Aerodynamic instability of tall structures with complex corner shapes

Thinzar Hnin

Abstract

In wind engineering for civil structures, many are treated as bluff bodies, with rectangular cylinders being a common cross-sectional shape. However, the rectangular cylinders could exhibit aerodynamic instabilities such as vortex-induced vibration (VIV) and galloping, depending on the side ratio (B/D) values. The reattachment of time-averaged flow influences the above-mentioned aerodynamic instabilities, and the interaction of VIV and galloping in rectangular cylinders is highlighted as a significant issue, requiring further research to address critical concerns. Hence, the current research investigates interactions between VIV and galloping instability by varying the Kármán-vortex shedding intensity through changes in the corner shape of the rectangular cylinder. In this research, the corners of the rectangular cylinder (B/D = 1.5) are modified into six different shapes, denoted as single recession (SR), double recession (DR), double recession II (DR II), double recession III (DR III), triple recession (TR) and chamfer (C). The effect of corner shape modification on the aerodynamic characteristics, the Kármán vortex shedding intensity, the Strouhal number, and the galloping onset of the rectangular and corner-cut cylinders are also discussed. This research covers both symmetric (zero angle of attack) and asymmetric (various angle of attack) bodies. Furthermore, the wind resistance and the flow field around an existing complex-shaped tall structure are also provided.

All studied corner-cut cylinders were found to reduce the aerodynamic force coefficients: longitudinal force coefficient (C_{Fx}), transverse force coefficient (C_{Fy}) and moment coefficient (C_M), of the original rectangular cylinder. The fluctuating transverse force coefficient which indicates the Kármán vortex shedding intensity (C'_{Fy}) of the original rectangular (R) section was also found to be reduced to approximately 63–90%. On the other hand, the Strouhal number (St) of all studied corner-cut cylinders was found to be larger than that of the original rectangular cylinder. A high value of the mass-damping parameter which is known as the Scruton number was required to completely decouple the Kármán vortex-induced vibration (KVIV) and galloping excitation range in the original rectangular cylinder. However, the corner-cut cylinders were found to require a comparatively smaller Scruton number than the original rectangular cylinder to decouple the KVIV and galloping. Moreover, all studied corner-cut cylinders were found to reduce the vibration response of the original rectangular cylinder. This can offer help in the optimization of the aerodynamic performance of structures.

In the sections with a strong Kármán vortex shedding intensity, it was found that the vibration of the model started around the onset reduced wind velocity of the Kármán vortex-induced vibration ($1/St$). On the other hand, the vibration of the model did not start at $1/St$ in the sections with a weak Kármán vortex shedding intensity. In both symmetric and asymmetric body conditions, it was found that Kármán vortices controlled the galloping instability when the Kármán vortex shedding intensity was strong. When the Kármán vortex shedding intensity was moderately strong, the Kármán and motion-induced vortices interacted with each other and controlled the galloping instability. When the Kármán vortex shedding intensity was weak, the motion-induced vortices mainly controlled the galloping instability. However, in the rectangular cylinder, the Kármán vortices dominate the galloping instability regardless of the Kármán vortex shedding intensity.

At the angle of attack just before the angle of attack where the reattachment occurs, the slope of the transverse force coefficient is considerably large and the Kármán vortex shedding is very weak. Moreover, the H_1^* obtained from the slope of the transverse force coefficient (the quasi-steady theory) was not asymptotic but rather parallel with the H_1^* obtained from the forced vibration tests even in the high reduced

wind velocity region. Therefore, the galloping instability might be difficult to describe by the quasi-steady theory at these angles of attack in both rectangular and corner-cut cylinders.

In this research, the flow field analysis of the existing complex-shaped tall structure was also carried out to study the effect of cross-sectional shape on the flow separation, flow reattachment and aerodynamic characteristics. The three-dimensional (3D) terrestrial laser scanning was performed to reproduce the 3D model of an existing Buddha statue. The time-averaged flow fields at different heights of the Buddha statue also showed that the size of the wake region was dependent not only on the width but also on the different corner shapes of the structure. It was also found that structure is likely to be affected by flow-induced vibrations when the angle of attack is increased to 90°. This lends a helping hand in the wind resistance evaluation of existing tall complex-shaped structures where wind tunnel testing and on-field measurement are infeasible.

Acknowledgements

Firstly, I would like to express my deepest gratitude to my supervisor, Prof. Tomomi Yagi, of the Bridge Engineering Laboratory, Department of Civil and Earth Resources Engineering, Graduate School of Engineering, Kyoto University, for his exceptional guidance, unwavering support, and scholarly insight throughout the entire journey of this Ph.D. thesis. This journey has not only been about academic growth but also personal development. Prof. Yagi has been more than a mentor; he has been a source of inspiration and encouragement. The constructive feedback, the countless discussions, and the patience displayed during challenging times have been invaluable. I am fortunate to have the privilege of working under the supervision of Prof. Yagi.

I extend my heartfelt thanks to Prof. Kunitomo Sugiura, of the Structures Management Engineering Laboratory, Department of Urban Management, Graduate School of Engineering, Kyoto University, for his insightful questions and comments. The unwavering commitment of Prof. Sugiura to the research has been a constant source of inspiration.

I express my gratitude to Prof. Yoshikazu Takahashi, of the Structural Dynamics Laboratory, Department of Civil and Earth Resources Engineering, Graduate School of Engineering, Kyoto University, for his insightful questions and comments. The mentorship of Prof. Takahashi has been a guiding light in this research.

I would like to express my gratitude to Assoc. Prof. Hisato Matsumiya, of the Bridge Engineering Laboratory, Department of Civil and Earth Resources Engineering, Graduate School of Engineering, Kyoto University, whose expertise has greatly enriched the depth and quality of this thesis. The collaborative and nurturing environment fostered under the guidance of Assoc. Prof. Matsumiya has allowed me to flourish as a researcher.

I also extend my sincere appreciation to Asst. Prof. Kyohei Noguchi, of the Bridge Engineering Laboratory, Department of Civil and Earth Resources Engineering, Graduate School of Engineering, Kyoto University, for his invaluable guidance, encouragement, and unwavering support throughout this academic journey.

Additionally, I wish to express my deepest gratitude to my late supervisor, Prof Hiromichi Shirato for patiently guiding me to the new research area in which I practically lacked experience, explaining topics carefully and thoroughly from the basics so that I could keep enthusiastic in the studies and giving critical attention to every progress of the studies.

A special note of thanks goes to Mrs. Tomoko Souda, a secretary of our laboratory and the unsung hero behind the scenes. Your efficiency, kindness, and dedication have made administrative processes smoother, allowing me to focus on my research.

I am also grateful to the members of our research group who have been instrumental in shaping the ideas and concepts presented in this thesis. Mr. Manoj Pradhan, Mr. Rintaro Kyotani, and Mr. Kaisei Shimobe, your collaboration has been intellectually stimulating, and I appreciate the camaraderie we have shared during the wind tunnel experiments.

I am thankful to my dearest friends in this lab, Ms. Yuxuan Yan and Ms. Minh Thu Dao, for their unwavering support, understanding, and countless moments of laughter have been a source of strength.

Getting to know both of you has been a constant reminder that the journey is just as important as the destination. I appreciate Mr. Hayata Omori, our fellow cat club member, for listening and laughing at all the crazy things that Dao-san and I shared. I also thank my lab mates and the former members of our laboratory, whose daily interactions have added both joy and depth to my research experience. Your insights, troubleshooting sessions, and shared victories have created a vibrant and collaborative atmosphere.

I would like to thank the Tokio Marine Kagami Memorial Foundation for providing the scholarship, which allowed me to pursue my studies without worries.

Last but certainly not least, my deepest gratitude goes to my parents, Mr. San Lin and Mrs. Hnin Kyi. Your unwavering belief in my abilities, sacrifices, and unconditional love have been the pillars of my success. This thesis is as much yours as it is mine.

To everyone who has played a role, big or small, in this academic endeavour, I offer my heartfelt thanks. Your contributions have made this journey memorable, and I am truly grateful for your presence in my life.

Table of Contents

List of Figures

Page

Chapter 1

Chapter 2

Chapter 3

Chapter 4

Chapter 5

Chapter 6

List of Tables

Page

Chapter 2

Chapter 4

Chapter 5

List of Symbols

B: width of the model

D: depth of the model

a: corner-cut length

l: span length of the model

α: the angle of attack

α_0: relative angle of attack

U: wind velocity

$\dot{\eta}$: body motion velocity

U_{rel}: relative wind velocity

F_y: transverse force

ρ: air density

L_{qs}: linear quasi-steady transverse force

m: mass per meter

c: structural damping coefficient

k_0: structural stiffness

St: Strouhal number

f_{st}: Kármán vortex shedding frequency

U_{cmv}: onset reduced wind velocity of the motion-induced vortices for the vertical motion

U_g: critical wind velocity calculated with quasi-steady theory

U_r: onset of Kármán vortex-induced vibration

C_L: lift force coefficient

C'_L: fluctuating lift force coefficient which indicates Kármán vortex shedding intensity

C_D: drag force coefficient

Re: Reynolds number

ν: kinematic viscosity of air

F_x: longitudinal force

F_y: transverse force

F_M: the pitching moment

C_{Fx}: longitudinal force coefficient or along-wind force coefficient

C_{Fy}: transverse force coefficient or across-wind force coefficient

C_M: moment coefficient

C'_{Fy}: fluctuating transverse force coefficient which corresponds to the Kármán vortex shedding intensity

H: Den Hartog criteria

U_{cr_quasi}: critical reduced wind velocity of galloping based on the quasi-steady theory

$S_{c\eta}$: Scruton number

m: equivalent mass per unit length

δ_η: structural damping in terms of the logarithmic decrement

f_n: heaving natural frequency obtained under no wind condition

L_{se}: self-excited transverse force per unit span

b: half of the model width

k: reduced frequency
ω: angular frequency
η: vertical displacement
$\dot{\eta}$: time differentiation of η
φ: torsional displacement
$\dot{\varphi}$: time differentiation of φ
H_i^* (i = 1~4): aerodynamic derivatives
F: inertial force acting on the vibrating model
F_0: amplitude of inertial force
Δ: digital phase lag between the displacement and the system
F_t: amplitude of the measured force (combination of the inertial and aerodynamic forces) in the windy condition
ψ_t: phase lag between the measured force F and displacement
F_a: amplitude of the aerodynamic force acting on the vibrating model in the windy condition
ψ_a: phase lag between the aerodynamic force and displacement
η_0: displacement amplitude
$L_{\eta 0}$: amplitude of the transverse force per unit length in vertical 1DOF direction
$\psi_{L\eta}$: phase lag between unsteady transverse force and the displacement
H_1^*: dimensionless aerodynamic damping
H_4^*: dimensionless aerodynamic stiffness
f: forced vibrating frequency
u_i: velocity
p: pressure
$\bar{u}_i$: filtered velocity
$\bar{p}$: filtered pressure
v_{SGS}: subgrid-scale eddy viscosity coefficient
f_s: van Driest damping function
k_{SGS}: sub-grid scale kinetic energy
$dC_{Fy}/d\alpha$: slope of the transverse force coefficient
f_{kv}: Kármán vortex shedding frequency
f_{vib}: vibration frequency
B_{avg}: average width of the Buddha statue
H: height of the Buddha statue
U^*: friction velocity
κ: von Karman's constant
z: vertical coordinate
z_0: surface roughness height
z_g: minimum z-coordinate
U_{ref}: reference wind velocity at z_{ref}
z_{ref}: reference height of 10 m
ν_T: turbulence kinematic viscosity
t: simulation time
L_r: recirculation region length
d': wake region width

d_{pair}: distance between the centres of the vortices

C_{Fi}: mean aerodynamic force coefficients

F_{ij} ($i = x, y$): mean aerodynamic forces acting on the cross-section j along x and y directions

A_j: frontal surface area of the cross-section j

U_{Hj}: mean wind velocity at the mid-height of the cross-section j

U_H: wind velocity at the height of the Buddha statue

f_v: vortex shedding frequency

Chapter 1

Introduction

1.1 General background

The towers of cable-stayed bridges and skyscrapers usually experience wind-induced vibrations during both in development and completion stages. In addition, the structural damping can be low and stiffness can be higher than expected in the early life of a tall concrete structure (Larose et al., 1998). However, even properly designed structures can be collapsed due to unforeseen/unknown reasons. After the collapse of the Tacoma Narrow Bridge in 1942, significant improvements have been made to the wind resistance design of infrastructures. However, there remain many issues to be addressed and some of the topics are still under discussion in many research fields.

In the field of wind engineering for civil engineering structures, most of the structures can be simplified as bluff bodies. Basic structural components such as beams and columns utilised rectangular cylinders as a common cross-sectional shape in the construction of most civil infrastructures. Furthermore, the cross-sectional shape of some of the tall infrastructures such as the bridge towers and high-rise buildings were also rectangular. However, this rectangular cross-sectional shape is known to exhibit the instabilities known as, vortex-induced vibration (VIV) and galloping instability (Mannini et al., 2016). The occurrence of the aforementioned instabilities is highly related to the side ratio (B/D, where B is the width and D is the depth) of the model (Nakaguchi et al., 1968; Bearman and Trueman, 1972; Mizota and Okajima, 1981; Igarashi, 1985; Parkinson, 1989; Matsumoto et al., 2006; Yagi et al., 2013).

Matsumoto et al. (1988, 2010) also mentioned that the reattachment of the time-averaged flow occurs when the side ratio is larger than 2.8 and the galloping does not appear. Hence, the separation and reattachment of flow around the rectangular cylinder highly influenced its aerodynamic instabilities. In addition, Mannini et al. (2014) reported that large amplitude vibrations were observed even at high mass-damping parameters in the rectangular cylinder with a B/D of 1.5. They also mentioned that the interaction of VIV and galloping in rectangular cylinders is a major issue in the field of flow-induced vibration and a lot of work is needed to shed some light on several critical issues. In the current study, the interactions between VIV and galloping instability are investigated by varying the Kármán-vortex shedding intensity of the rectangular cylinder by changing its corner shape. Flow field analysis of an existing tall structure is also discussed.

In the following sections, a brief overview of the VIV and galloping instability of the rectangular cylinders were described. In addition, literature reviews regarding the interaction between Kármán vortex-induced vibration (KVIV) and galloping, the Kármán vortex shedding suppression methods, the effect of corner modifications on the aerodynamic response of the rectangular cylinder and the effect of Reynolds number on the aerodynamic characteristics of the structures were also mentioned.

1.1.1 Galloping

In the high-wind-velocity region, a self-excited divergent oscillation known as galloping is observed in the transverse direction of the wind flow. Galloping has the potential to cause catastrophic structural failures as it represents a divergent form of vibration. Bearman and Trueman (1972) reported that the galloping instability is caused by the fluid interaction between the separated flow from the leading edge of the body and the tailing edge and sequential formation of the inner circulatory flow on a side surface of the body.

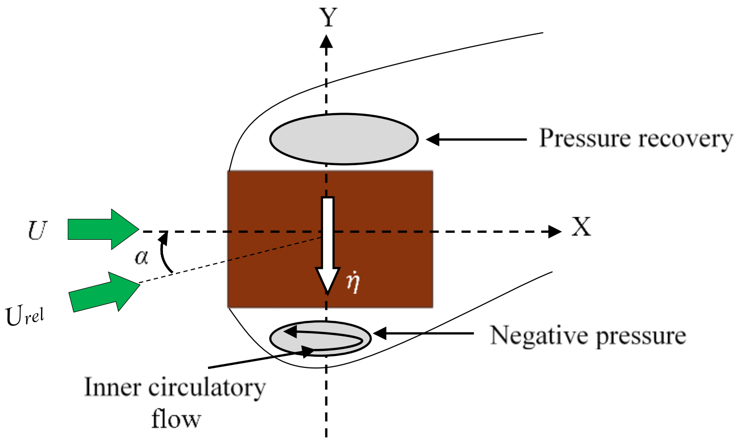

Fig. 1.1 Mechanism of galloping in the rectangular cylinder.

Fig. 1.1. shows the time-averaged flow field around a rectangular cylinder. At relatively high wind velocity, the downward motion causes the lower shear layer to move closer to the trailing edge while the upper shear layer moves away from the trailing edge. This makes the lower shear layer become more curved and the upper shear layer less curved. Subsequently, pressure recovery is observed at the upper surface and/or reduction in negative pressure is observed in the lower surface. The pressure difference on the upper and lower sides of the rectangular cylinder produces a downward force acting on it. Hence, the non-reattachment in the time-averaged flow field produces alternating motion-induced forces. These forces give rise to the galloping instability. Thus, the galloping instability of a rectangular cylinder is influenced by the side ratio and curvature of the separated shear layer (Bearman and Trueman, 1971; Igarashi, 1985; Matsumoto et al., 2006; Nakaguchi et al., 1968; Parkinson, 1989; Yagi et al., 2013).

Rectangular cylinders with a side ratio of less than 0.8 exhibit completely detached shear layers. This type of cross-section exhibits hard galloping, which requires a large initial amplitude to initiate the galloping instability (Nakamura and Tomonari, 1977; Parkinson, 1989). This hard galloping is also referred to as low-speed galloping since the vibrations start at wind velocity lower than the Kármán vortex resonance wind velocity (1/*St*), which will be described in the later sections.

When the side ratio of the rectangular cylinder is approximately between 0.8 and 2.8, the shear layers do not reattach in a time-averaged flow field (Matsumoto et al., 1988, 2010). This type of cross-section exhibits soft galloping, which does not require an initial amplitude to initiate the galloping instability (Nakamura and Tomonari, 1977; Parkinson, 1989). This soft galloping is also referred to as high-speed galloping.

In the rectangular cylinder with a side ratio greater than 2.8, the shear layers reattach in a time-averaged flow field and the galloping is stabilized.

Therefore, the curvature of the shear layers considerably affects the galloping instability of the rectangular cylinders.

In the high-wind-velocity region, the vortex shedding frequency is higher than the natural frequency of the vibrating system. Therefore, the interaction of the vortex shedding is absent and the transverse force acting on the cylinder can be calculated from the pressure distribution on the side surfaces of the cylinder. Den Hartog (1956, 1985) assumed that the instantaneous transverse force acting on the vibrating body can be considered the same as the transverse force acting on the stationary model under the relative angle of attack (α_0). The relative angle of attack and the relative wind velocity are expressed as follows:

$$\alpha_0 = \tan^{-1}\frac{\dot{\eta}}{U} \qquad \text{Eq. 1.1}$$

$$U_{rel} = \frac{U}{\cos\alpha_0} \qquad \text{Eq. 1.2}$$

where U is the wind velocity, $\dot{\eta}$ is the body motion velocity (positive in the downward direction), α_0 is the relative angle of attack (positive in the nose-up direction), and U_{rel} is the relative wind velocity.

The transverse force (F_y) for a stationary body and an oscillating body are written as follows:

$$F_y = \frac{1}{2}\rho U^2 Bl C_{F_y}(\alpha) \qquad \text{Eq. 1.3}$$

$$F_y = \frac{1}{2}\rho {U_{rel}}^2 Bl C_{F_y}(\alpha_0) = \frac{1}{2}\rho U^2 Bl C_{F_y}(\alpha_0)\sec^2(\alpha_0) \qquad \text{Eq. 1.4}$$

where F_y is the transverse force (positive in the upward direction), C_{F_y} is the transverse force coefficient, ρ is the air density, and B and l are the width and span length of the model.

When α_0 is small, the C_{F_y} and U_{rel} can be expressed as:

$$C_{F_y}(\alpha_0) = C_{F_y}\Big|_{\alpha=0^\circ} + \frac{dC_{F_y}}{d\alpha}\bigg|_{\alpha=0^\circ}\cdot\frac{\alpha_0}{1!} + \frac{d^2C_{F_y}}{d\alpha^2}\bigg|_{\alpha=0^\circ}\cdot\frac{\alpha_0}{2!} + \cdots \qquad \text{Eq. 1.5}$$

$$U_{rel}(\alpha_0) = U + \frac{d}{d\alpha}\left(\frac{U}{\cos\alpha_0}\right)\cdot\frac{\alpha_0}{1!} + \cdots \qquad \text{Eq. 1.6}$$

$$C_{F_y}(\alpha_0) \approx \alpha_0\frac{dC_{F_y}}{d\alpha}\bigg|_{\alpha=0^\circ} \qquad \text{Eq. 1.7}$$

$$U_{rel}(\alpha_0) \approx U \qquad \text{Eq. 1.8}$$

According to the small angle approximation:

$$\tan\alpha_0 \approx \alpha_0 \approx \frac{\dot{\eta}}{U} \qquad \text{Eq. 1.9}$$

By substituting Eq. 1.9 into Eq. 1.7,

$$C_{F_y}(\alpha_0) = \left.\frac{dC_{F_y}}{d\alpha}\right|_{\alpha=0^\circ} \cdot \frac{\dot{\eta}}{U} \qquad \text{Eq. 1.10}$$

The aerodynamic transverse force acting on the oscillating body is defined as positive in the downward direction. The linear quasi-steady transverse force acting on the oscillating body is expressed as:

$$L_{qs} = -\frac{1}{2}\rho {U_{rel}}^2 BlC_{F_y}(\alpha_0) = -\frac{1}{2}\rho UBl \left.\frac{dC_{F_y}}{d\alpha}\right|_{\alpha=0^\circ} \cdot \dot{\eta} \qquad \text{Eq. 1.11}$$

where L_{qs} is the linear quasi-steady transverse force, ρ is the air density, U_{rel} is the relative wind velocity, B and l are the width and span length of the model, C_{F_y} is the transverse force coefficient, and α_0 is the relative angle of attack.

The equation of motion for the system subjected to linear quasi-steady force is expressed as:

$$m\ddot{\eta} + c\dot{\eta} + k_0\eta = -\frac{1}{2}\rho UBl \left.\frac{dC_{F_y}}{d\alpha}\right|_{\alpha=0^\circ} \cdot \dot{\eta} \qquad \text{Eq. 1.12}$$

Eq. 1.12 can be rearranged as follows:

$$m\ddot{\eta} + \left(c + \frac{1}{2}\rho UBl \left.\frac{dC_{F_y}}{d\alpha}\right|_{\alpha=0^\circ}\right)\dot{\eta} + k_0\eta = 0 \qquad \text{Eq. 1.13}$$

where m is the mass per meter; c is the structural damping coefficient, and k_0 is the structural stiffness.

Hence, the body is unstable in conditions that;

$$\left.\frac{dC_{F_y}}{d\alpha}\right|_{\alpha=0^\circ} < 0 \qquad \text{Eq. 1.14}$$

Eq. 1.14 is known as the Den Hartog criterion, and its negative value indicates the presence of galloping instability in the model.

1.1.2 Vortex-induced vibration

Vortex-induced vibration (VIV) is an instability-induced excitation caused by the vortex shedding. VIV can be divided into two types known as Kármán vortex-induced vibrations (KVIV) and motion-induced vortex vibrations (MIV) (Komatsu and Kobayashi (1980), Shiraishi and Matsumoto (1983), Nakamura and Nakashima, (1986)). MIV is also known as impinging leading-edge vortices (Naudascher and Rockwell, 1994).

KVIV has the potential to induce fatigue damage in structures as it generates self-limiting vibrations that may surpass acceptable serviceability standards. In addition, unlike galloping instability, which occurs at higher wind velocities, KVIV appears in a lower wind velocity region. KVIV is also known as the two-shear layer instability since it is caused by the interference between the two separated shear layers from the leading edges (Fig 1.2). The time-dependent periodic vortices shed in the wake result in the formation of a vortex street aptly named after Theodore Von Kármán in 1911. This Kármán vortex shedding subsequently subjects fluctuating forces to the side surfaces of the cylinder, thereby exciting the cylinder into vibration. The shedding frequency of these vortices is inherently tied to the geometry of the cylinder and is directly proportional to the Strouhal number (*St*), a non-dimensional parameter which is defined as follows:

$$St = \frac{f_{st}D}{U} \qquad \text{Eq. 1.15}$$

where f_{st} is the Kármán vortex shedding frequency, D is the depth of the cylinder, U is the approaching wind velocity. Kármán vortex vibrations become obvious when the Kármán vortex shedding frequency coincides with the natural frequency of the cylinder or the vibration system. This is also known as the lock-in phenomenon. Hence, the onset of KVIV is known to occur at the reduced wind velocity of 1/*St*. However, the Kármán vortex shedding is subject to change depending on the flow regime encountered by the cylinder, which also depends on the Reynolds number (*Re*).

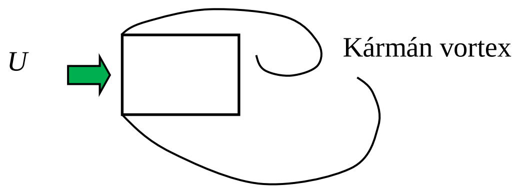

Fig. 1.2 Two-shear layer instability.

The second category of vortex-induced instability pertains to motion-induced vortex vibrations (MIV). As the term implies, motion-induced vortices arise when the movement of the cylinder interacts with the shear layers separating on its upper and lower sides. This is also known as the one-shear layer instability (Fig. 1.3). A study by Shiraishi and Matsumoto (1983) demonstrated that motion-induced vortices travel at a velocity equivalent to 60% of the approaching wind velocity along the side surfaces of the cylinder. These vortices subsequently merge with vortices originating from the trailing edge. These motion-induced vortices produce pressure fluctuations on the side surfaces of the cylinder. With increasing wind velocity, the motion-induced vortices travel at a frequency equal to 1/*N* times the natural frequency of the cylinder, thereby raising resonance vibrations in the heaving direction. Thus, the onset reduced wind velocity of the motion-induced vortices for the vertical motion can be written as follows;

$$U_{cmv} = \frac{1}{N}\frac{1}{0.6}\frac{B}{D} = \frac{1}{N}1.67\frac{B}{D} \qquad \text{Eq. 1.16}$$

where, *N* = 1, 2, 3, …, *B* and *D* are the width and depth of the cylinder.

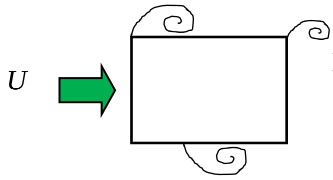

Fig. 1.3 One-shear layer instability.

1.1.3 KVIV-Galloping interaction

The initial documentation of Kármán vortex-induced vibration (KVIV) and its interaction with galloping can be traced back to 1964. Parkinson and Smith (1964) discovered that under conditions of low mass-damping, the square cylinder exhibited significant amplitude oscillations at a low reduced wind velocity region, which was significantly different from what was observed at higher mass-damping values. Shortly thereafter, in 1965, Scruton demonstrated that galloping oscillations commence at lower mass-damping values, specifically occurring at the inverse of the Strouhal number for the section (1/*St*), which is the onset wind velocity of the Kármán vortex-induced vibration (KVIV). Therefore, the onset of KVIV and the onset of galloping are associated with each other.

Furthermore, when the galloping onset predicted by the quasi-steady theory is lower than the onset of KVIV (1/*St*), especially when the mass-damping parameter (Scruton number, $S_{c\eta}$: which will be explained in Section 2.3.2) is low, the galloping instability does not initiate from the critical wind velocity predicted by the quasi-steady theory because of the Kármán vortices. In this case, the Kármán vortex shedding stabilizes the galloping until the KVIV onset wind velocity. On the other hand, the vibration increases unrestrictedly with the increasing wind velocity in the high-wind-velocity region. Corless and Parkinson (1988) referred to this phenomenon as the quenching effect, which results from the VIV and galloping interaction. Nakamura et al. (1991) also reported that the low-speed gallopingwas observed in a rectangular cylinder with a low side ratio. Thus, previous studies have indicated that the Kármán vortex shedding and galloping instability are closely associated.

In addition, previous studies primarily focused on VIV and galloping instability, offering significant insights as described in the following paragraphs.

Corless and Parkinson (1988) concentrated on the mathematical modelling of a square cross-section cylinder in crossflow. They combined the Hartlen-Currie model for VIV and the quasi-steady model of Parkinson and Smith for galloping, exploring the interaction between the two phenomena. Their mathematical model closely approximated the combined effects of VIV and galloping, although it had a slight over-prediction near resonance. This success suggested that the vortex street effects could be added to time-averaged shear layers to predict cylinder forces effectively.

In the rectangular cylinders with side ratios ranging from about 0.75 to 3, a high value of the mass-damping parameter was found to be necessary to fully decouple the ranges of excitation for VIV and galloping (Mannini et al. 2017). Hence, the mass-damping parameter played a critical role in ensuring that the quasi-steady theory accurately predicted the critical wind velocity for galloping. The spring-supported wind tunnel test results of rectangular cylinder (B/D = 1.5, short side perpendicular to the flow) for a wide range of mass-damping parameters ($S_{c\eta}$) indicated that the phenomenon of interference between KVIV and galloping was observed in the transverse degree of freedom (Mannini et al., 2016). The study yielded insights into the dynamics of the interaction between these two excitation mechanisms and revealed the presence of four distinct regimes of VIV-galloping interference. Hence, four different levels of interference between the mechanisms of VIV and galloping excitation as shown in Fig 1.4 were present in the rectangular cylinder (B/D = 1.5) depending on the values of the mass-damping parameters.

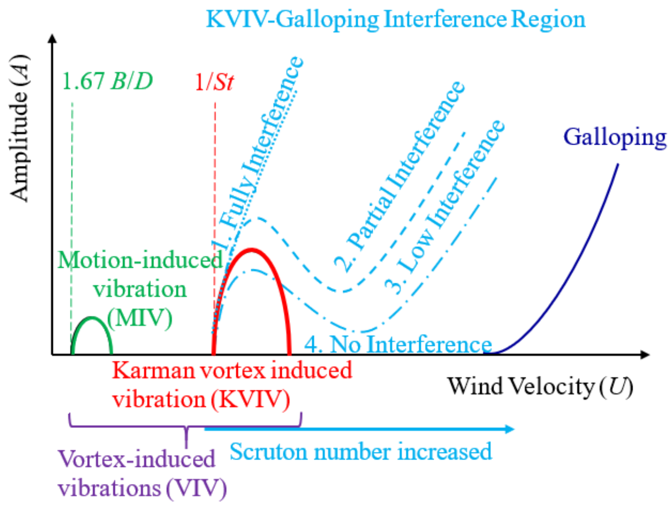

Fig. 1.4 Four distinct regimes of VIV-galloping interference (B/D = 1.5).

Mannini et al. (2014, 2015) explored side ratios in the range of 1-2 through an extensive literature review on rectangular cylinders. They particularly investigated the aerodynamic response of a 3:2 rectangular cylinder (B/D=1.5, short side perpendicular to the flow), focusing on the KVIV and galloping interference in both smooth and turbulent conditions. The study aimed to clarify the conditions under which velocity-unrestricted galloping-type vibrations could occur. In smooth flow conditions, a strong inclination towards a combined KVIV-galloping instability was observed. The vibrations are initiated at the onset of KVIV ($1/St$). Large-amplitude vibrations were also observed even at high mass-damping parameters. To prevent such galloping instability and its interaction with KVIV, a critical velocity ratio (U_g/U_r, where U_g is critical wind velocity calculated with quasi-steady theory and U_r is the onset of KVIV) between the two phenomena was found to be important. To prevent the interaction between KVIV and galloping, this ratio (U_g/U_r) was required to be within the range of 4.5-8.5. The authors mentioned that was significantly higher than the value of 1.5 suggested by Eurocode 1.

In the turbulent flow, from a quasi-steady perspective, static wind tunnel test results revealed the susceptibility to galloping instability even in highly turbulent flows (Mannini et al., 2018). They also indicated a reduction in the strength of vortex shedding while an increase in the tendency of VIV and galloping interaction when compared to smooth flow conditions. Spring-supported wind tunnel test results further confirmed this and highlighted the complex behaviour of the model in turbulent flows. Notably, it was observed that even higher values of the mass-damping parameter than the smooth flow condition were required for the quasi-steady theory to accurately predict the onset of galloping instability. The interference between vortex-induced vibration and galloping was also observed in turbulent flows, typically at higher wind velocity regions compared to cases with smooth flows. Hence, turbulence was also found to increase the onset of galloping instability, whether it interacted with vortex shedding or not. This unsteady galloping instability, rather than the classical quasi-steady galloping, is expected to pose a potential concern for large, slender, and lightweight civil engineering structures such as bridge pylons. Such a phenomenon must be appropriately considered in engineering codes and standards. Furthermore, the integral scale of turbulence was identified as a critical factor influencing the unsteady galloping behaviour of the examined rectangular cylinder. The model achieved stability within the observable wind velocity range when subjected to high turbulence intensity and a large integral length scale. The specific mechanism by which turbulence contributed to stabilization remained a topic of ongoing investigation.

Mannini et al. (2018) denoted the phenomenon of interference between VIV and galloping, which can occur in certain conditions involving bluff bodies in an airflow, especially rectangular cylinders with moderate side ratios, as “the unsteady galloping”. The term “unsteady galloping” was characterized by potentially significant vibration amplitudes in the wind velocity regions which were not predicted by classical theories. To predict the dynamic response of such rectangular cylinders effectively, a mathematical model was developed. This mathematical model provided a satisfactory qualitative estimate of structural vibration, and its parameter settings only required static tests and dynamic response data in the VIV range for a single value of the Scruton number. This approach simplifies the process compared to the extensive experimental campaigns typically needed to characterize this phenomenon. The researchers suggested that this modelling approach could prove valuable in the pre-design stage of wind-sensitive civil engineering structures or industrial applications in airflow. While they mentioned the potential extension of this approach to water flow systems, they noted that further investigation would be necessary in that context.

In their 2020 publication, Mannini et al. introduced a mathematical model that focused on a rectangular cylinder with a side ratio of 1.5, intending to investigate the interference between vortex-induced vibration and transverse galloping in turbulent flows. This research utilized a nonlinear wake-oscillator model and artificial random wind fields to advance the simulation of self-excited behaviour in such bodies, which had previously shown promising results in smooth flow conditions. The proposed model was designed to estimate the unsteady galloping behaviour of slender structures immersed in realistic large-scale turbulent flows, a scenario that is challenging to accurately replicate in wind tunnel experiments. However, the model could not account for the Scruton number-dependent increase in the onset of the instability beyond the onset of KVIV. This observation, which had also been noted for another cross-sectional geometry in smooth flow conditions (Chen et al., 2020), appeared to be unrelated to the fluctuating random wind field but rather attributed to the turbulence-induced modifications in the aerodynamics of the cylinder.

Marra et al. (2015) conducted experiments on a rectangular 4:1 cylinder in smooth flow conditions, covering various Scruton number values, to provide experimental results serving as a benchmark to validate the predictions of mathematical models and Computational Fluid Dynamics (CFD) simulations. The research sought to enhance the current methodology for assessing VIV in bridge decks. The extensive wind tunnel campaign significantly expanded the available dataset and served as a reference point for evaluating VIV predictions generated by different models and CFD techniques. In their study, for the lowest mass-damping parameter value, measurements were taken within and outside the lock-in range using a hot-wire anemometer inside and outside an elastically suspended sectional model. This allowed for the determination of the dominant frequency of flow velocity fluctuations. The research also found that the single-degree-of-freedom model developed by Scanlan in the 1980s was inadequate for predicting the VIV response of bridge decks when Scruton numbers deviated from those at which the model parameters were originally identified. As a result, an improved version of the model was proposed to address these discrepancies.

Therefore, many studies focused on KVIV and galloping instability to investigate the two phenomena and describe the interaction between them. However, the interaction between Kármán-vortex shedding and galloping for rectangular cylinders remained a major concern in flow-induced vibration research, necessitating further investigation to fully comprehend the physical causes of this phenomenon.

1.1.4 Suppression of Kármán vortex shedding

The curvature of the separated shear layer can significantly affect not only the galloping instability as mentioned in Section 1.1.1 but also the vortex shedding of a rectangular cylinder. Matsumoto et al. (2006) reported that the curvature of the separated shear layer is steep when the Kármán vortex shedding is strong. When the Kármán vortex shedding is suppressed, the curvature of the separated shear layer is mild.

Hence, the interaction between Kármán vortex shedding and galloping instability could be examined by mitigating the Kármán vortex shedding. Kármán vortex shedding of the rectangular cylinder can be suppressed by installing a splitter plate in the downstream direction (Yagi et al. 2013). On the other hand, the relative position of the splitter plate to the rectangular cylinder changed during the vibrations (Matsumoto et al. 2006). This raised concerns about whether installing a splitter plate and investigating the interference is suitable or not. Thus, alternative approaches to studying this interference are needed instead of relying solely on splitter plates.

Shiraishi et al. (1988) conducted wind tunnel tests on rectangular cylinders with various corner ratios (a/D, where a is the corner-cut length, and D is the model depth). It was found that modifying the shape of the corners in a rectangular cylinder by cutting them can effectively improve its aerodynamic behaviour by controlling the separated shear layers. Almost no KVIV was observed in the response of the corner-cut cylinder. Consequently, reducing the corner ratio also leads to lowering the aerodynamic force coefficients and increasing the onset reduced wind velocity of galloping. Thus, this corner-cutting method can be used as a means to suppress Kármán vortex shedding (Komatsu and Kobayashi, 1980). Therefore, cutting the corner of a rectangular cylinder might help in studying the interaction between vortices and galloping instability.

However, the influence of corner-cutting on the flow separation, reattachment and Kármán vortices has not been sufficiently investigated. Stabilizing the vibrations of the corner-cut cylinders for more than the zero angle of attack is still a work in progress so far. There are many unexplained parts which require further investigation.

1.1.5 Corner modification in rectangular cylinder

Corner-cutting is widely known as efficient in stabilizing aerodynamic instabilities. There has been considerable research on the corner modification of a rectangular cylinder as a means of minor aerodynamic modifications. This section describes literature reviews on the corner modification of rectangular cylinders. Most previous research has been conducted to identify an optimal corner-cut size, efficient corner-cut shape and so on. Furthermore, corner shapes such as recession corners, chamfer corners and rounded corners were commonly used in these studies (Fig. 1.5).

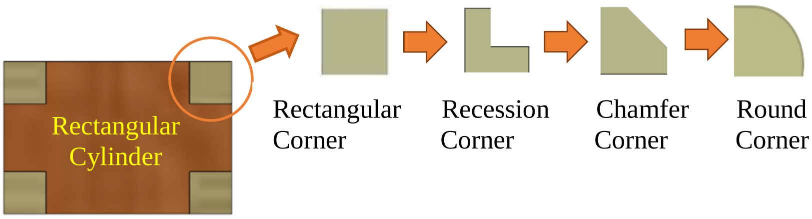

Fig. 1.5 Corner modifications in the rectangular cylinder.

Recession corner

The static wind tunnel test results showed that the C_L (lift force coefficient) value was considerably reduced and the C_D (drag force coefficient) value was only half that of the original rectangular cylinder when the corners were cut into a square shape, also known as a single recession (Shiraishi et al.,1988). The reduction in the drag coefficient of the rectangular cylinder suggests that the corner-cutting approach can be deemed effective for suppressing Kármán vortices (Komatsu and Kobayashi, 1980). The effectiveness of different corner-cut sizes in mitigating galloping was assessed by investigating the impact of corner-cut size on the vibrational response of the Higashi-Kobe bridge tower (Shiraiashi et al., 1988). The corner-cut sizes of $2/18D$ and $3/18D$, with D representing the characteristic depth of the section, were found to be the most effective in increasing the galloping onset reduced wind velocity into higher wind velocity region. This was believed to be due to the reattachment of the separated shear layer to the side surface near the trailing edge. Hence, cutting the corners of the rectangular section, controlled the circumferentially separated flow patterns, reduced the aerodynamic force coefficients and increased the galloping onset reduced wind velocity of the original rectangular section. However, increasing the corner ratio could induce instability at lower wind velocity regions.

When the VIV and galloping of the square (B/D = 1.0) and rectangular (B/D = 1.5) cylinders were investigated for a wide range of corner-cut sizes for recession, chamfer and rounder corners, it was found that aeroelastic instability of galloping combined with VIV was observed when the structural damping was low (Kawai, 1998). In the square cylinder, a small corner size effectively reduced vibration amplitude. On the other hand, a large corner size promoted instability at low wind velocity to reduce the onset wind velocity of the galloping when the structural damping was very small. The most effective corner modification type which can reduce the wind-induced vibrations of the square cylinder was the rounded corner type. In the case of rectangular cylinders, the galloping occurred at low wind velocity, but corner modifications stabilized the galloping and VIV at high wind velocity.

Small corner cuts and recessions were effective in enhancing aerodynamic damping and preventing instability, while larger cuts and recessions promoted instability. These modifications primarily affected instability at low wind velocity by impeding vortex shedding. Notably, motion-induced vortex vibration (MIV) was observed in the rectangular cylinder (B/D = 2) and remained relatively unaffected by corner modifications (Kawai, 1998). However, this might depend on the side ratio of the rectangular cylinder and the structural damping.

The effect of different blockage ratios at various angles of attack (α) for the square cylinder with a single recession corner type (single recession section) was studied by Choi and Kwon (1998). Regardless of the blockage ratio, the onset reduced velocity for galloping was the same for the rectangular cylinders with and without the single recession corner at $\alpha = 0^\circ \sim 10^\circ$. When the size of the corner was changed from 0.04D to 0.20D, an increase in steps of 0.02D, sections with corner-cut generally exhibited improved behaviour concerning the galloping phenomenon compared to the original section. However, the corner-cut method did not prevent VIV from occurring. For α values in the range of $0^\circ \sim 10^\circ$, increasing the corner-cut improved galloping stability, with the optimal size being 0.06D at $\alpha = 0^\circ$. However, the single recession corner shape had little impact on the VIV of the square cylinder at $\alpha > 15^\circ$ (Choi and Kwon, 1998).

For rectangular cylinders with B/D ratios of 1.5, and 2.0, various corner-cut sizes were considered to study the effect of the corner-cut size on the aerodynamics instability. For B/D = 1.0, the corner-cut size uniformly ranged from 0.00D to 0.20D, incremented by 0.02D. For B/D = 1.5 and 2.0, corner-cuts of 0.00D, 0.08D, 0.11D, 0.14D, 0.17D, and 0.20D were examined. The research found that as the attack angle (α) increased, the optimal size of the corner-cut also had to increase gradually. If a model with the optimal corner-cut size for $\alpha = 0^\circ$ was subjected to larger attack angles, significant separation occurred at the leading edge of the corner-cut, with no reattachment at the subsequent edge. Therefore, the optimal corner-cut size needed to be larger than that for $\alpha = 0^\circ$ to facilitate reattachment of the separated flow at the leading edge. Although it was challenging to pinpoint a single corner-cut size as the best for aerodynamic performance across all attack angles, corner-cutting remains an effective method for enhancing the aerodynamic behaviour of rectangular cylinders. The optimum corner-cut size of a single recession-type corner for aerodynamic stability varied with different α values, where the corner-cut size increased gradually as α increased (Choi and Kwon, 2000).

The basic principle of the single recession shape corner-cut effect is the minimization of separation width as the separation starts from the first edge of the corner-cut and reattaches to the second edge generated by the corner-cut, thus resulting in the decrease of vortex shedding interval behind the cylinder. Therefore, if a certain corner-cut size is effective in minimizing the separation width, the Strouhal number will become larger (Choi and Kwon, 2001).

Strouhal number (St) of the cylinders with various sizes of single recession shape corner-cut has a fluctuating trend as the angle of attack (α) changes (Choi and Kwon, 2003). In all studied corner-cut sizes, as the α of each corner-cut size increases above 15°, the St decreases gradually. In addition, three distinct characteristics of St variation can be identified, which are noted as Region I (St increases as α increases from 0° to 15°), Region II (St decreases as α increases from 15° to 30°), and Region III

(St relatively uniform in the range of α from 30˚ to 45˚). These trends are more noticeable in cylinders with larger corner-cut sizes. Whether a certain corner-cut size is more effective in reducing the wind-induced vibration than those of other corner-cut sizes can also be identified by larger St values. Furthermore, when only VIV is occurred, this type of corner-cut is effective in Region II and less effective in Region III (Choi and Kwon, 2003).

Chamfered and corner recession-type corner-cut are effective in significantly reducing both along-wind and cross-wind responses compared to the basic cylinder (Amin, J. A., et al., 2010). Moreover, modification of windward corners is very effective in reducing the drag and fluctuating lift. This is achieved by changing the characteristics of the separated shear layers to promote their reattachment and narrow the width of a wake. Hence, these types of corner modifications are effective in suppressing aeroelastic instability (Amin, J. A., et al., 2010).

Small corner-cut sizes of recession and round corner shapes at lower attack angles effectively stabilized instability by preventing the formation of strong vortices in the wake region and reducing the mean drag. However, as the corner recession size increased, this flow pattern significantly increased the lift force. At 15° for square cylinders with no recession, reattachment led to a large lift force due to differences in pressure difference on the top and bottom surfaces of the cylinder. This, in turn, resulted in reduced mean drag force. Similar flow pattern effects on a cross-shaped section and compared the recession size of the square cylinder to be similar to the thickness of the cross-type section. When the flow reattachment is near the corner, it leads to a significant reduction in drag and an increase in lift (Kawai and Fujinami, 2001).

Both single-recession and double-recession type corner-cuts led to a reduction in the coefficients of base moment and torque for the square cylinder (Zhang et al., 2012).

The wind tunnel experimental results of rectangular cylinders (B/D = 1.0, 1.5 and 2.0) with single recession-type corner-cut revealed distinct aerodynamic behaviour patterns for different attack angles, which can be categorized into three regions: the galloping dominant region (α = 0°~10°), the transient region (α = 15°, 20°), and the VIV dominant region (α = 25°~45°). The study findings indicate that corner cutting enhances aerodynamic stability, particularly in the galloping dominant region (α = 0°~10°). Certain corner-cut ratios effectively suppress galloping in this region. Moreover, an increase in B/D leads to a more pronounced effect of corner cutting on both galloping and VIV. The onset velocity of VIV is lower in cases with corner cuts than in the original section across the entire range of attack angles for both B/D=1.5 and 2.0. Additionally, corner cutting can help restrain torsional vibration (Choi and Kwon, 2000).

Chamfer corner

When the VIV and galloping of square and rectangular cylinders with chamfer type corner-cut were investigated, it was observed that VIV-Galloping instability occurred under conditions of low damping (0.03%) and low reduced wind velocity (Kawai, 1998). Smaller chamfer corners effectively reduced amplitudes at high reduced wind velocities, while larger chamfer corners led to galloping at low reduced wind velocities (Kawai, 1998).

Round corner

In the study focused on the round corner type corner-cut, where the corner radius (R) ranged from R/D = 0.0 (square) to 0.5 (circular) with increments of 0.1, the flow characteristics and vortex shedding were found to be significantly influenced by the corner radius (Mooneghi and Kargarmoakhar, 2016). In particular, a square cylinder exhibited the highest average drag value, while the opposite was observed in the case of a circular cylinder. Rounding the corner radius led to a reduction in aerodynamic forces (Mooneghi and Kargarmoakhar, 2016). In square and rectangular (B/D = 2.0) cylinders, increasing roundness improved stability, particularly at low reduced wind velocity, by mitigating vortex shedding, thereby reducing the occurrence of VIV and galloping (Kawai, 1998). In the study of the corner shape effect on galloping, which focused on square cylinders in the Reynolds number range of 1.7×10^4 to 2.3×10^5, it was observed that rounded corners led to a significant reduction in the onset velocity of galloping, primarily attributed to a decrease in the drag coefficient (Carassale and Marrè, 2013).

Kawai (1998) conducted experiments on square prisms with H/D = 10 and different B/D ratios of 1 and 2. Three types of corner modifications were examined: chamfer, single recession, and rounded corners. Among these, corner roundness was found to be the most effective in suppressing aeroelastic instability, with increased corner roundness leading to a reduction in wind-induced vibration amplitudes. Small corner cuts and recessions were effective in enhancing aerodynamic damping and preventing instability, while larger cuts and recessions promoted instability. These modifications primarily affected instability at low speeds by impeding vortex shedding. Notably, motion-induced vibration was observed for deep rectangular prisms and remained relatively unaffected by corner modifications.

To summarize, altering the corner shapes of a rectangular cylinder can contribute to the study of how Kármán vortices interfere with galloping instability.

1.1.6 Wind-induced vibrations in bridge tower

The vortex-induced vibration was serious during the development stage (Ogawa et al., 1990, Fujino, 2002). Higashi-Kobe Bridge is a cable-stayed bridge with a total length of 885 m and a tower height of 150 m. The B/D of the tower varied from 1.29 to 1.86, in accordance with height. During the under-construction condition, the tower of the Higashi-Kobe bridge was expected to have vibrations in the crosswind direction due to its low stiffness value (Ogawa et al., 1990). Shiraishi et al. (1988) proposed the single recession (SR) type corner with the corner ratio (a/D, where a is corner-cut length and D is model depth) of 2/18 and 3/18 as the optimum size for the Higashi-Kobe bridge tower (B/D ~1.5). Wind tunnel tests were carried out to investigate the effects of corner-cut on the aerodynamic stability of the free-standing tower (under construction) and the completed bridge tower (accomplished). In the completed bridge tower, vibrations occurred only in the along-wind direction (wind parallel to the bridge axis). Buffeting of the tower (random bending vibration) in the tower frame plane was observed in the grid turbulence and turbulent boundary layer. At the design wind velocity of 67 m/s, the maximum double-amplitude at the top of the tower was 0.3 m. When the corner-cuts were provided at the tower, no significant vibration occurred below the design wind velocity except buffeting in the higher wind velocity region (Ogawa et al., 1990). In the free-standing tower, the vibrations occurred both in the along-wind and across-wind directions (wind perpendicular to the bridge axis). In the along-wind direction, vortex-induced vibration occurred at 17-34 m/s, with a double-amplitude response higher than 2 m. When the corner-cuts were provided, only a small vortex-induced vibration occurred at 8 m/s, with a double-amplitude response smaller than 0.4 m. In the across-wind direction, the vortex-induced vibration of the 1st bending mode occurred at 10-14 m/s, 1st torsional mode at 14-21 m/s and 23-38 m/s, and 2nd bending model at 60-70 m/s. Hence, the application of corner cuts on the tower successfully/effectively stabilized the vibrations in the along-wind directions of both free-standing and completed bridge towers. However, the vibrations in the across-wind direction of the free-standing tower can only be reduced by installing the mechanical dampers. Takeuchi (1990) mentioned that the cruciform tandem column with a larger amount of corner-cut had better aerodynamic stability, especially at the angle of incidence between 40° and 50°. Hence, the cross-sectional shape of the tower plays an important role in the aerodynamic stability of the bridge tower. However, the discussion on the mass-damping parameter and the effect of wind direction are still insufficient and must be clarified.

In the case of the Akashi Kaikyo bridge, the vortex-induced vibration occurred at the top of the free-standing bridge tower (Kitagawa, 2004). The vibration continued to occur even in the completed bridge tower at a wind velocity below the design wind velocity of 66.7 m/s due to its low natural frequency. Improving the aerodynamic properties of the tower by cutting corners was also insufficient to suppress the vibration. Tuned mass dampers were installed to suppress the vibration of the first torsional mode (Kitagawa, 2004). Hence, whether the vortex-shedding can be suppressed or not depends not solely on the shape of the corners. Several other factors could be affecting the flow separation and reattachment, and this required further investigation.

Larose et al. (1995) mentioned that the three-dimensional (3D) aerodynamic behaviour of the bridge tower was dominated by the vortex-shedding excitation in the across-wind direction at the lower wind velocity region and in the torsional degree of freedom at higher wind velocity region. When the vortex-shedding was reduced by attaching the screens with 50% porosity to the round edges of the bridge tower, the stability of the bridge tower was confirmed for wind velocity larger than the design wind velocity of 60 m/s (Larose et al., 1995). Morgenthal and Yamasaki (2010) assessed the aerodynamic performance of the Stonecutters Bridge (Hong Kong) and Sutong Bridge (Suzhou) which were in typhoon-prone regions and strongly influenced by the wind effects during the free-standing conditions. The Stonecutters Bridge has a tapered and circular shape tower. The tapering of the tower reduced the vortex-shedding excitation by reducing the correlation of vortex-shedding throughout the tower height. In addition, the presence of construction equipment such as tower cranes and platforms also contributed to disturbing the vortex shedding. However, the numerical buffeting analyses of the partially erected tower of the Stonecutters Bridge showed that vibrations could occur due to galloping, vortex-shedding and internal resonance at a wide range of service wind speeds (Morgenthal and Yamasaki, 2010). Honda et al. (2012) described that the positions of the scaffolding and cranes for construction influenced the vortices and aerodynamic stability. During the erection, the bridge tower (tall steel pylon) required temporary mechanical control of wind-induced vibration for a short period rather than aerodynamic control (Fujino, 2002). The Forth suspension bridge used sliding-block-type dampers for the first time to control the vortex-induced vibration of its pylons during erection (Fujino, 2002). Although vortex-induced vibration of the tower may not create an instability problem, excessive vibration on the tower especially the steel one amid low damping may influence bridge service and eventually result in fatigue damage (Siringoringo et al., 2012). Hence, the aerodynamic behaviour of the bridge tower was dominated by vortex-shedding-induced oscillations and vortex-shedding should be suppressed with the available methods depending on the requirements.

The aerodynamic stability of the bridge towers could be improved by controlling their cross-sectional shapes throughout the height. However, a free-standing single-column bridge tower with various chamfered square cross sections showed the interactions between three-dimensional third-mode vortex-induced vibration and first-mode galloping (Ma et al., 2019). Independent of the structural damping ratio changes, divergent oscillation appeared at a nearly constant critical wind velocity that was approximately equal to the vortex resonance in the third mode of the structural vibration. In this case, considerable oscillations may be found within a wind-velocity range where their occurrence is not predicted by the existing classical models (Ma et al., 2019). Hence, the mechanism of VIV–galloping interaction is complex and further investigation is strongly required.

1.1.7 Wind-induced vibration in high-rise building

Various types of corner modifications were used in high-rise buildings to reduce wind-induced vibrations. Some of the minor aerodynamic modifications mostly used in the high-rise building included: attachments, chamfer corners, slotted corners, round corners and recession corners.

When single recession (SR) corners and openings were introduced to the square building, the across-wind coefficient became significantly smaller than that of the square model in the case of 0° to 22.5° (Miyashita et al., 1993). Amin and Ahuja (2010) mentioned that a single recession or chamfer or slots must be applied to about 10% of the building width to be useful. Single recession corners were effective in reducing the along-wind and across-wind forces of tall square buildings (Elshaer et al., 2017). In the rectangular section, single recession corners were more effective in reducing along-wind and across-wind forces than chamfer corners (Alminhana et al., 2018, Amin and Ahuja 2010). Double chamfered corners showed smaller separation zones and narrower wakes as compared to the square cylinder (Mooneghi and Kargarmoakhar, 2016). Double chamfered corners also reduced more than 30% of along and across wind responses (Elshaer et al., 2017). Cross-sections with recessed and double chamfer corners have smaller separation zones and narrower wakes as compared to the square cylinder. Thus, these were effective in reducing the along-wind and across-wind forces (Mooneghi and Kargarmoakhar, 2016).

Amin & Ahuja (2010) mentioned that the corner roundness is the most effective in suppressing the wind-induced vibrations of square buildings. They are also effective in reducing the across and along wind forces (Mooneghi and Kargarmoakhar, 2016; Elshaer et al., 2017, Zhang, 2013). Square buildings with smaller openings reduced the wind force coefficients of the model (Miyashita et al., 1993). Openings in the along-wind and across-wind directions significantly reduced wind excitations, especially at the top part of the building (Amin & Ahuja, 2010). Slotted corners are can also help to improve the wind performance of tall structures (Amin and Ahuja, 2010, Mooneghi and Kargarmoakhar, 2016, Elshaer et al., 2017).

Double recession corners reduced across-wind excitation dramatically compared to rounded and chamfered corners (Poon et al., 2004). Furthermore, the double recession corner reduced the wind-induced base moment by 25% (Irwin, 2008). The root mean square (rms) of across wind forces and the mean along wind forces on a building with a double recession type corner-cut decreased by up to 40% and 20%, respectively, when compared to a building with the original square configuration. This reduction in loading can be attributed to the disturbance in severe vortex shedding caused by the double recession type corner modification (Suresh Kumar et al., 2006).

1.1.8 Reynolds number

The Reynolds number (*Re*), a dimensionless number, is the ratio of inertial forces to the viscous forces of a fluid. It is used to classify the fluid flow around the model, flow velocity and flow pattern. In this study, the *Re* was calculated as follows;

$$Re = \frac{UD}{\nu} \qquad \text{Eq. 1.17}$$

where U is the wind velocity (m/s), D is the depth of the model (m) and ν is the kinematic viscosity of air (m^2/s).

Kármán vortex vibrations occur when time-dependent periodic vortices are shed in the wake, which is commonly referred to as the Kármán vortex street. This alternate shedding of vortices is contingent upon the flow regime encountered by the model. Concurrently, the flow regime around the model is dependent on the *Re*. As a consequence, the aerodynamic characteristics of a model and the aerodynamic instability encountered by the model might differ depending on the *Re* value.

Larose et al. measured the response of a free-standing bridge pylon, especially the vortex-induced vibration (VIV), in situ for 7 weeks. Then, the results from the full-scale observations were compared with that of the model-scale experiments. Although the Reynolds number of the model-scale experiments was 2000 times smaller than that of the full-scale values, the measured responses were found satisfactory (Larose, G. L., et al., 1998).

In the wind tunnel testing for the vortex-induced vibrations (VIV) of a yawed bridge tower, the *Re* effects were attentively considered both in the static and dynamic tests. However, no significant *Re* effect was observed within the investigated wind velocity range during the static tests. Therefore, the *Re* number dependency which is usually observed in the rounded bluff bodies was found to be negligible for the studied yawed bridge tower (Marra et al. 2017).

Matsuda et al. (2007) studied the *Re* number effects on the steady and unsteady aerodynamic forces on twin-box bridge section models of different scales. The authors mentioned that the flutter analysis carried out with the unsteady aerodynamic coefficients obtained from the low *Re* number region provides the evaluation on the safe side in the wind-resistance design. However, this is restricted to the bridge deck cross-sections investigated in their study.

Fujino (2002) mentioned that corner cutting is one of the well-known methods to reduce the vortex-induced vibration of pylons with rectangular sections. However, the effectiveness of the corner-cut depends upon the *Re* number and recommended to use a *Re* number greater than 10,000 in the wind tunnel experiments.

Practically, it is assumed that the *Re* number only has a slight influence on the aerodynamic characteristics of a structure, presuming the flow separation point is fixed. However, there are also cases where the *Re* number significantly influences the aerodynamic characteristics of a structure. In such cases, the aerodynamic characteristics differ for various *Re* numbers and there are also chances that the aerodynamic response of a structure may be under or over-estimated. Hence, the Reynolds number dependency is one of the important topics which need to be considered in evaluating the wind resistance design of a structure.

1.1.9 Computational fluid dynamics in wind engineering

Mannini et al. (2011) studied a 5:1 rectangular cylinder at Re = 26,400 using Computational Fluid Dynamics (CFD) simulation. They aimed to demonstrate the Detached Eddy Simulation (DES) applicability to bluff body flows, improving accuracy compared to 2-D and 3-D unsteady Reynolds-Averaged Navier-Stokes (RANS). Their results indicated that DES with a well-designed three-dimensional grid could provide fairly accurate results for this benchmark test case. However, this approach required fine three-dimensional meshes, small time steps, and statistical convergence for the flow field, making it computationally expensive, especially for bluff body simulations. The use of hybrid meshes and an unstructured solver showed promise for tackling detailed engineering structure aerodynamics and fluid-structure coupling issues at high Reynolds numbers, particularly for geometries with significantly rounded surfaces. The sensitivity of results to numerical schemes and the spanwise extension of the computational domain highlighted that state-of-the-art CFD simulations are not yet a complete replacement for wind tunnel experiments in bluff body flow research.

Yamagishi et al. (2009) investigated the surface flow around a square cylinder with corner-cuts (single recession and chamfer) by applying the Reynolds-Averaged Navier-Stokes (RANS) based turbulence model, RNG k–ε turbulent model. The simulation results show a tendency to agree well with the wind tunnel test results. Elshaer et al. (2014) used the k-epsilon turbulence model and mentioned that low-dimensional CFD modelling using steady flow can be considered useful for comparing different shapes (square, single recession, double recession, chamfer, and rounded corner) in the aerodynamic modification of tall buildings. Hence, RANS can provide fairly reliable simulation results even for complex 2D shapes. Alminhana et al. (2018) performed a large eddy simulation (LES) with a dynamic sub-grid scale model and calculated to aerodynamic performance of buildings with single recession and chamfer corners. The simulation gave relevant results with the experimental results. LES methods are more accurate than the RANS models for the prediction of unsteady forces at the cost of a higher computational burden (Mooneghi and Kargarmoakhar, 2016).

Therefore, it is important to carefully choose the appropriate turbulence model, numerical scheme, mesh type and time step to achieve statistical convergence and provide an accurate flow field.

1.2 Objective of the study

The tower of the long-span suspension and cable-stayed bridges usually suffered vibration caused by the wind along the bridge axis. However, the free-standing bridge tower in the construction state is generally characterized as having lower structural damping and natural vibration frequencies than the completed state. In this case, the tower is completely independent since the bridge deck and cables are not present. Hence, the tower is more vulnerable to wind-induced vibrations. This made the shape of the tower column sections play an important role in the aerodynamic stability of bridge towers. One of the common cross-sectional shapes utilised in such structures is the rectangular cylinder. However, this cross-sectional shape is known to be vulnerable to both VIV and transverse galloping.

As corner-cutting can reduce the drag coefficient of the rectangular cylinder, this method is considered one of the effective methods in reducing the Kármán vortex shedding (Komatsu and Kobayashi, 1980). According to previous research provided in Section 1.1.4, the corner-cutting method can suppress the Kármán vortex shedding depending on the corner shapes. Therefore, in this study, the effect of corner shape modification on the aerodynamic characteristics and the Kármán vortex shedding intensity of the rectangular cylinder is investigated. The corners of the rectangular cylinder are modified/altered into six different shapes, known as single recession (SR), double recession (DR), double recession II (DR II), double recession III (DR III), triple recession (TR) and chamfer (C).

Furthermore, as mentioned in Section 1.1.5, the aerodynamic instabilities of a rectangular cylinder can be reduced by applying the corner-cut to the rectangular cylinder. However, the mechanisms of aerodynamic stabilization of the corner-cutting method have not yet been clearly understood except for the flow separation. This raised questions about how the galloping stabilization mechanism of corner-cut sections may be associated with its Kármán vortices suppression. Thus, the effect of vortices on the onset reduced wind velocity of galloping is investigated by controlling the Kármán vortex shedding intensity via cutting the corners of the rectangular cylinder into various shapes. This may be able to provide information to develop solutions for the vibrations of real structures exposed to wind.

In the rectangular cylinder, a high value of the mass-damping parameter which is known as the Scruton number, is required to completely decouple the VIV and galloping excitation range (Mannini et al. 2016). In the corner-cut cylinder, the study related to the Scruton number and the aerodynamic instability is still lacking. Hence, in this research, the effect of Scruton number on the vibration amplitude of both rectangular and corner-cut cylinders is investigated. This can broaden our existing knowledge about the corner-cutting method in terms of VIV and galloping excitation range.

It is well known that the galloping instability is highly associated with the Kármán vortices. Moreover, the interaction between the Kármán vortex and galloping instability is also complex. In this study, the intensity of Kármán vortex shedding is controlled by altering the corner of the rectangular cylinder into various shapes. Moreover, at the angle of attack just before the angle of attack where the reattachment occurs, the slope of the transverse force coefficient is considerably large and a high galloping response is expected. On the other hand, the Kármán vortex shedding is found to be very weak at this angle of attack. Thus, the aerodynamic interactions between the galloping instability and the vortices are investigated at zero angle of attack (symmetric body) and various angles of attack (asymmetric body). This can be of help in clarifying how the vortices help in reducing the galloping instability.

Irwin (2008) mentioned that structures buffeted by steady wind winds experience lateral forces in the across-wind direction. Suction force, resulting from the well-organized vortices form in patterns, can induce dangerously large forces to the structures. Consequently, wind loading is considered one of the dominant lateral loadings in the design of high-rise structures. As described in section 1.1.7, the wind-induced vibration of the structures can be reduced by modifying the flow field around them by changing their corner shapes. In this research, the flow field analysis on the existing complex-shaped tall Buddha statue is carried out. The cross-sectional shape of the Buddha statue is varied throughout the overall height. This will provide a better understanding of the effect of cross-sectional shape on the flow separation, flow reattachment and the aerodynamic characteristics of the complex-shaped tall structure. Moreover, this can be of help in the wind-induced structural vibrations mitigation of the existing complex-shaped tall structure.

1.3 Thesis outline

This research is composed of seven chapters, each one providing a brief introduction of the content and finalized with a summary of findings. This dissertation is generally divided into three parts: the first part consists of Chapters 1 and 2, describing the general background and methodology of current research; the second part consists of Chapters 3, 4, 5, and 6, explaining the wind tunnel tests results, computational fluid dynamic simulations results and discussion; and the third part consists of Chapter 7, summarizing the findings and recommending future works.

In Chapter 1, the general background on the aerodynamics phenomenon which is necessary to understand this research is described. Then, the objectives and outlines of the current study are introduced.

In Chapter 2, the description of the models utilised in this research is introduced. Afterwards, the outlines of the wind tunnel tests and computational fluid dynamics simulations are provided.

In Chapter 3, the aerodynamic performance of a rectangular cylinder with side ratio B/D of 1.5, and corner-cut cylinders are reported in detail. The corners of a rectangular cylinder are modified into six different shapes with the expectation of reducing the Kármán vortex shedding intensity of the rectangular cylinder. Then, the aerodynamic force coefficients, Kármán vortex shedding intensity and Strouhal number of each section are discussed for the angle of attack range of $-3° \leq \alpha \leq +15°$.

In Chapter 4, the effect of Kármán vortex shedding intensity on the galloping onset of the rectangular cylinder is explained. Then, the effect of the mass-damping parameter, known as Scruton number ($S_{c\eta}$), on the Kármán vortex-induced vibration (KVIV) and galloping instability of rectangular and corner-cut cylinders is described. At last, the aerodynamic interactions between the vortices and the galloping instability are discussed for zero angle of attack (symmetric body).

In Chapter 5, the Kármán vortex shedding intensity of rectangular (R), triple recession (TR) and double recession III (DR III) are modified by changing the angle of attack into various values. This includes the angle of attack where the slope of the transverse force coefficient is the largest. Then, the effect of the Scruton number on the KVIV and galloping interference is described. Finally, the aerodynamic interactions between the vortices and the galloping instability are discussed for various angles of attack (asymmetric body).

In Chapter 6, the 3D terrestrial laser scanning, modelling and flow field analysis of complex-shaped tall structures are provided. Large eddy simulation procedures, aerodynamic characteristics, flow field visualisation, and wind resistance evaluation of complex-shaped structure are also briefly discussed.

Finally, conclusions and recommendations for future studies are provided in the last chapter.

Reference

Adeeb, E., Haider, B. A., & Sohn, C. H. (2018). Flow interference of two side-by-side square cylinders using IB-LBM – Effect of corner radius. *Results in Physics*, *10*(June), 256–263. https://doi.org/10.1016/j.rinp.2018.05.039

Alminhana, G. W., Braun, A. L., & Loredo-Souza, A. M. (2018). A numerical study on the aerodynamic performance of building cross-sections using corner modifications. *Latin American Journal of Solids and Structures*, *15*(7). https://doi.org/10.1590/1679-78254871

Amin, J. A., & Ahuja, A. K. (2010). Aerodynamic modifications to the shape of the buildings: A review of the state-of-the-art. *Asian Journal of Civil Engineering*, *11*(4), 433–450.

Bearman, P. W., & Trueman, D. M. (1972). An investigation of the flow around rectangular cylinders. *Aeronautical Quarterly*, 23(3), 229-237. https://doi.org/10.1017/S0001925900006119

Carassale, L., Freda, A., & Marrè-Brunenghi, M. (2013). Effects of free-stream turbulence and corner shape on the galloping instability of square cylinders. *Journal of Wind Engineering and Industrial Aerodynamics*, *123*, 274–280. https://doi.org/10.1016/j.jweia.2013.09.002.

Chen, C., Mannini, C., Bartoli, G., & Thiele, K. (2020). Experimental study and mathematical modeling on the unsteady galloping of a bridge deck with open cross section. *Journal of Wind Engineering and Industrial Aerodynamics*, 203, 104170. https://doi.org/10.1016/j.jweia.2020.104170.

Choi, C. K., & Kwon, D. K. (1998). Wind tunnel blockage effects on aerodynamic behavior of bluff body. *Wind and Structures, An International Journal*, *1*(4), 351–364. https://doi.org/10.12989/was.1998.1.4.351

Choi, C. K., & Kwon, D. K. (1999). Aerodynamic stability for square cylinder with various corner cuts. *Wind and Structures, An International Journal*, *2*(3), 173–187. https://doi.org/10.12989/was.1999.2.3.173

Choi, C. K., & Kwon, D. K. (2000). Aerodynamic Stability for Rectangular Cylinders with Various Corner Cuts. *The 4th International Colloquium on Bluff Body Aerodynamics and its Applications*, Bochum, Germany.

Choi, C. K., & Kwon, D. K. (2001). The Characteristics of Strouhal Number of Rectangular Cylinders with Various Corner Cuts. *The 5th Asia-Pacific Conference on Wind Engineering*, Kyoto, Japan.

Choi, C. K., & Kwon, D. K. (2003). Effects of corner cuts and angles of attack on the Strouhal number of rectangular cylinders. *Wind and Structures, An International Journal*, *6*(2), 127–140. https://doi.org/10.12989/was.2003.6.2.127.

Corless, R.M., & Parkinson, G. V., 1988. A model of the combined effects of vortex-induced oscillation and galloping. *J Fluids Struct 2*. https://doi.org/10.1016/S0889-9746(88)80008-2.

Den Hartog, J. P. (1956). Mechanical vibrations. McGraw-Hill, USA.

Den Hartog, J. P. (1985). Mechanical vibrations. Dover Publication, New York, USA.

Elshaer, A., Bitsuamlak, G., & Damatty, A. El. (2014). Wind Load Reductions due to Building Corner Modifications. *22nd Annual Conference of the CFD Society of Canada*, Toronto, Canada.

Elshaer, A., Bitsuamlak, G., & El Damatty, A. (2017). Enhancing wind performance of tall buildings using corner aerodynamic optimization. *Engineering Structures*, *136*, 133–148. https://doi.org/10.1016/j.engstruct.2017.01.019.

Fujino, Y. (2002). Vibration, control and monitoring of long-span bridges—recent research, developments and practice in Japan. *Journal of Constructional Steel Research*, 58 (1), 71-97. https://doi.org/10.1016/S0143-974X(01)00049-9.

Günter Schewe. (2013). Reynolds-number-effects in flow around a rectangular cylinder with aspect ratio 1:5. *Journal of Fluids and Structures*, 39, 15-26, https://doi.org/10.1016/j.jfluidstructs.2013.02.013.

Honda, A., Sugiyama, S., Shijo, R., Morishita, K. & Kato, M. (2012). Experiment, analysis and evaluation techniques to protect structures from windstorms and massive earthquakes. *Mitsubishi Heavy Industries Technical Review*, 49(4).

Igarashi, T. (1985). Characteristics of the flow around rectangular cylinders: the case of the angle of attack 0 deg. *Bulletin of JSME*, 28(242), 1690-1696.

Irwin, P. A. (2008). Bluff body aerodynamics in wind engineering. *Journal of Wind Engineering and Industrial Aerodynamics*, 96(6–7), 701–712. https://doi.org/10.1016/j.jweia.2007.06.008

Kawai, H. (1998). Effect of corner modifications on aeroelastic instabilities of tall buildings. *Journal of Wind Engineering and Industrial Aerodynamics*, *74–76*, 719–729. https://doi.org/10.1016/S0167-6105(98)00065-8

Kawai, H., & Fujinami, K. (2001). Wind Force on a Two-Dimensional Square Cylinder with Corner Recession and Corner Roundness in Smooth Flow. *Journal of Wind Engineering*, (89), 489-492.

Kawai, H., & Fujinami, K. (2001). Wind Force on a Two-Dimensional Square Cylinder with Corner Recession and Corner Roundness in Smooth Flow. *The fifth Asia Pacific Conference on Wind Engineering*, Kyoto, Japan.

Kitagawa, M. (2004). Technology of the Akashi Kaikyo bridge. *Structural control and health monitoring*, *11*(2), 75-90. https://doi.org/10.1002/stc.31.

Komatsu, S., & Kobayashi, H. (1980). Vortex-induced oscillation of bluff cylinders, *Journal of Wind Engineering and Industrial Aerodynamics*, 6, 3–4, 335-362. https://doi.org/10.1016/0167-6105(80)90010-0.

Larose, G. L., Falco, M., & Cigada, A. (1995). Aeroelastic response of the towers for the proposed bridge over Stretto di Messina. *Journal of wind engineering and industrial aerodynamics*, *57*(2-3), 363-373. https://doi.org/10.1016/0167-6105(94)00104-L.

Larose, G. L., Zasso, A., Melelli, S., & Casanova, D. (1998). Field measurements of the wind-induced response of a 254 m high free-standing bridge pylon. *Journal of Wind Engineering and Industrial Aerodynamics*, 74–76, 891-902, https://doi.org/10.1016/S0167-6105(98)00081-6.

Ma, C., Liu, Y., Yeung, N., & Li, Q. (2019). Experimental study of across-wind aerodynamic behavior of a bridge tower. *Journal of Bridge Engineering*, *24*(2), 04018116. https://doi.org/10.1061/(ASCE)BE.1943-5592.0001348.

Mannini, C. (2020). Incorporation of turbulence in a nonlinear wake-oscillator model for the prediction of unsteady galloping response. Journal of Wind Engineering and Industrial Aerodynamics, 200, 104141. https://doi.org/10.1016/j.jweia.2020.104141.

Mannini, C., Marra, A.M., & Bartoli, G. (2014). VIV–galloping instability of rectangular cylinders: Review and new experiments, *Journal of Wind Engineering and Industrial Aerodynamics*, 132, 109-124. https://doi.org/10.1016/j.jweia.2014.06.021.

Mannini, C., Marra, A. M., & Bartoli, G. (2015). Experimental investigation on VIV-galloping interaction of a rectangular 3: 2 cylinder. *Meccanica*, 50(3), 841-853. https://doi.org/10.1007/s11012-014-0025-8.

Mannini, C., Marra, A. M., Massai, T., & Bartoli, G. (2016). Interference of vortex-induced vibration and transverse galloping for a rectangular cylinder. *Journal of Fluids and Structures*, 66, 403-423, https://doi.org/10.1016/j.jfluidstructs.2016.08.002.

Mannini, C., Massai, T., Marra, A. M., & Bartoli, G. (2017). Interference of vortex-induced vibration and galloping: Experiments and mathematical modelling. *Procedia engineering*, 199, 3133-3138.

Mannini, C., Massai, T., & Marra, A. M. (2018). Unsteady galloping of a rectangular cylinder in turbulent flow. Journal of Wind Engineering and Industrial Aerodynamics, 173, 210-226. https://doi.org/10.1016/j.jweia.2017.11.010.

Mannini, C., Massai, T., & Marra, A. M. (2018). Modeling the interference of vortex-induced vibration and galloping for a slender rectangular prism. *Journal of Sound and Vibration*, 419, 493-509. https://doi.org/10.1016/j.jsv.2017.12.016.

Mannini, C., Soda, A, & Schewe, G. (2011), Numerical investigation on the three-dimensional unsteady flow past a 5:1 rectangular cylinder. *Journal of Wind Engineering and Industrial Aerodynamics*, 99, 469–482.

Marra, A. M., Mannini, C., & Bartoli, G. (2015). Measurements and improved model of vortex-induced vibration for an elongated rectangular cylinder. *Journal of Wind Engineering and Industrial Aerodynamics*, 147, 358-367. https://doi.org/10.1016/j.jweia.2015.08.007.

Marra, A. M., Mannini, C., & Bartoli, G. (2017). Wind tunnel modeling for the vortex-induced vibrations of a yawed bridge tower. *Journal of Bridge Engineering*, 22(5), https://doi.org/10.1061/(ASCE)BE.1943-5592.0001028.

Matsuda, K., Tokushige, M., & Iwasaki, T. (2007). Reynolds number effects on the steady and unsteady aerodynamic forces acting on the bridge deck sections of long-span suspension bridge. *IHI Engineering Review*, 40(1), 12-26.

Matsumoto, M., Shiraishi, N., & Shirato, H. (1988). Bluff body aerodynamics in pulsating flow. *Journal of Wind Engineering and Industrial Aerodynamics,* 28 (1–3), 261-270, https://doi.org/10.1016/0167-6105(88)90122-5.

Matsumoto, M., Yagi, T., Hatsuda, H., Shima, T., Tanaka, M., & Naito, H. (2010) Dry galloping characteristics and its mechanism of inclined/yawed cables. *Journal of Wind Engineering and Industrial Aerodynamics*, 98 (6–7), 317-327, https://doi.org/10.1016/j.jweia.2009.12.001.

Matsumoto, M., Yagi, T., Lee, J.H., Hori, K., & Kawashima, Y., 2006. Karman vortex effect on the aerodynamic forces to rectangular cylinders. American Society of Mechanical Engineers, *Pressure Vessels and Piping Division (Publication) PVP*. https://doi.org/10.1115/PVP2006-ICPVT-11-93783.

Miyashita, K., Katagiri, J., Nakamura, O., Ohkuma, T., Tamura, Y., Itoh, M., & Mimachi, T. (1993). Wind-induced response of high-rise buildings Effects of corner cuts or openings in square buildings. *Journal of Wind Engineering and Industrial Aerodynamics*, 50(C), 319–328. https://doi.org/10.1016/0167-6105(93)90087-5.

Mizota, T., & Okajima, A. (1981). Experimental studies of time mean flows around rectangular prisms. *Proceedings of the Japan Society of Civil Engineers*, 1981, 312, 39-47. https://doi.org/10.2208/jscej1969.1981.312_39.

Mooneghi, M. A., & Kargarmoakhar, R. (2016). Aerodynamic Mitigation and Shape Optimization of Buildings: Review. *Journal of Building Engineering*, 6, 225–235. https://doi.org/10.1016/j.jobe.2016.01.009.

Morgenthal, G., & Yamasaki, Y. (2010). Behaviour of very long cable-stayed bridges during erection. In *Proceedings of the Institution of Civil Engineers-Bridge Engineering*, 163, 4, 213-224. https://doi.org/10.1680/bren.2010.4.213.

Nakaguchi, H., Hashimoto, K., & Muto, S. (1968). An experimental study on aerodynamic drag of rectangular cylinders. *Journal of Japan Society for Aeronautical and Space Sciences*, 16, 1-5. https://doi.org/10.2322/jjsass1953.16.1 (In Japanese).

Nakamura, Y., Hirata, K., & Urabe, T., 1991. Galloping of rectangular cylinders inthe presence of a splitter plate. *J Fluids Struct* 5. https://doi.org/10.1016/S0889-9746(05)80004-0.

Nakamura Y, & Nakashima M. (1986). Vortex excitation of prisms with elongated rectangular, H and [vdash] cross-sections. *Journal of Fluid Mechanics*. 163, 149-169. https://doi:10.1017/S0022112086002252.

Nakamura, Y., & Tomonari, Y. (1977). Galloping of rectangular prisms in a smooth and in a turbulent flow, *Journal of Sound and Vibration*, 52, 2, 233-241. https://doi.org/10.1016/0022-460X(77)90642-3.

Naudascher, E., & Rockwell, D. (1994). Flow induced vibrations. Dover Publications, Inc. Mineola, New York.

Nidhul, K. (2014). Influence of corner geometry on the flow structure and flow characteristics for flow past a square cylinder at Re = 150. *International Journal of Research in Aeronautical and Mechanical Engineering*, 2 (12), 32-41,

Ogawa, K., Matsumoto, M., Kitazawa, M., & Yamasaki, T. (1990). Aerodynamic stability of the tower of a long-spanned cable-stayed bridge (Higashi-Kobe Bridge). *Journal of Wind Engineering and Industrial Aerodynamics*, 33 (1–2), 349-358, https://doi.org/10.1016/0167-6105(90)90050-M.

Parkinson, G., 1989. Phenomena and modelling of flow-induced vibrations of bluff bodies. Progress in Aerospace Sciences. https://doi.org/10.1016/0376-0421(89)90008-0

Parkinson, G. V., & Smith, J. D. (1964). The square prism as an aeroelastic non-linear oscillator. *The Quarterly Journal of Mechanics and Applied Mathematics*, 17(2), 225-239. https://doi.org/10.1093/qjmam/17.2.225.

Poon, D. C. K., Shieh, S., Joseph, L. M., & Chang, C. (2004). Structural design of Taipei 101, the world's tallest building. Proceedings of the CTBUH 2004 Seoul Conference, Seoul, Korea, 271–278.

Scanlan, R.H., (1981). On the State-of-the-Art Methods for Calculations of Flutter, Vortex-Induced and Buffeting Response of Bridge Structures. Technical Report, FHWA/RD-80/050, Nat. Tech. Information Service, Springfield, VA.

Scruton, C. (1965). On the Wind Excited Oscillations of Stacks, Towers, and Masts. Wind Effects on Buildings and Structures, Vol. 2, *Her Majesty's Stationery Office (Proc. Int. Conf. Wind Effects Buildings and Structures (1963))*, 798-832.

Shang, J., Zhou, Q., Alam, M. M., Liao, H., & Cao, S. (2019). Numerical studies of the flow structure and aerodynamic forces on two tandem square cylinders with different chamfered-corner ratios. *Physics of Fluids*, 31(7). https://doi.org/10.1063/1.5100266.

Shiraishi, N., Matsumoto, M., Shirato, H., & Ishizaki, H. (1988). On aerodynamic stability effects for bluff rectangular cylinders by their corner-cut. *Journal of Wind Engineering and Industrial Aerodynamics*, *28*(1-3), 371-380. https://doi.org/10.1016/0167-6105(88)90133-X.

Shiraishi, N., & Matsumoto, M. (1983). On classification of vortex-induced oscillation and its application for bridge structures, *Journal of Wind Engineering and Industrial Aerodynamics*, 14, 1–3, 419-430. https://doi.org/10.1016/0167-6105(83)90043-0.

Siringoringo, D. M., & Fujino, Y. (2012). Observed along-wind vibration of a suspension bridge tower. *Journal of wind engineering and industrial aerodynamics*, *103*, 107-121. https://doi.org/10.1016/j.jweia.2012.03.007.

Suresh Kumar, K., Irwin, P. A., & Davies, A. (2006). Design of tall building for wind: wind tunnel vs. codes/standards. In *Third National Conference on Wind Engineering, Calcutta, India* (pp. 318-325).

Takeuchi, T. (1990). Effects of geometrical shape on vortex-induced oscillations of bridge tower. *Journal of Wind Engineering and Industrial Aerodynamics*, *33*(1-2), 359-368. https://doi.org/10.1016/0167-6105(90)90051-D.

Yagi, T., Shinjo, K., & Narita, S., 2013. Interferences of vortex sheddings in galloping instability of rectangular cylinders. *Journal of structural engineering 59A*, 552–561. https://doi.org/https://doi.org/10.11532/structcivil.59A.552.

Yamagishi, Y., Kimura, S., Oki, M., & Hatayama, C. (2009). Effect of Corner Cutoffs on Flow Characteristics Around a Square Cylinder. *10th International Conference on Fluid Control, Measeuremnts and Visualisation*, 1–10.

Zhang, Z., Quan, Y., Gu, M., Tu, N., & Xiong, Y. (2012). Effects of corner recession modification on aerodynamic coefficients of square tall buildings. The Seventh International Colloquium on Bluff Body Aerodynamics and Applications, Shanghai, China.

Zhang, Z., Quan, Y., Gu, M., & Xiong, Y. (2013). Effects of corner chamfering and rounding modification on aerodynamic coefficients of square tall buildings. Tumu Gongcheng Xuebao/China Civil Engineering Journal, 46(9), 12–20.

Chapter 2

Methodology

2.1 Introduction

In this study, the corners of the rectangular cylinder with a side ratio (B/D) of 1.5 were altered into various shapes to reduce the Kármán vortex shedding intensity. Then, the effect of Kármán vortex shedding on the galloping onset, aerodynamic interference between the vortices and the galloping instability, and the aerodynamic characteristics of complex-shaped tall structures were discussed. Wind tunnel tests were conducted to evaluate the aerodynamic performance of rectangular cylinders with six different corner modifications. Computational fluid dynamics (CFD) simulations were carried out for the flow visualization. In this chapter, a detailed description of the models utilized in this study is provided in Section 2.2. In Sections 2.3 and 2.4, the outlines of the wind tunnel tests and the CFD simulations are described.

2.2 Model description

Two types of models, the two-dimensional (2D) and three-dimensional (3D) models, were used in this study. The following sections (Sections 2.2.1 and 2.2.2) described the rectangular and corner-cut cylinders, which were used to study the effect of vortices on the galloping instability. The 2D models explained in these two sections were used in the aerodynamic force measurement of a stationary model, vertical 1-DOF free vibration test of a spring-supported model, unsteady aerodynamic force measurement under forced vibration, and CFD simulations. Section 2.2.3 described the complex-shaped tall Buddha statue, which was used to study the effect of complex cross-sectional shapes on the flow field around the existing structure. The Buddha statue mentioned in this section, the 3D model, was used only in the CFD simulations.

2.2.1 Rectangular cylinder

Mannini et al. (2016) mentioned that the rectangular cylinder with a side ratio (B/D) of 1.5 is the vortex-induced vibration (VIV) and galloping instability-prone section. In this section, the time-averaged flow does not reattach to a side surface, and thus, the galloping instability occurs (Matsumoto et al. 1988, 2010). In addition, the onset reduced wind velocity of the motion-induced vortex vibration (MIV) calculated by Eq. 1.16 and that of the Kármán vortex-induced vibration (KVIV) calculated by Eq. 1.15 are also clearly separated from each other as shown in Fig. 2.1. Hence, it is easy to distinguish the effect caused by the motion-induced vortices and the Kármán vortex.

Moreover, as shown in Fig. 2.2, the fluctuating lift force coefficient which indicates Kármán vortex shedding intensity (C'_L) of B/D = 1.5 section is not too small and can further be reduced. Since one of the objectives of this study was to study the aerodynamic interactions between the galloping instability and vortices by varying the Kármán vortex shedding intensity, this cross-sectional shape

(*B*/*D* = 1.5) was selected as the most suitable one for the basic model. The specifications of the model were; the length (*L*) was 894 mm, the width (*B*) was 135 mm, and the depth (*D*) was 90 mm.

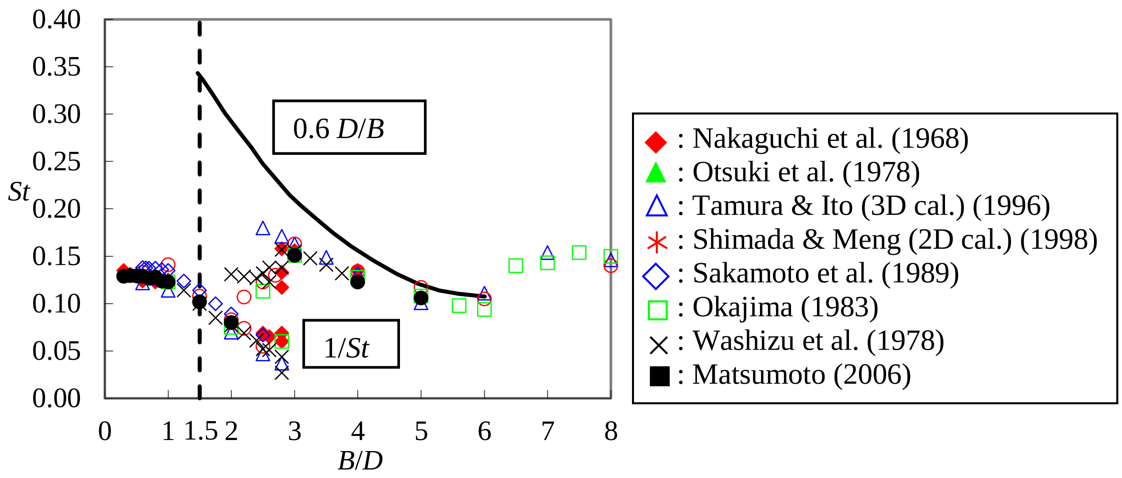

Fig. 2.1 Onset reduced wind velocity of Kármán vortex-induced vibration (1/*St*) and motion-induced vortex vibration (0.6 *D*/*B*) of rectangular cylinder for various side ratios.

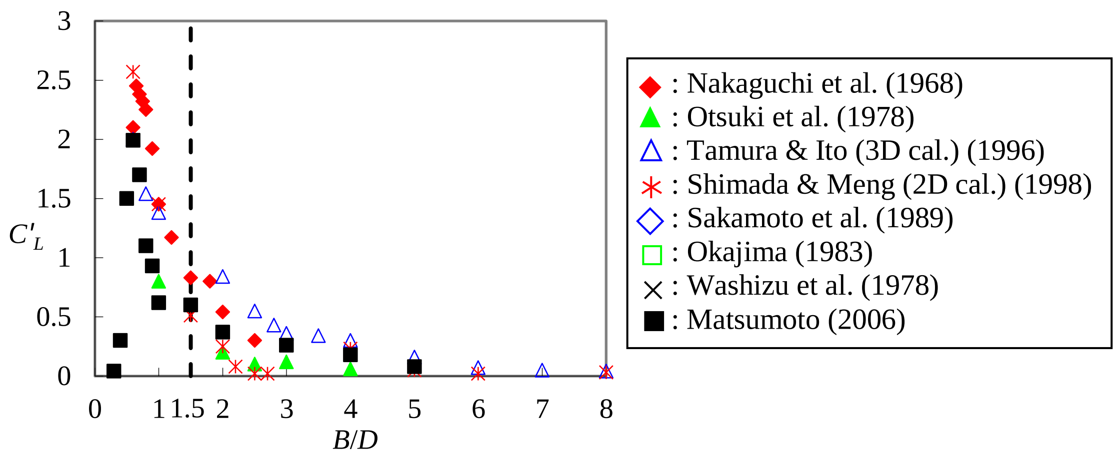

Fig. 2.2 The fluctuating lift force coefficient which indicated the Kármán vortex shedding intensity (C'_L) of rectangular cylinder for various side ratios.

2.2.2 Corner-shape altered section

In this study, the corners of the original rectangular section (*B*/*D* = 1.5) were modified into six different shapes while keeping the same *B*/*D* ratio. These corner shapes were generally divided into three groups as illustrated in Fig. 2.3. In the original rectangular (R) section, the shear layers separated from the leading edges were located far from the side surfaces of the model and had a wide wake region (Shiraishi et al., 1988). Based on the extensive literature reviews on the corner modification

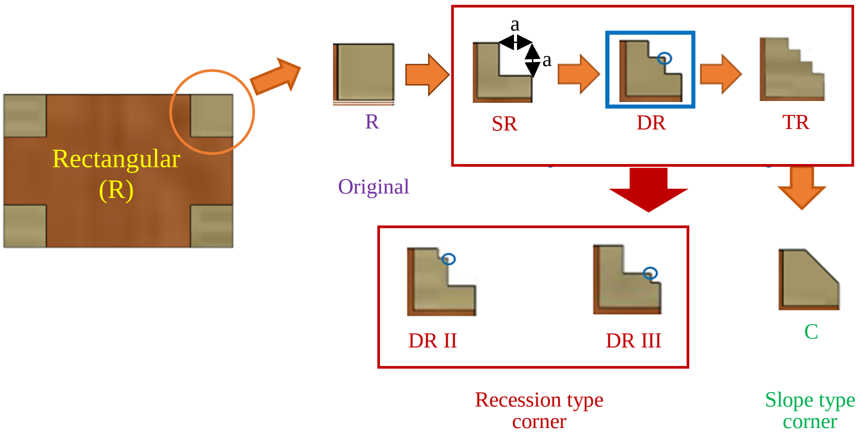

Fig. 2.3 Schematic representation of the corner-shape altering process.

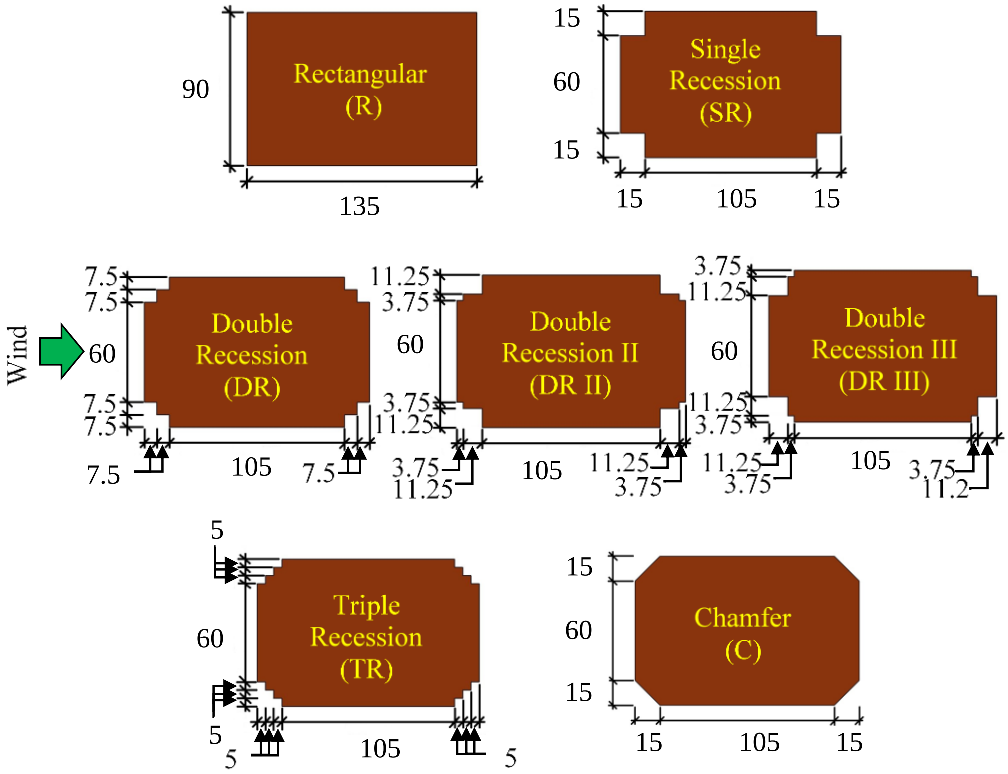

Fig. 2.4 Test models with different corner shapes (unit: mm).

topic, the single recession (SR) with the corner ratio (a/D, a = corner cut length and D = model depth) of 3/18 was chosen to keep the shear layers separated from the leading edges closer to the side surfaces of the model and suppress Kármán vortex shedding. Then, the corners of the SR section were filled with one step in double recession (DR) and two steps in triple recession (TR).

In addition, double recession II (DR II) and double recession III (DR III) were also used to investigate the sensitivity of the inner step orientation to the flow in the double recession type corners.

These five sections (SR, DR, DR II, DR III, and TR) were denoted as the recession-type corner-shape altered sections. Finally, the corners of the SR were connected with a straight line and altered into a chamfer (C) section. This section provided an infinite number of steps and was denoted as the slope-type corner-shape altered section.

According to Shiraishi et al. (1988), the size of a corner-cut affected the shear layer separation from the leading edge. Moreover, this considerably influenced the vibration response of the rectangular cylinder. In this study, the corner ratio (a/D) of each section, where the flow separation was likely to occur, was kept the same for all sections. However, the presence of different steps may also influence the flow separation to a certain extent. Therefore, the shear layers were expected to separate at different points in the leading edge. Since the flow separation highly affected the aerodynamic characteristics of a section, the aforementioned seven sections were expected to have different Kármán vortex shedding properties. The detailed cross-sectional shape of each model is illustrated in Fig. 2.4. For all models, the end plates were installed at both ends of the model to reduce the effect of the boundary layer on the wall of the wind tunnel. The end plate dimensions were; the width was 525 mm, the depth was 350 mm and the thickness (t) was 4 mm.

2.2.3 Complex-shaped tall structure

The Laykyun Sekkya Standing Buddha Statue, which is recorded as the third tallest statue as of 2023, is located on the Po Khaung Mountain, Monywa City, Sagaing Region, Myanmar (Fig. 2.5). According to Multi-Hazard Risk Assessment in Rakhine State of Myanmar written by United Nations Development Programme (UNDP, 2011), three storms affected Monywa with maximum sustained wind velocity of 35, 50 and 135 km/hr (9.72, 13.89 and 37.5 m/s). Hence, the Buddha statue is likely

(a) (b) (c)

Fig. 2.5 Laykyun Sekkya Standing Buddha Statue: (a) front view; (b) back view; and (c) side view.

to be affected by the storms in the near future. Therefore, this Buddha statue was chosen to use as the case study model in this research.

The Buddha statue is a hollow type structure. The width (B) and the length (L) of the statue at the base are 47.629 m and 43.468 m, respectively. The height of the statue is approximately 129 m including the throne and 116 m without it. It has a total of 31 storeys with an average storey height of approximately 3.66 m. Each storey has an estimated area of 39.93 m × 13.41 m. In this study, the flow field around and the aerodynamic characteristics of the Buddha statue were evaluated by performing 3D terrestrial laser scanning and computational fluid dynamic simulation. The Buddha statue was equally divided into 26 parts with an average height of around 4.96-5.04 m for each cross-section as illustrated in Fig. 2.5 (b) and (c). This is for the detailed representation of the aerodynamic characteristics produced by the complex shape of each part.

2.3 Outline of the wind tunnel test

In this section, the outline of wind tunnel tests conducted in this research are described. The room-circuit Eiffel-type wind tunnel (KWT-81) installed in the Department of Civil and Earth Resources Engineering, Graduate School of Engineering, Kyoto University was used.

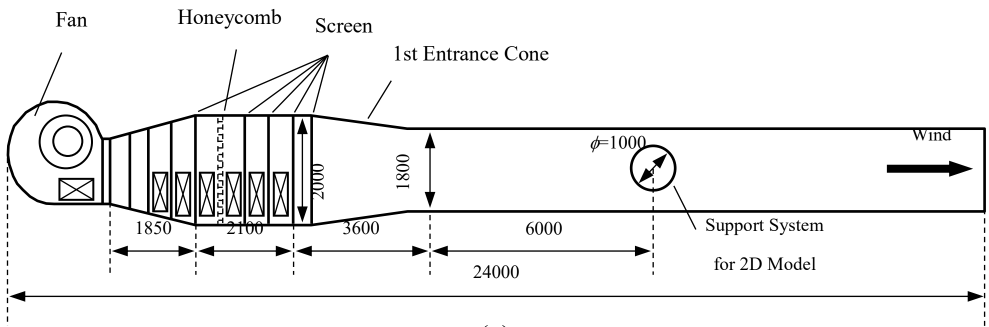

(a)

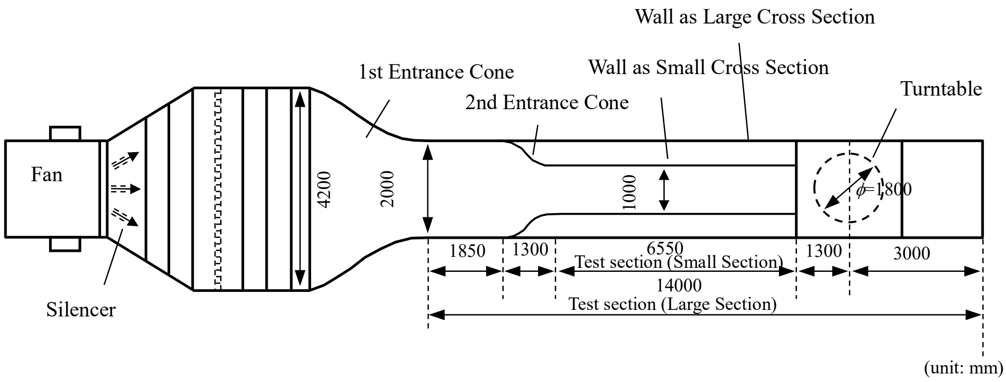

(b)

Fig. 2.6 The sketch of the room-circuit Eiffel-type wind tunnel: (a) side view; and (b) top view (unit: mm).

Fig. 2.6 shows the size of the test section with 1.80 m in height, 1.00 m in width, and 6.55 m in length. By controlling the rotation speed of the fan, it is possible to continuously change the wind velocity in the range of 0.2 to 30 m/s. To avoid the disturbance of the boundary turbulence on the side wall and the model support arm, a guide wall was installed at 35 mm from each side surface of the wind tunnel wall around the 2D testing section. The turbulence intensity is less than 0.3 % for the incoming wind velocity of 10 m/s.

An NPL pitot tube was used to measure the total pressure and static pressure. The differential pressure ΔP [Pa] was read with a digital manometer (OKANO WORKS, DP-20A). The wind velocity in the wind tunnel U [m/s] was calculated using the following formula.

$$U = \sqrt{\frac{2\Delta P}{\rho}} \qquad \text{Eq. 2.1}$$

where ρ is the air density (kg/m^3).

2.3.1 Aerodynamic force measurement of stationary model

Fig. 2.7 shows the set-up for the aerodynamic force measurement of the stationary model inside the wind tunnel. The aerodynamic forces acting on the model were recorded with two load cells (NISHO ELECTRIC WORKS CO. LTD MULTI COMPONENT LOADCELL MODEL LMC-3501-50N) attached to each side of the model as shown in Fig. 2.7 (a). The digital signal coming from the load cells was filtered through a 100 Hz low pass filter in the dynamic-strain measuring instrument (KYOWA, MCD-8A) and transferred to the A/D converter. The sampling frequency was 1,000 Hz and the recording time was 60 sec. The angle of attack (α) was defined as the nose-up positive in the upstream direction. During the measurement, the α value was changed from −3° to +15° at 1° intervals. The blockage ratio was between 4.47–6.05%.

(a)

Fig. 2.7 Set-up of each model for the static test: (a) rectangular; (b) single recession; (c) double recession; (d) double recession II; (e) double recession III; (f) triple recession; and (g) chamfer (1/2).

 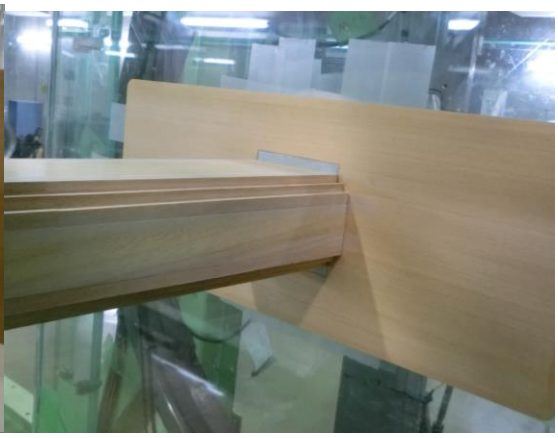

(b) (c)

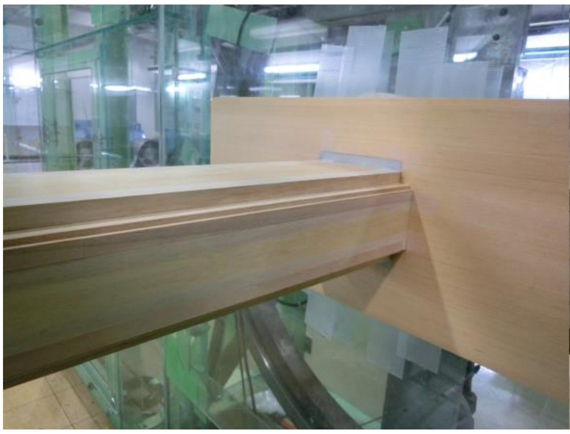 

(d) (e)

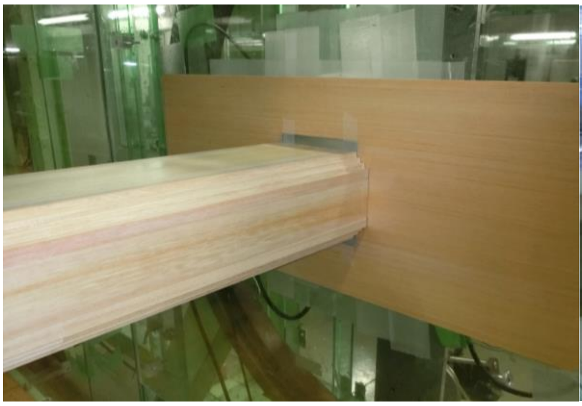 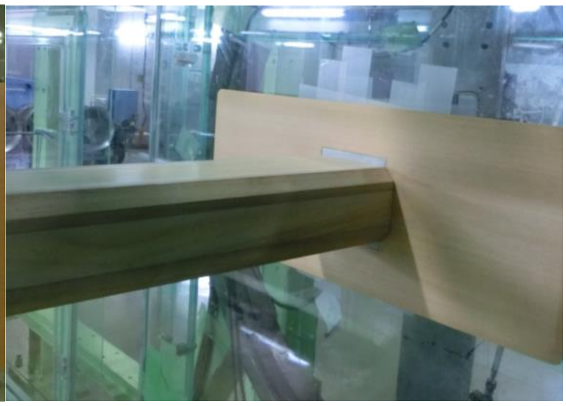

(f) (g)

Fig. 2.7 Set-up of each model for the static test: (a) rectangular; (b) single recession; (c) double recession; (d) double recession II; (e) double recession III; (f) triple recession; and (g) chamfer (2/2).

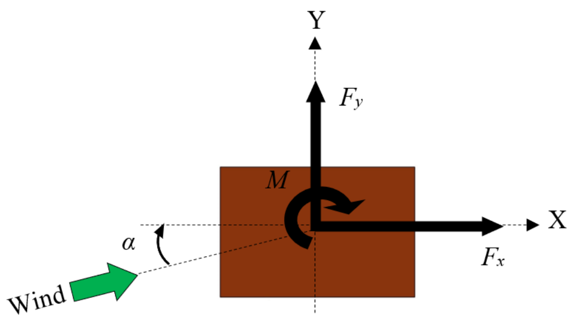

Fig. 2.8 Definition of aerodynamic forces on the structural axis.

All measurements were made on the structural axis as illustrated in Fig. 2.8 where F_x is positive in the streamwise direction, F_y is positive in the upward direction and F_M is positive in the nose-up direction. The aerodynamic force coefficients (C_{Fx}, C_{Fy} and C_M) and the fluctuating lift force coefficient (C'_{Fy}) which described the Kármán vortex shedding intensity are calculated as follows:

$$C_{Fx} = \frac{F_x}{\frac{1}{2}\rho U^2 Dl} \quad \text{Eq. 2.2}$$

$$C_{Fy} = \frac{F_y}{\frac{1}{2}\rho U^2 Bl} \quad \text{Eq. 2.3}$$

$$C_M = \frac{F_M}{\frac{1}{2}\rho U^2 B^2 l} \quad \text{Eq. 2.4}$$

$$C'_{Fy} = \frac{F_y(t)_{std}}{\frac{1}{2}\rho U^2 Bl} \quad \text{Eq. 2.5}$$

where, F_x is the longitudinal force (N), which indicates the time-averaged drag force defined on the longitudinal structural axis (x-direction); F_y is the transverse force (N), which indicates the time-averaged lift force defined on the transverse structural axis (y-direction); F_M is the pitching moment (Nm); $F_y(t)_{std}$ is the standard deviation of the fluctuating transverse force time series; C_{Fx} and C_{Fy} are the longitudinal and transverse force coefficients, respectively; C_M is moment coefficient; C'_{Fy} is the fluctuating transverse force coefficient, which corresponds to the Kármán vortex shedding intensity; ρ is the air density (kg/m^3); U is the wind velocity (m/s); and B, D, and l are the width (m), depth (m), and span length (m) of the model, respectively. According to the quasi-steady theory, galloping instability occurs when the slope of the lift force coefficient against the angle of attack has a negative value. The Den Hartog criteria (H) and critical reduced wind velocity of galloping based on the quasi-steady theory (U_{cr_quasi}) were calculated as follows:

$$H = \left.\frac{dC_{F_y}}{d\alpha}\right|_{\alpha=0°} \quad \text{Eq. 2.6}$$

$$U_{cr\_quasi} = \frac{2S_{c\eta}}{\left.\frac{dC_{F_y}}{d\alpha}\right|_{\alpha=0^\circ}} \frac{D}{B} \qquad \text{Eq. 2.7}$$

where $S_{c\eta}$ is the Scruton number, which will be explained in detail in the next section.

2.3.2 Free vibration test of spring-supported model

The vertical 1-DOF spring-supported free vibration tests were conducted to measure the vertical aerodynamic response of both rectangular and corner-cut cylinders. The endplates of the model were connected to the support arm on each side. The model was suspended with a total of eight springs, with four on each side. During the experiment, thin piano wires were used to restrain the movement of the model in the torsional direction and the model was allowed to vibrate freely only in the vertical 1DOF direction as shown in Fig. 2.9.

(a) (b)

Fig. 2.9 Vertical 1-DOF free vibration test set-up; (a) α = 0°; and (b) α = + 4°.

The vertical 1-DOF spring-supported free vibration tests were conducted to measure the vertical aerodynamic response of both rectangular and corner-cut cylinders. The endplates of the model were connected to the support arm on each side. The model was suspended with a total of eight springs, with four on each side. During the experiment, thin piano wires were used to restrain the movement of the model in the torsional direction and the model was allowed to vibrate freely only in the vertical 1DOF direction as shown in Fig. 2.9.

The vertical displacement of the model (η (mm)) was measured by using laser displacement sensors (KEYENCE, IL-300). The digital data from the sensors was sent to the A/D adapter with a sampling frequency of 1,000 Hz. The vibration amplitude is noted as $2A_\eta$ (mm), which is defined as the peak-to-peak amplitude of each wave of the model displacement. The Scruton number utilised in this study was calculated from the following formula:

$$S_{c\eta} = \frac{2m\delta_\eta}{\rho D^2} \qquad \text{Eq. 2.8}$$

where m is the equivalent mass per unit length (kg/m), δ_η is the structural damping in terms of the logarithmic decrement at $2A$ = 2 mm measured in no-wind condition, ρ is the air density (kg/m^3), and D is the model depth (m). The structural parameters of wind tunnel test cases for each corner-shape altered section are listed in Table 2.1-2.7.

In this study, a total of six Scruton numbers (6, 42, 56, 69, 90, and 130) were used to study the aerodynamic interference between the Kármán vortex-induced vibration (KVIV) and the galloping instability. The structural damping in the lower Scruton number case (6, and 42) was provided with an electro-magnetic damper. The structural damping in the larger Scruton number case (56, 69, 90, and 130) was achieved by using the oil dampers. A schematic representation of the oil damper set-up is illustrated in Fig. 2.10.

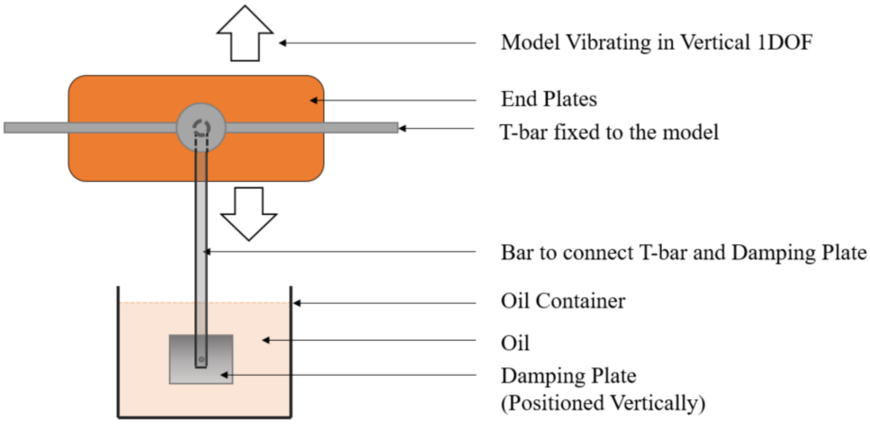

Fig. 2.10 Side view of the oil damper set-up (Manoj, 2022).

Table 2.1 Structural parameters of each test case for the vertical 1 DOF free vibration test of rectangular (R) section.

Attack angle, α [deg]	Equivalent mass, m [kg/m]	Natural frequency, f_n [Hz]	Logarithmic decrement, δ_η	$S_{c\eta}$
0	6.70	4.64	0.0043	6.07
0	6.83	4.58	0.0289	41.96
0	6.77	4.60	0.0385	55.40
0	6.82	4.58	0.0477	69.76
0	6.93	4.54	0.0606	90.13
0	7.01	4.51	0.0862	129.50
4	6.69	4.64	0.0045	6.18
4	6.72	4.64	0.0301	41.93
9	6.69	4.64	0.0044	6.11
9	6.68	4.64	0.0300	41.95

Table 2.2 Structural parameters of each test case for the vertical 1 DOF free vibration test of single recession (SR) section.

Attack angle, α [deg]	Equivalent mass, m [kg/m]	Natural frequency, f_n [Hz]	Logarithmic decrement, δ_η	$S_{c\eta}$
0	6.74	4.62	0.0043	6.18
0	6.79	4.60	0.0291	42.32
0	6.73	4.62	0.0385	55.60
0	6.76	4.60	0.0473	68.73
0	6.88	4.56	0.0609	89.97

Table 2.3 Structural parameters of each test case for the vertical 1 DOF free vibration test of double recession (DR) section.

Attack angle, α [deg]	Equivalent mass, m [kg/m]	Natural frequency, f_n [Hz]	Logarithmic decrement, δ_η	$S_{c\eta}$
0	6.81	4.59	0.0044	6.40
0	6.84	4.58	0.0288	42.15
0	6.79	4.60	0.0382	55.58
0	6.84	4.57	0.0473	69.96
0	6.90	4.54	0.0617	91.22

Table 2.4 Structural parameters of each test case for the vertical 1 DOF free vibration test of double recession II (DR II) section.

Attack angle, α [deg]	Equivalent mass, m [kg/m]	Natural frequency, f_n [Hz]	Logarithmic decrement, δ_η	$S_{c\eta}$
0	6.81	4.60	0.0044	6.37
0	6.84	4.58	0.0292	42.45
0	6.77	4.60	0.0384	55.65
0	6.78	4.59	0.0473	68.92
0	6.92	4.55	0.0590	87.48

Table 2.5 Structural parameters of each test case for the vertical 1 DOF free vibration test of double recession III (DR III) section.

Attack angle, α [deg]	Equivalent mass, m [kg/m]	Natural frequency, f_n [Hz]	Logarithmic decrement, δ_η	$S_{c\eta}$
0	6.81	4.60	0.0043	6.21
0	6.86	4.58	0.0291	42.46
0	6.76	4.60	0.0381	55.14
0	6.84	4.58	0.0468	68.87
0	6.94	4.55	0.0602	89.70
2	6.67	4.64	0.0043	5.98
2	6.71	4.63	0.0296	41.88
4	6.71	4.64	0.0044	6.20
4	6.74	4.63	0.0296	42.06

Table 2.6 Structural parameters of each test case for the vertical 1 DOF free vibration test of triple recession (TR) section.

Attack angle, α [deg]	Equivalent mass, m [kg/m]	Natural frequency, f_n [Hz]	Logarithmic decrement, δ_η	$S_{c\eta}$
0	6.84	4.58	0.0043	6.31
0	6.87	4.57	0.0288	42.42
0	6.81	4.59	0.0386	56.11
0	6.86	4.57	0.0470	69.68
0	6.96	4.53	0.0598	89.30
2	6.73	4.62	0.0043	5.98
2	6.73	4.6	0.0299	42.14
4	6.75	4.63	0.0042	5.98
4	6.73	4.63	0.0299	41.70

Table 2.7 Structural parameters of each test case for the vertical 1 DOF free vibration test of chamfer (C) section.

Attack angle, α [deg]	Equivalent mass, m [kg/m]	Natural frequency, f_n [Hz]	Logarithmic decrement, δ_η	$S_{c\eta}$
0	6.89	4.57	0.0042	6.26
0	6.93	4.55	0.0284	42.22
0	6.88	4.57	0.0377	55.55
0	6.91	4.55	0.0470	69.55
0	7.03	4.51	0.0595	89.57

2.3.3 Unsteady aerodynamic force measurement under forced vibration

The vertical 1-DOF forced vibration tests were conducted to measure the unsteady aerodynamic force acting on both rectangular and corner-cut cylinders. The model was fixed to the supporting system, which is present outside of the wind tunnel, as shown in Fig. 2.11. The rubber-toothed belt, also known as a timing belt, was used to link the ground motor (SPEEFFYNE, SD-400-11A) and the supporting system and allowed to vibrate the model in the vertical direction. Four laser gauges (KEYENCE, IL-300), two on each side of the model, were used to record the displacement of the model. The two load cells (NISHO ELECTRIC WORKS CO. LTD MULTI COMPONENT LOADCELL MODEL LMC-3501-50N) attached on each side of the model were used to measure the forces acting on the vibrating model. The sampling frequency was 1,000 Hz and the recording time was 180 sec.

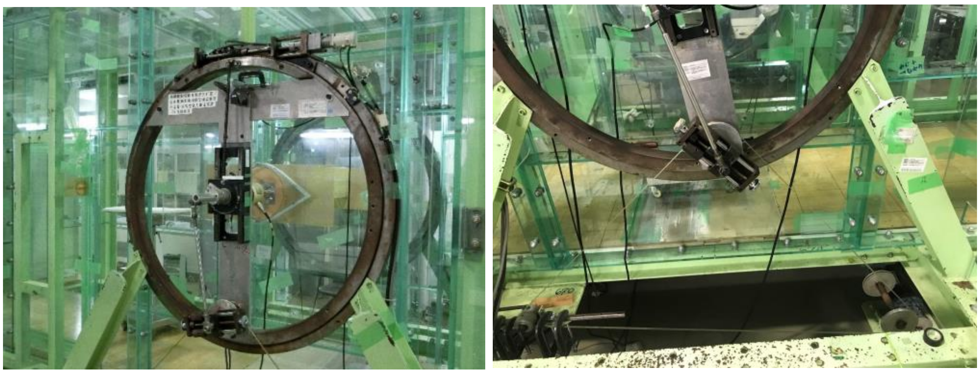

(a) (b)

Fig. 2.11 Vertical 1-DOF forced vibration test set-up; (a) model; and (b) motor.

Scanlan and Tomko (1971) described the self-excited aerodynamic forces acting on the vibrating model as follows:

$$L_{se} = \frac{1}{2}\rho(2b)U^2\left\{kH_1^*\frac{\dot{\eta}}{U} + kH_2^*\frac{b\dot{\varphi}}{U} + k^2H_3^*\varphi + k^2H_4^*\frac{\eta}{b}\right\} \quad \text{Eq. 2.9}$$

where L_{se} is the self-excited transverse force per unit span (N/m) (downward positive), ρ is the air density (kg/m^3), b is half of the model width B (m), U is the wind velocity (m/s), k is the reduced frequency ($b\omega/U$), ω is the angular frequency (rad/s), η is the vertical displacement (m) (downward positive), $\dot{\eta}$ is the time differentiation of η, φ is the torsional displacement (deg), $\dot{\varphi}$ is the time differentiation of φ, H_i^* (i = 1~4) is the aerodynamic derivatives. Scanlan and Tomoko (1971) mentioned that these aerodynamic derivatives can be used to check the presence of different aerodynamic instabilities in the tested model.

Generally, the force measured by the load cells during the measurement/test includes both the inertial and the aerodynamic forces. Hence, the aerodynamic force acting on the vibrating model was calculated by subtracting the inertial force from the measured force. Here, the inertial force acting on the vibrating model was obtained in no wind condition.

The digital system phase lag between the force and displacement was calculated by putting an additional mass of approximately 400g onto the model. This additional mass was put on the model to increase the measured force since the inertial force of the current model is small. The displacement is expressed as $disp = disp_0 e^{i\omega t}$. In the no wind condition, theoretically, there is no phase lag between the force and displacement. Then, the inertial force acting on the vibrating model can be written as:

$$F = F_0 \exp\big(i(\omega t - \Delta)\big) \qquad \text{Eq. 2.10}$$

where F_0 is the amplitude of inertial force, Δ is the digital phase lag between the displacement and the system. In the windy condition, the measured force F is expressed as:

$$F = F_t exp\big(i(\omega t - \psi_t)\big) \qquad \text{Eq. 2.11}$$

$$F = \{F_a exp\big(i(\omega t - \psi_a)\big) + F_0 exp(i(\omega t))\} exp(i(-\Delta)) \qquad \text{Eq. 2.12}$$

where F_t is the amplitude of the measured force (combination of the inertial and aerodynamic forces) in the windy condition, ψ_t is the phase lag between the measured force F and displacement, F_a is the amplitude of the aerodynamic force acting on the vibrating model in the windy condition, ψ_a is the phase lag between the aerodynamic force and displacement.

When the model is under vertical 1-DOF sinusoidal vibration, the displacement and the unsteady transverse force can be expressed as:

$$\eta(t) = \eta_0 \sin \omega t \qquad \text{Eq. 2.13}$$

$$L_{se} = L_{\eta 0}\, sin(\omega t - \psi_{L\eta}) \qquad \text{Eq. 2.14}$$

where η_0 is the displacement amplitude, $L_{\eta 0}$ is the amplitude of the transverse force per unit length in vertical 1DOF direction and $\psi_{L\eta}$ is the phase lag between unsteady transverse force and the displacement. Here, $L_{\eta 0}$ is positive in the downward direction. For a body oscillating in vertical 1DOF, by ignoring the torsional terms, Eq. 2.9 can be written as:

$$L_{se} = \frac{1}{2}\rho(2b)U^2 \left\{kH_1^* \frac{\dot{\eta}}{U} + k^2 H_4^* \frac{\eta}{b}\right\} \qquad \text{Eq. 2.15}$$

By equating equations Eq. 2.14 and Eq. 2.15, and substituting trigonometric functions obtained from the time-dependent derivative of Eq. 2.13, the equations of the aerodynamic derivatives were obtained.

In this study, the aerodynamic derivatives (H_1*and H_4*) were calculated using the following equations:

$$H_1^* = -\frac{L_{\eta 0}\, sin\, \psi_{L\eta}}{\rho b^2 \omega^2 \eta_0} \qquad \text{Eq. 2.16}$$

$$H_4^* = \frac{L_{\eta 0} \cos \psi_{L\eta}}{\rho b^2 \omega^2 \eta_0} \qquad \text{Eq. 2.17}$$

where H_1^* is the dimensionless aerodynamic damping, H_4^* is the dimensionless aerodynamic stiffness. The positive H_1^* value indicates the presence of aerodynamic instability in the vertical direction of the model. The negative H_1^* value indicates the model is stable.

Table 2.8 Structural parameter of each test for the vertical 1 DOF forced vibration test (1/2).

Section	Model configuration	Attack angle, α [deg]	Vibration frequency, f [Hz]	Vibration double amplitude, $2A$ [mm]		
Rectangular (R)		0	1.5	2.25	9	27
		0	2.0	2.25	9	27
		0	2.6	2.25	9	27
		+ 4	2.6	2.25	9	27
		+ 9	2.6	2.25	9	27
Single recession (SR)		0	1.5	2.25	9	27
		0	2.0	2.25	9	27
		0	2.6	2.25	9	27
Double recession (DR)	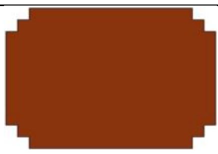	0	2.0	2.25	9	27
		0	2.6	2.25	9	27
Double recession II (DR II)	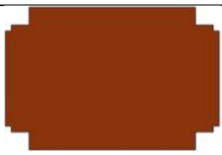	0	2.0	2.25	9	27
		0	2.6	2.25	9	27
Double recession III (DR III)		0	2.0	2.25	9	27
		0	2.6	2.25	9	27
		+ 2	2.6	2.25	9	27
		+ 4	2.6	2.25	9	27
Triple recession (TR)		0	2.0	2.25	9	27
		0	2.6	2.25	9	27
		+ 2	2.6	2.25	9	27
		+ 4	2.6	2.25	9	27

Table 2.8 Structural parameter of each test for the vertical 1 DOF forced vibration test (2/2).

Section	Model configuration	Attack angle, α [deg]	Vibration frequency, f [Hz]	Vibration double amplitude, $2A$ [mm]		
Chamfer (C)		0	2.0	2.25	9	27
		0	2.6	2.25	9	27

2.4 Outline of the computational fluid dynamics simulation

Nowadays, computational fluid dynamics (CFD) is widely used to calculate the aerodynamic performance and flow field characteristics around a particular structure. This reduces the number of wind tunnel experiments in certain situations. However, the need to regenerate meshes around the model every time the structure changes is time-consuming and demanding. In addition, the accuracy of CFD simulations is not guaranteed. Validation with wind tunnel test results is still required to determine whether these simulation results can be used in discussion or not. Since Large Eddy Simulation (LES) is efficient in handling the flow around complex shaped structures and provides highly accurate results, as mentioned in Section 1.1.9, LES was used in this study. In the following sections, a general description of the mesh type and numerical simulation method were provided.

2.4.1 Mesh algorithm

Hybrid meshes and unstructured solvers are also promising for geometries with significant rounded surfaces (Mannini et al., 2011). Both structured and unstructured meshes are widely used in CFD simulations. Structured meshes are simple and efficient. They offer high-accuracy simulation with low numerical error and require less computational memory. On the other hand, unstructured meshes provide flexibility in handling complex geometries. Hence, an O-type grid was used to generate meshes around the corner-shape altered sections. For the Buddha statue, the unstructured mesh type of anisotropic tetrahedral mesh generation (Garimella, 1998) was used.

For the unstructured mesh, delaunay, advancing front and advancing front ortho approaches, which were the functions of the Pointwise mesh generation software, were employed. Fig. 2.12 shows the graphical representation of these algorithms with triangle and quad cells in the 2D view. Delaunay and advancing front algorithms filled the interior of the domain with isotropic cells when triangles or triangles and quads cell types were used. When only triangles cell type was used, the advancing front algorithm produced equilateral triangles that were more uniform in appearance than the delaunay algorithm. Advancing front ortho algorithm filled the interior of the domain with right-angled isotropic cells using the triangles or triangles and quads cells (Pointwise, 2019).

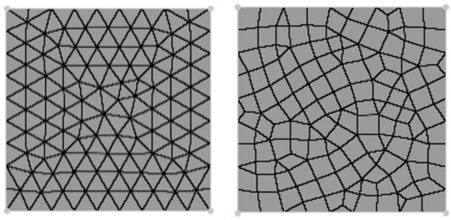

(a)

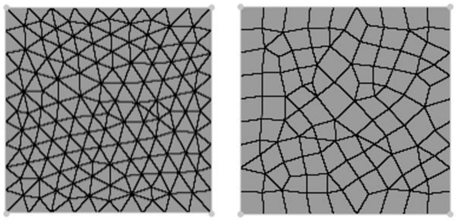

(b)

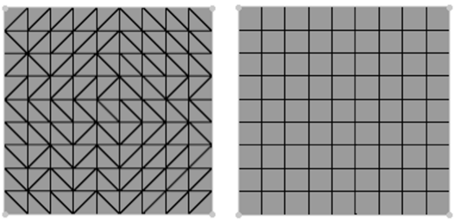

(c)

Fig. 2.12 Meshes composed with triangles (left side), and triangles and quads (right side) cells generated by; (a) delaunay; (b) advancing front; and (c) advancing front ortho algorithms (Pointwise, 2019).

2.4.2 Large eddy simulation

In the turbulent flows, the spinning or swirling fluid structures known as eddies are present. In the Large Eddy Simulation (LES), one of the turbulence mathematical models, the spatial filtering operation on the time-dependent flow equations was used to separate the large and small eddies. The large eddies, the length scale of which is greater than that of the filter cutoff width, are resolved. However, the small eddies are filtered out and destroyed. Hence, the sub-grid-scale or SGS stresses are produced due to the interaction between the large eddies (resolved) and small eddies (unresolved). This effect is described by the SGS model in the LES computation of turbulent flows. Since the contribution of the small-scale turbulence in the flow field is small, the errors introduced by this modelling are small (Versteeg and Malalasekera, 2007). Therefore, LES is chosen to be used in this study due to its small anticipated error and low computational cost.

For the incompressible flow, the Navier-Stokes equations can be expressed as:

$$\frac{\partial u_i}{\partial x_i} = 0 \qquad \text{Eq. 2.18}$$

$$\frac{\partial u_i}{\partial t} + u_j \frac{\partial u_i}{\partial x_j} = -\frac{1}{\rho}\frac{\partial p}{\partial x_i} + \frac{\partial}{\partial x_j}\left\{v\left(\frac{\partial u_i}{\partial x_j} + \frac{\partial u_j}{\partial x_i}\right)\right\} \qquad \text{Eq. 2.19}$$

where u_i is the velocity, v is the kinematic viscosity, p is the pressure, and ρ is the density.

Spatial filtering was used. The filtered incompressible Navier-Stokes equations and the equation of continuity are written as follows:

$$\frac{\partial \bar{u}_i}{\partial x_i} = 0 \qquad \text{Eq. 2.20}$$

$$\frac{\partial \bar{u}_i}{\partial t} + \bar{u}_j \frac{\partial \bar{u}_i}{\partial x_j} = -\frac{1}{\rho}\frac{\partial \bar{p}}{\partial x_i} + \frac{\partial}{\partial x_j}\left\{(v + v_{SGS})\left(\frac{\partial \bar{u}_i}{\partial x_j} + \frac{\partial \bar{u}_j}{\partial x_i}\right)\right\} \qquad \text{Eq. 2.21}$$

where $\bar{u}_i$ is the filtered velocity, v is the viscosity, $\bar{p}$ is the filtered pressure, ρ is the density, and v_{SGS} is the subgrid-scale eddy viscosity coefficient. The sub-grid scale stresses (SGS) are calculated by using the Smagorinsky Model (SM) (Smagorinsky, 1963) as follows:

$$v_{SGS} = (C_s \Delta)^2 |\bar{D}| \qquad \text{Eq. 2.22}$$

For the grid values close to the wall,

$$v_{SGS} = (C_s f_s \Delta)^2 |\bar{D}| \qquad \text{Eq. 2.23}$$

where f_s is the van Driest damping function and equal to $1 - e^{-y^+/A^+}$. In OpenFOAM 4.0 which is utilized in this research, v_{SGS} is represented as follows:

$$v_{SGS} = C_k \Delta \sqrt{k_{SGS}} \qquad \text{Eq. 2.24}$$

where the sub-grid scale kinetic energy k_{SGS} is obtained by assuming the balance between the sub-grid scale energy production and dissipation which is known as local equilibrium.

$$k_{SGS} = \frac{C_k \Delta^2 |\bar{D}|^2}{C_\epsilon} \qquad \text{Eq. 2.25}$$

By substituting Eq. 2.27 into Eq. 2.26,

$$v_{SGS} = C_k \sqrt{\frac{C_k}{C_\epsilon}} \Delta^2 |\bar{D}| \qquad \text{Eq. 2.26}$$

The relationship between C_k and C_S is written by comparing Eq. 2.24 and Eq. 2.28:

$$C_S^2 = C_k \sqrt{\frac{C_k}{C_\epsilon}} \qquad \text{Eq. 2.27}$$

In this study, C_S is set to 0.12 and the van Direst constant A^+ is 26.

Reference

Garimella, R. V. (1998). Anisotropic Tetrahedral Mesh Generation. Graduate Faculty of Rensselaer Polytechnic Institute, Rensselaer Polytechnic Institute, Troy, New York, December, 1998.

Mannini, C., Marra, A.M., Massai, T., & Bartoli, G. (2016). Interference of vortex-induced vibration and transverse galloping for a rectangular cylinder. *Journal of Fluids Structures*, 66. https://doi.org/10.1016/j.jfluidstructs.2016.08.002.

Mannini, C., Soda, A, & Schewe, G. (2011), Numerical investigation on the three-dimensional unsteady flow past a 5:1 rectangular cylinder. *Journal of Wind Engineering and Industrial Aerodynamics*, 99, 469–482.

Manoj, P. (2022). Effets of corner modifications on aerodynamic instability of rectangular cylinder. Master dissertation, Kyoto University, Japan.

Matsumoto, M., Shiraishi, N., & Shirato, H. (1988). Bluff body aerodynamics in pulsating flow. *Journal of Wind Engineering and Industrial Aerodynamics*, 28, 1–3, 261-270, https://doi.org/10.1016/0167-6105(88)90122-5.

Matsumoto, M., Yagi, T., Hatsuda, H., Shima, T., Tanaka, M., & Naito, H. (2010) Dry galloping characteristics and its mechanism of inclined/yawed cables. *Journal of Wind Engineering and Industrial Aerodynamics*, 98 (6–7), 317-327, https://doi.org/10.1016/j.jweia.2009.12.001.

Matsumoto, M., Yagi, T., Lee, J.H., Hori, K., & Kawashima, Y., 2006. Karman vortex effect on the aerodynamic forces to rectangular cylinders. *American Society of Mechanical Engineers, Pressure Vessels and Piping Division (Publication) PVP*. https://doi.org/10.1115/PVP2006-ICPVT-11-93783.

Nakaguchi, H., Hashimoto, K., & Muto, S. (1968). An experimental study on aerodynamic drag of rectangular cylinders. *Journal of Japan Society for Aeronautical and Space Sciences*, 16, 1-5. https://doi.org/10.2322/jjsass1953.16.1 (In Japanese).

Okajima, A. (1983). Flow around a rectangular cylinder with a section of various width/height ratios. *Journal of Wind Engineering (JAWE)*, 17, 1-19. (In Japanese) .

Otsuki, Y., Fujii, K., Washizu, K., & Ohaya, A. (1978). Wind tunnel experiments on aerodynamic forces and pressure distributions of rectangular cylinders in a uniform flow. *Proceedings of 5th Symposium on Wind Effects on Structures*, 169-176.

Pointwise (2019), https://www.pointwise.com/doc/user-manual/grid/solve/unstructured-domains/attributes-tab/algorithm.html. Accessed 2019.

Sakamoto, H., Haniu, H., & Kobayashi, Y. (1989). Fluctuating force acting on rectangular cylinders in uniform flow. *Transactions of the Japan Society of Mechanical Engineers*, 55(516), 2310–2317. https://doi.org/10.1299/kikaib.55.2310.

Scanlan, R.H., & Tomoko, J.J. (1971). Airfoil and bridge deck flutter derivatives. *Journal of Engineering Mechanics Division*, 97, 1717–1737. https://doi.org/10.1061/JMCEA3.0001526.

Shimada, K., & Meng, Y. (1998). Applicability of modified k-ε model on the estimation of aerodynamic properties of rectangular cylinders with various elongated cross sections. *Journal of Structural and Construction Engineering (Transactions of AIJ)*, 63 (514), 73-80.

Shiraishi, N., Matsumoto, M., Shirato, H., & Ishizaki, H. (1988). On aerodynamic stability effects for bluff rectangular cylinders by their corner-cut. *Journal of Wind Engineering and Industrial Aerodynamics*, 28. https://doi.org/10.1016/0167-6105(88)90133-X.

Smagorinsky, J. (1963): General circulation experiments with the primitive equation: I. The basic experiment. *Monthly weather review*, 91(3), 99-164.

Tamura, T., & Ito, Y. (1996). Aerodynamic characteristics and flow structures around a rectangular cylinder with a sesction of various depth/breadth ratios. *Journal of Structural and Construction Engineering (Transactions of AIJ)*, 61 (486), 153-162.

UNDP (United Nations Development Programme). (2011). Multi Hazard Risk Assessment in Rakhine State of Myanmar. Final Report, December.

Versteeg, H. K., & Malalasekera, W. (2007). An Introduction to Computational Fluid Dynamics: the Finite Volume Method. *Pearson Education Limited, Harlow, 2nd Edition.*

Washizu, K., Ohya, A., Otsuki, Y., & Fujii, K. (1978). Aeroelastic instability of rectangular cylinders in a heaving mode. *Journal of Sound and Vibration*, 59 (2), 198-210. https://doi.org/10.1016/0022-460X(78)90500-X.

Chapter 3
Aerodynamic performance of rectangular cylinder with corner modifications

3.1 Introduction

An overview of previous studies also revealed that the square and rectangular cylinders with corner modifications were effective in reducing aerodynamic force coefficients and efficient in mitigating aerodynamic instabilities of structures (Shiraishi et al., 1988; Hayashida and Iwasa, 1990; Choi and Kwon, 2001; Tse et al., 2009; Elshaer et al., 2014; Alminhana et al., 2018). The tower of the Higashi-Kobe bridge, a long-spanned cable-stayed bridge, also utilized corner-cut sections. It was found that cutting the corners of the bridge tower stabilized the wind-induced vibrations of the towers along the bridge axis not only after completion but also during the construction of the bridge (Ogawa et al. 1990). The aero-elastic study of the Messina Straits Bridge proved that improving the shape of the bridge deck and towers by adding plates or grid surfaces disturbed the formation of vortexes at their onset wind velocity (Diana et al., 2002). In this chapter, the effect of corner shape modification on the Kármán vortex shedding of the rectangular cylinder (B/D = 1.5, B is the width and D is the depth of the cylinder) was investigated.

The corner modification method has been widely used in bridge towers and high-rise buildings. However, the aerodynamic properties of corner-cut cylinders were likely to be sensitive to the Reynolds number depending on the side ratios and corner shapes (Shirato and Matsumoto, 1994; Cao and Tamura, 2018, Wang et al., 2020). In addition, the efficiency of the corner modification method in the mitigation of aerodynamic instabilities varied depending on the angle of attack (Choi and Kwon, 1999). When the angle of attack changed, the flow patterns around the cylinder and the effectiveness of the corner modification on the aerodynamic characteristics also changed (Alam et al., 2020). Therefore, it is necessary to investigate the effect of the corner shape modification on the aerodynamic characteristics of the rectangular cylinder and the flow field around it at various angles of attack for different Reynolds numbers. Hence, in this study, the aerodynamic characteristics (such as C_{Fx}, C_{Fy}, C_M, St, C'_{Fy}) of rectangular and corner-cut cylinders were discussed for the angle of attack of $-3° \leq \alpha \leq +15°$ and the Reynolds number of $36{,}000 \leq Re \leq 64{,}800$.

Wind tunnel experiments were carried out to describe the effect of the corner shape modification on the aerodynamic performance of the rectangular cylinder of side ratio (B/D) 1.5. In Section 3.2, the aerodynamic characteristics of the rectangular cylinder with different corner shapes are discussed for various attack angles. The Reynolds number effect on the aerodynamic characteristics of each section is also provided. Finally, Section 3.3 provides the summary and conclusion based on the objectives mentioned above.

3.2 Aerodynamic characteristics

Aerodynamic force measurements of stationary model were made for the seven types of corner-shape altered sections, including the original rectangular cylinder, for two different wind velocities, 6.0 m/s (*Re* = 36,000) and 10.8 m/s (*Re* = 64,800). The Reynolds number was defined according to Eq. 1.17. A total of seven sections, which were denoted as the rectangular (R), single recession (SR), double recession (DR), double recession II (DR II), double recession III (DR III), triple recession (TR), and chamfer (C), were utilised in this study. Detailed information for each section was provided in Section 2.2.2. Aerodynamic characteristics of each section such as the aerodynamic coefficients (C_{Fx}, C_{Fy}, C_M), the Kármán vortex shedding intensity (C'_{Fy}) and the Strouhal number (*St*) were discussed in the following sections.

3.2.1 Aerodynamic coefficients

Fig. 3.1 shows the effect of corner-shape modification on the aerodynamic force coefficients of the rectangular cylinder. Fig. 3.1 (a) shows the longitudinal force coefficient (C_{Fx}) for the wind velocity of 10.8 m/s (*Re* = 64,800). At $\alpha = 0°$, the R section has a C_{Fx} value of 1.72. This agrees with the experimental data reported by Mannini et al. (2016). When the number of recession steps was reduced in the order of TR, DR and SR, the C_{Fx} value was decreased to 1.23, 1.15 and 1.08, respectively. Hence, the reduction of the recession step number may decrease the Kármán vortex shedding.

When the DR section was modified into the DR II and DR III sections, the C_{Fx} values became 1.04 and 1.16. These three sections have the same double recession-type corners but the size and orientation of the inner step were different. Hence, the size and orientation as well as the number of the recession step affected the Kármán vortex shedding. In the section with the slope-type corner, the C section, the C_{Fx} value was 1.11. This value was slightly smaller than the TR section. Thus, the type of corner also played an important role in the Kármán vortex shedding reduction.

Overall, all corner-shape altered sections considerably reduced the C_{Fx} value of the original R section by about 17–40 % within the investigated attack angle range of $-3° \leq \alpha \leq +15°$. Among the all corner-shape altered sections, the SR and DR II sections were the most effective in decreasing the C_{Fx} value in the studied attack angle range.

Fig. 3.1 (b) shows the transverse force coefficient (C_{Fy}) for the wind velocity of 10.8 m/s (*Re* = 64,800). Hemon (2002) mentioned that when the flow reattaches on the model side surfaces, the transverse force coefficient slope becomes positive and galloping does not occur. In the R section, the transverse force coefficient slope changed from negative to positive at $\alpha = +10°$, where the flow reattachment was expected to occur. In the corner-shaped altered sections, the slope of the transverse force coefficient changed from negative to positive between +4° and +7°. Thus, in these sections, the flow is reattached at a smaller attack angle compared to the original rectangular section. Hence, the flow separated from the leading edge of these sections may appear closer to the side surfaces. This may produce a narrower wake region in the corner-shaped altered sections. The C_{Fy} values of all sections, except the DR section, were approximately zero at $\alpha = 0°$. Hence, the symmetric time-averaged flow was observed in these sections.

Fig. 3.1 (c) shows the moment coefficient (C_M) for the wind velocity of 10.8 m/s (*Re* = 10.8 m/s). The values of C_M were very small in all studied corner-shape altered sections. The aerodynamic coefficients of all sections at *U* = 6.0 m/s (*Re* = 36,000) and *U* = 10.8 m/s (*Re* = 64,800) were provided in Appendix B. The Reynolds number dependency was not observed in the investigated range of 36,000 ≤ *Re* ≤ 64,800 for all sections, except the DR section.

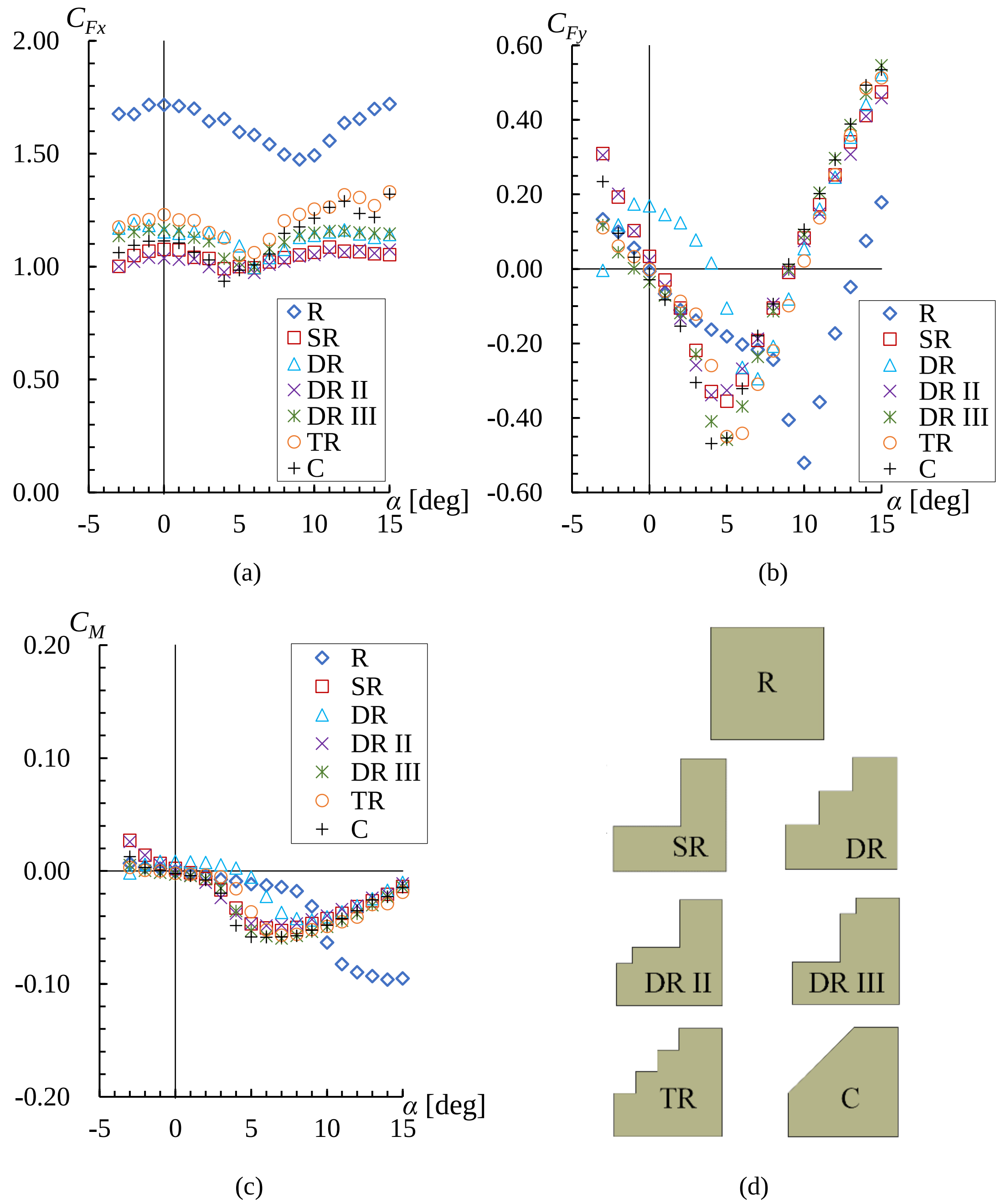

Fig. 3.1 Aerodynamic force coefficients (*U* = 10.80 m/s, *Re* = 64,800): (a) longitudinal force coefficient (C_{Fx}); (b) transverse force coefficient (C_{Fy}); (c) moment coefficient (C_M); and (d) corner configuration.

3.2.2 Reynolds number dependency of double recession type sections

Since a significant Reynolds number dependency was observed in the aerodynamic coefficients (C_{Fx}, C_{Fy} and C_M) of the DR section, additional measurements were made for DR, DR II and DR III sections within $-5° \leq \alpha \leq +5°$ considering the possibility of the sensitivity of the inner recession step to the flow separation. These measurements were made at four wind velocities, namely, 6.0, 10.0, 10.8 and 14 m/s to study the Reynolds number effect on the aerodynamic coefficients within the *Re* range of 36,000 and 84,000. Sketches of the studied double recession-type corners are illustrated in Fig. 3.2.

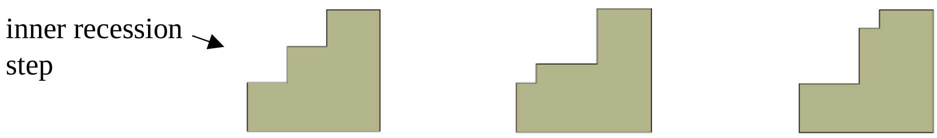

(a) (b) (c)

Fig. 3.2 Double recession type corners: (a) DR; (b) DR II; and (c) DR III.

Fig. 3.3 to 3.5 provide the aerodynamic force coefficients of the DR, DR II and DR III sections for different *Re*, respectively. For the C_{Fx} values, a small difference was present between Re = 36,000 and the other *Re* values as shown in Fig. 3.3 (a). In the DR II and DR III sections, as shown in Figs. 3.4 (a) and 3.5 (a), Reynolds number dependency was not observed. However, a small variation was present in the C_{Fx} value of the DR III section. Therefore, the along-wind forces (F_x) of these three sections were unlikely to vary much within the studied wind velocity range.

For the C_M values, the Reynolds number dependency was observed between Re = 36,000 and the other *Re* values in the attack angle below $\alpha = -2°$ and above $\alpha = +2°$ of the DR section as shown in Fig. 3.3 (c). On the other hand, the Reynolds number dependency was not observed in the DRII and DR III sections as shown in Figs. 3.4 (c) and 3.5 (c). Therefore, in the DR section, changes in the moment distribution were likely to be small only within $-2° \leq \alpha \leq +2°$.

For the C_{Fy} values, the Reynolds number dependency was observed at all angles of attack in the DR section as illustrated in Fig. 3.3 (b). In the DR II section, the C_{Fy} value changed a little with the Reynolds number within the angle of attack of $-4° \leq \alpha \leq -1°$ and $+2° \leq \alpha \leq +5°$ as shown in Fig. 3.4 (b). In the DR III section, as shown in Fig. 3.5 (b), the Reynolds dependency was not observed. Therefore, the flow patterns changed and the surface pressure distribution varied widely at the above-mentioned angles of attack of the DR and DR II sections. Hence, the location of the inner recession step was quite sensitive to the flow separation and affected the transverse force coefficient (C_{Fy}).

Therefore, if the double recession corner is intended to be applied in practical infrastructures, it is important to consider the Reynolds number effect in the wind-resistant design. Furthermore, the pressure distribution around the model surfaces should be investigated to study the mechanism of *Re* effects on the aerodynamic forces of these sections.

At $\alpha = 0°$, the slope of the transverse force coefficient ($dC_{Fy}/d\alpha$) of DR section have a negative value. When the *Re* was increased from 36,000 to 60,000, the $dC_{Fy}/d\alpha$ became positive. This positive sign of the $dC_{Fy}/d\alpha$ remained the same even when the Reynolds number was further increased. As the negative sign of the transverse force coefficient represents the possibility of galloping instability, the DR section might be stable after Re = 60,000 (U = 10 m/s) at α = 0°. On the other hand, the $dC_{Fy}/d\alpha$ of the DR II and DR III sections has a negative value throughout the studied Re range. Thus, these two sections were susceptible to galloping instability at α = 0°.

At α = 0°, the C_{Fy} of the DR section was non-zero at Re = 36,000. On the other hand, the C_{Fy} of the DR II and DR III sections were approximately zero at α = 0°. The only difference between DR, DR II and DR III sections was the position of the inner recession step as shown in Fig. 3.2. Hence, the

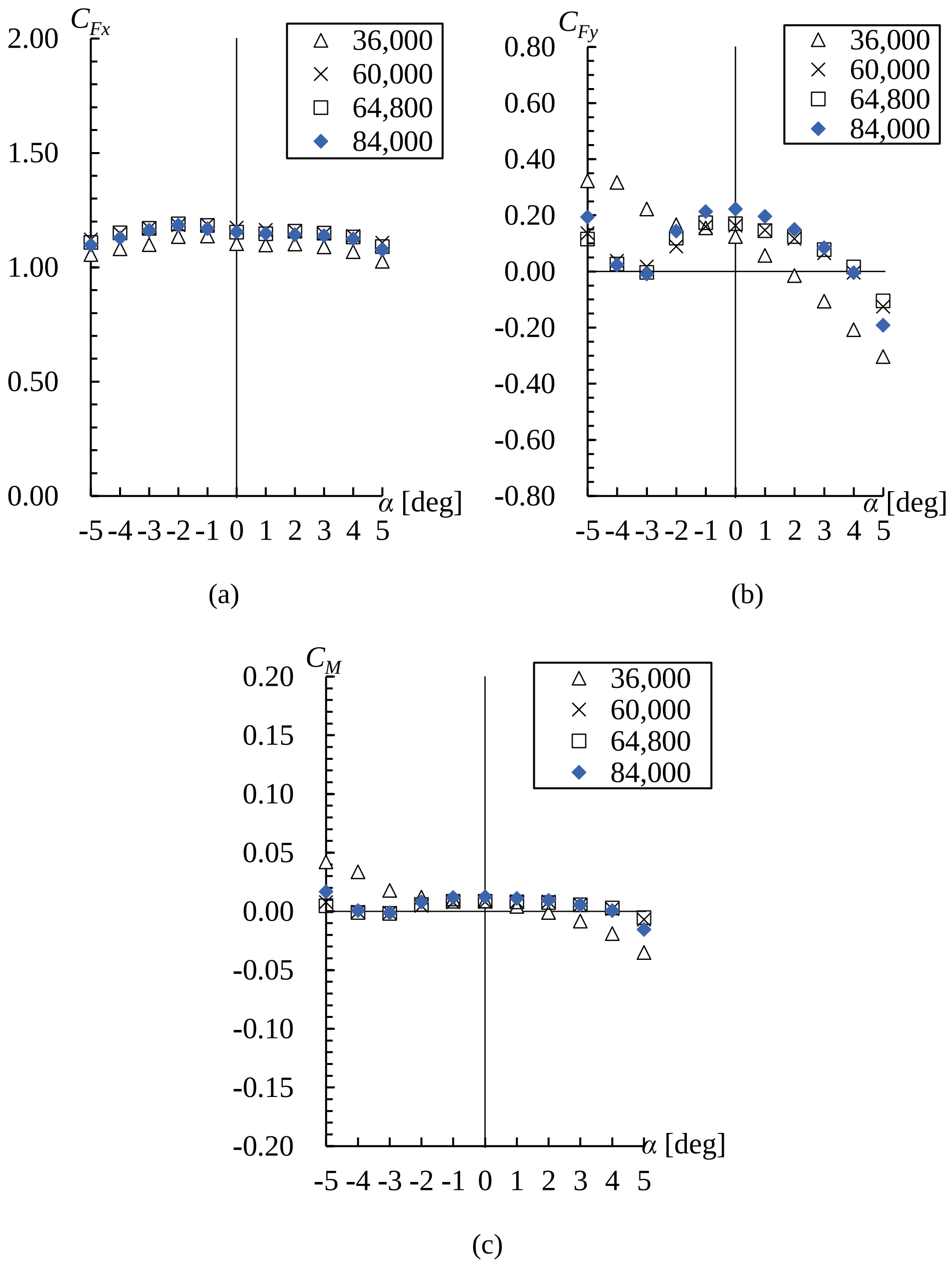

Fig. 3.3 Aerodynamic force coefficients of DR section for various Re: (a) longitudinal force coefficient (C_{Fx}); (b) transverse force coefficient (C_{Fy}); and (c) moment coefficient (C_M).

position of the inner recession step affected the symmetricity of the flow separation as the C_{Fy} of the DR section was non-zero while the C_{Fy} of DR II and DR III were approximately zero. Placing the inner recession step in the middle of the corner (Fig. 3.2 (a)) may produce the Reynolds number dependency but this may also stabilise the vibration of the section in the *Re* region higher than 60,000.

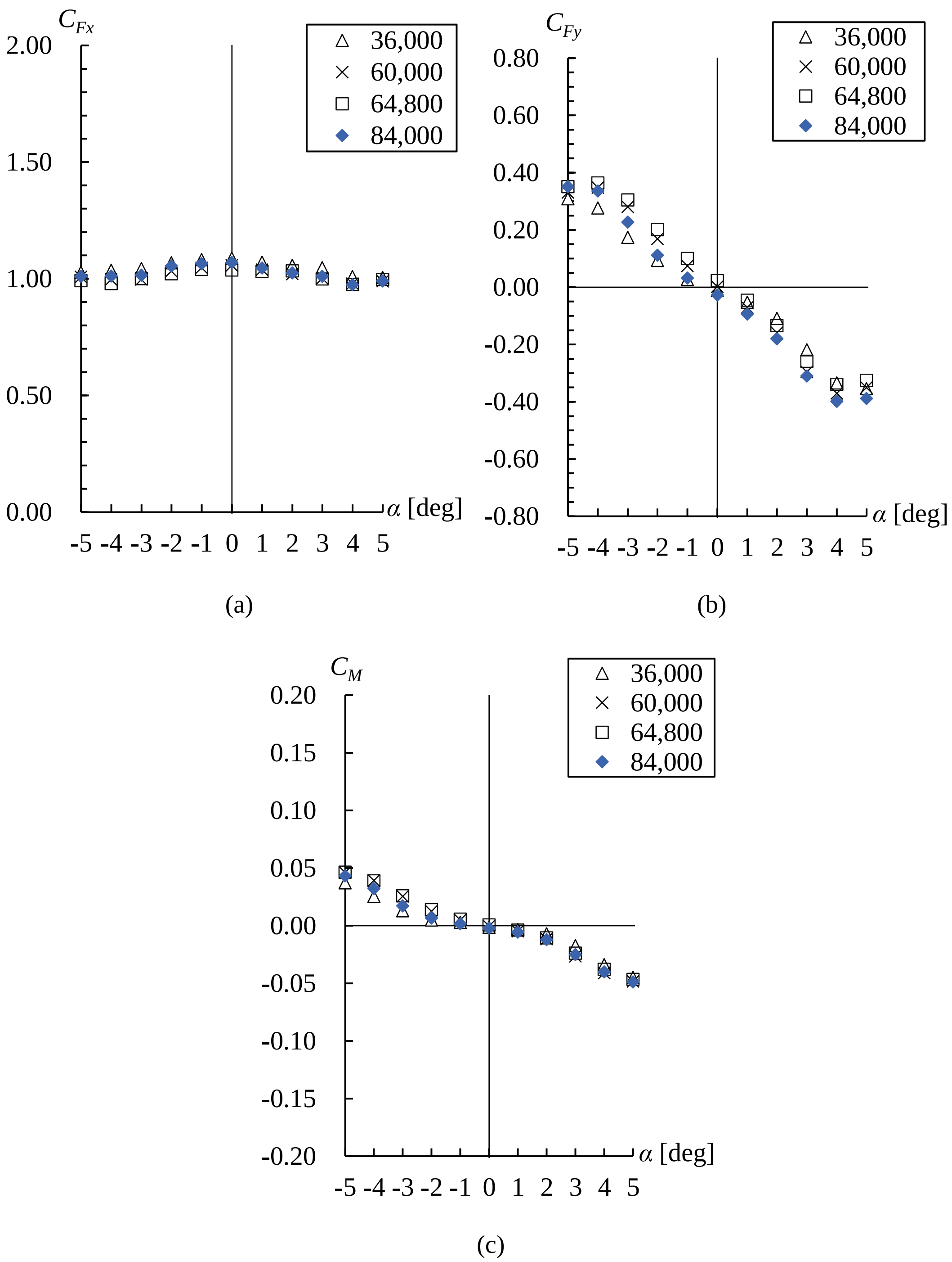

Fig. 3.4 Aerodynamic force coefficients of DR II section for various *Re*: (a) longitudinal force coefficient (C_{Fx}); (b) transverse force coefficient (C_{Fy}); and (c) moment coefficient (C_M).

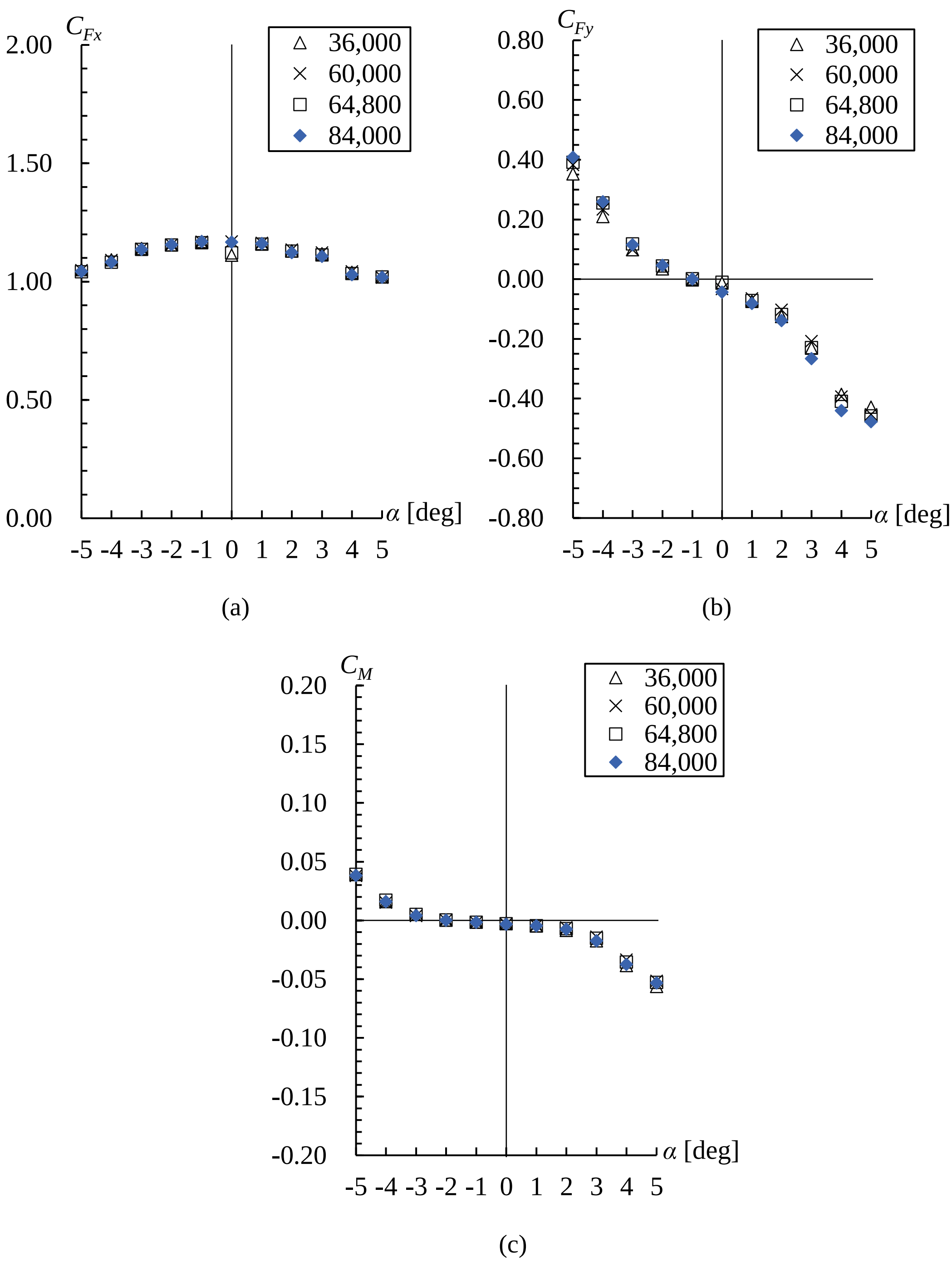

Fig. 3.5 Aerodynamic force coefficients of DR III section for various *Re*: (a) longitudinal force coefficient (C_{Fx}); (b) transverse force coefficient (C_{Fy}); and (c) moment coefficient (C_M).

The flow asymmetricity of the DR section was further studied by flipping the lower and upper surfaces of the model as shown in Fig. 3.6. Static force measurements were made at three wind velocities (U = 6.0, 10.0 and 14.0 m/s) for this inverted DR section. This covered the *Re* range of $36{,}000 \leq Re \leq 84{,}000$. The transverse force coefficient of the DR section for the normal case is shown in Fig. 3.7 (a) and the inverted case is shown in Fig. 3.7 (b). When the model was inverted, the C_{Fy}

graph also got reversed. Therefore, the asymmetric flow observed in the DR section may be caused by the geometrical issues of the model surface. This might also be one of the factors contributing to the Reynolds number dependency of the DR section. Hence, the DR section is highly sensitive to the shape and requires higher model precision.

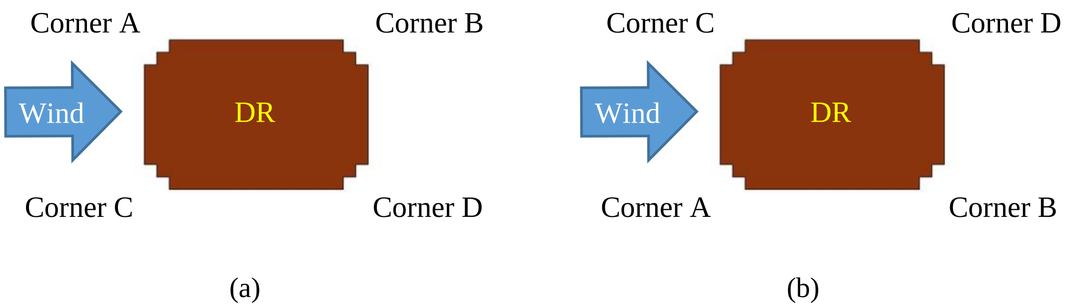

Fig. 3.6 Corner positions for DR section: (a) normal case; and (b) inverted case.

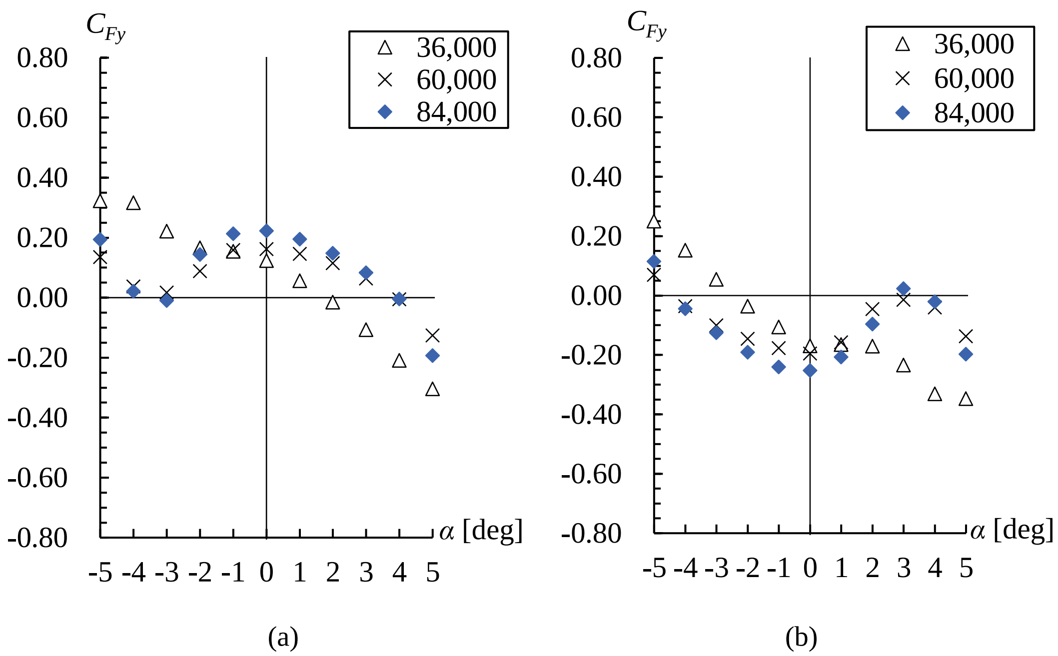

Fig. 3.7 Transverse force coefficient of DR section: (a) normal case; and (b) inverted case.

3.2.3 Kármán vortex shedding intensity and Strouhal number

The fluctuating transverse force coefficient (C'_{Fy}), which indicated the intensity of the Kármán vortex shedding and the Strouhal number (*St*) was calculated according to Eq. 2.5 and Eq. 1.15. In the following sections, the relation between the angle of attack (α), and the C'_{Fy} and *St* values were discussed for each cross-sectional shape. The power spectral density (PSD) of the transverse force was also provided for each section. The time-frequency scalograms of the transverse force for each corner modified section were also provided in Appendix C. The static wind tunnel measurements were made for two different wind velocities (U = 6.0 m/s and 10.8 m/s). However, two additional measurements

(U = 10.0 m/s and 14.0 m/s) were made for the double recession-type sections due to their Reynolds number dependency. Hence, the measured Re ranges from 36,000 to 84,000. In the following discussion, we mention the apparent side ratio of a section. For instance, as shown in Fig. 3.8, the Single Recession section (SR) has two possible corners where the flow separation occurs. Thus, the apparent side ratio of a section is probably different from that of the original rectangular cylinder with B/D = 1.5. According to Washizu et al. (1978), Tamura and Ito (1996), Shimada and Meng (1998), and Matsumoto et al. (2006), the Strouhal numbers of rectangular cylinders with B/D of 1.25, 1.5, and 2.5 were approximately 0.114–0.124, 0.100–0.108, and 0.047–0.180. These values are referred to in the following sections for a detailed discussion.

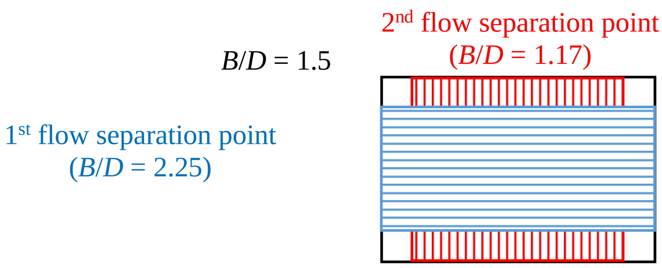

Fig. 3.8 Probable flow separation points based on the approximate B/D value.

(1) Rectangular (R)

In the R section, as shown in Fig. 3.9 (a), the fluctuating transverse force coefficient which indicated the Kármán vortex shedding intensity (C'_{Fy}) was the largest at α = 0° in both Re values. The C'_{Fy} value decreased with increasing angle of attack and reached its lowest value at α = +9°. From α = +10°, the C'_{Fy} value increased with increasing angle of attack. As for the Strouhal number (St), the values remained approximately the same within the angle of attack of $-3° \leq \alpha \leq +8°$. A sudden increase in St values was observed at α = +9°, reaching a maximum at α = +10°. Knisely (1990) mentioned that a rapid rise in the St occurred at a relatively small α. This rapid rise was associated with the reattachment of separated shear layers and was dependent on the side ratio (Knisely, 1990). Hence, the flow reattachment may occur at α = +9° in the R section. From α = +11°, the St value slightly decreased with increasing angle of attack. No significant Reynolds number dependency was observed in the R section within the studied Re range.

Fig. 3.9 (b) shows the power spectral density (PSD) of transverse force for the R section at α = 0° for U = 6.0 m/s. A large peak corresponding to St = 0.104 was observed. The time-frequency scalogram of the transverse force also showed a steady dominant frequency of 6.943 Hz (Fig. C.1 (a), Appendix C). Hence, the vortex shedding of the R section at α = 0° was strong and the flow separation might only occur at one fixed location. In addition, a small peak corresponding to a triple of the Strouhal component was also observed in this study. A similar phenomenon was also reported by Mannini et al (2016) for Re of 29,200 and 147,100.

Fig. 3.9 (c) shows the PSD of transverse force for the R section at α = +9° for U = 6.0 m/s. The frequency peak was not as clear as that at α = 0°. The time-frequency scalogram of the transverse force showed an unsteady weak frequency peak of 9.003 Hz (Fig. C.1 (c), Appendix C) which corresponded to the *St* of 0.135. Thus, the Kármán vortex shedding of the R section at α = +9° was weak compared to that of α = 0°. The flow patterns were unsteady and might change abruptly, and instantaneous and/or time-average flow reattachment might also be observed at α = +9°. In the R section, the time-averaged flow reattachment was known to occur at α = +10° based on the C_{Fy} value (Fig. B.1 (b)). When the flow reattachment occurred, a moderately strong frequency peak of 9.415 Hz was observed as shown in Fig. 3.9 (d) and Fig. C. 1 (e). This frequency corresponds to a sudden increase in the *St* of 0.141. In addition, a small and weak frequency peak corresponding to twice the Strouhal component was also observed. After the flow reattachment, the C'_{Fy} steadily increased while the *St* decreased. As 1/*St* denotes the onset of Kármán vortex-induced vibration, the onset reduced wind velocity of the R section might be small at the angles of attack in which the flow reattachment occurred.

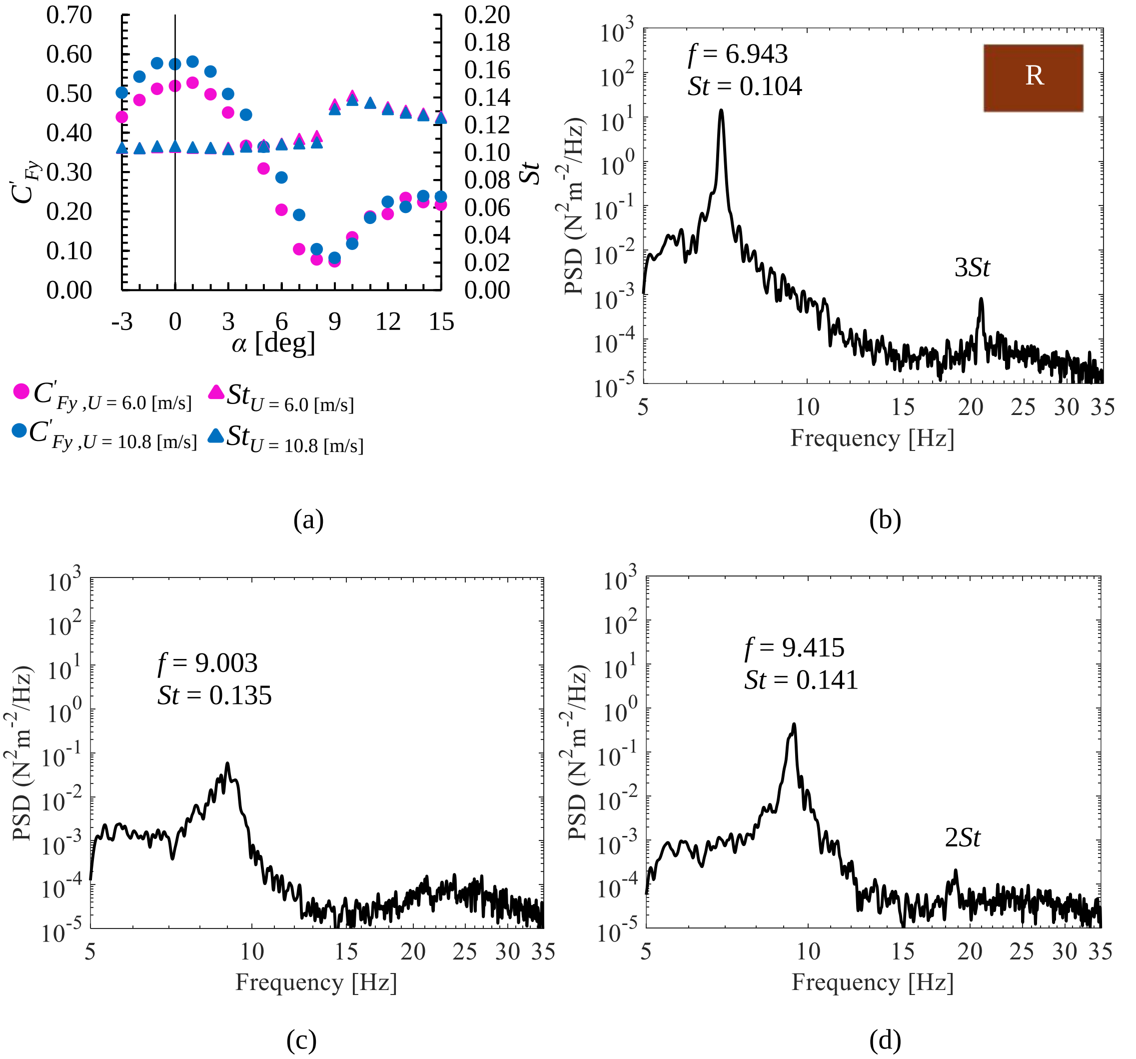

Fig. 3.9 R section: (a) the fluctuating transverse force coefficient which indicated Kármán vortex shedding intensity (C'_{Fy}) and Strouhal number (*St*); power spectra of transverse force for U = 6.0 m/s (*Re* = 36,000) at (b) α = 0°; (c) α = +9°; and (d) α = +10°.

(2) Single Recession (SR)

In the SR section, the C'_{Fy} was approximately 0.04–0.05 at α = 0° in both *Re* values as shown in Fig. 3.10 (a). The C'_{Fy} value remained approximately the same within the angle of attack of $-3° \leq \alpha \leq +4°$. Starting from α = +5°, the C'_{Fy} value increased with the increasing angle of attack. Abrupt changes in *St* values were observed within $-3° \leq \alpha \leq +3°$. An increase in *St* values was observed at α = +4°, having a maximum value at +5°. From α = +6°, the *St* value decreased with increasing angle of attack. No significant Reynolds number dependency was observed in the R section within the studied *Re* range.

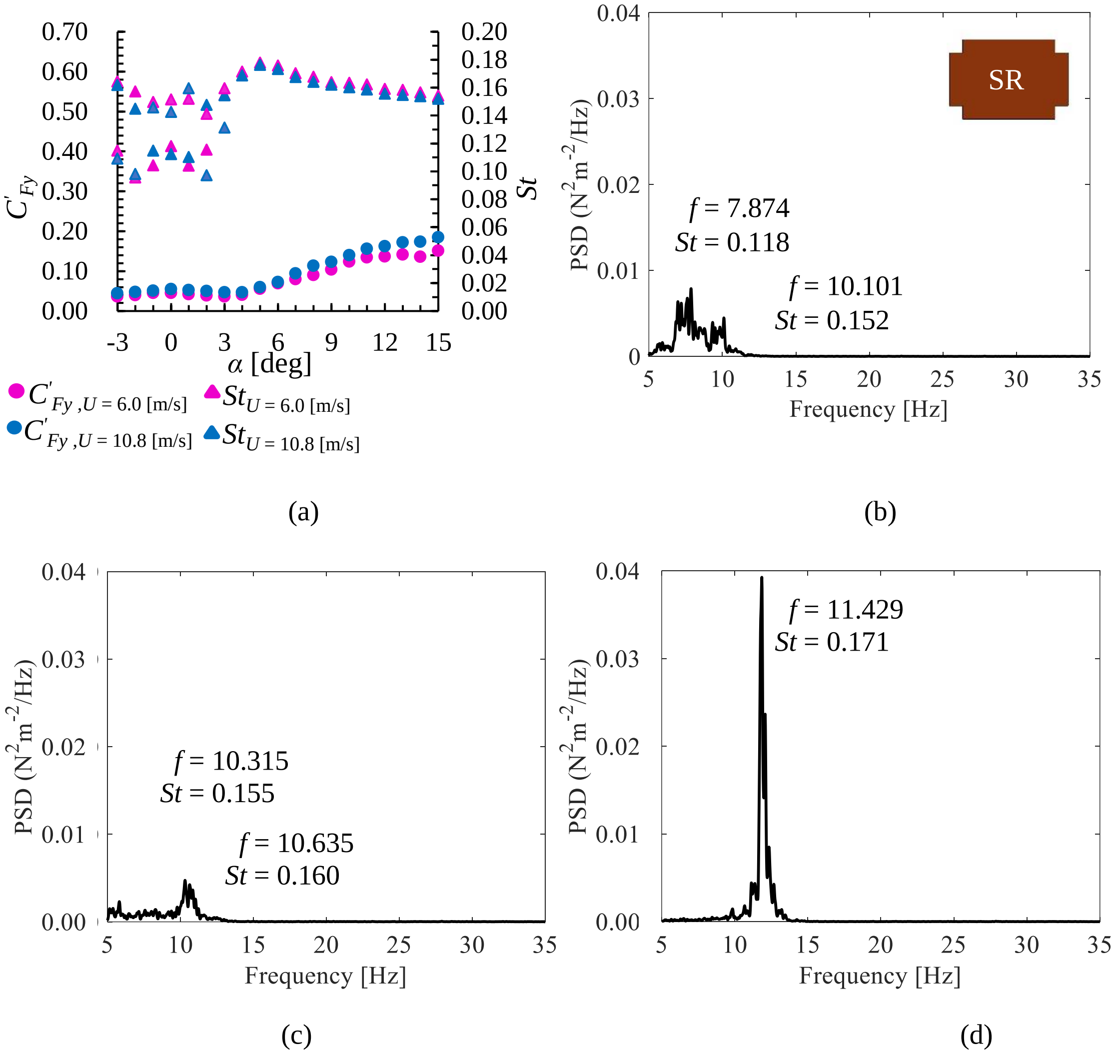

Fig. 3.10 SR section: (a) the fluctuating transverse force coefficient which indicated Kármán vortex shedding intensity (C'_{Fy}) and Strouhal number (*St*); power spectra of transverse force for U = 6.0 m/s (*Re* = 36,000) at (b) α = 0°; (c) α = +3°; and (d) α = +5°.

Weak wideband frequency peaks were observed in the PSD of transverse force for the SR section at α = 0° as shown in Fig. 3.10 (b). The *St* value also ranges from 0.112 to 0.153, with 0.112

being the dominating one. The time-frequency scalogram of transverse force showed unsteady weak frequency peaks (Fig. C.2 (a)). Therefore, the vortex shedding of the SR section at α = 0° was weak and unsteady. At α = 0°, the flow separated from the 2nd flow separation points of the SR section (Fig. 3.8) were likely to be in control of the flow around the SR section even though they were very weak.

The weak wideband frequency peaks were observed in the PSD of the transverse force (Fig. 3.10 (c)) and the scalogram of transverse force (Fig. C2. (b)) of the SR section at α = +3°. These frequency peaks corresponded the *St* of 0.155 and 0.160 and the C'_{Fy} was approximately 0.04. Thus, the vortex shedding of the SR section was weak compared to that of the R section and unsteady at this angle of attack. Also, the flow separated from the 1st flow separation points of the SR section (Fig. 3.8) was likely to dominate the flow field. In the SR section, the flow reattachment occurred at α = +5° based on the C_{Fy} value (Fig. B.2 (b)). When the flow reattachment occurred, the *St* was increased to 0.178, accompanied by a moderately strong frequency peak of 11.429 Hz as shown in Figs. 3.10 (d) and C.2 (e). This *St* was likely to be the result of flow separation at the 1st flow separation points. After the flow reattachment, the C'_{Fy} steadily increased while the *St* decreased gradually. Since 1/*St* denotes the onset of Kármán vortex-induced vibration, the onset reduced wind velocity of the SR section might be small at the angles of attack in which the flow reattachment occurred. Moreover, the onset reduced wind velocity of the SR section may be smaller than that of the original R section.

Within the studied *Re* range, the Reynolds number dependency was observed in the *St* value of the SR section at α = +2° and α = +3°. Furthermore, the vortex shedding of the SR section was unsteady and weak at angles of attack before the reattachment.

(3) Double Recession (DR)

According to Section 3.2.2, Reynolds number dependency was present in the DR section. Fig. 3.11 (a) shows the C'_{Fy} and the *St* values of the DR section for four wind velocities (36,000 ≤ *Re* ≤ 84,000). Reynolds number dependency in the C'_{Fy} and *St* values were observed within −5° ≤ α ≤ +5°, especially between U = 6 m/s (*Re* = 36,000) and the other wind velocities. In all wind velocities, the C'_{Fy} value decreased gradually with increasing α and reaching its lowest value at α = +5°. As for the *St* values, abrupt changes were observed at α = +4° and α = +5° in wind velocities except U = 6 m/s. From the C_{Fy} value of the DR section (Fig. B.3 (b)), it was found that the flow reattachment occurred at α = +5° (U = 6.0 m/s) and α = +7° (U = 10.8 m/s). When the flow reattachment occurred, the *St* reached its maximum value. After the flow reattachment, the C'_{Fy} steadily increased while the *St* decreased gradually.

From Fig. 3.11 (a), the C'_{Fy} of the DR section was 0.06–0.09 for α = 0°. Figs. 3.11 (b–c) shows the PSD of transverse force for α = 0° at 6.0 and 10.8 m/s. A weak frequency peak was observed at U = 6.0 m/s and moderately strong wideband frequency peaks were observed at U = 10.8 m/s. Similar unsteady frequency peaks were also observed in the time-frequency scalograms of transverse force as shown in Figs. C.3 (a–b). These frequency peaks corresponded to the *St* of 0.152 at U = 6.0 m/s and 0.125 at U = 10.8 m/s. Therefore, the flow separated from the 1st flow separation points (Fig. 3.8) dominates the flow at U = 6.0 m/s. On the other hand, the flow separated from the 2nd flow separation points (Fig. 3.8) was likely to dominate the flow at 10.8 m/s. Hence, Kármán vortex shedding was weak and unsteady in this attack angle.

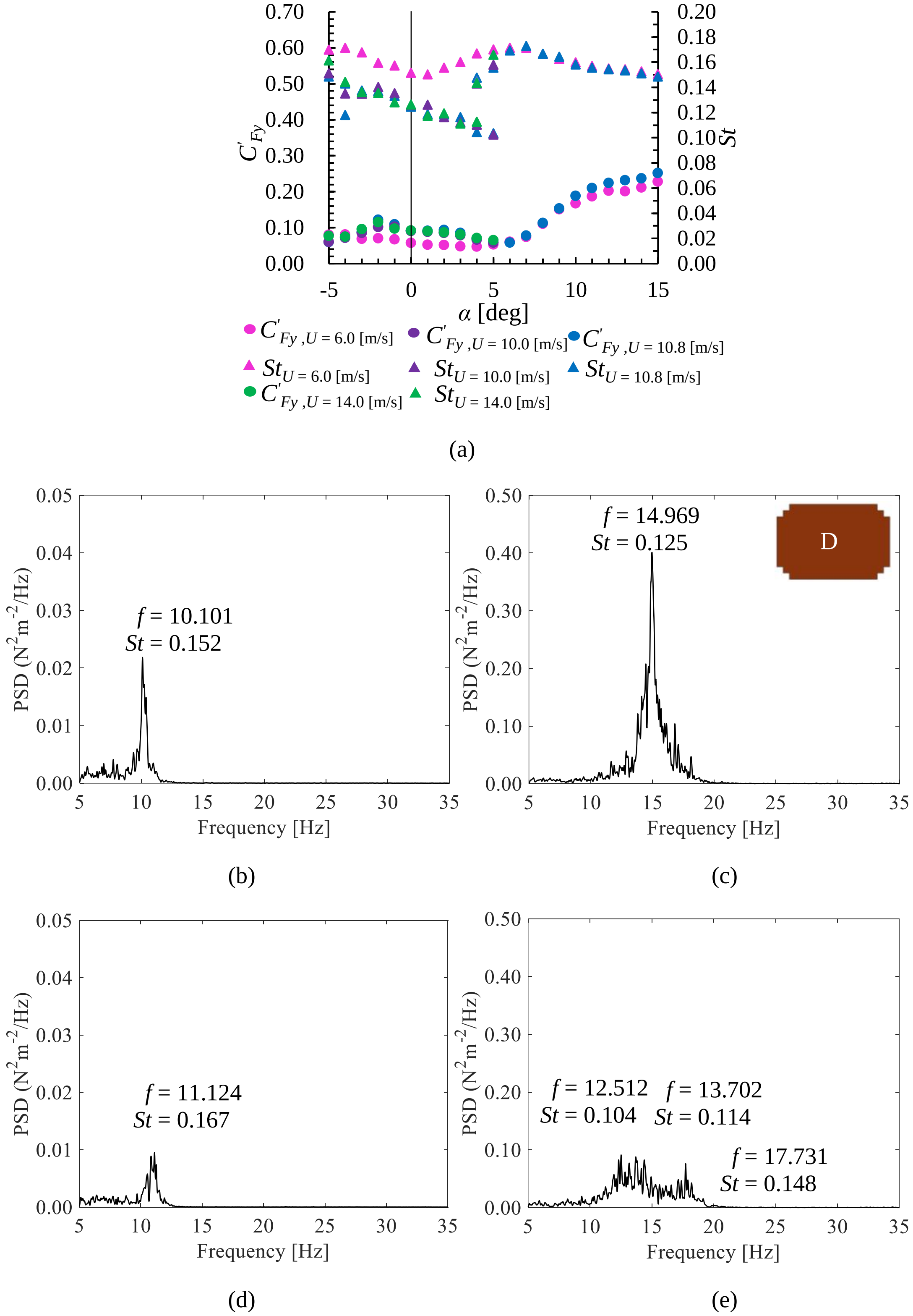

Fig. 3.11 DR section: (a) the fluctuating transverse force coefficient which indicated Kármán vortex shedding intensity (C'_{Fy}) and Strouhal number (*St*); power spectra of transverse force at α = 0° for (b) U = 6.0 m/s and (c) U =10.8 m/s; power spectra of transverse force at α = +4° for (d) U = 6.0 m/s and (e) U =10.8 m/s; power spectra of transverse force at α = +5° for (f) U = 6.0 m/s and (g) U =10.8 m/s; and power spectra of transverse force at α = +7° for (h) U = 6.0 m/s and (i) U =10.8 m/s (1/2).

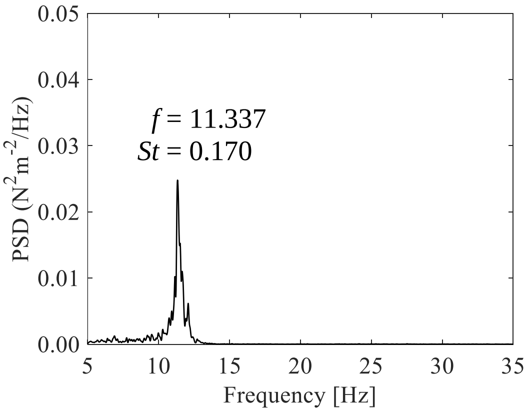

(f)

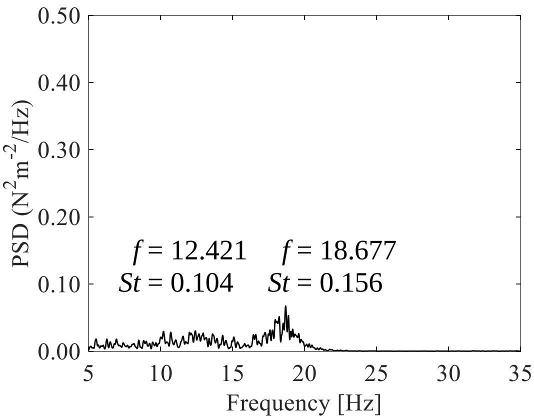

(g)

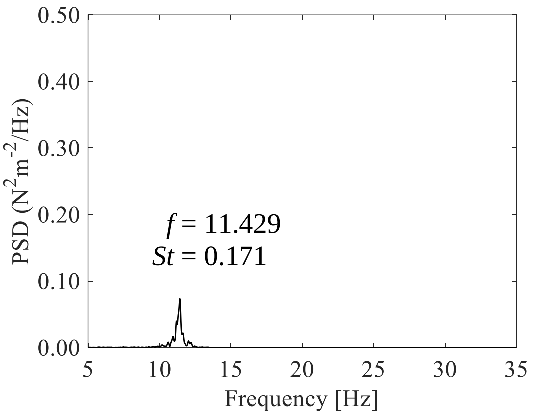

(h)

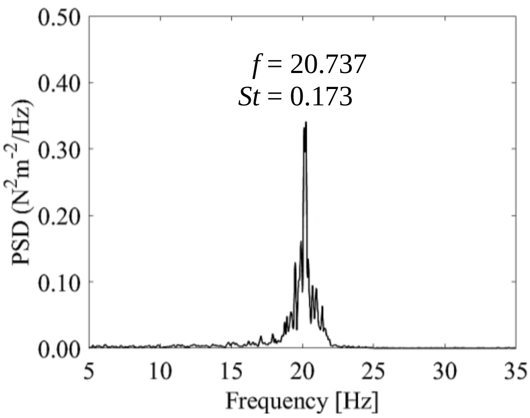

(i)

Fig. 3.11. DR section: (a) the fluctuating transverse force coefficient which indicated Kármán vortex shedding intensity (C'_{Fy}) and Strouhal number (*St*); power spectra of transverse force at α = 0° for (b) *U* = 6.0 m/s and (c) *U* =10.8 m/s; power spectra of transverse force at α = +4° for (d) *U* = 6.0 m/s and (e) *U* =10.8 m/s; power spectra of transverse force at α = +5° for (f) *U* = 6.0 m/s and (g) *U* =10.8 m/s; and power spectra of transverse force at α = +7° for (h) *U* = 6.0 m/s and (i) *U* =10.8 m/s (2/2).

Figs. 3.11(d–e) show the PSD and Figs. C.3 (c–d) show the time-frequency scalogram of transverse force for α = +4° at 6.0 and 10.8 m/s. A weak dominating frequency peak was observed at 11.124 Hz (*St* = 0.167) in *U* = 6.0 m/s. Hence, the flow separated from the 1st flow separation points (Fig. 3.8) probably dominates the flow at *U* = 6 m/s. Several weak wideband frequency peaks of 12.512 Hz (*St* = 0.104), 13.702 Hz (*St* = 0.114), and 17.731 Hz (*St* = 0.148) were observed at *U* = 10.8 m/s. These *St* values correspond to the *St* of *B*/*D* = 1.5, 1.25 and 2.5. Hence, the flow separation points were likely to change frequently, and Kármán vortex shedding was highly unsteady in these attack angles.

In the DR section, the flow reattachment occurred at α = +5° (*U* = 6.0 m/s) and α = +7° (*U* = 10.8 m/s). When the flow reattachment occurred, the dominating frequency peaks gave the highest *St* values. These frequencies were weak and unsteady, especially at α = +5° (*U* = 10.8 m/s), as shown in the PSD (Figs. 3.11 (f–i)) and the scalogram (Figs. C.3 (e–h)) of the transverse force. To summarize, the Kármán vortex shedding of the DR section was weak compared to that of the R section and highly unsteady at attack angles before the flow reattachment. Since $1/St$ denotes the onset of Kármán vortex-induced vibration, the onset reduced wind velocity of the DR section might be small at the attack angles where the flow reattachment occurred, except U = 6.0 m/s. In U = 6.0 m/s, the onset reduced wind velocity of the DR section might be smaller than that of the original R section for all studied attack angles.

(4) Double Recession II (DR II)

In the DR II section, as shown in Fig. 3.12 (a), the C'_{Fy} values remained approximately the same within the angle of attack of $-4° \leq \alpha \leq +4°$. As for the Strouhal number (St), the values went up and down within $-5° \leq \alpha \leq +5°$. From the C_{Fy} value (Fig. B.4 (b)), the flow reattachment was known

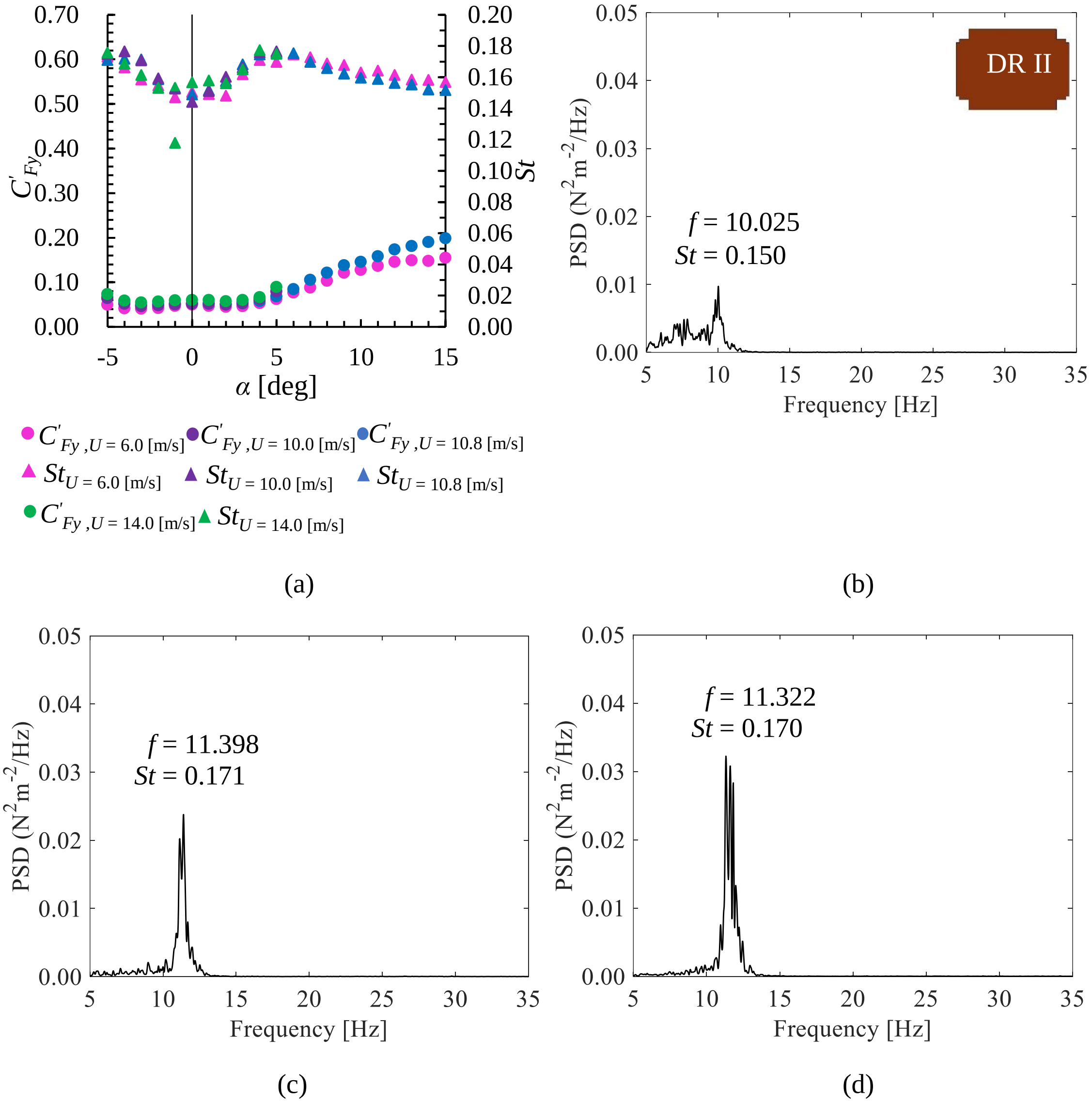

Fig. 3.12 DR II section: (a) the fluctuating transverse force coefficient which indicated Kármán vortex shedding intensity (C'_{Fy}) and Strouhal number (St); power spectra of transverse force for U = 6.0 m/s at (b) α = 0°; (c) α = +4°; and (d) α = +5°.

to occur at α = +5° in the DR II section. From α = +6°, the C'_{Fy} value increased with increasing angle of attack while the *St* value decreased with increasing angle of attack. No significant Reynolds number dependency was observed in the DR II section within the studied *Re* range.

Fig. 3.12 (b) shows the PSD of transverse force for the DR II section at α = 0° while Fig. C.4 (a) shows the scalogram. A weak frequency peak corresponding to the *St* of 0.118 (7.858 Hz) and the dominating frequency peak corresponding to the *St* of 0.150 (10.025 Hz) were observed in both plots. At α = +4° and α = +5°, weak dominating frequency peaks corresponding to the *St* of 0.170 were observed as shown in Figs. 3.12 (c–d) and C.4 (c and e). Therefore, the flow separated from the 1st flow separation points (Fig. 3.8) probably dominates the flow. The Kármán vortex shedding of the DR II section was weak compared to that of the R section but the flow separation was likely to be steady and occurred at a fixed location. Moreover, the onset reduced wind velocity of the DR II section may be smaller than that of the original R section as 1/*St* denotes the onset of Kármán vortex-induced vibration.

(5) Double Recession III (DR III)

As shown in Fig. 3.13 (a), the C'_{Fy} was 0.09–0.12 at α = 0° in the DR III section. The C'_{Fy} value reached its lowest at α = −4° and α = +4°. Abrupt changes in *St* values were observed at α = −4°, α = −3°, α = −2°, α = +2° and α = +3°. From the C_{Fy} value (Fig. B.5 (b)), the flow reattachment occurred at α = +5° in the DR III section. When the flow reattachment occurred, the *St* reached its maximum value. After the flow reattachment, the C'_{Fy} steadily increased while the *St* decreased gradually. No significant Reynolds number dependency was observed in the DR III section within the studied *Re* range.

Fig. 3.13 (b) shows the PSD of transverse force for the DR III section at α = 0°. A sharp and moderately strong dominating frequency peak of 7.568 Hz was observed. A similar steady frequency peak was observed in the scalogram of transverse force as shown in Fig. C.5 (a). This frequency corresponds to a *St* of 0.114. Hence, the flow separated from the 2nd flow separation points (Fig. 3.8) probably dominates the flow. Figs. 3.13 (c–d) show the PSD and Figs. 3.13 (c and e) show the scalogram of transverse force for the DR III section at α = +4°, and α = +5°. Weak frequency peaks corresponding to the *St* of 0.167–0.169 were observed and the flow separated from the 1st flow separation point (Fig. 3.8) was likely to dominate the flow. Therefore, the Kármán vortex shedding of the DR III section was likely to be steady and moderate with one significant peak, except for the angles of attack near the flow reattachment.

Within the attack angle range of $-1° \le \alpha \le +1°$, the onset reduced wind velocity of the DR III section may be close to the original R section. However, the onset reduced wind velocity of the DR III section might decrease once the flow reattachment about to and/or occurred. In addition, the onset reduced wind velocity of the DR III section might be small at the angles of attack in which the flow reattachment occurred.

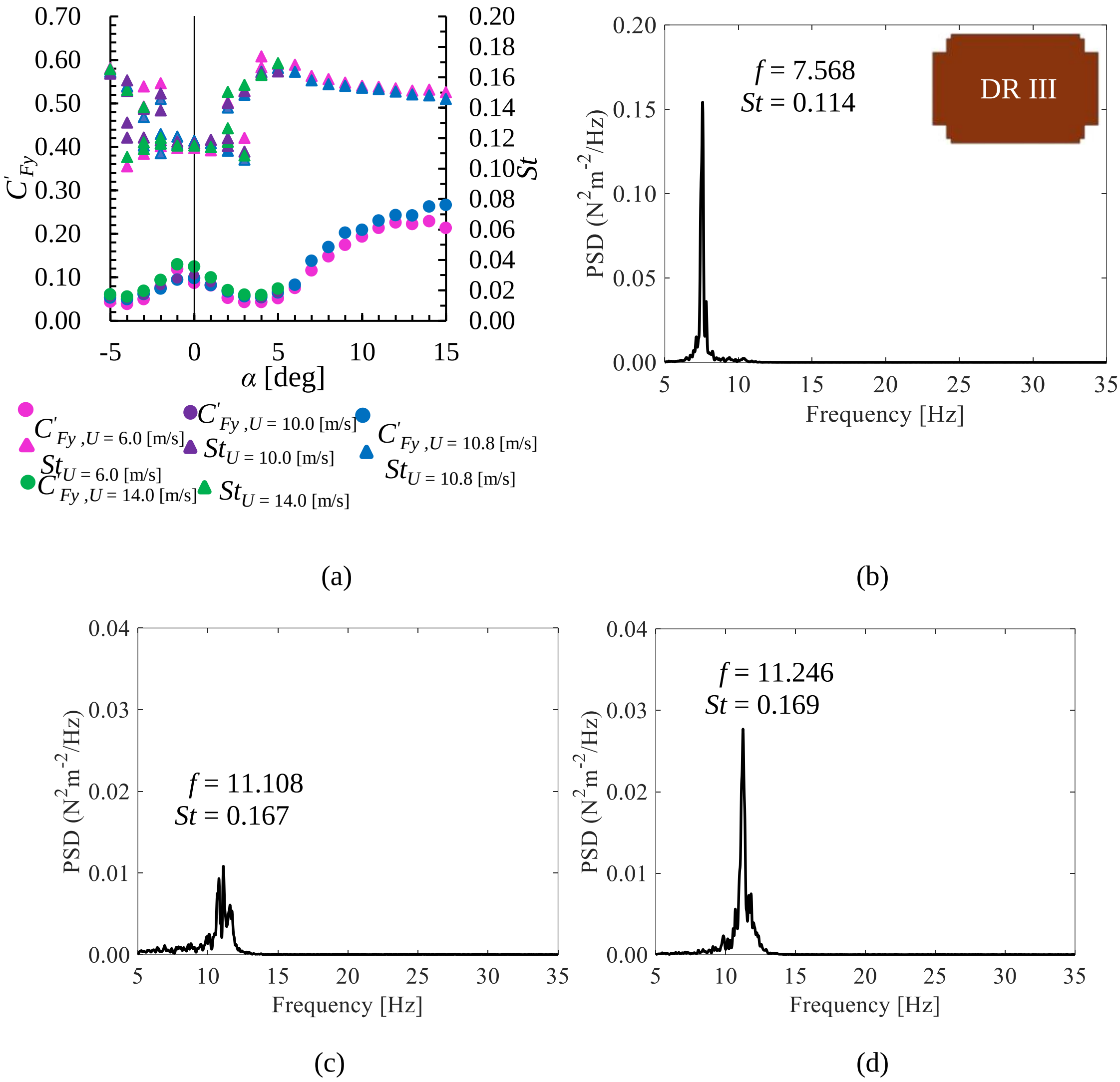

Fig. 3.13 DR III section: (a) the fluctuating transverse force coefficient which indicated Kármán vortex shedding intensity (C'_{Fy}) and Strouhal number (St); power spectra of transverse force for U = 6.0 m/s at (b) α = 0°; (c) α = +4°; and (d) α = +5°.

(6) Triple Recession (TR)

In the TR section, as shown in Fig. 3.14 (a), the C'_{Fy} was 0.19–0.25 at α = 0°. Within the attack angle range of $0° \leq \alpha \leq +4°$, the C'_{Fy} value decreases with increasing α and reaches its lowest value at α = +4°. In addition, abrupt changes in St values were observed at α = +3° and α = +4°. From the C_{Fy} value as shown in Fig. B.6 (b), the flow reattachment occurred around α = +6° (U = 6.0 m/s) and α = +5° (U = 10.8 m/s) in the TR section. When the flow reattachment occurred, the St value increased to the highest. After the flow reattachment, the C'_{Fy} steadily increased while the St gradually decreased. No significant Reynolds number dependency was observed in the TR section within the studied Re range.

Figs. 3.14 (b–d) show the PSD and Figs. C.6 (a, c and e) show the time-frequency scalogram of transverse force for the TR section at α = 0°, α = +4° and α = +5° for U = 6.0 m/s. At α = 0°, a strong, sharp and steady frequency peak of 7.828 Hz which corresponds to St of 0.117 was observed in both PSD and scalogram. Therefore, the flow separated from the 2nd flow separation points (Fig. 3.8) may dominate the flow. At α = +4°, weak and unsteady frequency peaks of 7.462 Hz and 10.208 Hz which correspond to St of 0.112 and 0.153 were observed. Hence, the flow separation was likely to switch between the flow separated from the 1st and 2nd flow separation points (Fig. 3.8). Since 10.208 Hz (St = 0.153) was the dominating frequency, the flow separated from the 1st flow separation point may dominate the flow field. At α = +5°, a weak frequency peak of 10.483 Hz which corresponds to St of 0.157 was observed. Hence, the flow separated from the 1st flow separation points (Fig. 3.8) may dominate the flow similar to the α = +4° case.

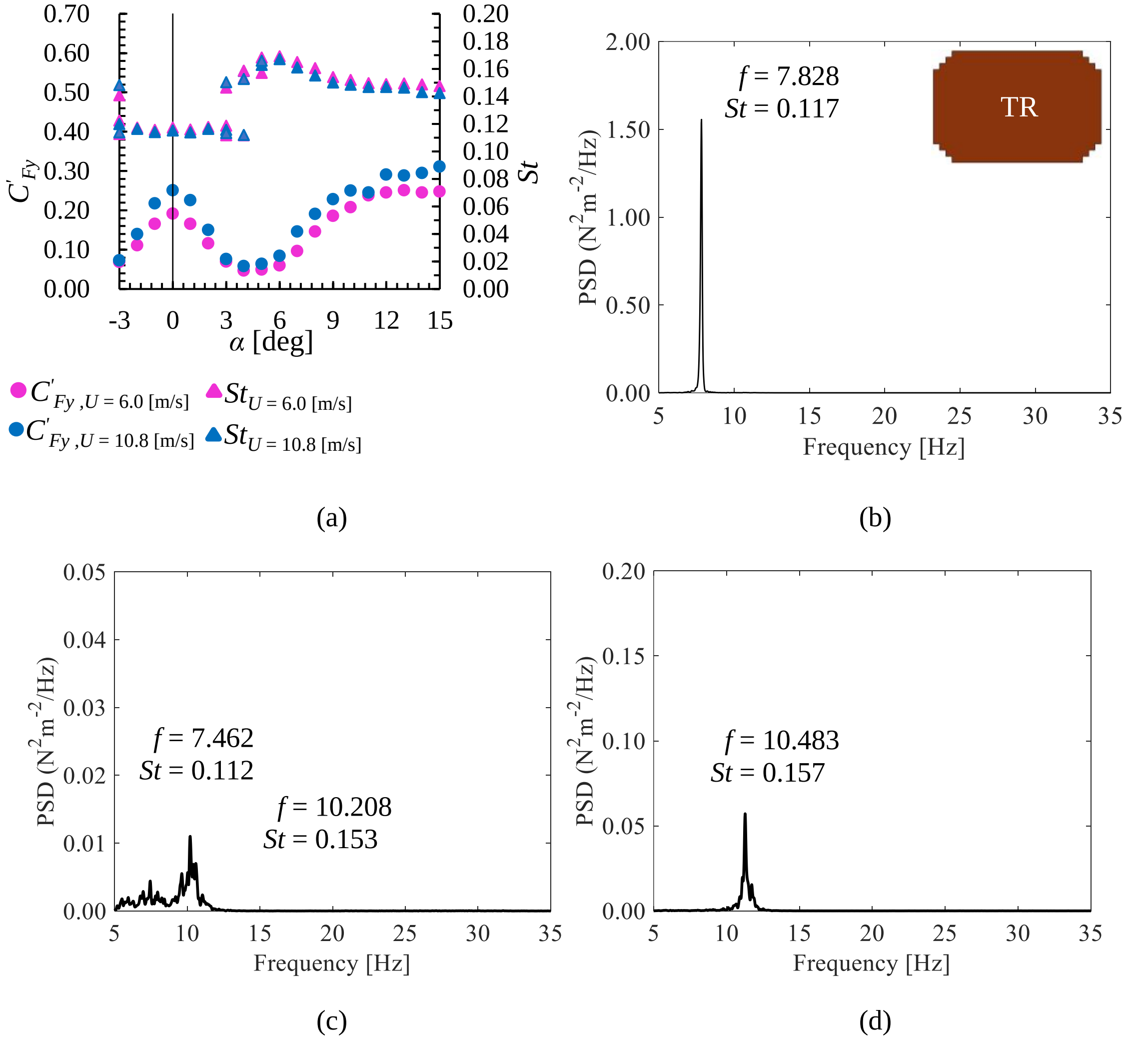

Fig. 3.14 TR section: (a) the fluctuating transverse force coefficient which indicated Kármán vortex shedding intensity (C'_{Fy}) and Strouhal number (St); power spectra of transverse force for U = 6.0 m/s at (b) α = 0°; (c) α = +4°; and (d) α = +6°.

To summarize, the vortex shedding of the TR section was strong and steady with one significant peak at α = 0°. On the other hand, the Kármán vortices were weak and unsteady at α = +4° while weak but steady at α = +5°. Within −2° ≤ α ≤ +2°, the TR section might have a similar onset reduced wind velocity as the original R section. However, the onset reduced wind velocity of the TR section might be small at the attack angles in which the flow reattachment occurred.

(7) Chamfer (C)

In the C section, the C'_{Fy} was 0.04–0.16 at α = 0° as shown in Fig. 3.15 (a). Hence, significant Reynolds number dependency was observed in the C'_{Fy} values between U = 6.0 m/s (Re = 36,000) and U = 10.8 m/s (Re = 64,800). For U = 10.8 m/s, the C'_{Fy} value decreased gradually with increasing α and reaching its lowest value at α = +4°. From the C_{Fy} value of the C section (Fig. B.7 (b)), the flow reattachment occurred at α = +4°. When the flow reattachment occurred, the St reached its maximum value. After flow reattachment, the C'_{Fy} increased steadily while the St decreased gradually. Reynolds number dependency was observed in the C'_{Fy} values within −1° ≤ α ≤ +1° and +7° ≤ α ≤ +9°.

Figs. 3.15 (b–c) show the PSD and Figs. C.7 (a–b) show the time-frequency scalogram of transverse force of C section at α = 0° for U = 6.0 and U = 10.8 m/s. In U = 6.0 m/s, two weak and unsteady peaks of 7.187 Hz (St = 0.106) and 10.483 Hz (St = 0.157) were observed while the former was the dominating one. In U = 10.8 m/s, two frequency peaks of 13.412 Hz (St = 0.112) and 18.936 Hz (St = 0.158) were observed while the former one being the steady, stronger and dominating. Therefore, the St values of 0.106–0.112 dominated the flow in both wind velocities. Hence, the flow separation was unsteady, and the flow separated from the 2nd flow separation points (Fig. 3.8) may dominate the flow. At α = +3° (U = 6.0 m/s), an unsteady and weak wideband frequency peak of 12.604 Hz, corresponding to St of 0.189 was observed as shown in Figs. 3.15 (d) and C.7 (c). This

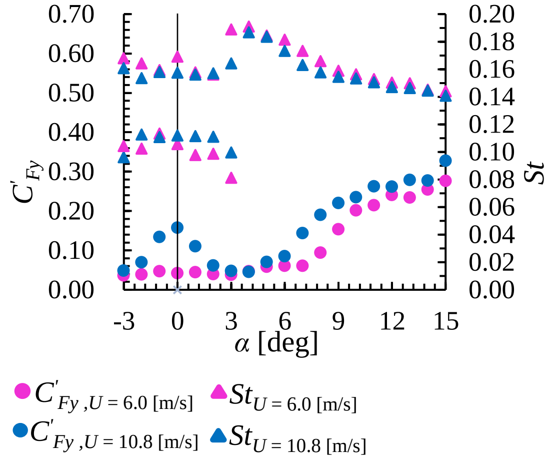

(a)

Fig. 3.15 C section: (a) the fluctuating transverse force coefficient which indicated Kármán vortex shedding intensity (C'_{Fy}) and Strouhal number (St); power spectra of transverse force at α = 0° for (b) U = 6.0 m/s and (c) U =10.8 m/s; and power spectra of transverse force at (d) α = +3° and (e) α = +4° for U = 6.0 m/s (1/2).

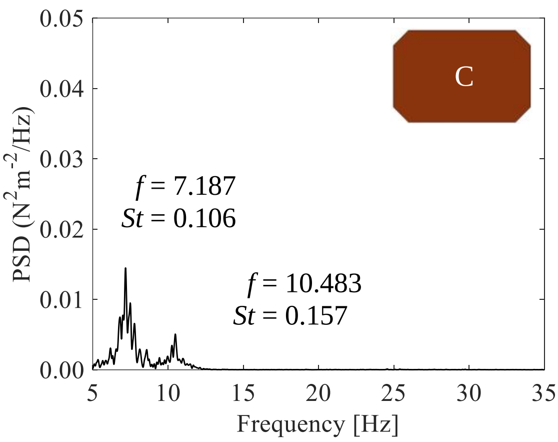

(b)

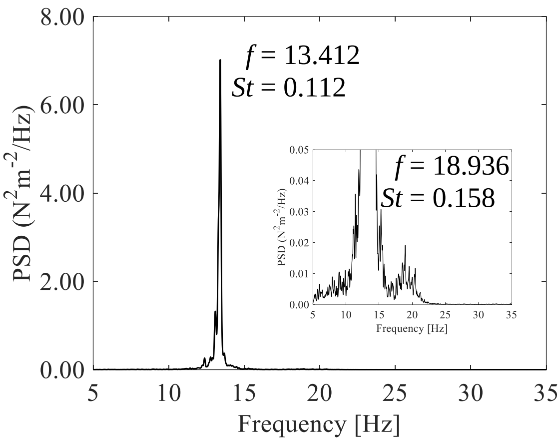

(c)

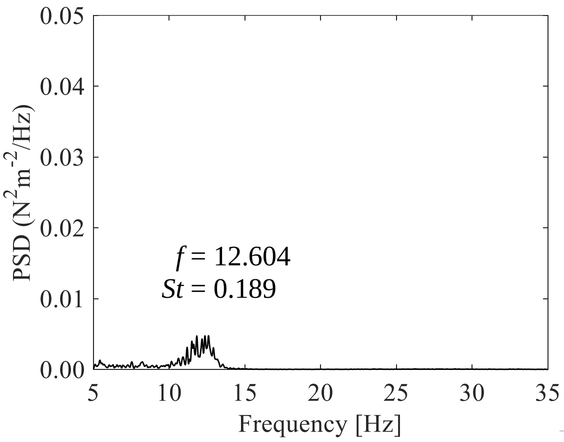

(d)

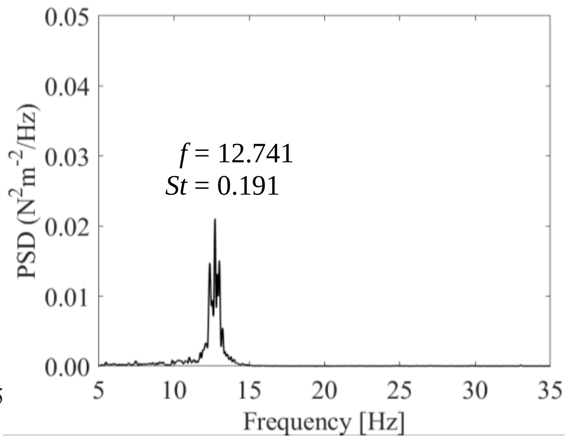

(e)

Fig. 3.15 C section: (a) the fluctuating transverse force coefficient which indicated Kármán vortex shedding intensity (C'_{Fy}) and Strouhal number (*St*); power spectra of transverse force at α = 0° for (b) U = 6.0 m/s and (c) U =10.8 m/s; and power spectra of transverse force at (d) α = +3° and (e) α = +4° for U = 6.0 m/s (2/2).

frequency peak may be due to the flow separation at 1st flow separation points (Fig. 3.8). Similar phenomenon was observed within $-3° \leq \alpha \leq +3°$. Hence, the vortex shedding of the C section was weak and unsteady within $-3° \leq \alpha \leq +3°$.

At α = +4° (U = 6.0 m/s), a weak frequency peak of 12.741 Hz which corresponds to *St* of 0.191 was observed at +4° as shown in Figs. 3.15 (e) and C.7 (e). Since 1/*St* denotes the onset of Kármán vortex-induced vibration, the onset reduced wind velocity of the C section may be smaller than that of the original R section. In addition, the onset reduced wind velocity might be small at the angles of attack in which the flow reattachment occurred.

(8) Summary

To summarize, all studied sections with corner modifications significantly reduced the Kármán vortex shedding intensity (C'_{Fy}) value against the original rectangular (R) section within $-3° \le \alpha \le +15°$. Furthermore, a gradual increase in the C'_{Fy} values was observed at the angles of attack where the flow reattachment occurred and larger. As for the Strouhal number (*St*) value, all studied sections with corner modifications have larger *St* values than the original R section within $-3° \le \alpha \le +15°$. Furthermore, the *St* value reached the maximum value at the angle of attack where the flow reattachment occurred. In addition, between $-3° \le \alpha \le +15°$, there also exists a certain angle of attack range in each studied section where the C'_{Fy} value was the smallest and the *St* value was the largest. This angle of attack range is observed around the angle of attack where the flow reattachment occurred. Within this angle of attack range, the *St* values fluctuate significantly. Hence, the flow separation points were unsteady and likely to change abruptly in these attack angle cases.

The effect of corner shape modification on the C'_{Fy} and *St* of the rectangular cylinder at $\alpha = 0°$ was shown in Fig. 3.16. Significant Reynolds number dependency was observed in the C'_{Fy} value of the C section and the *St* value of the DR section. For $U = 6$ m/s at $\alpha = 0°$, the TR, DR III and DR sections reduced 63%, 77% and 88% of the original C'_{Fy} value. The DR II, SR and C section effectively reduced 90% of the original C'_{Fy} value. The sections with double recession-type corners, DR II and DR III, reduced the C'_{Fy} value differently although the inner step size was identical while orientation was different. Hence, placing the inner step closer to the windward surface at the leading edge might be more effective in reducing the Kármán vortex shedding intensity. On the other hand, The *St* of all corner modified sections were higher than that of the R section and two *St* frequencies were observed in the SR and C sections. Since 1/*St* denotes the onset of Kármán vortex-induced vibration, the onset reduced wind velocities of sections with corner modification may be smaller than that of the original R section.

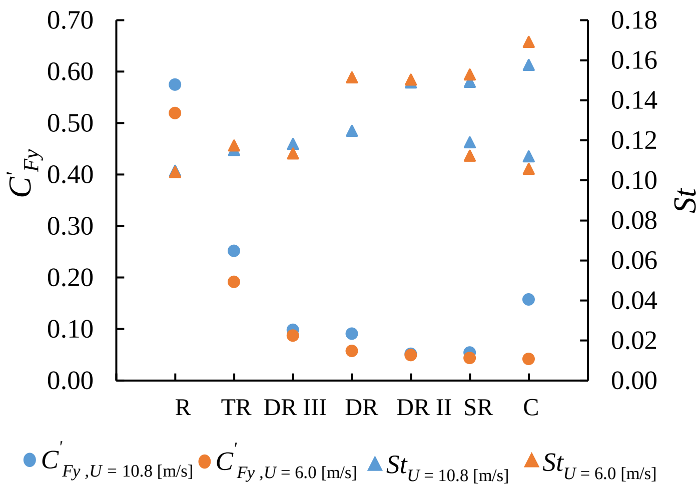

Fig. 3.16 Fluctuating transverse force coefficient which indicated Kármán vortex shedding intensity (C'_{Fy}) and Strouhal number (*St*) of the corner modified sections at $\alpha = 0°$.

3.3 Concluding remarks

To summarize, all studied sections with corner modifications considerably reduced the aerodynamic force coefficients: longitudinal force coefficient (C_{Fx}), transverse force coefficient (C_{Fy}) and moment coefficient (C_M), of the original rectangular cylinder.

The fluctuating transverse force coefficient which indicates the Kármán vortex shedding intensity (C'_{Fy}) of the original rectangular (R) section was also reduced to approximately 63–90% when various corner modifications were applied (U = 6.0 m/s, Re = 36,000). The Kármán vortex shedding intensity of a section can be noticeably affected by changing not only the recession step number but also the recession step size and orientation. In a section with the double recession-type corners, putting the inner recession step closer to the windward surface at the leading edge is more effective in reducing the Kármán vortex shedding intensity. At the angles of attack which were just after the angles of attack where the flow reattachment occurred, the C'_{Fy} values increased gradually. Thus, the flow reattachment in the asymmetric flow separation might have some relation with the Kármán vortex shedding intensity.

Significant Reynolds number dependency was observed in the C_{Fy}, C'_{Fy} and St values of the double recession (DR) section within the attack angle of −5° to +5°, especially in the higher wind velocity regions (starting from U = 10.0 m/s, Re = 60,000). This Reynolds number dependency may be due to the asymmetric flow caused by the geometrical issues of the model surface. In the double recession II (DR II) section, the Reynolds number dependency was also observed in the C_{Fy} value within the attack angle of $-4° \leq \alpha \leq -1°$ and $+2° \leq \alpha \leq +5°$. However, Reynolds number dependency was not observed in the double recession III (DR III) section. Hence, the flow separation of the section with a double recession-type corner might be sensitive to the placement of the inner step. Reynolds number dependency was also observed in the C'_{Fy} value of the chamfer (C) section within the attack angle of −1° to +1°, between 6 m/s (Re = 36,000) and 10.8 m/s (Re = 64,800). Therefore, the Reynolds number effect must be considered in the wind-resistant design of structures with these types of corner modifications.

The Strouhal number (St) of all sections with corner modifications was larger than that of the original R section. Hence, the onset reduced wind velocity of sections with corner modification was expected to be smaller than that of the original R section as $1/St$ denotes the onset of Kármán vortex-induced vibration. In addition, the maximum St value was found at the attack angle where the flow reattachment occurred and the value gradually decreased with an increase in the attack angle. Hence, the onset reduced wind velocity of each section might become lower once the flow is reattached and/or about to reattach the side surfaces.

The single recession (SR), double recession II (DR II), and chamfer (C) sections have two different St values and exhibited unsteady vortex shedding at certain attack angles before the flow field reattachment. In the SR and C sections, the flow separated from the second flow separation point dominated the flow field since this flow has the vortex shedding frequency peak with the largest power in the power spectral density. On the other hand, the flow separated from the first flow separation point dominated the vortex shedding in the DR II section. In the double recession III (DR III) and triple recession (TR) sections, the flow is separated from the first flow separation point.

Reference

Alam, M. M., Abdelhamid, T., & Sohankar, A. (2020). Effect of cylinder corner radius and attack angle on heat transfer and flow topology. *International Journal of Mechanical Sciences*, *175*, 105566. https://doi.org/10.1016/j.ijmecsci.2020.105566.

Alminhana, G. W., Braun, A. L., & Loredo-Souza, A. M. (2018). A numerical study on the aerodynamic performance of building cross-sections using corner modifications. *Latin American Journal of Solids and Structures*, *15*(7). https://doi.org/10.1590/1679-78254871.

Cao, Y., & Tamura, T. (2018). Aerodynamic characteristics of a rounded-corner square cylinder in shear flow at subcritical and supercritical Reynolds numbers. *Journal of Fluids and Structures*, *82*, 473-491. https://doi.org/10.1016/j.jfluidstructs.2018.07.012.

Choi, C. K., & Kwon, D. K. (1999). Aerodynamic stability for square cylinder with various corner cuts. *Wind and Structures, An International Journal*, *2*(3), 173–187. https://doi.org/10.12989/was.1999.2.3.173.

Choi, C. K., & Kwon, D. K. (2001). The Characteristics of Strouhal Number of Rectangular Cylinders with Various Corner Cuts. *The 5th Asia-Pacific Conference on Wind Engineering*, Kyoto, Japan.

Diana, G., Falco, M., Cheli, F., & Cigada, A. (2003). The aeroelastic study of the Messina Straits Bridge. *Natural hazards*, *30*, 79-106. https://doi.org/10.1023/A:1025014411143.

Elshaer, A., Bitsuamlak, G., & Damatty, A. El. (2014). Wind Load Reductions due to Building Corner Modifications. *22nd Annual Conference of the CFD Society of Canada*, Toronto, Canada.

Hayashida, H., & Iwasa, Y. (1990). Aerodynamic shape effects of tall building for vortex induced vibration. *Journal of Wind Engineering and Industrial Aerodynamics*, 33(1-2), 237-242. https://doi.org/10.1016/0167-6105(90)90039-F.

Hémon, P., & Santi, F. (2002). On the aeroelastic behaviour of rectangular cylinders in cross-flow. *Journal of Fluids and Structures*, *16*(7), 855-889. https://doi.org/10.1006/jfls.2002.0452.

Knisely, C. W. (1990). Strouhal numbers of rectangular cylinders at incidence: a review and new data. *Journal of fluids and structures*, *4*(4), 371-393. https://doi.org/10.1016/0889-9746(90)90137-T.

Matsumoto, M., Yagi, T., Lee, J.H., Hori, K., & Kawashima, Y., 2006. Karman vortex effect on the aerodynamic forces to rectangular cylinders. *American Society of Mechanical Engineers, Pressure Vessels and Piping Division (Publication) PVP*. https://doi.org/10.1115/PVP2006-ICPVT-11-93783.

Mannini, C., Marra, A. M., Massai, T., & Bartoli, G. (2016). Interference of vortex-induced vibration and transverse galloping for a rectangular cylinder. *Journal of Fluids and Structures*, 66, 403-423, https://doi.org/10.1016/j.jfluidstructs.2016.08.002.

Ogawa, K., Matsumoto, M., Kitazawa, M., & Yamasaki, T. (1990). Aerodynamic stability of the tower of a long-spanned cable-stayed bridge (Higashi-Kobe Bridge). *Journal of Wind Engineering and Industrial Aerodynamics,* 33 (1–2), 349-358, https://doi.org/10.1016/0167-6105(90)90050-M.

Shimada, K., & Meng, Y. (1998). Applicability of modified k-ε model on the estimation of aerodynamic properties of rectangular cylinders with various elongated cross sections. *Journal of Structural and Construction Engineering (Transactions of AIJ),* 63 (514), 73-80.

Shiraishi, N., Matsumoto, M., Shirato, H., & Ishizaki, H. (1988). On aerodynamic stability effects for bluff rectangular cylinders by their corner-cut. *Journal of Wind Engineering and Industrial Aerodynamics*, 28. https://doi.org/10.1016/0167-6105(88)90133-X.

Shirato, H., & Matsumoto, M. (1994). Reynolds Number Effect on Aerodynamic Properties of 2-D Rectangular Section with Corner-Cut. *Wind Engineers, JAWE*, *1994*(59), 5-9. https://doi.org/10.5359/jawe.1994.59_5.

Tamura, T., & Ito, Y. (1996). Aerodynamic characteristics and flow structures around a rectangular cylinder with a section of various depth/breadth ratios. *Journal of Structural and Construction Engineering (Transactions of AIJ),* 61 (486), 153-162.

Tse, K. T., Hitchcock, P. A., Kwok, K. C., Thepmongkorn, S., & Chan, C. M. (2009). Economic perspectives of aerodynamic treatments of square tall buildings. *Journal of Wind Engineering and Industrial Aerodynamics*, *97*(9-10), 455-467. https://doi.org/10.1016/j.jweia.2009.07.005.

Wang, Y., Hu, Z., & Thompson, D. (2020). Numerical investigations on the flow over cubes with rounded corners and the noise emitted. *Computers & Fluids*, *202*, 104521. https://doi.org/10.1016/j.compfluid.2020.104521.

Washizu, K., Ohya, A., Otsuki, Y., & Fujii, K. (1978). Aeroelastic instability of rectangular cylinders in a heaving mode. *Journal of Sound and Vibration*, 59 (2), 198-210. https://doi.org/10.1016/0022-460X(78)90500-X.

Chapter 4

Aerodynamic interaction between the galloping instability and the vortices at zero angle of attack

4.1 Introduction

For the design and construction of structures in the field of civil engineering, the relationship between aerodynamic forces and structural instabilities has been one of the complex topics. When the wind blows over a certain structure, it applies positive and negative pressure to the surface of that structure. This leads to the wind-induced vibration of the structures, especially in the case of the high-rise structure.

Galloping instability is a large amplitude vibration observed in the structures exposed to a flow such as wind and water. This vibration has the potential to cause collapse and failures and is usually observed in the higher wind velocity regions. In lower wind velocity regions, an aerodynamic phenomenon known as vortex-induced vibration (VIV) is observed. The VIV can be further divided into two groups, known as Kármán vortex-induced vibration (KVIV) and motion-induced vortex vibration (MIV). While the amplitudes of VIV are generally smaller than that of the galloping, VIV can lead to fatigue failures of the structures. Therefore, it is important to consider these aerodynamic phenomena in the structural designs of structures. This should be considered in a way that these structures can mitigate and/or withstand the wind-induced vibrations and ensure stability throughout their lifetimes.

The interaction of the VIV and galloping may result in large amplitude vibrations even in low wind velocity region. Mannini, et al. (2014) mentioned that the interaction between VIV and galloping in the rectangular cylinder is a complex phenomenon and additional studies are still required to describe various critical issues. To the best knowledge of the author, there have been almost no studies regarding the VIV and galloping instability by controlling the Kármán vortex shedding intensity of the rectangular cylinder with a side ratio (B/D) of 1.5. In this study, the Kármán vortex shedding intensity of the rectangular cylinder was reduced by modifying the corners into six different shapes, denoted as triple recession (TR), double recession (III), double recession (DR), double recession II (DR II), single recession (SR) and chamfer (C). In addition, the effect of Scruton number (mass-damping parameter) on the response amplitude and the onset reduced wind velocity of galloping were also investigated by increasing the structural damping. In this chapter, the wind tunnel tests: the static, vertical 1 degree-of-freedom (1 DOF) forced vibration and free vibration tests were conducted at α = 0°, where α = angle of attack (symmetric body).

In Section 4.2, the effect of corner shape modification on the steady aerodynamic characteristics of the rectangular cylinder is provided. Section 4.3 explains the effect of Scruton number on the response amplitude of rectangular and corner-cut cylinders. Section 4.4 reports the effect of corner shape modification on the unsteady aerodynamic characteristics such as the aerodynamic derivatives (H_1^* and H_4^*). Section 4.5 explains the effect of Kármán vortex shedding intensity on the motion-induced vortices and galloping onset wind velocity based on the 1DOF forced vibration test results. Finally, Section 4.6 provides the conclusion remarks. Some of the experimental results and conclusions about the aerodynamic interactions between the galloping instability and Kármán and motion-induced vortices at $\alpha = 0°$ mentioned in this chapter are summarized in the work by Hnin et al. (Under review).

4.2 Effect of corner shape modification on the steady aerodynamic characteristics of rectangular cylinder

According to previous studies, it is undeniable that there is an interaction between the vortices and the galloping instability. Hence, in this study, the aerodynamic interaction between the vortices and the galloping instability was investigated by controlling the Kármán vortex shedding intensity. The Kármán vortex (KV) shedding was modified by changing the corners of the rectangular section into different shapes. The following sections described the effect of corner shape modification on the Kármán vortex shedding intensity and the quasi-steady galloping instability for two wind tunnel wind velocities of 6.0 m/s (Re = 36,000) and 10.8 m/s (Re = 64,800).

4.2.1 Kármán vortex shedding intensity and Strouhal number

Fig. 4.1 shows the fluctuating transverse force coefficient which indicated the Kármán vortex shedding intensity (C'_{Fy}) and Strouhal number (St) of all studied sections. The original rectangular (R) section has C'_{Fy} = 0.52 and St = 0.104 for U = 6 m/s (Re = 36,000). This was similar to the results reported by Matsumoto et al. (2006) for the Reynolds number range of approximately 2.5–4.0×10^4. For U = 10.8 m/s (Re = 64,800), the R section has C'_{Fy} = 0.57 and St = 0.105. This also agreed with the results by Mannini et al. (2016) for the Reynolds number of 58,200.

As shown in Fig. 4.1, the Kármán vortex shedding intensity (C'_{Fy}) was significantly decreased when the corners of the original R section were cut into various shapes. The C'_{Fy} reduction percentage from the R section for U = 6.0 m/s was as follows: TR (63%), DR III (77%), DR (88%), and DRII, SR and C (90%). For U = 10.8 m/s, the values were as follows: TR (55%), DR III (83%), DR (84%), DR II and SR (91%), and C (72%), respectively. Hence, significant Reynold number dependency was observed between 36,000 (U = 6.0 m/s) and 64,800 (U = 10.8 m/s) in the C'_{Fy} values of C sections. In addition, there is a general tendency for the C'_{Fy} value to decrease with the decrease in the recession steps number, especially in the recession-type corner-shaped sections such as TR, DR III, DR, DR II and SR. When the C'_{Fy} values of the double recession-type corner-shaped sections (DR, DR II and DR III) were compared, the DR II section had the smallest C'_{Fy} values. Hence, it was more suitable to put the inner step closer to the windward and leeward surfaces of the model for the effective reduction of Kármán vortex shedding intensity in the DR-type corner-shaped sections.

On the other hand, the Strouhal number (St) increased steadily when the corners of the original R section were cut into various shapes as shown in Fig. 4.1. Significant Reynolds number dependency between 36,000 and 64,800 was also observed in the St values of the DR section. In the case of SR and C sections, two Kármán vortex shedding frequency peaks were observed in the power spectral density (PSD) diagram as mentioned previously in Section 3.2.3.

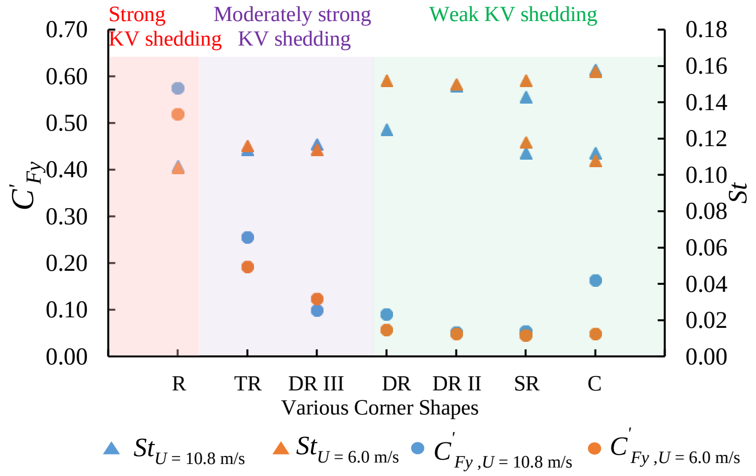

Fig. 4.1 The fluctuating transverse force coefficient which indicated the Kármán vortex shedding intensity (C'_{Fy}) and Strouhal number (St) at α = 0°.

Hence, changing the corner geometry of the rectangular cylinder reduced the Kármán vortex shedding intensity (C'_{Fy}), which can be divided into three regions as shown in Fig 4.1, and increased the Strouhal number (St). Since $1/St$ represents the onset of the Kármán vortex-induced vibration (KVIV), the onset reduced wind velocity of the corner-cut sections was expected to be lower than that of the original R section.

4.2.2 Slope of transverse force coefficient

The slope of the transverse force coefficient ($dC_{Fy}/d\alpha$) was used in the quasi-steady theory to determine the critical reduced wind velocity of galloping (U_{cr_quasi}). In this study, the angle of attack range of $-3° \leq \alpha \leq +15°$ was used to describe the slope of the transverse force coefficient at α = 0° as shown in Fig.4.2 for a wind velocity of 6.0 and 10.8 m/s. The slope of the transverse force coefficient for various wind velocities are listed in Table 4.1. No significant Reynolds number dependency was

Table 4.1 Slope of transverse force coefficient at α = 0°.

Section	Slope of transverse force coefficient, $dC_{Fy}/d\alpha$ [rad^{-1}]			
	U = 6.0 m/s (Re = 36,000) ($-3° \leq \alpha \leq +15°$)	U = 10.0 m/s (Re = 60,000) ($-3° \leq \alpha \leq +15°$)	U = 10.8 m/s (Re = 64,800) ($-3° \leq \alpha \leq +15°$)	U = 14.0 m/s (Re = 84,000) ($-3° \leq \alpha \leq +15°$)
R	−3.28	-	−3.74	-
TR	−1.97	-	−2.95	-
DR III	−2.08	-	−2.08	-
DR	−3.08	−0.76	−1.20	−0.61
DR II	−4.32	-	−3.97	-
SR	−2.76	-	−3.68	-
C	−3.17	-	−3.45	-

observed, except the DR section. Therefore, the U_{cr_quasi} value of the DR section was expected to vary depending on the targeted wind velocity.

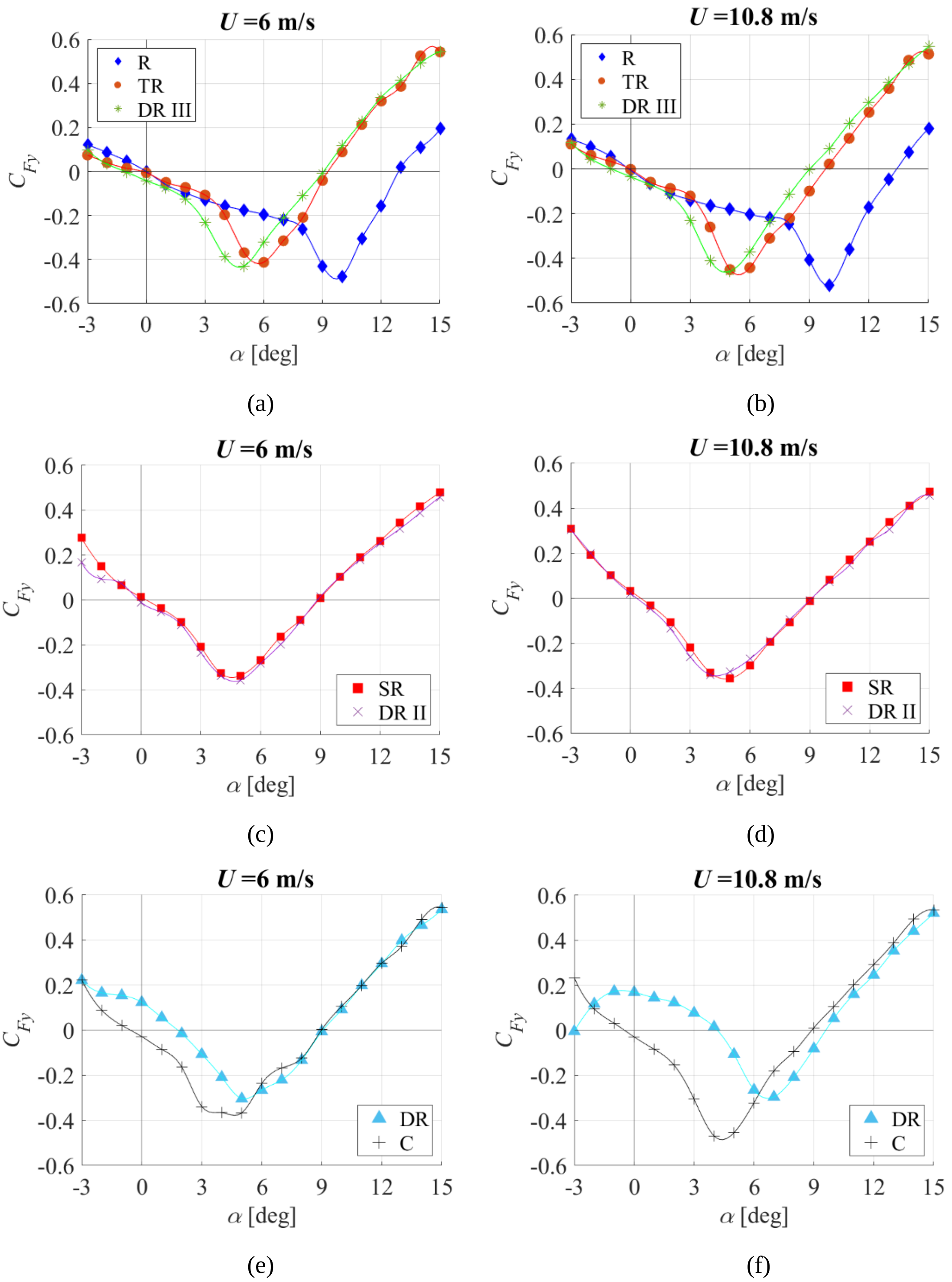

Fig. 4.2 Slope of the transverse force coefficient ($dC_{Fy}/d\alpha$) at $\alpha = 0°$ within $-3° \leq \alpha \leq +15°$ for: (a) R, DR III and TR (U = 6.0 m/s); (b) R, DR III and TR (U = 10.8 m/s); (c) SR and DR II (U = 6.0 m/s); (d) SR and DR II (U = 10.8 m/s); (e) DR and C (U = 6.0 m/s); and (f) DR and C (U = 10.8 m/s).

4.2.3 Critical reduced wind velocity of galloping

This section describes the effect of corner shape modification on the onset of galloping using quasi-steady theory, as mentioned in previous chapters. The critical reduced wind velocity of galloping based on the quasi-steady theory (U_{cr_quasi}) was calculated using Eq. 2.7. Tables 4.2 and 4.3 listed the onset reduced wind velocity of the Kármán vortex-induced vibration ($1/St$) and the critical reduced wind velocity of galloping based on the quasi-steady theory (U_{cr_quasi}) for U = 6.0 m/s (Re = 36,000) and 10.8 m/s (Re = 64,800) at various Scruton numbers ($S_{c\eta}$).

Table 4.2 Comparison of the onset reduced wind velocity of the Kármán vortex-induced vibration ($1/St$) and the critical reduced wind velocity of galloping based on the quasi-steady theory (U_{cr_quasi}) at α = 0° for various Scruton number values (U = 6.0 m/s, Re = 36,000).

Section	$1/St$	U_{cr_quasi}					
		$S_{c\eta}$ = 6	$S_{c\eta}$ = 42	$S_{c\eta}$ = 56	$S_{c\eta}$ = 69	$S_{c\eta}$ = 90	$S_{c\eta}$ = 130
R	9.60	2.47	17.07	22.54	28.39	36.68	52.70
TR	8.52	4.27	28.70	37.97	47.14	60.42	-
DR III	8.81	3.99	27.26	35.41	44.23	57.60	-
DR	6.60	2.77	18.26	24.08	30.31	39.52	-
DR II	6.65	1.97	13.11	17.19	21.29	27.03	-
SR	8.47, 6.60	2.98	20.42	26.82	33.16	43.41	-
C	9.28, 6.36	2.63	17.75	23.35	29.23	37.64	-

Table 4.3 Comparison of the onset reduced wind velocity of the Kármán vortex-induced vibration ($1/St$) and the critical reduced wind velocity of galloping based on the quasi-steady theory (U_{cr_quasi}) at α = 0° for various Scruton number values (U = 10.8 m/s, Re = 64,800).

Section	$1/St$	U_{cr_quasi}					
		$S_{c\eta}$ = 6	$S_{c\eta}$ = 42	$S_{c\eta}$ = 56	$S_{c\eta}$ = 69	$S_{c\eta}$ = 90	$S_{c\eta}$ = 130
R	9.53	2.16	14.96	19.74	24.86	32.13	46.16
TR	8.77	2.86	19.20	25.39	31.53	40.41	-
DR III	8.46	3.99	27.25	35.39	44.21	57.57	-
DR	8.02	7.08	46.66	61.52	77.45	100.98	-
DR II	6.72	2.14	14.26	18.70	23.16	29.39	-
SR	8.91, 7.02	2.24	15.35	20.16	24.93	32.63	-
C	8.95, 6.34	2.42	16.30	21.45	26.85	34.58	-

At a very low Scruton number ($S_{c\eta}$ = 6), the U_{cr_quasi} is significantly lower than that of $1/St$ excluding the DR section at U = 10.8 m/s. However, the side ratio of the target section was 1.5, and was larger than 0.6. Thus, the low-speed galloping (Nakamura and Hirata, 1989, 1994) is expected to not occur. Instead, the Kármán vortex-induced vibration (KVIV) and galloping might be appeared altogether in the response amplitude. When the Scruton number was further increased from 6, the value of U_{cr_quasi} became larger than $1/St$. Therefore, the KVIV and galloping were expected to separate from each other. This will be further discussed in Section 4.3. On the other hand, the fact that the U_{cr_quasi} value of the DR section was higher than that of $1/St$ at U = 10.8 m/s might be related to the Reynolds number dependency and further investigation is still needed.

4.3 Effect of Scruton number on the response amplitude of rectangular cylinder with corner modifications

Washizu et al. (1978) reported that for a rectangular cylinder with a side ratio of 2.0, instabilities were observed in two distinct wind velocity ranges when the Scruton number was sufficiently low. However, as the Scruton number increased, the instability in the lower wind velocity range ceased to exist. This instability was referred to as motion-induced vortex vibration (MIV) by Komatsu and Kobayashi (1980). Shiraishi and Matsumoto (1983) explained the onset velocity of MIV, and this phenomenon is also known as impinging leading-edge vortices (Naudascher and Rockwell, 1994). Furthermore, Washizu et al. (1978) observed that for a rectangular cylinder with a side ratio of 2.0 and a sufficiently large Scruton number, the instability in the high wind velocity range split into two unstable regions. One of these regions was located near the onset wind velocity of Kármán vortex-induced vibration (KVIV), while the other corresponded to galloping.

In this section, the effects of the Scruton number ($S_{c\eta}$) on the MIV, KVIV and galloping response of the rectangular cylinder with various corner modifications were described for α = 0°. Vertical 1DOF free vibration tests were carried out within the reduced wind velocity range of $0 \leq U/fD \leq 41$, in which the maximum Reynolds number corresponds to 99,000. The $S_{c\eta}$ value was calculated according to Eq. 2.8. A wide range of $S_{c\eta}$, ranging from 6 to 130 as listed in Tables 2.1-2.7, was considered in this study. The target $S_{c\eta}$ values were achieved by increasing the structural damping. For $S_{c\eta}$ = 6 and 42, the structural damping was modified by increasing the voltage of the electromagnetic damper. For the remaining $S_{c\eta}$ cases, the structural damping was modified by increasing the plate size of the oil damper. The damping values of each case are provided in Appendix A. There is only limited information in the literature on the galloping instability/characteristics of corner-cut cylinders for the $S_{c\eta}$ range used in current study, even for the common single recession (SR) section. In addition, the threshold of the aerodynamic instability caused by the Kármán vortex interference on the galloping instability has not yet been studied by controlling the Kármán vortex shedding intensity by cutting the corners of the rectangular section. Hence, in this section, the interference between Kármán vortex-induced vibration (KVIV) and the galloping instability was discussed for both rectangular and corner-cut cylinders for various $S_{c\eta}$ values. In the following sections, the heaving natural frequency obtained under no wind condition was represented in f_n, and the Kármán vortex shedding frequency and the vibration frequency obtained from the power spectral density (PSD) at each wind velocity were represented in f_{kv} and f_{vib}. In the free vibration test, the onset wind velocity was considered when the minimum vertical displacement of the model was over 2.25 mm and/or the vertical displacement difference between two consecutive wind velocities was more than 5 mm.

4.3.1 Response amplitude of rectangular section

The rectangular (R) section has the strongest Kármán vortex shedding intensity (C'_{Fy} = 0.57, U = 10.8 m/s) among all studied sections. Fig. 4.3 shows the response amplitude of the R section for various $S_{c\eta}$ cases. The f_{kv} and f_{vib} values obtained from the power spectral density (PSD) at each wind velocity were provided in Fig. 4.4 (a) for without initial vibration and Fig. 4.4 (b) for with initial vibration conditions. Fig. 4.5 illustrates the enlarged view of Fig. 4.4. The f_{kv} and f_{vib} of the R section for each $S_{c\eta}$ were also provided in Figs. G.1-G.6 of Appendix-G.

The motion-induced vortex vibration (MIV) was observed around the reduced wind velocity of 1.67B/D at $S_{c\eta}$ = 6 as shown in Fig. 4.3. For low $S_{c\eta}$ cases (6 and 42), the vibration of the model started from the onset reduced wind velocity of the Kármán vortex-induced vibration (1/St). This vibration increased linearly with the increasing wind velocity. A slight decrease in vibration frequency (frequency drop) was observed between $9 \leq U/f_nD \leq 11$ as shown in Fig. 4.5. In addition, the Karman vortex shedding frequency (f_{kv}) was not observed in the PSDs of the measured wind velocities after the lock-in as shown in Fig. 4.4. In the velocity-amplitude diagram (Fig. 4.3), the lock-in occurred at 1/St and the model showed the KVIV-galloping response for the increasing wind velocity. Hence, the KVIV and galloping fully interfered with each other at low $S_{c\eta}$ values (6 and 42) in the R section.

For the $S_{c\eta}$ values of 56 and 69, the vibration of the model started from 1/St similar to the previous $S_{c\eta}$ cases (6 and 42). When lock-in occurred, a slight frequency drop in vibrating frequency was observed between $9 \leq U/f_nD \leq 11$ as shown in Fig. 4.5. The f_{kv} was observed in the PSDs of U/f_nD starting from 17.41 in the $S_{c\eta}$ = 56 and 14.56 in the $S_{c\eta}$ = 69 cases as shown in Fig. 4.4. Hence, the lock-in might be considered to finish at these reduced wind velocities. However, the magnitude of the response amplitude decreased only for a few measured wind velocities and later increased with the increasing wind velocity (Fig. 4.3). Therefore, the KVIV and galloping partially interfered with each other at mid-$S_{c\eta}$ values (56 and 69) in R section.

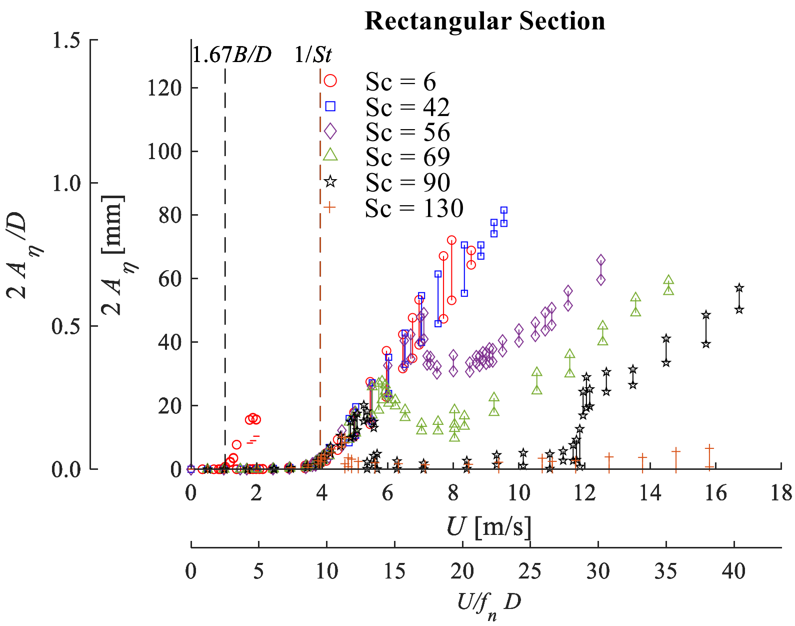

Fig. 4.3 Vibration amplitude of R section for various Scruton numbers at α = 0°.

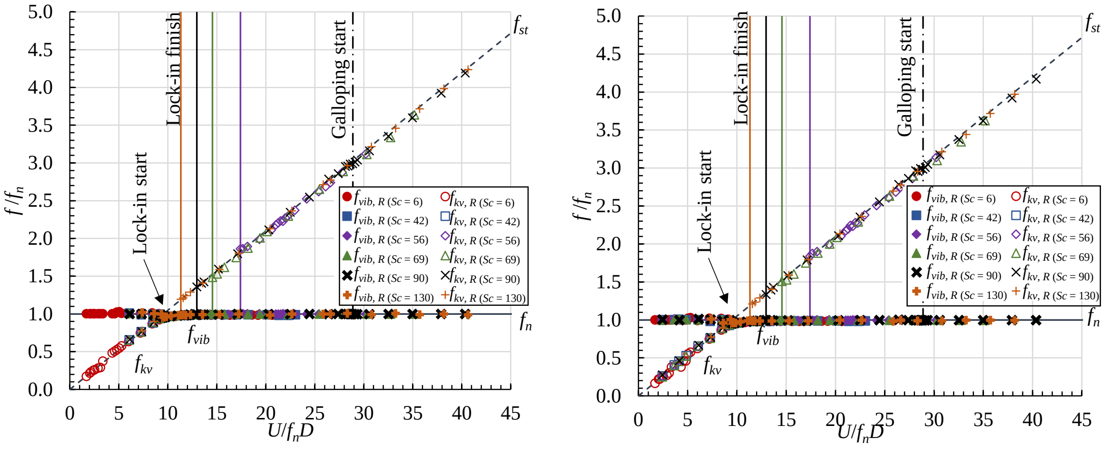

(a) (b)

Fig. 4.4 Kármán vortex shedding frequency (circle) and vibrating frequency (filled circle) (dash slope line: stationary, circle and filled circle: vibrating) of R section under (a) Without, and (b) With initial vibration conditions.

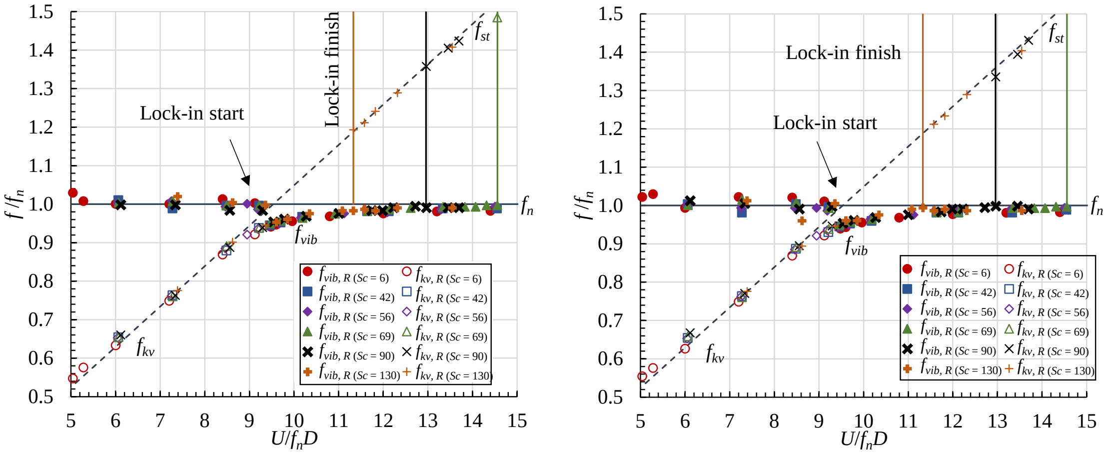

(a) (b)

Fig. 4.5 Enlarged view for Kármán vortex shedding frequency (circle) and vibrating frequency (filled circle) (dash slope line: stationary, circle and filled circle: vibrating) of R section under (a) Without, and (b) With initial vibration conditions.

For high $S_{c\eta}$ cases (90 and 130), the vibration of the model still started from $1/St$ in both cases. However, galloping was only observed in the $S_{c\eta}$ = 90 case at U/f_nD = 28.86. When lock-in occurred, a slight frequency drop in the vibrating frequency was observed between $9 \leq U/f_nD \leq 11$ as shown in Fig. 4.5 in both $S_{c\eta}$ cases. The f_{kv} was observed in the PSDs of U/f_nD starting from 12.96 in the $S_{c\eta}$ = 90 and 11.33 in the $S_{c\eta}$ = 130 cases as shown in Fig. 4.4. In response amplitude diagram (Fig. 4.3), the KVIV was distinctly observed and no vibration was observed with the increasing wind velocity: up to the galloping onset. Hence, the KVIV and galloping did not interfere with each other at high $S_{c\eta}$ values (90 and 130) in the R section.

The critical reduced wind velocity of galloping based on the quasi-steady theory (U_{cr_quasi}) and the onset reduced wind velocity obtained from the free vibration test for the R section at α = 0° were listed in Table 4.4. According to Fig. 4.3, $S_{c\eta}$ of around 90 and 130 was required to decouple KVIV and galloping in the R section. Thus, the U_{cr_quasi} and the galloping onset reduced wind velocity obtained from the velocity-amplitude diagram became close to each other at $S_{c\eta}$ of around 90 and 130.

Table 4.4 The critical reduced wind velocity of galloping based on the quasi-steady theory (U_{cr_quasi}) and the onset reduced wind velocity obtained from the free vibration test for the R section at α = 0°.

$S_{c\eta}$	U_{cr_quasi}		Free vibration test	
	U = 6.0 m/s (Re = 36,000)	U = 10.8 m/s (Re = 64,800)	Without initial vibration	With initial vibration
6	2.47	2.16	9.96	9.96
42	17.08	14.96	9.70	9.70
56	22.54	19.74	9.66	9.66
69	28.39	24.86	9.70	9.70
90	36.68	32.13	28.88	28.88
130	52.70	46.16	-	-

4.3.2 Response amplitude of triple recession section

The triple recession (TR) section had the second strongest Kármán vortex shedding intensity (C'_{Fy} = 0.25, U = 10.8 m/s). Fig. 4.6 shows the response amplitude of the TR section for various $S_{c\eta}$ cases. The f_{kv} and f_{vib} values obtained from the PSD at each wind velocity of the TR section for all $S_{c\eta}$ cases were provided in Fig. 4.7 (a) for without initial vibration and Fig. 4.7 (b) for with initial vibration conditions. Fig. 4.8 illustrates the enlarged view of Fig. 4.7. The f_{kv} and f_{vib} of the TR section for each $S_{c\eta}$ were also provided in Figs. G.7-G.11 of Appendix-G.

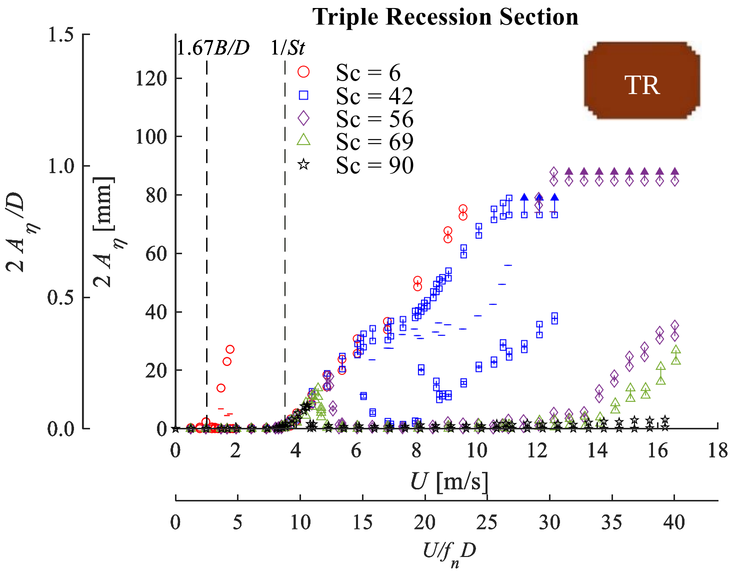

Fig. 4.6 Vibration amplitude of TR section for various Scruton numbers at α = 0°.

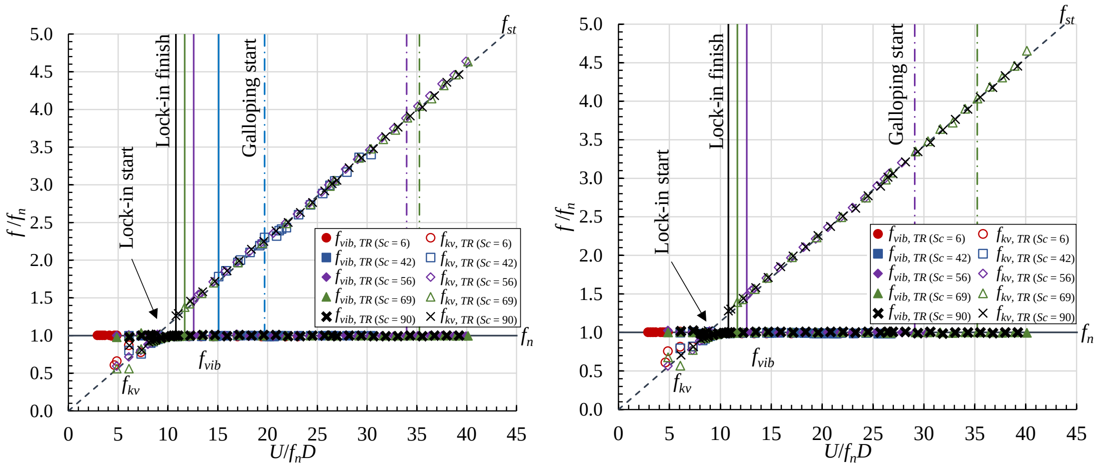

(a) (b)

Fig. 4.7 Kármán vortex shedding frequency (circle) and vibrating frequency (filled circle) (dash slope line: stationary, circle and filled circle: vibrating) of TR section under (a) Without, and (b) With initial vibration conditions.

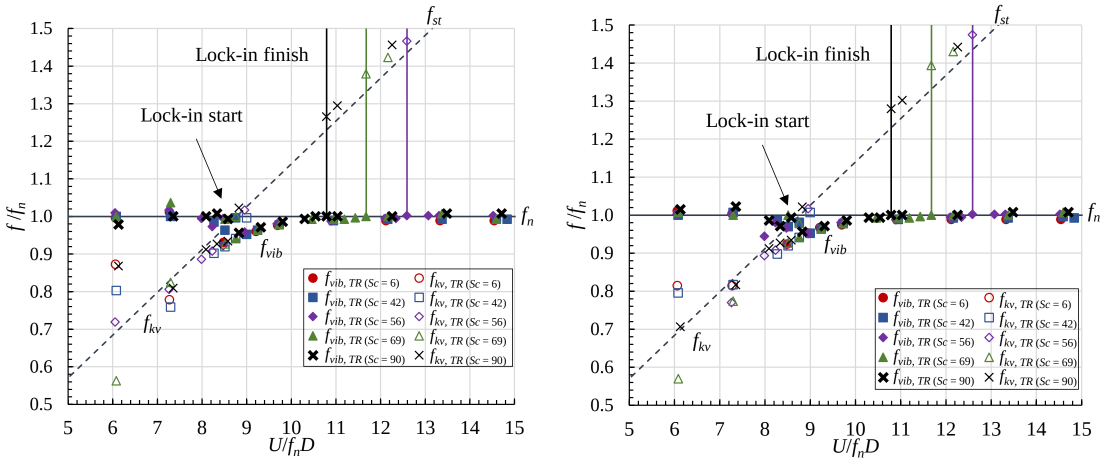

(a) (b)

Fig. 4.8 Enlarged view for Kármán vortex shedding frequency (circle) and vibrating frequency (filled circle) (dash slope line: stationary, circle and filled circle: vibrating) of TR section under (a) Without, and (b) With initial vibration conditions.

MIV was observed around the reduced wind velocity of 1.67B/D at $S_{c\eta}$ = 6 in the TR section as shown in Fig. 4.6. Moreover, the vibration of the model started from the onset reduced wind velocity of the Kármán vortex-induced vibration (1/St) and the vibration increased linearly with the increasing wind velocity. A slight frequency drop was observed between $8.5 \leq U/f_nD \leq 9.5$ as shown in Fig. 4.8. In addition, f_{kv} was not observed in the PSDs of the measured wind velocities after the lock-in as shown in Fig. 4.7. In the velocity-amplitude diagram, the lock-in occurred and the model showed the KVIV-galloping response (Fig. 4.6). Hence, the KVIV and galloping fully interfered with each other at a low $S_{c\eta}$ value of 6 in the TR section.

At $S_{c\eta}$ = 42, the vibration of the model started from $1/St$ similar to the $S_{c\eta}$ = 6 case. When lock-in occurred, a slight frequency drop was observed between $8.5 \leq U/f_nD \leq 9.5$ as shown in Fig. 4.8. In the without initial vibration case, as shown in Fig. 4.7 (a), the f_{kv} was observed in the PSDs between $15.08 \leq U/f_nD \leq 19.70$ and $20.92 \leq U/f_nD \leq 30.40$. Hence, lock-in may be considered to finish at U/f_nD = 15.08 and no vibration was observed between $15.08 \leq U/f_nD \leq 19.70$ in Fig. 4.6. In the case with initial vibration as shown in Fig. 4.7 (b), the f_{kv} was not observed in the PSDs of the measured wind velocities after the lock-in. Also, the vibration amplitude increased linearly with the increasing wind velocity (Fig. 4.6). So, in the TR section, the KVIV and galloping partially interfered with each other in the absence of initial vibration and fully interfered with each other in the presence of initial vibration.

For $S_{c\eta}$ of 56, 69 and 90, the vibration of the model started from $1/St$. As shown in Fig. 4.8, a slight frequency drop in the vibrating frequency was observed between $8.5 \leq U/f_nD \leq 9.5$ when lock-in occurred. As shown in Fig 4.7, the f_{kv} was observed in the PSDs of U/f_nD starting from 12.59, 11.68 and 10.79, respectively. In Fig. 4.6, the KVIV was distinctly observed and no vibration was observed with the increasing wind velocity until the galloping onset. At $S_{c\eta}$ = 90, galloping was not observed within the measured wind velocity range. Hence, the KVIV and galloping did not interfere with each other at these $S_{c\eta}$ values.

The critical reduced wind velocity of galloping based on the quasi-steady theory (U_{cr_quasi}) and the onset reduced wind velocity obtained from the free vibration test for the TR section at α = 0° were listed in Table 4.5. Due to the presence of Reynolds dependency in the $dC_{Fy}/d\alpha$ value (Table 4.1), significant different in the U_{cr_quasi} values were observed between two measured wind velocities. According to Fig. 4.6, the $S_{c\eta}$ value of around 42 was required to separate KVIV and galloping in the TR section. Therefore, the U_{cr_quasi} and the galloping onset reduced wind velocity obtained from the velocity-amplitude diagram became close to each other starting from $S_{c\eta}$ of 42 in the absence of initial vibration and 56 in the presence of initial vibration (Table 4.5). Therefore, a smaller mass-damping parameter than the R section is required to decouple KVIV and galloping instability in the TR section.

Table 4.5 The critical reduced wind velocity of galloping based on the quasi-steady theory (U_{cr_quasi}) and the onset reduced wind velocity obtained from free vibration test for the TR section at α = 0°.

$S_{c\eta}$	U_{cr_quasi}		Free vibration test	
	U = 6.0 m/s (Re = 36,000)	U = 10.8 m/s (Re = 64,800)	Without initial vibration	With initial vibration
6	4.27	2.86	9.70	9.70
42	28.70	19.20	19.69	9.73
56	37.97	25.39	30.33	29.11
69	47.14	31.53	35.25	35.25
90	60.42	40.41	-	-

4.3.3 Response amplitude of double recession III section

The double recession III (DR III) section has the Kármán vortex shedding intensity of 0.12 at U = 10.8 m/s. Fig. 4.9 shows the response amplitude of the DR III section for various $S_{c\eta}$ cases. The f_{kv} and f_{vib} values obtained from the PSD at each wind velocity of the DR III section for all $S_{c\eta}$ cases were provided in Fig. 4.10 (a) for without initial vibration and Fig. 4.10 (b) for with initial vibration conditions. Fig. 4.11 illustrates the enlarged view of Fig. 4.10. The f_{kv} and f_{vib} of the DR III section for each $S_{c\eta}$ were also provided in Figs. G.12-G.16 of Appendix-G.

MIV was observed around the reduced wind velocity of 1.67*B/D* at $S_{c\eta}$ = 6 in the DR III section as shown in Fig. 4.9. The vibration of the model started from the onset reduced wind velocity of the Kármán vortex-induced vibration (1/*St*) and the vibration increased linearly with the increasing wind velocity. A slight frequency drop was observed between $8.5 \leq U/f_nD \leq 9.5$ as shown in Fig. 4.11. The f_{kv} was not observed in the PSDs of measured wind velocities after the lock-in as shown in Fig. 4.10.

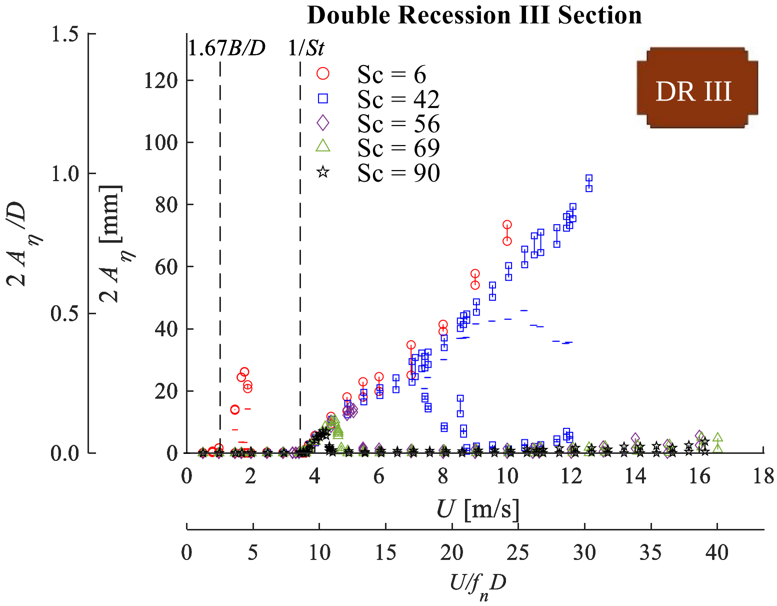

Fig. 4.9 Vibration amplitude of DR III section for various Scruton numbers at α = 0°.

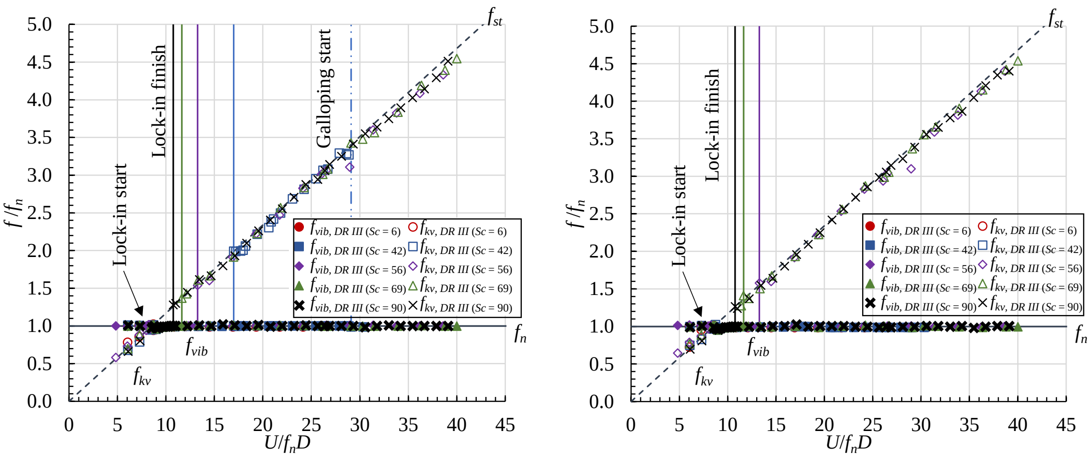

(a) (b)

Fig. 4.10 Kármán vortex shedding frequency (circle) and vibrating frequency (filled circle) (dash slope line: stationary, circle and filled circle: vibrating) of DR III section under (a) Without, and (b) With initial vibration conditions.

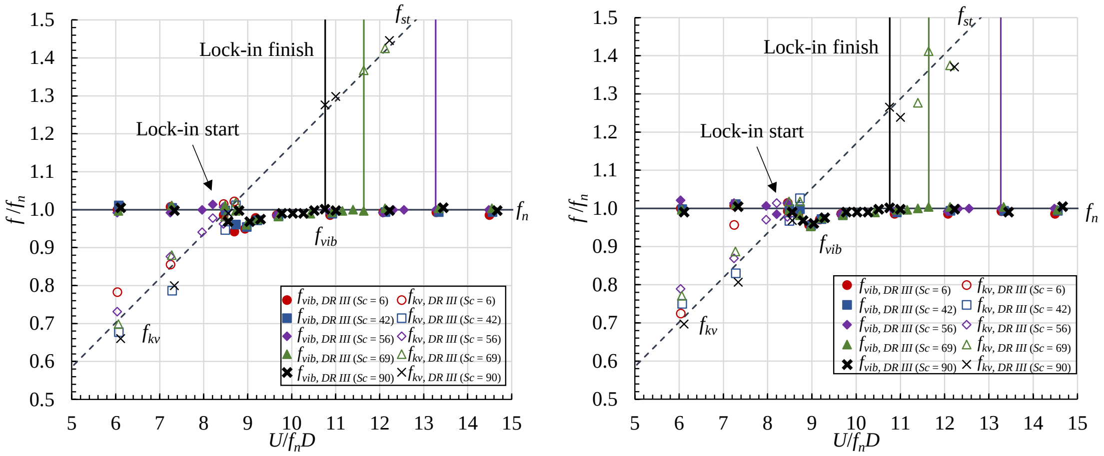

(a) (b)

Fig. 4.11 Enlarged view for Kármán vortex shedding frequency (circle) and vibrating frequency (filled circle) (dash slope line: stationary, circle and filled circle: vibrating) of DR III section under (a) Without, and (b) With initial vibration conditions.

Moreover, the lock-in occurred and the model showed the KVIV-galloping response in the velocity-amplitude diagram as shown in Fig. 4.9. Hence, the KVIV and galloping fully interfered with each other in the DR III section at $S_{c\eta} = 6$.

As shown in Fig. 4.9, the vibration of the model started from $1/St$ at $S_{c\eta} = 42$. A slight frequency drop was observed between $8.5 \leq U/f_nD \leq 9.5$ as shown in Fig. 4.11 when lock-in occurred. Since f_v was observed in the PSDs starting from $U/f_nD = 16.98$ in the without initial vibration case (Fig. 4.10 (a)), lock-in may be considered to finish. Vibration also decreased with increasing wind velocity and no vibration was observed in the response amplitude diagram (Fig. 4.9). On the other hand, f_{kv} was not observed in the PSDs of the measured wind velocities after the lock-in in with initial vibration case (Fig. 4.10 (b)). The vibration amplitude increased linearly with the increasing wind velocity (Fig. 4.9). Hence, the KVIV and galloping partially interfered with each other in the absence of initial vibration and fully interfered with each other in the presence of initial vibration at $S_{c\eta} = 42$ in the DR III section.

In the case of $S_{c\eta} = 56$, 69 and 90, the vibration of the model started from $1/St$ (Fig. 4.9). A slight frequency drop in the vibrating frequency was observed between $8.5 \leq U/f_nD \leq 9.5$ when lock-in occurred (Fig. 4.11). In the PSDs, f_{kv} was observed starting from U/f_nD of 13.27, 11.64 and 10.76, respectively as shown in Fig. 4.10. The KVIV was distinctly observed in the response amplitude diagram (Fig. 4.9) and galloping was not observed within the measured wind velocity range. Hence, the KVIV and galloping did not interfere with each other at these $S_{c\eta}$ values in the DR III section.

The critical reduced wind velocity of galloping based on the quasi-steady theory (U_{cr_quasi}) and the onset reduced wind velocity obtained from the free vibration test for the DR III section at $\alpha = 0°$ were listed in Table 4.6. According to response amplitude (Fig. 4.9), $S_{c\eta}$ of around 42 was required to separate KVIV and galloping in the DR III section. Thus, the U_{cr_quasi} and the galloping onset reduced wind velocity obtained from the velocity-amplitude diagram became close to each other at $S_{c\eta}$ of 42 in the absence of initial vibration (Table 4.6). Hence, a smaller mass-damping parameter than the R section is required to decouple KVIV and galloping instability in the DR III section.

Table 4.6 The critical reduced wind velocity of galloping based on the quasi-steady theory (U_{cr_quasi}) and the onset reduced wind velocity obtained from free vibration test for the DR III section at α = 0°.

$S_{c\eta}$	U_{cr_quasi}		Free vibration test	
	U = 6.0 m/s (Re = 36,000)	U = 10.8 m/s (Re = 64,800)	Without initial vibration	With initial vibration
6	3.99	3.99	9.66	9.66
42	27.26	27.25	29.11	9.70
56	35.41	35.39	-	-
69	44.23	44.21	-	-
90	57.60	57.57	-	-

4.3.4 Response amplitude of double recession section

The double recession (DR) section has the Kármán vortex shedding intensity of 0.06 at U = 6.0 m/s and 0.09 at U = 10.8 m/s. Fig. 4.12 shows the response amplitude of the DR section for various $S_{c\eta}$ cases. The f_{kv} and f_{vib} values obtained from the PSD at each wind velocity of the DR section for all $S_{c\eta}$ cases were provided in Fig. 4.13 (a) for without initial vibration and Fig. 4.13 (b) for with initial vibration conditions. The f_{kv} and f_{vib} of the DR section for each $S_{c\eta}$ were also provided in Figs. G.17-G.21 of Appendix-G. As shown in Fig. 4.12, MIV was hardly observed around the reduced wind velocity of 1.67B/D in the DR section even at $S_{c\eta}$ = 6. The vibration of the model did not start from the onset reduced wind velocity of the Kármán vortex-induced vibration (1/St). When vibration occurred, it increased with the increasing wind velocity. The f_{kv} was also not observed in the PSDs of the measured wind velocities as shown in Fig. 4.13. In the velocity-amplitude diagram (Fig. 4.12), the model showed the KVIV-galloping response. Therefore, the KVIV and galloping might fully interfere with each other in the DR section at $S_{c\eta}$ = 6.

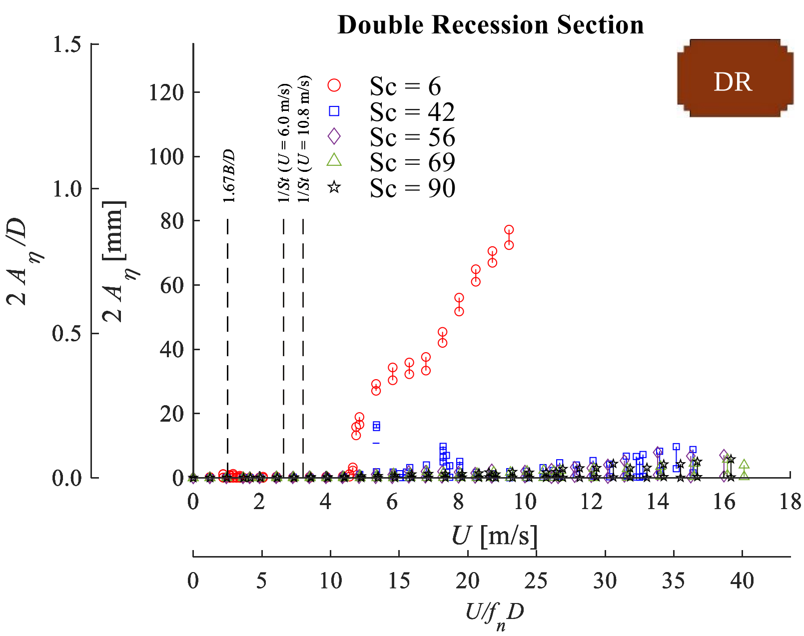

Fig. 4.12 Vibration amplitude of DR section for various Scruton numbers at α = 0°.

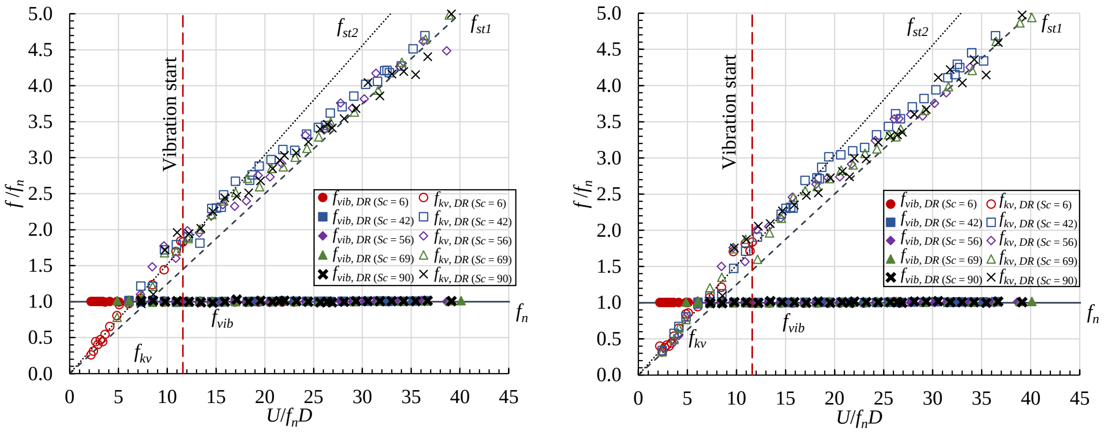

(a) (b)

Fig. 4.13 Kármán vortex shedding frequency (circle) and vibrating frequency (filled circle) (dash slope line: stationary, circle and filled circle: vibrating) of DR section under (a) Without, and (b) With initial vibration conditions.

Table 4.7 The critical reduced wind velocity of galloping based on the quasi-steady theory (U_{cr_quasi}) and the onset reduced wind velocity obtained from the free vibration test for the DR section at α = 0°.

$S_{c\eta}$	U_{cr_quasi}		Free vibration test	
	U = 6.0 m/s (Re = 36,000)	U = 10.8 m/s (Re = 64,800)	Without initial vibration	With initial vibration
6	2.77	7.08	11.62	11.62
42	18.26	46.66	-	-
56	24.08	61.52	-	-
69	30.31	77.45	-	-
90	39.52	100.98	-	-

For the remaining Scruton number cases (42, 56, 69 and 90), no significant vibration of the model was observed (Fig. 4.12). The f_v was also observed in the PSD of each measured wind velocity (Fig. 4.13). In Table 4.7, the critical reduced wind velocity of galloping based on the quasi-steady theory (U_{cr_quasi}) and the onset reduced wind velocity obtained from the free vibration test for the DR section at α = 0° were listed. Since Reynolds number dependency was present in the $dC_{Fy}/d\alpha$ value, significant different in the U_{cr_quasi} values were observed between the two measured wind velocities. Vibrations were also only observed in the $S_{c\eta}$ of 6 as the $dC_{Fy}/d\alpha$ is negative only in the lower wind velocity region. It is also difficult to study the KVIV and galloping interference in the DR section.

4.3.5 Response amplitude of double recession II section

The double recession II (DR II) section has the Kármán vortex shedding intensity of 0.05 at U = 10.8 m/s. The response amplitude of the DR II section for various $S_{c\eta}$ cases is shown in Fig. 4.14. The f_{kv} and f_{vib} values obtained from the PSD at each wind velocity of the DR II section for all $S_{c\eta}$

cases were provided in Fig. 4.15 (a) for without initial vibration and Fig. 4.15 (b) for with initial vibration conditions. The f_{kv} and f_{vib} of the DR II section for each $S_{c\eta}$ was also provided in Figs. G.22-G.26 of Appendix-G.

At $S_{c\eta}$ = 6, MIV was observed around the reduced wind velocity of 1.67*B/D* as shown in Fig. 4.14. The vibration of the model did not start from the onset reduced wind velocity of the Kármán vortex-induced vibration (1/*St*). Once vibration occurred, it increased with the increasing wind velocity and f_{kv} was not observed in the PSDs as shown in Fig. 4.15. In the velocity-amplitude diagram (Fig. 4.14), the model showed the KVIV-galloping response. Therefore, the KVIV and galloping fully interfered with each other in the DR II section at $S_{c\eta}$ = 6.

For $S_{c\eta}$ of 42, 56, and 69, the wind velocity limited vibration response similar to KVIV was observed between $10.67 \leq U/f_nD \leq 14.56$ in $S_{c\eta}$ = 42, and $11.11 \leq U/f_nD \leq 12.08$ in $S_{c\eta}$ = 56 as shown in Fig. 4.14. As shown in Fig. 4.15, the f_{kv} was observed in the PSDs starting from U/f_nD of 15.77 and 12.56, respectively. In the response amplitude diagram (Fig. 4.14), the vibration appeared to be galloping was observed around U/f_nD of 23 and 30. Thus, the wind velocity limited vibration response similar to KVIV and galloping did not interfere with each other at these $S_{c\eta}$ values in the DR II section. In $S_{c\eta}$ = 90 case, no significant vibration response was observed within measured wind velocity range.

The critical reduced wind velocity of galloping based on the quasi-steady theory (U_{cr_quasi}) and the onset reduced wind velocity obtained from the free vibration test for the DR II section at α = 0° were listed in Table 4.8. The U_{cr_quasi} and the galloping onset reduced wind velocity obtained from the velocity-amplitude diagram did not become close to each other in the DR II section. According to response amplitude (Fig. 4.14), $S_{c\eta}$ of around 42 was required to separate the wind velocity limited vibration similar to the KVIV and galloping in the DR II section. In the DR II section, a smaller mass-damping parameter than the R section ($S_{c\eta}$ = 42) is required to decouple the two phenomenon.

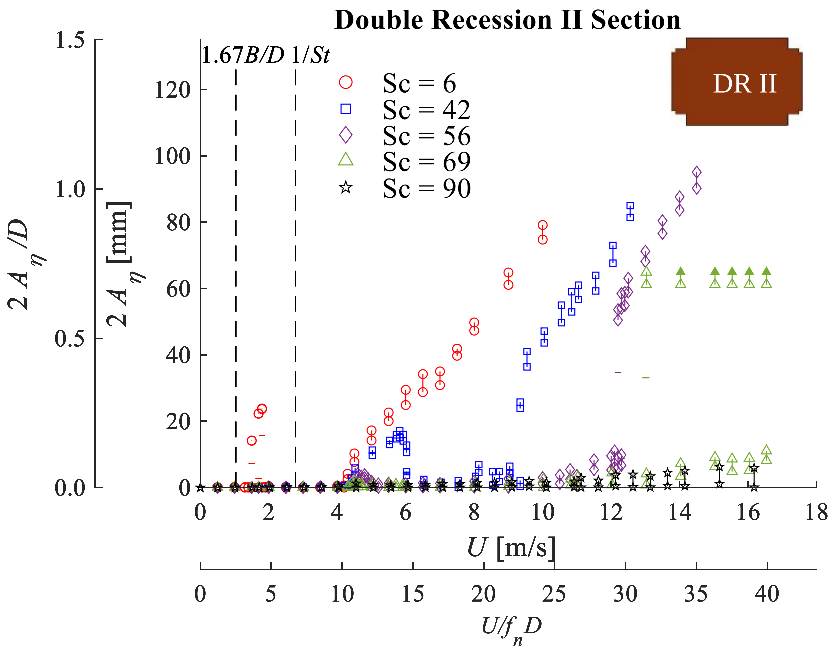

Fig. 4.14 Vibration amplitude of DR II section for various Scruton numbers α = 0°.

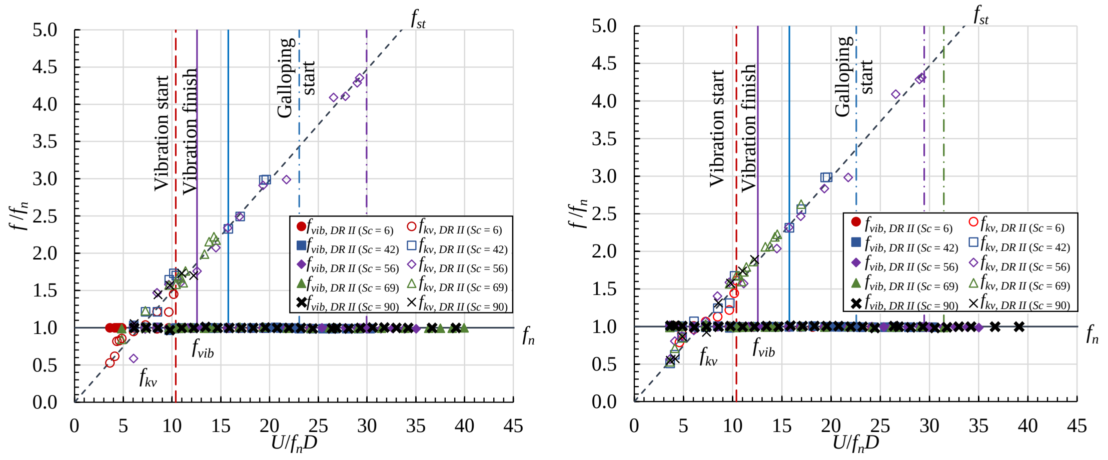

(a) (b)

Fig. 4.15 Kármán vortex shedding frequency (circle) and vibrating frequency (filled circle) (dash slope line: stationary, circle and filled circle: vibrating) of DR II section under (a) Without, and (b) With initial vibration conditions.

Table 4.8 The critical reduced wind velocity of galloping based on the quasi-steady theory (U_{cr_quasi}) and the onset reduced wind velocity obtained from free vibration test for the DR II section at α = 0°.

$S_{c\eta}$	U_{cr_quasi}		Free vibration test	
	U = 6.0 m/s (Re = 36,000)	U = 10.8 m/s (Re = 64,800)	Without initial vibration	With initial vibration
6	1.97	2.14	10.39	10.39
42	13.11	14.26	23.05	22.56
56	17.19	18.70	27.78	27.78
69	21.29	23.16	33.89	31.47
90	27.03	29.39	-	-

4.3.6 Response amplitude of single recession section

The single recession (SR) section has the C'_{Fy} of 0.05 at U = 10.8 m/s. The response amplitude of the SR section for various $S_{c\eta}$ cases is shown in Fig. 4.16. The f_{kv} and f_{vib} values obtained from the PSD at each wind velocity of the SR section were provided in Fig. 4.17 (a) for without initial vibration and Fig. 4.17 (b) for with initial vibration conditions. At $S_{c\eta}$ = 6, the MIV was observed around the reduced wind velocity of 1.67B/D in the SR section as shown in Fig. 4.16. Kármán vortex-induced vibration (1/St) and the vibration amplitude increased with the increasing wind velocity. As shown in Fig. 4.17, f_{kv} was also not observed in the PSDs. The model showed the KVIV-galloping response in the velocity-amplitude diagram (Fig. 4.16). Thus, the KVIV and galloping fully interfered with each other at $S_{c\eta}$ = 6 in the SR section.

Since the Kármán vortex shedding of the SR section was very weak, the KVIV was not observed in this section at $S_{c\eta}$ = 42, 56, 69, and 90 cases (Fig. 4.16). At $S_{c\eta}$ = 42 and 56, the vibration of the model started from U/f_nD of 19.56 and 29.35. Then, the vibration amplitude linearly increased with the increasing wind velocity. At $S_{c\eta}$ = 69 and 90, no significant vibration response was observed within the measured wind velocity range.

In addition, f_{kv} was observed in the PSDs until U/f_nD of approximately 20 in the $S_{c\eta}$ cases of 42–90 (Fig. 4.17). Thus, the KVIV and galloping did not interfere with each other at these $S_{c\eta}$ values in the SR section. The f_{kv} and f_{vib} values obtained from the PSD at each wind velocity of the SR section for each $S_{c\eta}$ were also provided in Figs. G.27-G.31 of Appendix-G.

The critical reduced wind velocity of galloping based on the quasi-steady theory (U_{cr_quasi}) and the onset reduced wind velocity obtained from the free vibration test for the SR section at α = 0° were listed in Table 4.9. Due to the presence of Reynolds number dependency in the $dC_{Fy}/d\alpha$ value (Table 4.1), significant different in the U_{cr_quasi} values were observed between the two measured wind

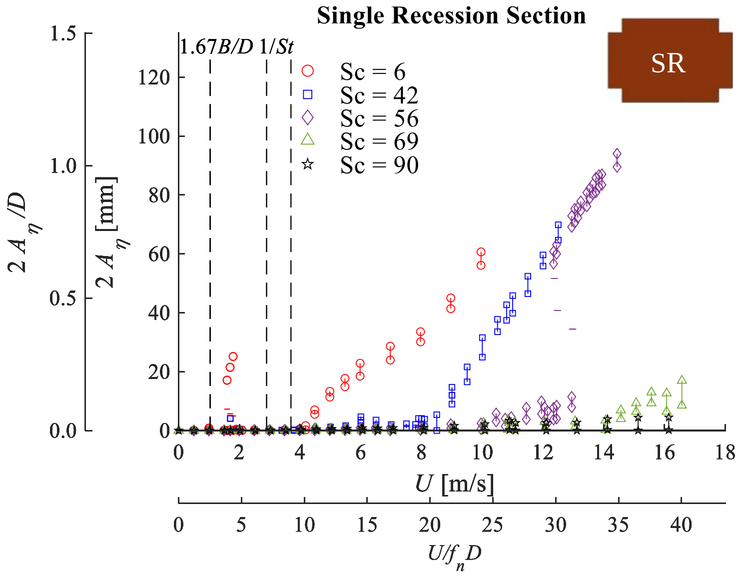

Fig. 4.16 Vibration amplitude of SR section for various Scruton numbers at α = 0°.

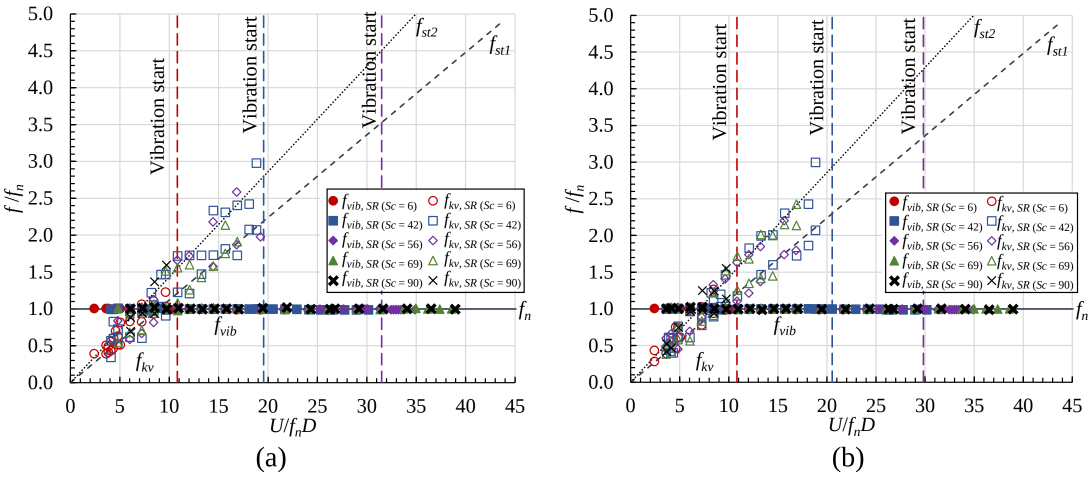

Fig. 4.17 Kármán vortex shedding frequency (circle) and vibrating frequency (filled circle) (dash slope line: stationary, circle and filled circle: vibrating) of SR section under (a) Without, and (b) With initial vibration conditions.

velocities. In the SR section, KVIV was hardly observed and $S_{c\eta}$ of around 42 was required to separate KVIV and galloping as shown in Fig. 4.16. However, the U_{cr_quasi} and the galloping onset reduced wind velocity obtained from the velocity-amplitude diagram did not become close to each other in the SR section. A smaller mass-damping parameter than the R section ($S_{c\eta}$ = 42) is required to decouple KVIV and galloping instability in the SR section.

Table 4.9 The critical reduced wind velocity of galloping based on the quasi-steady theory (U_{cr_quasi}) and the onset reduced wind velocity obtained from the free vibration test for the SR section at α = 0°.

$S_{c\eta}$	U_{cr_quasi}		Free vibration test	
	U = 6.0 m/s (Re = 36,000)	U = 10.8 m/s (Re = 64,800)	Without initial vibration	With initial vibration
6	2.98	2.24	10.82	10.82
42	20.42	15.35	19.57	20.53
56	26.82	20.16	30.06	29.82
69	33.16	24.93	-	-
90	43.41	32.63	-	-

4.3.7 Response amplitude of chamfer section

The chamfer (C) section has the Kármán vortex shedding intensity of 0.04 at U = 6.0 m/s and 0.16 at U = 10.8 m/s. The response amplitude of the C section for various $S_{c\eta}$ cases is shown in Fig. 4.18. The f_{kv} and f_{vib} values obtained from the PSD at each wind velocity of the C section for all $S_{c\eta}$ cases were provided in Fig. 4.19 (a) for without initial vibration and Fig. 4.19 (b) for with initial vibration conditions. The f_{kv} and f_{vib} values obtained from the PSD at each wind velocity of the C section for each $S_{c\eta}$ were also provided in Figs. G.32-G.36 of Appendix-G.

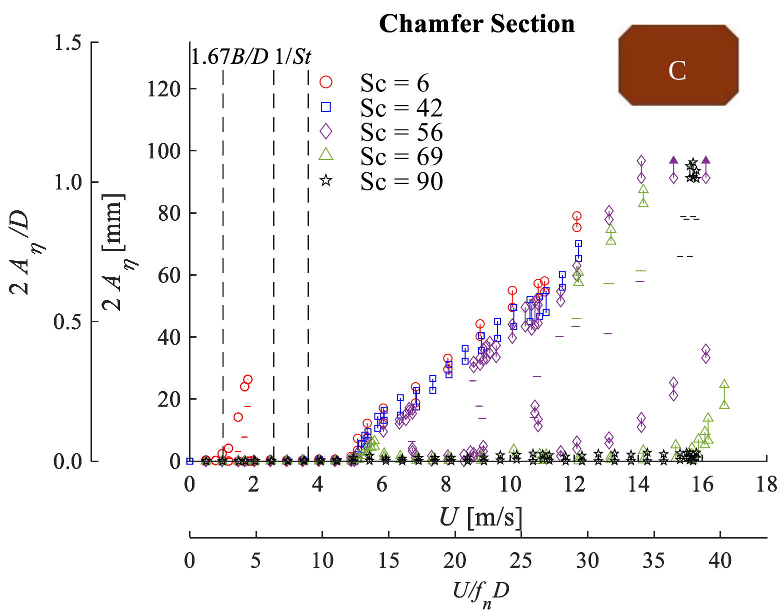

Fig. 4.18 Vibration amplitude of C section for various Scruton numbers at α = 0°.

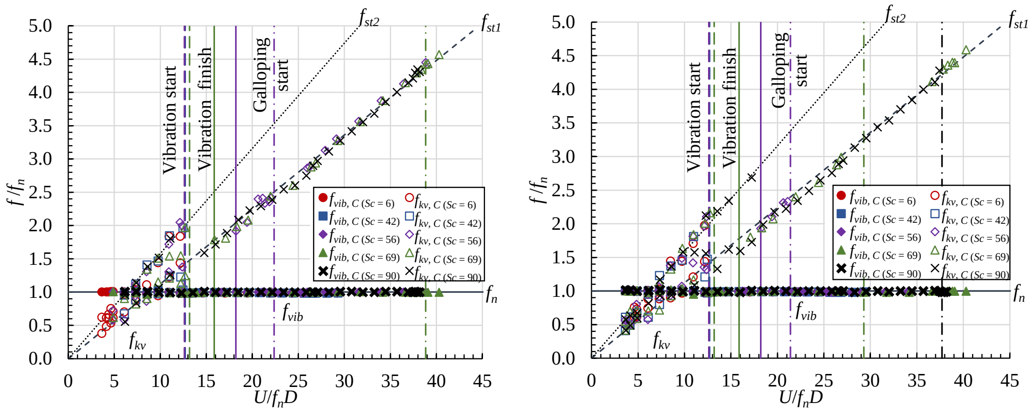

(a) (b)

Fig. 4.19 Kármán vortex shedding frequency (circle) and vibrating frequency (filled circle) (dash slope line: stationary, circle and filled circle: vibrating) of C section under (a) Without, and (b) With initial vibration conditions.

As shown in Fig. 4.18, MIV was observed around the reduced wind velocity of 1.67*B/D* at $S_{c\eta}$ = 6. The vibration of the model did not start from the onset reduced wind velocity of the Kármán vortex-induced vibration (1/*St*) and the vibration increase linearly with the increasing wind velocity both in $S_{c\eta}$ = 6 and 42 cases. Once the vibration occurred, it linearly increased with the increasing wind velocity and f_v was not observed in the PSDs as shown in Fig. 4.19. In the velocity-amplitude diagram (Fig. 4.18), the model showed the KVIV-galloping response. Hence, the KVIV and galloping fully interfered with each other in the C section at $S_{c\eta}$ = 6 and 42 cases.

In $S_{c\eta}$ = 56 and 69 cases, the KVIV type vibration response was observed between 12.62 ≤ U/f_nD ≤ 16.99 in $S_{c\eta}$ = 56, and 13.19 ≤ U/f_nD ≤ 14.65 in $S_{c\eta}$ = 69 as shown in Fig. 4.18. At $S_{c\eta}$ = 56, the f_{kv} was observed in the PSDs between 18.21 ≤ U/f_nD ≤ 22.09 and U/f_nD ≥ 25.97 in the without initial vibration case as shown in Fig. 4.19 (a) and U/f_nD ≥ 18.21 in the with initial vibration case as shown in Fig. 4.19 (b). At $S_{c\eta}$ = 69, the f_{kv} was observed in the PSDs of U/f_nD ≤ 15.87 in the without initial vibration case as shown in Fig. 4.19 (a), and between 17.09 ≤ U/f_nD ≤ 26.86 and U/f_nD ≥ 36.63 in the with initial vibration case as shown in Fig. 4.19 (b). Therefore, KVIV can be considered to finish at U/f_nD = 18.21 in $S_{c\eta}$ = 56 case and around U/f_nD = 17.09 in $S_{c\eta}$ = 69 case. In $S_{c\eta}$ = 90 case, no significant vibration response was observed within the measured wind velocity range in the without initial vibration case. On the other hand, galloping was observed at U/f_nD = 37.69 in the with initial vibration case. Hence, in the C section, the KVIV and galloping did not interfere with each other from $S_{c\eta}$ = 56.

The critical reduced wind velocity of galloping based on the quasi-steady theory (U_{cr_quasi}) and the onset reduced wind velocity obtained from the free vibration test for the C section at α = 0° were listed in Table 4.10. According to the response amplitude diagram (Fig. 4.18), $S_{c\eta}$ of around 56 was required to separate KVIV and galloping in the C section. Therefore, the U_{cr_quasi} and the galloping onset reduced wind velocity obtained from the velocity-amplitude diagram became close to each other starting from $S_{c\eta}$ of 56. A smaller mass-damping parameter than the R section is required to decouple KVIV and galloping instability in the C section.

Table 4.10 The critical reduced wind velocity of galloping based on the quasi-steady theory (U_{cr_quasi}) and the onset reduced wind velocity obtained from the free vibration test for the C section at α = 0°.

$S_{c\eta}$	U_{cr_quasi}		Free vibration test	
	U = 6.0 m/s (Re = 36,000)	U = 10.8 m/s (Re = 64,800)	Without initial vibration	With initial vibration
6	2.63	2.42	12.64	12.64
42	17.75	16.30	12.94	12.94
56	23.35	21.45	22.12	21.40
69	29.23	26.85	38.83	29.30
90	37.64	34.58	>38	37.69

4.3.8 Summary

In this study, the effect of Kármán vortex shedding on the galloping onset wind velocity was discussed by modifying the Kármán vortex shedding intensity (C'_{Fy}) of a section. This was accomplished by altering the corner shapes of the rectangular cylinder into different shapes as illustrated in Figs. 2.4 and 4.1. To summarize, the response amplitudes of the studied sections were divided into two groups: (i) sections which vibrated at 1/*St* and (ii) sections which did not vibrate at 1/*St*. Fig 4.20 shows the division of two groups for the lowest Scruton number ($S_{c\eta}$ = 6) case.

As shown in Fig 4.20 (a), the R, TR and DR III sections vibrated at the onset reduced wind velocity of the Kármán vortex-induced vibration (1/*St*). The Kármán vortex shedding of these three sections was the strongest among all studied sections (Fig. 4.1). Hence, the galloping onsets of these sections may be controlled by the Kármán vortex. The remaining sections, DR, DRII, SR and C

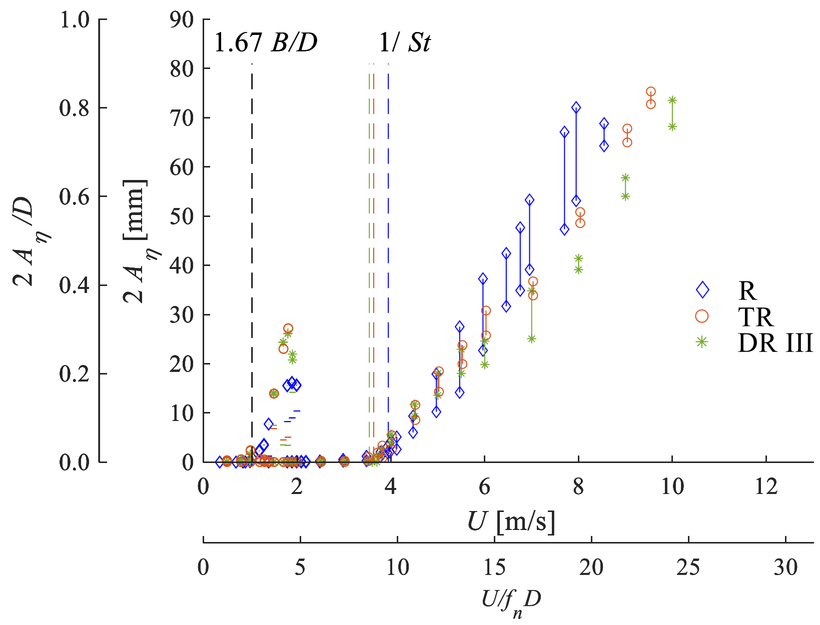

(a)

Fig. 4.20 Vibration amplitude of (a) R, TR, and DR III, and (b) DR, DR II, SR, and C sections at $S_{c\eta}$ = 6 (1/2).

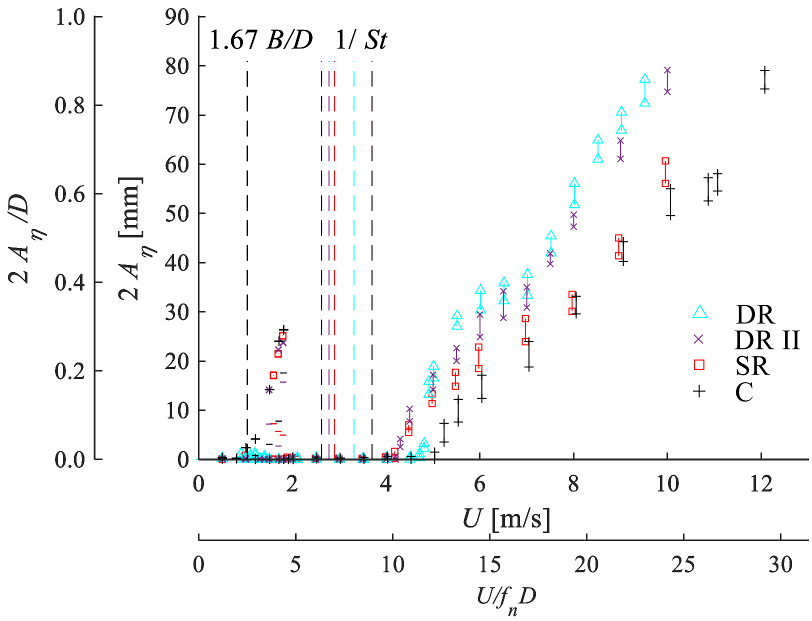

(b)

Fig. 4.20 Vibration amplitude of (a) R, TR, and DR III, and (b) DR, DR II, SR, and C sections at $S_{c\eta}$ = 6 (2/2).

sections, did not vibrate at 1/*St* as shown in Fig 4.20 (b). In these sections, the Kármán vortex shedding was very weak, except in the C section due to its Reynolds number dependency (Fig. 4.1). Therefore, another factor other than the Kármán vortex may affect the galloping onset of these sections.

4.4 Effect of corner shape modification on the unsteady aerodynamic characteristics of rectangular cylinder

In this section, the effects of corner shape modifications on the unsteady aerodynamic characteristics such as H_1^* and H_4^* were discussed for α = 0°. Vertical 1DOF forced vibration tests were carried out for double amplitude of $2\eta_0$ = 2.25, 9, and 27 mm ($2\eta_0/D$ = 0.025, 0.1, and 0.3, respectively), and vibration frequency of f = 1.5, 2.0, and 2.6 Hz at α = 0° (Table 2.8). The measured reduced wind velocity range was $0 \leq U/fD \leq 105$, in which the maximum Reynolds number corresponds to 84,000. The aerodynamic derivatives, H_1^* and H_4^* were calculated according to Eqs. 2.16 and 2.17. The aerodynamic damping parameter (H_1^*) was used to evaluate whether or not galloping would occur. When H_1^* is positive, aerodynamic instability is observed in the section. There is only limited literature concerning the aerodynamic derivatives for the corner-cut and rectangular cylinders of side ratio 1.5. Therefore, in the following sections, the frequency dependency/Reynolds number dependency and amplitude dependency of H_1^* for each section were described. Then, the effects of corner shape modification on the aerodynamic derivatives were discussed.

4.4.1 Reynolds number and amplitude dependencies

(1) Rectangular (R)

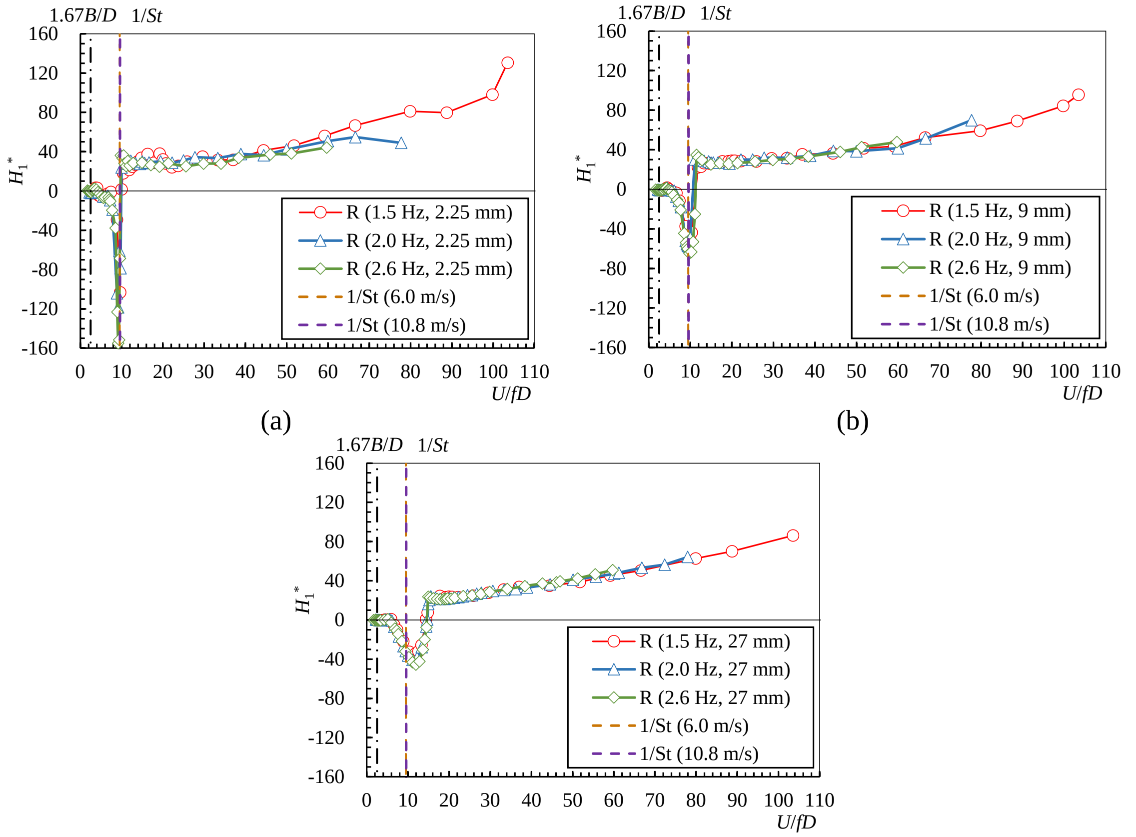

(c)

Fig. 4.21 Aerodynamic damping H_1^* of R section for the forced vibrating frequencies of 1.5, 2.0, and 2.6 Hz at the forced vibrating double amplitude ($2\eta_0$) of: (a) 0.025D; (b) 0.1D; and (c) 0.3D.

For the R section as shown in Fig. 4.21, the amplitude dependency was present in the onset reduced wind velocity. No Reynolds number dependency was also observed at the onset and the H_1^* values within the studied reduced wind velocity range at all three amplitudes. The amplitude dependency of R section was also provided in Figs. E.1 and E3 of Appendix E.

(2) Triple Recession (TR)

For the TR section as shown in Fig. 4.22, the amplitude dependency was present in the onset reduced wind velocity. A slight Reynolds number dependency was also observed around the onset region, especially at $2\eta_0$ of 2.25, and 9 mm. A larger vibration frequency value gave a smaller galloping onset value. On the other hand, no Reynolds number dependency was found in the H_1^* values at all three amplitudes. The amplitude dependency of TR section was also provided in Figs. E.4 and E5 of Appendix E.

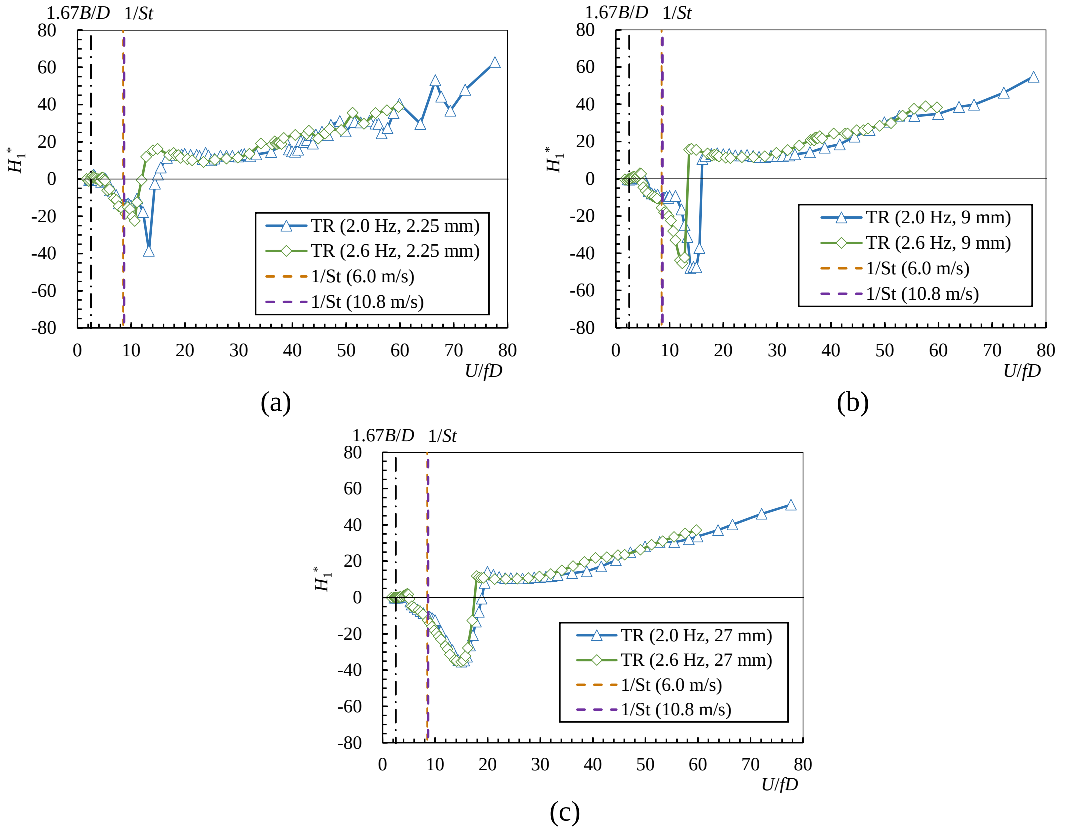

Fig. 4.22 Aerodynamic damping H_1^* of TR section for the forced vibrating frequencies of 1.5, 2.0, and 2.6 Hz at the forced vibrating double amplitude ($2\eta_0$) of: (a) 0.025*D*; (b) 0.1*D*; and (c) 0.3*D*.

(3) Double Recession III (DR III)

For the DR III section as shown in Fig. 4.23, the amplitude dependency was present in the onset reduced wind velocity. A slight Reynolds number dependency was also observed around the onset region and in the H_1^* values of higher reduced wind velocity (U/fD > 40) at all three amplitudes. A larger vibration frequency value gave a smaller galloping onset value. The amplitude dependency of DR III section was also provided in Figs. E.6 and E7 of Appendix E.

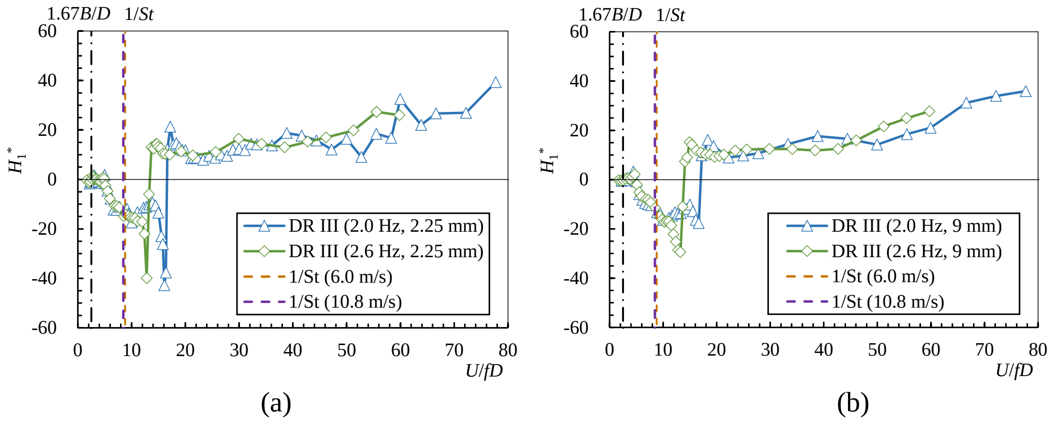

Fig. 4.23 Aerodynamic damping H_1^* of DRIII section for the forced vibrating frequencies of 1.5, 2.0, and 2.6Hz at the forced vibrating double amplitude ($2\eta_0$) of: (a) 0.025*D*; (b) 0.1*D*; and (c) 0.3*D*(1/2).

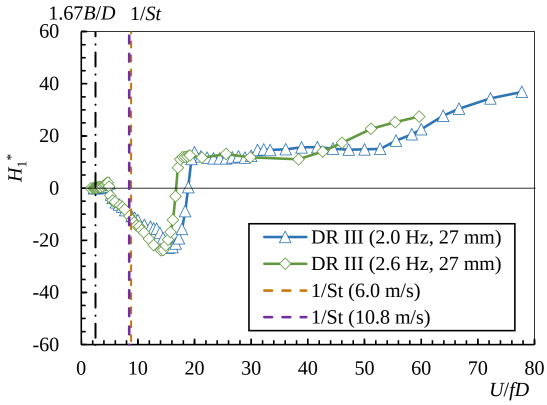

(c)

Fig. 4.23 Aerodynamic damping H_1^* of DRIII section for the forced vibrating frequencies of 1.5, 2.0, and 2.6Hz at the forced vibrating double amplitude ($2\eta_0$) of: (a) 0.025*D*; (b) 0.1*D*; and (c) 0.3*D*(2/2).

(4) Double Recession (DR)

As mentioned in Section 3.2.2, Reynolds number dependency was present in the aerodynamic force coefficients of the DR section. As shown in Fig. 4.24, the amplitude dependency was present in the onset reduced wind velocity. A slight Reynolds number dependency was also observed around the onset region, especially at $2\eta_0$ of 2.25, and 9 mm. A larger vibration frequency value gave a smaller

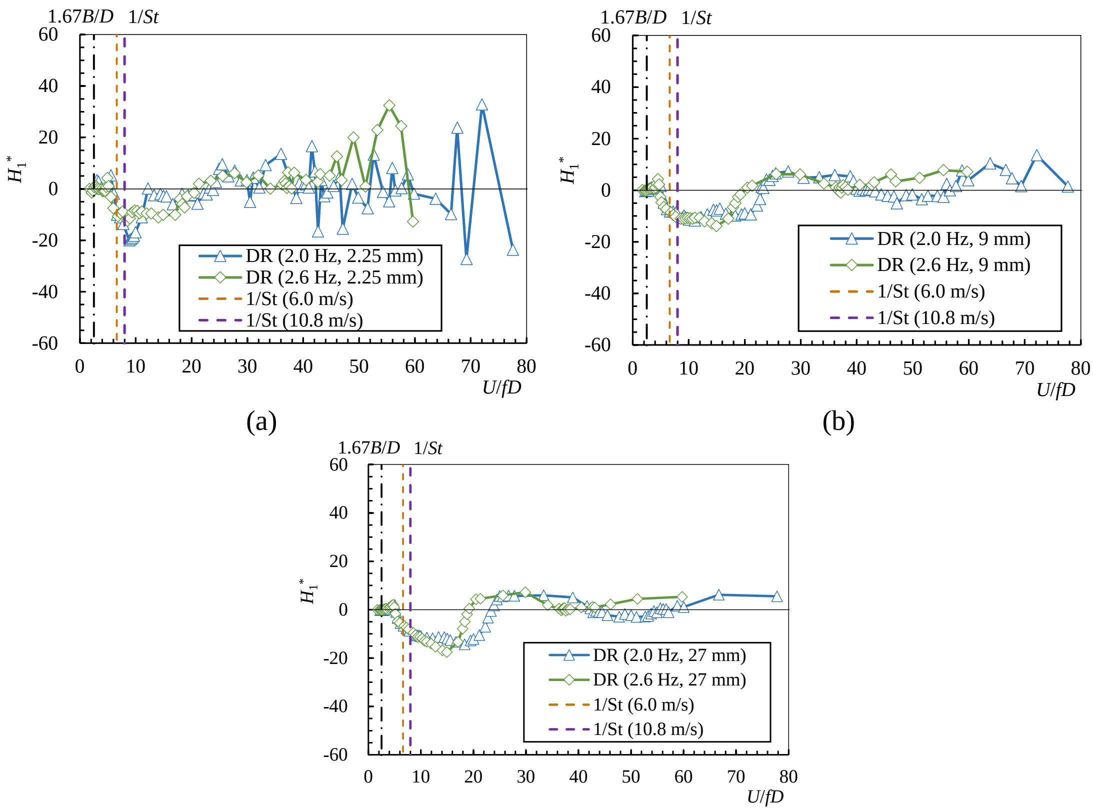

(c)

Fig. 4.24 Aerodynamic damping H_1^* of DR section for the forced vibrating frequencies of 2.0, and 2.6 Hz at the forced vibrating double amplitude ($2\eta_0$) of: (a) 0.025*D*; (b) 0.1*D*; and (c) 0.3*D*.

galloping onset value. Since the H_1^* values of the DR section were very small, it was difficult to describe the Reynolds number dependency in H_1^* values. The amplitude dependency of DR section was also provided in Figs. E.8 and E9 of Appendix E.

(5) Double Recession II (DR II)

As shown in Fig. 4.25, amplitude dependency in the onset reduced wind velocity was present in the DR II section, especially between $2\eta_0$ of 2.25, and 9 mm. A slight Reynolds number dependency was observed around the onset region at three amplitudes. A larger vibration frequency value gave a smaller galloping onset value. No Reynolds number dependency was found in the H_1^* values at all three amplitudes. The amplitude dependency was also provided in Figs. E.10 and E11 of Appendix E.

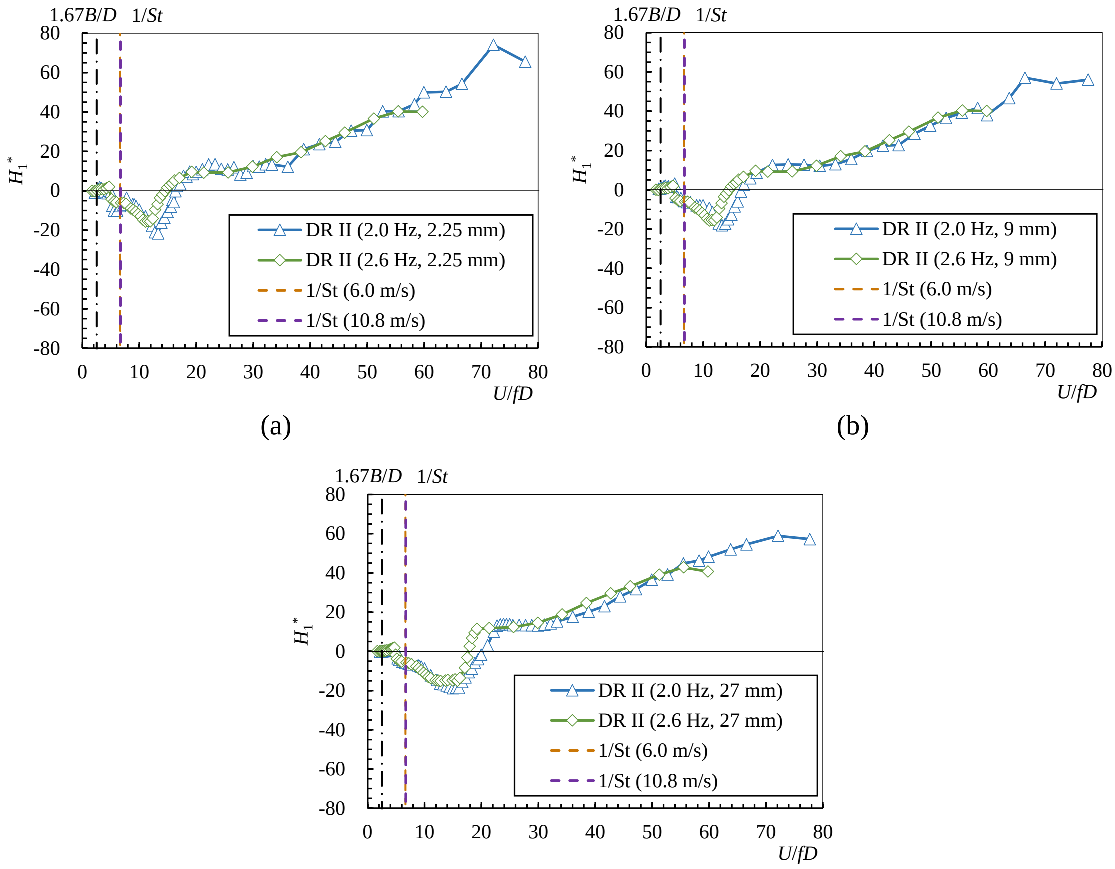

(c)

Fig. 4.25 Aerodynamic damping H_1^* of DR II section for the forced vibrating frequencies of 2.0, and 2.6 Hz at the forced vibrating double amplitude ($2\eta_0$) of: (a) 0.025D; (b) 0.1D; and (c) 0.3D.

(6) Single Recession (SR)

As shown in Fig. 4.26, small amplitude dependency in the onset reduced wind velocity was present in the SR section (Figs. E.12 and E14). A slight Reynolds number dependency was observed around the onset region at all three amplitudes. A larger vibration frequency value gave a smaller galloping onset value. No Reynolds number dependency was found in the H_1^* values.

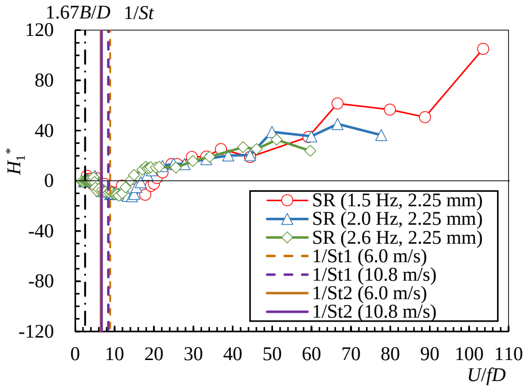

(a)

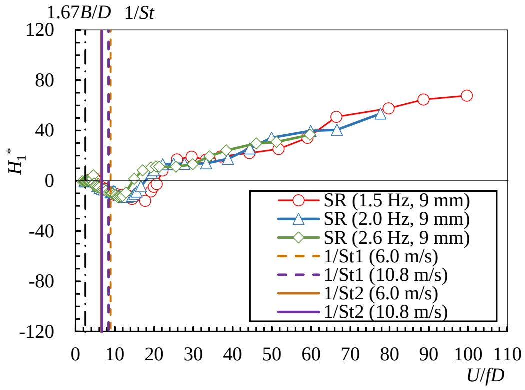

(b)

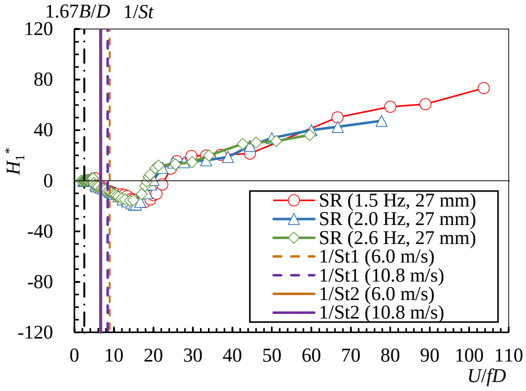

(c)

Fig. 4.26 Aerodynamic damping H_1^* of SR section for the forced vibrating frequencies of 1.5, 2.0, and 2.6 Hz at the forced vibrating double amplitude ($2\eta_0$) of: (a) 0.025D; (b) 0.1D; and (c) 0.3D.

(7) Chamfer (C)

Amplitude dependency in the onset reduced wind velocity was present in the C section as shown in Figs. E.15 and E.16. This was the maximum among all studied corner-cut sections. As shown in As shown in Fig. 4.27, a slight Reynolds number dependency was observed around the onset, especially at $2\eta_0$ of 9 mm; a larger vibration frequency gave a smaller galloping onset. Reynolds number dependency was found in the H_1^* values at all three amplitudes.

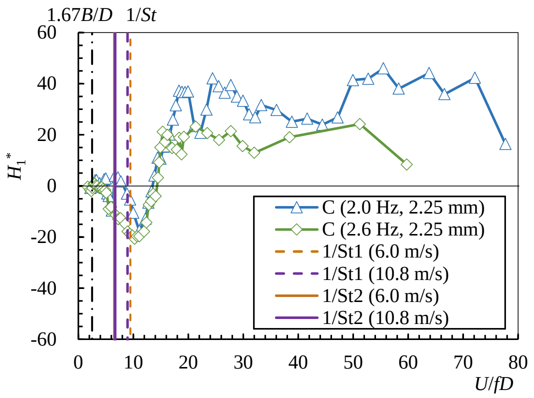

(a)

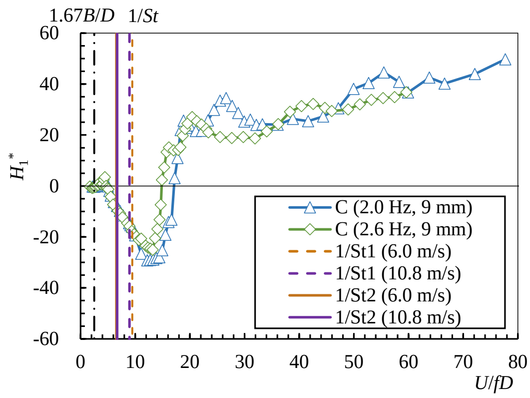

(b)

Fig. 4.27 Aerodynamic damping H_1^* of C section for the forced vibrating frequencies of 2.0, and 2.6 Hz at the forced vibrating double amplitude ($2\eta_0$) of: (a) 0.025D; (b) 0.1D; and (c) 0.3D (1/2).

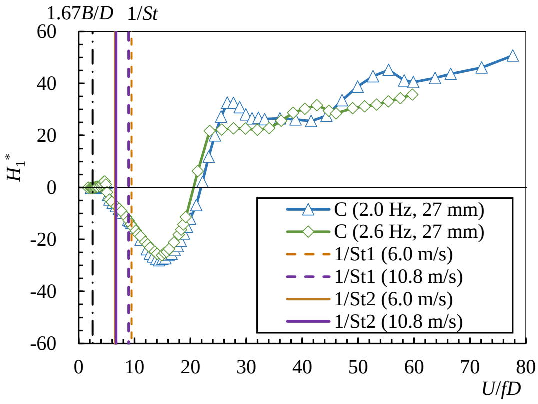

(c)

Fig. 4.27 Aerodynamic damping H_1^* of C section for the forced vibrating frequencies of 2.0, and 2.6 Hz at the forced vibrating double amplitude ($2\eta_0$) of: (a) 0.025*D*; (b) 0.1*D*; and (c) 0.3*D* (2/2).

(8) Summary

The amplitude dependency was present in the onset reduced wind velocity of both rectangular and corner-cut cylinders. A slight frequency dependency/Reynolds number dependency was observed in the onset reduced wind velocity of all studied corner-cut cylinders except the rectangular cylinder. No Reynolds number dependency was observed in the H_1^* values of R, TR, DR II and SR sections at all three amplitudes. On the other hand, Reynolds number dependency was found in the H_1^* values of C (within the measured wind velocity range) and DR III ($U/fD > 40$) sections. In the DR section, Reynolds number dependency of H_1^* values was difficult to investigate due to small H_1^* values.

4.4.2 Comparison of galloping onset

The onset reduced wind velocity of both rectangular and corner-cut cylinders may change based on the Scruton number. Hence, the onset reduced wind velocity of galloping based on the quasi-steady theory, the onset reduced wind velocity obtained from the vertical 1DOF free vibration and forced vibration tests were compared for various Scruton numbers (*Sc* or $S_{c\eta}$) in this section.

As shown in Figs 4.28 to 4.34, the amplitude dependency in the H_1^* value was observed at the onset reduced wind velocity region of both rectangular and corner-cut cylinders. Once the H_1^* value became positive, it increased with the increasing wind velocity in all sections, except the DR. As mentioned in Section 4.3, the Kármán vortex-induced vibration (KVIV) and galloping separated from each other starting from Scruton number ($S_{c\eta}$) of around 90 in the rectangular (R) section, 56 in the triple recession (TR) and chamfer (C) sections, and 42 in the double recession III (DR III), double recession II (DR II) and single recession (SR) sections. The onset reduced wind velocity of all sections, except the DR section, obtained from the H_1^* values were approximately the same as the onset reduced wind velocity of the Kármán vortex-induced vibration (1/*St*) obtained from the respective velocity-amplitude diagram in these $S_{c\eta}$ values. This is listed in Table 4.11. In addition, the onset reduced wind velocity of a section depends on its Kármán vortex shedding intensity. Depending on the Kármán vortex shedding intensity of a section, the onset reduced wind velocity of a section can be started either from 1/*St* or not. Therefore, in the corner-cut sections, the onset reduced wind velocity could not be controlled solely by Kármán vortex shedding.

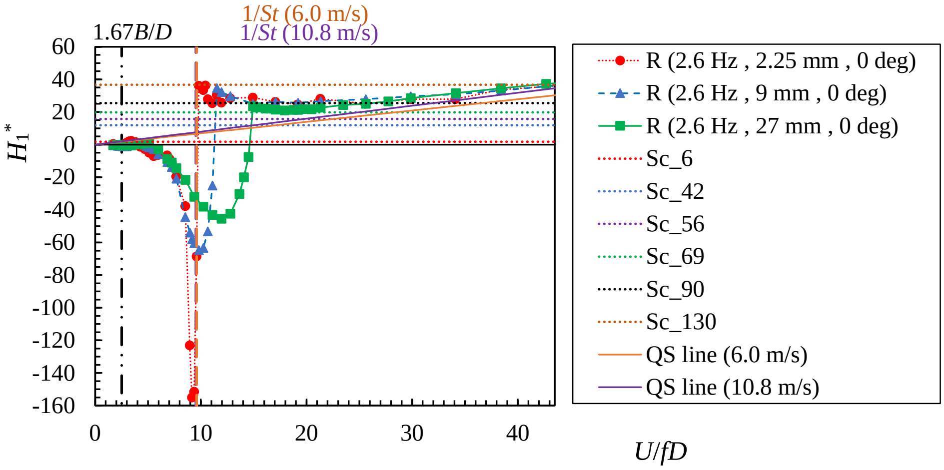

Fig. 4.28 Aerodynamic damping H_1^* of R section obtained from forced vibration test (marker) for the forced vibrating double amplitudes ($2\eta_0$) of 0.025*D*, 0.1*D*, and 0.3*D* at the forced vibrating frequency (f) of 2.6 Hz, H_1^* calculated based on quasi-steady theory (inclined solid line), and Scruton number (dot line).

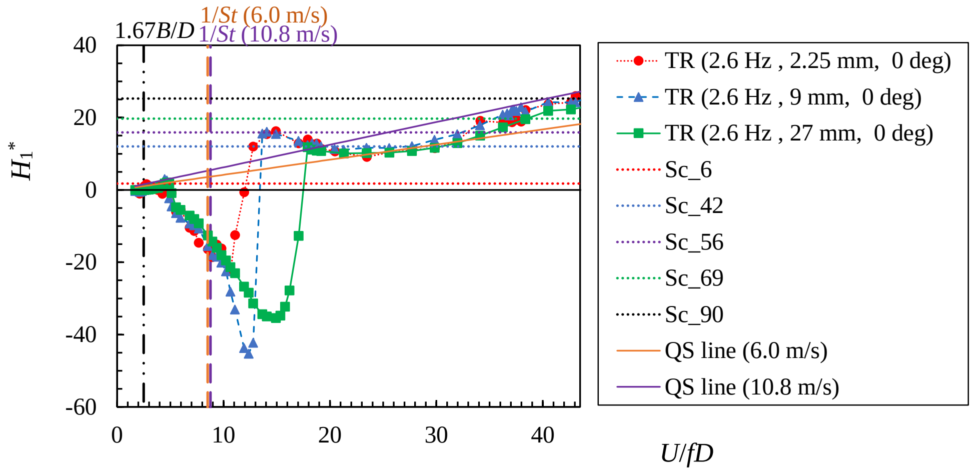

Fig. 4.29 Aerodynamic damping H_1^* of TR section obtained from forced vibration test (marker) for the forced vibrating double amplitudes ($2\eta_0$) of 0.025*D*, 0.1*D*, and 0.3*D* at the forced vibrating frequency (f) of 2.6 Hz, H_1^* calculated based on quasi-steady theory (inclined solid line), and Scruton number (dot line).

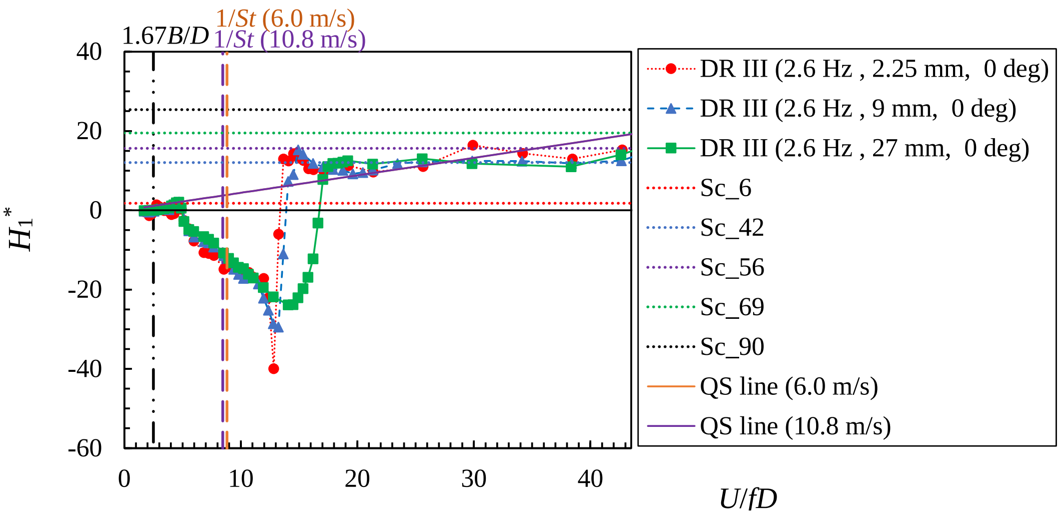

Fig. 4.30 Aerodynamic damping H_1^* of DR III section obtained from forced vibration test (marker) for the forced vibrating double amplitudes ($2\eta_0$) of 0.025D, 0.1D, and 0.3D at the forced vibrating frequency (f) of 2.6 Hz, H_1^* calculated based on quasi-steady theory (inclined solid line), and Scruton number (dot line).

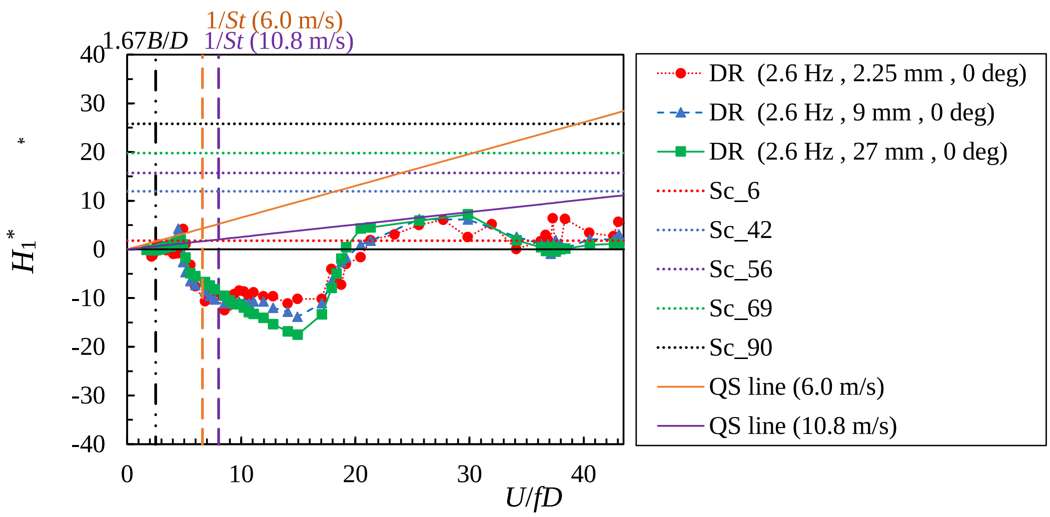

Fig. 4.31 Aerodynamic damping H_1^* of DR section obtained from forced vibration test (marker) for the forced vibrating double amplitudes ($2\eta_0$) of 0.025D, 0.1D, and 0.3D at the forced vibrating frequency (f) of 2.6 Hz, H_1^* calculated based on quasi-steady theory (inclined solid line), and Scruton number (dot line).

In the DR section, Reynolds number dependency was found in the transverse force coefficient (Fig. 3.3 (b) and Table 4.1). The slope of the transverse force coefficient have a negative value at Re = 36,000 and small positive value in high Reynolds number region (Re = 60,000-84,000). In the free vibration test, the DR section only vibrated from U/fD = 11.86 at the lowest Scruton number ($S_{c\eta}$ = 6). At $S_{c\eta}$ = 6, the maximum measured wind velocity is 10 m/s (Re = 60,000, U/fD = 24). In the forced vibration test, the maximum Reynolds number of DR was 84,000. Moreover, the H_1^* values were very small and almost equal to zero at all vibration amplitudes. Therefore, the discrepancies between the free and forced vibration tests may be due to the Reynolds number dependency of the DR section.

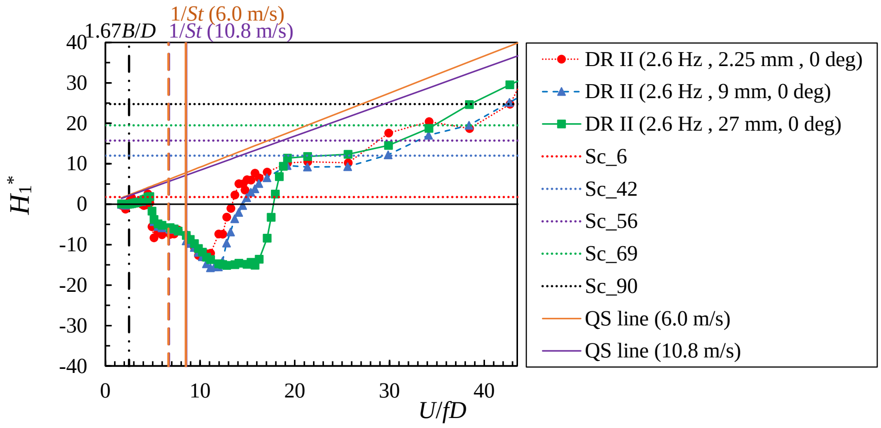

Fig. 4.32 Aerodynamic damping H_1^* of DR II section obtained from forced vibration test (marker) for the forced vibrating double amplitudes ($2\eta_0$) of 0.025D, 0.1D, and 0.3D at the forced vibrating frequency (f) of 2.6 Hz, H_1^* calculated based on quasi-steady theory (inclined solid line), and Scruton number (dot line).

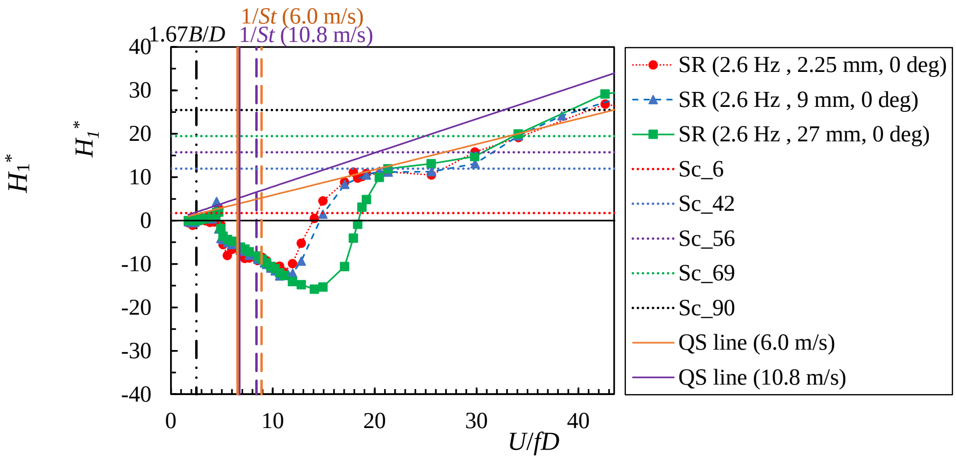

Fig. 4.33 Aerodynamic damping H_1^* of SR section obtained from forced vibration test (marker) for the forced vibrating double amplitudes ($2\eta_0$) of 0.025D, 0.1D, and 0.3D at the forced vibrating frequency (f) of 2.6 Hz, H_1^* calculated based on quasi-steady theory (inclined solid line), and Scruton number (dot line).

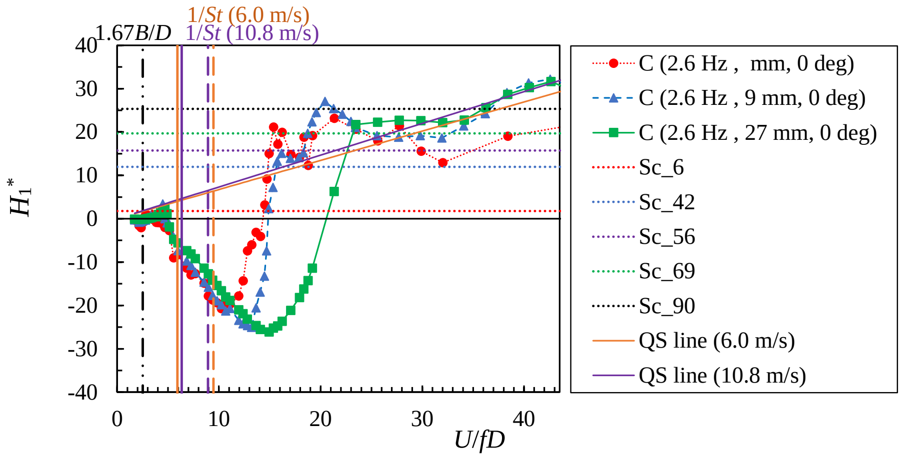

Fig. 4.34 Aerodynamic damping H_1^* of C section obtained from forced vibration test (marker) for the forced vibrating double amplitudes ($2\eta_0$) of 0.025D, 0.1D, and 0.3D at the forced vibrating frequency (f) of 2.6 Hz, H_1^* calculated based on quasi-steady theory (inclined solid line), and Scruton number (dot line).

Table 4.11 The critical reduced wind velocity of galloping based on the quasi-steady theory (U_{cr_quasi}), the onset reduced wind velocity obtained from the vertical 1DOF free vibration and forced vibration tests for rectangular and corner-cut cylinders at α = 0°.

Section and α	$S_{c\eta}$	U_{cr_quasi}		Free vibration test, $2\eta_0$ [mm]						Forced vibration test, $2\eta_0$ [mm]		
		U = 6.0 m/s (Re = 36,000)	U = 10.8 m/s (Re = 64,800)	Without initial vibration			With initial vibration			2.25	9	27
				2.25	9	27	2.25	9	27			
R (0°)	6	2.47	2.16	9.96	12.00	15.60	9.96	12.00	15.60	9.80	11.52	14.93
	42	17.08	14.96	9.70	12.13	15.77	9.70	12.13	15.77	9.80	11.52	14.93
	56	22.54	19.74	9.66	12.08	15.70	9.66	12.08	15.70	9.80	11.52	14.93
	69	28.39	24.86	9.70	19.41	27.90	9.70	19.41	27.90	9.80	11.52	14.93,21.37
	90	36.68	32.13	28.88	28.88	35.00	28.88	28.88	35.00	9.80,29.91	11.52,29.91	29.91
	130	52.70	46.16	-	-	-	-	-	-	46.02	46.09	46.09
TR (0°)	6	4.27	2.86	9.70	12.13	16.98	9.70	12.13	16.98	12.80	13.64	17.91
	42	28.70	19.20	19.69	19.65	19.89	9.73	12.16	15.07	14.08,32.05	13.64,32.05	32.05
	56	37.97	25.39	30.33	33.96	38.82	29.11	29.11	29.11	14.93,34.19	14.07,34.19	36.25
	69	47.14	31.53	35.25	36.47	>40	35.25	36.47	>40	36.69	36.23	40.51
	90	60.42	40.41	-	-	-	-	-	-	43.08	44.78	49.04
DR III (0°)	6	3.99	3.99	9.66	10.87	19.32	9.66	10.87	19.32	13.68	14.07	17.05
	42	27.26	27.25	29.11	29.11	29.11	9.70	12.13	17.71	13.68,29.91	14.93,29.91	18.76,29.91
	56	35.41	35.39	-	-	-	-	-	-	29.92	46.07	46.04
	69	44.23	44.21	-	-	-	-	-	-	51.29	51.19	51.15
	90	57.60	57.57	-	-	-	-	-	-	55.57	59.73	59.68
DR (0°)	6	2.77	7.08	11.62	11.86	13.31	11.62	11.86	13.31	21.31	25.64	25.64
	42	18.26	46.66	-	-	-	-	-	-	46.02	-	-

Table 4.11 Continued.

Section and α	$S_{c\eta}$	U_{cr_quasi}		Free vibration test, $2\eta_0$ [mm]						Forced vibration test, $2\eta_0$ [mm]		
		U = 6.0 m/s	U = 10.8 m/s	Without initial vibration			With initial vibration			2.25	9	27
		(Re = 36,000)	(Re = 64,800)	2.25	9	27	2.25	9	27			
DR (0°)	56	24.08	61.52	-	-	-	-	-	-	49.00	-	-
	69	30.31	77.45	-	-	-	-	-	-	49.00	-	-
	90	39.52	100.98	-	-	-	-	-	-	55.40	-	-
DR II (0°)	6	1.97	2.14	10.39	12.08	15.70	10.39	12.08	15.70	13.67	15.35	17.94
	42	13.11	14.26	23.05	23.05	23.05	22.56	22.56	23.05	29.91	29.86	25.63
	56	17.19	18.70	27.78	29.95	29.95	27.78	29.47	29.47	29.91	34.13	34.17
	69	21.29	23.16	33.89	-		31.47	31.47	31.47	34.18	38.39	38.44
	90	27.03	29.39	-	-	-	-	-	-	46.14	42.66	42.71
SR (0°)	6	2.98	2.24	10.82	12.03	19.24	10.82	12.03	19.24	14.92	17.06	18.75
	42	20.42	15.35	19.57	22.95	24.15	20.53	22.95	24.15	29.83	29.85	25.55
	56	26.82	20.16	30.06	31.51	31.51	29.82	29.82	29.82	29.83	34.11	34.08
	69	33.16	24.93	-	-	-	-	-	-	34.11	34.11	34.08
	90	43.41	32.63	-	-	-	-	-	-	42.62	46.05	42.60
C (0°)	6	2.63	2.42	12.64	13.37	19.45	12.64	14.59	19.45	14.51	14.89	21.32
	42	17.75	16.30	12.94	14.16	19.54	12.94	14.16	19.54	14.94	15.74	23.46
	56	23.35	21.45	22.12	22.37	22.37	21.40	21.40	21.40	15.37,38.46	18.72	23.46
	69	29.23	26.85	38.83	39.07	>40	29.30	29.30	29.30	15.37,40.00	18.72,34.05	23.46
	90	37.64	34.58	>38	>38	>38	37.69	37.69	37.69	-	20.43,38.31	36.25

4.4.3 Aerodynamic derivatives

In this section, the effect of Kármán vortex shedding intensity (corner shape modification) on the aerodynamic derivatives is described. The aerodynamic derivatives which represent aerodynamic damping (H_1^*) and aerodynamic stiffness (H_4^*) of the studied sections were divided into two groups: (i) sections which vibrated at the onset of Kármán vortex-induced vibration (1/*St*) and (ii) sections which did not vibrate at 1/*St*. Galloping vibration occurs when the sign of H_1^* changes from negative to positive. H_1^* also represents the generating force of galloping. The applicability of the quasi-steady theory in the corner-cut sections was also investigated by converting the aerodynamic force coefficients into H_1^* values.

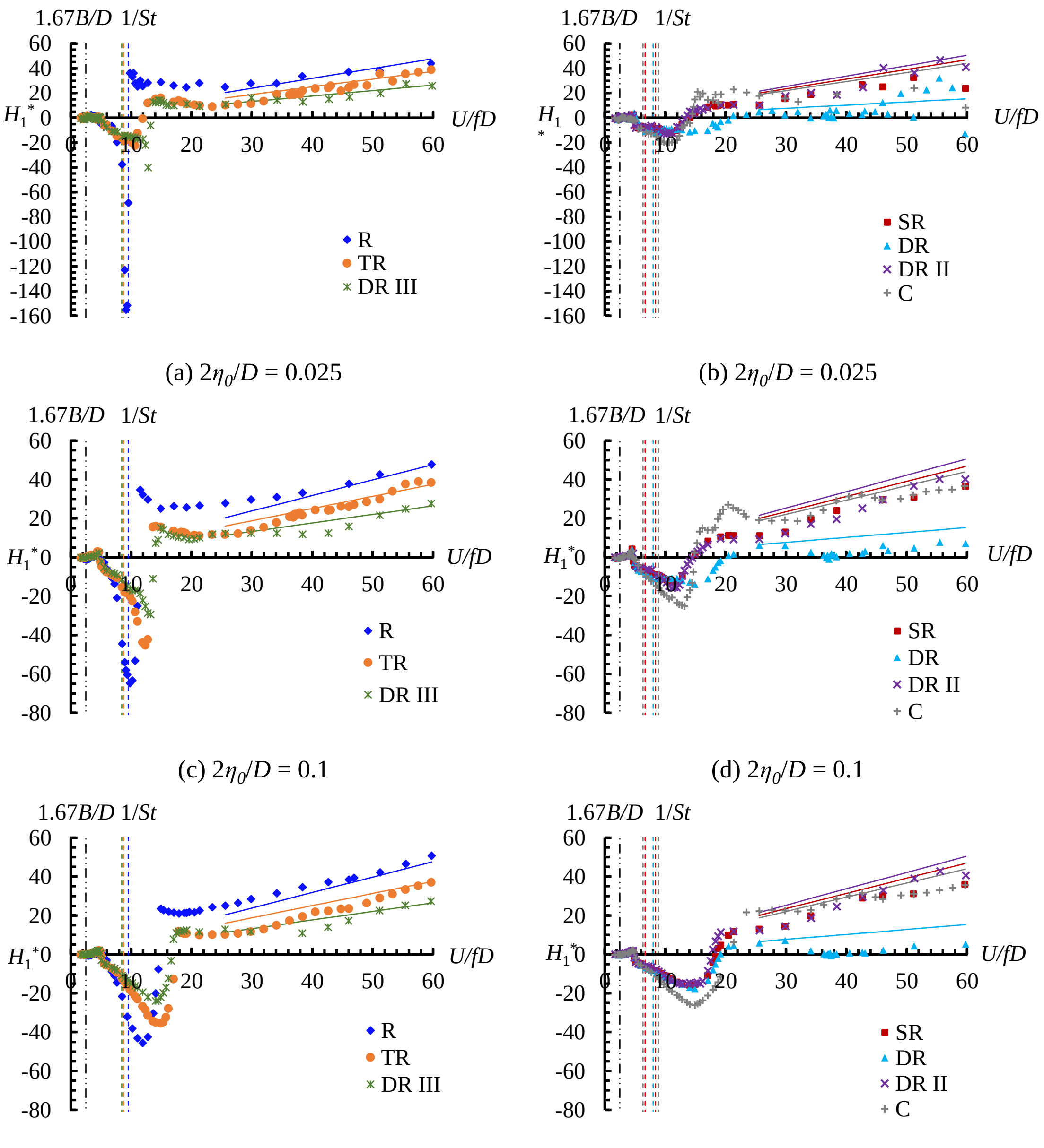

(a) $2\eta_0/D = 0.025$ (b) $2\eta_0/D = 0.025$

(c) $2\eta_0/D = 0.1$ (d) $2\eta_0/D = 0.1$

(e) $2\eta_0/D = 0.3$ (f) $2\eta_0/D = 0.3$

Fig. 4.35 Aerodynamic derivative H_1^* obtained from forced vibration test (marker) and calculated based on quasi-steady theory (solid line) for (a) R, TR, DR III and (b) DR, DR II, SR, C sections.

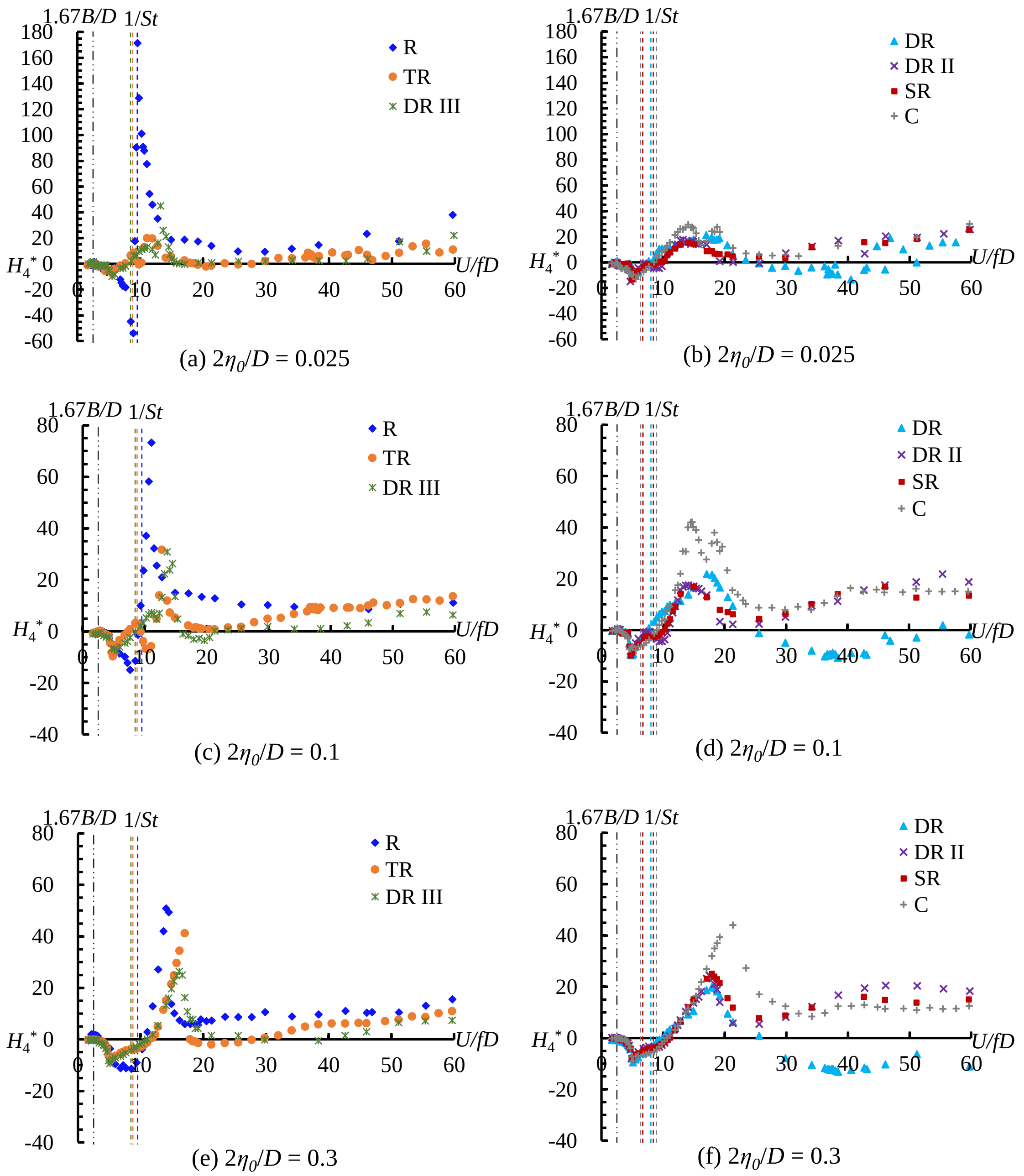

Fig. 4.36 Aerodynamic derivative H_4^* obtained from forced vibration test for (a) R, TR, DR III and (b) DR, DR II, SR, C sections.

As shown in Fig. 4.35, positive H_1^* values were observed around $U/fD = 1.67B/D$ in all sections. Thus, the existence of MIV in the studied sections was confirmed both in the H_1^* values (forced vibration test results) and response amplitude diagrams (free vibration test results). When the measured wind velocity was increased, the H_1^* values of all sections became negative within $5 < U/fD < 20$. Among them, R has the largest negative H_1^* value followed by the TR and DR III sections as shown in Fig. 4.35 (a), (c), and (e). These sections also have a strong Kármán vortex shedding as shown in Fig. 4.1. In these sections, the H_1^* value sharply changed from negative to positive around U/fD = 9.59, 11.94, and 13.25, respectively (Fig. 4.35 (a)). These U/fD values were relatively close to the onset reduced wind velocity of the Kármán vortex-induced vibration (1/*St*). In addition, vibrations of these three sections started from 1/*St* in the velocity-amplitude diagram as shown in Figs. 4.4, 4.7, and 4.10. Moreover, a slight decrease in vibration frequency (frequency drop) was also observed around 1/*St* as shown in Figs. 4.6, 4.9, and 4.12. This corresponds to a sharp increase in the positive H_4^* value around 1/*St* as shown in Fig. 4.36 (a). Hence, the Kármán vortex was highly associated with the vibration of R, TR, and DR III sections. Thus, the galloping instability of these sections was suppressed by the Kármán vortex until 1/*St*.

In the DR, DRII, and SR sections, the Kármán vortex shedding intensity was weak as shown in Fig. 4.1. Hence, the negative H_1^* values of DR, DR II and SR section were comparatively smaller than those of R, TR and DR III sections as shown in Fig. 4.35 (b), (d) and (f). On the other hand, Reynolds number dependency was present in the Kármán vortex shedding intensity of the C section. Therefore, the Kármán vortex shedding of the C section is weak in the low wind velocity region (U = 6 m/s) and strong in the high wind velocity region (U = 10.8 m/s). However, the H_1^* value of these four sections (DR, DR II, SR and C) gradually changed from negative to positive. The upper reduced wind velocity limits of negative H_1^* value were around *U/fD* of 20.46, 13.24, 12.79, and 14.10, respectively (Fig. 4.28 (a)). These *U/fD* values were larger than that of their respective 1/*St* value. In the velocity-amplitude diagram, vibrations of these sections did not start from 1/*St* as shown in Figs. 4.13, 4.15, 4.17, and 4.19. Moreover, a frequency drop in the vibration frequency was also not observed in these sections as shown in Figs. 4.14, 4.16, 4.18 and 4.20. The positive H_4^* values were also smaller than that of R, TR and DR III sections as provided in Figs. 4.36 (b), (d), and (f). Hence, the Kármán vortex may not be completely associated with the vibration of DR, DRII, SR, and C sections. Hence, the galloping instability got suppressed far beyond 1/*St* due to another factor than the Kármán vortex. This will be discussed in Section 4.5.

As shown in Fig. 4.35, reducing the Kármán vortex shedding intensity of the R section by providing various corner shapes lowered the H_1^* values and reduced the instability of the original R section. Moreover, the H_1^* values of all sections obtained from the force vibration test were asymptotic to the H_1^* values calculated from the slope of transverse force coefficients, particularly in the higher wind velocity region, at all three vibration amplitudes as shown in Figs. 4.35 (b), (d) and (f). It was also worth noting that the two H_1^* graphs of the SR and DR II sections were closely parallel with each other while both were still asymptotic. Hence, the galloping instability of the corner-cut sections in the high reduced wind velocity region could be described with the quasi-steady theory.

4.5 Effect of Kármán vortex shedding on the motion-induced vortices and the galloping onset

In this section, the effect of Kármán vortex shedding on the motion-induced vortices and the galloping onset were discussed based on the aerodynamic damping (H_1^*), non-dimensionalized transverse force amplitude, and phase lag between the unsteady transverse force and vertical displacement. These values were evaluated from vertical 1DOF force vibration measurements which were taken at the vibration double amplitudes of 0.025D, 0.1D, and 0.3D, respectively. When H_1^* values change from negative to positive and the phase lag changes from positive to negative, aerodynamic instability is known to occur.

4.5.1 Sections with strong Kármán vortex shedding

Fig. 4.37 illustrates the aerodynamic derivative (H_1^*), non-dimensionalized transverse force amplitude and phase lag between the unsteady transverse force and vertical displacement of R, TR and DR III sections at $2\eta_0/D$ = 0.025, 0.1, and 0.3. The Kármán vortex sheddings of these three sections were strong as they have the largest C'_{Fy} values among all sections. In the R section, section with the strongest Kármán vortex shedding intensity, vibration stated at the onset reduced wind velocity of the Kármán vortex-induced vibration (1/*St*). Moreover, the maximum non-dimensionalized transverse force amplitude was found at 1/*St* as shown in Fig. 37 (a). The phase turned from a positive sign to a negative sign at 1/*St* as shown in Fig. 37 (b) and the vibration of the R section began at 1/*St*.

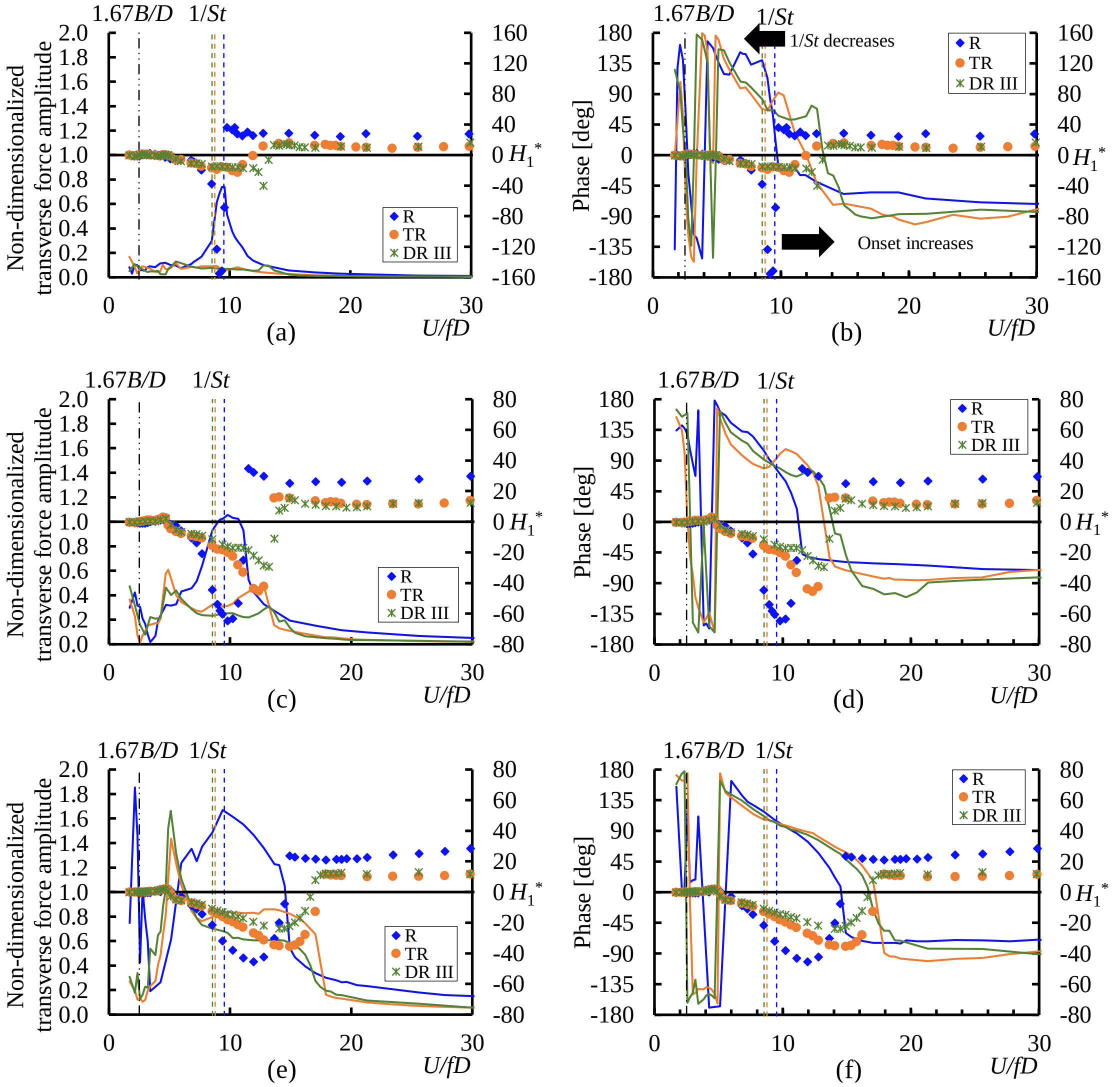

Fig. 4.37 Aerodynamic damping H_1^* (marker) for sections with strong Kármán vortex shedding (a) Non-dimensionalized transverse force amplitude (solid line) and (b) Phase (solid line) at $2\eta_0/D$ = 0.025, (c) Non-dimensionalized transverse force amplitude (solid line) and (d) Phase (solid line) at $2\eta_0/D$ = 0.1, and (e) Non-dimensionalized transverse force amplitude (solid line) and (f) Phase (solid line) at $2\eta_0/D$ = 0.3.

The onset reduced wind velocity values were dependent on the vibration amplitude (Figs. 4.37 (a-f)). The non-dimensionalized transverse force amplitude also increased with an increase in the vibration amplitude (Figs. 37 (a), (c) and (e)). Hence, the instability caused by the Kármán vortex, which is also known as two-shear layer instability, was dominant in the vibration of the R section.

When the Kármán vortex shedding intensity was further reduced, TR and DRIII sections, the non-dimensionalized transverse force amplitude at 1/*St* was also significantly decreased as shown in Fig. 4.37 (a). Similar to the R section, the non-dimensionalized transverse force amplitude of TR and DR III sections increased with an increase in the vibration amplitude. However, contrary to the R section, the maximum non-dimensionalized transverse force amplitude of these sections was found between 1.67*B*/*D* and 1/*St* as shown in Figs. 4.37 (c) and (e). Additionally, the second largest peak was observed at wind velocity higher than 1/*St* (Figs. 4.37 (c)). Hence, the phase changed from a positive sign to a negative sign at higher wind velocity compared to that of the R section (Figs. 4.37 (b), (d), and (f)). Therefore, the instability caused by the motion-induced vortex, which is also known as one-shear layer instability, was dominant in the vibrations while the effect of the Kármán vortex was still present in the TR and DR III sections.

4.5.2 Sections with weak Kármán vortex shedding

Fig. 4.38 shows the aerodynamic derivative (H_1^*), non-dimensionalized transverse force amplitude and phase lag between the unsteady transverse force and vertical displacement of DR, DR II, SR and C sections at $2\eta_0/D$ = 0.025, 0.1, and 0.3. The Kármán vortex sheddings of DR, DR II and SR sections were weak as they have the smallest C'_{Fy} values among all sections. On the other hand, the C section has weak Kármán vortex shedding only in the lower wind velocity region due to its Reynolds number dependency. Hence, the vibration did not start at 1/*St* in the DR, DR II, SR and C sections.

The maximum non-dimensionalized transverse force amplitude of these sections was found between 1.67*B*/*D* and 1/*St* as shown in Figs. 4.38 (a), (c), and (e). The phase also changed from a positive sign to a negative sign at wind velocity higher than that of 1/*St* as shown in Figs. 4.38 (b), (d), and (f)). Since the Kármán vortex sheddings of these four sections were weak and no significant second peak was observed at 1/*St* and/or wind velocity higher than that of 1/*St*, the effect of the Kármán vortex was absent in the vibrations of these sections. Therefore, the motion-induced vortex, which is also known as one-shear layer instability, was dominant in the vibration of DR, DR II, SR and C sections.

Hence, the Kármán vortex shedding intensity of a section can affect the range of motion-induced vortex influence. Furthermore, the Kármán and motion-induced vortices may interfere with each other, depending on the Kármán vortex shedding intensity of a section. This interference may affect the onset reduced wind velocity of galloping of the respective section.

Matsumoto et al. (2012) mentioned the presence of an aerodynamic interaction between the Kármán and motion-induced vortices associated with a rectangular cylinder. When a splitter plate was attached to the wake region of the rectangular cylinder with *B/D* = 2 to suppress Kármán vortex shedding, a similar phenomenon of the galloping onset reduced wind velocity was observed in the high reduced wind velocity region because the influence of the motion-induced vortices was found. In the rectangular cylinder, two transverse force amplitude peaks corresponding to the motion-induced and Kármán vortices were observed. However, a peak at *1/St* was not observed when the Kármán vortices were suppressed by installing the splitter plate (Yagi et al., 2013). This is similar to the observations of the current study.

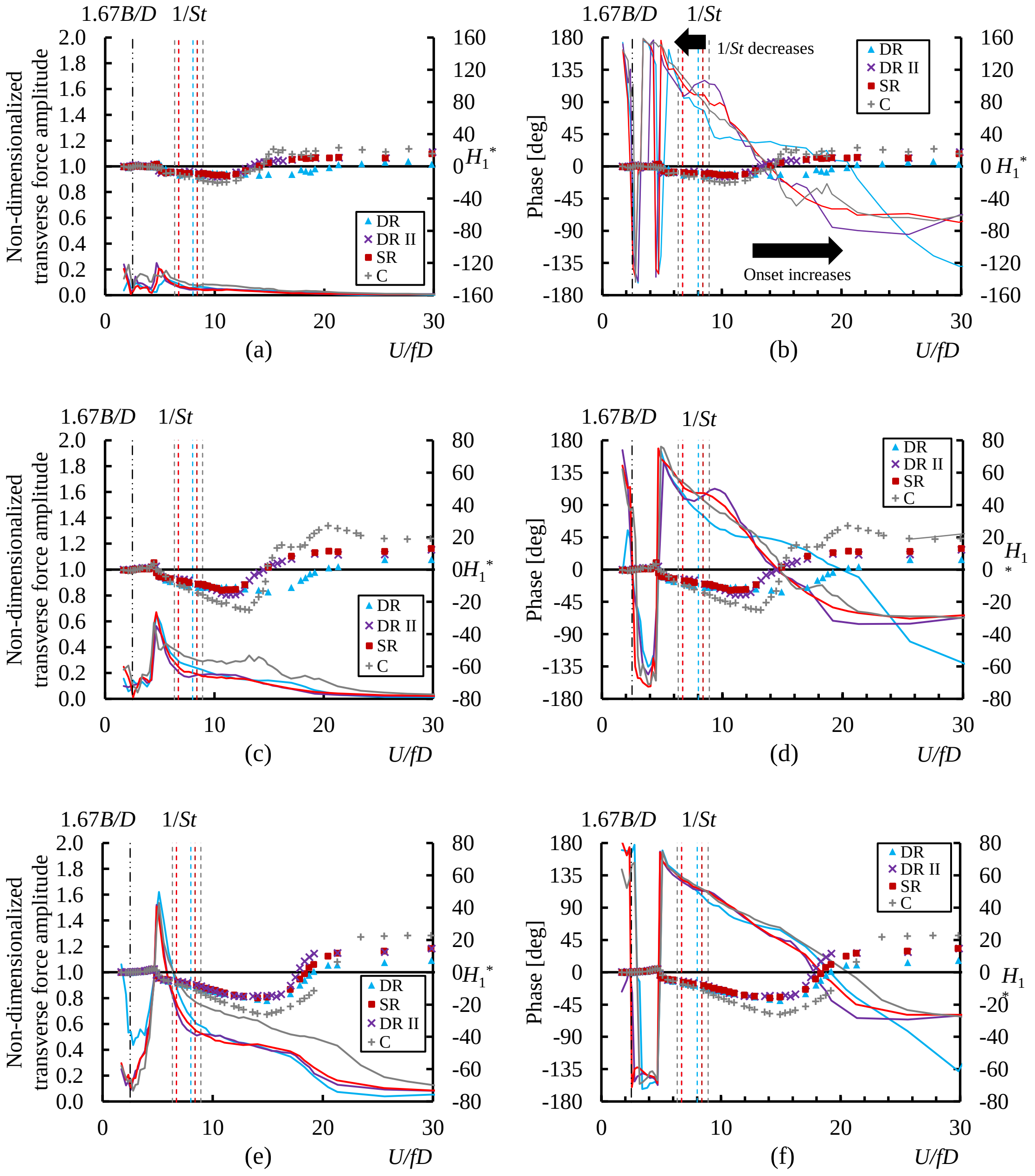

Fig. 4.38 Aerodynamic damping H_1^* (marker) for sections with weak Kármán vortex shedding (a) Non-dimensionalized transverse force amplitude (solid line) and (b) Phase (solid line) at $2\eta_0/D$ = 0.025, (c) Non-dimensionalized transverse force amplitude (solid line) and (d) Phase (solid line) at $2\eta_0/D$ = 0.1, and (e) Non-dimensionalized transverse force amplitude (solid line) and (f) Phase (solid line) at $2\eta_0/D$ = 0.3.

4.6 Concluding remarks

All studied corner shapes reduced the vibration response (vertical response amplitude) of the original rectangular cylinder (R) at zero angle of attack (symmetric body). These corner shapes include triple recession (TR), double recession III (DR III), double recession (DR), double recession II (DR II), single recession (SR) and chamfer (C) shapes. The DR section is the most effective in reducing the vertical response amplitude since the section vibrated into large amplitude only at the lowest Scruton number ($S_{c\eta}$ = 6). The motion-induced vortex vibration (MIV), which is also known as one shear layer instability, was observed around the reduced wind velocity of 1.67B/D only at the lowest $S_{c\eta}$ value of 6 in both rectangular and corner-cut cylinders. The current investigation revealed that the minimum $S_{c\eta}$ required to separate the Kármán vortex-induced vibration (KVIV) and galloping was different for each section. Each section has specific characteristics influencing the KVIV and galloping instability. The minimum $S_{c\eta}$ value required was around 90 in the R section, 56 in the TR and C sections, and 42 in the DR III, DR II and SR sections. Hence, the corner-cut cylinders required a lower mass-damping parameter ($S_{c\eta}$) than the original R section to decouple the KVIV and galloping. Hence, corner-cut cylinders were effective in separating the KVIV and galloping instability.

The corner-cut cylinders have lower aerodynamic damping (H_1^*) values compared to that of the original rectangular cylinder. Among them, the DR section has the lowest H_1^* values. Since aerodynamic damping produces a dissipative force that tends to reduce vibration, the vibration responses of the corner-cut cylinder were supposed to be larger than that of the original rectangular cylinder. This is contrary to the general knowledge that higher aerodynamic damping reduces the vibrations and stabilizes the structure.

For all sections, the H_1^* obtained from the forced vibration tests was asymptotic to the H_1^* obtained from the slope of the transverse force coefficient (the quasi-steady theory) in the high reduced wind velocity region. In the SR and DR II sections, although the two H_1^* graphs were asymptotic, they were closely parallel with each other. Therefore, the galloping instability of both rectangular and corner-cut cylinders can be described by the quasi-steady theory.

Although the H_1^* values of the DR section obtained from the forced vibration test and the quasi-steady theory were asymptotic, discrepancies in the onset reduced wind velocity were observed between the free and forced vibration tests. This may be due to the different measured wind velocity ranges between the forced vibration test (U < 14 m/s) and the free vibration test (U < 10 m/s at $S_{c\eta}$ = 6). Therefore, further investigation and discussion may be required for the DR section.

In the free vibration test of the current study, the onset reduced wind velocity of a section is determined at a double amplitude of 2.25 mm. In the forced vibration test of the current study, the onset reduced wind velocity of a section is determined as the reduced wind velocity where the H_1^* value of that section changed from negative sign to positive sign at $2\eta_0/D$ = 0.025. In the sections with a strong Kármán vortex shedding intensity (R, TR and DR III), the vibration of the model was found to be started around the onset reduced wind velocity of the Kármán vortex-induced vibration (1/St) both in the vertical response amplitude and the H_1^* diagrams. In the sections with a weak Kármán vortex shedding intensity (DR, DRII, SR and C), the vibration of the model did not start at 1/St both in the vertical response amplitude and the H_1^* diagrams. In addition, the onset reduced wind velocity of corner-cut cylinders did not decrease despite an increase in the Strouhal number compared to the original rectangular cylinder both in the vertical response amplitude and the H_1^* diagrams. This was contrary to the static force measurement results.

In the section with the strongest Kármán vortex shedding intensity (R), it was found that the galloping instability was mainly controlled by the Kármán vortex, which is also known as two-shear layer instability. In the sections with relatively strong Kármán vortex shedding intensity (TR and DR III), it was found that the galloping instability was controlled by both Kármán and motion-induced vortices. In the sections with weak Kármán vortex shedding intensity (DR, DR II, SR and C), it was found that the galloping instability was significantly controlled by the motion-induced vortices, which is also known as one-shear layer instability.

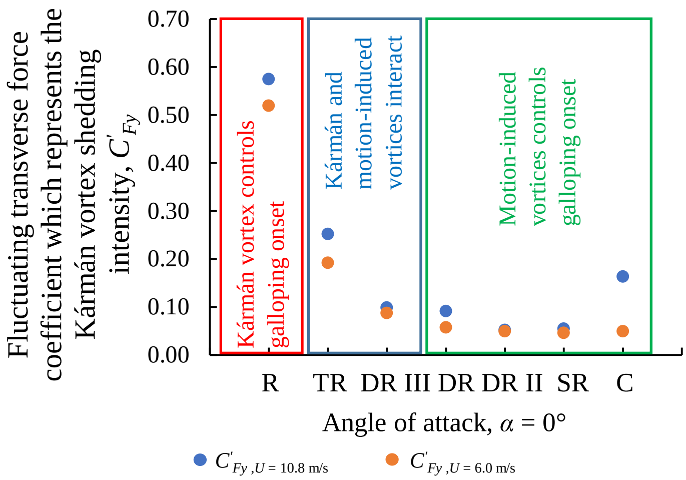

Fig. 4.39 Interaction between vortices and galloping onset at zero angle of attack.

To summarize, the interactions between the vortices and galloping in the rectangular and corner-cut cylinders can be divided into three groups depending on the Kármán vortex shedding intensity of a model as shown in Fig. 4.39. This can offer a range of aerodynamic instability mitigation measures to ensure the safety, reliability and optimization of the aerodynamic performance of structures.

Reference

Komatsu, S., & Kobayashi, H. (1980). Vortex-induced oscillation of bluff cylinders, *Journal of Wind Engineering and Industrial Aerodynamics*, 6, 3–4, 335-362. https://doi.org/10.1016/0167-6105(80)90010-0.

Mannini, C., Marra, A.M., & Bartoli, G. (2014). VIV–galloping instability of rectangular cylinders: Review and new experiments, *Journal of Wind Engineering and Industrial Aerodynamics*, 132, 109-124. https://doi.org/10.1016/j.jweia.2014.06.021.

Matsumoto, M., Yagi, T., Lee, J.H., Hori, K., & Kawashima, Y., (2006). Karman vortex effect on the aerodynamic forces to rectangular cylinders. *American Society of Mechanical Engineers, Pressure Vessels and Piping Division (Publication) PVP*. https://doi.org/10.1115/PVP2006-ICPVT-11-93783.

Mannini, C., Marra, A. M., Massai, T., & Bartoli, G. (2016). Interference of vortex-induced vibration and transverse galloping for a rectangular cylinder. *Journal of Fluids and Structures*, 66, 403-423. https://doi.org/10.1016/j.jfluidstructs.2016.08.002.

Nakamura, Y., & Hirata, K. (1989). Critical geometry of oscillating bluff bodies. *Journal of Fluid Mechanics*, 208, 375-393. https://doi.org/10.1017/S0022112089002879.

Nakamura, Y., & Hirata, K. (1994). The aerodynamic mechanism of galloping. *Trans. Jpn. Soc. Aeronaut. Space Sci*, 114 237-269.

Naudascher, E., & Rockwell, D. (1994). Flow induced vibrations. Dover Publications, Inc. Mineola, New York.

Shiraishi, N., & Matsumoto, M. (1983). On classification of vortex-induced oscillation and its application for bridge structures, *Journal of Wind Engineering and Industrial Aerodynamics*, 14, 1–3, 419-430. https://doi.org/10.1016/0167-6105(83)90043-0.

Washizu, K., Ohya, A., Otsuki, Y., & Fujii, K. (1978). Aeroelastic instability of rectangular cylinders in a heaving mode. *Journal of Sound and Vibration*, 59 (2), 198-210. https://doi.org/10.1016/0022-460X(78)90500-X.

Chapter 5
Aerodynamic interaction between the galloping instability and the vortices at various angles of attack

5.1 Introduction

In Chapter 4, the Kármán vortex shedding intensity of the rectangular cylinder was modified by altering its corners into various shapes. Then, the aerodynamic interactions between the galloping instability of the vortices were investigated for the zero angle of attack (α = 0°, symmetric body). It was found that the Kármán vortex can affect the influence of motion-induced vortices on the galloping onset depending on the intensity of Kármán vortex shedding.

At α = 0°, the time-averaged flow separated from the upper and lower side surfaces of the rectangular and square cylinders was symmetric (Shiraishi et al. 1988, Bruno et al. 2010, Yamur et al. 2015, Yamagishi et al. 2009, Nidhul 2014). Similar symmetric flow patterns in the time-averaged flow field were also observed in the single recession (Shiraishi et al. 1988, Yamagishi et al. 2009, Nidhul 2014), and chamfer (Yamagishi et al. 2009, Nidhul 2014) sections at α = 0°. When the angle of attack was changed from α = 0° to different values, the Strouhal number of the single recession section dramatically changed (Choi and Kwon, 2003). Furthermore, the inverse of the Strouhal number (1/*St*) represents the onset of the Kármán vortex-induced vibration (KVIV). Moreover, the KVIV and the galloping onset were closely associated with each other (Nidhul 2014, Mannini et al. 2016, Chen et al. 2023). Hence, changing the angle of attack into different values could affect the KVIV and the galloping onset. However, limited information was available in literature on the galloping instability of rectangular and corner-cut cylinders for only common the angle of attack range of $-3° \leq \alpha \leq +3°$.

In this chapter, sections with the strong Kármán vortex shedding, (R, TR and DR III) were chosen with the aim of reducing the Kármán vortex shedding intensity by changing the angle of attack (α) into various values. Then, the effect of Kármán and motion-induced vortices on the galloping instability was investigated for various α values. When α was changed from 0° to various values, the model was asymmetric to the incoming flow. The effect of Scruton number (structural damping) on the response amplitude and the onset reduced wind velocity of galloping instability were also investigated by increasing the structural damping. The static force measurement, vertical 1 degree-of-freedom (1 DOF) forced vibration and free vibration tests of each section were carried out at various attack angles for the R, TR and DR III sections.

This chapter is organised as follows: the effect of angle of attack on the steady aerodynamic characteristics such as the fluctuating transverse force coefficient (C'_{Fy}) which represented the Kármán vortex shedding intensity and the Strouhal number (*St*) of the R, TR and DR III sections are briefly described in Section 5.2, the effect of Scruton number on the response amplitude of R, TR and DR III sections at various angles of attack is provided in Section 5.3, and the effect of angle of attack on the unsteady aerodynamic derivatives such as H_1^* and H_4^* is mentioned in Section 5.4. Finally, the effect of Kármán vortex shedding on the motion-induced vortices and galloping onset for various attack angle cases is discussed based on the 1DOF forced vibration test results in Section 5.5.

5.2 Effect of angle of attack on the steady aerodynamic characteristics of rectangular and corner-cut cylinder

In this section, the effect of the angle of attack (symmetric and asymmetric body) on the steady aerodynamic characteristics was described. Aerodynamic force measurements of stationary model were conducted for a second time by increasing the angle of attack (α) of the rectangular (R) section from α = 0° to +4° and +9°. In the triple recession (TR) and double recession (DR III) sections, the α was increased from α = 0° to +2° and +4°, respectively. According to Section 3.2.1, the slope of the transverse force coefficient was the largest at α = +9° in the R section, and α = +4° in the TR and DR III sections. The following sections provided the effect of the angle of attack on the Kármán vortex shedding intensity and the quasi-steady galloping instability of R, TR and DR III sections for two wind tunnel wind velocities of 6.0 m/s (*Re* = 36,000) and 10.8 m/s (*Re* = 64,800).

5.2.1 Kármán vortex shedding intensity and Strouhal number

Fig. 5.1 shows the fluctuating transverse force coefficient (C'_{Fy}), which represented the Kármán vortex shedding intensity and the Strouhal number (*St*) of R, TR, and DR III sections. The power spectral density (PSD) of each section was provided in Figs. F.1 to F6 of Appendix F. When α of the

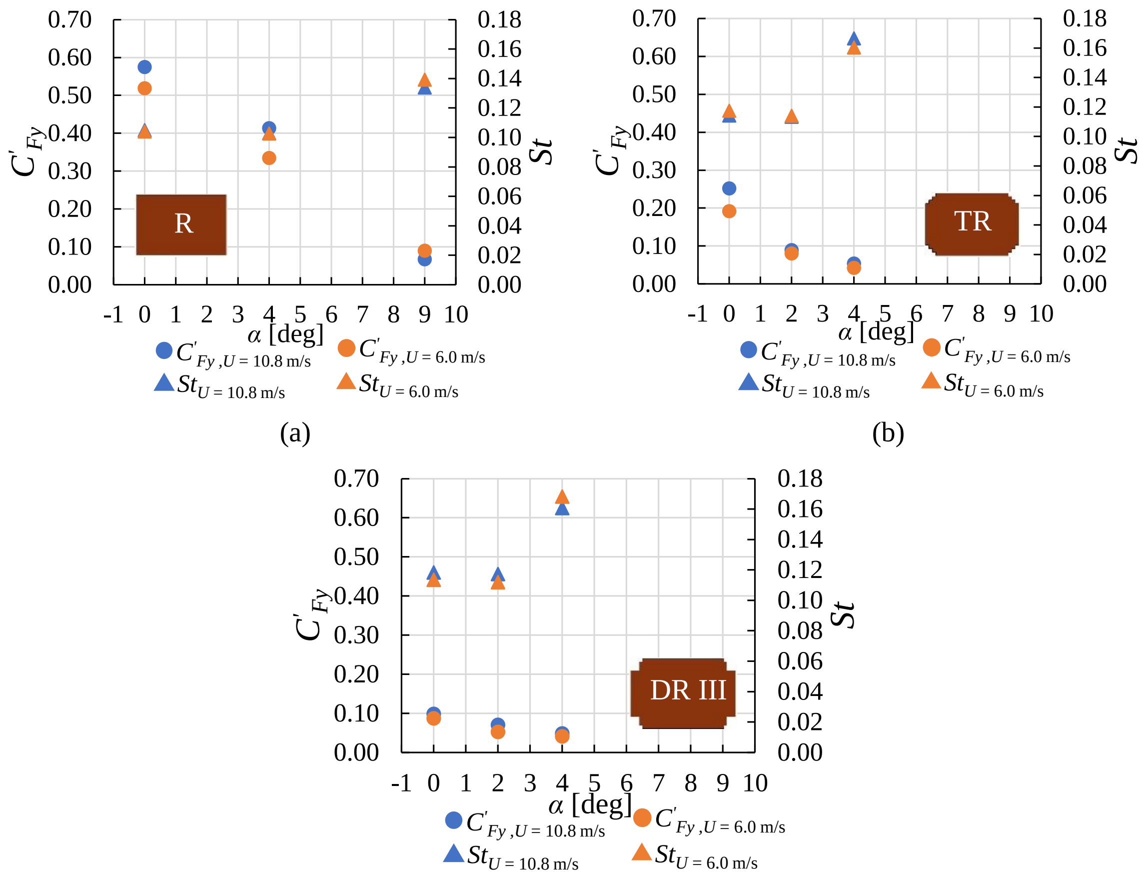

(c)

Fig. 5.1 Kármán vortex shedding intensity (C'_{Fy}: fluctuating transverse force coefficient) and Strouhal number (*St*) at various angles of attack for (a) R (b) TR, and (c) DR III sections.

R section was increased from α = 0° to +4° and +9°, the C'_{Fy} was significantly decreased while the *St* was increased (Fig. 5.1 (a)). A similar phenomenon occurred in the TR and DR III sections when the α of the respective section was increased from α = 0° to +2° and +4° (Fig. 5.1 (b) and (c)). Hence, the Kármán vortex shedding intensity of a section can significantly be decreased when the angle of attack of the respective section is increased. On the other hand, the Strouhal number of a section was increased by increasing the angle of attack. In both C'_{Fy} and *St* values of R, TR and DR III sections for various α, no significant Reynolds number dependency between 36,000 (U = 6.0 m/s) and 64,800 (U = 10.8 m/s) was observed. As the onset reduced wind velocity of the Kármán vortex-induced vibration (KVIV) was denoted in (1/*St*), the onset reduced wind velocity of KVIV of these three sections at the studied angle of attack cases was anticipated to be much lower than that of the α = 0° case.

5.2.2 Slope of transverse force coefficient

In this section, the slopes of the transverse force coefficient ($dC_{Fy}/d\alpha$) of R, TR and DR III sections (Fig. 5.2) at α = +2°, +4° and +9° were calculated within various angles of attack ranges. The $dC_{Fy}/d\alpha$ values of each section at respective α for various attack angle ranges were provided in Appendix F for both polynomial and spline curve fitting (Tables F.1 to F.12). In this study, the slope of the transverse force coefficient at each targeted angle of attack (α = 0°, +2°, +4° and +9°) was calculated with spline curve fitting by considering 19 consecutive points (the angle of attack range of $-3° \leq \alpha \leq +15°$) as shown in Fig. 5.2 at two different wind velocities (U = 6.0 m/s and U = 10.8 m/s). These $dC_{Fy}/d\alpha$ values are listed in Table 5.1.

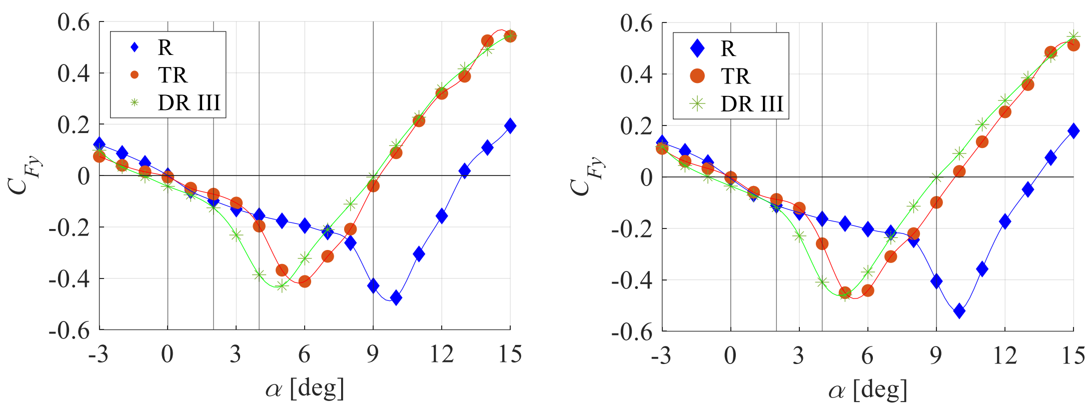

(a) (b)

Fig. 5.2 Slope of transverse force coefficient ($dC_{Fy}/d\alpha$) calculated within $-3° \leq \alpha \leq +15°$ for α = 0° in R, TR and DR III sections, α = +2° in TR and DR III sections, α = +4° in R, TR and DR III sections, and α = +9° in R section:(a) U = 6.0 m/s; and (b) U = 10.8 m/s.

A slight difference in the $dC_{Fy}/d\alpha$ values of TR and DR III sections was observed at α = +4° and R section at α = +9° for all considered angle of attack ranges. Since the critical reduced wind velocity of galloping based on the quasi-steady theory (U_{cr_quasi}) was calculated by using the $dC_{Fy}/d\alpha$ value as mentioned in Eq. 2.7, the U_{cr_quasi} values may slightly vary based on the targeted wind velocity in TR and DR III sections at α = +4°, and R section at α = +9° (Table 5.1). Furthermore, the R, TR and DR III sections (especially at the above-mentioned angles of attack) were expected to be highly prone to galloping instability as they have a large slope of transverse force coefficient at these angles of attack. This will be further discussed in section 5.3.

Table 5.1 Slope of transverse force coefficient at various angles of attack for U = 6.0 m/s (Re = 36,000) and U = 10.8 m/s (Re = 64,800).

Angle of attack (α)	U [ms^{-1}]	Slope of transverse force coefficient, $dC_{Fy}/d\alpha$ [rad^{-1}]		
		R	TR	DR III
α = 0° ($-3° \leq \alpha \leq +15°$)	6.0	−3.28	−1.97	−2.08
	10.8	−3.74	−2.95	−2.08
α = +2° ($-3° \leq \alpha \leq +15°$)	6.0	-	−1.25	−4.11
	10.8	-	−0.90	−3.88
α = +4° ($-3° \leq \alpha \leq +15°$)	6.0	−1.29	−8.56	−7.07
	10.8	−1.19	−11.43	−7.94
α = +9° ($-3° \leq \alpha \leq +15°$)	6.0	−8.78	-	-
	10.8	−10.97	-	-

Furthermore, the transverse force coefficients (C_{Fy}) of the angles of attack next to the targeted angle of attack were modified ± 5% to ± 10%. This was to investigate whether the variation in the C_{Fy} values in the vicinity of the targeted angle of attack influences the calculation of the $dC_{Fy}/d\alpha$. The $dC_{Fy}/d\alpha$ values were calculated within the angle of attack range of $-3° \leq \alpha \leq +15°$. As shown in Figs. 5.3 and 5.4 (Table. 5.2), the $dC_{Fy}/d\alpha$ values of the three sections calculated with the modified C_{Fy} did not significantly differ from the one calculated with the original measured values. Hence, the effect of the variation of the vicinity C_{Fy} value on the $dC_{Fy}/d\alpha$ calculation of the targeted angle of attack may be insignificant. This will be further discussed in the following sections.

Table 5.2 Slope of transverse force coefficient at various angles of attack.

Transverse force coefficient, C_{Fy}	Slope of transverse force coefficient, $dC_{Fy}/d\alpha$ [rad^{-1}]					
	R (α = +9°)		TR (α = +4°)		DR III (α = +4°)	
	6.0 m/s	10.8 m/s	6.0 m/s	10.8 m/s	6.0 m/s	10.8 m/s
−10% of original	−7.79	−9.70	−7.36	−9.91	−6.16	−6.88
−5% of original	−8.29	−10.33	−7.96	−10.67	−6.61	−7.41
Original	−8.78	−10.97	−8.56	−11.43	−7.07	−7.94
+5% of original	−9.27	−11.60	−9.16	−12.18	−7.52	−8.46
+10% of original	−9.76	−12.24	−9.76	−12.94	−7.98	−8.99

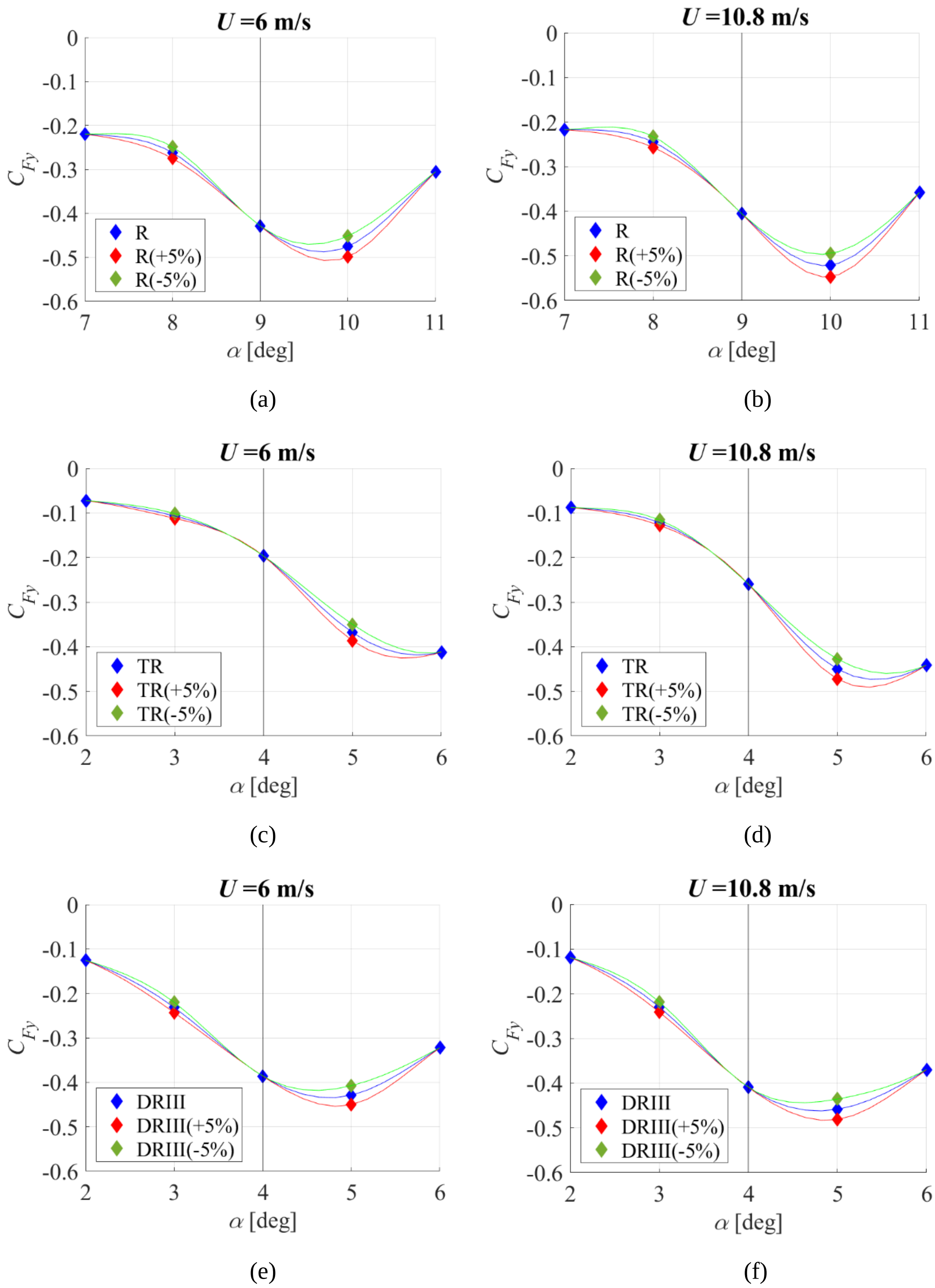

Fig. 5.3 Enlarged slope of 5 % modified transverse force coefficient ($dC_{Fy}/d\alpha$) calculated within $-3° \leq \alpha \leq +15°$ for R section at α = +9° (a) U = 6.0 m/s and (b) U = 10.8 m/s; TR section at α = +4° (c) U = 6.0 m/s and (d) U = 10.8 m/s; and DR III section at α = +4°: (e) U = 6.0 m/s and (f) U = 10.8 m/s.

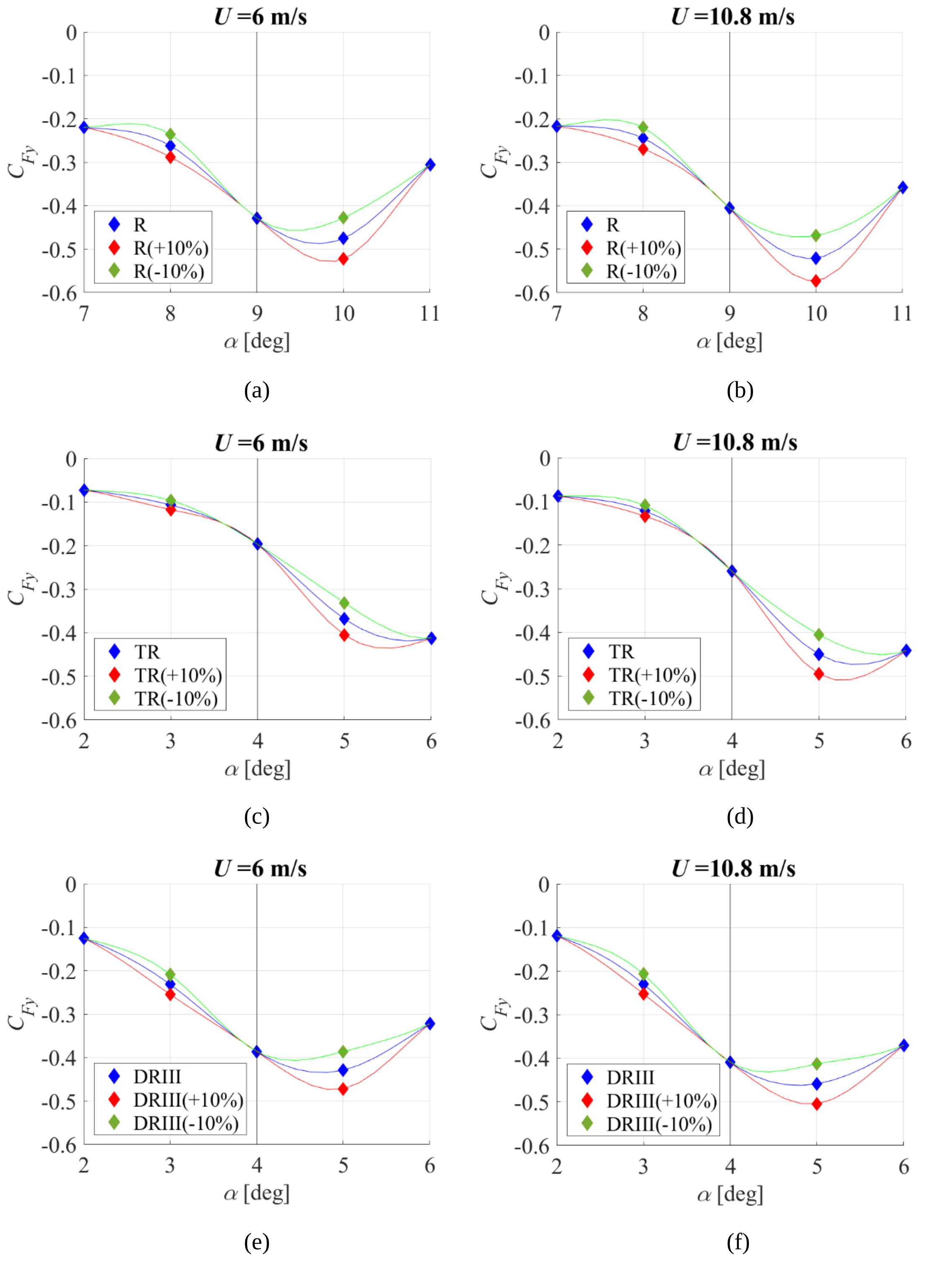

Fig. 5.4 Enlarged slope of 10 % modified transverse force coefficient ($dC_{Fy}/d\alpha$) calculated within $-3° \le \alpha \le +15°$ for R section at α = +9° (a) U = 6.0 m/s and (b) U = 10.8 m/s; TR section at α = +4° (c) U = 6.0 m/s and (d) U = 10.8 m/s; and DR III section at α = +4°: (e) U = 6.0 m/s and (f) U = 10.8 m/s.

5.2.3 Critical reduced wind velocity of galloping

This section describes the effect of the angle of attack on the quasi-steady galloping instability. The onset reduced wind velocity of the Kármán vortex-induced vibration ($1/St$) and the critical reduced wind velocity of galloping based on the quasi-steady theory (U_{cr_quasi}) (calculated according to Eq. 2.7) for U = 6.0 m/s (Re = 36,000) and 10.8 m/s (Re = 64,800) for the Scruton numbers of 6 and 42 were shown in Figs. 5.5 and 5.6.

At a very low Scruton number ($S_{c\eta}$ = 6), the U_{cr_quasi} is lower than that of $1/St$ under asymmetric flow separation (asymmetric body, α = +2°, +4° and +9°), excluding the TR section at α = +4° (U = 10.8 m/s). Therefore, the vibration of the model could be started at $1/St$. This situation is similar to that of the respective section under symmetric flow separation (symmetric body, α = 0°). Hence, at a very low Scruton number ($S_{c\eta}$ = 6), the Kármán vortex-induced vibration (KVIV) and galloping might be observed altogether in the response amplitude. This will be further investigated in the following Section 5.3.

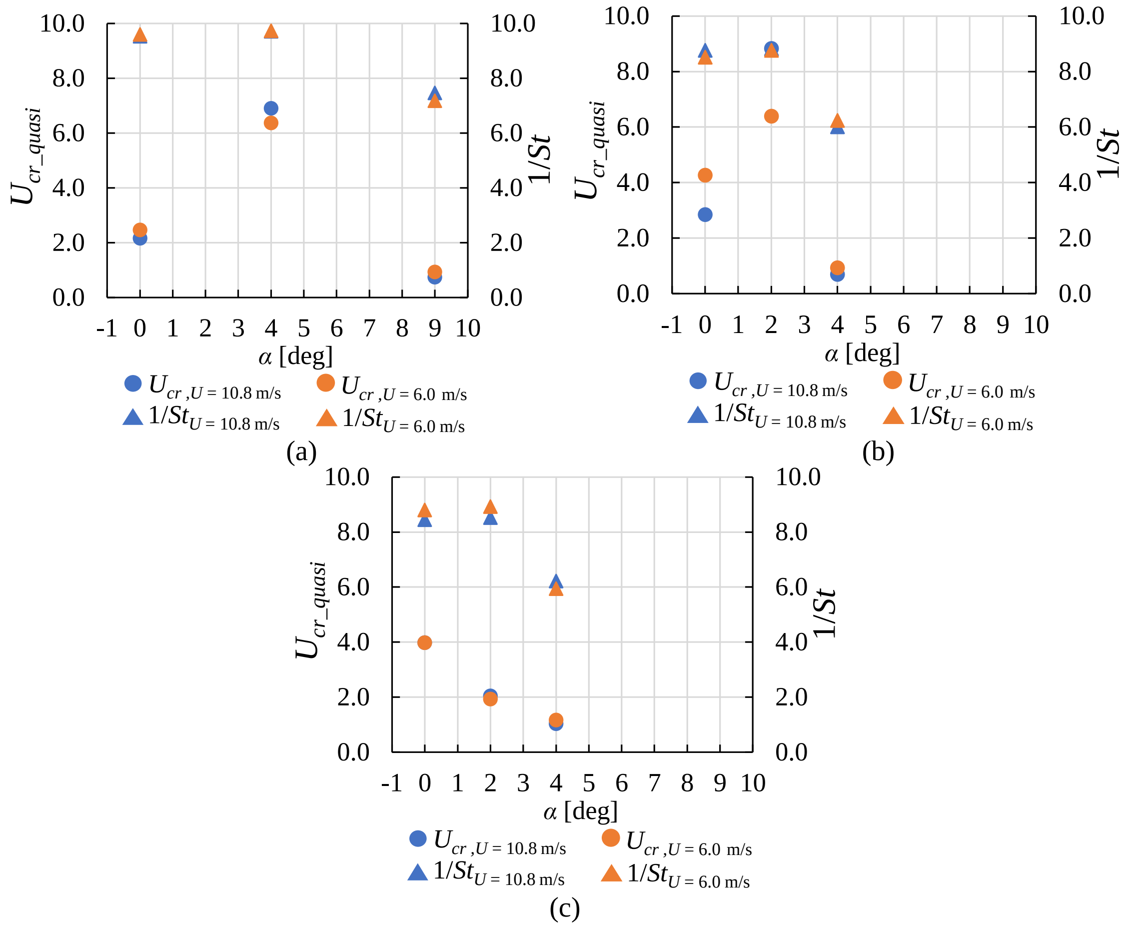

Fig. 5.5 Comparison of the onset reduced wind velocity of the Kármán vortex-induced vibration ($1/St$) and the critical reduced wind velocity of galloping based on the quasi-steady theory (U_{cr_quasi}) under various angles of attack (α) for $S_{c\eta}$ = 6: (a) R; (b) TR; and (c) DR III.

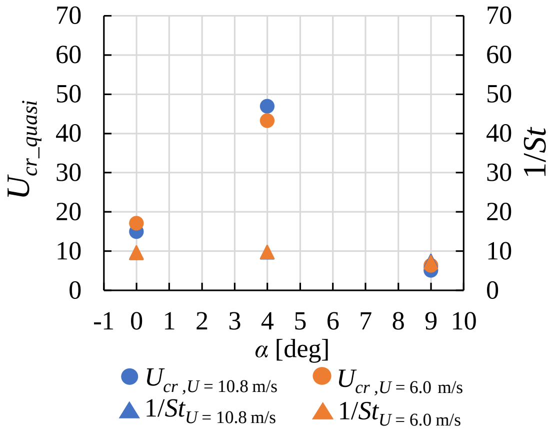

(a)

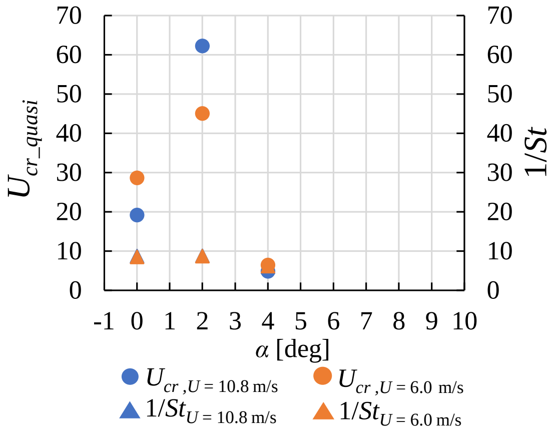

(b)

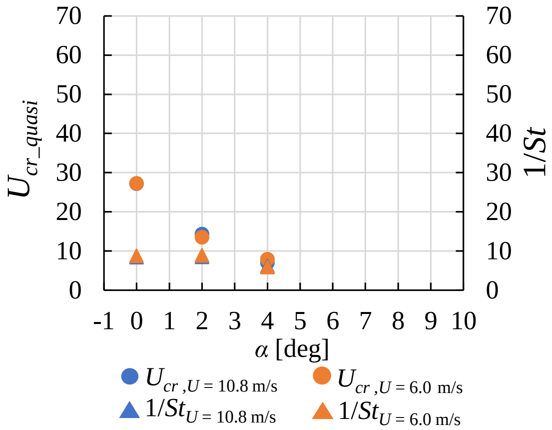

(c)

Fig. 5.6 Comparison of the onset reduced wind velocity of the Kármán vortex-induced vibration ($1/St$) and the critical reduced wind velocity of galloping based on the quasi-steady theory (U_{cr_quasi}) under various angles of attack (α) for $S_{c\eta}$ = 42: (a) R; (b) TR; and (c) DR III.

When $S_{c\eta}$ was increased to 42, U_{cr_quasi} became significantly higher than that of $1/St$ at $\alpha = +4°$ in the R section, and at $\alpha = +2°$ in the TR section as shown in Fig 5.6. The U_{cr_quasi} values were also larger than $1/St$ in the remaining attack angle cases of these three sections. Therefore, the vibration of the section will start at $1/St$. In addition, the KVIV and galloping were expected to be observed separately in the response amplitude. This will be further investigated in the following Section 5.3.

5.3 Effect of angle of attack and Scruton number on the response amplitude of rectangular cylinder with corner modifications

Massai et al. (2018) mentioned that altering the angle of attack affected flow-induced vibrations (FIVs) in the sharp-edged rectangular cylinders of side ratios spanning from 0.67 to 1.5. In this section, the effect of changing the angle of attack (α) and the mass-damping parameter (Scruton number, $S_{c\eta}$) on the two common FIV phenomena, namely Kármán vortex-induced vibration (KVIV) and galloping were investigated. The KVIV and galloping response of the rectangular (R), triple recession (TR), and double recession III (DR III) sections were investigated for α = +2° (TR, DR III), +4° (R, TR, DR III), and +9° (R). Vertical 1DOF free vibration tests were conducted for the reduced wind velocity range of $0 \leq U/fD \leq 39$, in which the maximum Reynolds number corresponds to 96,000. The $S_{c\eta}$ was calculated according to Eq. 2.8. An Electromagnetic damper was used to modify the structural damping. At α = 0°, the KVIV and galloping separated from each other at $S_{c\eta}$ = 42 in the TR and DR III sections under without initial vibration condition. Therefore, two $S_{c\eta}$ cases, denoted as 6 and 42, were considered to study the interference between the KVIV and the galloping instability of rectangular and corner-cut sections at various attack angles (asymmetric body). The structural parameters of each targeted case were listed in Tables 2.1, 2.5 and 2.6, and respective damping values were provided in Figs. A.1(a-b), A.5(a-b), A.6(a-b), and A.8 to A.13 of Appendix A. In subsequent sections, the heaving natural frequency obtained under no wind condition was represented in f_n, and the Kármán vortex shedding frequency and the vibration frequency obtained from the power spectral density (PSD) at each wind velocity were represented in f_{kv} and f_{vib}. In this section, the model was assumed to vibrate when the minimum vertical displacement was larger than 2.25 mm and/or the vertical displacement difference between two consecutive wind velocities was larger than 5 mm.

5.3.1 Response amplitude of rectangular section at various angles of attack

The changes in the response amplitude of the R section at $S_{c\eta}$ = 6 when the angle of attack (α) was increased from α = 0° to +4° and +9° were shown in Fig. 5.7. The f_{kv} and f_{vib} values obtained from the power spectral density (PSD) at each wind velocity of R section for all attack angle cases were provided in Fig. 5.8 (a) for without initial vibration and Fig. 5.8 (b) for with initial vibration conditions at $S_{c\eta}$ = 6. The f_{kv} and f_{vib} of each angle of attack were also provided in Figs. H.1-H.3 of Appendix H. At α = +4°, the motion-induced vortex vibration (MIV) was observed around the reduced wind velocity of 1.67B/D (Fig. 5.7). The vibration of the model also started from the 1/St (lock-in) and the vibration increased linearly with the increasing wind velocity. As shown in Fig 5.8 (a) and (b), the Kármán vortex shedding frequency (f_{kv}) was not observed in the PSDs of the measured wind velocities after the lock-in. Therefore, the KVIV- galloping type response, similar to α = 0°, was observed in the velocity-amplitude diagram (Fig. 5.7). When α was further increased into +9°, MIV was not observed at 1.67B/D while a small KVIV was observed at 1/St (Fig. 5.7). Then, the galloping instability occurred at U/fD = 23.95. In Fig 5.8 (a) and (b), f_{kv} was observed at all measured wind velocities, except around 1/St as shown in Fig 5.9 (a) and (b). Hence, the KVIV and galloping response were separately observed in the velocity-amplitude diagram (Fig. 5.7).

Fig. 5.10 showed the response amplitude and Fig. 5.11 provided the f_{kv} and f_{vib} values obtained from the PSD at each wind velocity of R section for all attack angle cases at $S_{c\eta}$ = 42. The f_{kv} and f_{vib} of each angle of attack were also provided in Figs. H.4-H.6 of Appendix H. At α = +4°, except for the disappearance of MIV (Fig. 5.10), the other phenomenon remained the same as that of $S_{c\eta}$ = 6 (Figs. 5.8 and 5.11). Therefore, the KVIV and galloping fully interfere with each other at α = +4° in both $S_{c\eta}$ cases of the R section, like α = 0°. When α = +9°, the onset of galloping instability was increased to U/fD of 28.25 (Fig. 5.10) while the other phenomenon remained the same with that of $S_{c\eta}$ = 6 (Figs. 5.8 and 5.11). Hence, the KVIV and galloping did not interfere with each other at α = +9° in both $S_{c\eta}$ cases of the R section.

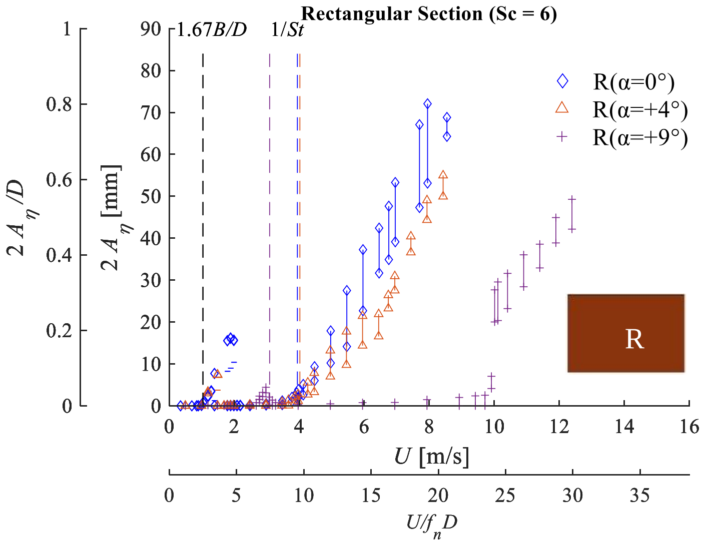

Fig. 5.7 Vibration amplitude of R section at $S_{c\eta}$ = 6 for various attack angles.

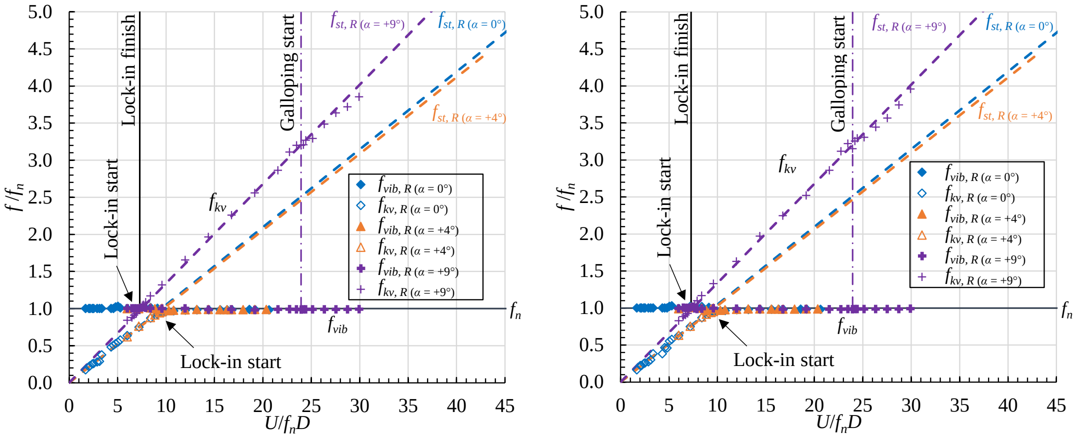

(a) (b)

Fig. 5.8 Kármán vortex shedding frequency (circle) and vibrating frequency (filled circle) (dash slope line: stationary, circle and filled circle: vibrating) of R section under (a) Without, and (b) With initial vibration conditions at $S_{c\eta}$ = 6 for various attack angles.

At U = 10.8 m/s, the Strouhal number (St) of the rectangular (R) section was changed from 0.105 (α = 0°) to 0.103 (α = +4°) and 0.134 (α = +9°) as the attack angle was increased. Since $1/St$ represents the onset reduced wind velocity of KVIV, the onset reduced wind velocity of R was expected to be observed in the lower wind velocity region at α = +9°. As shown in Figs. 5.7 and 5.10, the onset reduced wind velocity of KVIV for the R section at α = +9° was lower than that of the α = 0° and +4°. In addition, the KVIV was observed around $1/St$ in the response amplitude of the R section at the lowest Scruton number ($S_{c\eta}$ = 6) although the Kármán vortex shedding intensity was weak at α = +9° (Fig. 5.1 (a)). Therefore, the two-shear layer instability, also known as the KVIV, may control the galloping of the R section even under the asymmetric flow and weak Kármán vortex sheddings. The f_{kv} and f_{vib} of each angle of attack were also provided in Figs. H.1-H.6 of Appendix H.

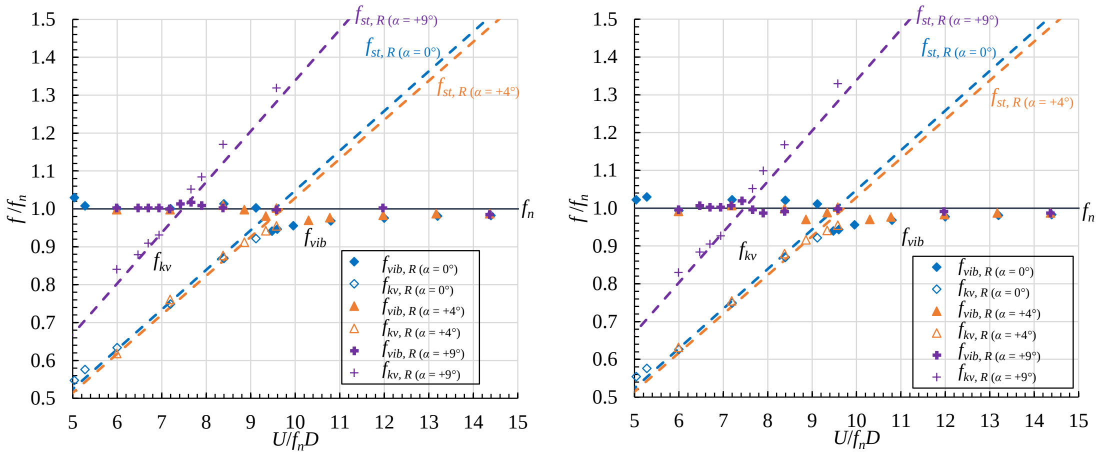

(a)

(b)

Fig. 5.9 Enlarged view for Kármán vortex shedding frequency (circle) and vibrating frequency (filled circle) (dash slope line: stationary, circle and filled circle: vibrating) of R section under (a) Without, and (b) With initial vibration conditions at $S_{c\eta}$ = 6 for various attack angles.

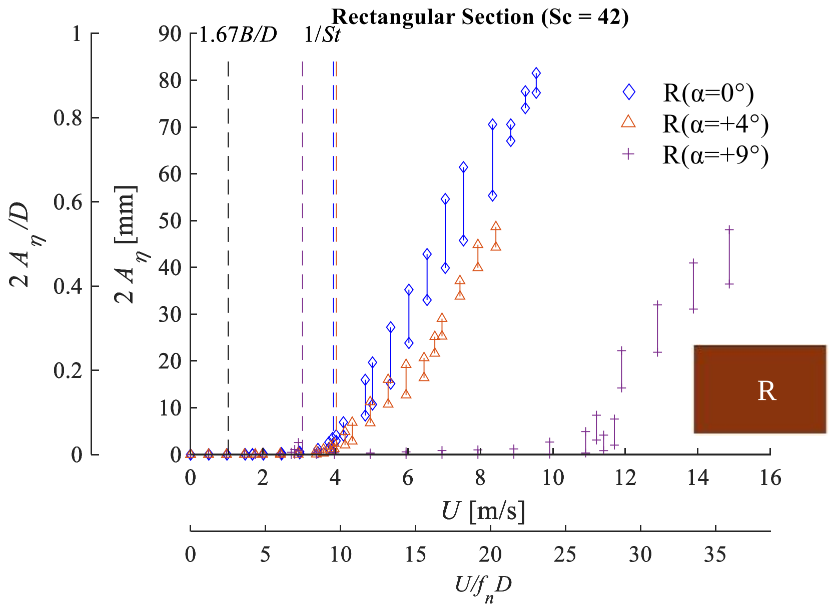

Fig. 5.10 Vibration amplitude of R section at $S_{c\eta}$ = 42 for various attack angles.

Moreover, the slope of the transverse force coefficient ($dC_{Fy}/d\alpha$) was also changed from −3.28 (α = 0°) to −1.29 (α = +4°) and −8.78 (α = +9°) at wind velocity of 6.0 m/s, and from −3.74 (α = 0°) to −1.19 (α = +4°) and −10.97 (α = +9°) at wind velocity of 10.8 m/s. Since $dC_{Fy}/d\alpha$ is the largest at α = +9° in both measured wind velocities, the critical reduced wind velocity of galloping based on the quasi-steady theory (U_{cr_quasi}) of R section was expected to be in the lower wind velocity region at α = +9° (Figs. 5.5 (a) and 5.6 (a)). However, the galloping onset was observed in the higher wind velocity region for both Scruton number cases as shown in Figs. 5.7 and 5.10. Therefore, it is speculated that the quasi-steady theory may not be able to describe the galloping instability of the R section at α = +9°. This will be further investigated in Section 5.4.

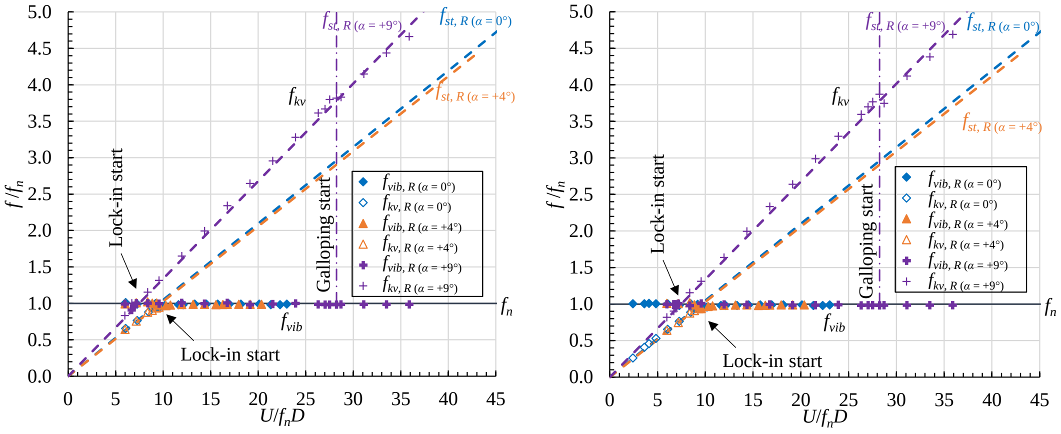

(a) (b)

Fig. 5.11 Kármán vortex shedding frequency (circle) and vibrating frequency (filled circle) (dash slope line: stationary, circle and filled circle: vibrating) of R section under (a) Without, and (b) With initial vibration conditions at $S_{c\eta}$ = 42 for various attack angles.

5.3.2 Response amplitude of triple recession section at various angles of attack

Fig. 5.12 shows the response amplitude of the TR section at $S_{c\eta}$ = 6 for α = 0°, +4° and +9°. The f_{kv} and f_{vib} values obtained from the power spectral density (PSD) at each wind velocity of the TR section were also shown in Fig. 5.13 (a) for without initial vibration and Fig. 5.13 (b) for with initial vibration conditions at $S_{c\eta}$ = 6. The f_{kv} and f_{vib} of each angle of attack were also provided in Figs. H.7-H.9 of Appendix H. At α = +2°, as shown in Fig. 5.12, the motion-induced vortex vibration (MIV) was observed around the reduced wind velocity of 1.67*B*/*D*. Then, the model vibrated at 1/*St* (lock-in) and the vibration amplitude linearly increased with the increasing wind velocity. After the lock-in, the Kármán vortex shedding frequency (f_{kv}) was not observed in the PSDs of the measured wind velocities

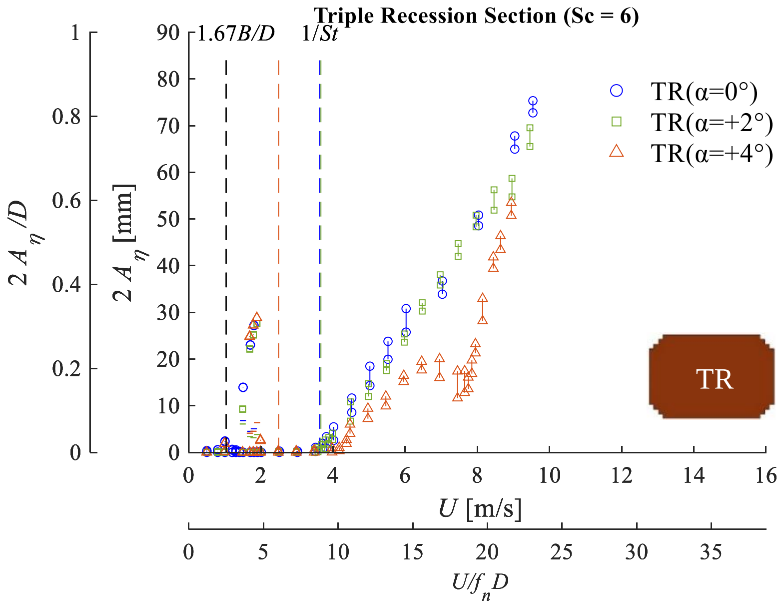

Fig. 5.12 Vibration amplitude of TR section at $S_{c\eta}$ = 6 for various attack angles.

as shown in Fig 5.13 (a) and (b). Hence, the Kármán vortex-induced vibration (KVIV) and galloping fully interfered with each other in the TR section at α = +2° and the KVIV-galloping type response was observed in the velocity-amplitude diagram similar to α = 0° case. At α = +4°, MIV was still observed at 1.67B/D in the response amplitude as in the +2° case (Fig. 5.12). However, the vibration of the model did not start at 1/St and a response amplitude similar to KVIV was observed within $10 \leq U/fD \leq 19$. As shown in Fig 5.13 (a) and (b), f_{kv} was not observed within this region. Afterwards, the vibration amplitude steeply increased with increasing wind velocity (Fig. 5.12). Therefore, for $S_{c\eta}$ = 6, the wind velocity limited vibration similar to KVIV and galloping partially interference with each other in the TR section at α = +4°.

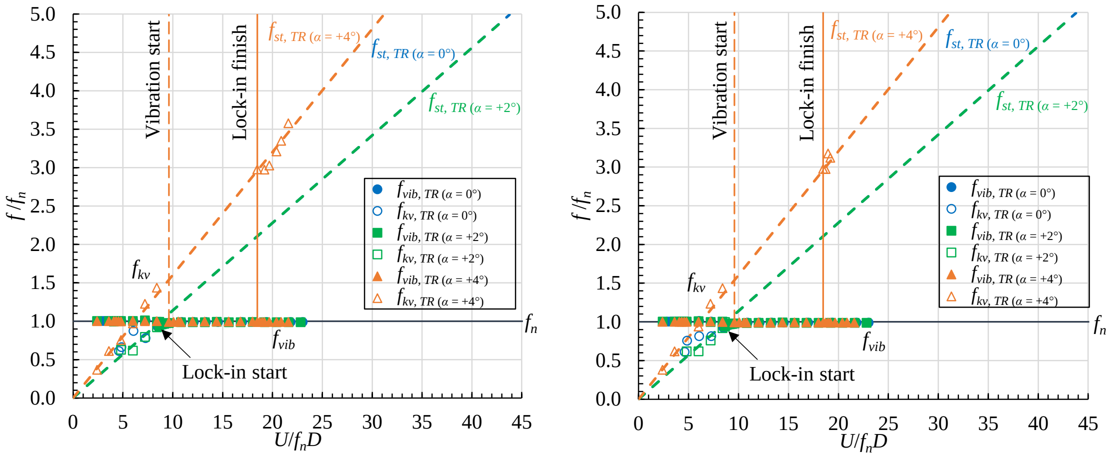

(a) (b)

Fig. 5.13 Kármán vortex shedding frequency (circle) and vibrating frequency (filled circle) (dash slope line: stationary, circle and filled circle: vibrating) of TR section under (a) Without, and (b) With initial vibration conditions at $S_{c\eta}$ = 6 for various attack angles.

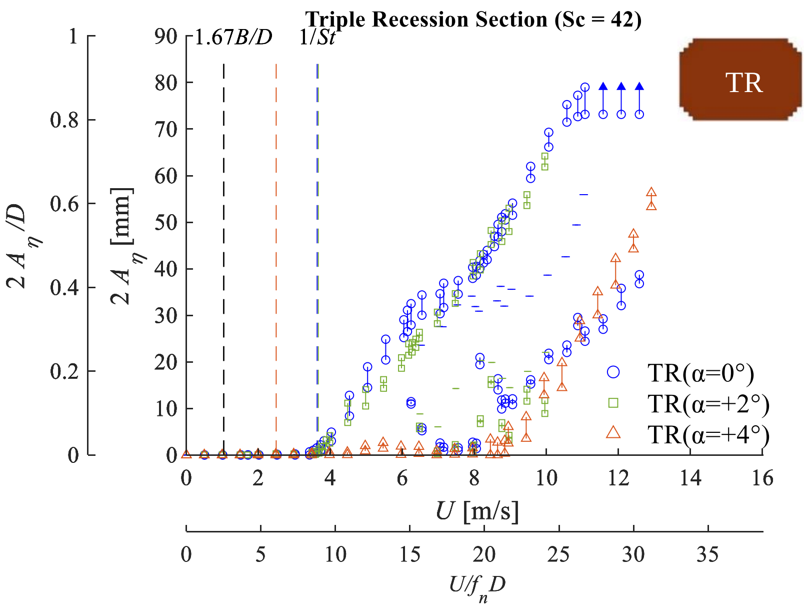

Fig. 5.14 Vibration amplitude of TR section at $S_{c\eta}$ = 42 for various attack angles.

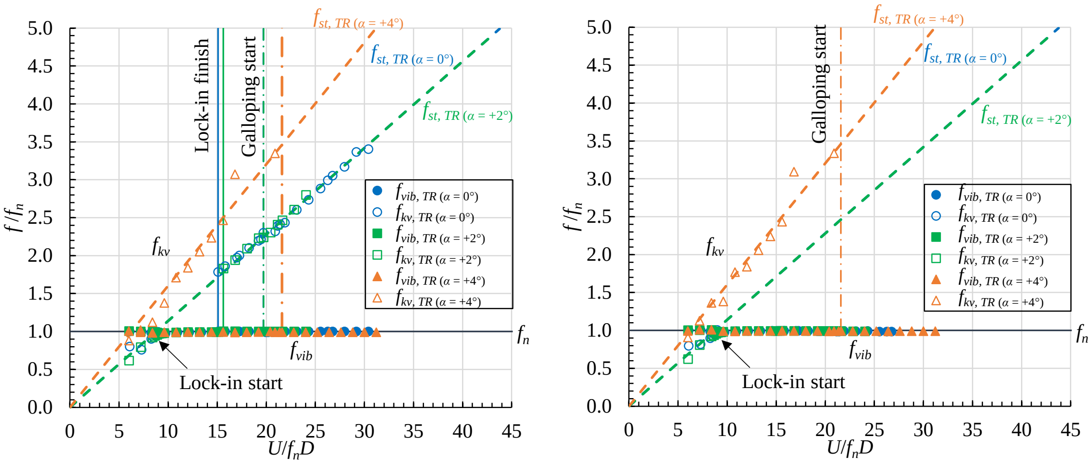

(a) (b)

Fig. 5.15 Kármán vortex shedding frequency (circle) and vibrating frequency (filled circle) (dash slope line: stationary, circle and filled circle: vibrating) of TR section under (a) Without, and (b) With initial vibration conditions at $S_{c\eta}$ = 42 for various attack angles.

The response amplitude of the TR section and the f_{kv} and f_{vib} values obtained from the PSD at each wind velocity for all attack angle cases at $S_{c\eta}$ = 42 were shown in Figs. 5.14 and 5.15. The f_{kv} and f_{vib} of each angle of attack were also provided in Figs. H.10-H.12 of Appendix H.

At α = +2°, the vibration of the model (lock-in) started from 1/*St* (Fig. 5.14). After the lock-in, the f_{kv} was observed in the PSDs of $U/fD \leq 15.63$ in the without initial vibration case as shown in Fig. 5.15 (a)). Therefore, lock-in can be considered to finish at U/fD = 15.63, and vibrations smaller than 20 mm were observed in the response amplitude diagram afterwards (Fig. 5.14). In the with initial vibration case (Fig. 5.15 (b)), the f_{kv} was not observed in the PSDs of the measured wind velocities after the lock-in. In the velocity-amplitude diagram, the vibrations increased linearly with the increasing wind velocity (Fig. 5.14). Thus, at α = +2° of the TR section for $S_{c\eta}$ = 42, the KVIV and galloping partially interfered with each other in the absence of initial vibration and fully interfered with each other in the presence of initial vibration. This phenomenon is the same as that of α = 0° case. When α = +4°, the KVIV was hardly observed in the response amplitude and the onset of galloping instability was increased to U/fD of 21.60 (Fig. 5.14). The f_{kv} was also observed in the PSDs of the measured wind velocities as shown in Fig. 5.15. Therefore, for $S_{c\eta}$ = 42, the KVIV and galloping did not interfere with each other at α = +4° in the TR section.

When the attack angle was increased, the Strouhal number (*St*) of the triple recession (TR) section was changed from 0.114 (α = 0°) to 0.113 (α = +2°) and 0.166 (α = +4°) at U = 10.8 m/s. Since 1/*St* represents the onset reduced wind velocity of KVIV, the onset reduced wind velocity of TR was expected to be observed in the lower wind velocity region at α = +4°. However, the TR section vibrated at the reduced wind velocity higher than that of 1/*St* at α = +4° in both Scruton number cases as shown in Figs. 5.12 and 5.14. Since the Kármán vortex shedding intensity of the TR section was very weak at α = +4° (Fig. 5.1 (b)), another factor aside from the Kármán vortex may control the galloping of this section.

Moreover, the slope of the transverse force coefficient ($dC_{Fy}/d\alpha$) was also changed from −1.97 (α = 0°) to −1.25 (α = +2°) and −8.56 (α = +4°) at wind velocity of 6.0 m/s, and from −2.95 (α = 0°) to −0.90 (α = +2°) and −11.43 (α = +4°) at wind velocity of 10.8 m/s. Since $dC_{Fy}/d\alpha$ is the largest at α = +4°, the critical reduced wind velocity of galloping based on the quasi-steady theory (U_{cr_quasi}) of the TR section was expected to be in the lower wind velocity region at α = +4° (Figs. 5.5 (b) and 5.6 (b)). However, the section vibrated at the reduced wind velocity higher than U_{cr_quasi} as shown in Figs. 5.12 and 5.14. Therefore, it is speculated that the quasi-steady theory may not be able to describe the galloping instability of the TR section at α = +4°. This will be further investigated in the Section 5.4.

5.3.3 Response amplitude of double recession III section at various angles of attack

The changes in the response amplitude of the DR III section when the angle of attack (α) was increased from 0° to +2° and +4° were shown in Fig. 5.16 for $S_{c\eta}$ = 6, and Fig. 5.18 for $S_{c\eta}$ = 42. The f_{kv} and f_{vib} values obtained from the PSD at each wind velocity are shown in Figs. 5.17 and 5.19: (a) for without and (b) for with initial vibration conditions. The f_{kv} and f_{vib} of each angle of attack were also provided in Figs. H.13-H.15 of Appendix H.

As shown in Fig. 5.16, the motion-induced vortex vibration (MIV) was observed around the reduced wind velocity of 1.67*B*/*D* in all attack angle cases at $S_{c\eta}$ = 6. The model vibrated at 1/*St* (lock-in) and the vibration amplitude linearly increased with the increasing wind velocity at α = 0° and +2°. After the lock-in, the Kármán vortex shedding frequency (f_{kv}) was not observed in the PSDs of the measured wind velocities as shown in Fig 5.17 (a) and (b). The KVIV-galloping type response was observed in the velocity-amplitude diagram of the DR III section at α = 0° and +2° for $S_{c\eta}$ = 6. At α = +4°, the model did not vibrate at 1/*St* and a sudden jump in the response amplitude was observed around U/fD = 31.13 under the initial vibration condition (Fig. 5.16). The f_{kv} was also observed in the PSD of nearly all measured wind velocities (Fig. 5.16). Therefore, for $S_{c\eta}$ = 6, the KVIV and galloping did not interfere with each other at α = +4° in the DR III section.

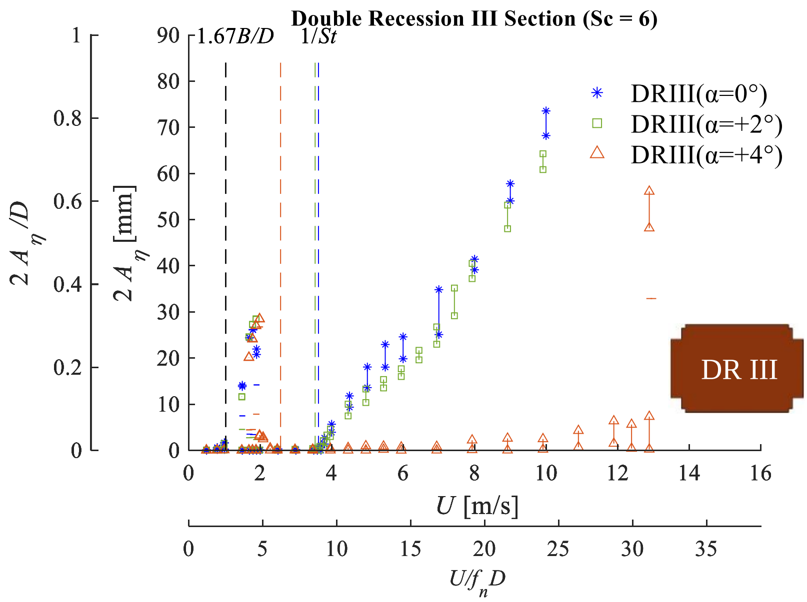

Fig. 5.16 Vibration amplitude of DR III section at $S_{c\eta}$ = 6 for various attack angles.

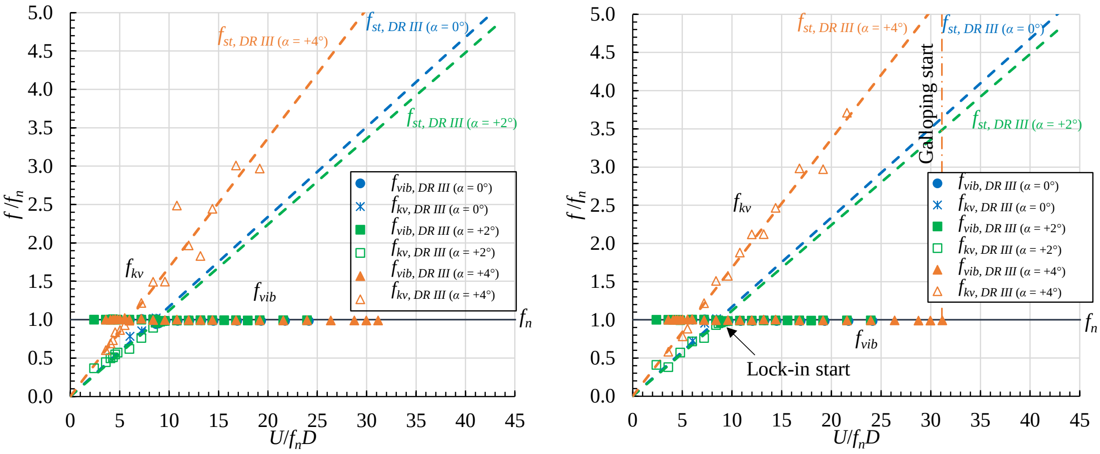

(a) (b)

Fig. 5.17 Kármán vortex shedding frequency (circle) and vibrating frequency (filled circle) (dash slope line: stationary, circle and filled circle: vibrating) of DR III section under (a) Without, and (b) With initial vibration conditions at $S_{c\eta}$ = 6 for various attack angles.

When the $S_{c\eta}$ was increased to 42 as shown in Fig. 5.18, MIV was not observed in all attack angle cases. At α = 0°, the model vibrated at $1/St$ (lock-in) and the vibration amplitude linearly increased with the increasing wind velocity under the initial vibration condition. After the lock-in, f_{kv} was also not observed in the PSDs (Fig. 5.19 (b)). Thus, the KVIV-galloping type response was observed in the velocity-amplitude diagram (Fig. 5.18). On the other hand, in the absence of initial vibration, the model vibrated at $1/St$ (lock-in). However, after the lock-in, the f_{kv} was observed in the PSDs of $U/fD \leq 16.98$ (Fig. 5.19(a)). Hence, lock-in was considered to finish at U/fD = 16.98, and vibrations smaller than 20 mm were observed in the response amplitude diagram until U/fD = 29.11 (Fig. 5.18). Thus, for $S_{c\eta}$ = 42, the KVIV and galloping partially interfered with each other at α = 0° in the DR III section. At α = +2°, the model vibrated at $1/St$ in both types of initial conditions. However, the galloping-type instability was only observed at U/fD = 25.20 under the initial vibration condition. In addition, the f_{kv} was not observed in the PSDs within $9.11 \leq U/f_hD \leq 17.27$ (Fig. 5.19). Therefore, for $S_{c\eta}$ = 42, the KVIV and galloping hardly interfered with each other at α = +2° in the DR III section. At α = +4°, as shown in Fig. 5.18, the model vibrated around U/fD = 35.92 and KVIV was not observed at $1/St$. Moreover, the f_{kv} was also observed in the PSD of nearly all measured wind velocities (Fig. 5.19). Therefore, for $S_{c\eta}$ = 42, the KVIV and galloping did not interfere with each other at α = +4° in the DR III section. The f_{kv} and f_{vib} of each α were also provided in Figs. H.16-H.18 of Appendix H.

Strouhal number (St) of the double recession III (DR III) section at U = 10.8 m/s was changed from 0.118 (α = 0°) to 0.117 (α = +2°) and 0.161 (α = +4°) when the attack angle was increased. Since $1/St$ represents the onset reduced wind velocity of KVIV, the onset reduced wind velocity of the DR III section was expected to be observed in the lower wind velocity region at α = +4°. However, the DR III section vibrated at the reduced wind velocity higher than that of $1/St$ at α = +4° in both Scruton number cases as shown in Figs. 5.16 and 5.18. Since the Kármán vortex shedding intensity of the DR III section was very weak at α = +4° (Fig. 5.1 (c)), another factor apart from the Kármán vortex may control the galloping of this section.

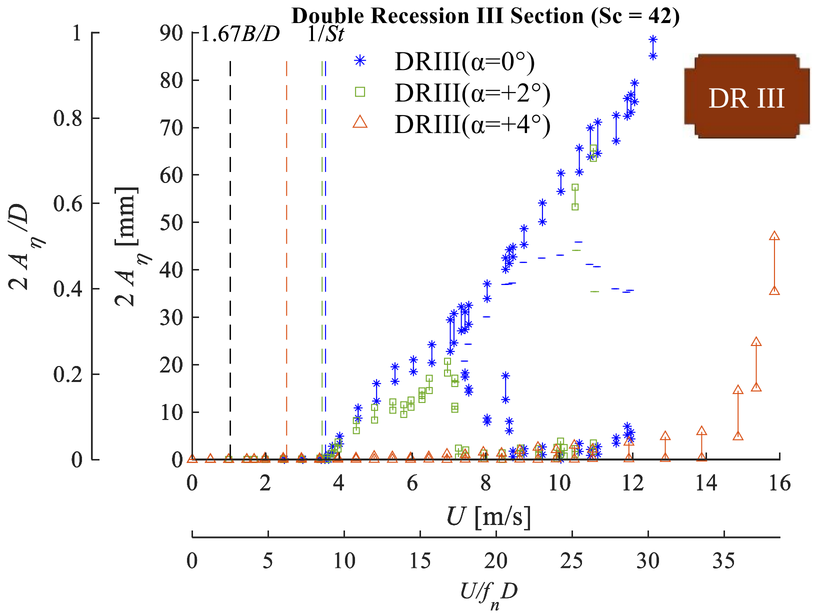

Fig. 5.18 Vibration amplitude of DR III section at $S_{c\eta}$ = 42 for various attack angles.

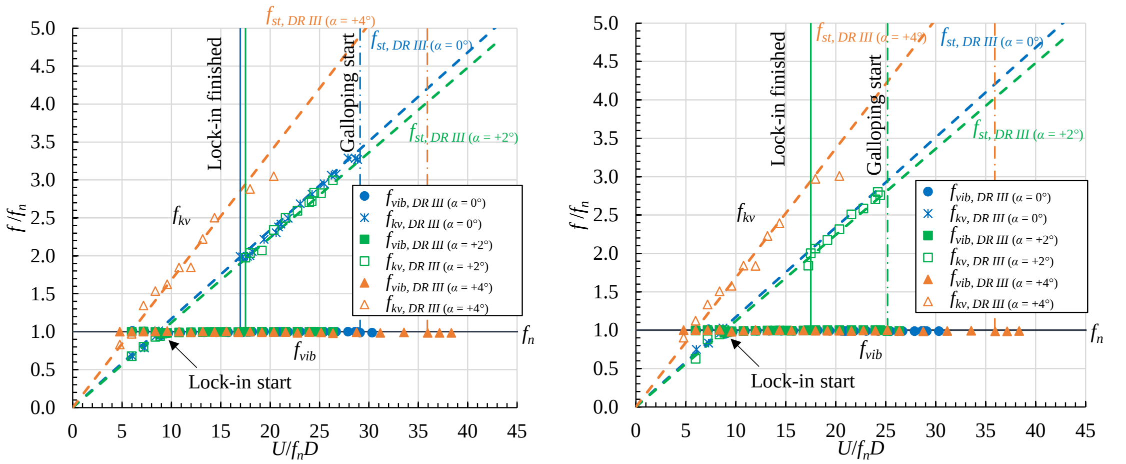

(a) (b)

Fig. 5.19 Kármán vortex shedding frequency (circle) and vibrating frequency (filled circle) (dash slope line: stationary, circle and filled circle: vibrating) of DR III section under (a) Without, and (b) With initial vibration conditions at $S_{c\eta}$ = 42 for various attack angles.

Moreover, the slope of the transverse force coefficient ($dC_{Fy}/d\alpha$) was also changed from −2.08 (α = 0°) to −4.11 (α = +2°) and −7.07 (α = +4°) at wind velocity of 6.0 m/s, and from −2.08 (α = 0°) to −3.88 (α = +2°) and −7.94 (α = +4°) at wind velocity of 10.8 m/s. Since $dC_{Fy}/d\alpha$ is the largest at α = +4°, the critical reduced wind velocity of galloping based on the quasi-steady theory (U_{cr_quasi}) of the DR III section was expected to be in the lower wind velocity region at α = +4° (Figs. 5.5 (c) and 5.6 (c)). However, the DR III section vibrated at the reduced wind velocity significantly higher than U_{cr_quasi} as shown in Figs. 5.16 and 5.18. Thus, the quasi-steady theory may not be able to describe the galloping instability of the DR III section at α = +4°.

5.3.4 Summary

In rectangular (R) section, the KVIV and galloping fully interfered with each other at α = 0° and +4° within the studied Scruton number range ($S_{c\eta}$ = 6 and 42). At α = +9°, the KVIV and galloping did not interfere with each other in both Scruton numbers. In the triple recession (TR) section, the KVIV and galloping fully interfered with each other at α = 0° and +2° in the case of $S_{c\eta}$ = 6. When the Scruton number was increased to 42, the KVIV and galloping partially interfered with each other in the absence of initial vibration and fully interfered with each other in the presence of initial vibration at α = 0° and +2°. At α = +4° of the TR section, the KVIV and galloping partially interfered with each other when $S_{c\eta}$ = 6 and did not interfere with each other when $S_{c\eta}$ was increased to 42. In the double recession III (DR III) section, the KVIV and galloping fully interfered with each other at α = 0° and +2° when $S_{c\eta}$ = 6. When the Scruton number was increased to 42, the KVIV and galloping partially interfered with each other at α = 0° and hardly interfered with each other at α = +2°. At α = +4° of the DR III section, the KVIV and galloping did not interfere with each other in both Scruton numbers. An increase in the angle of attack and/or Scruton number resulted in different amplitude responses.

When the Kármán vortex shedding intensity was decreased to minimum value by increasing the angle of attack (α) from 0° to +9° in the R section, and 0° to +4° in TR and DR III sections, the Strouhal number (St) of the respective section were increased. Since $1/St$ represents the onset reduced wind velocity of KVIV, the onset reduced wind velocity of these sections was expected to be observed in the lower wind velocity regions. At α = +9° of the R section, despite the weak Kármán vortex shedding, KVIV was observed around $1/St$ in the $S_{c\eta}$ = 6 case. Hence, the two-shear layer instability, also known as the Kármán vortex shedding, may control the galloping. At α = +4° of TR and DR III sections, the model vibrated at the reduced wind velocity higher than that of $1/St$ in both Scruton number cases. Since the Kármán vortex shedding intensity of both TR and DR III sections were very weak at α = +4° and KVIV was not observed in the response amplitude, factors other than the Kármán vortex may control the galloping of these sections.

On the other hand, the slope of the transverse force coefficient ($dC_{Fy}/d\alpha$) became the largest when the attack angle (α) was increased from 0° to +9° in the R section, and 0° to +4° in the TR and DR III sections. Therefore, the critical reduced wind velocity of galloping based on the quasi-steady theory (U_{cr_quasi}) of all sections at respective the angle of attack was expected to be in the lower wind velocity region. However, the galloping onset of all sections was observed in the higher wind velocity region. Thus, the quasi-steady theory may not be able to describe the galloping instability of the R section at α = +9°, and TR and DR III sections at α = +4°. This will be further investigated in the Section 5.4.

5.4 Effect of angle of attack on the unsteady aerodynamic force characteristics of the rectangular and corner-cut cylinders

In this section, the effects of the angle of attack on the unsteady aerodynamic characteristics such as the aerodynamic derivatives which represent aerodynamic damping (H_1^*) and aerodynamic stiffness (H_4^*) of the rectangular (R), triple recession (TR) and double recession III (DR III) were discussed. Vertical 1DOF forced vibration tests were carried out for double amplitude of $2\eta_0$ = 2.25, 9, and 27 mm ($2\eta_0/D$ = 0.025, 0.1, and 0.3, respectively), and vibration frequency of f = 2.6 Hz (Table 2.8). The measured reduced wind velocity range was $0 \leq U/fD \leq 60$, in which the maximum Reynolds number corresponds to 84,000. The aerodynamic derivatives, H_1^* and H_4^* were calculated according to Eqs. 2.16 and 2.17. The positive value of H_1^* represents the presence of galloping in the study section under forced vibration conditions. There is almost no literature concerning the study of aerodynamic derivatives of rectangular and corner-cut cylinders of side ratio 1.5 at the studied angles of attack (α = 0°, +4° and +9° for R section, and α = 0°, +2° and +4° for TR and DR III). Therefore, the amplitude dependency of each section at each angle of attack was also provided. Then the effects of angles of attack (asymmetric body) on the aerodynamic derivatives, the critical reduced wind velocity of galloping based on the quasi-steady theory (U_{cr_quasi}), the onset reduced wind velocity obtained from the vertical 1DOF free vibration and forced vibration tests of both rectangular and corner-cut cylinders were discussed in the following sections.

5.4.1 Rectangular cylinder

As shown in Fig. 5.20, amplitude dependency was present in the onset reduced wind velocity at α = 0° (symmetric body) and +4° (asymmetric body) of the rectangular (R) section. At α = +9° (asymmetric body and large $dC_{Fy}/d\alpha$), no amplitude dependency was observed both in the onset reduced wind velocity and aerodynamic damping (H_1^*) values. In the R section, the positive H_1^* values around 1.67B/D were only observed in the angle of attack of 0° and +4° cases. Therefore, the existence of MIV in these two angles of attack was confirmed both in the H_1^* values (forced vibration test results) and response amplitude diagrams (free vibration test results). However, α = +9°, the MIV was not observed in both tests. The H_1^* values of the R section became negative within $5 < U/fD < 15$ when the measured wind velocity was increased. The α = 0° case has the largest negative H_1^* value at $1/St$ (the onset reduced wind velocity of KVIV) while the α = +9° case has the smallest negative H_1^* value at $1/St$ as shown in Fig. 5.20. This corresponds with the Kármán vortex shedding intensity of respective section as shown in Fig. 5.1 (a).

In the case with strong Kármán vortex shedding intensity (α = 0° and +4°), the H_1^* value sharply changed from a negative to a positive sign at $1/St$ ($2\eta_0/D$ = 0.025) as shown in Figs. 5.20 (a) and (b). This corresponds to a sharp increase in the positive H_4^* value around $1/St$ as shown in Fig. 5.21 (a) and (b). Since vibrations of these three two angles of attack cases started from $1/St$ in the velocity-amplitude diagram (Fig. 5.7 and 5.10) the Kármán vortex was highly associated with the vibration of the model. Thus, the galloping instability of these two cases was suppressed by the Kármán vortex until $1/St$.

In the case with weak Kármán vortex shedding intensity (α = +9°), the H_1^* value gradually changed from a negative to a positive sign at the reduced wind velocity higher than $1/St$ as shown in Figs. 5.20 (c). As shown in Fig. 5.21 (c), the H_4^* value around $1/St$ was also extremely small. In the velocity-amplitude diagram (Fig. 5.7 and 5.10), only a small Kármán vortex-induced vibration (KVIV) was observed at $1/St$. Hence, the KVIV and galloping were completely separated from each other.

The H_1^* values obtained from the force vibration test were asymptotic to the H_1^* values calculated from the slope of transverse force coefficients, particularly in the higher wind velocity region, at all three vibration amplitudes only at α = 0° case as shown in Fig. 5.20 (a). At α = +4° and +9°, the two H_1^* values only paralleled with each other. Hence, the galloping instability might be difficult to describe with the quasi-steady theory in these two angles of attack cases. At α = +9°, the H_1^* values obtained from the $dC_{Fy}/d\alpha$ modified ±5% to ±10% also paralleled with the H_1^* values obtained from the force vibration test (Figs. H.19, H.22, H.25 and H.28). Hence, the ±5% to ±10% variation of the C_{Fy} values next to the targeted angle of attack did not affect the comparison of the two H_1^* values.

The onset reduced wind velocity obtained from the H_1^* values was approximately the same as 1/*St* obtained from the respective velocity-amplitude diagram for both $S_{c\eta}$ values in the α = 0° and +4° cases. At α = +9°, the difference of around U/fD = 5 was observed as listed in Table 5.3.

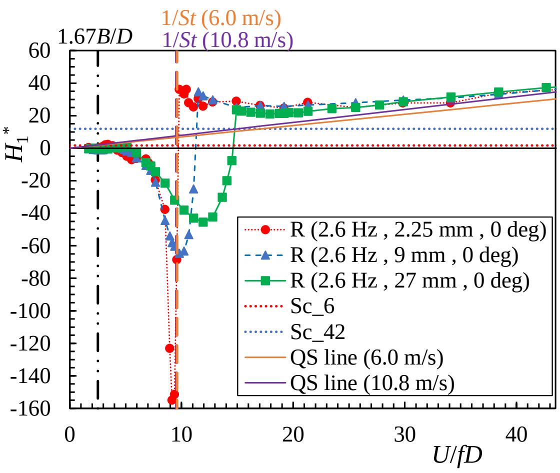

(a)

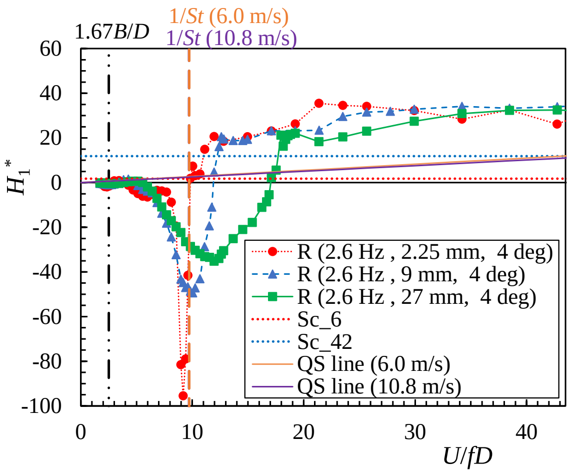

(b)

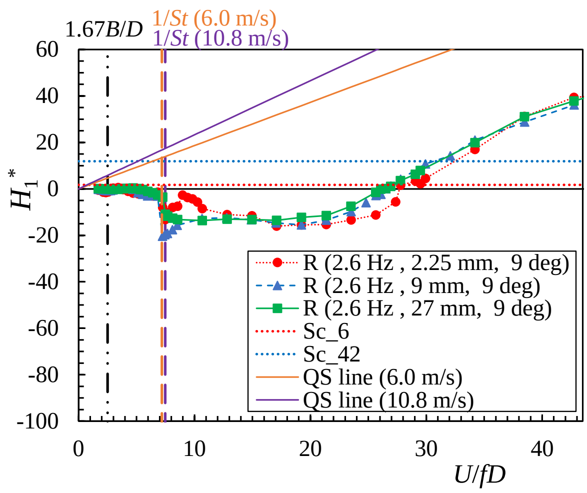

(c)

Fig. 5.20 Aerodynamic damping H_1^* of R section obtained from forced vibration test (marker) for the forced vibrating double amplitudes ($2\eta_0$) of 0.025*D*, 0.1*D*, and 0.3*D*, H_1^* calculated based on quasi-steady theory (inclined solid line), and Scruton number (dot line) at (a) α = 0°, (b) α = +4°, and (c) α = +9°.

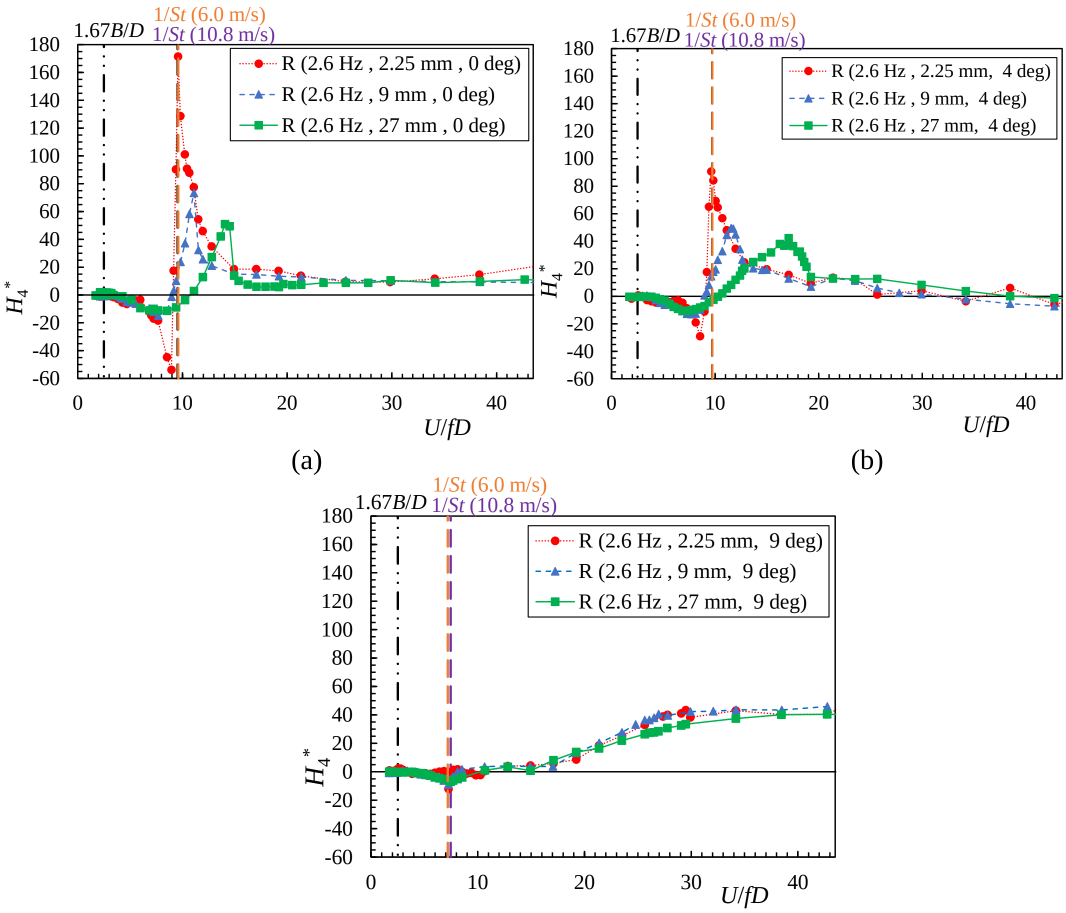

(c)

Fig. 5.21 Aerodynamic stiffness H_4^* of R section obtained from forced vibration test (marker) for the forced vibrating double amplitudes ($2\eta_0$) of 0.025D, 0.1D, and 0.3D at (a) α = 0°, (b) α = +4°, and (c) α = +9°.

5.4.2 Corner-cut cylinders

(1) Triple Recession (TR)

As shown in Fig. 5.22, amplitude dependency was present in the onset reduced wind velocity at α = 0° (symmetric body) and +2° (asymmetric body) of the triple recession section. At α = +4° (asymmetric body and large $dC_{Fy}/d\alpha$), no amplitude dependency was observed both in the onset reduced wind velocity and aerodynamic damping (H_1^*) values. In the TR section, the positive H_1^* values around 1.67B/D were only observed in all cases. Therefore, the existence of MIV was confirmed both in the H_1^* values (forced vibration test results) and response amplitude diagrams (free vibration test results).

The H_1^* values of the TR section became negative within 5 < U/fD < 20 when the measured wind velocity was increased. Among them, the α = 0° and +2° case has the largest negative H_1^* value while the α = +4° case has the smallest as shown in Fig. 5.22. The negative H_1^* region corresponds to the reduced wind velocity region where an increase in the positive H_4^* value was observed as shown in Fig. 5.23 (a) and (b). The amount of negative H_1^* value corresponds with the Kármán vortex shedding intensity of the respective section as shown in Fig. 5.1 (b). Since vibrations of these two angles of attack cases started from 1/St in the velocity-amplitude diagram (Fig. 5.12 and 5.14) the

Kármán vortex is associated with the vibration of the model. Thus, the galloping instability of these two cases was suppressed by the Kármán vortex until 1/*St*.

In the case with weak Kármán vortex shedding intensity (α = +4°), the H_1^* value gradually changed from a negative to a positive sign at the reduced wind velocity higher than 1/*St* as shown in Figs. 5.22 (c). As shown in Fig. 5.23 (c), the H_4^* value around 1/*St* was also negative. In the velocity-amplitude diagram (Fig. 5.12 and 5.14), KVIV was not observed at 1/*St*. Hence, the KVIV and galloping were completely separated from each other. Thus, the vibration of this section may be associated with other factors in addition to the Kármán vortex.

The H_1^* values obtained from the force vibration test were asymptotic to the H_1^* values calculated from the slope of transverse force coefficients, particularly in the higher wind velocity region, at all three vibration amplitudes at α = 0° and +2° as shown in Fig. 5.22 (a) and (b). At α = +4°, the two H_1^* values are only parallel with each other. Thus, the galloping instability might be difficult to describe with the quasi-steady theory in TR section at α = +4°. At α = +4°, the H_1^* values obtained from the $dC_{Fy}/d\alpha$ modified ±5% to ±10% also paralleled with the H_1^* values obtained from the force

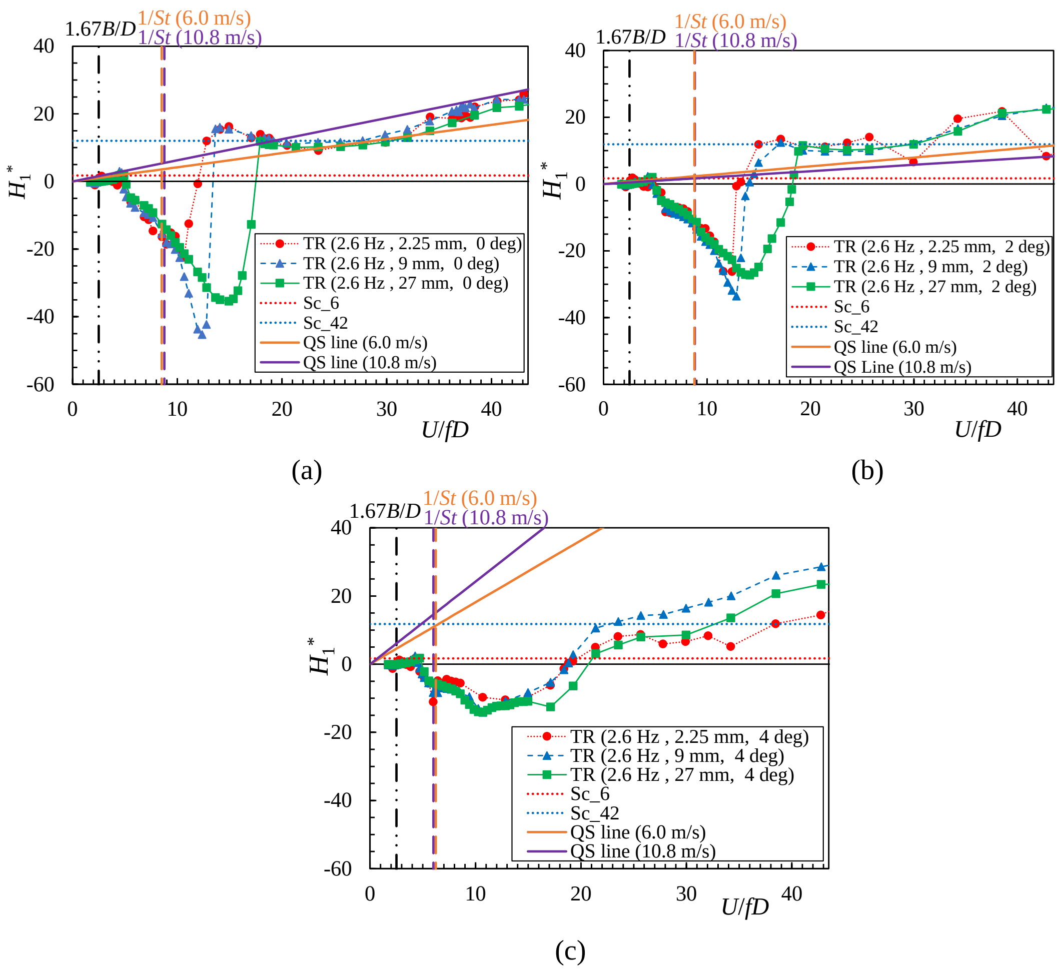

Fig. 5.22 Aerodynamic damping H_1^* of TR section obtained from forced vibration test (marker) for the forced vibrating double amplitudes ($2\eta_0$) of 0.025*D*, 0.1*D*, and 0.3*D*, H_1^* calculated based on quasi-steady theory (inclined solid line), and Scruton number (dot line) at (a) α = 0°, (b) α = +2°, and (c) α = +4°.

vibration test (Figs. H.20, H.23, H.26 and H.29). Hence, the ±5% to ±10% variation of the C_{Fy} values next to the targeted angle of attack did not affect the comparison of the two H_1^* values in TR. The onset reduced wind velocity obtained from the H_1^* values of the force vibration test was approximately the same as 1/*St* obtained from the respective velocity-amplitude diagram for both $S_{c\eta}$ values at α = 0°. At α = +2° and +4° cases, a difference of around U/fD = 5 was observed as listed in Table 5.3.

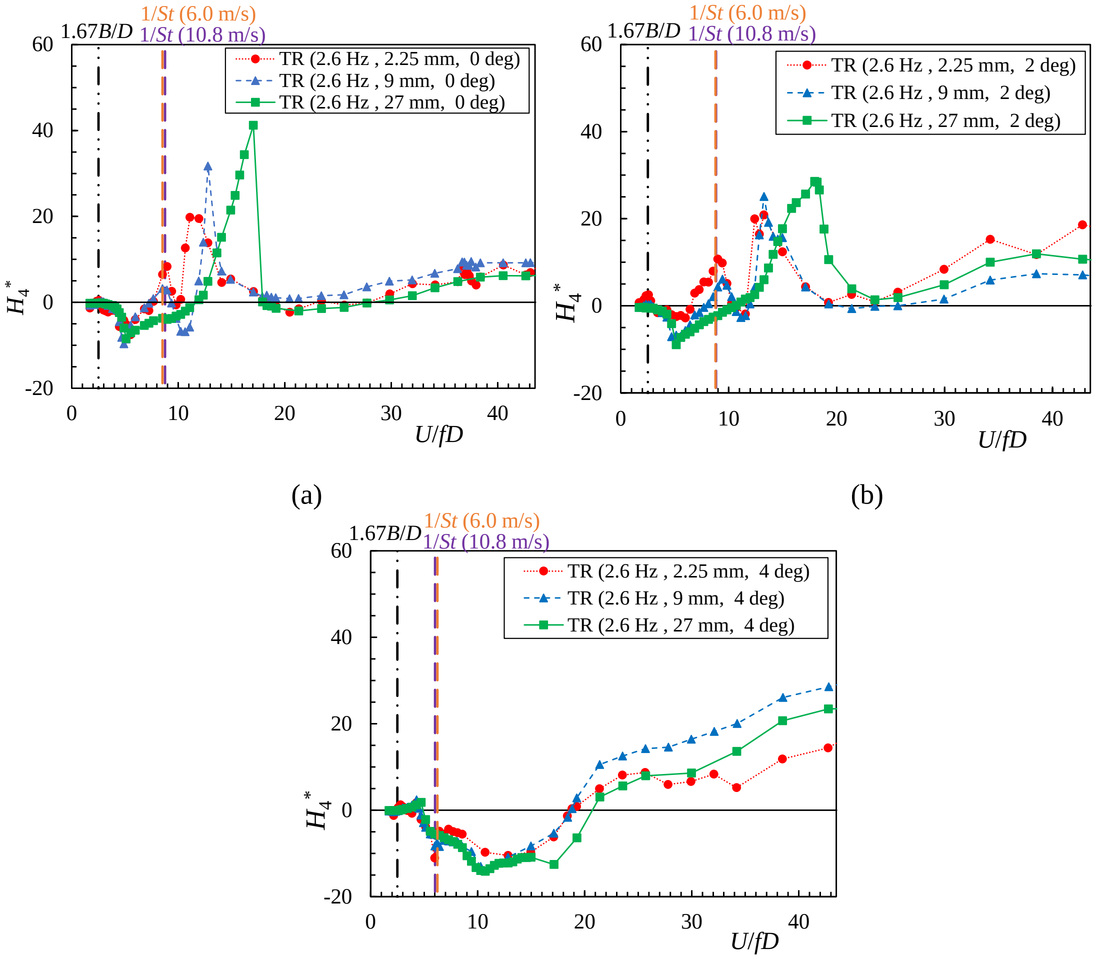

(c)

Fig. 5.23 Aerodynamic stiffness H_4^* of TR section obtained from forced vibration test (marker) for the forced vibrating double amplitudes ($2\eta_0$) of 0.025*D*, 0.1*D*, and 0.3*D* at (a) α = 0°, (b) α = +2°, and (c) α = +4°.

(2) Double Recession III (DR III)

As shown in Fig. 5.24, amplitude dependency was present in the onset reduced wind velocity at α = 0° (symmetric body) and +2° (asymmetric body) of the double recession III section, especially between vibrating double amplitude of 9mm and 27 mm. At α = +4° (asymmetric body and large $dC_{Fy}/d\alpha$), no amplitude dependency was observed both in the onset reduced wind velocity and aerodynamic damping (H_1^*) values. In the DR III section, the positive H_1^* values around 1.67*B*/*D* were only observed in all cases. Therefore, the existence of MIV was confirmed both in the H_1^* values (forced vibration test results) and response amplitude diagrams (free vibration test results).

The H_1^* values of the DR III section became negative within $5 < U/fD < 30$ when the measured wind velocity was increased. Among them, the $\alpha = 0°$ and $+2°$ case has the largest negative H_1^* value while the $\alpha = +4°$ case has the smallest as shown in Fig. 5.24. The negative H_1^* region corresponds to the reduced wind velocity region where an increase in the positive H_4^* value was observed as shown in Fig. 5.25 (a) and (b). The amount of negative H_1^* value corresponds with the Kármán vortex shedding intensity of the respective section as shown in Fig. 5.1 (c). Since vibrations of these two angles of attack cases started from $1/St$ in the velocity-amplitude diagram (Fig. 5.12 and 5.14) the Kármán vortex is associated with the vibration of the model. Thus, the galloping instability of these two cases was suppressed by the Kármán vortex until $1/St$.

In the case with weak Kármán vortex shedding intensity ($\alpha = +4°$), the H_1^* value gradually changed from a negative to a positive sign at the reduced wind velocity higher than $1/St$ as shown in Figs. 5.24 (c). As shown in Fig. 5.25 (c), the H_4^* value around $1/St$ was also negative. In the velocity-

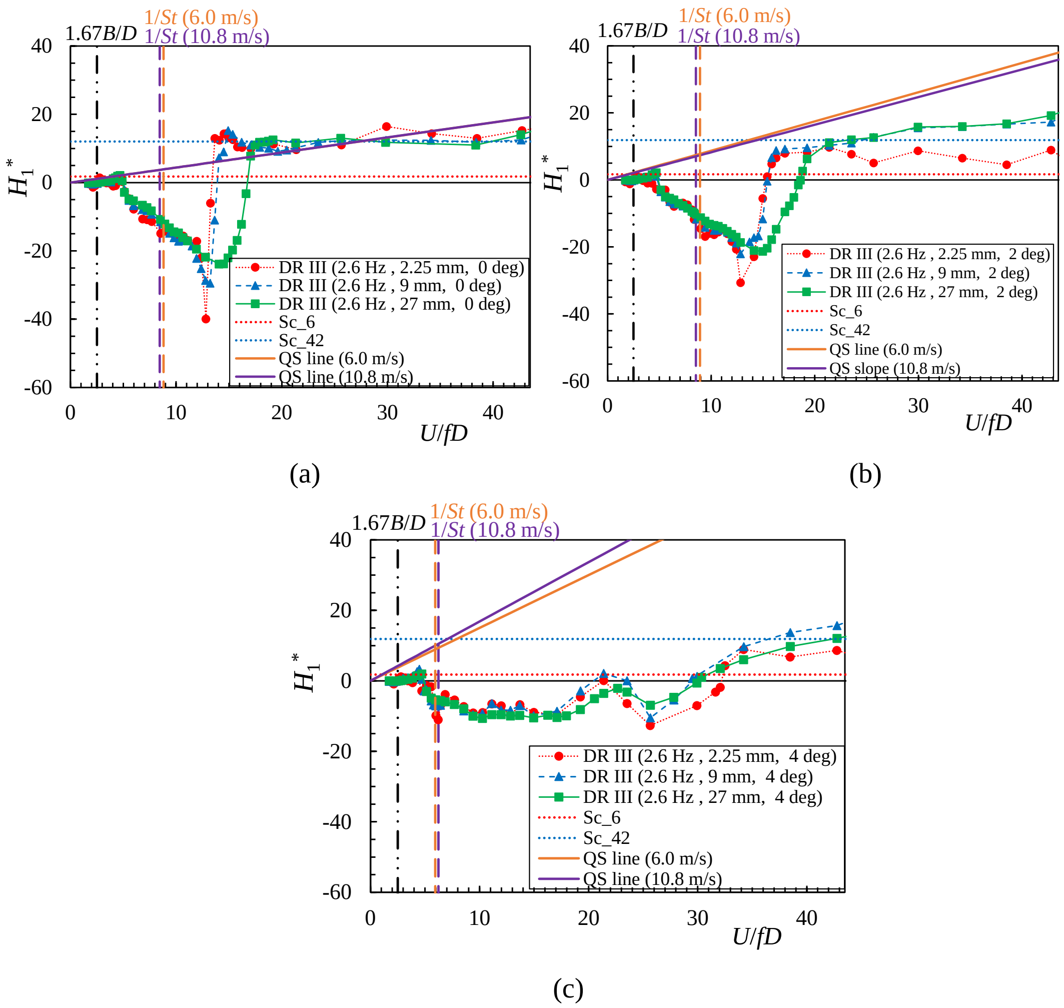

Fig. 5.24 Aerodynamic damping H_1^* of DR III section obtained from forced vibration test (marker) for the forced vibrating double amplitudes ($2\eta_0$) of 0.025D, 0.1D, and 0.3D, H_1^* calculated based on quasi-steady theory (inclined solid line), and Scruton number (dot line) at (a) $\alpha = 0°$, (b) $\alpha = +2°$, and (c) $\alpha = +4°$.

amplitude diagram (Fig. 5.16 and 5.18), KVIV was not observed at 1/*St*. Hence, the KVIV and galloping were completely separated from each other. Thus, the vibration of this section may be associated with other factors in addition to the Kármán vortex similar to α = +4° of the TR section.

The H_1^* values obtained from the force vibration test were asymptotic to the H_1^* values calculated from the slope of transverse force coefficients, particularly in the higher wind velocity region, at all three vibration amplitudes at α = 0° as shown in Fig. 5.24 (a). At α = +2° and +4°, the two H_1^* values only paralleled with each other. Hence, the galloping instability might be difficult to describe with the quasi-steady theory in the DR III section at these two angles of attack. At α = +4°, the H_1^* values obtained from the $dC_{Fy}/d\alpha$ modified ±5% to ±10% also paralleled with the H_1^* values obtained from the force vibration test (Figs. H.21, H.24, H.27 and H.30). Hence, the ±5% to ±10% variation of the C_{Fy} values next to the targeted angle of attack did not affect the comparison of the two H_1^* values in DR III. This was similar with +9° of R and +4° of TR sections. The onset reduced wind velocity obtained from the H_1^* values was larger around *U*/*fD* of 5 than the onset reduced wind velocity of the Kármán vortex-induced vibration (1/*St*) obtained from the respective velocity-amplitude diagram for both $S_{c\eta}$ values at all angles of attack in DR III section. This is listed in Table 5.3.

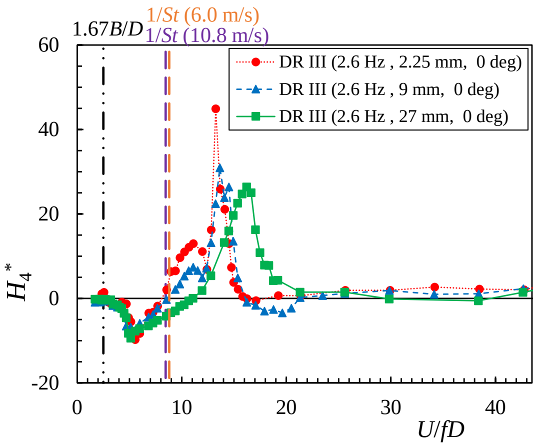

(a)

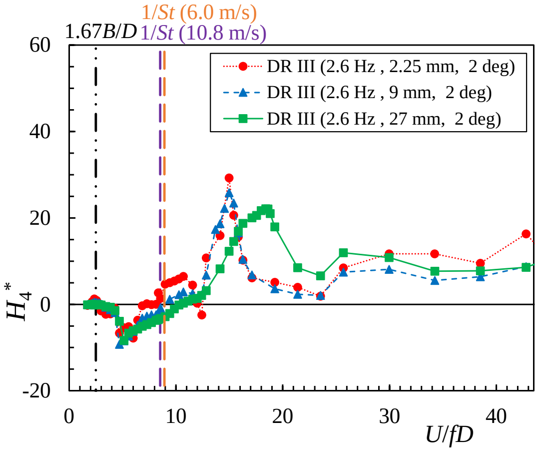

(b)

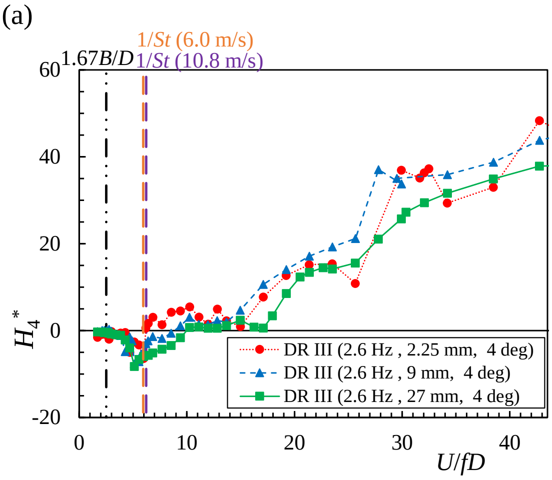

(c)

Fig. 5.25 Aerodynamic stiffness H_4^* of DR III section obtained from forced vibration test (marker) for the forced vibrating double amplitudes ($2\eta_0$) of 0.025*D*, 0.1*D*, and 0.3*D* at (a) α = 0°, (b) α = +2°, and (c) α = +4°.

Table 5.3 The critical reduced wind velocity of galloping based on the quasi-steady theory (U_{cr_quasi}), the onset reduced wind velocity obtained from the vertical 1DOF free vibration and forced vibration tests for rectangular (R), triple recession (TR) and double recession III (DR III) sections at various angles of attack.

Section and α	$S_{c\eta}$	U_{cr_quasi}		Free vibration test, $2\eta_0$ [mm]						Forced vibration test, $2\eta_0$ [mm]		
		U = 6.0 m/s (Re = 36,000)	U = 10.8 m/s (Re = 64,800)	Without initial vibration			With initial vibration			2.25	9	27
				2.25	9	27	2.25	9	27			
R (0°)	6	2.47	2.16	9.96	12.00	15.60	9.96	12.00	15.60	9.80	11.52	14.93
	42	17.07	14.96	9.70	12.13	15.77	9.70	12.13	15.77	9.80	11.52	14.93
R (+4°)	6	6.37	6.91	10.30	13.17	16.76	10.30	13.17	16.76	9.83	11.97	17.10
	42	43.23	46.87	10.30	13.17	17.96	10.30	13.17	17.96	11.11	12.40	17.96
R (+9°)	6	0.93	0.74	23.95	24.19	26.34	23.95	24.19	26.34	29.07	27.80	27.78
	42	6.37	5.10	28.74	28.74	33.52	28.74	28.74	33.52	34.20	32.07	34.20
TR (0°)	6	4.27	2.86	9.70	12.13	16.98	9.70	12.13	16.98	12.80	13.64	17.91
	42	28.70	19.20	19.69	19.65	19.89	9.73	12.16	15.07	14.08,32.05	13.64,32.05	32.05
TR (+2°)	6	6.39	8.84	9.62	12.03	15.63	9.62	12.03	15.63	14.97	14.55	18.40
	42	45.06	62.27	19.72	20.44	>24	9.62	12.03	16.84	17.11	17.12,29.96	34.24
TR (+4°)	6	0.93	0.70	10.80	13.20	19.68	10.80	13.20	19.68	21.37	19.26	21.40
	42	6.50	4.87	21.60	24.00	27.60	21.60	24.00	27.60	38.46	23.54	34.21
DR III (0°)	6	3.99	3.99	9.66	10.87	19.32	9.66	10.87	19.32	13.68	14.07	17.05
	42	27.26	27.25	29.11	29.11	29.11	9.70	12.13	17.71	13.68,29.91	14.93,29.91	18.76,29.91
DR III (+2°)	6	1.94	2.05	9.58	11.97	17.96	9.58	11.97	17.96	15.83	15.83	18.83
	42	13.58	14.38	>26	>26	>26	25.20	25.20	25.20	-	25.67	23.53
DR III (+4°)	6	1.17	1.04	>31	>31	>31	31.13	31.13	31.13	32.49	34.22	32.07
	42	7.93	7.07	35.92	37.12	38.31	35.92	37.12	38.31	-	38.50	42.76

5.5 Effect of Kármán vortex shedding on the motion-induced vortices and the galloping onset at various angles of attack

In this section, the effect of Kármán vortex shedding on the motion-induced vortices and the galloping onset were discussed for various attack angle cases (asymmetric body) based on the aerodynamic damping (H_1^*), non-dimensionalized transverse force amplitude, and phase lag between the unsteady transverse force and vertical displacement of the respective section. The discussions were made for three vibration double amplitudes of 0.025*D*, 0.1*D*, and 0.3*D*. The aerodynamics instability is present in the model when the H_1^* values change from negative to positive and the phase lag changes from positive to negative.

5.5.1 Rectangular cylinder

Fig. 5.26 illustrates the aerodynamic derivative (H_1^*), non-dimensionalized transverse force amplitude and phase lag between the unsteady transverse force and vertical displacement of R section at $2\eta_0/D$ = 0.025, 0.1, and 0.3 for α = 0°, +4°, and +9°. The Kármán vortex shedding of the R section was strong as it has the largest C'_{Fy} value at 0° (symmetric body) and +4° (asymmetric body) as shown in Fig. 5.1 (a). At these two angles of attack, the vibration stated at the onset reduced wind velocity of the Kármán vortex-induced vibration (1/*St*). Moreover, the maximum non-dimensionalized transverse force amplitude was found at 1/*St* as shown in Fig. 5.26 (a). The phase also turned from a positive sign to a negative sign at 1/*St* as shown in Fig. 5.26 (b) and the vibration began at 1/*St*. As shown in Figs. 5.26 (a-f), the onset reduced wind velocity values were dependent on the vibration amplitude. The non-dimensionalized transverse force amplitude also increased with an increase in the vibration amplitude (Figs. 5.26 (a), (c) and (e)). Hence, the instability caused by the Kármán vortex, which is also known as two-shear layer instability, was dominant in the vibration of the R section at α = 0° and +4°.

When the Kármán vortex shedding intensity was significantly reduced by changing the angle of attack to α = +9° (asymmetric body), the non-dimensionalized transverse force amplitude at 1/*St* was significantly decreased as shown in Fig. 5.26 (a). The phase changes from a positive sign to a negative sign around 1/*St* was observed in the phase diagram as shown in Fig. 5.26 (b). However, the phase did not change from positive to negative sharply as in α = 0° and +4° cases. It is also worth noting that the phase did not correspond to −90° and the onset reduced wind velocity values were independent of the vibration amplitude at +9° of the R section. On the other hand, the non-dimensionalized transverse force amplitude increased with an increase in the vibration amplitude similar to 0° and +9° cases of the R section. Therefore, the instability caused by the Kármán vortex, which is also known as two-shear layer instability, was dominant in the vibration of the R section at α = +9°, regardless of the weak Kármán vortex shedding intensity. Hence, the Kármán vortices dominate the vibration of the R section both in the symmetric (α = 0°) and asymmetric (α = +4° and +9°) body conditions.

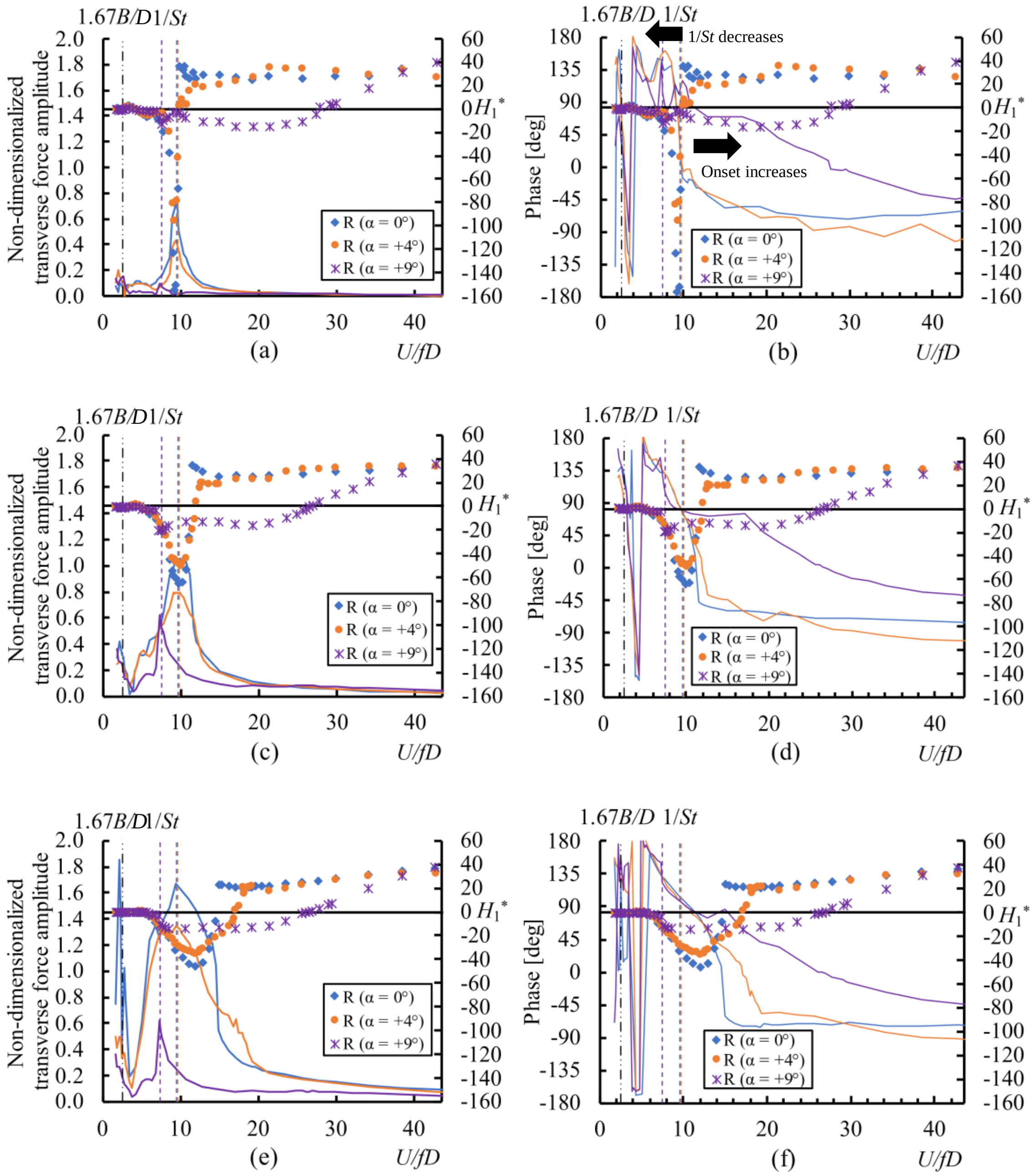

Fig. 5.26 Aerodynamic damping H_1^* (marker) for R section (a) Non-dimensionalized transverse force amplitude (solid line) and (b) Phase (solid line) at $2\eta_0/D$ = 0.025, (c) Non-dimensionalized transverse force amplitude (solid line) and (d) Phase (solid line) at $2\eta_0/D$ = 0.1, and (e) Non-dimensionalized transverse force amplitude (solid line) and (f) Phase (solid line) at $2\eta_0/D$ = 0.3 for various attack angles.

5.5.2 Corner-cut cylinders

(1) Triple Recession (TR)

Fig. 5.27 illustrates the aerodynamic derivative (H_1^*), non-dimensionalized transverse force amplitude and phase lag between the unsteady transverse force and vertical displacement of TR section at $2\eta_0/D$ = 0.025, 0.1, and 0.3 for α = 0°, +2°, and +4°. The Kármán vortex shedding of the TR section was relatively strong as it has the second largest C'_{Fy} value at 0° as shown in Fig. 5.1 (b). On the other hand, the Kármán vortex shedding of the TR section was weak at α = +2° and +4° as they have the smallest C'_{Fy} values. In the response amplitude diagram, the vibration of the model started around 1/*St* at α = 0° and +2° cases. At α = +4°, the vibration of the model did not start at 1/*St*.

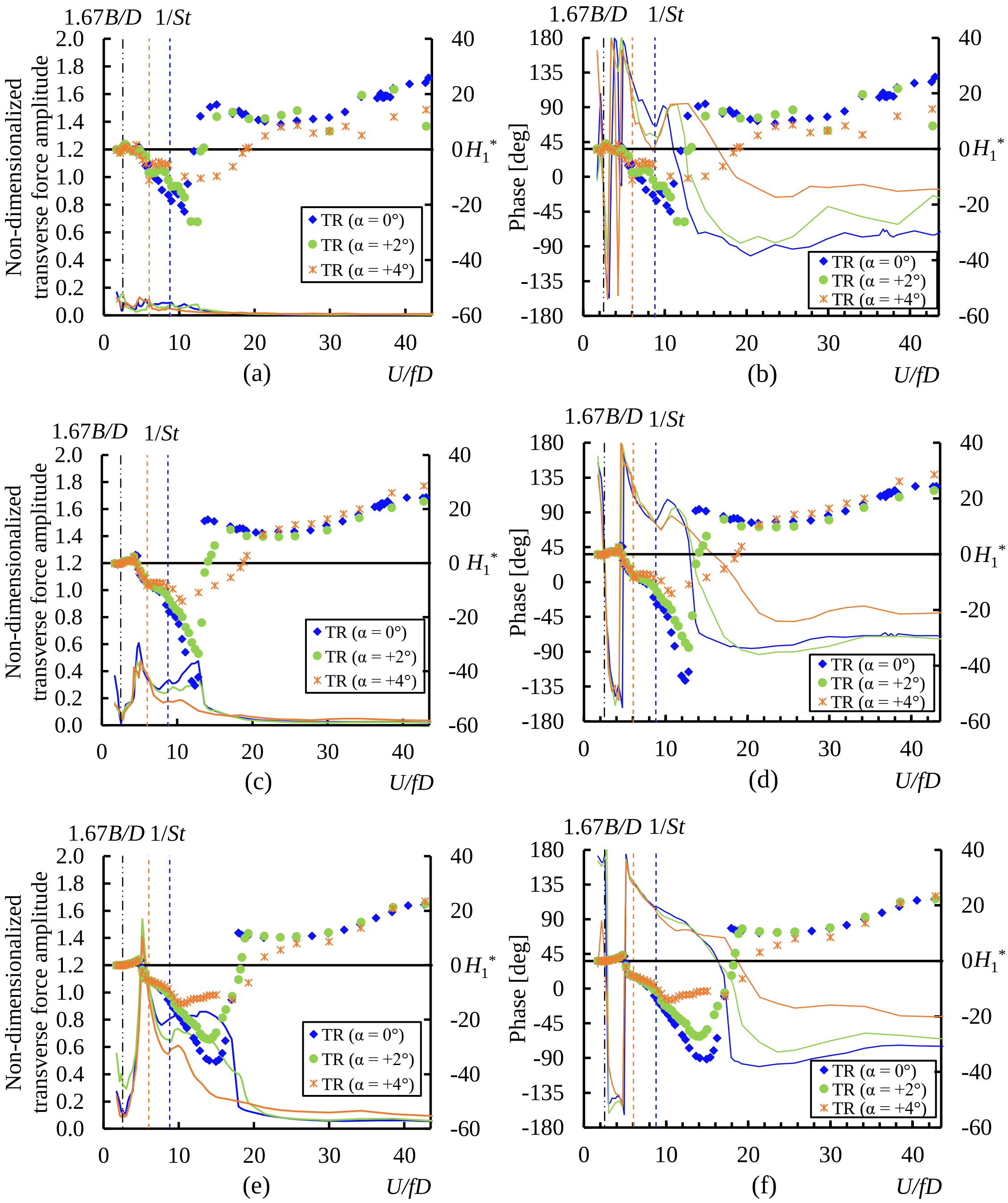

Fig. 5.27 Aerodynamic damping H_1^* (marker) for TR section (a) Non-dimensionalized transverse force amplitude (solid line) and (b) Phase (solid line) at $2\eta_0/D$ = 0.025, (c) Non-dimensionalized transverse force amplitude (solid line) and (d) Phase (solid line) at $2\eta_0/D$ = 0.1, and (e) Non-dimensionalized transverse force amplitude (solid line) and (f) Phase (solid line) at $2\eta_0/D$ = 0.3 for various attack angles.

The maximum non-dimensionalized transverse force amplitude of the TR section for all studied angles of attack was found between 1.67*B*/*D* and 1/*St* as shown in Figs. 5.27 (a), (c), and (e). Additionally, the second-largest peak was observed at wind velocity higher than 1/*St*. The phase also changed from a positive sign to a negative sign at wind velocity higher than 1/*St* (Figs. 5.27 (c), (d), and (f)). At α = 0° and +2°, the onset reduced wind velocity values were dependent on the vibration amplitude as shown in Figs. 5.27 (a-f). The non-dimensionalized transverse force amplitude also increased with an increase in the vibration amplitude (Figs. 5.27 (a), (c) and (e)). At α = +4°, the second-largest peak was hardly observed. In addition, the phase did not correspond to −90° and the onset reduced wind velocity values were independent of the vibration amplitude. This is similar to +9° of the R section.

Since the maximum non-dimensionalized transverse force amplitude of the TR section originated from 1.67*B*/*D*, the instability caused by the motion-induced vortex, which is also known as one-shear layer instability, was dominant in the vibrations while the effect of the Kármán vortex was still present. Therefore, motion-induced vortices dominate the vibration of the TR section while the effect of Kármán vortices was still observed at α = 0° and +2°. On the other hand, the motion-induced vortices dominate the vibration of the TR section at α = +4°.

(2) Double Recession III (DR III)

Fig. 5.28 illustrates the aerodynamic derivative (H_1^*), non-dimensionalized transverse force amplitude and phase lag between the unsteady transverse force and vertical displacement of DR III section at $2\eta_0/D$ = 0.025, 0.1, and 0.3 for α = 0°, +2°, and +4°. The Kármán vortex shedding of the DR III section was relatively strong as it has the third largest C'_{Fy} value at 0° as shown in Fig. 5.1 (c). On the other hand, the Kármán vortex shedding of the DR III section was weak at α = +2° and +4° as they have the smallest C'_{Fy} values as shown in Fig. 5.1 (c). In the response amplitude diagram, the vibration of the model started around 1/*St* at α = 0° and +2° cases. At α = +4°, the vibration of the model did not start at 1/*St*.

The maximum non-dimensionalized transverse force amplitude of the DR III section for all studied angles of attack was found between 1.67*B*/*D* and 1/*St* as shown in Figs. 5.28 (a), (c), and (e). Additionally, the second largest peak was observed at wind velocity higher than 1/*St* (Figs. 5.28 (a), (b) and (c)). The phase also changed from a positive sign to a negative sign at wind velocity higher than 1/*St* (Figs. 5.28 (c), (d), and (f)). This is similar to the TR section. However, the magnitude of the second largest peak was comparatively smaller as the Kármán vortex shedding of the DR III section was smaller than the TR section. At α = 0° and +2°, the onset reduced wind velocity values were dependent on the vibration amplitude (Figs. 5.28 (a-f)) and the non-dimensionalized transverse force amplitude increased with an increase in the vibration amplitude (Figs. 5.28 (a), (c) and (e)). The second-largest peak was hardly observed at α = +4° of the DR III section. In addition, the phase did not correspond to −90° and the onset reduced wind velocity values were independent of the vibration amplitude. This is similar to +9° of the R and +4° of the TR sections.

Therefore, the instability caused by the motion-induced vortex, which is also known as one-shear layer instability, was dominant in the vibrations of DR III sections while the effect of the Kármán vortex was still present. At α = 0° and +2°, the motion-induced vortices dominated the vibration of the

DR III section while the effect of Kármán vortices was still observed. On the other hand, the motion-induced vortices dominate the vibration of the DR III section at α = +4°.

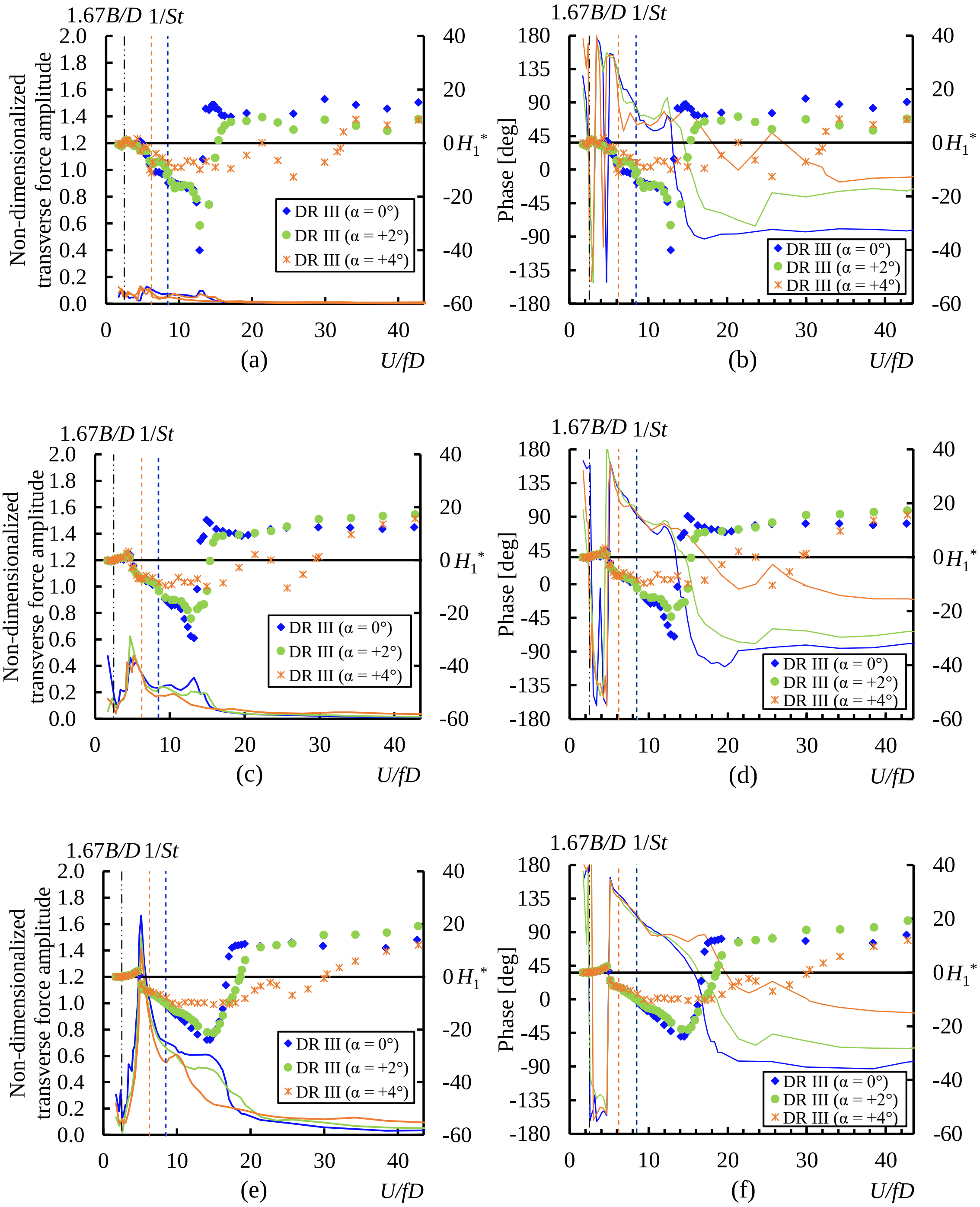

Fig. 5.28 Aerodynamic damping H_1^* (marker) for DR III section (a) Non-dimensionalized transverse force amplitude (solid line) and (b) Phase (solid line) at $2\eta_0/D$ = 0.025, (c) Non-dimensionalized transverse force amplitude (solid line) and (d) Phase (solid line) at $2\eta_0/D$ = 0.1, and (e) Non-dimensionalized transverse force amplitude (solid line) and (f) Phase (solid line) at $2\eta_0/D$ = 0.3 for various attack angles.

Hence, the Kármán vortex shedding intensity of a section can affect the range of motion-induced vortex influence. Furthermore, the Kármán and motion-induced vortices may interfere with each other, depending on the Kármán vortex shedding intensity of a section. This interference may affect the onset of reduced wind velocity of the respective section.

5.6 Concluding remarks

In this chapter, the aerodynamic interactions between the galloping instability and the vortices were investigated by increasing the angle of attack from 0° (symmetric body) to various values (asymmetric body). The angles of attack with the largest slope of transverse force coefficient, α = +9° in the rectangular (R) section, and +4° in the triple recession (TR) and double recession III (DR III) sections, were the most effective in reducing the vertical response amplitude. The static force measurements at R (+9°), TR (+4°), and DR III (+4°) show that these three sections were highly prone to galloping instability based on the perspective of the quasi-steady theory. However, the Kármán vortex shedding intensity of these cases was observed to be very small and the response amplitudes obtained from the vertical 1 DOF free vibration tests show a low tendency of galloping even at very low Sc case (Sc = 6). This behaviour is complex and there remain unexplainable phenomena. In addition, a small KVIV was present around $1/St$ in the response amplitude of the R section at the lowest Scruton number ($S_{c\eta}$ = 6) although the Kármán vortex shedding intensity was reduced by increasing the attack angle from 0° to +9°. According to the response amplitude diagram, the KVIV and galloping separated from each other even in a very small mass-damping parameter ($S_{c\eta}$) of 6 at α = +9° of the R section.

For all sections, the H_1^* obtained from the forced vibration tests was asymptotic to the H_1^* obtained from the slope of the transverse force coefficient (the quasi-steady theory) in the high reduced wind velocity region at α = 0° (symmetric body). When the angle of attack was increased (asymmetric body), they were no longer asymptotic but closely parallel with each other. Therefore, the galloping instability might be difficult to describe by the quasi-steady theory in these angle-of-attack cases. It is also worth noting that the phase did not correspond to −90° at +9° of R, and +4° of TR and DR III sections. At these angles of attack, the onset reduced wind velocity values were also independent of the vibration amplitude.

For the original rectangular (R) section, it was found that the galloping instability was mainly controlled by the Kármán vortex, which is also known as two-shear layer instability, in all studied angles of attack. In the TR and DR III sections, it was found that the galloping instability was controlled by both Kármán and motion-induced vortices at α = 0° and +2°. At α = +4° of the TR and DR III sections, it was found that the galloping instability was significantly controlled by the motion-induced vortices, which is also known as one-shear layer instability.

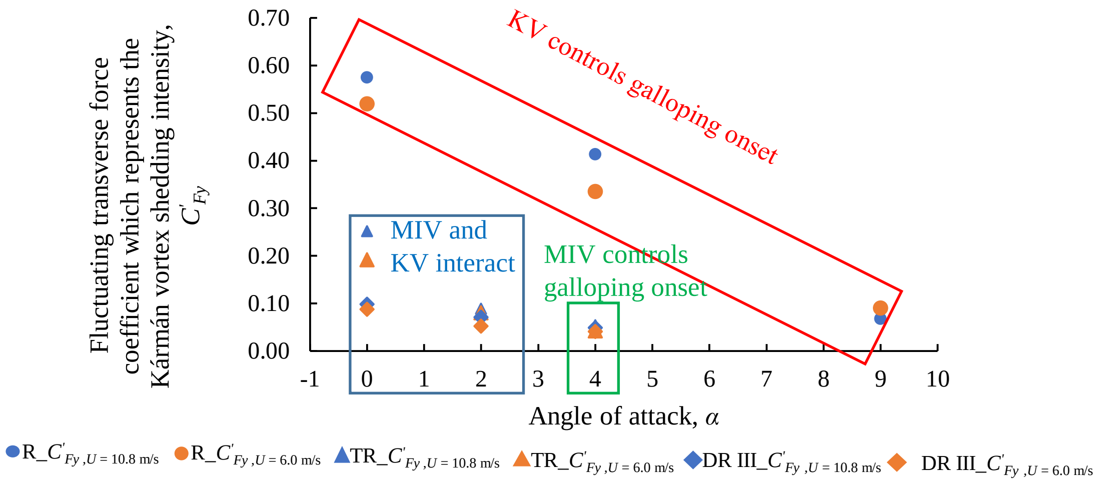

Fig. 5.29 Interaction between vortices and galloping onset at various angles of attack.

To summarize, the interactions between the vortices and galloping in the rectangular and corner-cut cylinders can be divided into three groups depending on the Kármán vortex shedding intensity of a model as shown in Fig. 5.29. This is similar to the zero-angle of attack case. This can offer a range of aerodynamic instability mitigation measures to ensure the safety, reliability and optimization of the aerodynamic performance of structures.

Reference

Choi, Chang-Koon & Kwon, Dae Kun. (2003). Effects of corner cuts and angles of attack on the Strouhal number of rectangular cylinders. Wind and Structures An International Journal. 6. 127-140. 10.12989/was.2003.6.2.127.

Claudio Mannini, Antonino Maria Marra, Tommaso Massai, Gianni Bartoli, Interference of vortex-induced vibration and transverse galloping for a rectangular cylinder, Journal of Fluids and Structures, Volume 66, 2016, Pages 403-423, ISSN 0889-9746, https://doi.org/10.1016/j.jfluidstructs.2016.08.002.

Luca Bruno, Davide Fransos, Nicolas Coste, Arianna Bosco, 3D flow around a rectangular cylinder: A computational study, Journal of Wind Engineering and Industrial Aerodynamics, Volume 98, Issues 6–7, 2010, Pages 263-276, ISSN 0167-6105, https://doi.org/10.1016/j.jweia.2009.10.005.

Shiraishi, N., Matsumoto, M., Shirato, H., & Ishizaki, H. (1988). On aerodynamic stability effects for bluff rectangular cylinders by their corner-cut. *Journal of Wind Engineering and Industrial Aerodynamics*, *28*(1-3), 371-380, ISSN 0167-6105, https://doi.org/10.1016/0167-6105(88)90133-X.

Weilin Chen, Yuhan Wei, Chunning Ji, Yawei Zhao, Mass ratio effects on flow-induced vibrations of an equilateral triangular prism, Journal of Fluids and Structures, Volume 116, 2023, 103808, ISSN 0889-9746, https://doi.org/10.1016/j.jfluidstructs.2022.103808.

Yagmur, Sercan & Dogan, Sercan & Aksoy, Muharrem & Canli, Eyüb & Ozgoren, Muammer. (2015). Experimental and Numerical Investigation of Flow Structures around Cylindrical Bluff Bodies. EPJ Web of Conferences. 92. 02113. 10.1051/epjconf/20159202113.

Yamagishi, Y., Kimura, S., Oki, M., & Hatayama, C. (2009, August). Effect of corner cutoffs on flow characteristics around a square cylinder. In *10th International Conference on Fluid Control, Measurements, and Visualization*.

Chapter 6

Flow field analysis and wind resistance evaluation of complex-shaped structure

6.1 Introduction

In previous chapters, the discussions were made mainly for the two-dimensional (2D) models. However, in the practical designs and applications, the structure has finite height and was a three-dimensional (3D) model. Moreover, some structures have sharp corners, which produce wide flow separation, and lead to strong wind-structure interaction. Hence, the wind-induced vibrations and wind loads acting on these structures should be considered significantly in their structural designs. In this study, the flow field around and the aerodynamic characteristics of the Buddha statue were evaluated by performing 3D terrestrial laser scanning and computational fluid dynamic simulation. The Buddha statue was equally divided into 26 parts with an average height of around 4.96-5.04 m for each cross-section for the detailed representation of the aerodynamic characteristics produced by the cross-sectional configuration of each part.

In this chapter, the static wind forces acting on the 3D model and the flow field around it were discussed. Two types of 3D models, namely the circular cylinder and the Buddha statue, were utilized in this study. In the Buddha statue model, the shape, especially the corners, were varying throughout the overall height of the statue. Thus, this chapter describes the effect of cross-sectional shape changes on the flow separation, flow reattachment, and aerodynamic characteristics of the complex-shaped 3D structure. The acquisition of the external configuration data by using the terrestrial laser scanning method and the 3D modelling from the scanned data are described in Section 6.2. The large eddy simulation conditions of the complex-shaped Buddha statue are introduced in Section 6.3. Section 6.4 discussed the flow field analysis results of the Buddha statue. Section 6.5 provided the aerodynamic characteristics of the Buddha statue. Some of the flow visualization results of the Buddha statue and conclusions provided in this chapter are summarized in the academic article by Hnin et al. (2023).

6.2 Three-dimensional laser scanning and modelling

The architectural and structural drawings are usually required to create the 3D model for Computational Fluid Dynamic (CFD) simulation or experimental purposes. However, there are cases where such type of information is unavailable when the structure is too old/ancient and the blueprints are lost or destroyed. In such cases, the digital data from the Geographic Information System (GIS), Light Detection and Ranging (LIDAR), Airborne Laser Scanning (ALS) and Terrestrial Laser Scanning (TLS) can be used to create a 3D model of the targeted structure. In the current study, the external configuration of one of the proposed models, the Buddha statue, was obtained by using the TLS method. Then, the 3D model of the complex-shaped Buddha statue was generated from the scan data.

6.2.1 Complex-shaped tall structure

The Laykyun Sekkya Standing Buddha Statue, which is recorded as the third tallest statue as of 2023, is located on the Po Khaung Mountain, Monywa City, Sagaing Region, Myanmar as shown in Fig. 6.1. According to Multi-Hazard Risk Assessment in Rakhine State of Myanmar written by the United Nations Development Programme (UNDP, 2011), three storms affected Monywa City with a maximum sustained wind velocity of 35, 50 and 135 km/hr. Hence, the Buddha statue is likely to be affected by the storms in the near future. Therefore, this Buddha statue was chosen to use as the case study model in this research. The Buddha statue is a hollow type structure. The width (B) and the length (L) of the statue at the base are 47.629 m and 43.468 m, respectively. The height of the statue is approximately 129 m including the height of the throne and 116 m without it. It has a total of 31 storeys with an average storey height of approximately 3.66 m. Each storey has an estimated area of 39.93 m × 13.41 m.

(a) (b)

Fig. 6.1 Laykyun Sekkya Standing Buddha Statue: (a) front view; and (b) back view.

6.2.2 Terrestrial laser scanning

The Faro Focus 3D X330, the terrestrial type of phase-shift laser scanner, was used to scan the configuration of the Buddha statue. The targetless scanning was carried out with at least 60% overlap between the two consecutive scans. The scan provided a set of points, denoted as point cloud, which contained the location coordinates. The scanning range in the current measurement was within 303.74 m. The maximum probable error for a single point from a single scan was around 24.3 mm. The global positioning system (GPS), compass, inclinometer and altimeter sensors were used during the 3D laser scanning process to obtain the highly accurate location of the points. The necessary density of the data points required for the 3D modelling was achieved by using the "½ resolution" which is equivalent to approximately 3.07 mm point spacing at a 10 m distance. The noise in the measurement was determined by the incoming signal strength which depends on the observation time. In the current measurement, the scan quality factor of "3×" which has an observation time of approximately 6 μs per scan point was used.

Different parts of the Buddha statue were scanned from the 36 locations as shown in Fig. 6.2. When the laser scanner was positioned at the locations marked with the blue colour, the scanning was focused on the lower parts of the Buddha statue. When the laser scanner was positioned at the locations marked with the violet colour, the middle parts of the Buddha statue were scanned in detail. When the laser scanner was positioned at the locations marked with yellow colour, the scanning was focused on the top parts of the Buddha statue. The red marks indicated the scans which have high obstruction due to the walking humans and animals. Fig. 6.3 shows the output image of one arbitrary scan of the Buddha statue taken from the location marked with the blue colour.

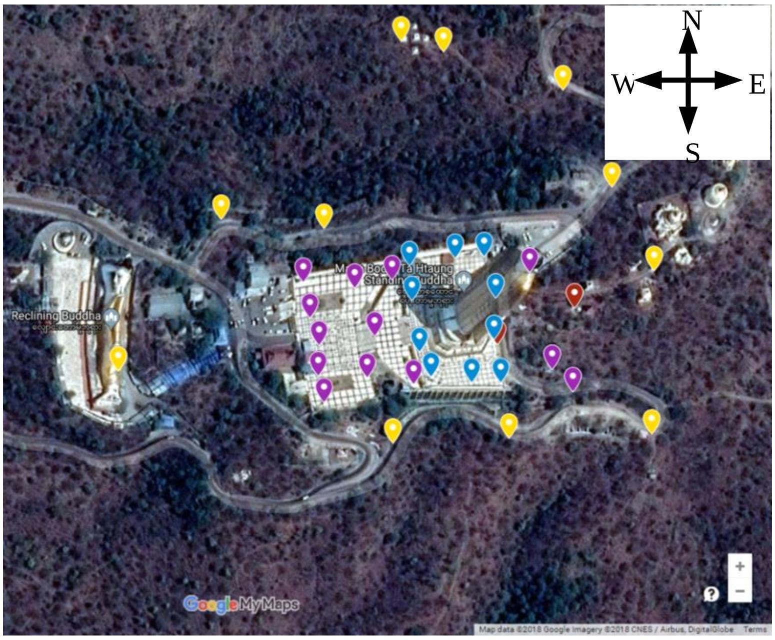

Fig. 6.2 Position of the scanner during the 3D terrestrial laser scanning (Maps Data: Google, ©2018 CNES/ Airbus, DigitalGlobe).

Fig. 6.3 Image of random scan taking the front side of the Buddha statue.

6.2.3 Three-dimensional modelling

The commercial 3D modelling software, FARO SCENE, was used to extract the point cloud data from the scans. The dark scan point filter and distance filter were used to remove the undesirable and overlapping points. Two scans denoted with red as shown in Fig. 6.2 had high obstruction and hindered the point recognition. Thus, these two scans were discarded. The remaining scans were divided into four clusters and then manually registered into the 3D stereolithography (stl) model. The total alignment error of the Buddha statue was approximately 23.4 mm, which was about 0.02–0.05 % of the overall dimension of the Buddha statue.

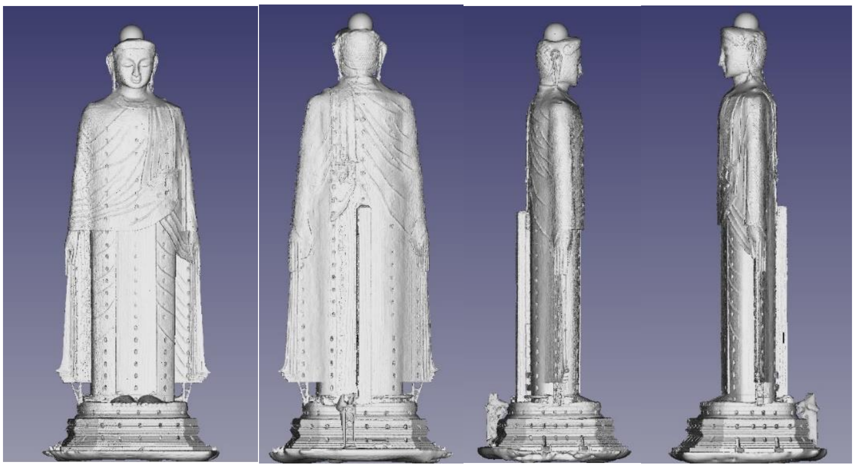

(a) (b) (c) (d)

Fig. 6.4 3D model of the Buddha statue; (a) front; (b) back; (c) left; and (d) right side.

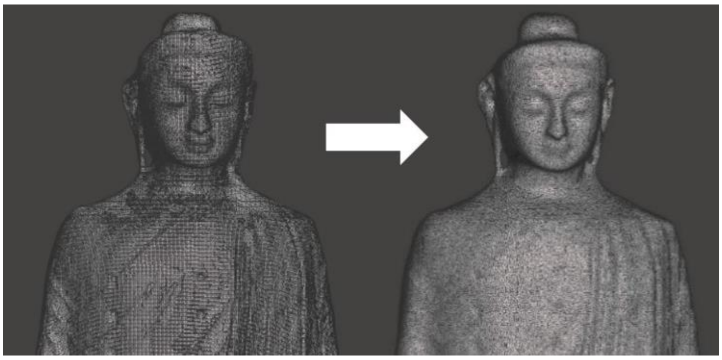

Fig. 6.5 Mesh smoothing.

Due to the lower point density caused by the reflectivity of the black surface at the top part of the Buddha statue, the hair of the Buddha statue was manually reproduced with the FreeCAD software. The final 3D model of the Buddha statue is shown in Fig. 6.4. The Autodesk Meshmixer software was used to repair the twisted and overlapped surface meshes present in the 3D model. The surface meshes of the exterior and interior surface of the Buddha statue were uniformly smoothened into the 22 mm meshes for better control of the complexity of the shape as illustrated in Fig. 6.5. The width (B), side length (L), and height (H) of the Buddha statue were 47.63, 43.47 and 129 m, respectively.

The FreeCAD software was used to create the 3D model of the finite circular cylinder. The diameter of the finite circular cylinder was set as the average width of the Buddha statue (B_{avg} = 30.22 m). The height was set the same as the height of the Buddha statue (H = 129 m). The purpose of the finite circular cylinder is to validate the numerical simulation results of the Buddha statue.

6.3 Numerical simulation

Large Eddy Simulation (LES) model is efficient in handling the flow around complex shaped structures. Hence, LES was chosen to calculate the flow field around the Buddha statue. OpenFOAM software was used for the LES simulation. In this study, LES is performed on the 3D statue model obtained from the 3D terrestrial laser scanning. The following sections describe the computational domain size, surface and volume meshes, boundary condition, numerical algorithms, y^+ values, simulation time and convergence of the simulation.

6.3.1 Computational domain

In the case study area of the Buddha statue, the tropical cyclones mostly come from the south-west wind direction (UNDP, 2011). The wind direction used in the design of the Buddha statue was the west direction. Hence, four types of wind direction, denoted as along-wind direction (α = 0°), west direction (α = 5°), south-west direction (α = 50°) and across-wind direction (α = 90°), were considered during the flow field analysis of the Buddha statue. For the finite circular cylinder, only the along-wind direction (α = 0°) was considered. The meshes around the proposed models are shown in Fig. 6.6. The guidelines issued by the Architecture Institute of Japan (AIJ) were considered in the determination of the computational domain size for the Buddha statue (AIJ, 2017). Fig. 6.7 illustrates the computational domain. The upstream distance was 10B (B is the width of the Buddha statue). The downstream distance was 5H (H is the height of the Buddha statue). The side distance on both sides of the Buddha statue was 10B. The height of the computational domain was 2H. The blockage ratio was between 1.57-2.50%.

The triangle and quad mesh cells were used in the surface mesh. The average spacing (Δs) was 0.25 m. In this study, the windows of the Buddha statue were assumed not to affect the flow separation and simplified as a plain surface. 3D anisotropic tetrahedral extrusion method, T-rex hybrid meshing,

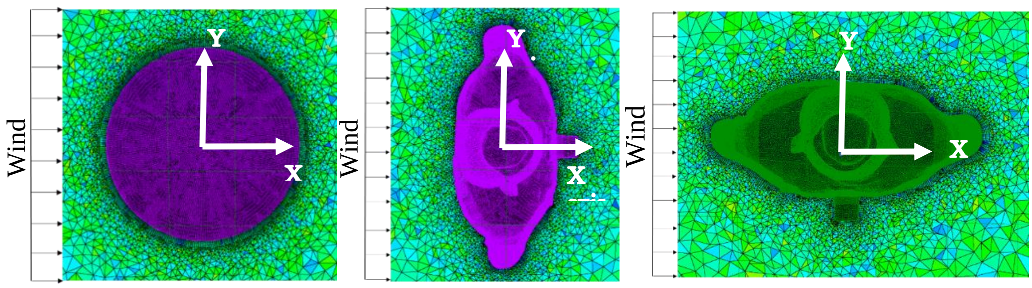

(a) (b) (c)

Fig. 6.6 Mesh around the models; (a) finite circular cylinder in the along-wind direction (α = 0°); Buddha statue in the (b) along-wind direction (α = 0°); and (c) across-wind direction (α = 90°).

was used to generate the volume mesh. The unstructured meshes composed of tetrahedra, pyramids, prisms and hexahedra cells were used in the volume mesh. The first cell height was 0.09 m (*B*/530) and the last cell height of the computation domain was 10 m (*B*/5). The total mesh number was 8.78×10^6 for 0°, 9.41×10^6 for 5°, 10.16×10^6 for 50° and 9.42×10^6 for the 90° attack angle case in the Buddha statue. For each simulation case, the maximum aspect ratio was 132.04, 137.24, 130.25 and 134.14, the maximum mesh non-orthogonality was 84.98, 84.23, 81.08 and 78.82, and maximum skewness was 1.12, 1.18, 1.20 and 1.34, respectively. For the finite circular cylinder, the total mesh number was 8.21×10^6, the maximum aspect ratio was 126.97, the maximum mesh non-orthogonality was 80.30, and the maximum skewness was 1.12.

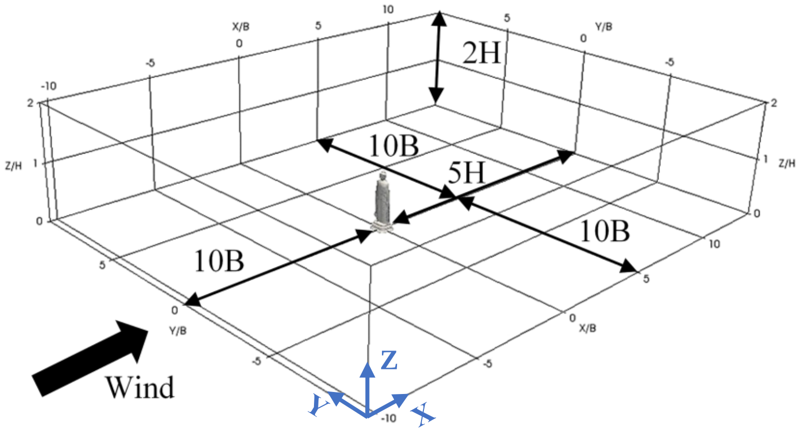

Fig. 6.7 Dimension of the computation domain (Not in scale).

6.3.2 Boundary condition

As recommended by the Myanmar National Building Code (MNBC), the logarithmic law was used to calculate the inlet flow profile of the case study area as follows:

$$U = \frac{U^*}{\kappa} ln\left(\frac{z - z_g + z_0}{z_0}\right) \quad \text{Eq. 6.1}$$

$$U^* = \kappa \frac{U_{ref}}{ln\left(\frac{z_{ref} + z_0}{z_0}\right)} \quad \text{Eq. 6.2}$$

where U is the wind velocity, U^* is the friction velocity, κ is the von Karman's constant, z is the vertical coordinate, z_0 is the surface roughness height, z_g is the minimum z-coordinate in meter, U_{ref} is the reference wind velocity at z_{ref} and z_{ref} is the reference height of 10 m. The ratio of the mean wind velocity (U) to the mean wind velocity at the Buddha statue height (U_H) for the LES inlet wind profile (blue dot) and fitted log law profile (red solid line) is shown in Fig. 6.8.

Since the location of the Buddha statue is in an unpopulated area with few low-rise buildings and paddy fields, it can be classified as the Terrain category II by the Myanmar National Building Code (MNBC). As the case study area was the open terrain with the exposure category of C (MNBC, 2016), the "nutkAtmRoughWallFunction" with a roughness length of 0.01m was used for the ground surface. This wall function provides turbulence kinematic viscosity (ν_T) for atmospheric velocity profiles. On the Buddha statue surface, the "nutUSpaldingWallFunction" which was proposed by Spalding (1961) was used. This wall function considers u^+ to be equal to y^+ in the viscous layer area and $\frac{Ey^+}{\kappa}$ in the log area.

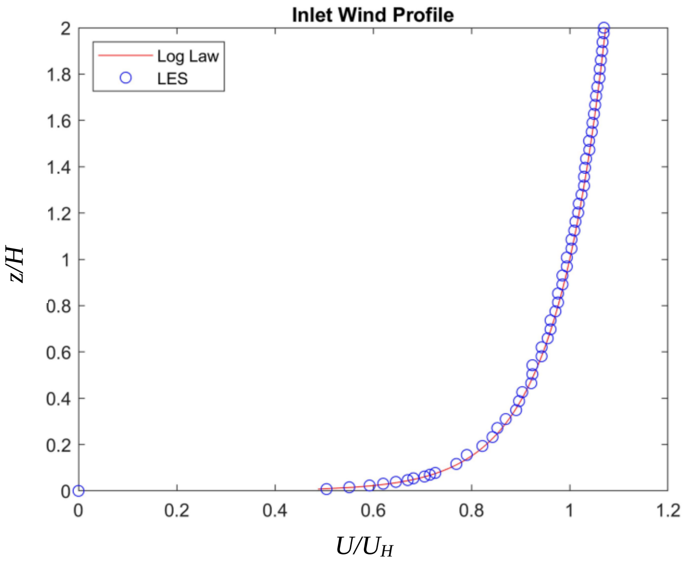

Fig. 6.8 Inlet wind profile.

6.3.3 Numerical algorithm

For the time advancement, the first-order implicit Euler method was used. For the gradient terms, the second-order least squares discretization scheme was used. The divergence schemes were calculated with the second-order linear upwind scheme. The pressure-implicit with splitting of operators (PISO) algorithm (Irwin, 2010) was used to calculate pressure-velocity coupling. All the simulations were carried out for approximately 200t^* for the statistical convergence and full flow field development, where $t^*=U_H t/B$ and t is the simulation time. After the preliminary calculation of 50t^*, an average duration of approximately 150t^* was used to calculate the aerodynamic force coefficients. The maximum Courant number during the simulation was around 1.5. The maximum y^+ value for the Buddha statue was 4.34. The sampling frequency was 100 Hz.

6.4 Flow field analysis

Flow visualization was performed to obtain a full picture of the flow around the Buddha statue and the finite circular cylinder. The shape of the Buddha statue was highly complex and significantly varied throughout the overall height. Hence, the model of the Buddha statue was further divided into 26 cross-sectional parts with an equivalent height of 0.04H (5 m) to simplify the complex shape. For the lowest part (01), the height was measured from the base to the mid-height of the upper part. For the remaining parts, the height was measured from the mid-height to mid-height of the two consecutive cross-sectional parts. Each cross-sectional shape of the Buddha statue and the finite cylinder were shown with different colours in Fig. 6.9.

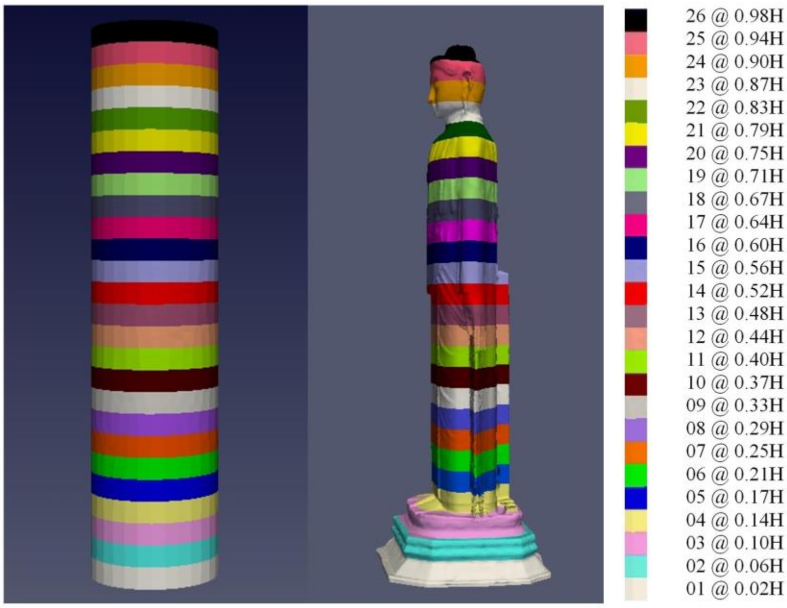

Fig. 6.9 Parts of a finite circular cylinder and Buddha statue models represented in different colours.

The flow structures for different cross-sectional shapes throughout the overall height of the Buddha statue and finite circular cylinder were investigated by using time-averaged normalized velocity magnitude and streamlines (Smits &. Lim, 2000). The flow structures included vertical and horizontal flow separation, reattachment, vortices, and the formation of the wake region behind the Buddha statue. In this study, the distance between the centre of the Buddha statue and the near-wake saddle point in the time average flow field was defined as the length of the recirculation region (L_r) (Yoon et al., 2010). The lateral distance at a given streamwise location between two points situated on the opposite sides of the model centerline was defined as the width of the wake region (d') (Roshko, 1954). The distance between the centres of the vortices in each vortex pair was denoted as the distance between the vortex pair (d_{pair}).

6.4.1 Three-dimensional flow visualization around the finite circular cylinder

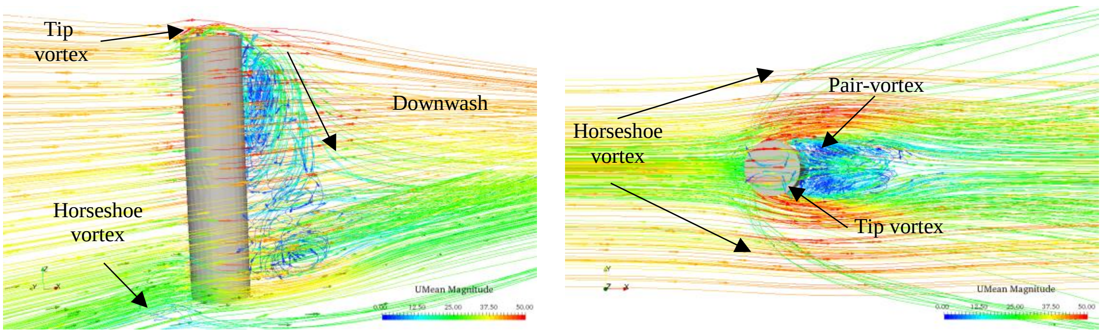

(a) (b)

Fig. 6.10 3D time-averaged velocity streamlines around the finite circular cylinder (a) side view; and (b) top view at α = 0°.

Fig. 6.10 illustrates the 3D time-averaged velocity streamlines around the finite circular cylinder for α = 0°. At the top of the finite circular cylinder, the flow was separated at the leading edge and reattached at the trailing edge. Then, the flow came downward with a steady slope. This downwash produced a wake region with vortices behind it. Hence, drag forces were still expected on the finite cylinder at α = 0°. A Horseshoe vortex was also observed near the front base of the finite circular cylinder. Thus, the presence of 3D boundary layer separation could be confirmed. The flow field structures around the current finite circular cylinder agreed well with the results provided by the previous studies (Pattenden et al. 2005).

6.4.2 Three-dimensional flow visualization around the Buddha statue

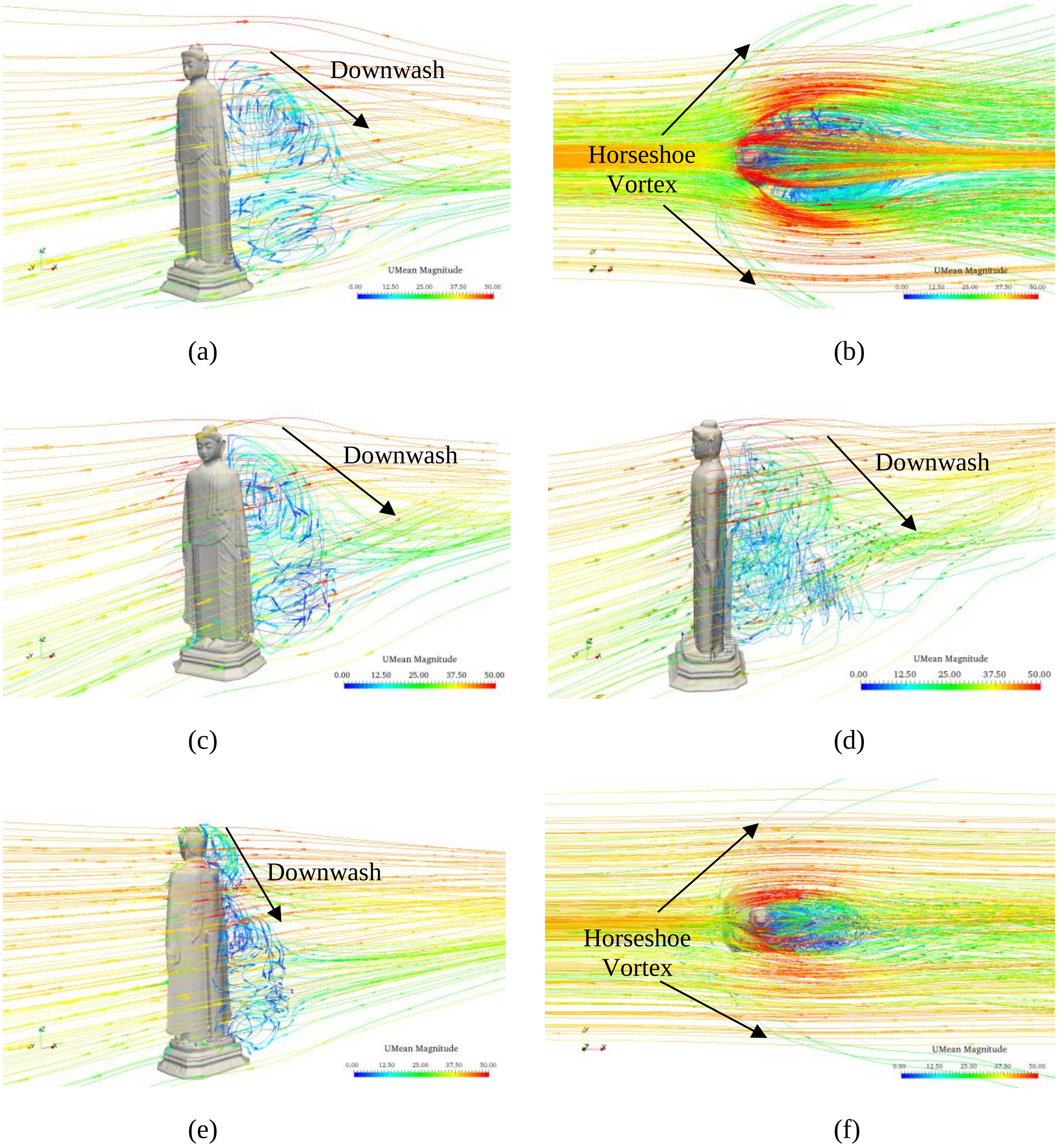

Fig. 6.11 3D time-averaged velocity streamlines around the Buddha statue (a) side view; and (b) top view at α = 0°; (c) side view at α = 5°; (d) side view at α = 50°; and (e) side view; and (f) top view at α = 90°.

Fig. 6.11 illustrates the 3D time-averaged velocity streamlines around the Buddha statue for $\alpha = 0°$, 5°, 50° and 90° cases. At $\alpha = 0°$, as shown in Fig 6.11 (a), the flow was separated at the top of the Buddha statue and came downward with a steady slope. This downwash produced a large wake region behind the Buddha statue. Hence, larger drag forces were expected on the Buddha statue at $\alpha = 0°$. Similarly, the flow separation occurred at the top of the Buddha statue at $\alpha = 5°$ and 50°, as shown in Fig 6.11 (c and d). However, the slope of the downwash became steeper and the wake region became smaller with the increasing angle of attack. Hence, the drag forces on the Buddha statue at $\alpha = 5°$ and 50° cases were likely to be slightly smaller than that of the $\alpha = 0°$ case. At $\alpha = 90°$, the orientation of the Buddha statue was like a streamlined body. Moreover, the flow separated from the top of the Buddha statue came down steeply. Thus, the wake region behind the Buddha statue was relatively small compared to the $\alpha = 0°$ case. Hence, the drag forces acting on the Buddha statue at $\alpha = 90°$ may be significantly smaller than that of the Buddha statue at $\alpha = 0°$. A horseshoe vortex was observed near the front at the base of the Buddha statue in all attack angle cases. Hence, the 3D boundary layer separation was present in all attack angle cases of the Buddha statue. No tip vortices were observed at the top of the Buddha statue in both cases.

6.4.3 Flow separation and reattachment and vortices around each cross-sectional shape of the finite circular cylinder

The flow field visualization around the finite circular cylinder at $\alpha = 0°$ is provided in Fig. 6.12. The time-averaged flow field around the finite circular cylinder on the *xz*-plane at $y/B = 0$ is shown in Fig. 6.12 (a). Flow separation was observed at the leading edge and reattachment was found at the trailing edge of the finite circular cylinder. In the wake region of the finite circular cylinder, two vertical vortices were observed. The centers of the lower vertical vortex were around 0.40*H* and 0.75*H* while the center of the upper vertical vortex was around 0.83*H*.

Fig. 6.12 (b–f) shows the time-averaged flow field around the finite circular cylinder on the *xy*-plane at different heights. At 0.006*H*, the horseshoe vortex was observed in front of the finite circular cylinder at 0.88o*B* in the upstream direction. On the *xy*-plane, the two symmetric vortices known as paired vortex, were observed in the wake region. Within 0.06–0.37*H*, this paired vortex has an increasing wake region width (d') of 0.75*B* to 0.80*B*, and recirculation region length (L_r) of 1.68*B* to 1.75*B*. After 0.37*H*, the values started decreasing. Since the reduction in the wake width indicated a reduction in the time-averaged momentum loss in the wake region, smaller loadings could be expected on the finite circular cylinder in these regions.

The distance between the centres of the vortices (d_{pair}) increased from 0.25*B* to 0.55*B* between the ground surface and 0.37*H*. After 0.37*H*, the value decreased with the increase in height. The minimum d_{pair} value was 0.33*B* at 0.83*H*. Hence, it can be concluded that these two vortices combined and became an arch vortex as mentioned in the existing literature (Pattenden et al., 2005). After 0.83*H*, no obvious vortices were observed in the wake region in the *xy*-plane. At the top of the finite circular cylinder (1.01*H*), two tip vortices were observed.

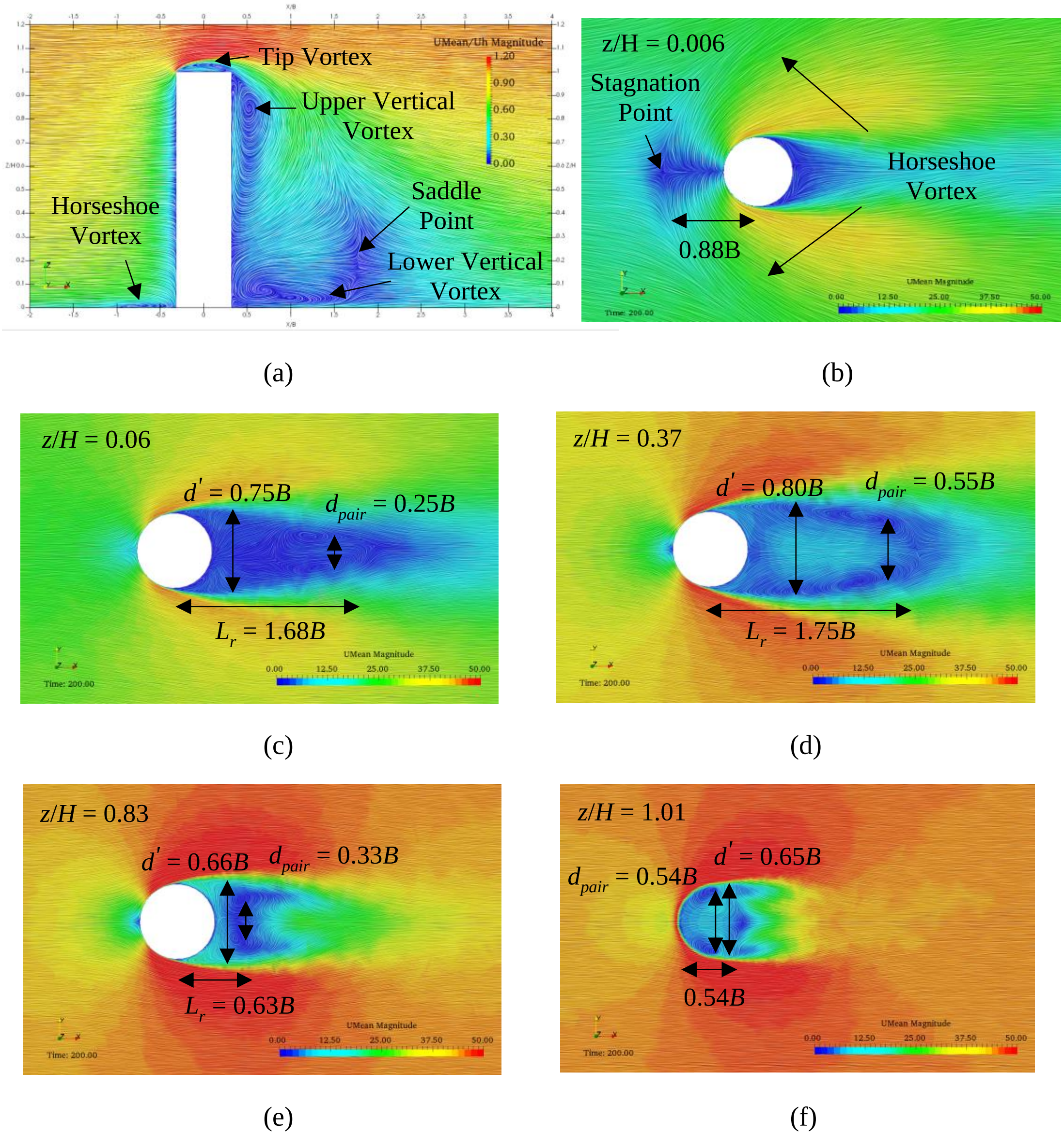

Fig. 6.12 Time-averaged flow field around the finite circular cylinder at $\alpha = 0°$ on (a) *xz*-plane at $y/B = 0$; and *xy*-plane at (b) $0.006H$; (c) $0.06H$; (d) $0.37H$; (e) $0.83H$; and (f) $1.01H$.

6.4.4 Flow separation and reattachment and vortices around each cross-sectional shape of the Buddha statue

Fig. 6.13 provides the flow field visualization around the Buddha statue at $\alpha = 0°$. Fig. 6.13 (a) shows the time-averaged flow field around the Buddha statue on the *xz*-plane at $y/B = 0$. At the top of the Buddha statue, the flow separation occurred near the tailing edge of the head. Two vertical vortices were observed in the wake region. The center of the lower vertical vortex was at $0.02H$ and the upper vertical vortex was at $0.72H$.

Fig. 6.13 (b–j) shows the time-averaged flow field around the Buddha statue on the *xy*-plane at different cross-sectional shapes of the Buddha statue. The horseshoe vortex was present in the upstream direction of $1.29B$. The cross-sectional shape of the Buddha statue was similar to the rectangular cylinder with chamfered corners until $0.08H$. In this section, flow separation occurred at

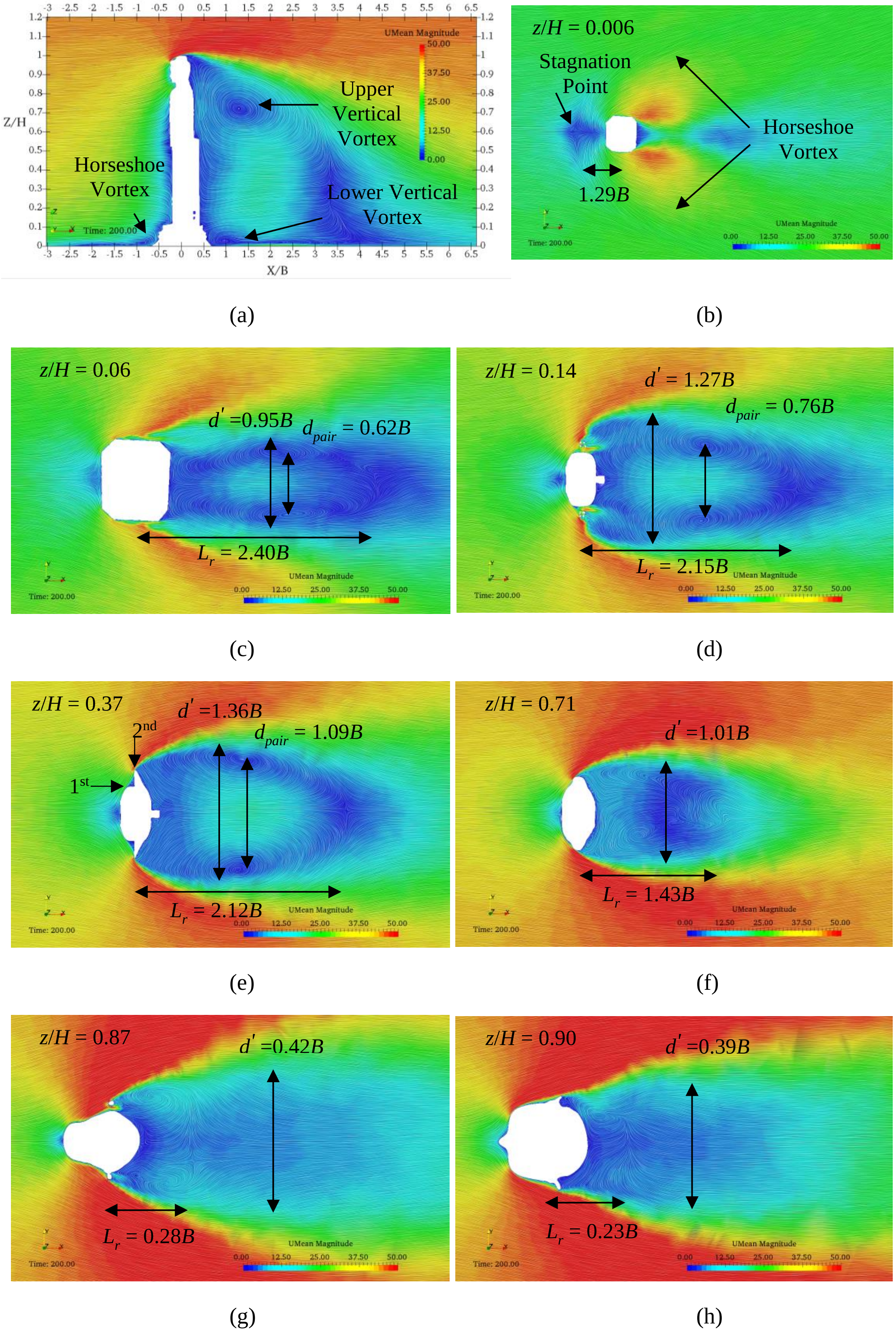

Fig. 6.13 Time-averaged flow field around the Buddha statue at α = 0° on (a) *xz*-plane at y/B = 0; and *xy*-plane at (b) 0.006*H*; (c) 0.06*H*; (d) 0.14*H*; (e) 0.37*H*; (f) 0.71*H*; (g) 0.87*H*; (h) 0.90*H*; (i) 0.98*H*; and (j) 1.01*H* (1/2).

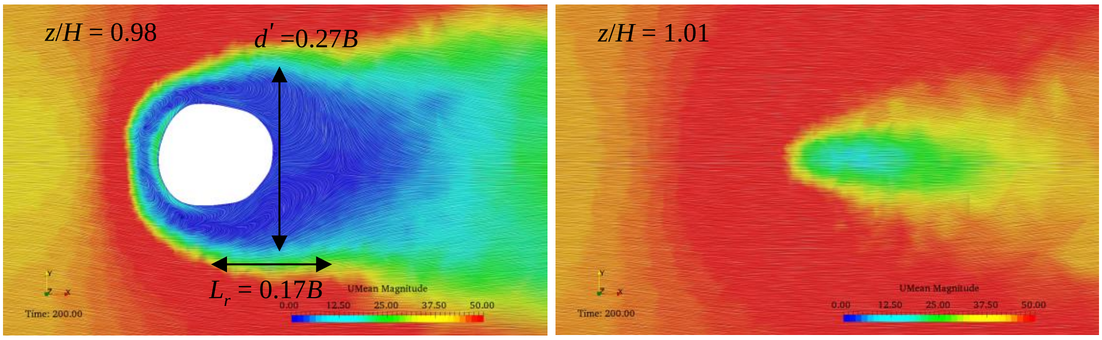

(i) (j)

Fig. 6.13 Time-averaged flow field around the Buddha statue at $\alpha = 0°$ on (a) *xz*-plane at $y/B = 0$; and *xy*-plane at (b) 0.006*H*; (c) 0.06*H*; (d) 0.14*H*; (e) 0.37*H*; (f) 0.71*H*; (g) 0.87*H*; (h) 0.90*H*; (i) 0.98*H*; and (j) 1.01*H* (2/2).

the chamfered corner near the trailing edge (Fig. 6.13 (c)). At 0.06*H*, the length of the recirculation region (L_r) was 2.40*B* and the width of the wake region (d') was 0.95*B*. An uneven pair vortex was observed in the wake region with a distance between the vortex pair (d_{pair}) of 0.62*B*.

At 0.14*H*, columns on both sides of the Buddha statue served as the aerodynamic appendages (Fig. 6.13 (d)). In this section, flow separation occurred not only at rounded chamfered corners near the trailing edge but also close to these columns. This increased the d' value to 1.27*B* and the d_{pair} value to 0.76*B*. The L_r was 2.15*B* and small vortices were present near the setback in the wake region.

Between 0.15–0.56*H*, single recession-type corners were present near the corners of the windward surface on both sides of the Buddha statue. In this type of cross-sectional shape, flow separation occurred at the 2nd flow separation point and a pair vortex was present in the wake region as shown in Fig. 6.13 (e). Small recirculation regions and vortices were also present near the single recession corners in the windward surface and the setback in the leeward surface. Within 0.57–0.85*H*, the setback in the wake region was discontinued and the shape of the Buddha statue was alike the elliptical shape. After 0.85*H*, the shape of the Buddha statue was closer to the circular cylinder. In these regions, flow separation occurred at the side surfaces.

At 0.71*H*, the pair vortex in the wake region combined into one as illustrated in Fig. 6.13 (f). As the width of the Buddha statue became smaller, the L_r and d' values were also decreased to 1.43*B* and 1.01*B*, respectively. Subsequently, no obvious vortices were observed in the wake region afterwards. In all cross-sectional shapes, flow reattachment was hardly observed at the side surfaces. As shown in Fig. 6.13 (j), tip vortices were not observed at the top of the Buddha statue.

Fig. 6.14 provides the flow field visualization around the Buddha statue at $\alpha = 5°$. Fig. 6.14 (a) shows the time-averaged flow field around the Buddha statue on the *xz*-plane at $y/B = 0$. Similar to the $\alpha = 0°$ case, the flow separation occurred near the tailing edge at the head of the Buddha statue and two vertical vortices were present in the wake region. The centre of the lower vertical vortex was at 0.02*H* and the upper vertical vortex was at 0.70*H*. Fig. 6.14 (b–d) shows the time-averaged flow field around the Buddha statue on the *xy*-plane at different cross-sectional shapes of the Buddha statue. At 0.006*H*, the horseshoe vortex was present in the upstream direction of 1.09*B* (Fig. 6.14 (b)). Contrary to the α = 0° case, only one vortex was observed on the *xy*-plane at 0.06*H* (Fig. 6.14 (c)). At 0.10*H*, an uneven vortex was observed (Fig. 6.14 (d)). This uneven pair vortex was developed into vortices similar to that of α = 0° case with increasing height. The two vortices of the uneven pair vortex combined and became an arch vortex between 0.67*H* and 0.71*H*. Afterwards, no obvious vortices were observed in the wake region.

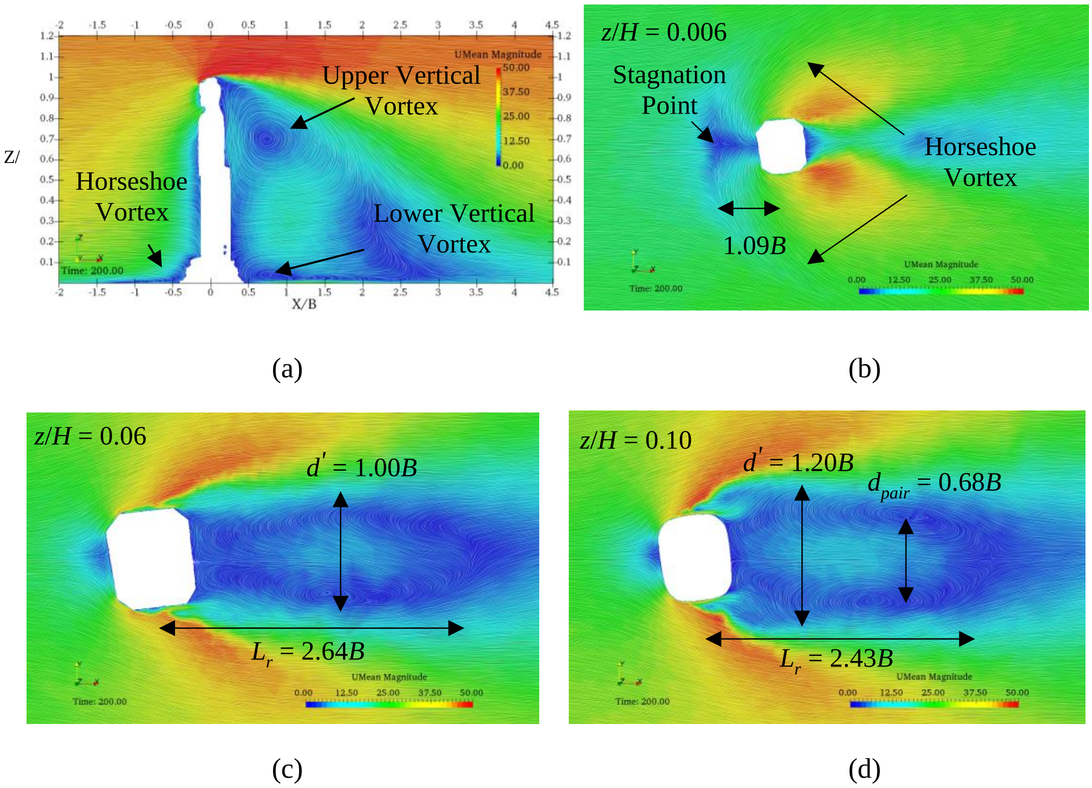

Fig. 6.14 Time-averaged flow field around the Buddha statue at α = 5° on (a) *xz*-plane at *y*/*B* = 0; and *xy*-plane at (b) 0.006*H*; (c) 0.06*H*; and (d) 0.10*H*.

The flow field visualization around the Buddha statue at α = 50° is shown in Fig. 6.15. Fig. 6.15 (a) shows the time-averaged flow field around the Buddha statue on the *xz*-plane at *y*/*B* = 0. On the *xz*-plane, the flow separation occurred near the tailing edge at the head of the Buddha statue and no tip vortices were observed at the top. Two vertical vortices were present in the wake region similar to the previous attack angle cases. The centre of the lower vertical vortex was at 0.025*H* and the upper vertical vortex was at 0.65*H*. Fig. 6.15 (b–f) shows the time-averaged flow field around the Buddha statue on the *xy*-plane at different cross-sectional shapes of the Buddha statue. At 0.006*H*, the horseshoe vortex was present in the upstream direction of 1.05*B* (Fig. 6.15 (b)). Similar to the α = 5° case, only one vortex was observed on the *xy*-plane at 0.06*H* (Fig. 6.15 (c)). This vortex was fully developed into a pair vortex at 0.14*H* (Fig. 6.15 (d)). This pair vortex was dissolved into one vortex at 0.56*H* (Fig. 6.15 (e)). The size of this vortex was reduced with increasing height and moved closer toward the Buddha statue between 0.60*H* and 0.67*H*. No obvious vortices were observed in the wake region within 0.71–0.83*H*. Afterwards, small vortices were found around the statue in the wake region. The formation of vortices in this case was complex compared to the other attack angle cases.

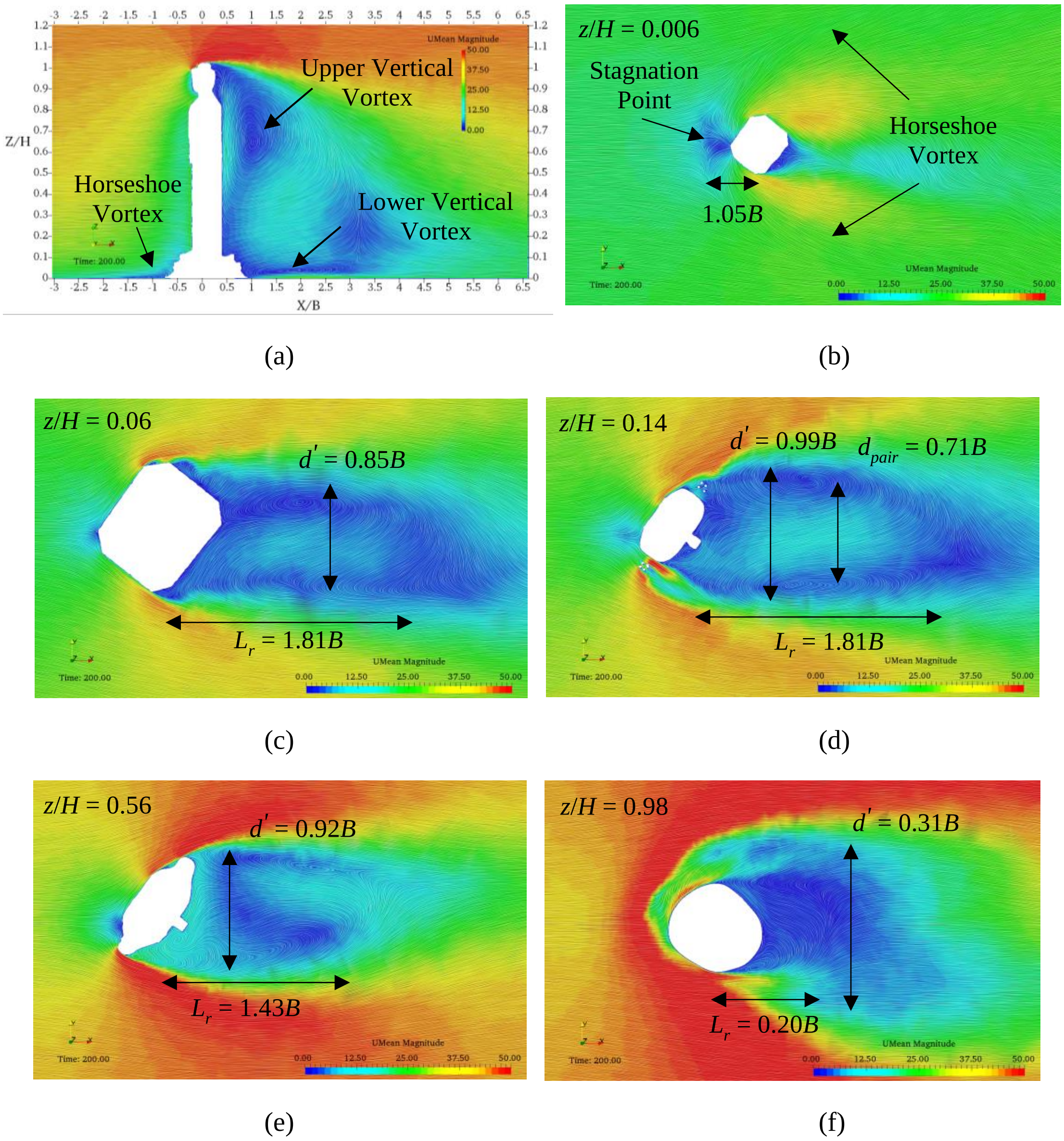

Fig. 6.15 Time-averaged flow field around the Buddha statue at α = 50° on (a) *xz*-plane at $y/B = 0$; and *xy*-plane at (b) 0.006H; (c) 0.06H; (d) 0.14H; (e) 0.56H; and (f) 0.98H.

Fig. 6.16 (a) shows the time-averaged flow field around the Buddha statue on the *xz*-plane at $y/B = 0$ for α = 90°. Flow separation at the top of the Buddha statue occurred near the tailing edge of the head. Three vertical vortices were observed in the wake region. The centre of the lower vertical vortex was at 0.07H, the middle vertical vortex was at 0.52H and the upper vertical vortex was at 0.95H. The wake region was small compared to the α = 0°. The horseshoe vortex was present in the upstream direction at 0.95B as shown in Fig. 6.16 (b).

Fig. 6.16 (b–k) shows the time-averaged flow field around the Buddha statue on the *xy*-plane at different cross-sectional shapes of the Buddha statue at α = 90°. In the chamfered corner section, the flow separation occurred at the 2nd flow separation point in the leading edge and then the flow was reattached to the side surfaces, especially to the upper side surfaces. Then, the flow separation occurred once more at the trailing edge as shown in Fig. 6.16 (c). This produced the recirculation region length (L_r) of 1.01*B* and the wake region width (d') of 0.60*B*. In the rounded chamfered corner section, flow separation occurred at the trailing edge as shown in Fig. 6.16 (d). This increased the L_r value to 1.24*B* and the d' value to 0.70*B*. In the wake region, a pair vortex was observed with a distance between the vortex pair (d_{pair}) of 0.39*B*. When the columns are present in the upstream direction, the flow separation occurred at the rounded corner in the leading edge and the columns did not affect the flow separation.

In the section with the single recession corners, the shape of the Buddha statue is similar to the streamlined body and the pointed leading separates the incoming flow. Small recirculation regions were observed near the upstream single recession corner and the setback. Later, the flow got separated once again at the rounded corner on the upper side surface and then set back on the lower side surface as shown in Fig. 6.16 (e). The pair vortex was present in the wake region between 0.10–0.33*H* with the increasing L_r value of 1.24*B* to 1.31*B*, the decreasing d' value of 0.70*B* to 0.56*B*, and the d_{pair} value of 0.39*B* to 0.37*B* as illustrated in Figs. 6.16 (d and e). At 0.52*H* (Fig. 6.16 (f)), only one vortex with L_r of 1.03*B* and d' of 0.50*B* was observed in the wake region. No vortex was observed in the wake region at 0.56–0.67*H* (Fig. 6.16 (g)). One small vortex emerged on the upper side of the wake region at 0.71*H*. This was developed into an uneven pair vortex with d_{pair} of 0.17*B* at 0.75*H*, the elliptical cross-sectional shape, as shown in Fig. 6.16 (h). This pair vortex was reduced into one vortex between 0.79–0.83*H*. Afterwards, this vortex progressed into a pair vortex once more between 0.86–0.90*H*. At 0.94*H*, no obvious vortex was present in the wake region. On the other hand, a small pair vortex was found in the wake region of 0.98*H*.

To sum up, not only the width of the cross-section but also the cross-sectional shape of the Buddha statue affected the width of the wake region. The formation of vortices in the wake region of the Buddha statue was complex in both attack angle cases.

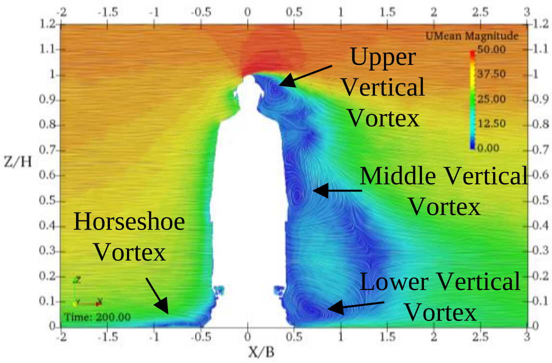

(a)

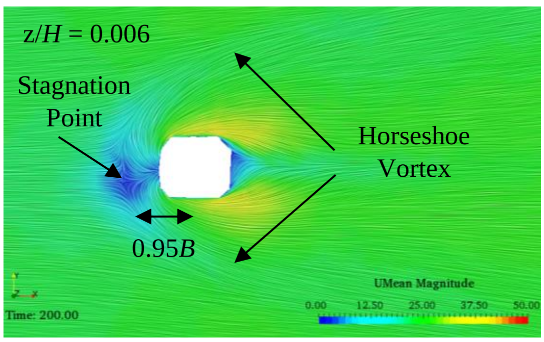

(b)

Fig. 6.16 Time-averaged flow field around the Buddha statue at α = 90° on (a) *xz*-plane at *y*/*B* = 0; and *xy*-plane at (b) 0.006*H*; (c) 0.06*H*; (d) 0.10*H*; (e) 0.33*H*; (f) 0.52*H*; (g) 0.56*H*; (h) 0.75*H*; (i) 0.94*H*; and (j) 0.98*H* (1/2).

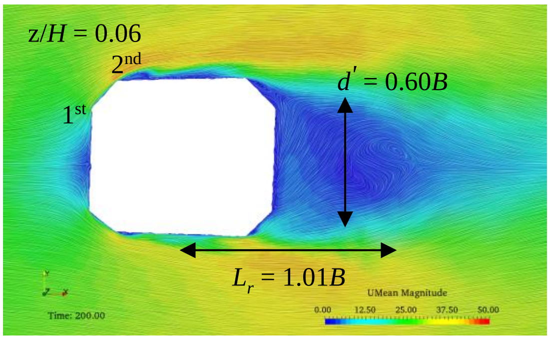

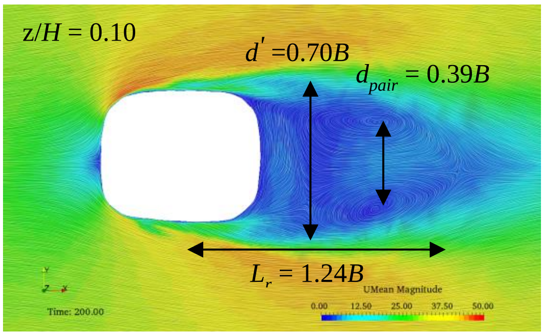

(c) (d)

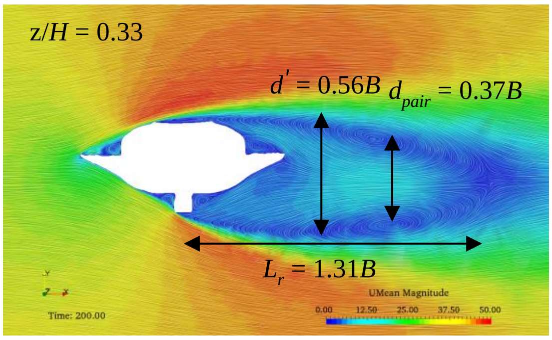

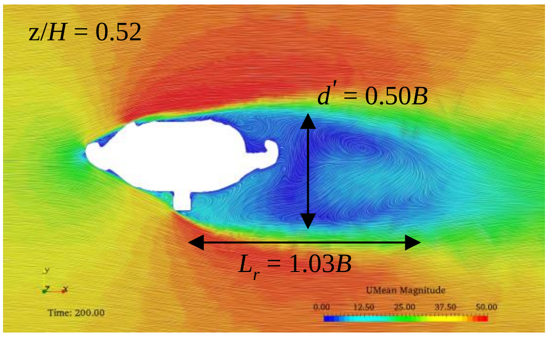

(e) (f)

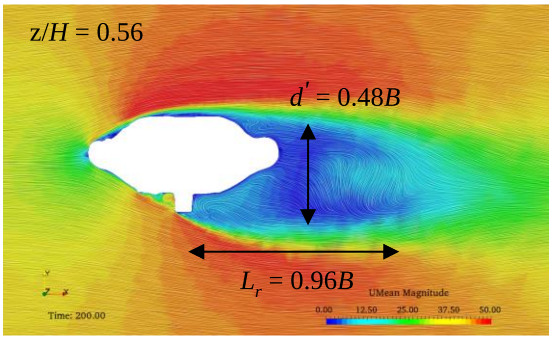

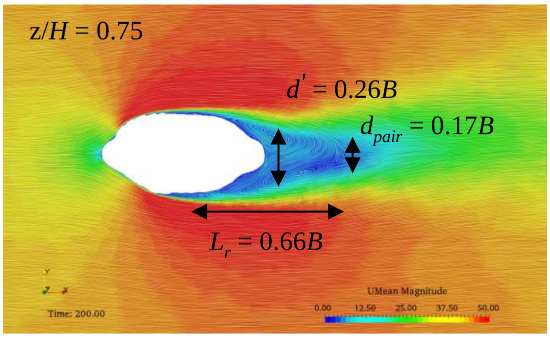

(g) (h)

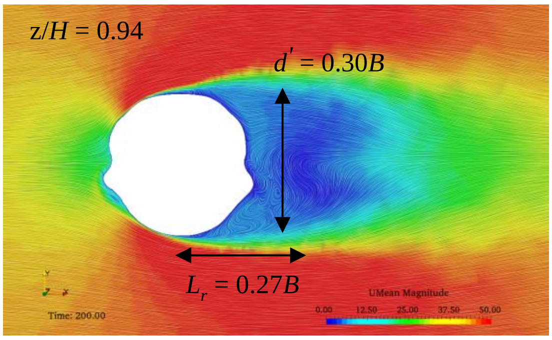

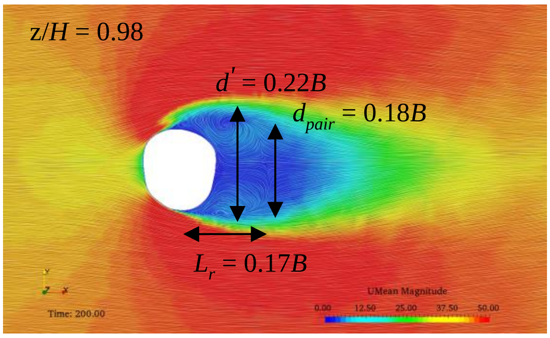

(i) (j)

Fig. 6.16 Time-averaged flow field around the Buddha statue at $\alpha = 90°$ on (a) *xz*-plane at $y/B = 0$; and *xy*-plane at (b) 0.006*H*; (c) 0.06*H*; (d) 0.10*H*; (e) 0.33*H*; (f) 0.52*H*; (g) 0.56*H*; (h) 0.75*H*; (i) 0.94*H*; and (j) 0.98*H* (2/2).

6.5 Aerodynamic characteristics of the Buddha statue

The aerodynamic force coefficients of the Buddha statue were calculated for each cross-sectional shape throughout the overall height of the statue. The mean aerodynamic forces acting on each cross-sectional shape were calculated by integrating the pressure around each cross-sectional surface area of the Buddha statue. The mean aerodynamic force coefficients were calculated as follows:

$$C_{Fi} = \frac{2F_{ij}}{\rho U_{Hj}^2 A_j} \qquad \text{Eq. 6.3}$$

where F_{ij} ($i = x, y$) is the mean aerodynamic forces acting on the cross-section j along x and y directions, A_j is the frontal surface area of the cross-section j, ρ is the air density and U_{Hj} is the mean wind velocity at the mid-height of the cross-section j. In this study, the Reynolds number is defined as follows:

$$Re = \frac{U_H B}{v} \qquad \text{Eq. 6.4}$$

where U_H is the wind velocity at the height of the Buddha statue of 129 m (42.88 m/s), B is the width of the Buddha statue (47.63 m), and v is the kinematic viscosity (0.1 m^2/s). Hence, the Reynolds number of a finite circular cylinder and Buddha statue were approximately 13,000 and 20,400. Two probes, located on the left (50 m, 50 m) and right (-50 m, 50 m) sides of the model behind the Buddha statue, were used to measure the velocity fluctuation in the wake region.

6.5.1 Aerodynamic force coefficient

The mean along-wind force coefficient (C_{Fx}) and across-wind force coefficient (C_{Fy}) for each cross-sectional shape throughout the overall height of the Buddha statue and the finite circular cylinder are shown in Fig. 6.17. For the finite circular cylinder, the C_{Fx} value varied between 0.69–1.53 and between 0.02–0.98H. The C_{Fx} value has a decreasing trend until 0.33H. After 0.33H, this trend was changed into an increasing trend. According to flow visualization results, the upper and lower vertical vortices are reattached on the *xz*-plane at this height. The decrease in C_{Fx} value to 0.69 at 0.98H might also be associated with the horizontal vortex pair disappearance on the *xy*-plane. As for the C_{Fy} value, the value was approximately zero throughout the overall height of the finite circular cylinder. The flow separation around the finite circular cylinder in the across-wind direction was symmetrical and the pressure distributions around it were also equal.

The C_{Fx} values were varied along the height of the Buddha statue in all attack angle cases. Since the wake region behind the Buddha statue of 0° case was the largest and the 90° case was the smallest among all attack angle cases as shown in Fig. 6.13 (a), Fig. 6.14 (a), Fig. 6.15 (a) and Fig. 6.16 (a), the C_{Fx} values of the 0° attack angle case was the largest and the 90° case was the smallest. The C_{Fx} values of the Buddha statue changed drastically within 0.14–0.25H and 0.83–0.90H in all attack angle cases. Between 0.14H and 0.25H, the cross-sectional shape changed from the rectangular to elliptical shape. Between 0.83H and 0.90H, the upper vertical vortex reattached on the *xz*-plane and the horizontal pair vortex also weakened on the *xy*-plane. Thus, the C_{Fx} values drastically increased within these regions. Since the wake region and vortex size decreased between 0.25H and 0.83H, the C_{Fx} value also decreased steadily in all attack angle cases. In particular, the C_{Fx} value of the α = 90° case was constant within 0.29–0.52H. At 0.56H, the setback at the back of the Buddha statue was discontinued and the horizontal pair vortex was transformed into a single vortex. Hence, the C_{Fx} value fluctuates between 0.56H and 0.87H. Moreover, the C_{Fx} values of the Buddha statue were approximately close to each other in all attack angle cases between 0.85–1.00H. Within this region, the cross-sectional shape of the Buddha statue was similar to that of the circular cylinder. Thus, the C_{Fx} values of the Buddha statue were likely to be independent of the attack angle. In the C_{Fy} values of the Buddha statue, sudden changes similar to the C_{Fx} values were observed within 0.14–0.25H and 0.83–0.90H in all attack angle cases. Furthermore, the symmetric time-averaged flow was observed only in the 0° attack angle, especially between 0.19H and 0.77H.

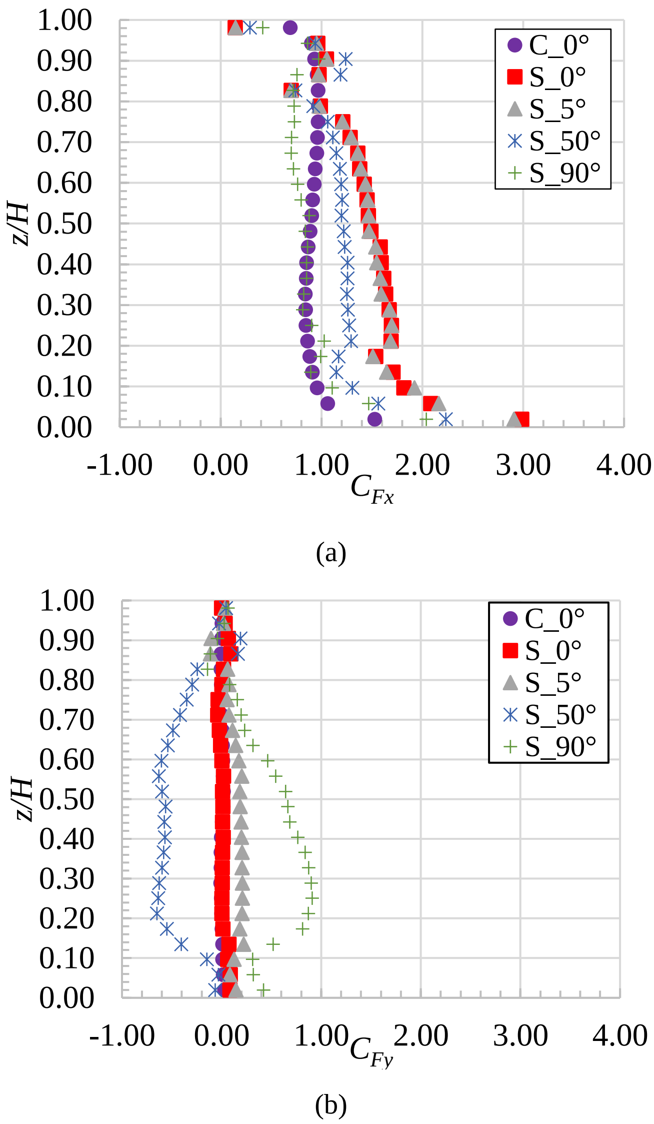

Fig. 6.17 Mean aerodynamic force coefficients of the Buddha statue and finite circular cylinder; (a) mean along-wind force coefficient (C_{Fx}); and (b) mean across-wind force coefficient (C_{Fy}).

When the attack angle was varied from 0° to 90°, the recirculation region length (L_r) decreased as a result of an increase in the downwash slope. The wake region width (d') and distance between vortex pair (d_{pair}) also decreased as the width of the Buddha statue was decreased. Therefore, the 3D wake region became narrower with increasing angle of attack. As a result, the mean global along-wind force coefficient decreased steadily from 1.35 (α = 0°), 1.35 (α = 5°), 1.08 (α = 50°), and 0.80 (α = 90°). The mean global across-wind force coefficient varied from 0.01 (α = 0°), 0.14 (α = 5°), -0.40 (α = 50°), and 0.40 (α = 90°).

Hence, the less bluff and comparatively streamline-like structural shape of the Buddha statue at α = 90° reduces approximately 50% of the along-wind force coefficient. The symmetric flow separation was still observed in the α = 0° case of the Buddha statue despite its complex shape. On the other hand, the presence of the setback in the α = 90° case produced an asymmetric flow field around the Buddha statue. This may cause asymmetric pressure distribution which has a negative impact on the stability of the Buddha statue.

6.5.2 Vortex shedding frequency and the Strouhal number

A structure can be vulnerable to large vibrations when the vortex shedding frequency is close to the natural frequency of that structure (Irwin, 2010). The natural frequency of a structure is mainly dependent on the structural system and mass distribution. The natural frequency of an existing structure can be measured with an impact test, accelerometer, and vibration monitoring equipment. Since the Buddha statue becomes slender and the setback behind it is discontinued with the increasing height, the natural frequency of it is expected to be smaller as the height increases. In this study, the vortex shedding frequency (f_v) values were obtained from the power spectral density analysis of wind velocity recordings at the two probes, provided on the left and right sides of the model.

Fig. 6.18 (a) shows the vortex shedding frequency (f_v) of each cross-sectional shape throughout the overall height of the Buddha statue and the finite circular cylinder. The f_v values of the Buddha statue in the α = 0° and 5° cases were approximately constant throughout the overall height. The values were also about half that of a finite circular cylinder. Due to the discontinuation of the setback behind the Buddha statue and the changes in the formation of the vortices, a sudden increase in the f_v values was found between 0.40H and 0.70H in the α = 50° case. Due to the uneven vortex shedding in the wake region of the α = 90° case as shown in Fig. 6.16 (c) and (h–i), the Buddha statue has different f_v values for the left and right-side probes between ground level–0.04 H and 0.70–0.97 H. After the discontinuation of the setback, the vortex shedding was not observed until 0.70H in the α = 90° case. After 0.70H, a sudden increase in the f_v values was observed. This may be related to the presence of asymmetric vortices like α = 50° case. It should be noted that the power of these frequencies was weak.

Hence, the natural frequency of the Buddha statue should not be close to either of the f_v values shown in Fig. 6.18 (a) to avoid the resonance wind load (lock-in). Proper maintenance and renovation plans for the Buddha statue can be implemented for each story level based on these f_v values to provide occupant comfort, increase serviceability, and prevent structural failure.

Fig. 6.18 (b) shows the Strouhal number (St) of each cross-sectional shape throughout the overall height of the Buddha statue and the finite circular cylinder. Since the St value considered the width of the model, inflow wind velocity and the vortex shedding frequency, variations were observed in the St values of both models. Due to the influence of the 3D boundary layer separation, the St values of all cases steadily decreased between the ground surface and 0.16H. Ma et al., 2017 reported that the *St* of the elliptical cylinder was 0.18 at α = 26° for a Reynolds number of 124,000. The *St* of the finite circular cylinder with an aspect ratio of 10 was approximately 0.150 for a Reynolds number of 44,000 at y/D of 3 (Fox and West, 1993). For the finite circular cylinder with an aspect ratio of 4 and Reynolds number of 10,400, the *St* was approximately 0.145 (Morton et al, 2018). Hence, the *St* of the finite circular cylinder used in the current study concurred with the previous research.

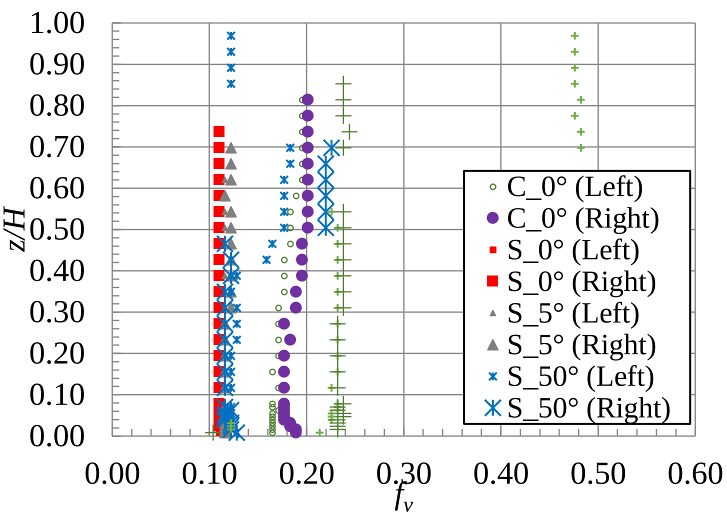

(a)

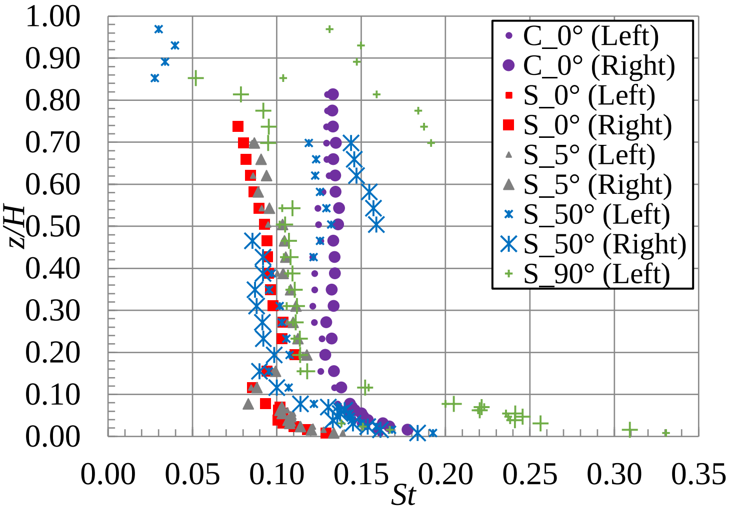

(b)

Fig. 6.18 Mean aerodynamic force coefficients of the Buddha statue and finite circular cylinder; (a) vortex shedding frequency (f_v); and (b) Strouhal number (*St*).

Fig. 6.18 (b) shows the Strouhal number (*St*) of each cross-sectional shape throughout the overall height of the Buddha statue and the finite circular cylinder. Since the *St* value considered the width of the model, inflow wind velocity and the vortex shedding frequency, variations were observed in the *St* values of both models. Due to the influence of the 3D boundary layer separation, the *St* values of all cases steadily decreased between the ground surface and 0.16*H*. Ma et al., 2017 reported that the *St* of the elliptical cylinder was 0.18 at α = 26° for a Reynolds number of 124,000. The *St* of the finite circular cylinder with an aspect ratio of 10 was approximately 0.150 for a Reynolds number of 44,000 at y/D of 3 (Fox and West, 1993). For the finite circular cylinder with an aspect ratio of 4 and Reynolds number of 10,400, the *St* was approximately 0.145 (Morton et al, 2018). Hence, the *St* of the finite circular cylinder used in the current study concurred with the previous research.

As for the Buddha statue, the St values of all attack angle cases except α = 50° were closely resembling each other between 0.16 and 0.74*H* (Fig. 6.18 (b)). In the α = 50° case, the *St* value was close to others only between 0.16–0.47*H*. Hence, independent of the presence of the setback, the *St* values were close to each other (0.094–0.118) within 0.16–0.47*H* in all attack angle cases. Hence, the statue may vibrate at a wind velocity lower than its design wind velocity within this height range. After the discontinuation of the setback, the *St* value was increased approximately twice around 0.50*H* in the α = 50° case and 0.70*H* in the α = 90° case. This abrupt increase moved toward the top of the Buddha statue as the attack angle increased. This may be due to the presence of a setback to the incoming flow. Afterwards, the *St* value decreased gradually in the remaining height. Hence, the wind-induced vibration responses of the Buddha statue may vary significantly depending on the height and attack angle.

6.6 Maintenance, renovation, and management

The Buddha statue was likely to get large along-wind forces at 0° and 5° attack angle cases according to the flow field analysis results. Both C_{Fx} and C_{Fy} values suddenly change within 0.14–0.25*H* and 0.83–0.90*H*. Moreover, the C_{Fx} values were the highest at the base. Hence, the base (under 0.2*H*), the connection between the lotus throne and the feet (0.14–0.25*H*), and the neck (0.83–0.90*H*) of the Buddha statue should be strengthened during the maintenance and renovation processes. The vertical and diagonal bracings could be added inside the hollow Buddha statue at these locations and increase the wind load resistance.

Flow patterns around the Buddha statue showed the presence of different corner shapes throughout the overall height and setback behind it. This moderately influenced the vortex shedding frequency and the Strouhal number. The vortex-shedding frequency of the Buddha statue became higher as the attack angle increased. The resonant (lock-in) wind load can arise when this vortex-shedding frequency approaches the natural frequency of the Buddha statue. Therefore, the natural frequency of the Buddha statue should be checked with either an accelerometer, impact test or modal analysis if possible. Afterwards, the resonant wind load can be determined and appropriate maintenance and renovation plans can be implemented for each story level of the Buddha statue. At α = 50° and 90° cases, abrupt changes in the *St* values were found. Since the increase in *St* is an increase in instability, aerodynamic modifications such as slotted corners, baffles, and fins can be added during the renovation to reduce the instability.

The horseshoe vortex moved towards the Buddha statue in the upstream direction with an increasing angle of attack. Hence, the base part of the Buddha statue should be strengthened periodically to withstand material deterioration and avoid structural damage during tropical cyclones. In addition, the wake of the Buddha statue has the recirculation region length (L_r) of 2.64*B* and the wake region width (d') of 1.36B. This large wake might affect the wind loading and flow field around the surrounding structures. Thus, the effect of the wake region of the Buddha statue on the surrounding structures should also be studied in detail in the future.

6.7 Concluding remarks

Moving obstacles such as walking humans and animals must be prevented during the 3D laser scanning. Since the scanner operates on a laser light line, such obstacles produce occlusion and hinder the registration of the points into one global coordinate. In this study, the 3D terrestrial laser scanning could not record enough point data to generate the head of the Buddha statue. Aside from that 3D terrestrial laser scanning can reproduce adequately precise 3D models of a complex-shaped structure like the Buddha statue within a short period of time. However, the imperfections in the generated 3D model were recommended to be refined. Furthermore, the unstructured meshing can successfully handle the shape complexity of the Buddha statue.

The changes in the cross-sectional shapes, especially near the corners, of the statue in accordance with height, created different flow separation points throughout the overall height of the Buddha statue. The corners of the cross-section may significantly affect the aerodynamic characteristics of it. The Buddha statue acted as a bluff body at α = 0°, 5° and 50° while it acted as a streamlined body at α = 90°. Thus, the α = 90° case had the smallest wake region size and minimum along-wind force coefficient compared to the 0° case. Based on the across-wind force coefficient, the symmetric time-averaged flow was only observed within 0.19–0.77H in the α = 0° case.

The time-averaged flow fields in the *xz*-plane and *xy*-plane at different heights of the Buddha statue showed that the size of the wake region was dependent not only on the width of the statue but also on the flow separation conditions produced by the different corner shapes of the statue. The wake region also contained many small vortices, and the 3D arch vortex in the wake region intertwined in a complex manner. When the angle of attack increased, the wake region size decreased and the horseshoe vortex moved closer towards the Buddha statue. A small recirculation zone was observed on the windward side at the top. However, no tip vortices were observed at the top of the Buddha statue. Flow patterns around the statue showed that the presence of different corner shapes throughout the height of the Buddha statue can influence the vortex shedding frequency and Strouhal number. The Strouhal number of the Buddha statue increased with increased with the increasing attack angles. After the discontinuation of the setback, an abrupt increase in the Strouhal number was observed in the α = 50° and 90° cases. This abrupt increase moved towards the top of the Buddha statue as the attack angle was increased. Therefore, the Buddha statue is likely to be affected by flow-induced vibrations when the attack angle is increased to 90° and this should be considered in the renovation and maintenance plans.

With an increased demand for cost-effective and time-efficient methods in the wind resistance evaluation, the methods mentioned in the chapter can be used in the wind resistance evaluation of existing tall complex-shaped structures where wind tunnel testing and on-field measurement are difficult or infeasible. This will help in the structural health monitoring, life-cycle performance evaluation, and risk analysis of existing unique structures.

Reference

AIJ (Architectural Institute of Japan). (2017). Guidebook of Recommendations for Loads on Buildings 2. Wind-induced Response and Load Estimation/Practical Guide of CFD for Wind Resistant Design, Architectural Institute of Japan, (in Japanese).

Fox, T. A., and G. S. West. (1993). Fluid-Induced loading of cantilevered circular cylinders in a low-turbulence uniform flow. Part 1: Mean loading with aspect ratios in the range 4 to 30. *Journal of Fluids and Structures*, 7 (1). https://doi.org/10.1006/jfls.1993.1001.

Irwin, P. A. (2010). Vortices and tall buildings: A recipe for resonance. *Physics Today*, 63 (9). https://doi.org/10.1063/1.3490510.

Ma, W., J. H. G. Macdonald, and Q. Liu. (2017). Aerodynamic characteristics and excitation mechanisms of the galloping of an elliptical cylinder in the critical Reynolds number range. *Journal of Wind Engineering and Industrial Aerodynamics*, 171. https://doi.org/10.1016/j.jweia.2017.10.006.

MNBC (Myanmar National Building Code). (2016). Part 3: Structural Design, Myanmar National Building Code, Second Edition, Yangon, Myanmar.

Morton, C., and et al. (2018). Wake dynamics of a cantilevered circular cylinder of aspect ratio 4. *International Journal of Heat and Fluid Flow*, 72. https://doi.org/10.1016/j.ijheatfluidflow.2018.05.014.

Pattenden, R. J., S. R. Turnock, and X. Zhang. (2005). Measurements of the flow over a low-aspect-ratio cylinder mounted on a ground plane. *Experiments in Fluids*, 39 (1). https://doi.org/10.1007/s00348-005-0949-9.

Roshko, A. (1954). On the drag and shedding frequency of two-dimensional bluff bodies. *NACA Technical Note 3169*.

Smits, A. J., and Lim, T. T. (2000). Flow Visualization: Techniques and Examples, Imperial College Press, First edition.

Spalding, D. B. (1960). A single formula for the ‘law of the wall’. *Journal of Applied Mechanics, Transactions ASME*, 28 (3). https://doi.org/10.1115/1.3641728.

UNDP (United Nations Development Programme). (2011). Multi Hazard Risk Assessment in Rakhine State of Myanmar, Final Report, December.

Yoon, D. H., K. S. Yang, and C. B. Choi. (2010). Flow past a square cylinder with an angle of incidence. Physics of Fluids, 22 (4). https://doi.org/10.1063/1.3388857.

Chapter 7

Conclusions and future topics

7.1 Conclusions

This study presents the various shapes of corner-cut modification that can be used for reducing the wind-induced vibration of structures. In this study, the effect of corner shape modification on the aerodynamic characteristic of the rectangular cylinder was mainly investigated. Six different corner-cuts, denoted as single recession (SR), double recession (DR), double recession II (DR II), double recession III (DR III), triple recession (TR) and chamfer (C), were used to modify the corners of the rectangular (R) cylinder. The corners of the rectangular cylinder were modified into the above-mentioned six different shapes in order to reduce the Kármán vortex shedding intensity of the original rectangular cylinder. Then, the effect of Kármán vortex shedding intensity on the vertical response amplitude of the rectangular and corner-cut cylinders was also studied. Moreover, the interference between the vortices and galloping instability was discussed for both symmetric (zero angle of attack) and asymmetric (various angles of attack) bodies. Finally, the effect of cross-sectional shape on the flow field and aerodynamic characteristics were studied for an existing complex-shaped tall structure. The calculations were carried out in both wind tunnel testing and computational fluid dynamics simulation.

In Chapter 3, the effect of corner shape modification on the aerodynamic force coefficients acting on the stationary body and the Kármán vortex shedding of the rectangular cylinder was discussed. As mentioned in Chapter 3, the corner shape modification significantly decreased the absolute value of the aerodynamic force coefficients (C_{Fx}, C_{Fy}, and C_M) of the original rectangular cylinder. Moreover, the fluctuating transverse force coefficient which represents the Kármán vortex shedding intensity (C'_{Fy}) was also reduced up to the maximum of 90% at zero angle of attack. Significant Reynolds number dependency was observed in C_{Fy} values of the DR section, C'_{Fy} values of the C section, and *St* values of the DR section. This indicated that these two corner-cut sections were sensitive to the approaching wind velocity. When the angle of attack of R, TR and DR III sections was changed from zero to different values, as provided in Chapter 3, the Kármán vortex shedding intensity of the respective section was significantly decreased. When the Kármán vortex shedding intensity was reduced, the Strouhal number (*St*) of the respective section became increasing. Thus, these sections were expected to have smaller onset reduced wind velocities of Kármán vortex-induced vibration (1/*St*). This expectation was clarified in the following chapters.

In Chapter 4, the effect of Kármán vortex shedding intensity on the galloping onset reduced wind velocity, and the aerodynamic interactions between the galloping instability and the vortices were discussed for zero angle of attack. At zero angle of attack, the model was symmetric and the time-averaged flow field around it was also symmetric. In this study, six different mass-damping parameters or Scruton numbers ($S_{c\eta}$ = 6, 42, 56, 69, 90 and 130), were used to study its effect on the interference between the Kármán vortex-induced vibration (KVIV) and galloping instability for both rectangular and corner-cut cylinders. In terms of vertical response amplitude, all corner-cut types significantly reduced the onset reduced wind velocity and the vibration response of the original rectangular cylinder in all studied Scruton number values.

The motion-induced vortex vibration (MIV), which is also known as one shear layer instability, was observed around the reduced wind velocity of 1.67B/D only at the lowest mass-damping parameter ($S_{c\eta}$ = 6) in both the rectangular and the corner-cut cylinders. The original rectangular cylinder required a large value of the mass-damping parameter ($S_{c\eta}$ = 90) to separate the KVIV and galloping instability. On the other hand, corner-cut cylinders only required small values: $S_{c\eta}$ of 56 in the TR and C sections, and 42 in the DR III, DR II and SR sections. Hence, corner-cut cylinders were effective in separating the KVIV and galloping instability.

In the sections with strong Kármán vortex shedding intensity (R, TR, and DR III sections), vibrations start around the onset reduced wind velocity of Kármán vortex-induced vibration (1/*St*). Among these sections, the section with the strongest Kármán vortex shedding (R section), the galloping instability is largely controlled by the two-shear layer instability (Kármán vortices). Among these sections, the section with moderately strong Kármán vortex shedding intensity (TR and DR III sections), both one-shear layer instability (motion-induced vortices) and two-shear layer instability (Kármán vortices) are observed in the transverse force amplitude. Hence, motion-induced vortices and Kármán vortices interact with each other and control the vibration of the section.

In sections with weak Kármán vortex shedding intensity (DR, DR II, SR and C sections), vibrations start from the wind velocity higher than the onset reduced wind velocity of Kármán vortex-induced vibration (1/*St*). In these sections, the galloping instability is significantly controlled by the one-shear layer instability (motion-induced vortices).

In Chapter 5, the effect of Kármán vortex shedding intensity on the galloping onset reduced wind velocity, and the aerodynamic interactions between the galloping instability and the vortices in the R, TR and DR III sections were discussed for various angles of attack. Under various angles of attack, both the model and the flow field around it were asymmetric. The studied angle of attack included the angle of attack (α = +9° in R, and +4° in TR and DR III sections) just before the angle of attack where the reattachment occurs and the slope of the transverse force coefficient is considerably large. Although these cases were highly prone to galloping instability from the perspective of the quasi-steady theory, the response amplitudes showed a low tendency of galloping even at a very low Scruton number ($S_{c\eta}$ = 6). Moreover, in the high reduced wind velocity region, the H_1^* obtained from the slope of the transverse force coefficient (the quasi-steady theory) was not asymptotic but rather parallel with the H_1^* obtained from the forced vibration tests. Hence, galloping instability might be difficult to describe by the quasi-steady theory in these angles of attack.

In the sections with the strongest Kármán vortex shedding intensity at α = 0° (R section), the Kármán vortex shedding intensity considerably decreased when the angle of attack was increased to +4° and +9°. However, the two-shear layer instability (Kármán vortices) dominates the galloping instability of the rectangular cylinder, regardless of the reduction in the Kármán vortex shedding intensity.

In the sections with strong Kármán vortex shedding at α = 0° (TR and DR III sections), the Kármán vortex shedding intensity significantly decreased when the angle of attack was increased to +2° and +4°. In these two sections, the one-shear layer instability (motion-induced vortices) and two-shear layer instability (Kármán vortices) interact with each other and dominate the galloping when Kármán vortex shedding was strong (α = +2°). On the other hand, when the Kármán vortex shedding was weak (α = +4°), the one-shear layer instability (motion-induced vortices) influenced the galloping.

Hence, similar interactions between vortices and galloping were observed both in the zero angle of attack (symmetric body) and various angles of attack (asymmetric body) of the corner-cut cylinders. Thus, the Kármán vortex shedding intensity of a section plays an important role in controlling the galloping onset of that section, especially in corner-cut cylinders. When the section with weak Kármán vortex shedding intensity was intended to be used in the wind resistance design of a structure, caution should be exercised.

Furthermore, the galloping instability of a model might be difficult to desctibe by the quasi-steady theory at certain attack, which is the angle of attack where the slope of the transverse force coefficient is large and just before the angle of attack where the flow reattachment of known to be occurred.

In Chapter 6, the effect of cross-sectional shape on the flow separation, flow reattachment, and aerodynamic characteristics of the existing complex-shaped tall structure was discussed. The 3D model of the Buddha statue utilised in the numerical simulation was obtained by performing the 3D laser scanning of the actual Buddha statue. As for the 3D terrestrial laser scanning of the complex-shaped tall structure, it was found that obstacles like moving humans or animals can obstruct the laser line of the scanner. This caused occlusion and hindered point registration. Despite challenges in capturing enough data for the head of the Buddha statue, the 3D terrestrial laser scanning could efficiently produce a precise model of the complex-shaped structure. However, it should be noted that the imperfections in the model needed to be refined. In addition, the unstructured meshing effectively handled the complexity of the statue shape.

Changes in the cross-sectional shape of the Buddha statue, especially near corners, influence the aerodynamic characteristics of the Buddha statue. Different corner shapes throughout the height of the Buddha statue produced different flow separation points, affecting wake region size, vortex shedding frequency, and Strouhal number. Furthermore, the Buddha statue behaves as a bluff body at α = 0° (wind approaching from the front surface of the Buddha statue) and less bluff or comparatively streamlined at α = 90° (wind approaching from the side surface of the Buddha statue). Hence, the wake region size and along-wind force coefficient are minimized at α = 90°. Increasing the angle of attack (α) may lead to flow-induced vibrations at the upper and lower part of the Buddha statue. This could impact the renovation and maintenance plans of the Buddha statue.

Given the growing need for economical and time-saving approaches in assessing wind resistance, the 3D terrestrial laser scanning method offers valuable options for evaluating the wind resistance of tall, complex-shaped structures where conventional methods like wind tunnel testing and on-site measurements pose challenges.

7.2 Future topics

The pressure distribution around the model surfaces of the DR section should be conducted to study the mechanism of *Re* effects on the aerodynamic forces and response amplitude.

At the angles of attack which were larger than the angle of attack where the time-averaged flow reattachment occurred, the C'_{Fy} values began to increase gradually. Thus, the effect of flow reattachment on the Kármán vortex shedding intensity and response amplitude should be further investigated for the asymmetric body. The large discrepancy between the quasi-steady and unsteady aerodynamic forces in the asymmetric body, especially at α = +9° for R, and +4° for TR and DR III sections, also needs to be addressed in future studies.

Flow visualisation during forced vibration should be performed to discuss whether Kármán vortex-induced vibration (KVIV) is self-excited or motion-induced type. This can be carried out either by the Particle image velocimetry (PIV) and/or Computational Fluid Dynamics (CFD) simulation. It is also necessary to investigate whether the wind velocity limited vibration in the double recession II (DR II) and chamfer (C) sections is either KVIV or not.

Appendix A

Structural damping of rectangular cylinder with corner modifications during the vertical 1DOF free vibration test

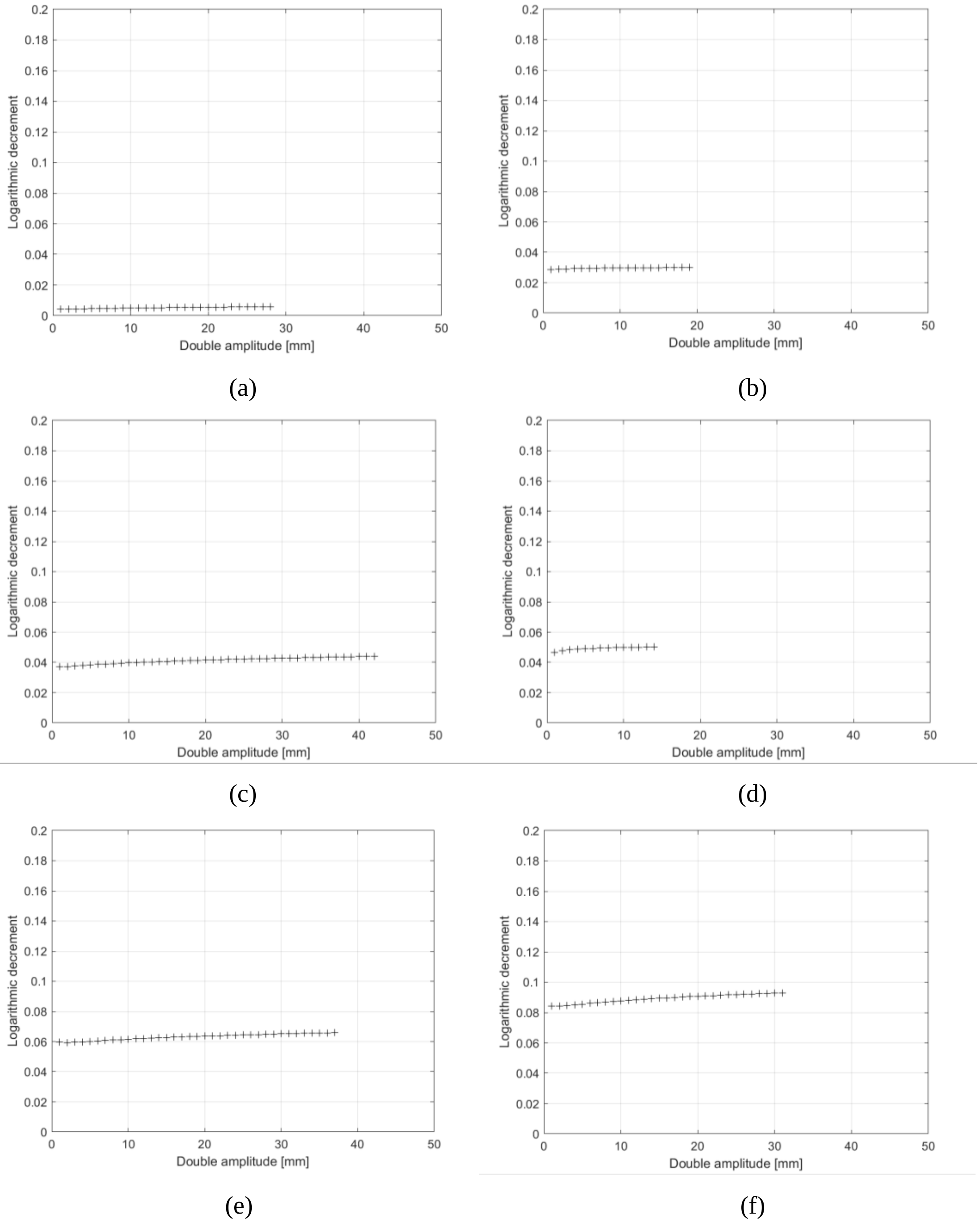

Fig. A.1 Structural damping in terms of the logarithmic decrement for rectangular section (α = 0°) at S_c of (a) 6; (b) 42; (c) 56; (d) 69; (e) 90; and (f) 130.

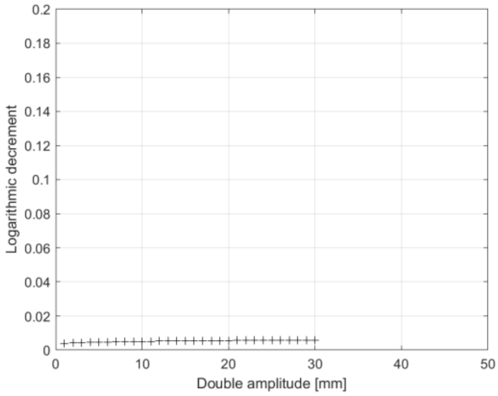

(a)

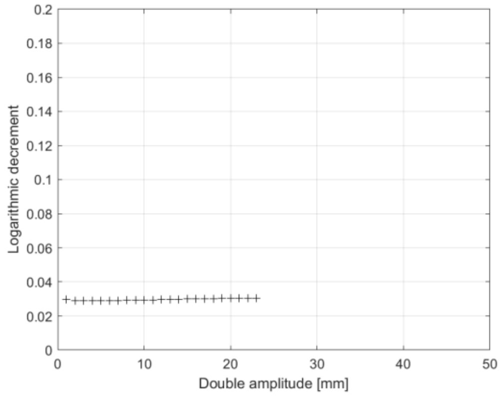

(b)

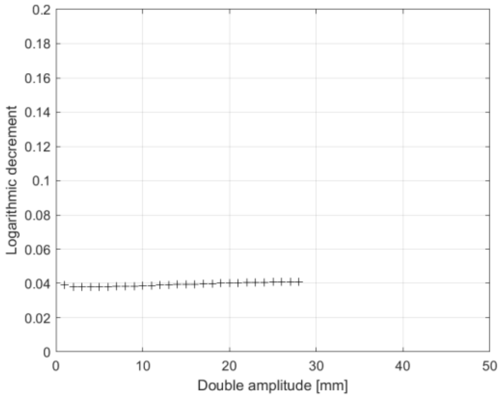

(c)

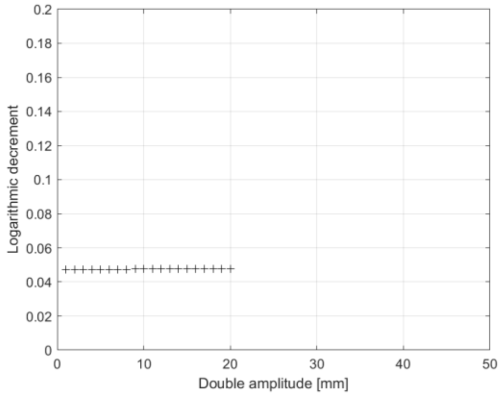

(d)

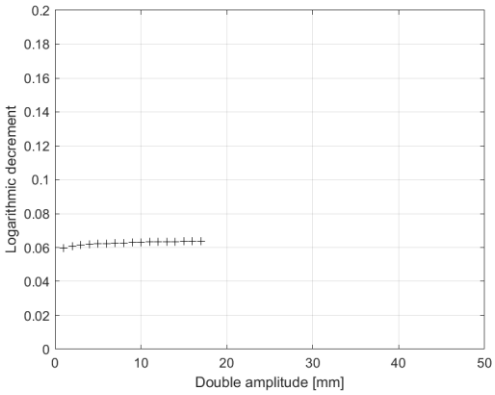

(e)

Fig. A.2 Structural damping in terms of the logarithmic decrement for single recession section (α = 0°) at S_c of (a) 6; (b) 42; (c) 56; (d) 69; and (e) 90.

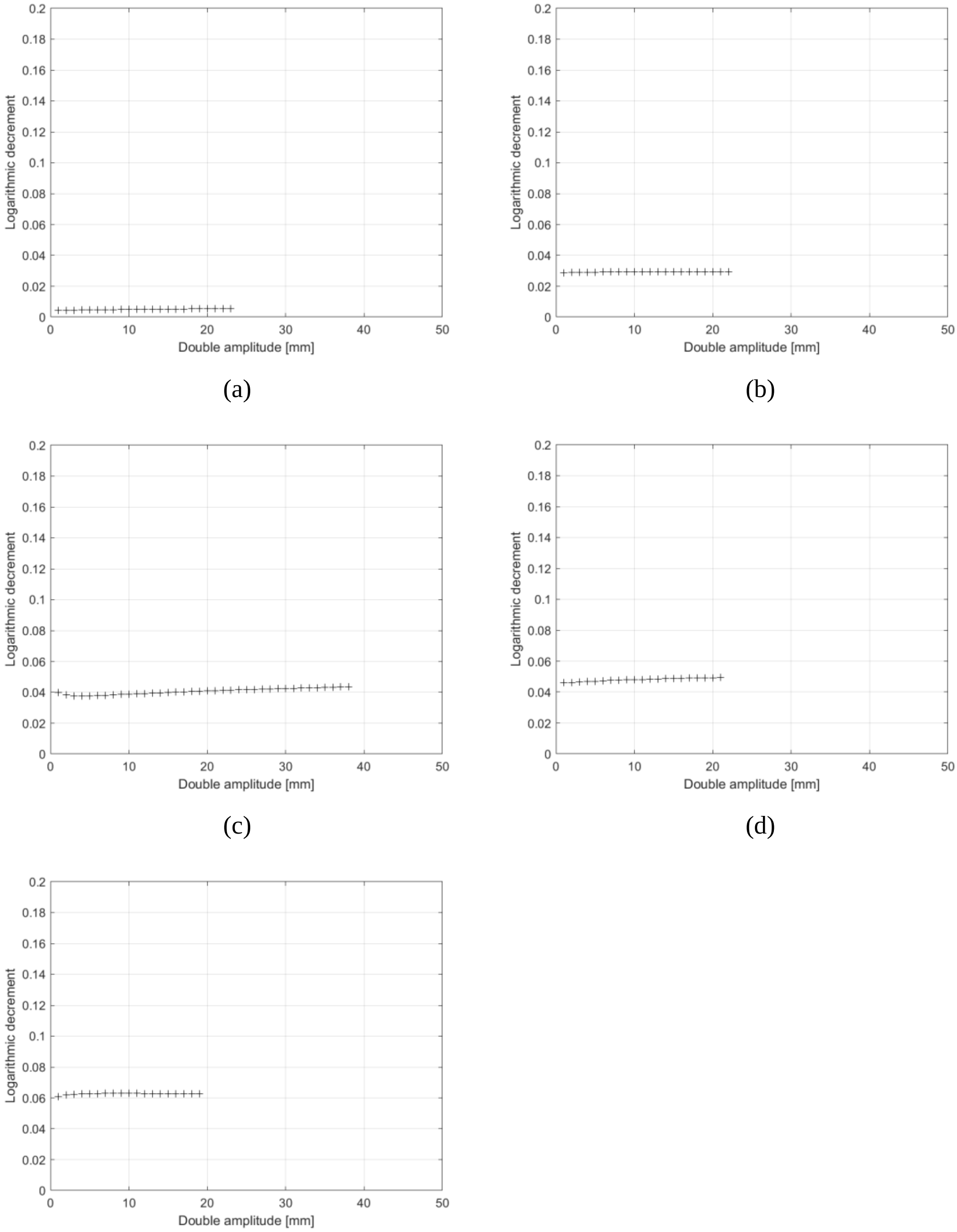

(a) (b) (c) (d) (e)

Fig. A.3 Structural damping in terms of the logarithmic decrement for double recession section (α = 0°) at S_c of (a) 6; (b) 42; (c) 56; (d) 69; and (e) 90.

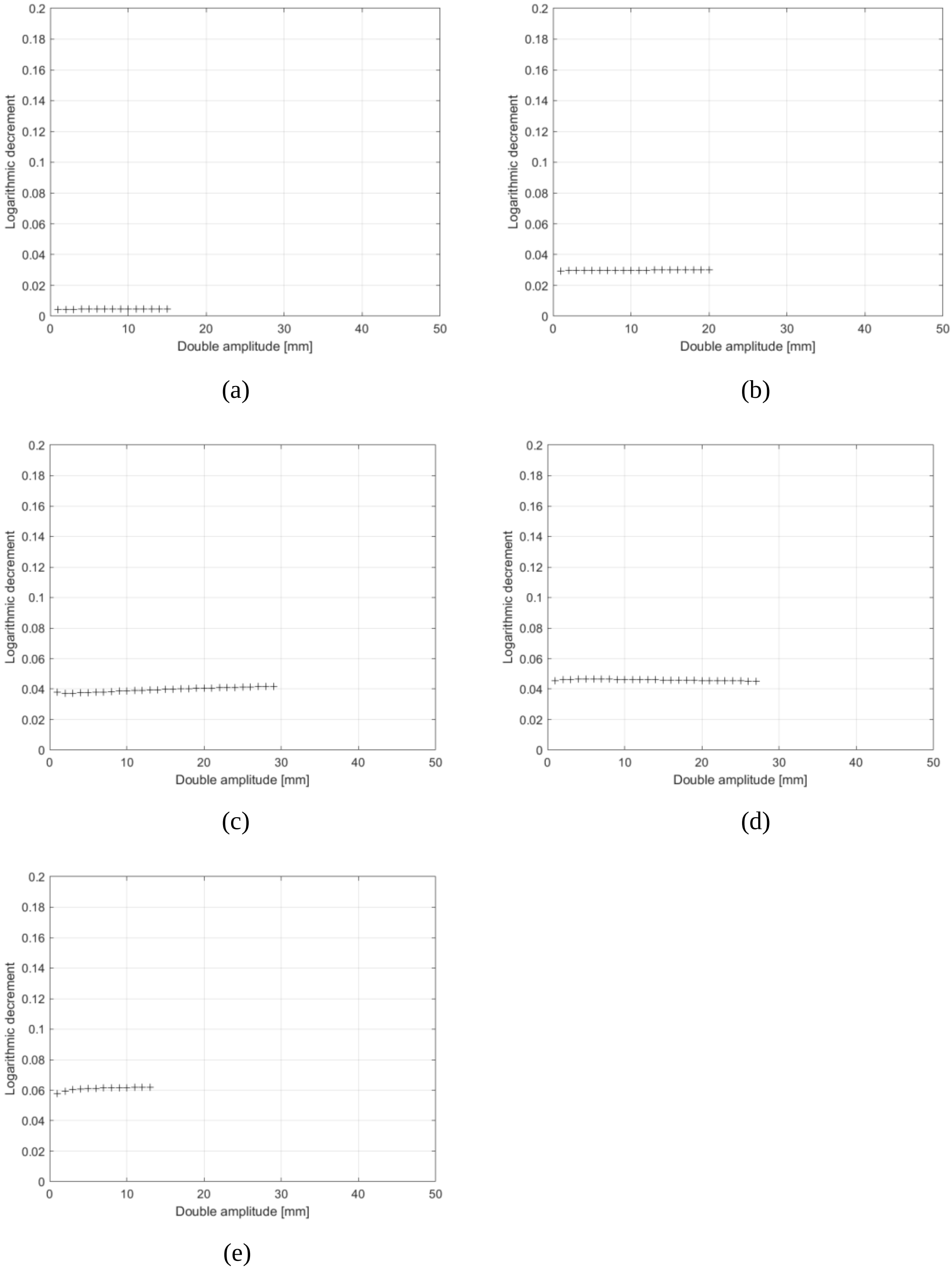

Fig. A.4 Structural damping in terms of the logarithmic decrement for double recession II section (α = 0°) at S_c of (a) 6; (b) 42; (c) 56; (d) 69; and (e) 90.

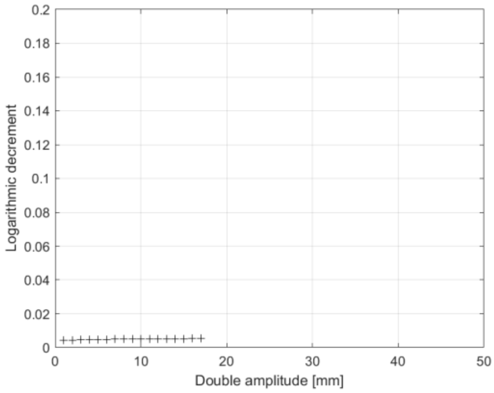

(a)

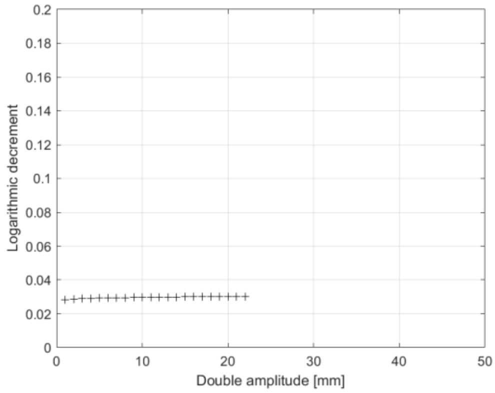

(b)

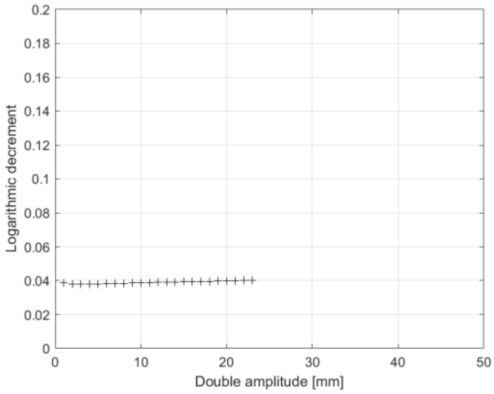

(c)

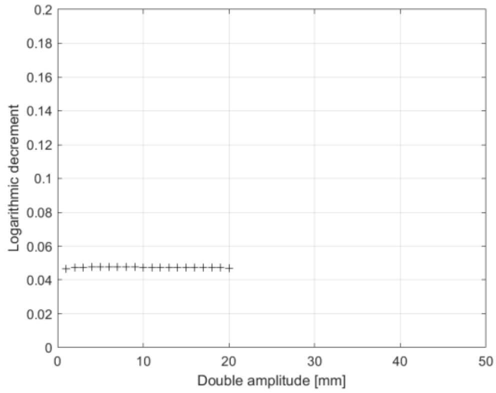

(d)

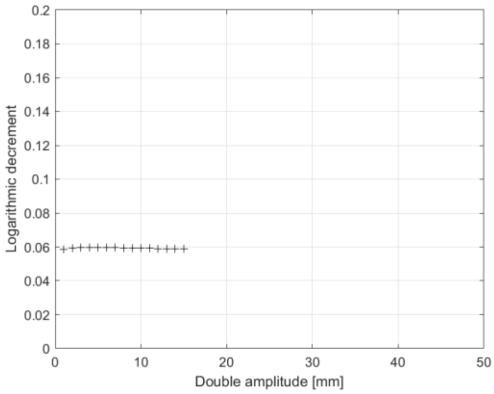

(e)

Fig. A.5 Structural damping in terms of the logarithmic decrement for double recession III section (α = 0°) at S_c of (a) 6; (b) 42; (c) 56; (d) 69; and (e) 90.

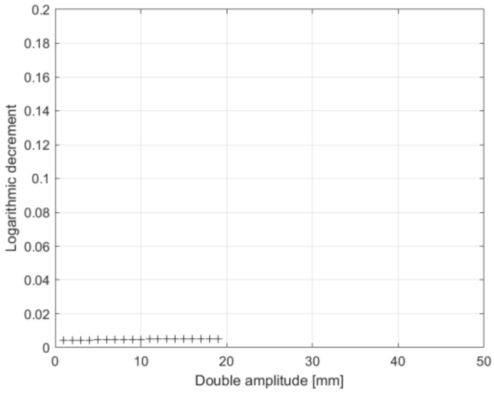

(a)

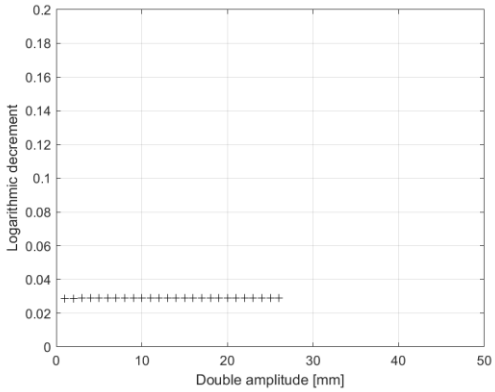

(b)

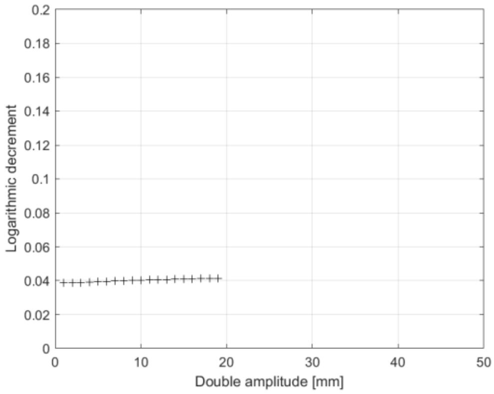

(c)

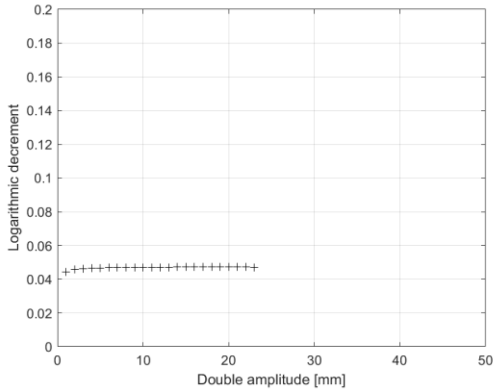

(d)

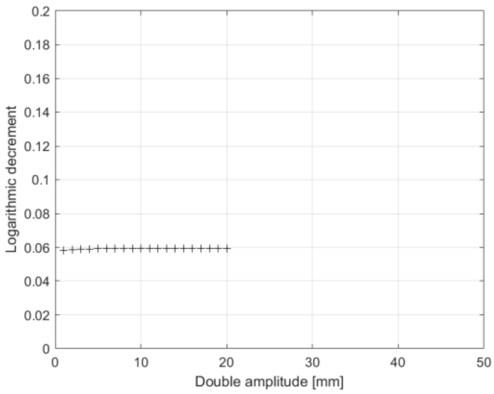

(e)

Fig. A.6 Structural damping in terms of the logarithmic decrement for triple recession section (α = 0°) at S_c of (a) 6; (b) 42; (c) 56; (d) 69; and (e) 90.

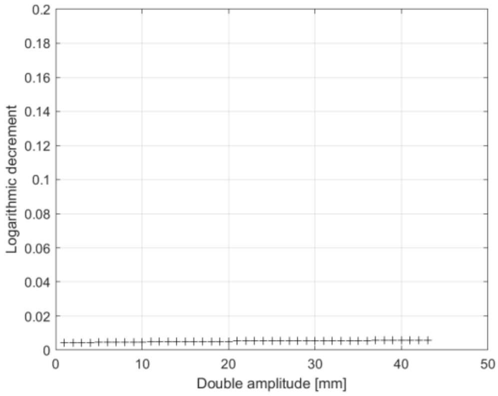

(a)

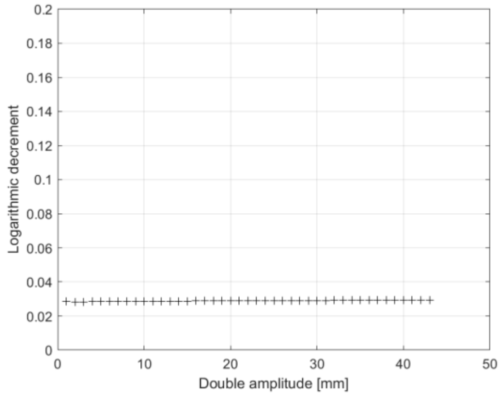

(b)

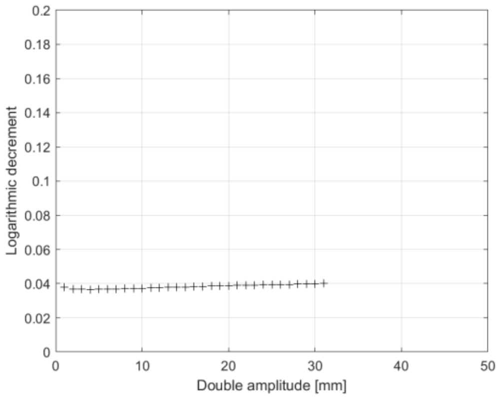

(c)

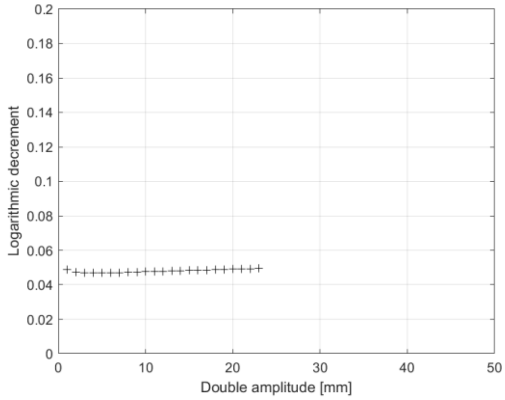

(d)

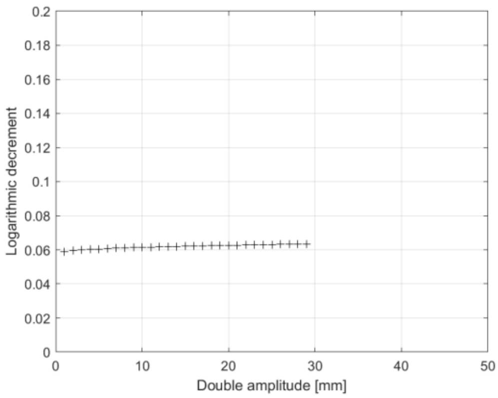

(e)

Fig. A.7 Structural damping in terms of the logarithmic decrement for chamfer section (α = 0°) at S_c of (a) 6; (b) 42; (c) 56; (d) 69; and (e) 90.

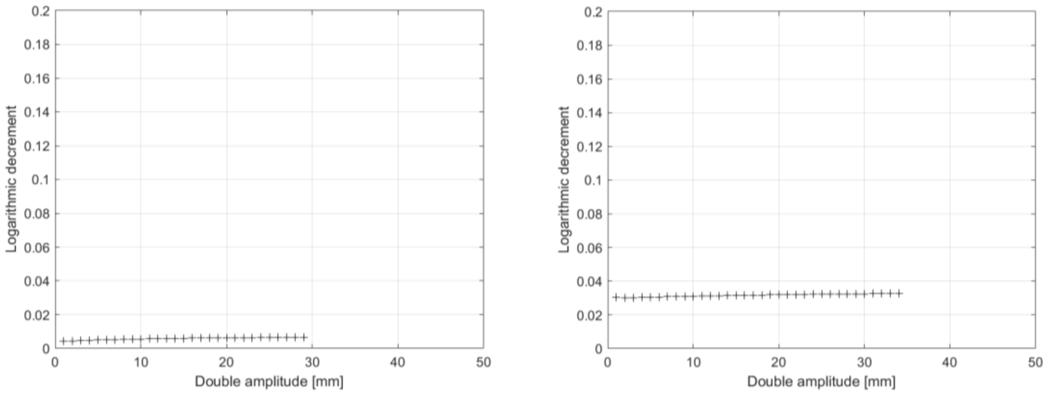

(a) (b)

Fig. A.8 Structural damping in terms of the logarithmic decrement for rectangular section (α = +4°) at S_c of (a) 6; and (b) 42.

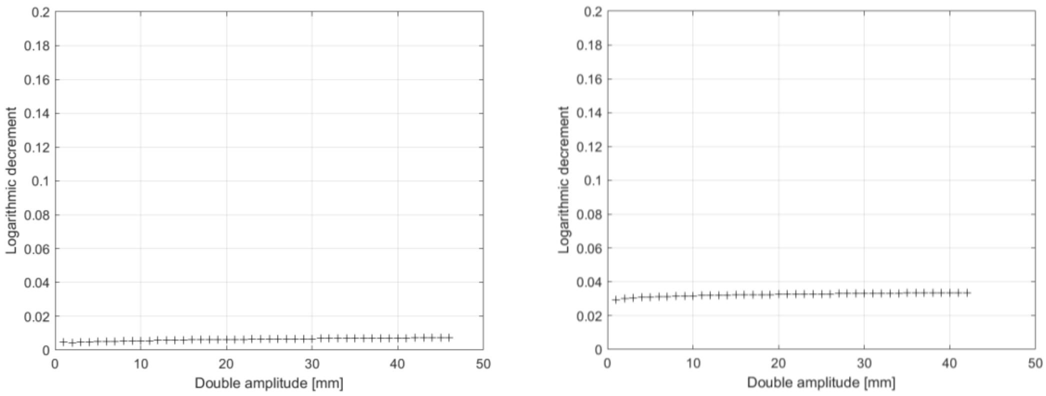

(a) (b)

Fig. A.9 Structural damping in terms of the logarithmic decrement for rectangular section (α = +9°) at S_c of (a) 6; and (b) 42.

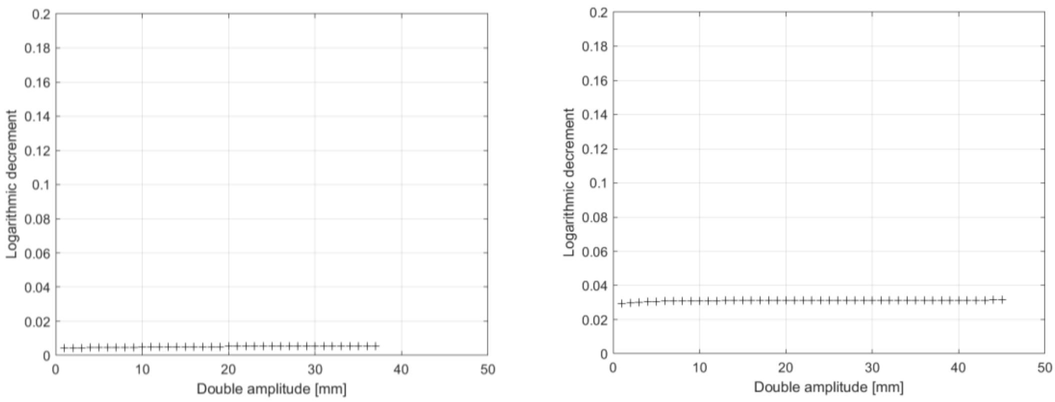

(a) (b)

Fig. A.10 Structural damping in terms of the logarithmic decrement for triple recession section (α = +2°) at S_c of (a) 6; and (b) 42.

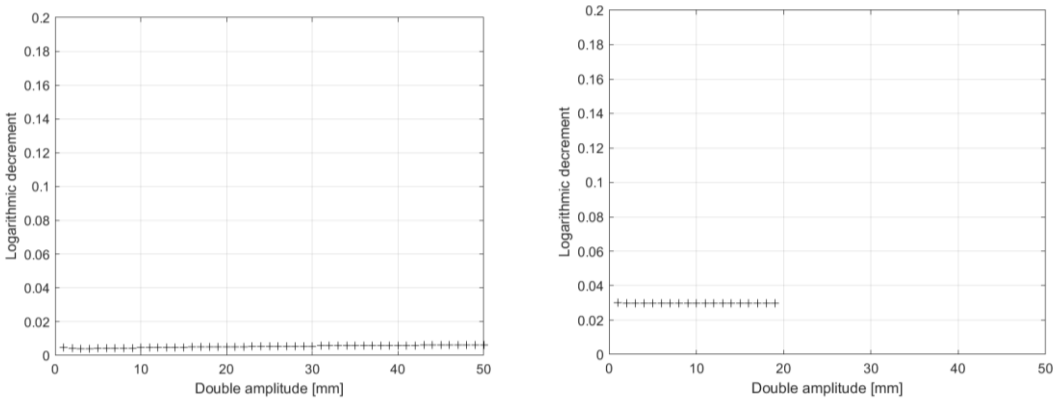

(a) (b)

Fig. A.11 Structural damping in terms of the logarithmic decrement for triple recession section (α = +4°) at S_c of (a) 6; and (b) 42.

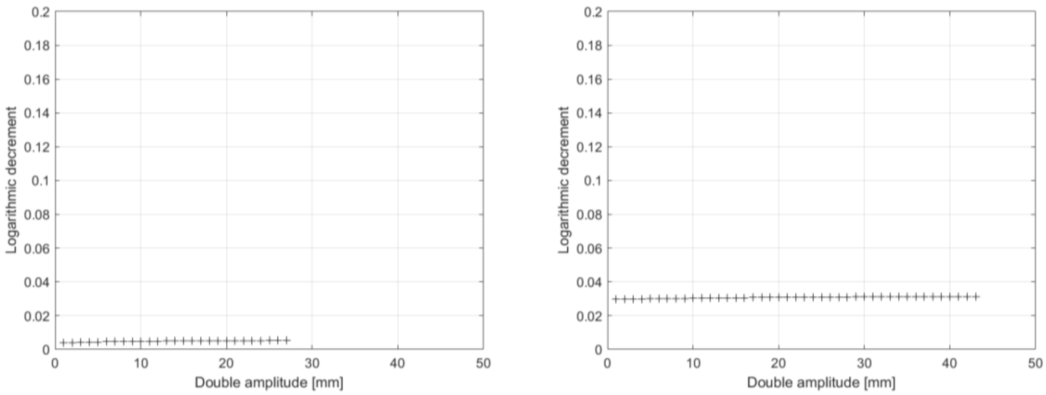

(a) (b)

Fig. A.12 Structural damping in terms of the logarithmic decrement for double recession III section (α = +2°) at S_c of (a) 6; and (b) 42.

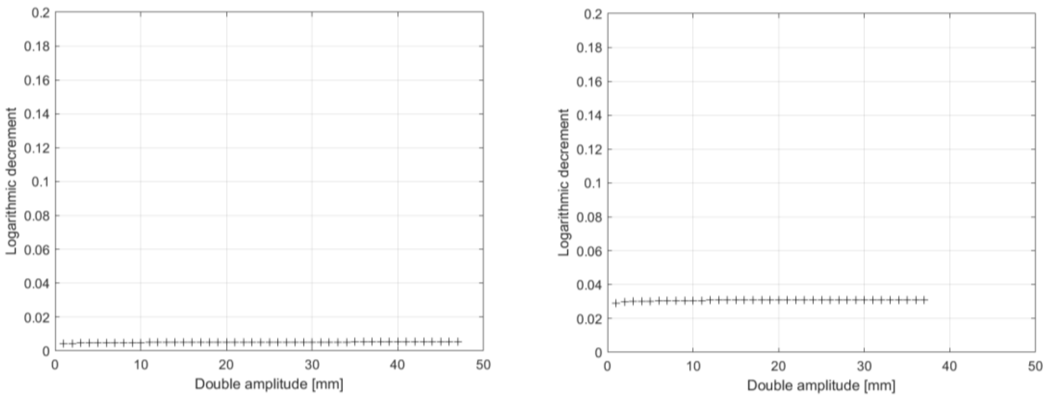

(a) (b)

Fig. A.13 Structural damping in terms of the logarithmic decrement for double recession III section (α = +4°) at S_c of (a) 6; and (b) 42.

Appendix B

Aerodynamic coefficients of rectangular cylinder with corner modifications

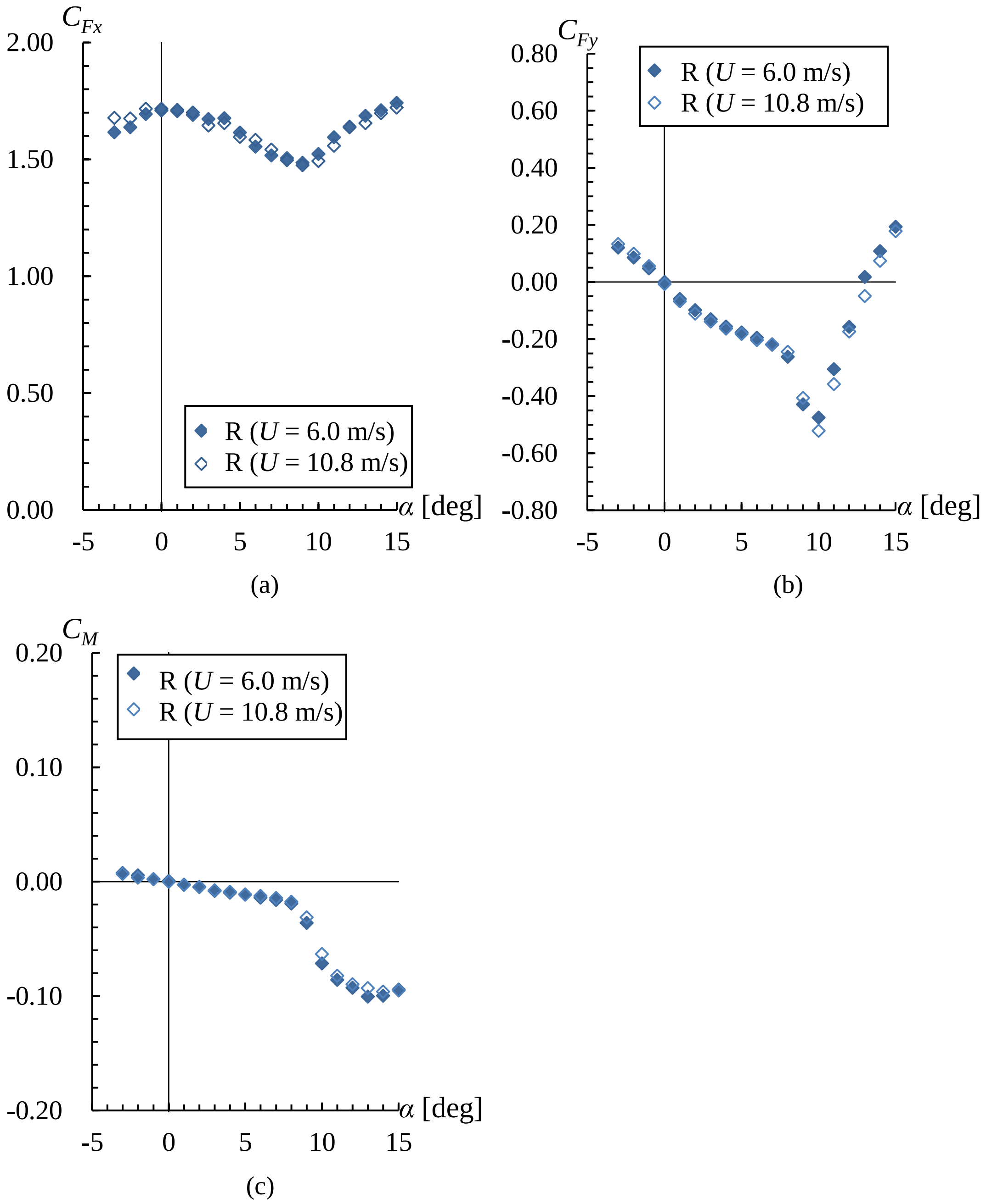

Fig. B.1 Aerodynamic coefficients of rectangular section at U = 6.0 m/s (Re = 36,000) and U = 10.8 m/s (Re = 64,800): (a) longitudinal force coefficient (C_{Fx}); (b) transverse force coefficient (C_{Fy}); and (c) moment coefficient (C_M).

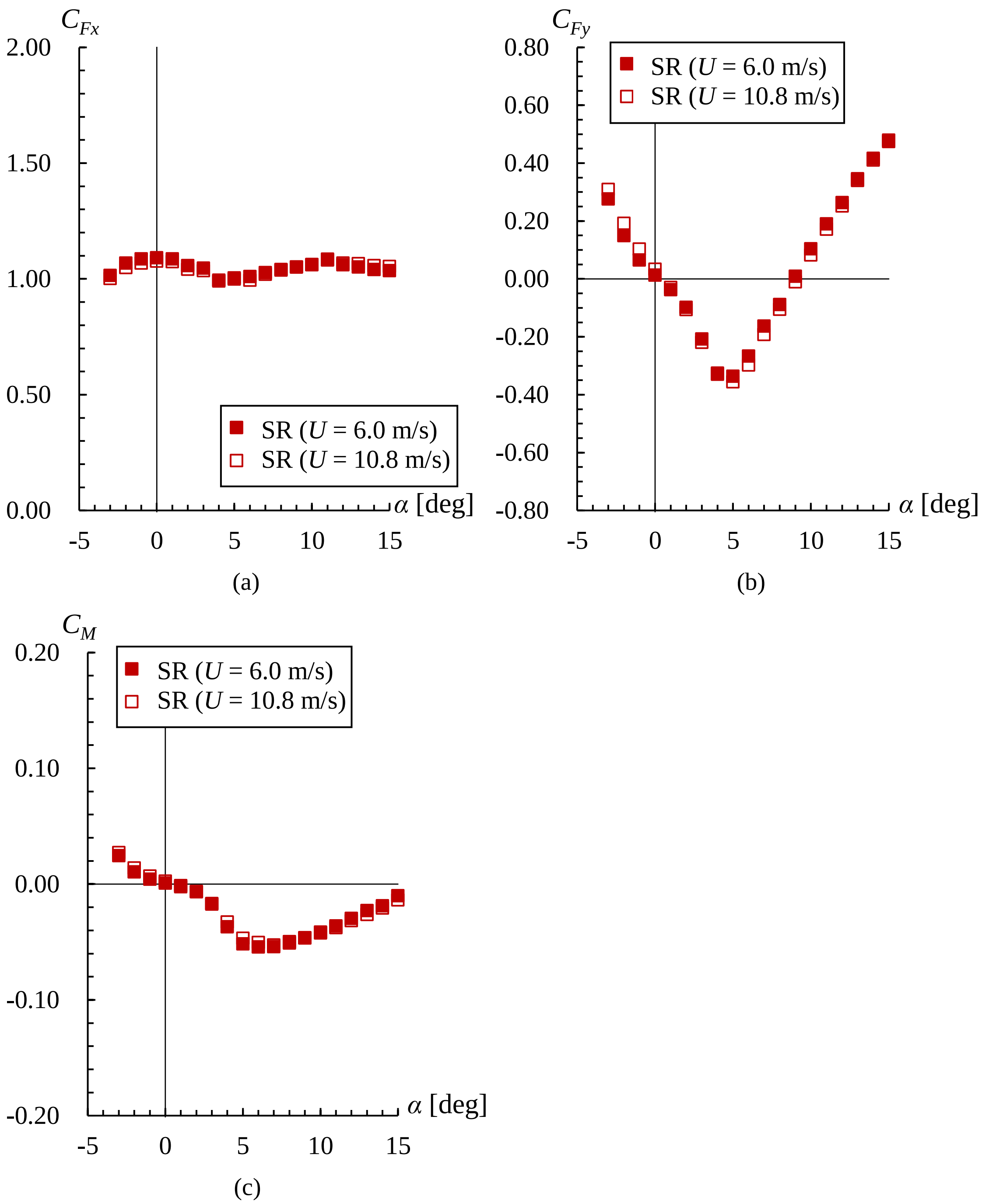

Fig. B.2 Aerodynamic coefficients of single recession section at U = 6.0 m/s (Re = 36,000) and U = 10.8 m/s (Re = 64,800): (a) longitudinal force coefficient (C_{Fx}); (b) transverse force coefficient (C_{Fy}); and (c) moment coefficient (C_M).

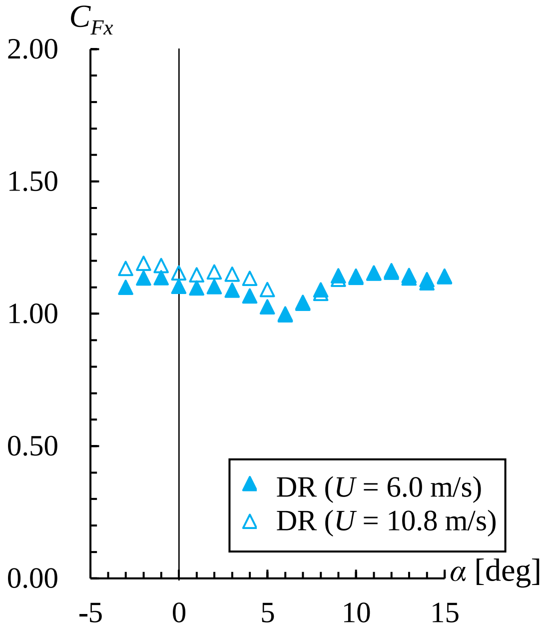

(a)

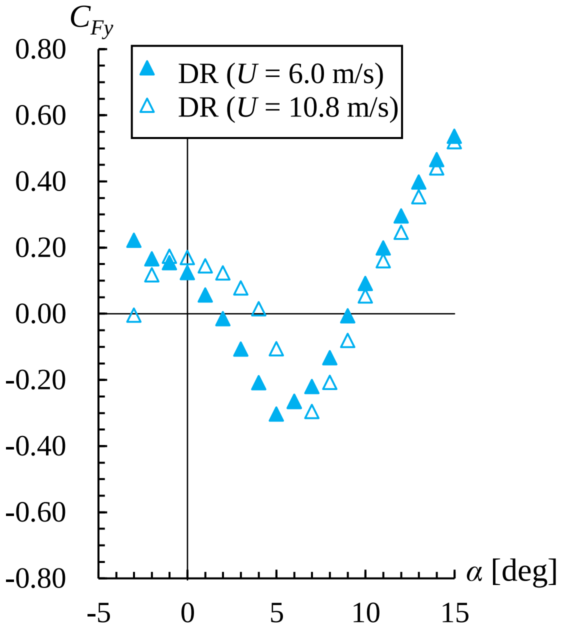

(b)

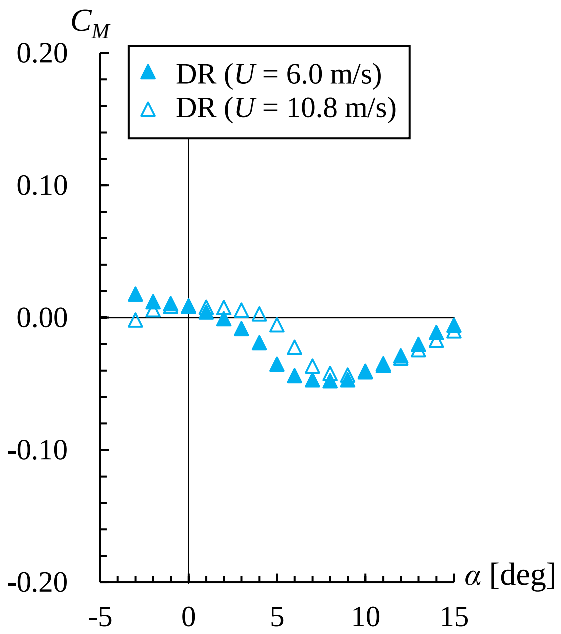

(c)

Fig. B.3 Aerodynamic coefficients of double recession section at U = 6.0 m/s (Re = 36,000) and U = 10.8 m/s (Re = 64,800): (a) longitudinal force coefficient (C_{Fx}); (b) transverse force coefficient (C_{Fy}); and (c) moment coefficient (C_M).

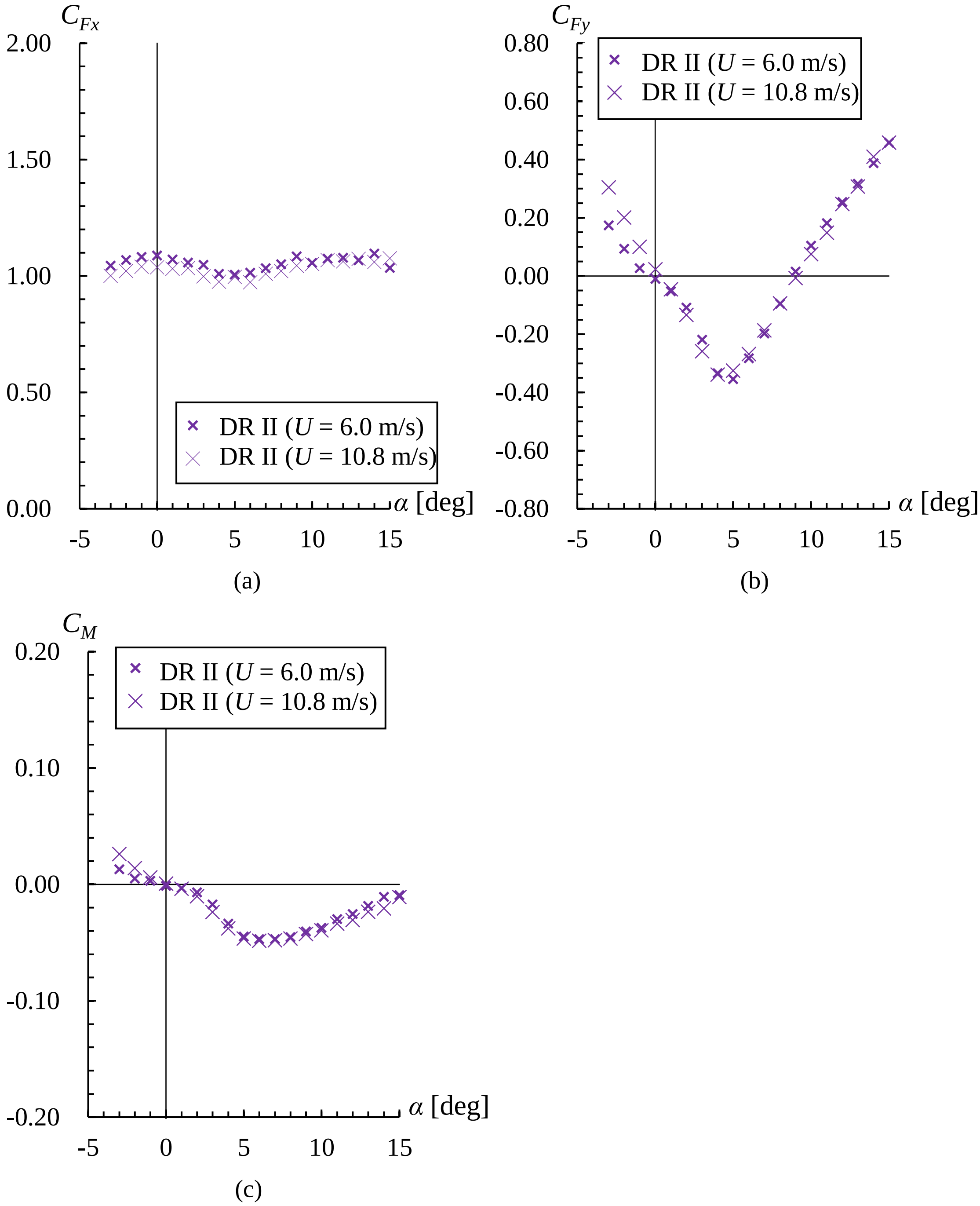

Fig. B.4 Aerodynamic coefficients of double recession II section at U = 6.0 m/s (Re = 36,000) and U = 10.8 m/s (Re = 64,800): (a) longitudinal force coefficient (C_{Fx}); (b) transverse force coefficient (C_{Fy}); and (c) moment coefficient (C_M).

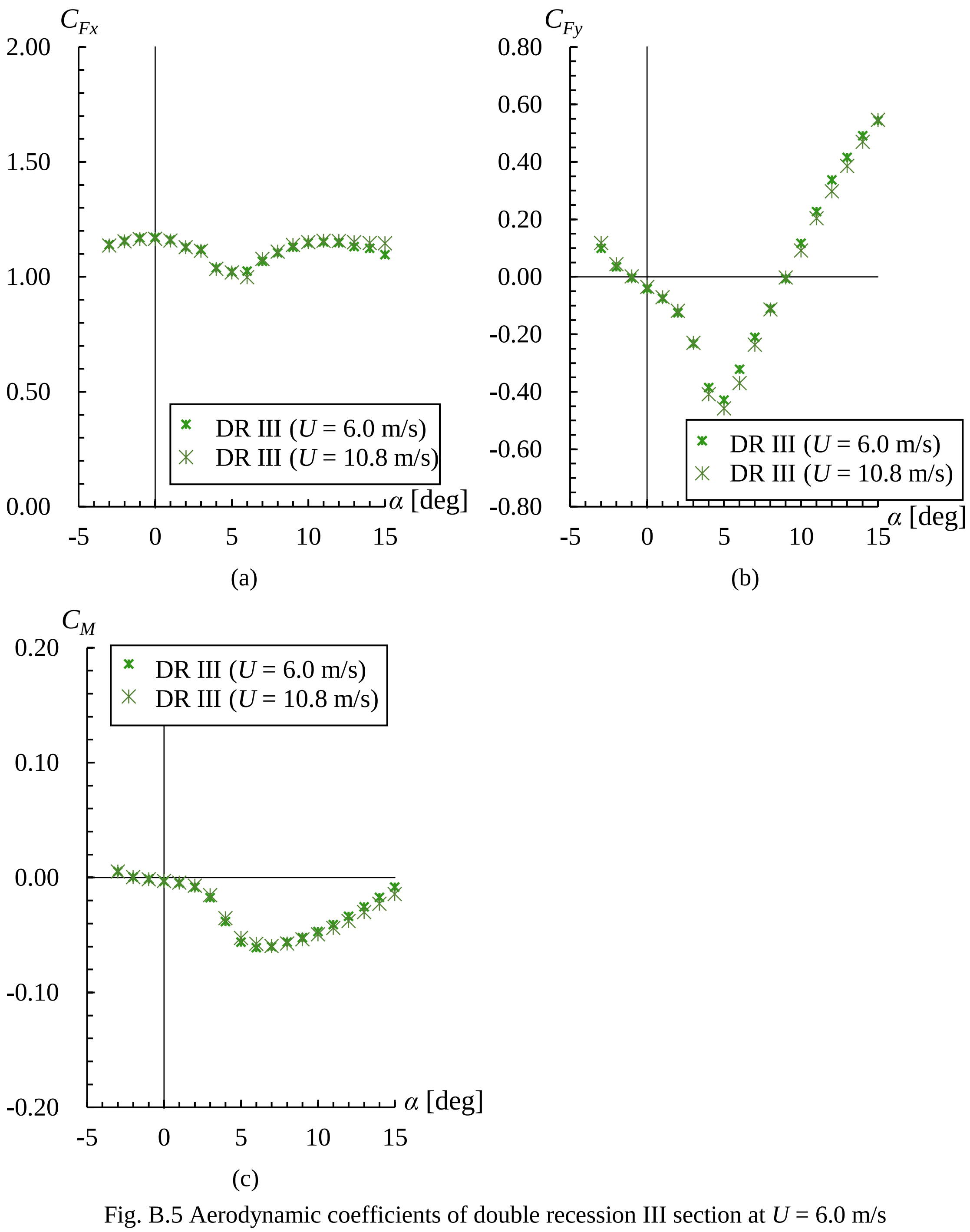

Fig. B.5 Aerodynamic coefficients of double recession III section at U = 6.0 m/s (Re = 36,000) and U = 10.8 m/s (Re = 64,800): (a) longitudinal force coefficient (C_{Fx}); (b) transverse force coefficient (C_{Fy}); and (c) moment coefficient (C_M).

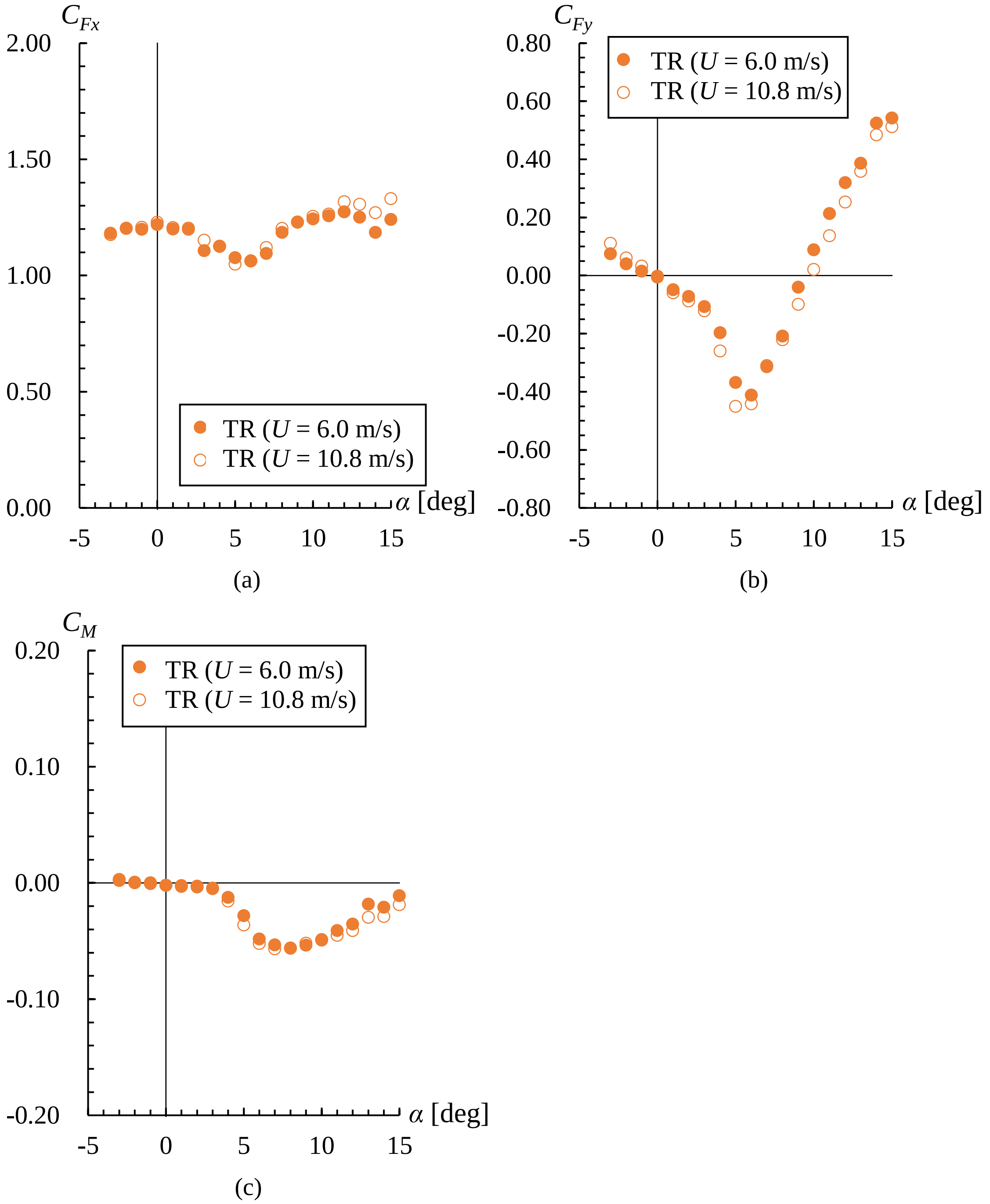

Fig. B.6 Aerodynamic coefficients of triple recession section at U = 6.0 m/s (Re = 36,000) and U = 10.8 m/s (Re = 64,800): (a) longitudinal force coefficient (C_{Fx}); (b) transverse force coefficient (C_{Fy}); and (c) moment coefficient (C_M).

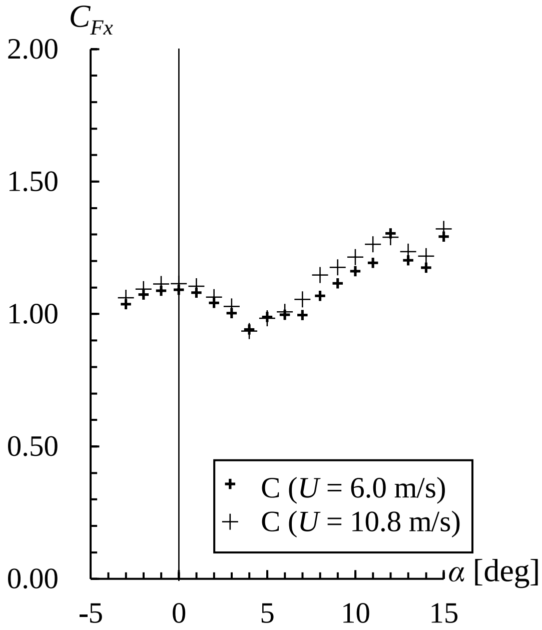

(a)

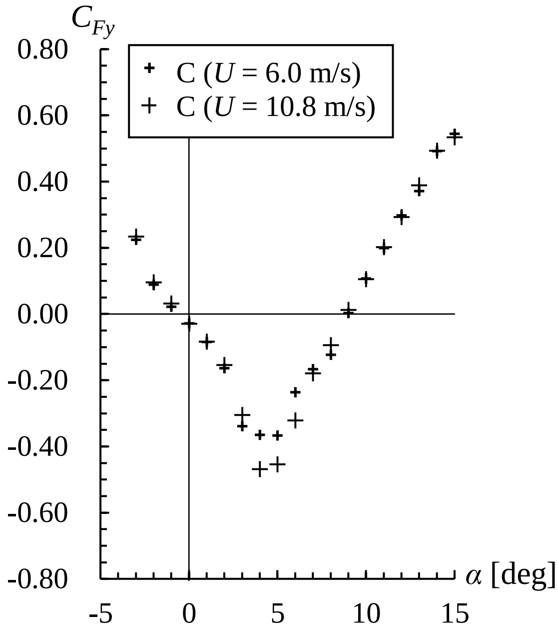

(b)

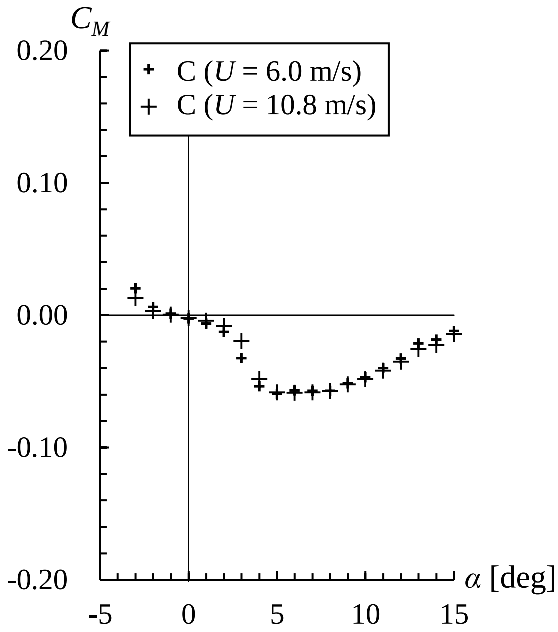

(c)

Fig. B.7 Aerodynamic coefficients of chamfer section at U = 6.0 m/s (Re = 36,000) and U = 10.8 m/s (Re = 64,800): (a) longitudinal force coefficient (C_{Fx}); (b) transverse force coefficient (C_{Fy}); and (c) moment coefficient (C_M).

Appendix C

Scalogram of transverse force for rectangular cylinder with corner modifications

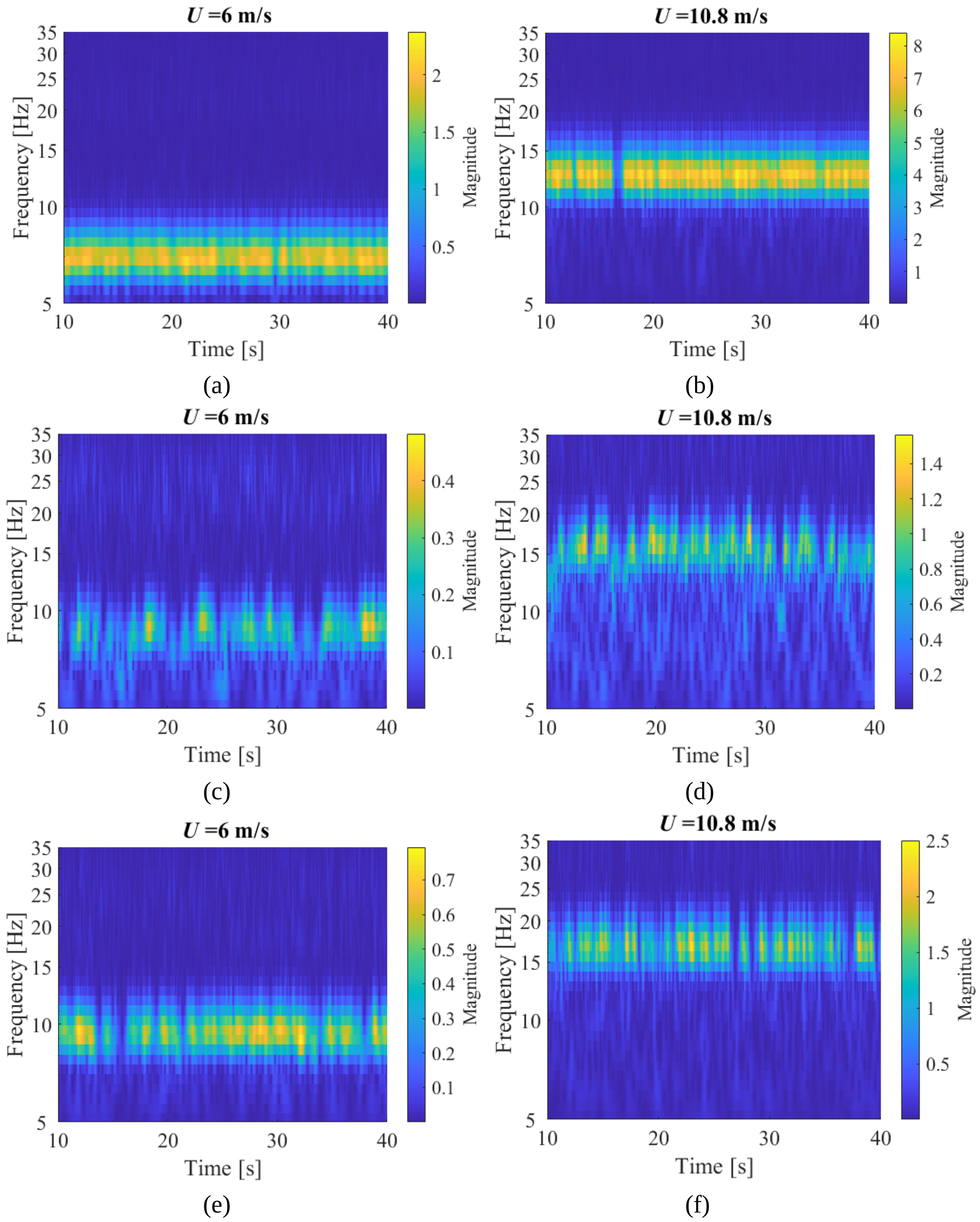

Fig. C.1 R section: Scalogram of transverse force at α = 0° for (a) U = 6.0 m/s and (b) U = 10.8 m/s; at α = +9° for (c) U = 6.0 m/s and (d) U = 10.8 m/s; and at α = +10° for (e) U = 6.0 m/s and (f) U = 10.8 m/s.

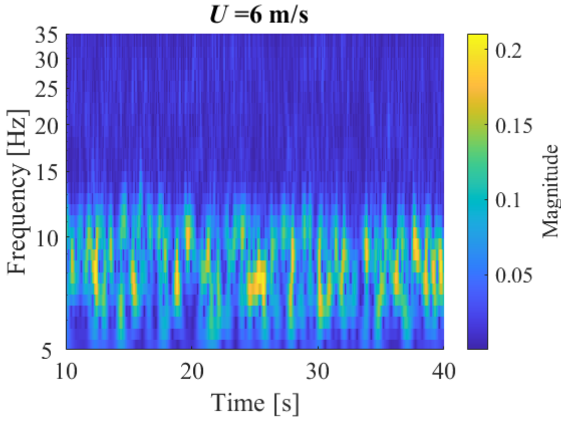

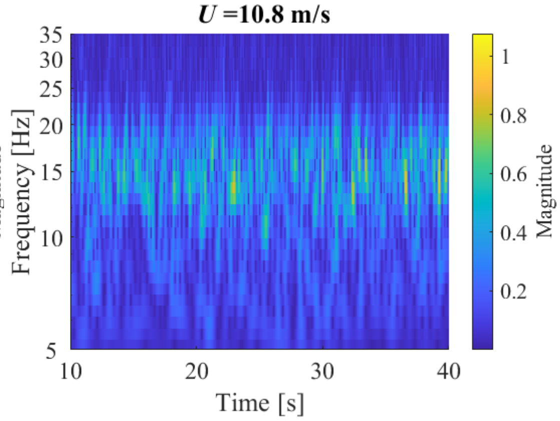

(a) (b)

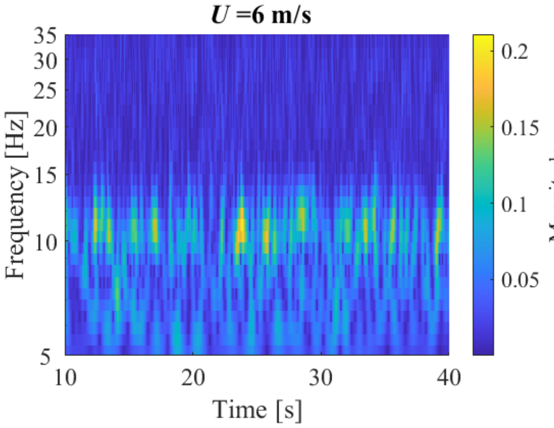

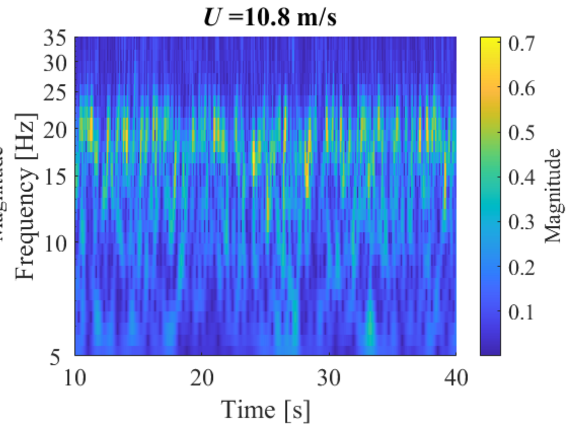

(c) (d)

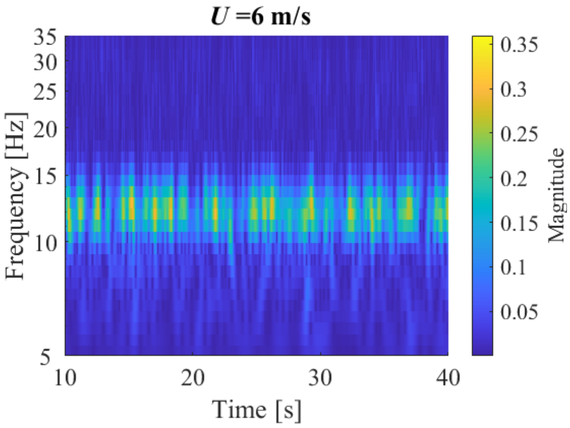

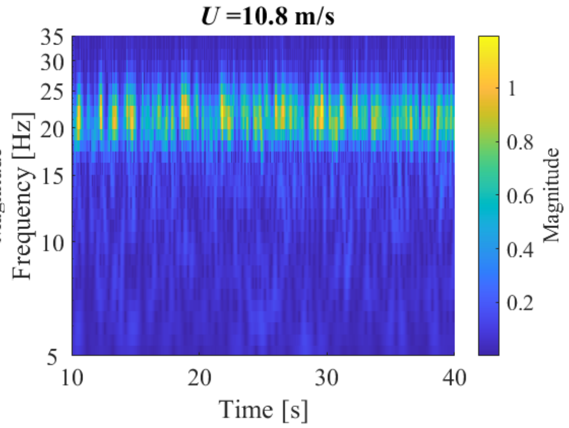

(e) (f)

Fig. C.2 SR section: Scalogram of transverse force at α = 0° for (a) U = 6.0 m/s and (b) U = 10.8 m/s; at α = +3° for (c) U = 6.0 m/s and (d) U = 10.8 m/s; and at α = +5° for (e) U = 6.0 m/s and (f) U = 10.8 m/s.

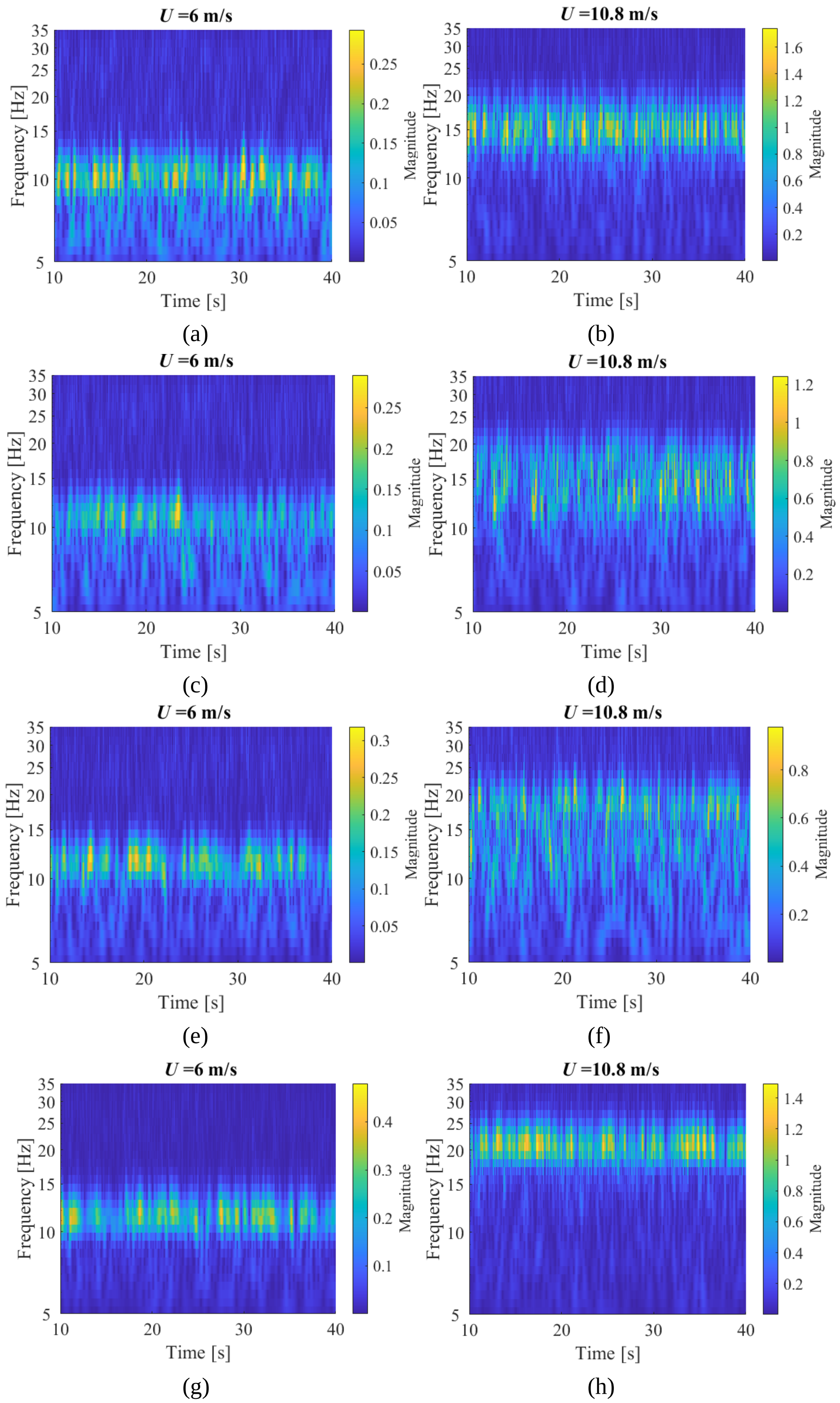

Fig. C.3 DR section: Scalogram of transverse force at α = 0° for (a) U = 6.0 m/s and (b) U = 10.8 m/s; at α = +4° for (c) U = 6.0 m/s and (d) U = 10.8 m/s; at α = +5° for (e) U = 6.0 m/s and (f) U = 10.8 m/s; and at α = +7° for (g) U = 6.0 m/s and (h) U = 10.8 m/s.

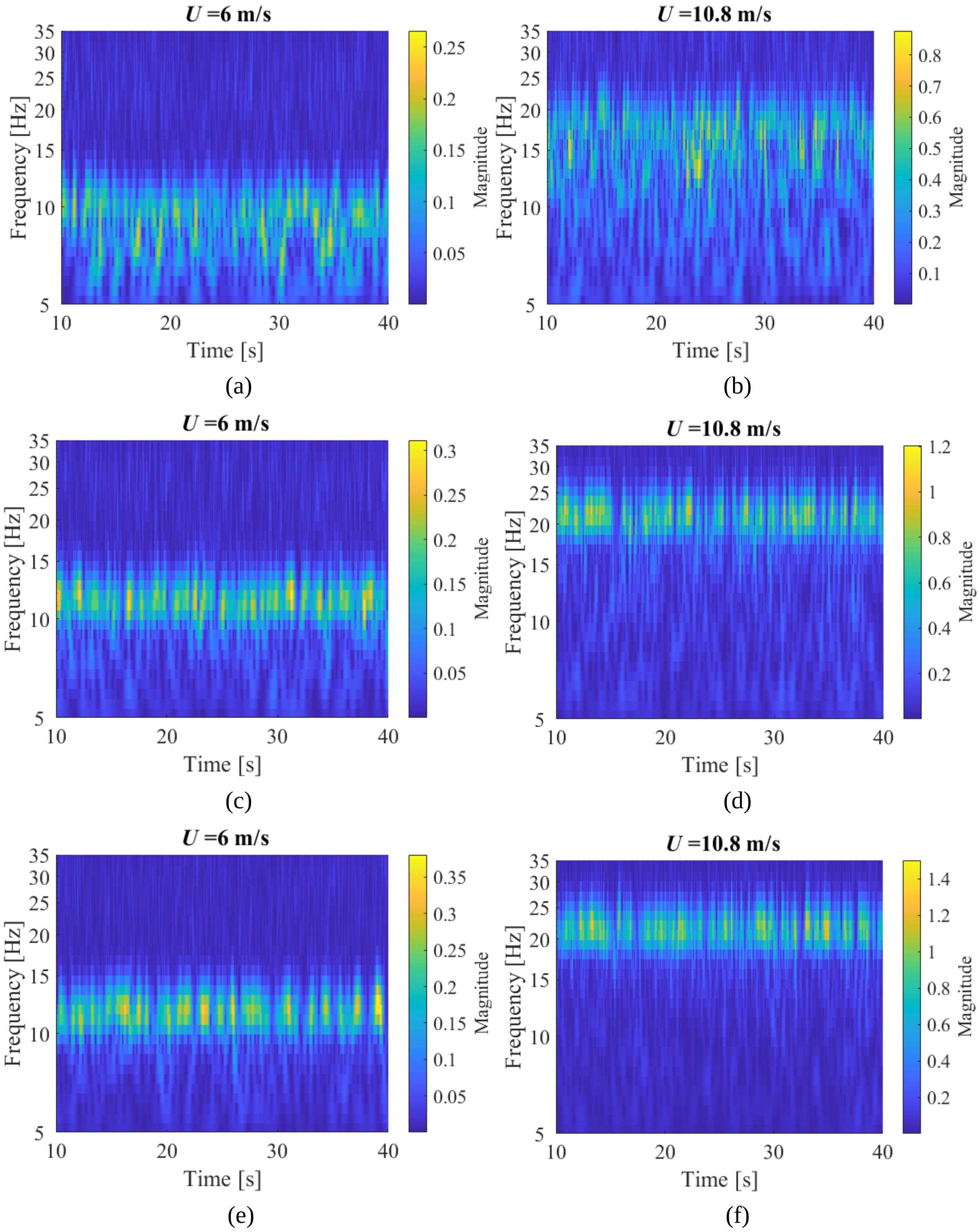

Fig. C.4 DR II section: Scalogram of transverse force at α = 0° for (a) U = 6.0 m/s and (b) U = 10.8 m/s; at α = +4° for (c) U = 6.0 m/s and (d) U = 10.8 m/s; and at α = +5° for (e) U = 6.0 m/s and (f) U = 10.8 m/s.

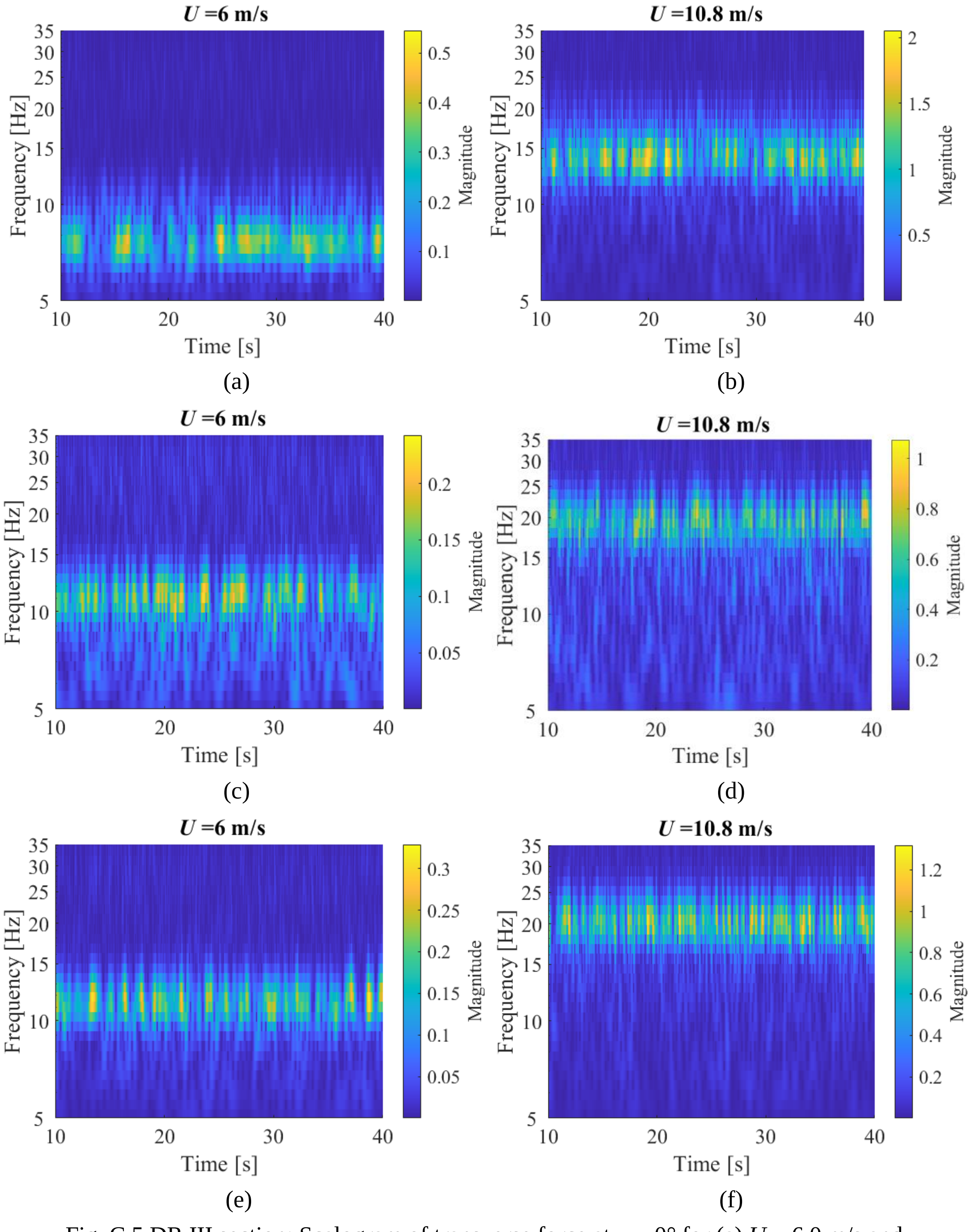

Fig. C.5 DR III section: Scalogram of transverse force at α = 0° for (a) U = 6.0 m/s and (b) U = 10.8 m/s; at α = +4° for (c) U = 6.0 m/s and (d) U = 10.8 m/s; and at α = +5° for (e) U = 6.0 m/s and (f) U = 10.8 m/s.

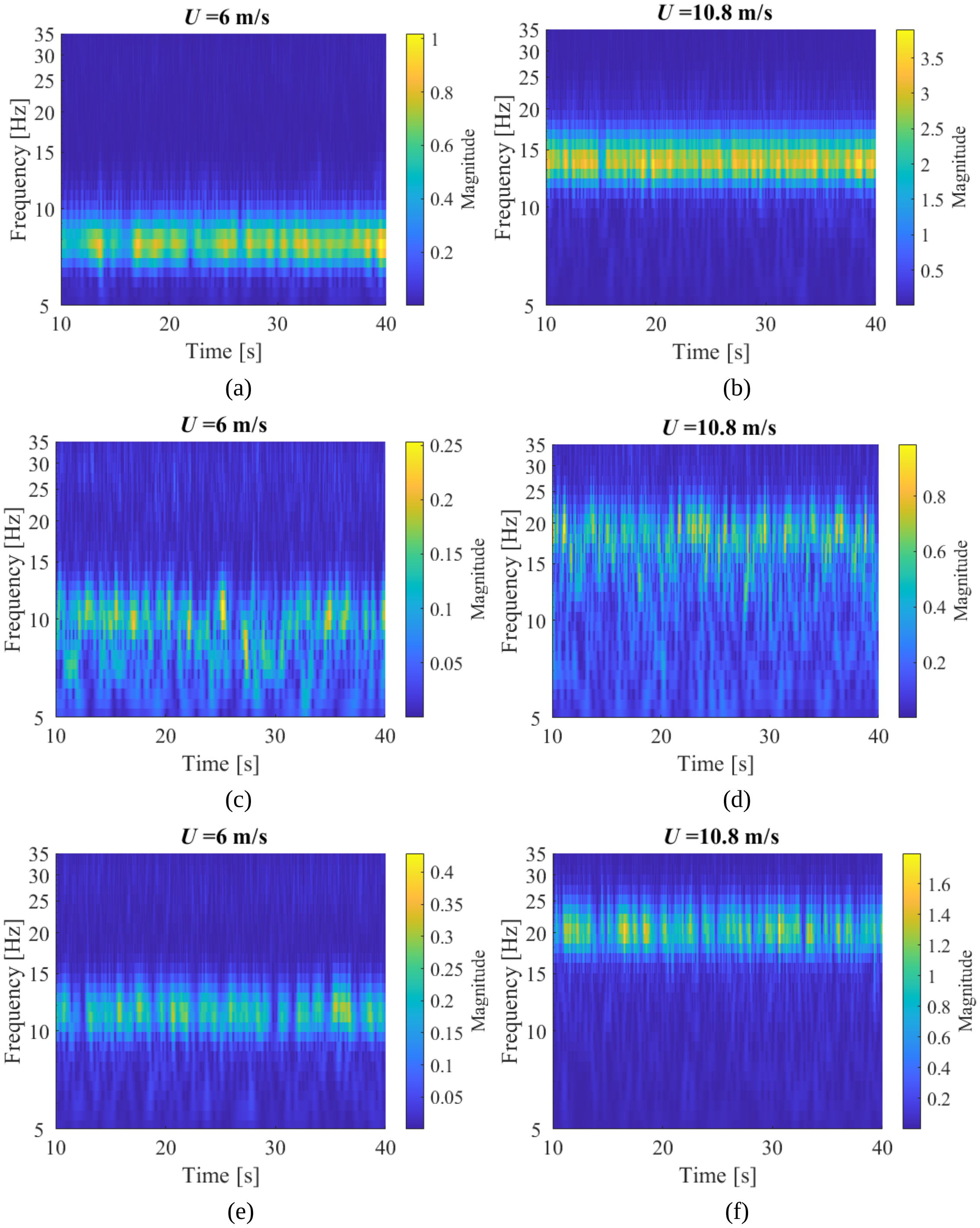

Fig. C.6 TR section: Scalogram of transverse force at α = 0° for (a) U = 6.0 m/s and (b) U = 10.8 m/s; at α = +4° for (c) U = 6.0 m/s and (d) U = 10.8 m/s; and at α = +6° for (e) U = 6.0 m/s and (f) U = 10.8 m/s.

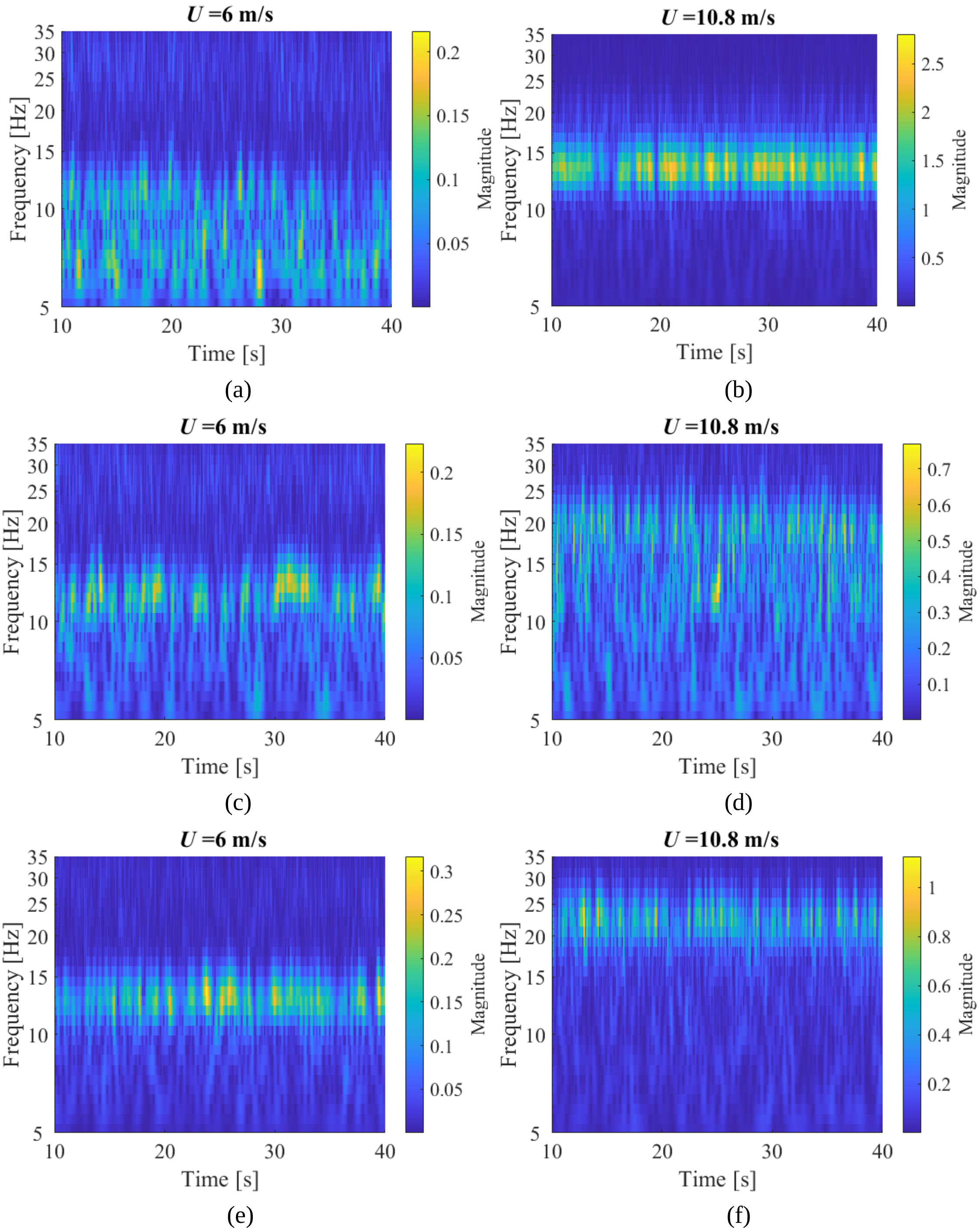

Fig. C.7 C section: Scalogram of transverse force at α = 0° for (a) U = 6.0 m/s and (b) U = 10.8 m/s; at α = +3° for (c) U = 6.0 m/s and (d) U = 10.8 m/s; and at α = +4° for (e) U = 6.0 m/s and (f) U = 10.8 m/s.

Appendix D

Slope of transverse force coefficient for rectangular cylinder with corner modifications at zero angle of attack

The $dC_{Fy}/d\alpha$ value was calculated within the angle of attack ranges of $-1° \leq \alpha \leq +1°$, $-2° \leq \alpha \leq +2°$, $-3° \leq \alpha \leq +3°$ and $-3° \leq \alpha \leq +15°$ by using spline and polynomial curve fitting. The $dC_{Fy}/d\alpha$ values were also listed in Table D.1 to D.4 of Appendix D. Spline curve fitting was found to be more suitable to describe the slope of the transverse force coefficient. According to Table D.1 and D.2, a variation in the $dC_{Fy}/d\alpha$ values was observed between the angle of attack range of $-1° \leq \alpha \leq +1°$, $-2° \leq \alpha \leq +2°$ and $-3° \leq \alpha \leq +15°$. On the other hand, the $dC_{Fy}/d\alpha$ values of $-3° \leq \alpha \leq +3°$ and $-3° \leq \alpha \leq +15°$ were found to be almost identical. Therefore, the $dC_{Fy}/d\alpha$ value is dependent on the number of points used in the calculation. At least three points on each side of the targeted angle (α = 0°) should be used to calculate the slope of the transverse force coefficient.

Table D.1. Slope of transverse force coefficient for rectangular cylinder with various corner modifications at α = 0° by spline curve fitting (U = 6.0 m/s, Re = 36,000).

Section	Slope of transverse force coefficient, $dC_{Fy}/d\alpha$ [rad^{-1}]			
	Angle range ($-1° \leq \alpha \leq +1°$)	Angle range ($-2° \leq \alpha \leq +2°$)	Angle range ($-3° \leq \alpha \leq +3°$)	Angle range ($-3° \leq \alpha \leq +15°$)
R	−3.07	−3.31	−3.27	−3.28
TR	−1.83	−1.95	−1.99	−1.97
DR III	−2.06	−1.93	−2.12	−2.08
DR	−2.82	−2.95	−3.08	−3.08
DR II	−3.65	−4.08	−4.32	−4.32
SR	−2.93	−2.57	−2.79	−2.76
C	−3.05	−2.72	−3.10	−3.17

Table D.2. Slope of transverse force coefficient for rectangular cylinder with various corner modifications at α = 0° by spline curve fitting (U = 10.8 m/s, Re = 64,800).

Section	Slope of transverse force coefficient, $dC_{Fy}/d\alpha$ [rad^{-1}]			
	Angle range ($-1° \leq \alpha \leq +1°$)	Angle range ($-2° \leq \alpha \leq +2°$)	Angle range ($-3° \leq \alpha \leq +3°$)	Angle range ($-3° \leq \alpha \leq +15°$)
R	−3.52	−3.81	−3.74	−3.74
TR	−2.65	−2.95	−2.99	−2.95
DR III	−2.07	−1.92	−2.14	−2.08
DR	−0.82	−1.33	−1.21	−1.20
DR II	−4.20	−3.85	−3.96	−3.97
SR	−3.80	−3.53	−3.69	−3.68
C	−3.30	−3.14	−3.49	−3.45

Table D.3. Slope of transverse force coefficient for rectangular cylinder with various corner modifications at α = 0° by polynomial curve fitting (U = 6.0 m/s, Re = 36,000).

Section	Slope of transverse force coefficient, $dC_{Fy}/d\alpha$ [rad^{-1}]			
	Angle range ($-1° \leq \alpha \leq +1°$)	Angle range ($-2° \leq \alpha \leq +2°$)	Angle range ($-3° \leq \alpha \leq +3°$)	Angle range ($-3° \leq \alpha \leq +15°$)
R	−3.07	−2.72	−2.96	−2.31
TR	−1.83	−1.65	−1.64	−1.93
DR III	−2.06	−2.24	−1.72	−1.88
DR II	−3.65	−3.06	−2.77	−2.15
SR	−2.93	−3.43	−2.70	−1.75
DR	−2.82	−2.64	−2.41	−1.81
C	−3.05	−3.50	−2.43	−4.07

Table D.4. Slope of transverse force coefficient for rectangular cylinder with various corner modifications at α = 0° by polynomial curve fitting (U = 10.8 m/s, Re = 64,800).

Section	Slope of transverse force coefficient, $dC_{Fy}/d\alpha$ [rad^{-1}]			
	Angle range ($-1° \leq \alpha \leq +1°$)	Angle range ($-2° \leq \alpha \leq +2°$)	Angle range ($-3° \leq \alpha \leq +3°$)	Angle range ($-3° \leq \alpha \leq +15°$)
R	−3.52	−3.11	−3.46	−2.83
TR	−2.65	−2.23	−2.32	−2.06
DR III	−2.07	−2.28	−1.70	−1.57
DR II	−4.20	−4.68	−4.22	−3.86
SR	−3.80	−4.18	−3.65	−2.63
DR	−0.82	−0.10	−0.70	−0.80
C	−3.30	−3.51	−2.61	−3.48

Appendix E

Amplitude dependencies of rectangular cylinder with corner modifications at zero angle of attack

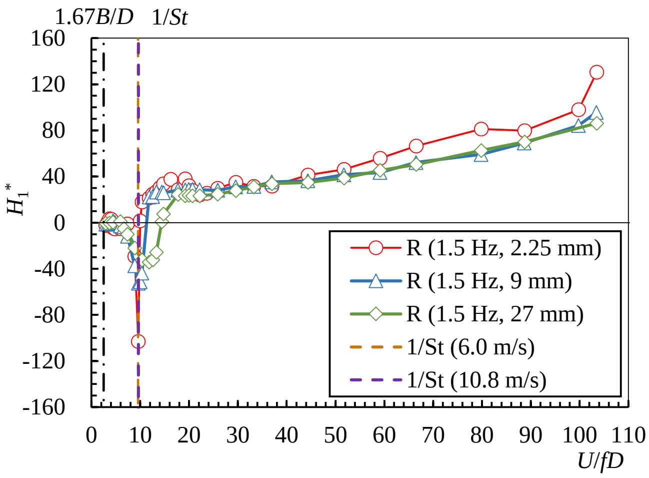

Fig. E.1 Aerodynamic damping H_1^* of R section for the forced vibrating double amplitudes ($2\eta_0$) of 0.025*D*, 0.1*D*, and 0.3*D* at the forced vibrating frequency (*f*) of 1.5 Hz.

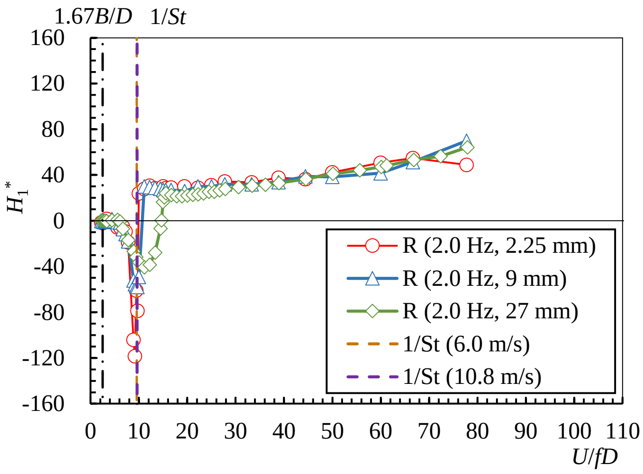

Fig. E.2 Aerodynamic damping H_1^* of R section for the forced vibrating double amplitudes ($2\eta_0$) of 0.025*D*, 0.1*D*, and 0.3*D* at the forced vibrating frequency (*f*) of 2.0 Hz.

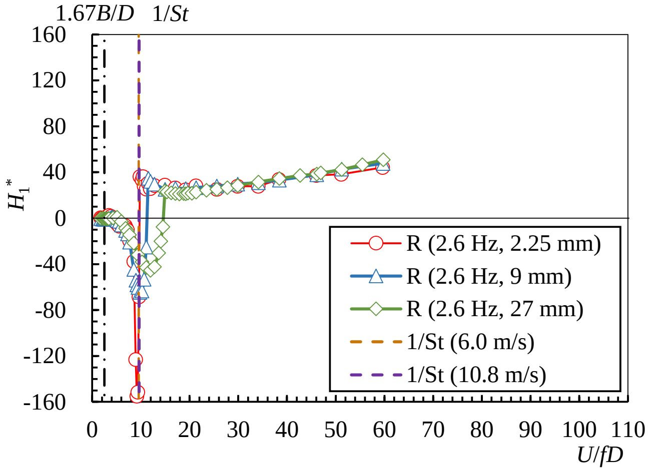

Fig. E.3 Aerodynamic damping H_1^* of R section for the forced vibrating double amplitudes ($2\eta_0$) of 0.025*D*, 0.1*D*, and 0.3*D* at the forced vibrating frequency (*f*) of 2.6 Hz.

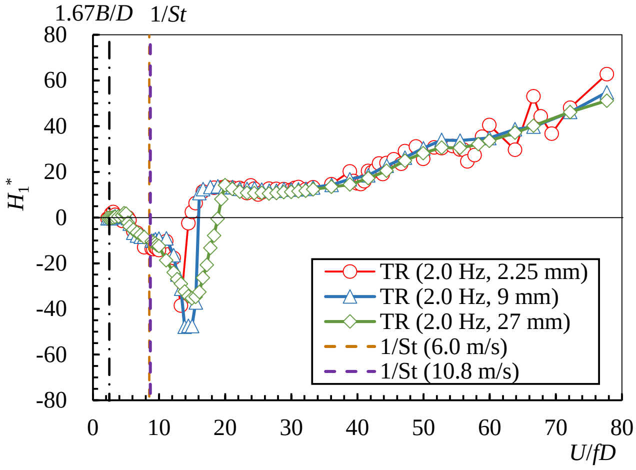

Fig. E.4 Aerodynamic damping H_1^* of TR section for the forced vibrating double amplitudes ($2\eta_0$) of 0.025*D*, 0.1*D*, and 0.3*D* at the forced vibrating frequency (*f*) of 2.0 Hz.

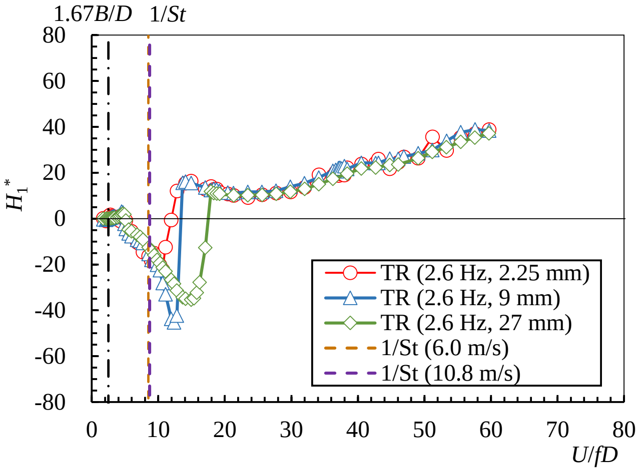

Fig. E.5 Aerodynamic damping H_1^* of TR section for the forced vibrating double amplitudes ($2\eta_0$) of 0.025*D*, 0.1*D*, and 0.3*D* at the forced vibrating frequency (*f*) of 2.6 Hz.

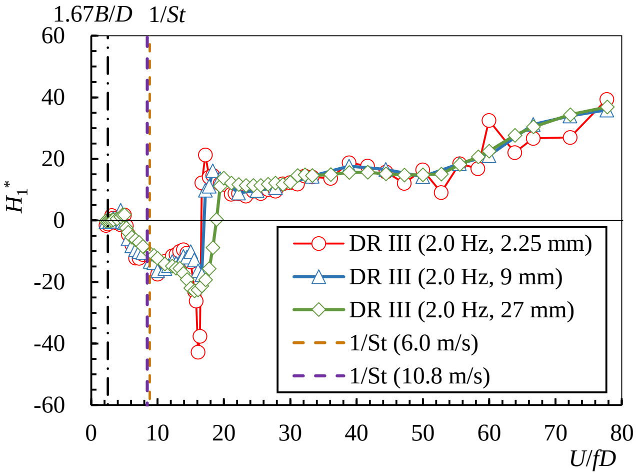

Fig. E.6 Aerodynamic damping H_1^* of DR III section for the forced vibrating double amplitudes ($2\eta_0$) of 0.025D, 0.1D, and 0.3D at the forced vibrating frequency (f) of 2.0 Hz.

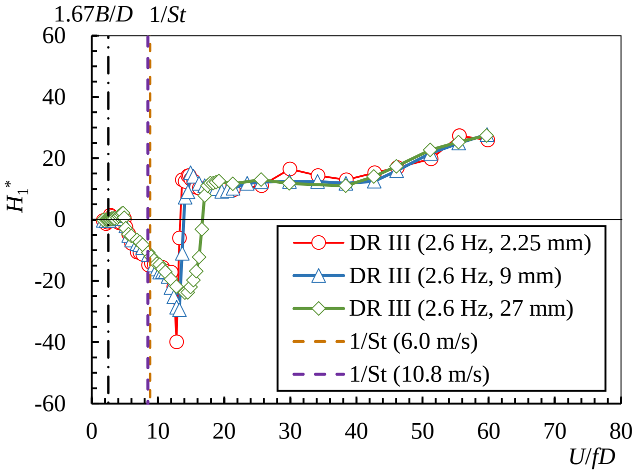

Fig. E.7 Aerodynamic damping H_1^* of DR III section for the forced vibrating double amplitudes ($2\eta_0$) of 0.025D, 0.1D, and 0.3D at the forced vibrating frequency (f) of 2.6 Hz.

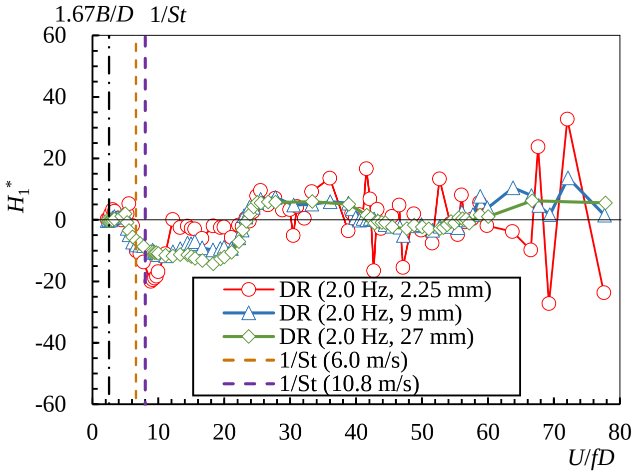

Fig. E.8 Aerodynamic damping H_1^* of DR section for the forced vibrating double amplitudes ($2\eta_0$) of 0.025D, 0.1D, and 0.3D at the forced vibrating frequency (f) of 2.0 Hz.

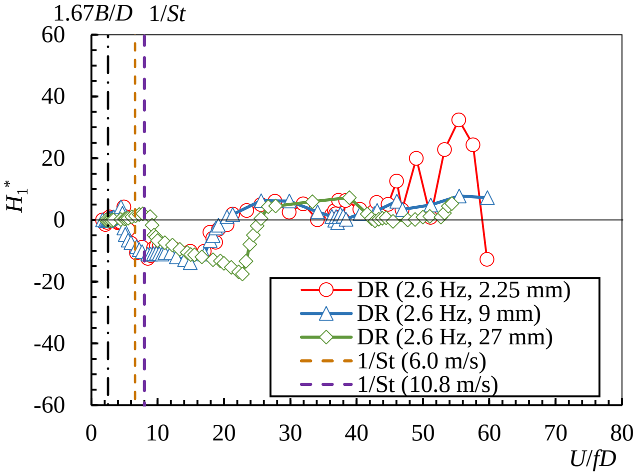

Fig. E.9 Aerodynamic damping H_1^* of DR section for the forced vibrating double amplitudes ($2\eta_0$) of 0.025*D*, 0.1*D*, and 0.3*D* at the forced vibrating frequency (*f*) of 2.6 Hz.

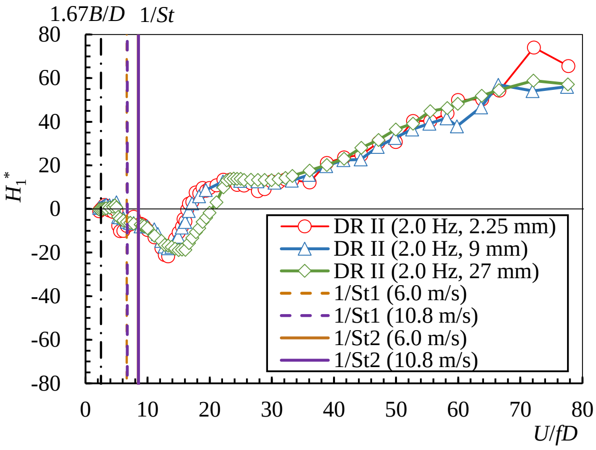

Fig. E.10 Aerodynamic damping H_1^* of DR II section for the forced vibrating double amplitudes ($2\eta_0$) of 0.025*D*, 0.1*D*, and 0.3*D* at the forced vibrating frequency (*f*) of 2.0 Hz.

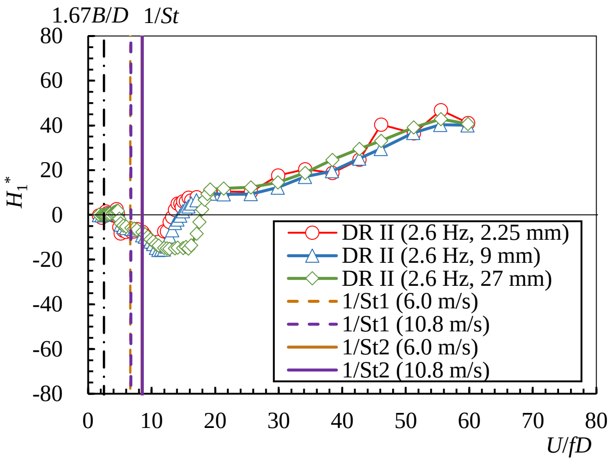

Fig. E.11 Aerodynamic damping H_1^* of DR II section for the forced vibrating double amplitudes ($2\eta_0$) of 0.025*D*, 0.1*D*, and 0.3*D* at the forced vibrating frequency (*f*) of 2.6 Hz.

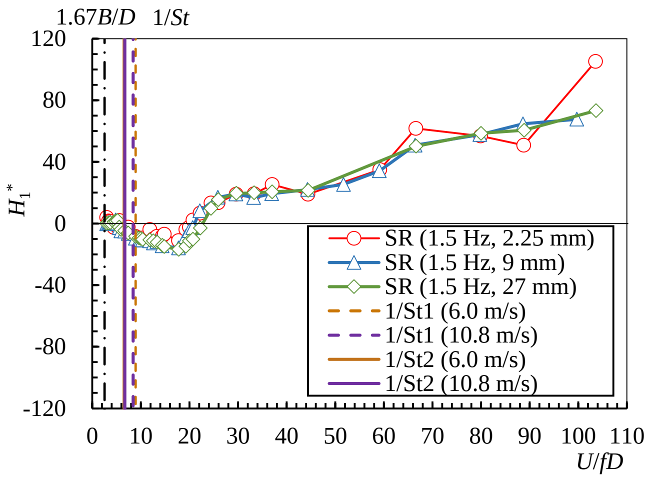

Fig. E.12 Aerodynamic damping H_1^* of SR section for the forced vibrating double amplitudes ($2\eta_0$) of 0.025D, 0.1D, and 0.3D at the forced vibrating frequency (f) of 1.5 Hz.

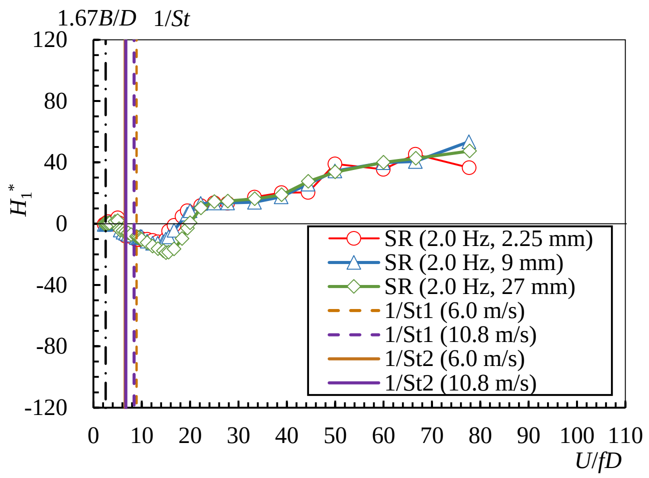

Fig. E.13 Aerodynamic damping H_1^* of SR section for the forced vibrating double amplitudes ($2\eta_0$) of 0.025D, 0.1D, and 0.3D at the forced vibrating frequency (f) of 2.0 Hz.

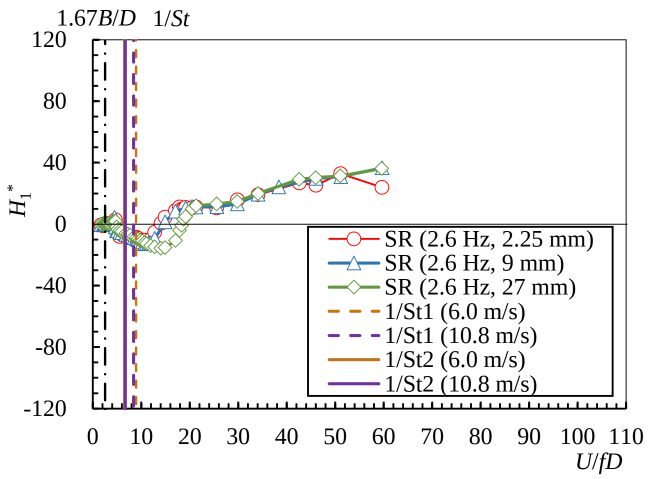

Fig. E.14 Aerodynamic damping H_1^* of SR section for the forced vibrating double amplitudes ($2\eta_0$) of 0.025D, 0.1D, and 0.3D at the forced vibrating frequency (f) of 2.6 Hz.

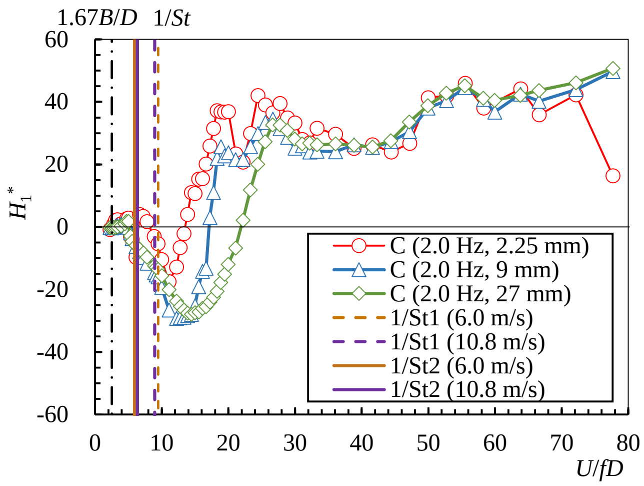

Fig. E.15 Aerodynamic damping H_1^* of C section for the forced vibrating double amplitudes ($2\eta_0$) of 0.025*D*, 0.1*D*, and 0.3*D* at the forced vibrating frequency (*f*) of 2.0 Hz.

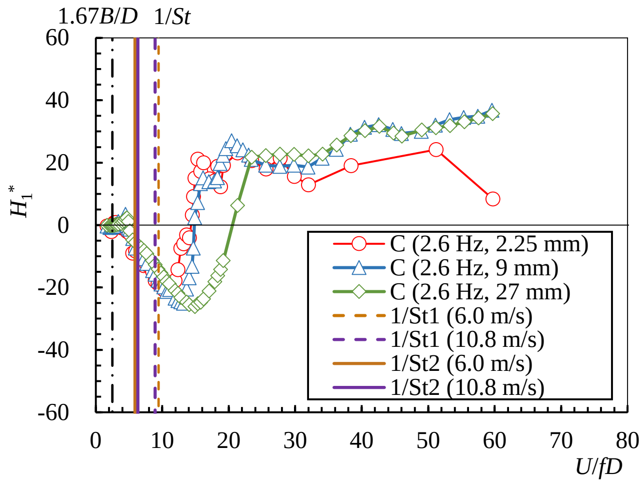

Fig. E.16 Aerodynamic damping H_1^* of C section for the forced vibrating double amplitudes ($2\eta_0$) of 0.025*D*, 0.1*D*, and 0.3*D* at the forced vibrating frequency (*f*) of 2.6 Hz.

Appendix F

Power spectral density and slope of transverse force coefficient for rectangular, triple recession and double recession III modifications at various angles of attack

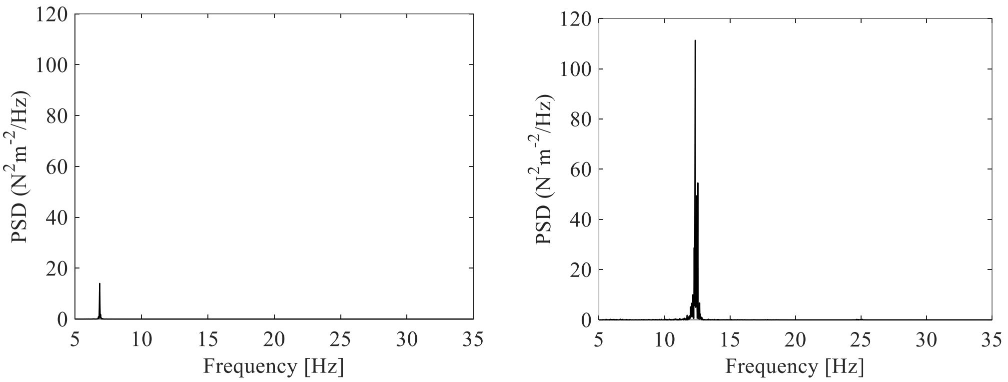

Fig. F.1 Power spectra of transverse force of R section at α = +4° for (a) U = 6.0 m/s; and (b) U = 10.8 m/s.

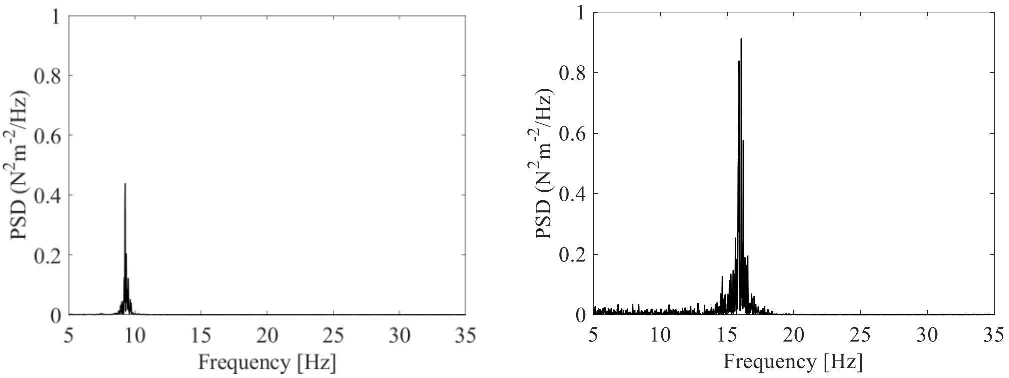

Fig. F.2 Power spectra of transverse force of R section at α = +9° for (a) U = 6.0 m/s; and (b) U = 10.8 m/s.

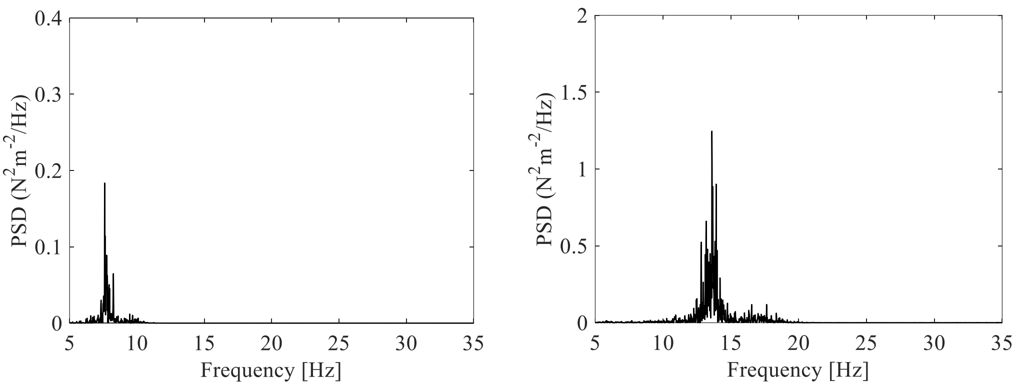

Fig. F.3 Power spectra of transverse force of TR section at α = +2° for (a) U = 6.0 m/s; and (b) U = 10.8 m/s.

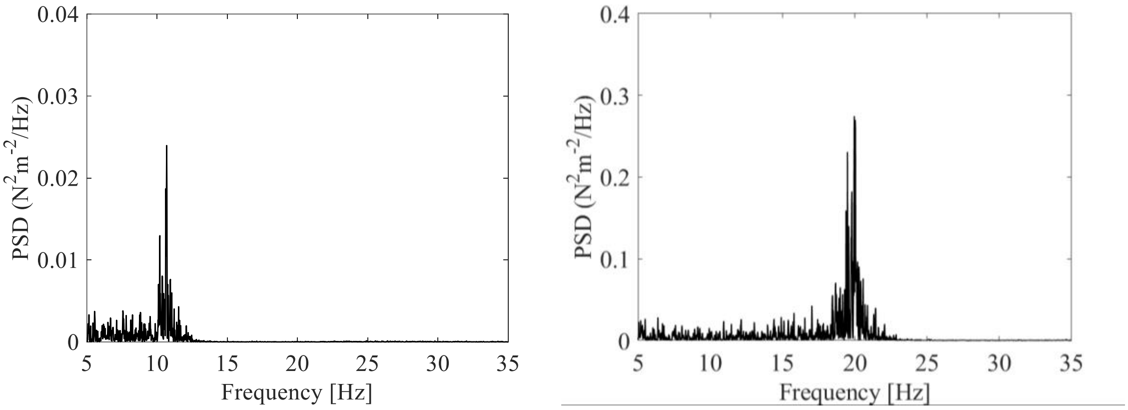

Fig. F.4 Power spectra of transverse force of R section at α = +4° for (a) U = 6.0 m/s; and (b) U = 10.8 m/s.

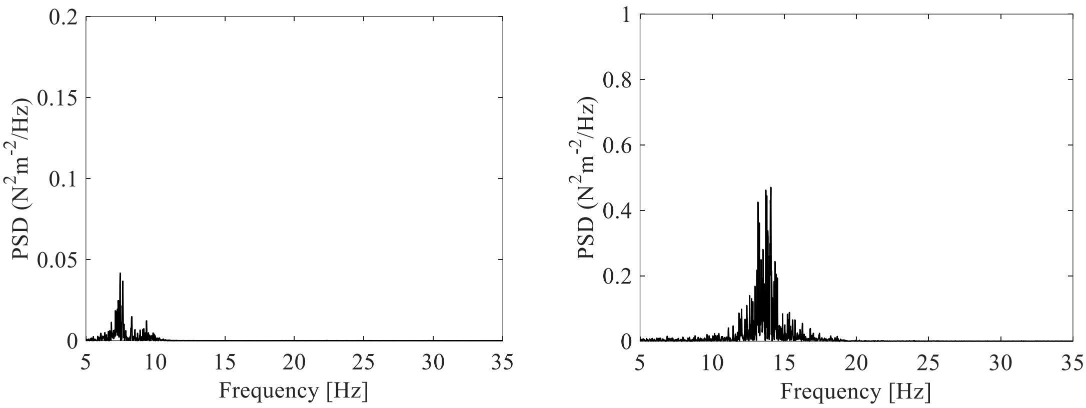

Fig. F.5 Power spectra of transverse force of DR III section at α = +2° for (a) U = 6.0 m/s; and (b) U = 10.8 m/s.

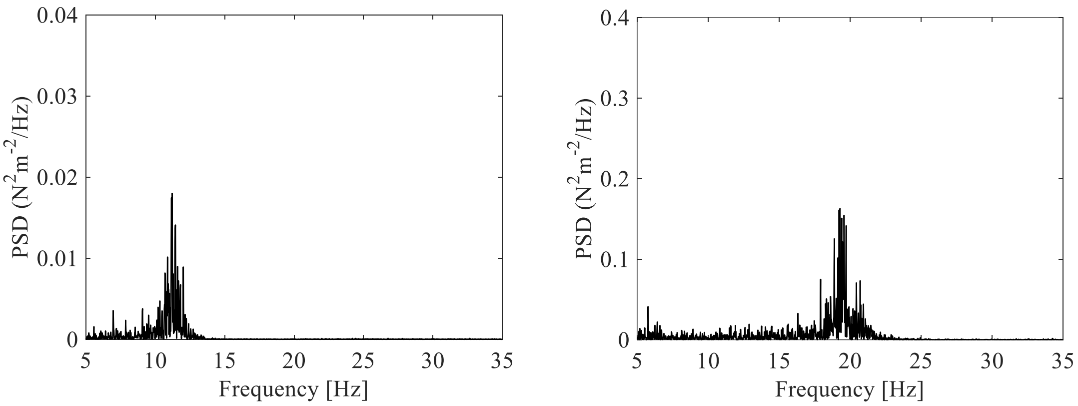

Fig. F.6 Power spectra of transverse force of DR III section at α = +4° for (a) U = 6.0 m/s; and (b) U = 10.8 m/s.

The $dC_{Fy}/d\alpha$ value of TR and DR III sections at α = +2° was calculated within the angle of attack ranges of +1° ≤ α ≤ +3° (3 points), 0° ≤ α ≤ +4° (5 points), −1° ≤ α ≤ +5° (7 points), and −3° ≤ α ≤ +15° (19 points) by using spline curve fitting and polynomial curve fitting. The $dC_{Fy}/d\alpha$ value of R, TR and DR III sections at α = +4° was calculated within the angle of attack ranges of +3° ≤ α ≤ +5°

(3 points), +2° ≤ α ≤ +6° (5 points), +1° ≤ α ≤ +7° (7 points), and −3° ≤ α ≤ +15° (19 points). The $dC_{Fy}/d\alpha$ value of the R section at α = +9° was calculated within the angle of attack ranges of +8° ≤ α ≤ +10° (3 points), +7° ≤ α ≤ +11° (5 points), +6° ≤ α ≤ +12° (7 points), and −3° ≤ α ≤ +15° (19 points). It was found that the $dC_{Fy}/d\alpha$ values varied slightly based on the attack angle range considered during the calculation of the slope of the transverse force coefficient as listed in Tables F.1-F.6 of Appendix F. When the slope of the transverse force coefficient was calculated considering 3 and 5 consecutive points, a notable variation in the $dC_{Fy}/d\alpha$ values was observed with the rest (7 and 19 consecutive points) in the +4° of TR and DR III sections (Table F.3 and F.4). On the other hand, the $dC_{Fy}/d\alpha$ values calculated considering 7 and 19 consecutive points were similar to each other. A similar phenomenon in the $dC_{Fy}/d\alpha$ values was also observed in the +9° of the R section (Table F.5 and F.6). These attack angles (+4° in TR and DR III, +9° in R) were just before the attack angle where flow reattachment was known to be observed (+5° in TR and DR III, +10° in R). In these angles, the number of points (the number of angles of attack) considered to calculate the slope can affect the $dC_{Fy}/d\alpha$ values. Thus, the U_{cr_quasi} values could also fluctuate depending on the considered angle of attack range in the slope calculation.

Table F.1. Slope of transverse force coefficient for TR and DR III sections at α = +2° by spline curve fitting (U = 6.0 m/s, Re = 36,000).

Section	Slope of transverse force coefficient, $dC_{Fy}/d\alpha$ [rad^{-1}]			
	Angle range (+1° ≤ α ≤ +3°)	Angle range (0° ≤ α ≤ +4°)	Angle range (−1° ≤ α ≤ +5°)	Angle range (−3° ≤ α ≤ +15°)
TR	−1.66	−1.04	−1.20	−1.25
DR III	−4.48	−4.23	−4.01	−4.11

Table F.2. Slope of transverse force coefficient for TR and DR III sections at α = +2° by spline curve fitting (U = 10.8 m/s, Re = 64,800).

Section	Slope of transverse force coefficient, $dC_{Fy}/d\alpha$ [rad^{-1}]			
	Angle range (+1° ≤ α ≤ +3°)	Angle range (0° ≤ α ≤ +4°)	Angle range (−1° ≤ α ≤ +5°)	Angle range (−3° ≤ α ≤ +15°)
TR	−1.77	−0.68	−0.81	−0.90
DR III	−4.52	−4.05	−3.79	−3.88

Table F.3. Slope of transverse force coefficient for R, TR and DR III sections at α = +4° by spline curve fitting (U = 6.0 m/s, Re = 36,000).

Section	Slope of transverse force coefficient, $dC_{Fy}/d\alpha$ [rad^{-1}]			
	Angle range (+3° ≤ α ≤ +5°)	Angle range (+2° ≤ α ≤ +6°)	Angle range (+1° ≤ α ≤ +7°)	Angle range (−3° ≤ α ≤ +15°)
R	−1.31	−1.27	−1.30	−1.29
TR	−7.49	−8.99	−8.57	−8.56
DR III	−5.66	−7.29	−7.06	−7.07

Table F.4. Slope of transverse force coefficient for R, TR and DR III sections at α = +4° by spline curve fitting (U = 10.8 m/s, Re = 64,800).

Section	Slope of transverse force coefficient, $dC_{Fy}/d\alpha$ [rad^{-1}]			
	Angle range (+3° ≤ α ≤ +5°)	Angle range (+2° ≤ α ≤ +6°)	Angle range (+1° ≤ α ≤ +7°)	Angle range (−3° ≤ α ≤ +15°)
R	−1.23	−1.17	−1.19	−1.19
TR	−9.41	−11.90	−11.47	−11.43
DR III	−6.57	−8.26	−7.93	−7.94

Table F.5. Slope of transverse force coefficient for R section at α = +9° by spline curve fitting (U = 6.0 m/s, Re = 36,000).

Section	Slope of transverse force coefficient, $dC_{Fy}/d\alpha$ [rad^{-1}]			
	Angle range (+8° ≤ α ≤ +10°)	Angle range (+7° ≤ α ≤ +11°)	Angle range (+6° ≤ α ≤ +12°)	Angle range (−3° ≤ α ≤ +15°)
R	−6.12	−8.91	−8.76	−8.78

Table F.6. Slope of transverse force coefficient for R section at α = +9° by spline curve fitting (U = 10.8 m/s, Re = 64,800).

Section	Slope of transverse force coefficient, $dC_{Fy}/d\alpha$ [rad^{-1}]			
	Angle range (+8° ≤ α ≤ +10°)	Angle range (+7° ≤ α ≤ +11°)	Angle range (+6° ≤ α ≤ +12°)	Angle range (−3° ≤ α ≤ +15°)
R	−7.92	−11.29	−11.02	−10.97

Table F.7. Slope of transverse force coefficient for TR and DR III sections at α = +2° by polynomial curve fitting (U = 6.0 m/s, Re = 36,000).

Section	Slope of transverse force coefficient, $dC_{Fy}/d\alpha$ [rad^{-1}]			
	Angle range (+1° ≤ α ≤ +3°)	Angle range (0° ≤ α ≤ +4°)	Angle range (−1° ≤ α ≤ +5°)	Angle range (−3° ≤ α ≤ +15°)
TR	−1.66	−2.52	−1.76	−1.85
DR III	−4.48	−4.84	−4.17	−6.45

Table F.8. Slope of transverse force coefficient for TR and DR III sections at α = +2° by polynomial curve fitting (U = 10.8 m/s, Re = 64,800).

Section	Slope of transverse force coefficient, $dC_{Fy}/d\alpha$ [rad^{-1}]			
	Angle range (+1° ≤ α ≤ +3°)	Angle range (0° ≤ α ≤ +4°)	Angle range (−1° ≤ α ≤ +5°)	Angle range (−3° ≤ α ≤ +15°)
TR	−1.77	−3.31	−2.33	−3.05
DR III	−4.52	−5.19	−4.01	−6.99

Table F.9. Slope of transverse force coefficient for R, TR and DR III sections at α = +4° by polynomial curve fitting (U = 6.0 m/s, Re = 36,000).

Section	Slope of transverse force coefficient, $dC_{Fy}/d\alpha$ [rad^{-1}]			
	Angle range (+3° ≤ α ≤ +5°)	Angle range (+2° ≤ α ≤ +6°)	Angle range (+1° ≤ α ≤ +7°)	Angle range (−3° ≤ α ≤ +15°)
R	−1.31	−1.29	−1.28	−0.36
TR	−7.49	−8.36	−7.30	−6.98
DR III	−5.66	−6.61	−6.93	−3.46

Table F.10. Slope of transverse force coefficient for R, TR and DR III sections at α = +4° by polynomial curve fitting (U = 10.8 m/s, Re = 64,800).

Section	Slope of transverse force coefficient, $dC_{Fy}/d\alpha$ [rad^{-1}]			
	Angle range (+3° ≤ α ≤ +5°)	Angle range (+2° ≤ α ≤ +6°)	Angle range (+1° ≤ α ≤ +7°)	Angle range (−3° ≤ α ≤ +15°)
R	−1.23	−1.19	−1.23	−0.22
TR	−9.41	−10.86	−8.48	−7.58
DR III	−6.57	−7.56	−7.85	−4.31

Table F.11. Slope of transverse force coefficient for R section at α = +9° by polynomial curve fitting (U = 6.0 m/s, Re = 36,000).

Section	Slope of transverse force coefficient, $dC_{Fy}/d\alpha$ [rad^{-1}]			
	Angle range (+8° ≤ α ≤ +10°)	Angle range (+7° ≤ α ≤ +11°)	Angle range (+6° ≤ α ≤ +12°)	Angle range (−3° ≤ α ≤ +15°)
R	−6.12	−7.75	−8.40	−5.11

Table F.12. Slope of transverse force coefficient for R section at α = +9° by polynomial curve fitting (U = 10.8 m/s, Re = 64,800).

Section	Slope of transverse force coefficient, $dC_{Fy}/d\alpha$ [rad^{-1}]			
	Angle range (+8° ≤ α ≤ +10°)	Angle range (+7° ≤ α ≤ +11°)	Angle range (+6° ≤ α ≤ +12°)	Angle range (−3° ≤ α ≤ +15°)
R	−7.92	−9.88	−10.64	−8.26

Appendix G

Kármán vortex shedding frequency (f_{kv}) and vibrating frequency (f_{vib}) of the rectangular cylinder with corner modifications at zero angle of attack

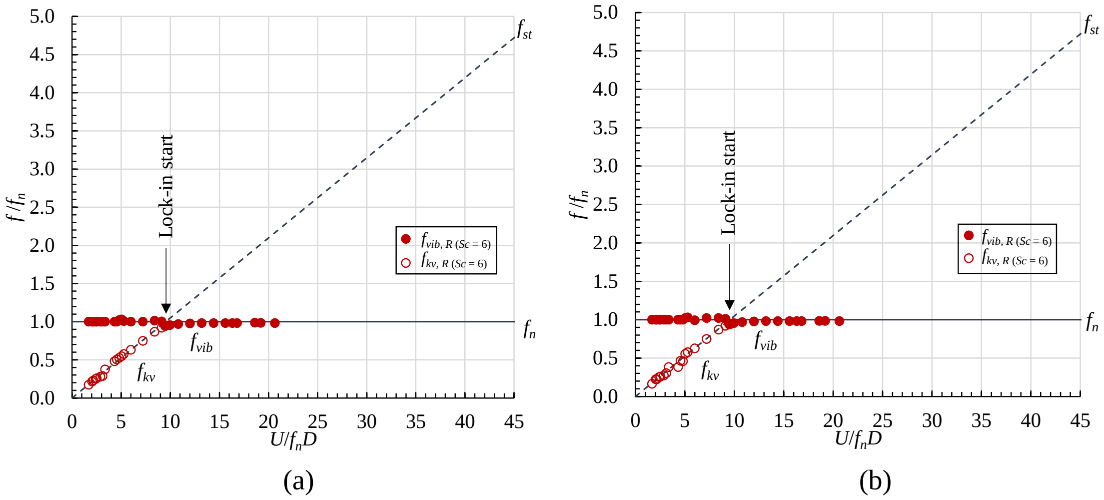

Fig. G.1 Kármán vortex shedding frequency (circle) and vibrating frequency (filled circle) (dash slope line: stationary, circle and filled circle: vibrating) of R section for $S_{c\eta}$ = 6 under (a) Without, and (b) With initial vibration conditions.

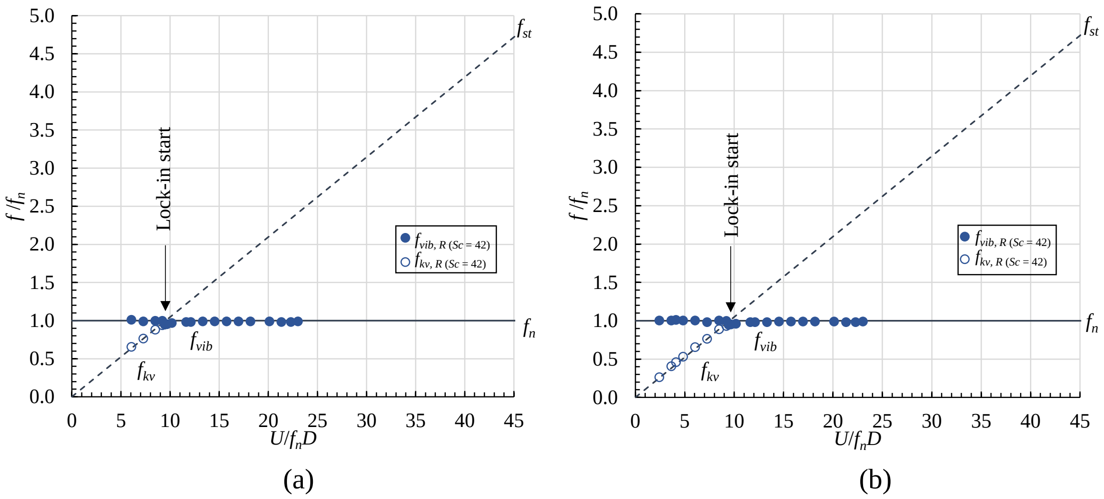

Fig. G.2 Kármán vortex shedding frequency (circle) and vibrating frequency (filled circle) (dash slope line: stationary, circle and filled circle: vibrating) of R section for $S_{c\eta}$ = 42 under (a) Without, and (b) With initial vibration conditions.

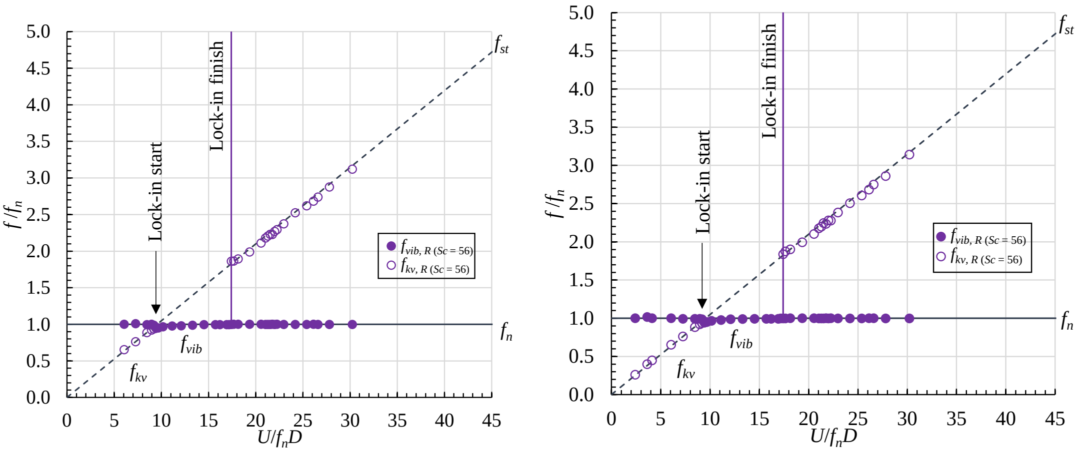

(a) (b)

Fig. G.3 Kármán vortex shedding frequency (circle) and vibrating frequency (filled circle) (dash slope line: stationary, circle and filled circle: vibrating) of R section for $S_{c\eta}$ = 56 under (a) Without, and (b) With initial vibration conditions.

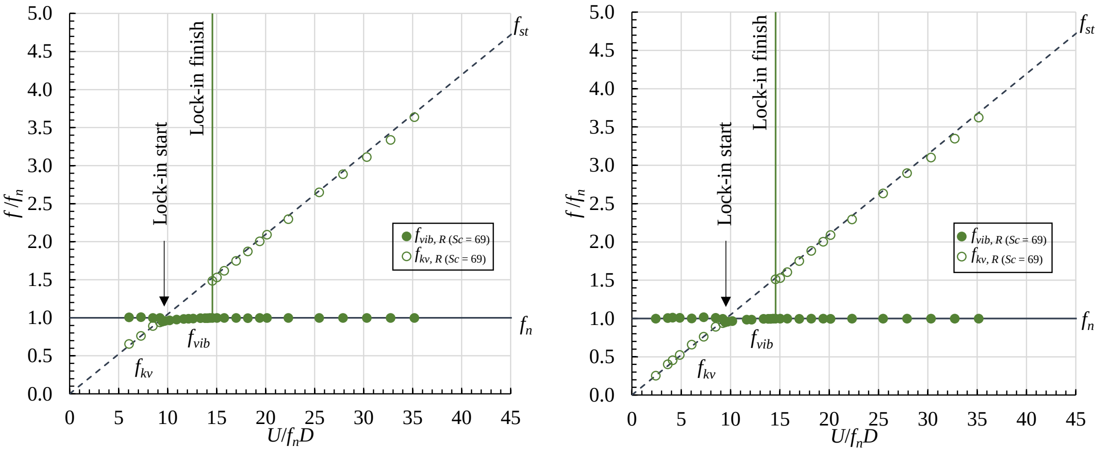

(a) (b)

Fig. G.4 Kármán vortex shedding frequency (circle) and vibrating frequency (filled circle) (dash slope line: stationary, circle and filled circle: vibrating) of R section for $S_{c\eta}$ = 69 under (a) Without, and (b) With initial vibration conditions.

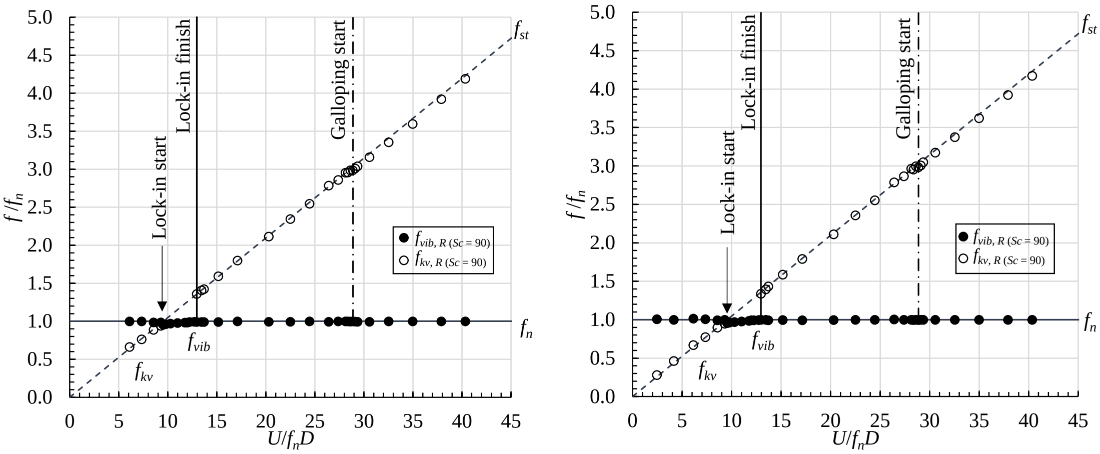

(a) (b)

Fig. G.5 Kármán vortex shedding frequency (circle) and vibrating frequency (filled circle) (dash slope line: stationary, circle and filled circle: vibrating) of R section for $S_{c\eta}$ = 90 under (a) Without, and (b) With initial vibration conditions.

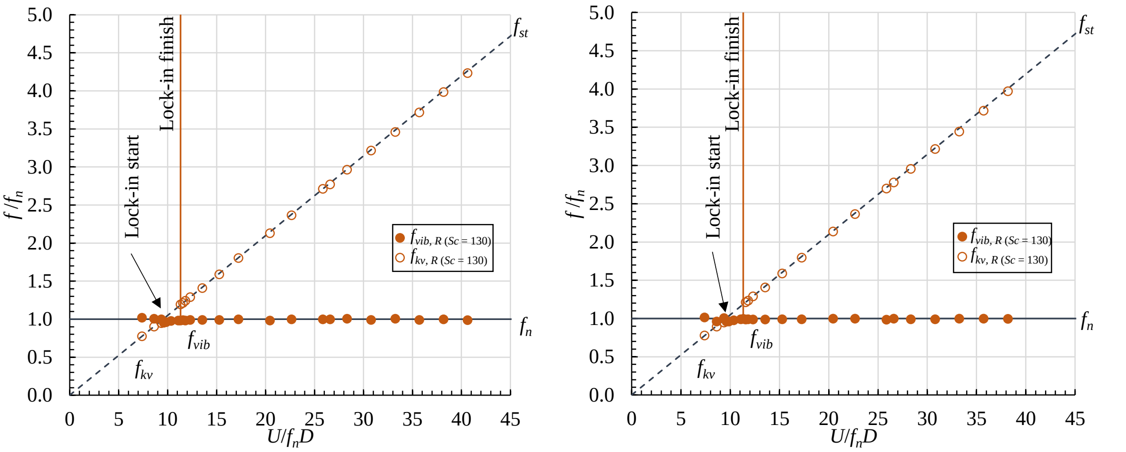

(a) (b)

Fig. G.6 Kármán vortex shedding frequency (circle) and vibrating frequency (filled circle) (dash slope line: stationary, circle and filled circle: vibrating) of R section for $S_{c\eta}$ = 130 under (a) Without, and (b) With initial vibration conditions.

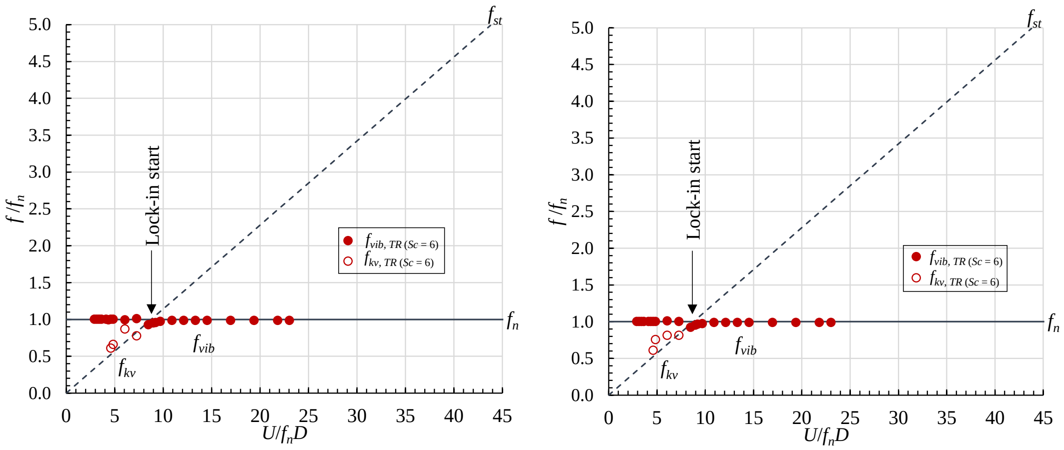

(a) (b)

Fig. G.7 Kármán vortex shedding frequency (circle) and vibrating frequency (filled circle) (dash slope line: stationary, circle and filled circle: vibrating) of TR section for $S_{c\eta}$ = 6 under (a) Without, and (b) With initial vibration conditions.

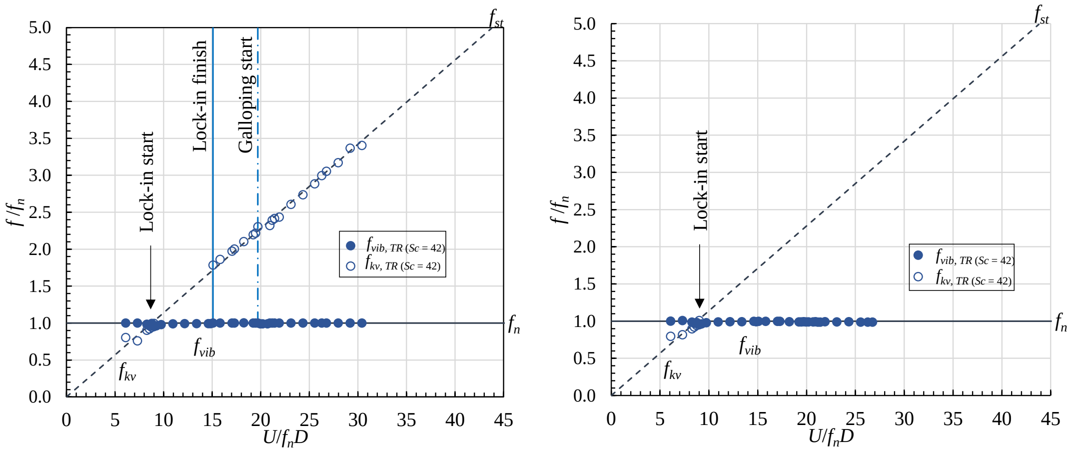

(a) (b)

Fig. G.8 Kármán vortex shedding frequency (circle) and vibrating frequency (filled circle) (dash slope line: stationary, circle and filled circle: vibrating) of TR section for $S_{c\eta}$ = 42 under (a) Without, and (b) With initial vibration conditions.

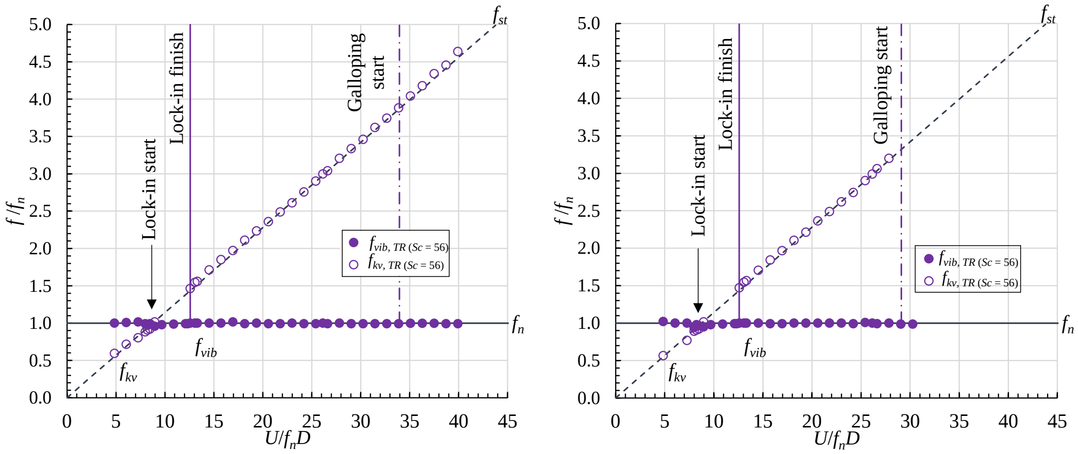

(a) (b)

Fig. G.9 Kármán vortex shedding frequency (circle) and vibrating frequency (filled circle) (dash slope line: stationary, circle and filled circle: vibrating) of TR section for $S_{c\eta}$ = 56 under (a) Without, and (b) With initial vibration conditions.

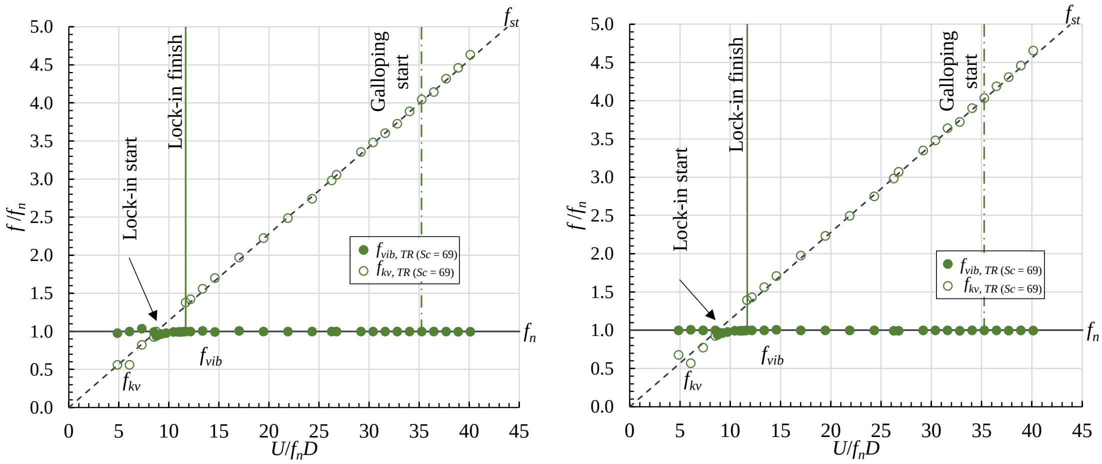

(a) (b)

Fig. G.10 Kármán vortex shedding frequency (circle) and vibrating frequency (filled circle) (dash slope line: stationary, circle and filled circle: vibrating) of TR section for $S_{c\eta}$ = 69 under (a) Without, and (b) With initial vibration conditions.

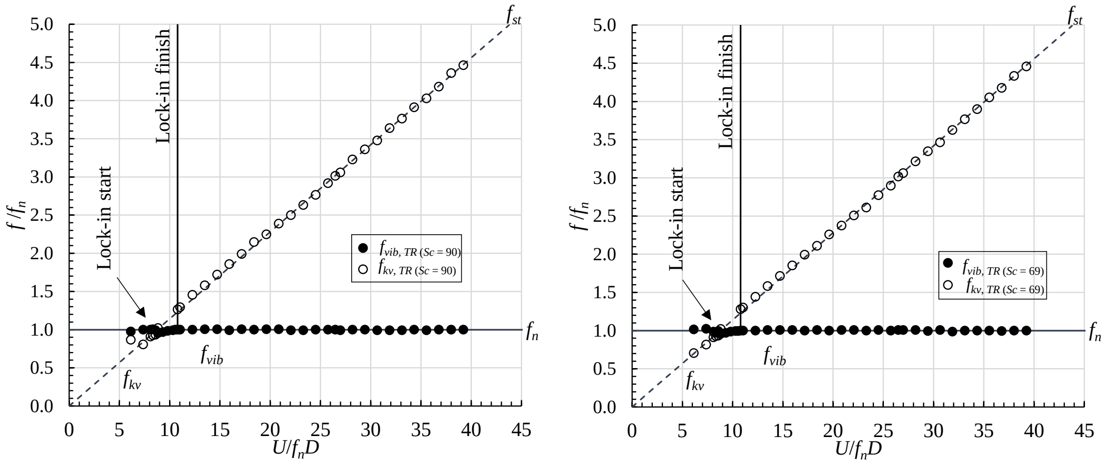

(a) (b)

Fig. G.11 Kármán vortex shedding frequency (circle) and vibrating frequency (filled circle) (dash slope line: stationary, circle and filled circle: vibrating) of TR section for $S_{c\eta}$ = 90 under (a) Without, and (b) With initial vibration conditions.

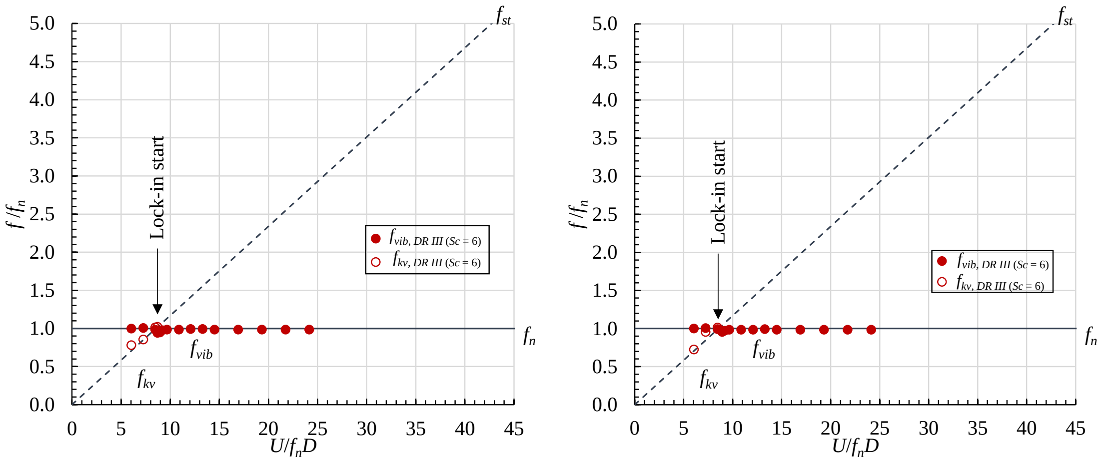

(a) (b)

Fig. G.12 Kármán vortex shedding frequency (circle) and vibrating frequency (filled circle) (dash slope line: stationary, circle and filled circle: vibrating) of DR III section for $S_{c\eta}$ = 6 under (a) Without, and (b) With initial vibration conditions.

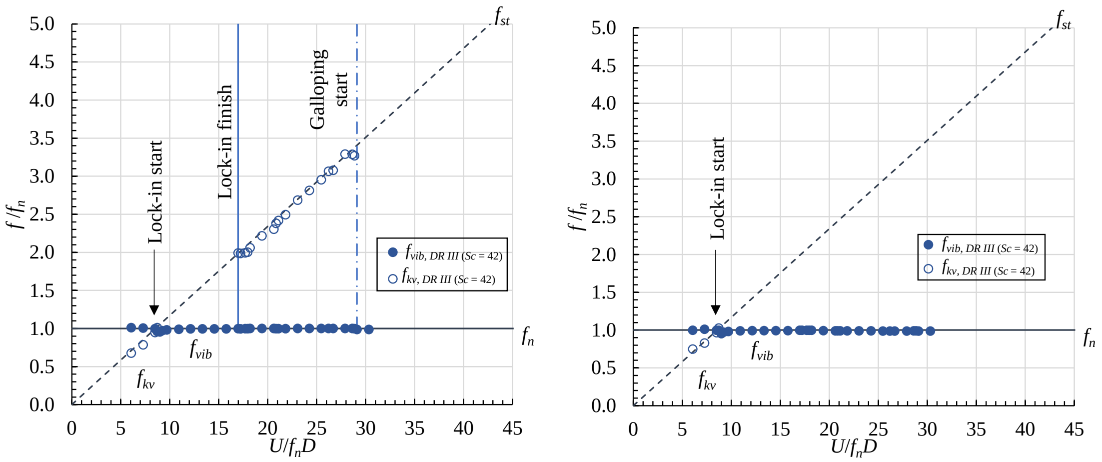

(a) (b)

Fig. G.13 Kármán vortex shedding frequency (circle) and vibrating frequency (filled circle) (dash slope line: stationary, circle and filled circle: vibrating) of DR III section for $S_{c\eta}$ = 42 under (a) Without, and (b) With initial vibration conditions.

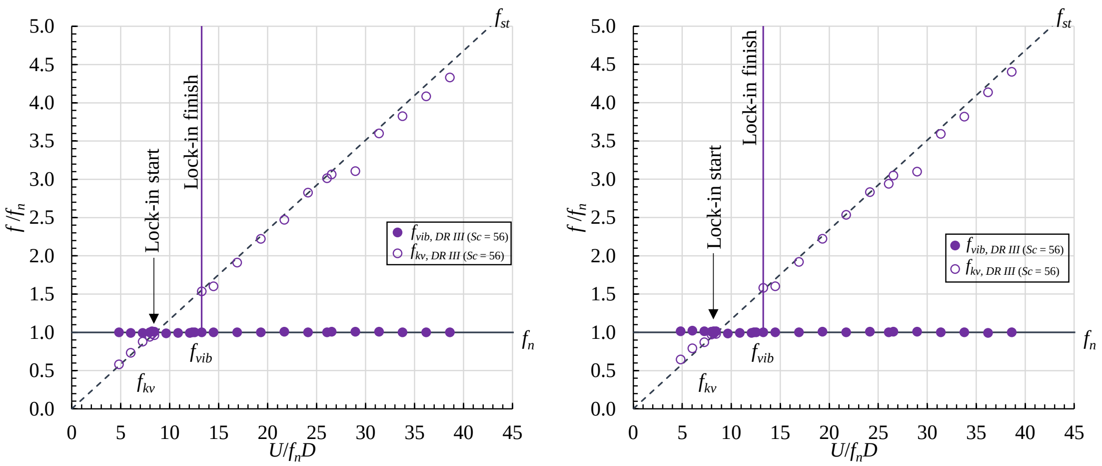

(a) (b)

Fig. G.14 Kármán vortex shedding frequency (circle) and vibrating frequency (filled circle) (dash slope line: stationary, circle and filled circle: vibrating) of DR III section for $S_{c\eta}$ = 56 under (a) Without, and (b) With initial vibration conditions.

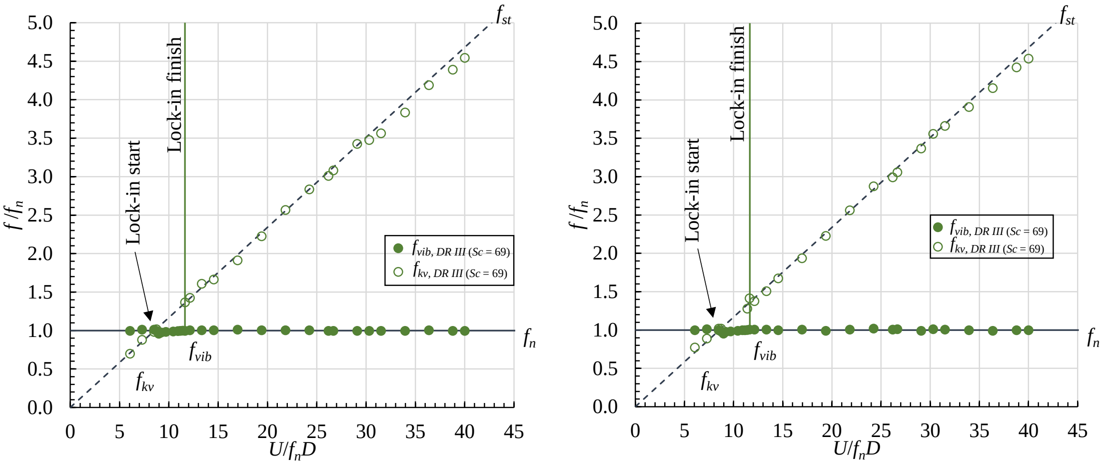

(a) (b)

Fig. G.15 Kármán vortex shedding frequency (circle) and vibrating frequency (filled circle) (dash slope line: stationary, circle and filled circle: vibrating) of DR III section for $S_{c\eta}$ = 69 under (a) Without, and (b) With initial vibration conditions.

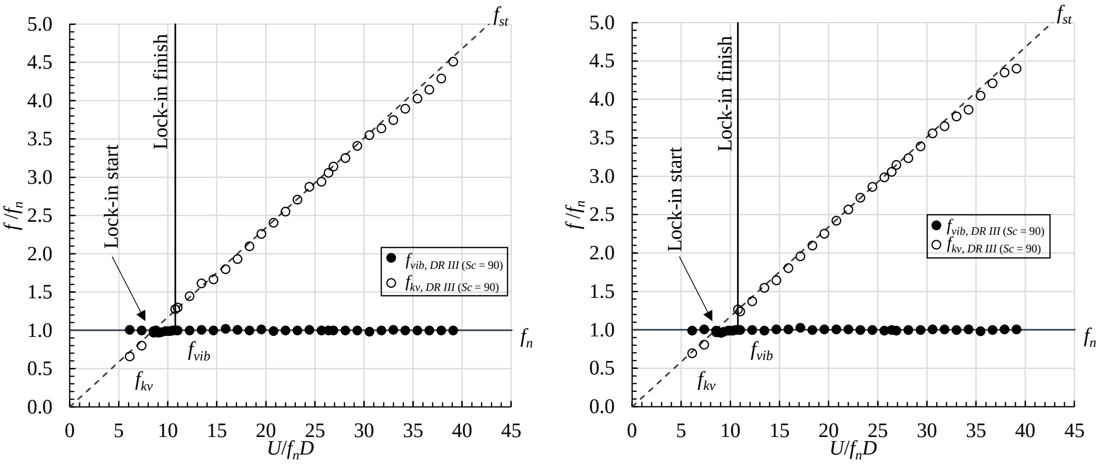

(a) (b)

Fig. G.16 Kármán vortex shedding frequency (circle) and vibrating frequency (filled circle) (dash slope line: stationary, circle and filled circle: vibrating) of DR III section for $S_{c\eta}$ = 90 under (a) Without, and (b) With initial vibration conditions.

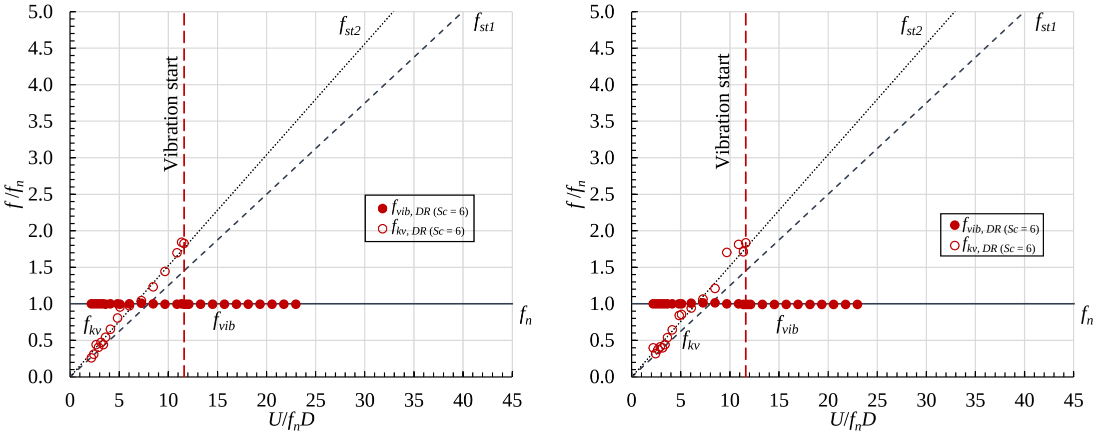

(a) (b)

Fig. G.17 Kármán vortex shedding frequency (circle) and vibrating frequency (filled circle) (dash slope line: stationary, circle and filled circle: vibrating) of DR section for $S_{c\eta}$ = 6 under (a) Without, and (b) With initial vibration conditions.

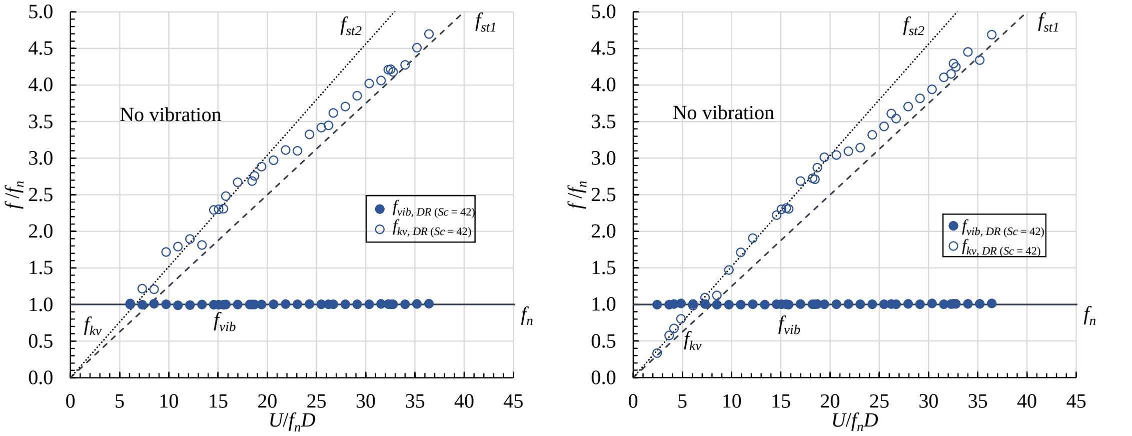

(a) (b)

Fig. G.18 Kármán vortex shedding frequency (circle) and vibrating frequency (filled circle) (dash slope line: stationary, circle and filled circle: vibrating) of DR section for $S_{c\eta}$ = 42 under (a) Without, and (b) With initial vibration conditions.

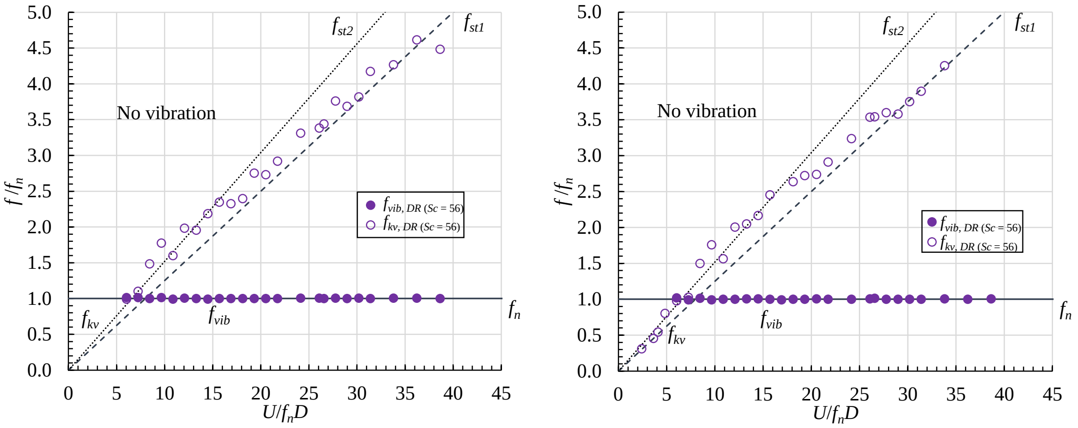

(a) (b)

Fig. G.19 Kármán vortex shedding frequency (circle) and vibrating frequency (filled circle) (dash slope line: stationary, circle and filled circle: vibrating) of DR section for $S_{c\eta}$ = 56 under (a) Without, and (b) With initial vibration conditions.

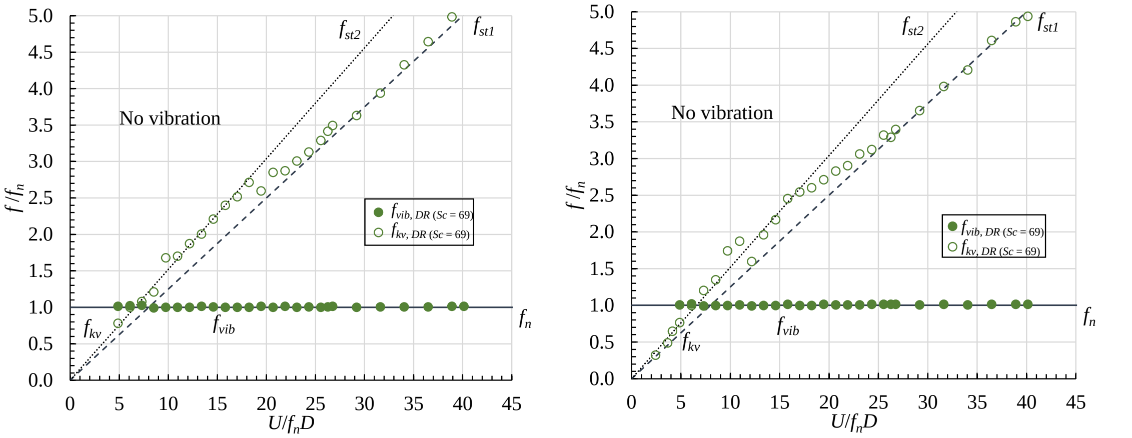

(a) (b)

Fig. G.20 Kármán vortex shedding frequency (circle) and vibrating frequency (filled circle) (dash slope line: stationary, circle and filled circle: vibrating) of DR section for $S_{c\eta}$ = 69 under (a) Without, and (b) With initial vibration conditions.

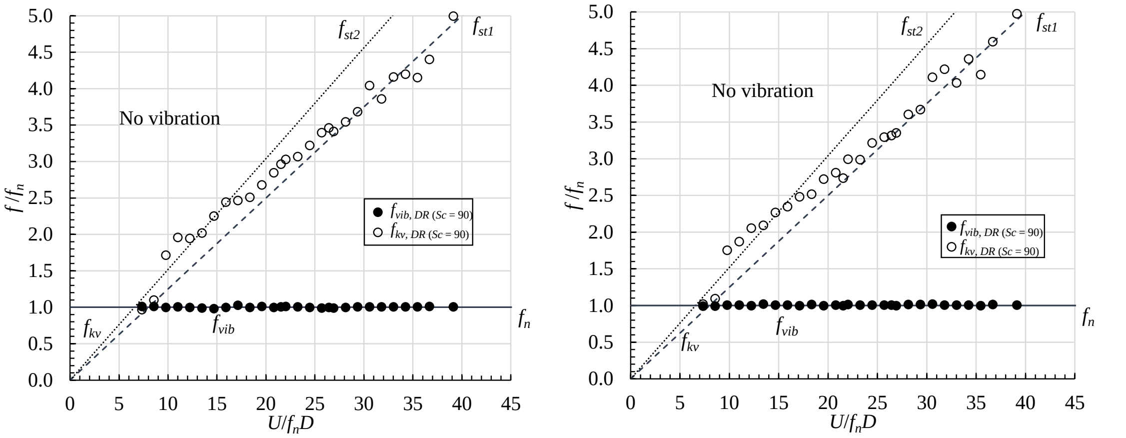

(a) (b)

Fig. G.21 Kármán vortex shedding frequency (circle) and vibrating frequency (filled circle) (dash slope line: stationary, circle and filled circle: vibrating) of DR section for $S_{c\eta}$ = 90 under (a) Without, and (b) With initial vibration conditions.

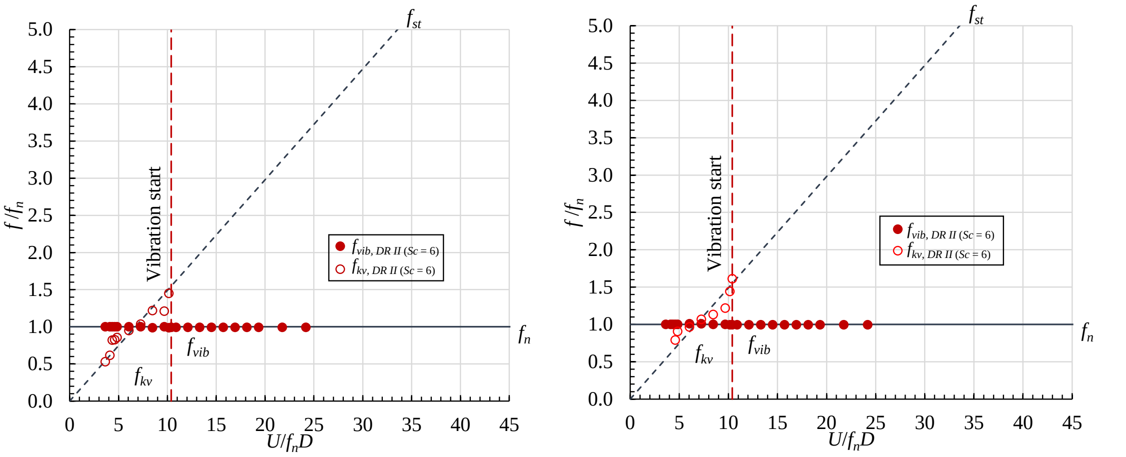

(a) (b)

Fig. G.22 Kármán vortex shedding frequency (circle) and vibrating frequency (filled circle) (dash slope line: stationary, circle and filled circle: vibrating) of DR II section for $S_{c\eta}$ = 6 under (a) Without, and (b) With initial vibration conditions.

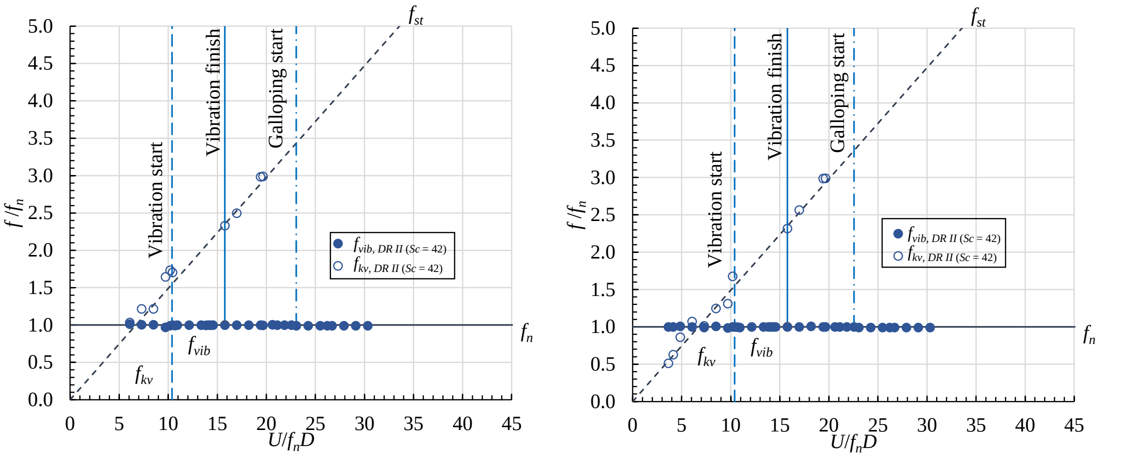

(a) (b)

Fig. G.23 Kármán vortex shedding frequency (circle) and vibrating frequency (filled circle) (dash slope line: stationary, circle and filled circle: vibrating) of DR II section for $S_{c\eta}$ = 42 under (a) Without, and (b) With initial vibration conditions.

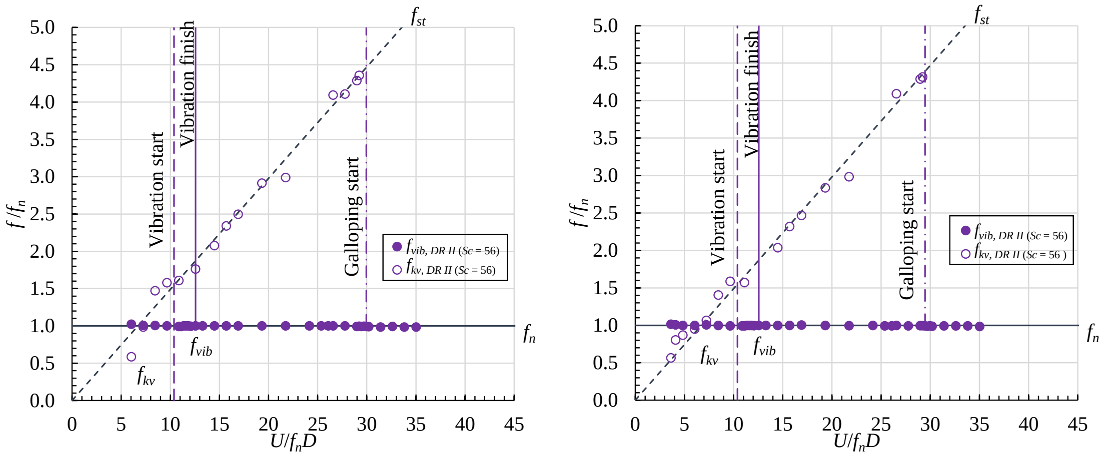

(a) (b)

Fig. G.24 Kármán vortex shedding frequency (circle) and vibrating frequency (filled circle) (dash slope line: stationary, circle and filled circle: vibrating) of DR II section for $S_{c\eta}$ = 56 under (a) Without, and (b) With initial vibration conditions.

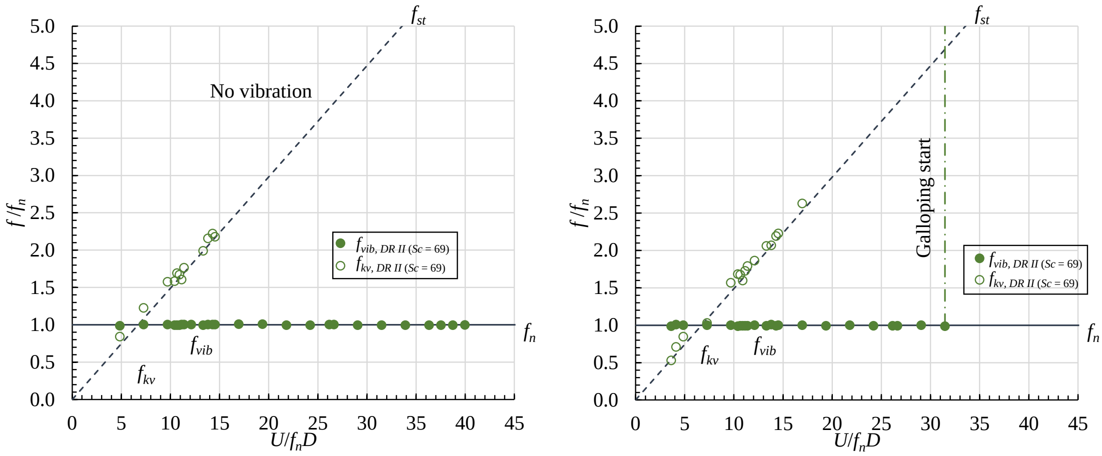

(a) (b)

Fig. G.25 Kármán vortex shedding frequency (circle) and vibrating frequency (filled circle) (dash slope line: stationary, circle and filled circle: vibrating) of DR II section for $S_{c\eta}$ = 69 under (a) Without, and (b) With initial vibration conditions.

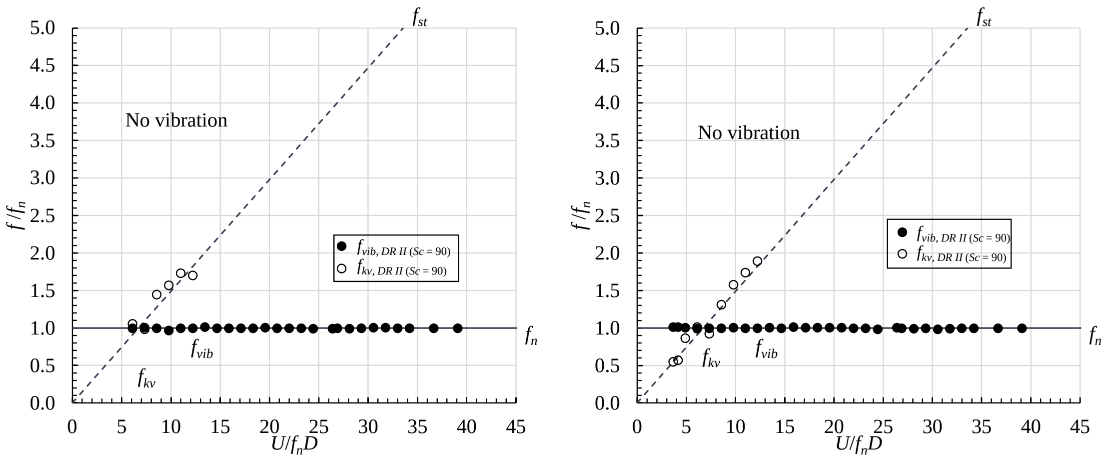

(a) (b)

Fig. G.26 Kármán vortex shedding frequency (circle) and vibrating frequency (filled circle) (dash slope line: stationary, circle and filled circle: vibrating) of DR II section for $S_{c\eta}$ = 90 under (a) Without, and (b) With initial vibration conditions.

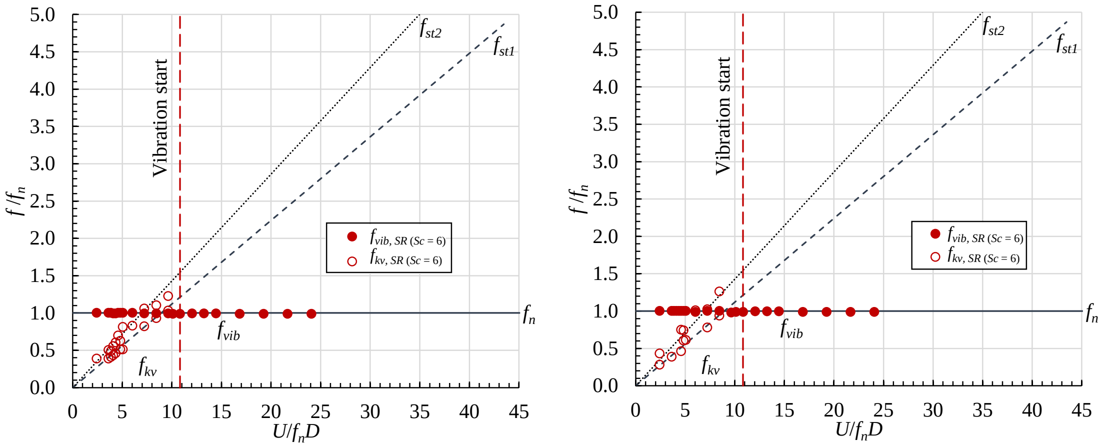

(a) (b)

Fig. G.27 Kármán vortex shedding frequency (circle) and vibrating frequency (filled circle) (dash slope line: stationary, circle and filled circle: vibrating) of SR section for $S_{c\eta}$ = 6 under (a) Without, and (b) With initial vibration conditions.

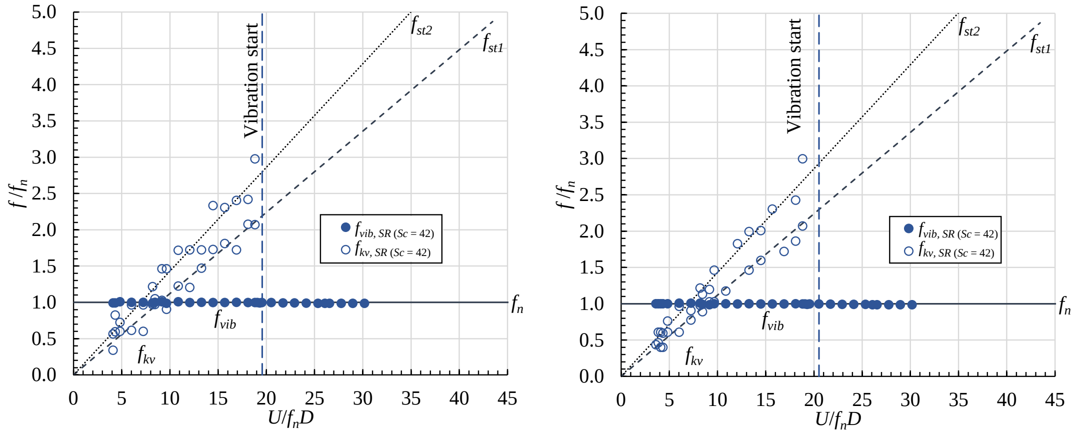

(a) (b)

Fig. G.28 Kármán vortex shedding frequency (circle) and vibrating frequency (filled circle) (dash slope line: stationary, circle and filled circle: vibrating) of SR section for $S_{c\eta}$ = 42 under (a) Without, and (b) With initial vibration conditions.

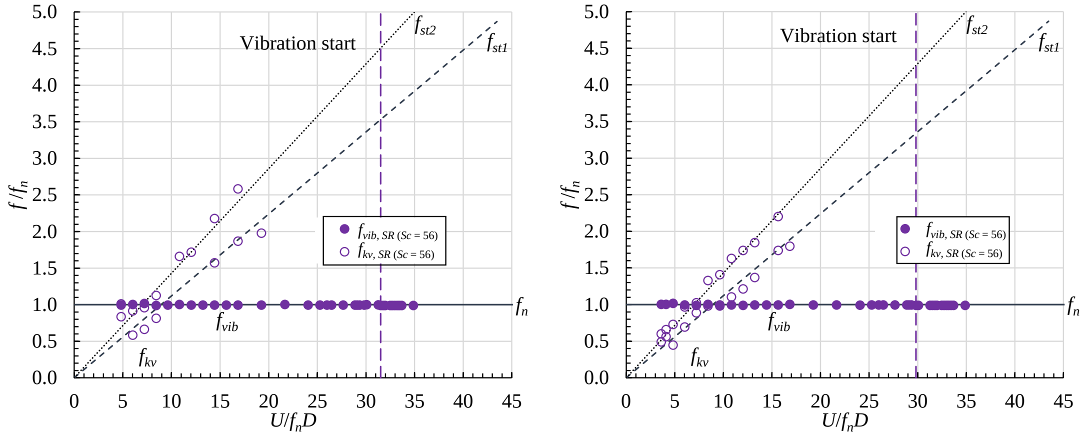

(a) (b)

Fig. G.29 Kármán vortex shedding frequency (circle) and vibrating frequency (filled circle) (dash slope line: stationary, circle and filled circle: vibrating) of SR section for $S_{c\eta}$ = 56 under (a) Without, and (b) With initial vibration conditions.

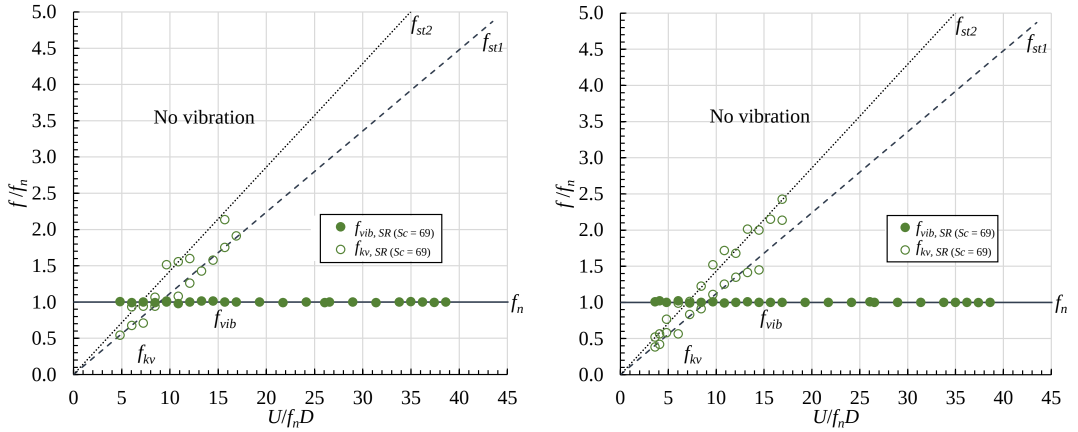

(a) (b)

Fig. G.30 Kármán vortex shedding frequency (circle) and vibrating frequency (filled circle) (dash slope line: stationary, circle and filled circle: vibrating) of SR section for $S_{c\eta}$ = 69 under (a) Without, and (b) With initial vibration conditions.

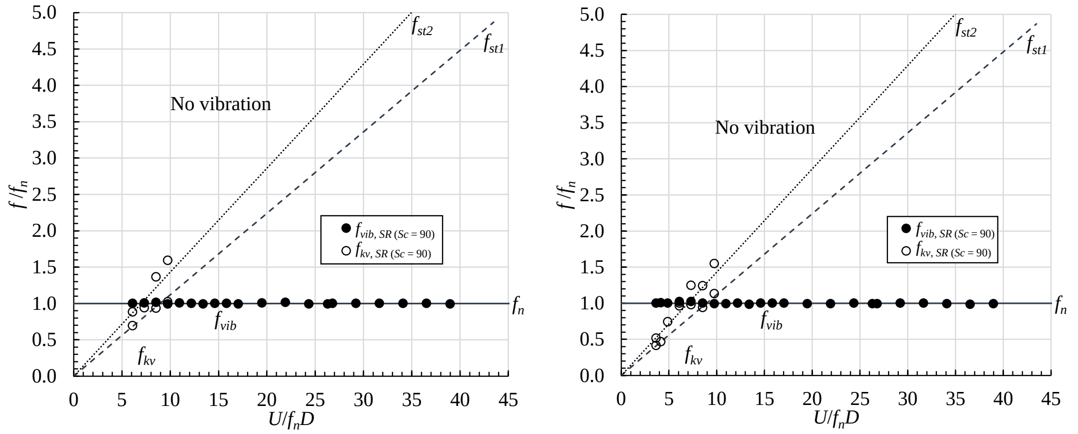

(a) (b)

Fig. G.31 Kármán vortex shedding frequency (circle) and vibrating frequency (filled circle) (dash slope line: stationary, circle and filled circle: vibrating) of SR section for $S_{c\eta}$ = 90 under (a) Without, and (b) With initial vibration conditions.

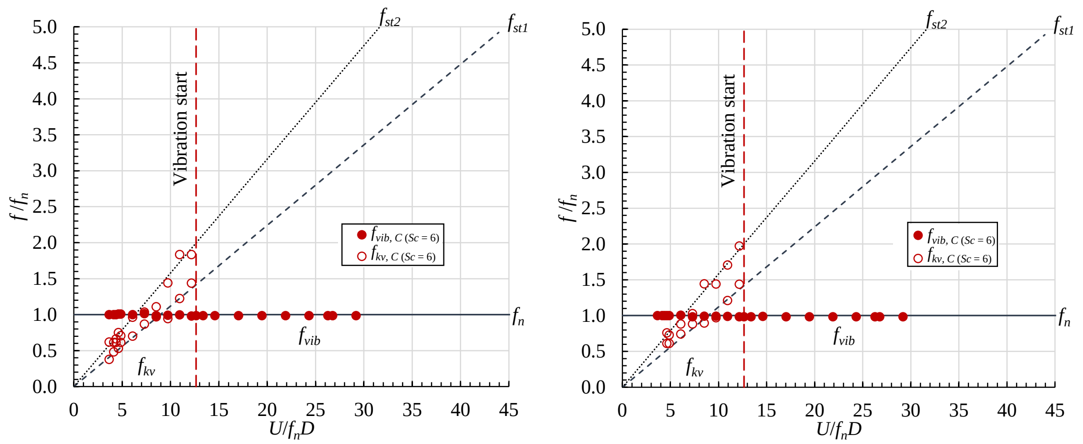

(a) (b)

Fig. G.32 Kármán vortex shedding frequency (circle) and vibrating frequency (filled circle) (dash slope line: stationary, circle and filled circle: vibrating) of C section for $S_{c\eta}$ = 6 under (a) Without, and (b) With initial vibration conditions.

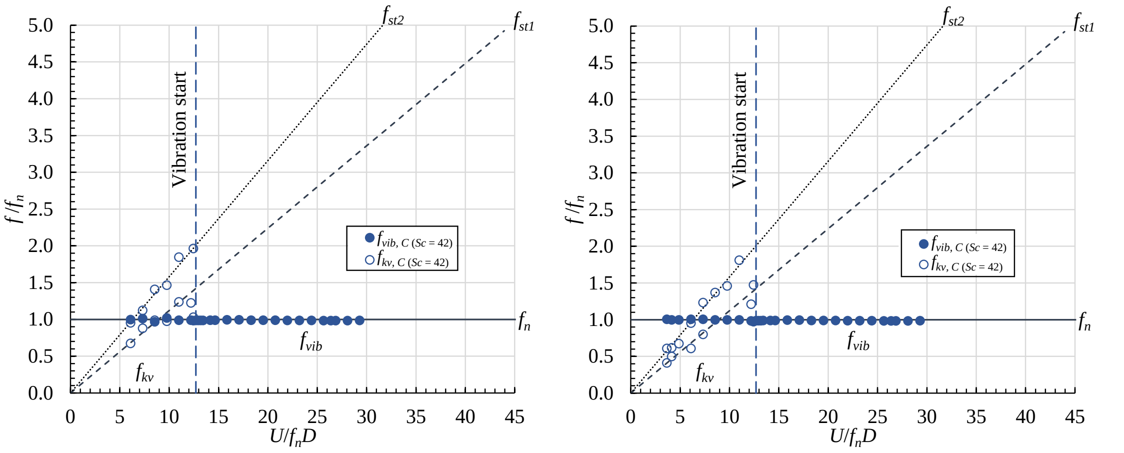

(a) (b)

Fig. G.33 Kármán vortex shedding frequency (circle) and vibrating frequency (filled circle) (dash slope line: stationary, circle and filled circle: vibrating) of C section for $S_{c\eta}$ = 42 under (a) Without, and (b) With initial vibration conditions.

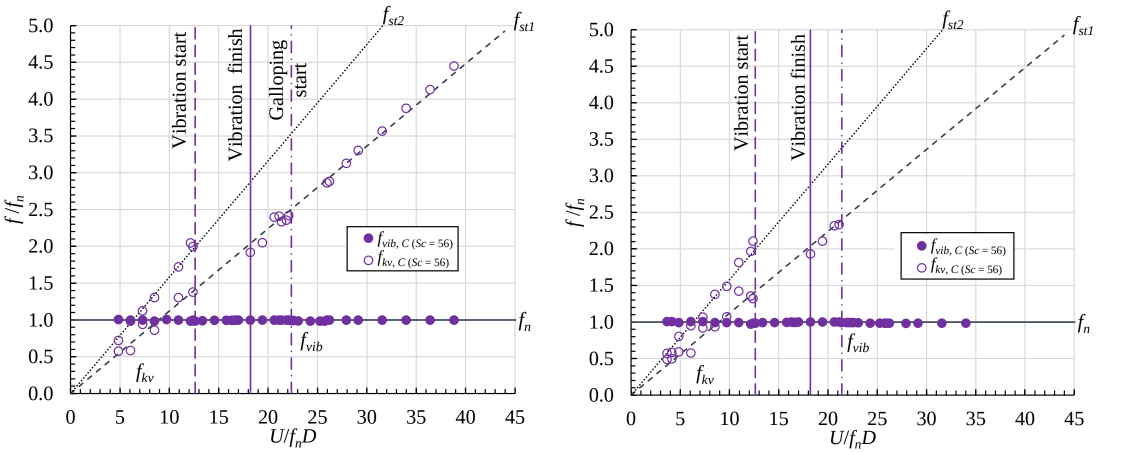

(a) (b)

Fig. G.34 Kármán vortex shedding frequency (circle) and vibrating frequency (filled circle) (dash slope line: stationary, circle and filled circle: vibrating) of C section for $S_{c\eta}$ = 56 under (a) Without, and (b) With initial vibration conditions.

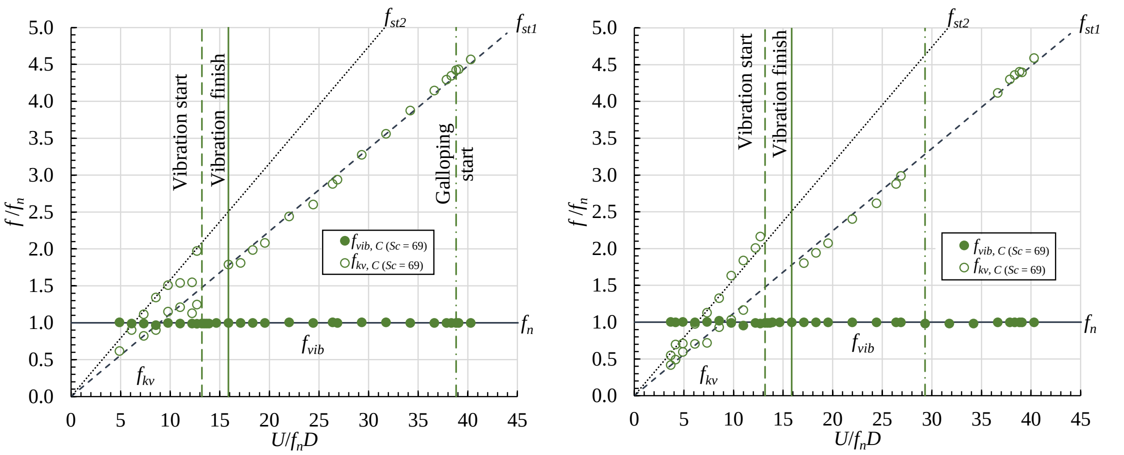

(a) (b)

Fig. G.35 Kármán vortex shedding frequency (circle) and vibrating frequency (filled circle) (dash slope line: stationary, circle and filled circle: vibrating) of C section for $S_{c\eta}$ = 69 under (a) Without, and (b) With initial vibration conditions.

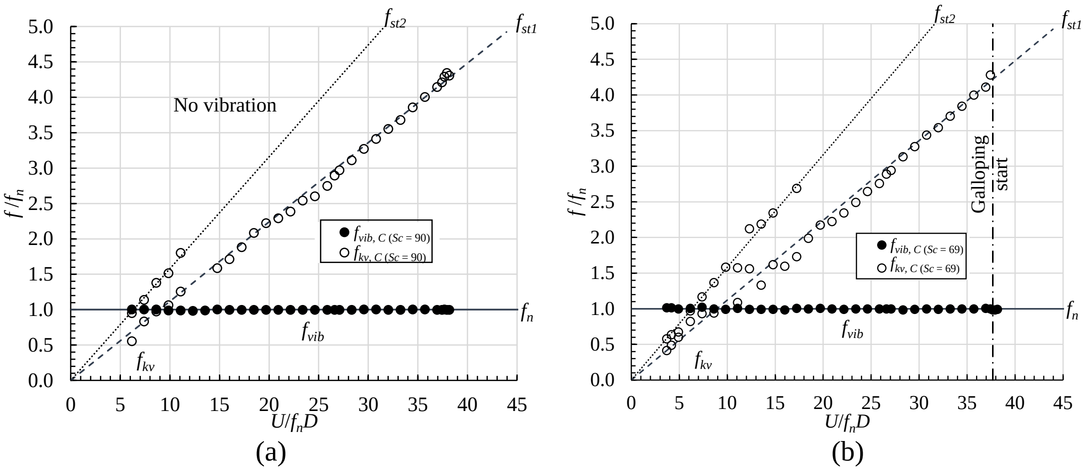

Fig. G.36 Kármán vortex shedding frequency (circle) and vibrating frequency (filled circle) (dash slope line: stationary, circle and filled circle: vibrating) of C section for $S_{c\eta}$ = 90 under (a) Without, and (b) With initial vibration conditions.

Appendix H

Kármán vortex shedding intensity (f_{kv}) and vibrating frequency (f_{vib}) of rectangular cylinder with corner modifications at various angles of attack

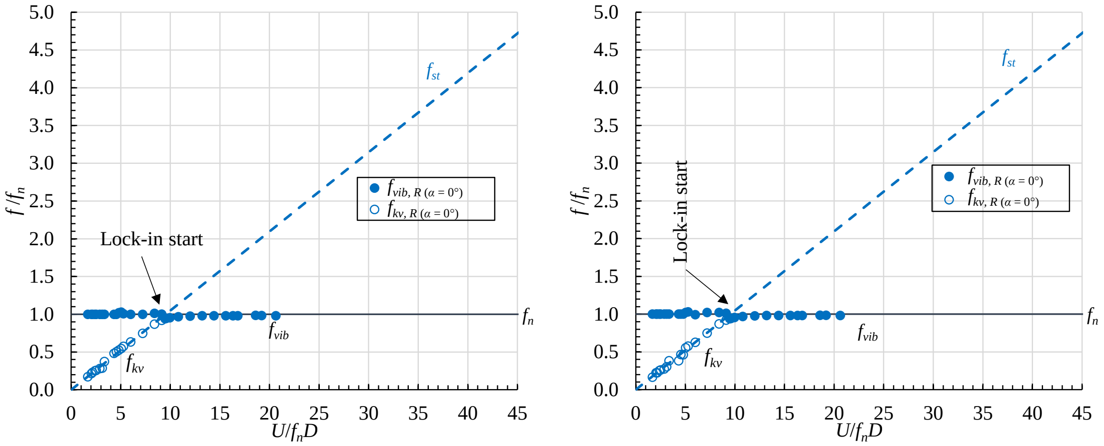

(a) (b)

Fig. H.1 Kármán vortex shedding frequency (circle) and vibrating frequency (filled circle) (dash slope line: stationary, circle and filled circle: vibrating) of R section under (a) Without, and (b) With initial vibration conditions at $S_{c\eta}$ = 6 for α = 0°.

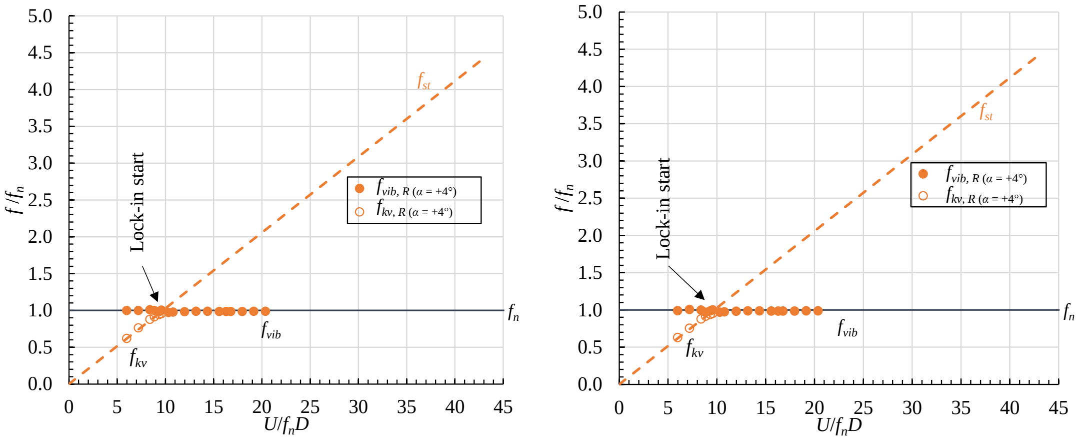

(a) (b)

Fig. H.2 Kármán vortex shedding frequency (circle) and vibrating frequency (filled circle) (dash slope line: stationary, circle and filled circle: vibrating) of R section under (a) Without, and (b) With initial vibration conditions at $S_{c\eta}$ = 6 for α = +4°.

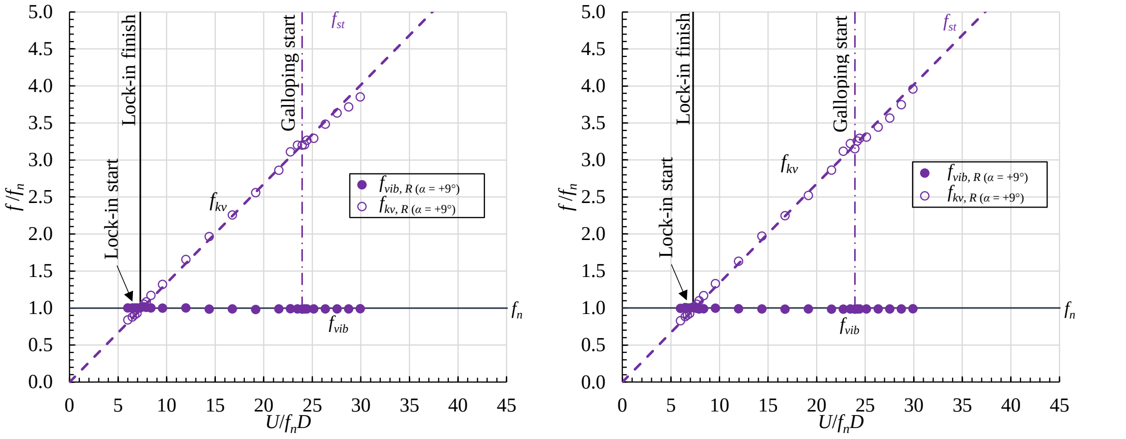

(a) (b)

Fig. H.3 Kármán vortex shedding frequency (circle) and vibrating frequency (filled circle) (dash slope line: stationary, circle and filled circle: vibrating) of R section under (a) Without, and (b) With initial vibration conditions at $S_{c\eta}$ = 6 for α = +9°.

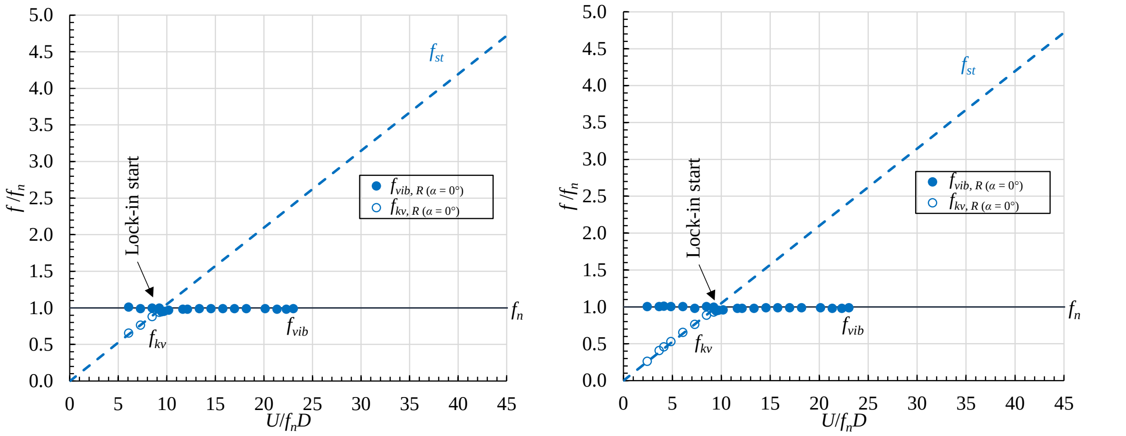

(a) (b)

Fig. H.4 Kármán vortex shedding frequency (circle) and vibrating frequency (filled circle) (dash slope line: stationary, circle and filled circle: vibrating) of R section under (a) Without, and (b) With initial vibration conditions at $S_{c\eta}$ = 42 for α = 0°.

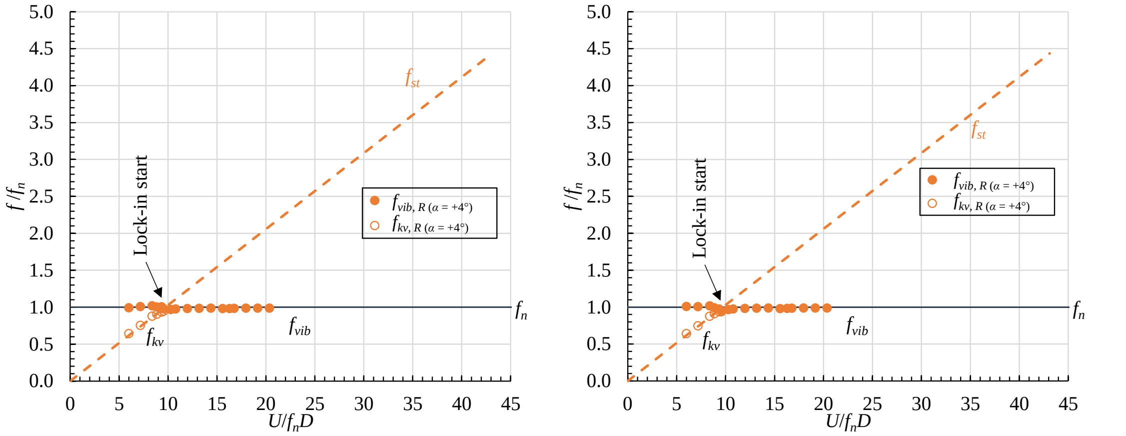

(a) (b)

Fig. H.5 Kármán vortex shedding frequency (circle) and vibrating frequency (filled circle) (dash slope line: stationary, circle and filled circle: vibrating) of R section under (a) Without, and (b) With initial vibration conditions at $S_{c\eta}$ = 42 for α = +4°.

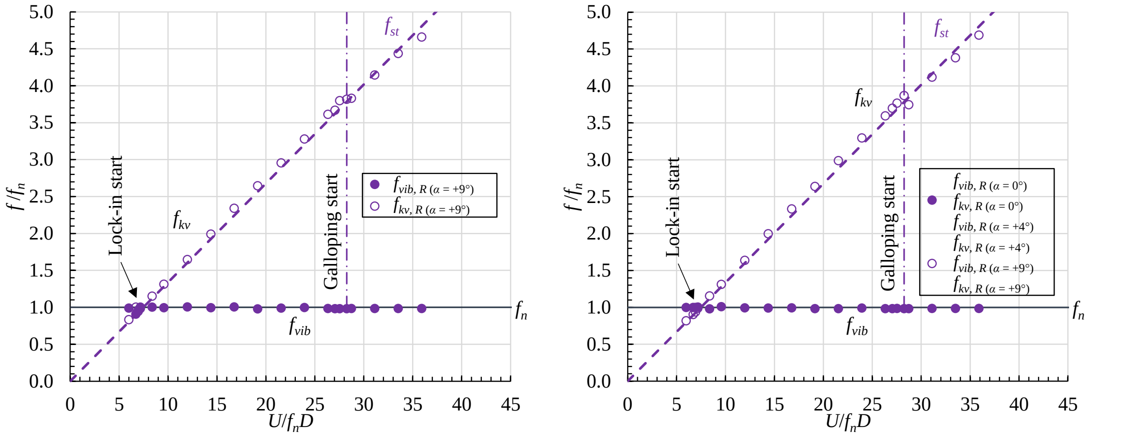

(a) (b)

Fig. H.6 Kármán vortex shedding frequency (circle) and vibrating frequency (filled circle) (dash slope line: stationary, circle and filled circle: vibrating) of R section under (a) Without, and (b) With initial vibration conditions at $S_{c\eta}$ = 42 for α = +9°.

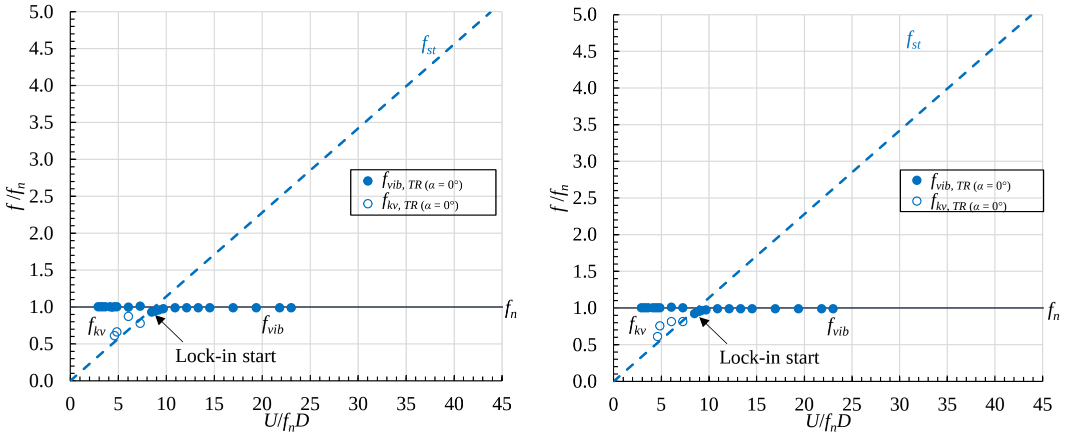

(a) (b)

Fig. H.7 Kármán vortex shedding frequency (circle) and vibrating frequency (filled circle) (dash slope line: stationary, circle and filled circle: vibrating) of TR section under (a) Without, and (b) With initial vibration conditions at $S_{c\eta}$ = 6 for α = 0°.

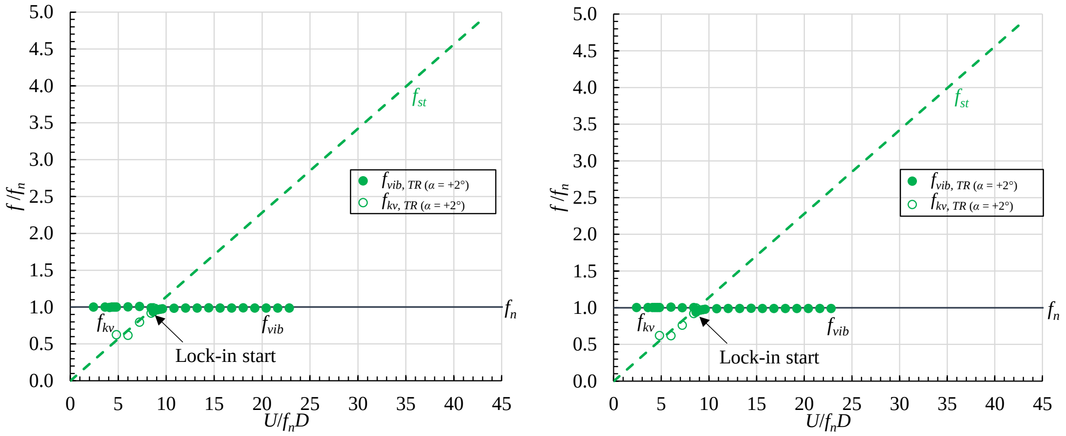

(a) (b)

Fig. H.8 Kármán vortex shedding frequency (circle) and vibrating frequency (filled circle) (dash slope line: stationary, circle and filled circle: vibrating) of TR section under (a) Without, and (b) With initial vibration conditions at $S_{c\eta}$ = 6 for α = +2°.

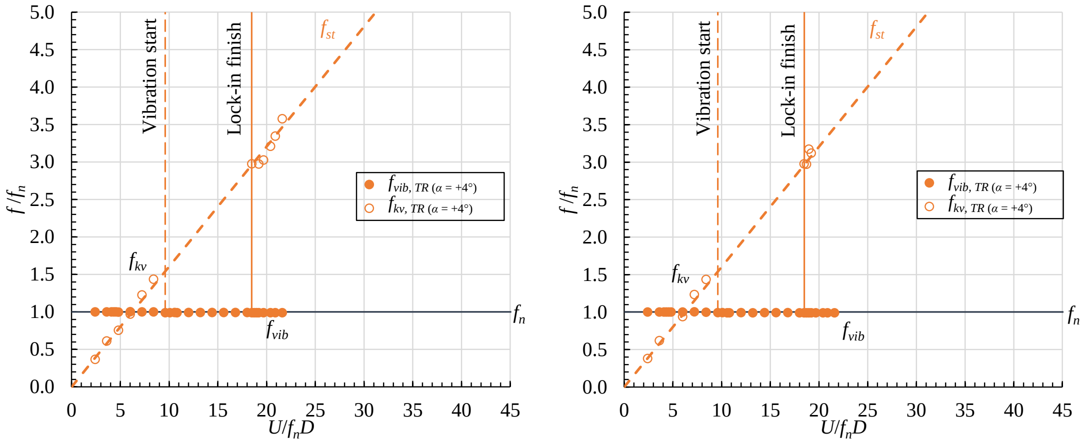

(a) (b)

Fig. H.9 Kármán vortex shedding frequency (circle) and vibrating frequency (filled circle) (dash slope line: stationary, circle and filled circle: vibrating) of TR section under (a) Without, and (b) With initial vibration conditions at $S_{c\eta}$ = 6 for α = +4°.

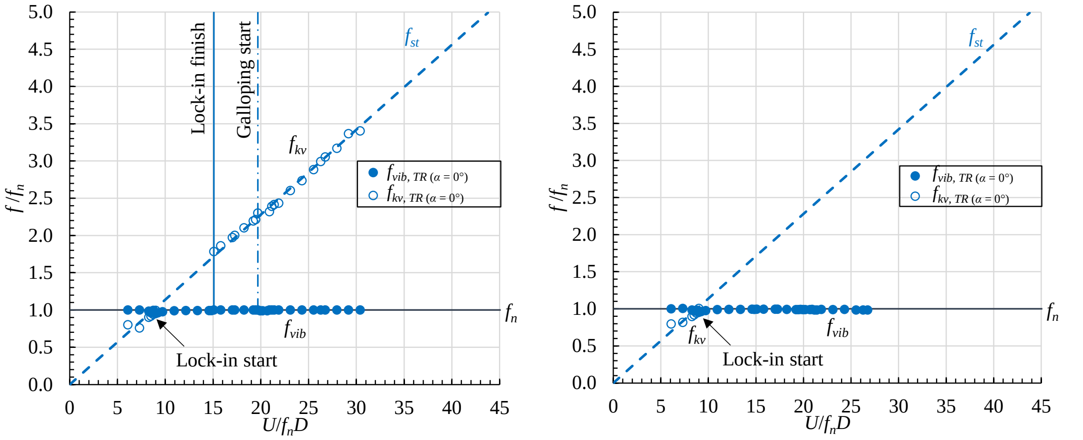

(a) (b)

Fig. H.10 Kármán vortex shedding frequency (circle) and vibrating frequency (filled circle) (dash slope line: stationary, circle and filled circle: vibrating) of TR section under (a) Without, and (b) With initial vibration conditions at $S_{c\eta}$ = 42 for α = 0°.

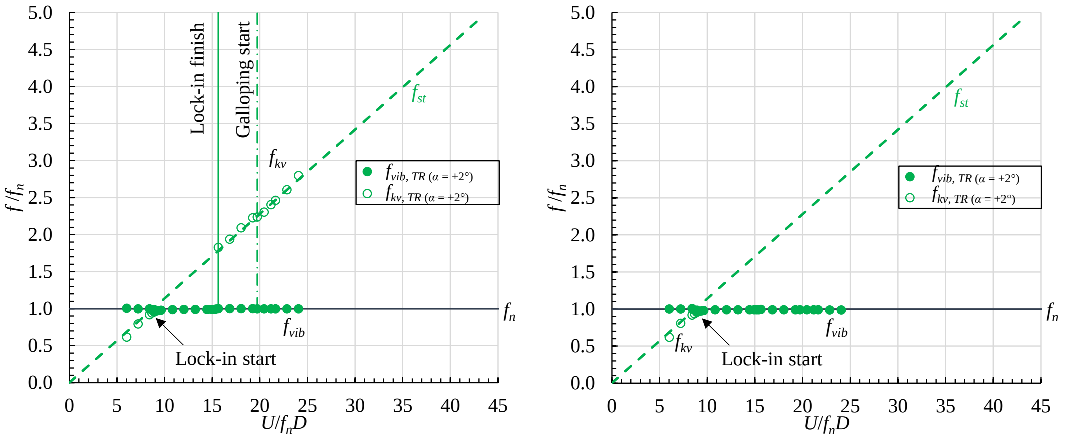

(a) (b)

Fig. H.11 Kármán vortex shedding frequency (circle) and vibrating frequency (filled circle) (dash slope line: stationary, circle and filled circle: vibrating) of TR section under (a) Without, and (b) With initial vibration conditions at $S_{c\eta}$ = 42 for α = +2°.

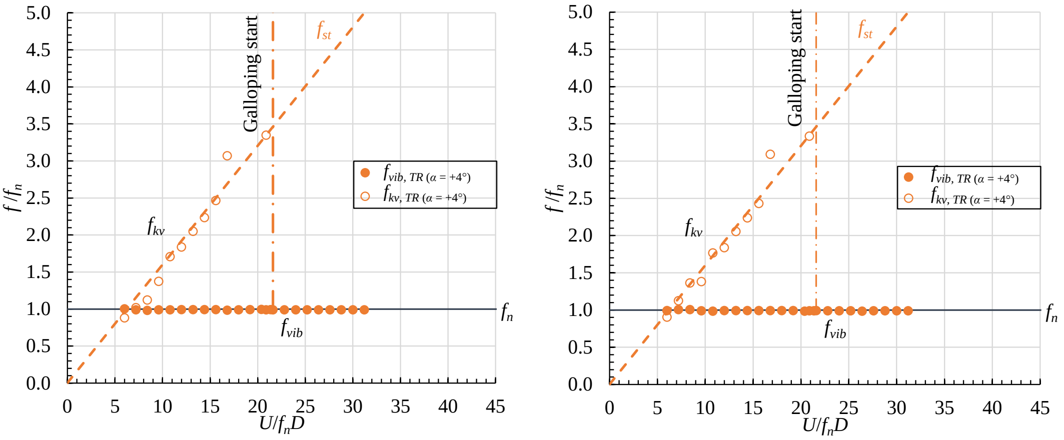

(a) (b)

Fig. H.12 Kármán vortex shedding frequency (circle) and vibrating frequency (filled circle) (dash slope line: stationary, circle and filled circle: vibrating) of TR section under (a) Without, and (b) With initial vibration conditions at $S_{c\eta}$ = 42 for α = +4°.

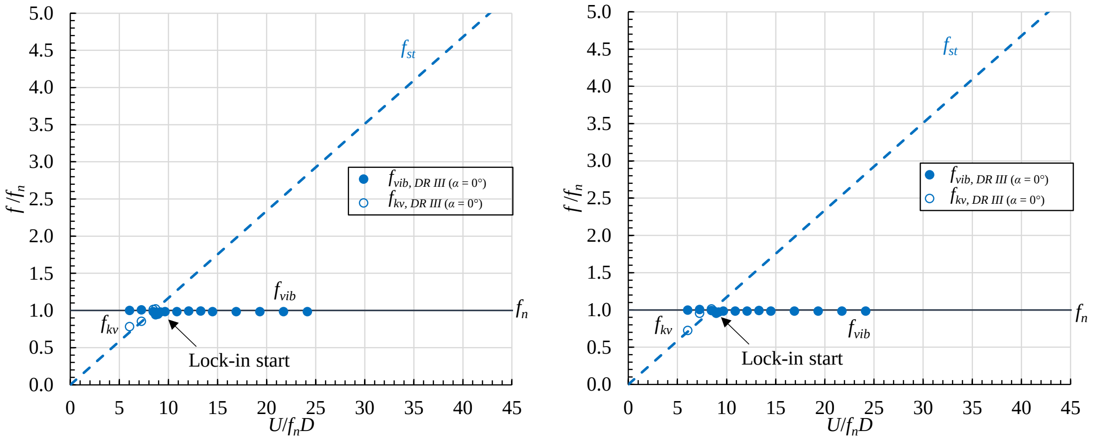

(a) (b)

Fig. H.13 Kármán vortex shedding frequency (circle) and vibrating frequency (filled circle) (dash slope line: stationary, circle and filled circle: vibrating) of DR III section under (a) Without, and (b) With initial vibration conditions at $S_{c\eta}$ = 6 for α = 0°.

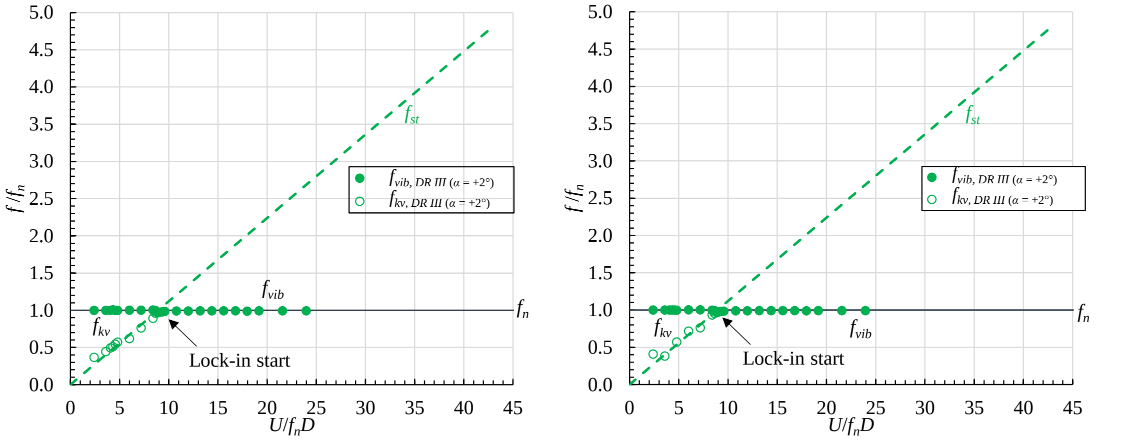

(a) (b)

Fig. H.14 Kármán vortex shedding frequency (circle) and vibrating frequency (filled circle) (dash slope line: stationary, circle and filled circle: vibrating) of DR III section under (a) Without, and (b) With initial vibration conditions at $S_{c\eta}$ = 6 for α = +2°.

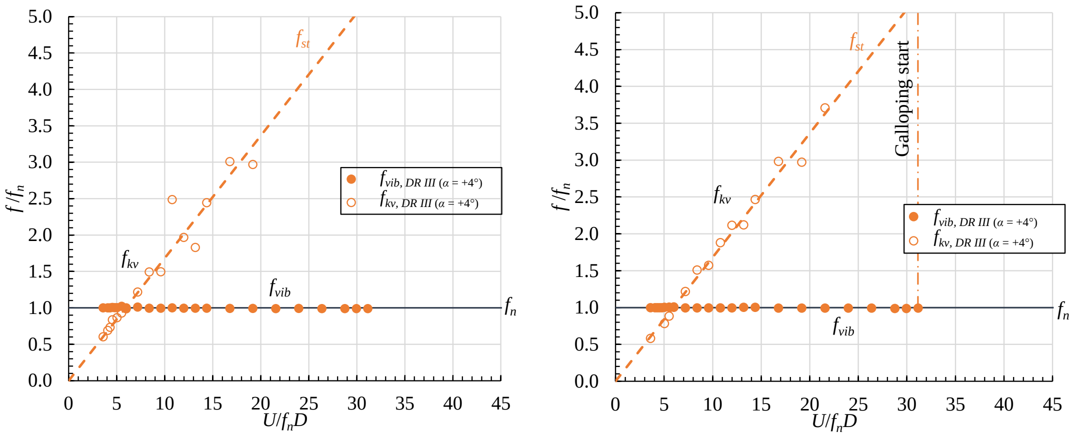

(a) (b)

Fig. H.15 Kármán vortex shedding frequency (circle) and vibrating frequency (filled circle) (dash slope line: stationary, circle and filled circle: vibrating) of DR III section under (a) Without, and (b) With initial vibration conditions at $S_{c\eta}$ = 6 for α = +4°.

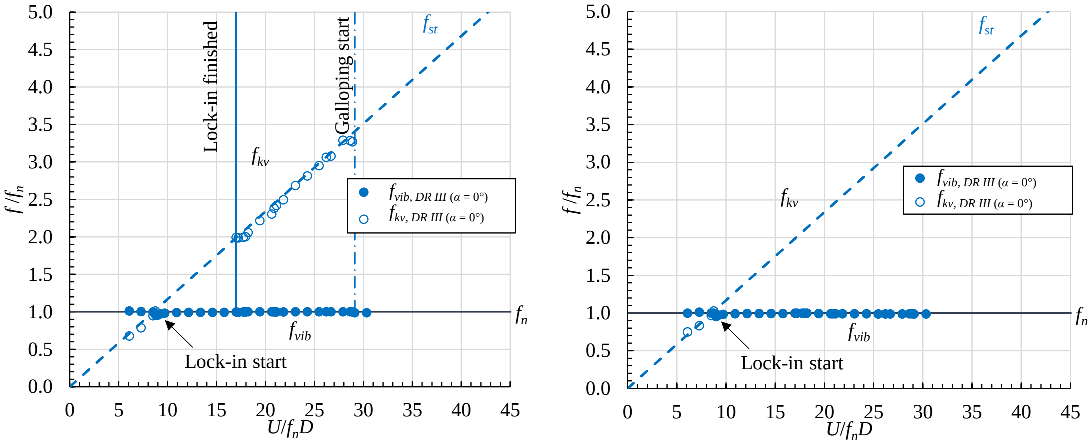

(a) (b)

Fig. H.16 Kármán vortex shedding frequency (circle) and vibrating frequency (filled circle) (dash slope line: stationary, circle and filled circle: vibrating) of DR III section under (a) Without, and (b) With initial vibration conditions at $S_{c\eta}$ = 42 for α = 0°.

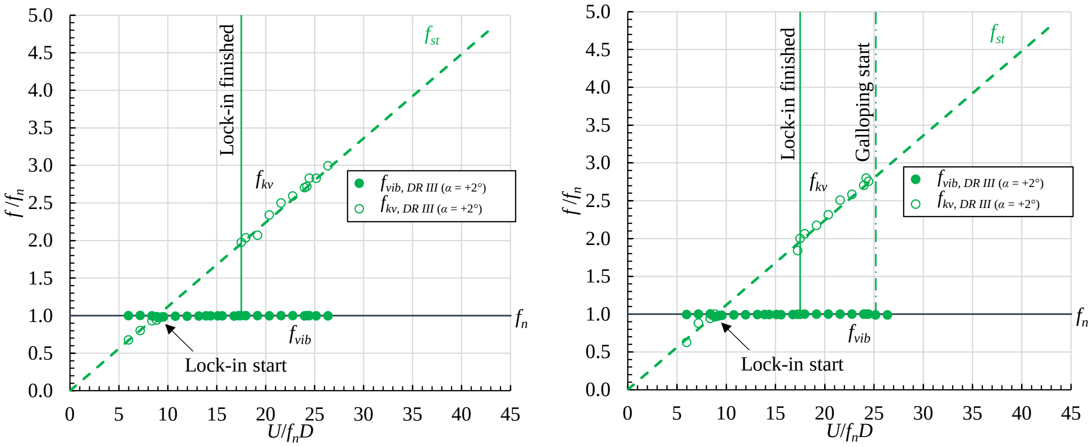

(a) (b)

Fig. H.17 Kármán vortex shedding frequency (circle) and vibrating frequency (filled circle) (dash slope line: stationary, circle and filled circle: vibrating) of DR III section under (a) Without, and (b) With initial vibration conditions at $S_{c\eta}$ = 42 for α = +2°.

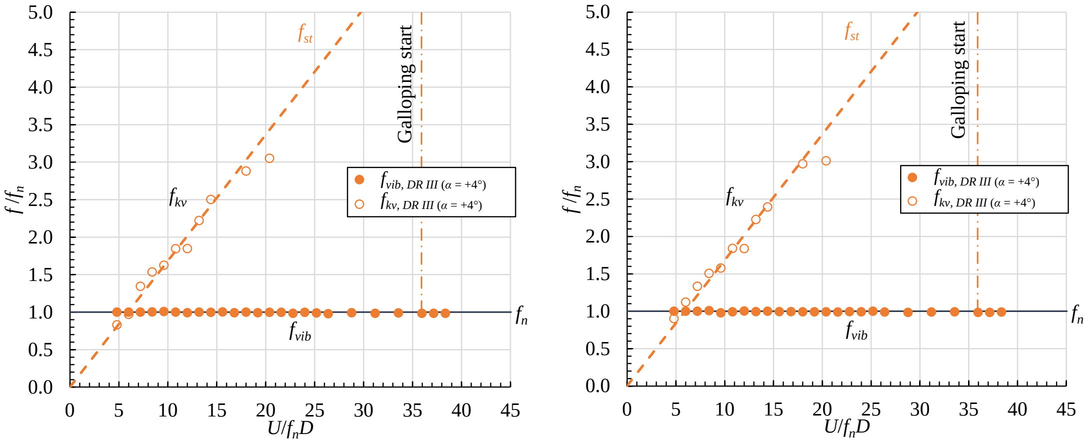

(a) (b)

Fig. H.18 Kármán vortex shedding frequency (circle) and vibrating frequency (filled circle) (dash slope line: stationary, circle and filled circle: vibrating) of DR III section under (a) Without, and (b) With initial vibration conditions at $S_{c\eta}$ = 42 for α = +4°.

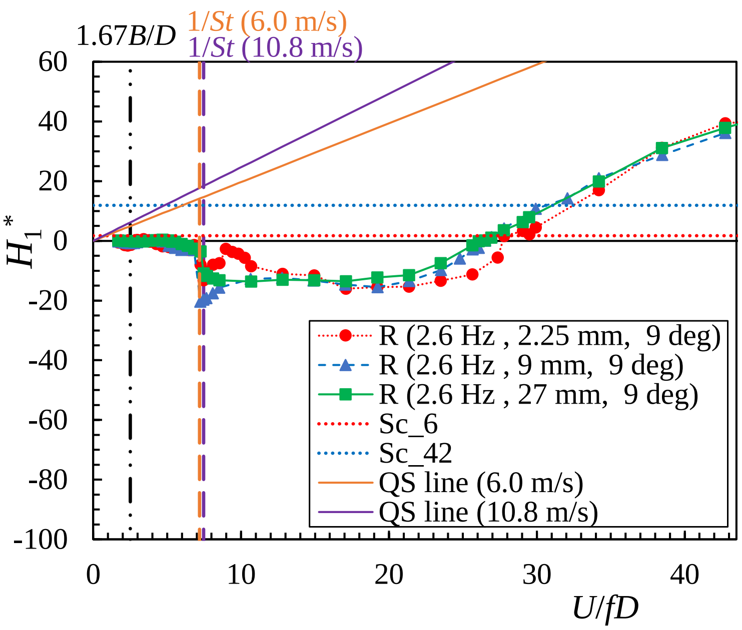

Fig. H.19 Aerodynamic damping H_1^* of R section obtained from forced vibration test (marker) for the forced vibrating double amplitudes ($2\eta_0$) of 0.025D, 0.1D, and 0.3D, H_1^* calculated based on quasi-steady theory from 5% increased $dC_{Fy}/d\alpha$ (inclined solid line), and Scruton number (dot line) at α = +9°.

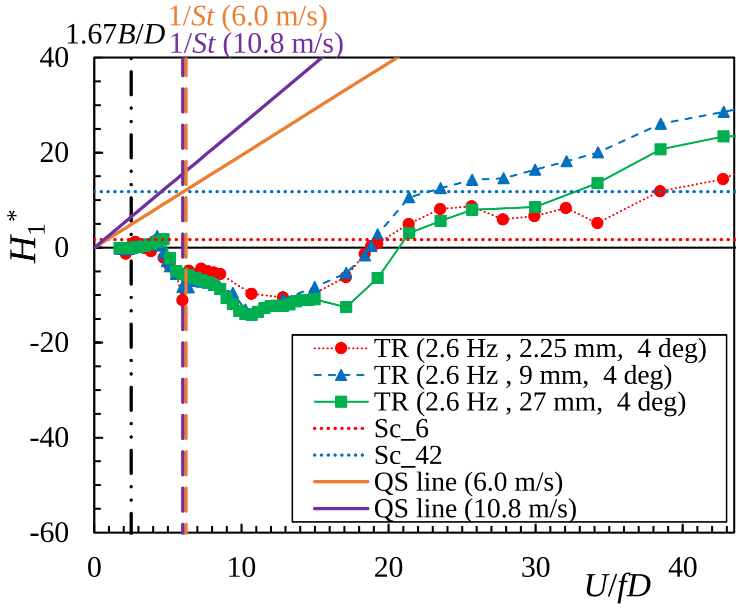

Fig. H.20 Aerodynamic damping H_1^* of TR section obtained from forced vibration test (marker) for the forced vibrating double amplitudes ($2\eta_0$) of 0.025D, 0.1D, and 0.3D, H_1^* calculated based on quasi-steady theory from 5% increased $dC_{Fy}/d\alpha$ (inclined solid line), and Scruton number (dot line) at α = +4°.

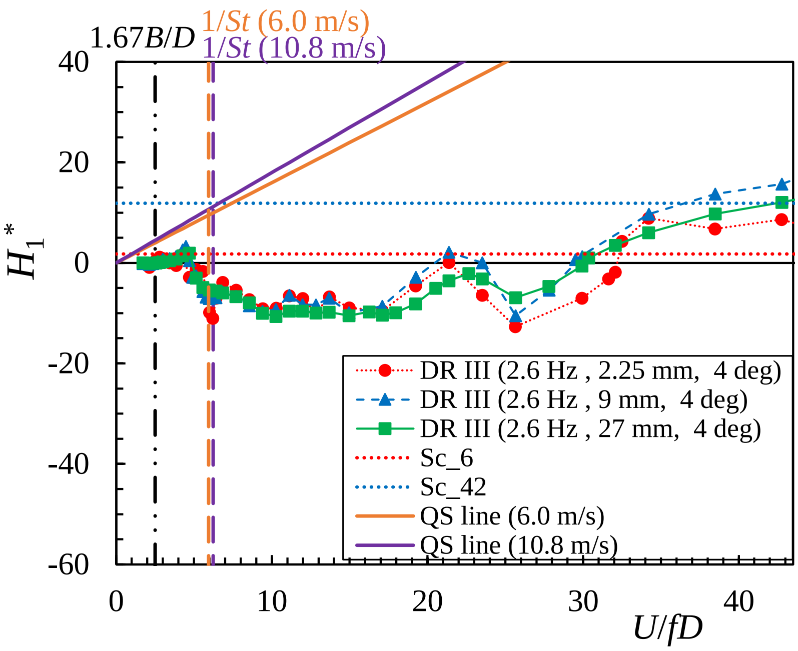

Fig. H.21 Aerodynamic damping H_1^* of DR III section obtained from forced vibration test (marker) for the forced vibrating double amplitudes ($2\eta_0$) of 0.025D, 0.1D, and 0.3D, H_1^* calculated based on quasi-steady theory from 5% increased $dC_{Fy}/d\alpha$ (inclined solid line), and Scruton number (dot line) at α = +4°.

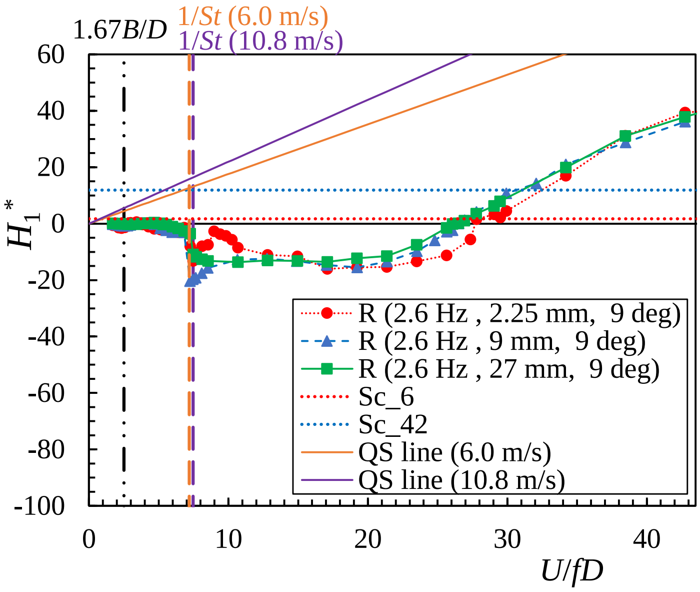

Fig. H.22 Aerodynamic damping H_1^* of R section obtained from forced vibration test (marker) for the forced vibrating double amplitudes ($2\eta_0$) of 0.025D, 0.1D, and 0.3D, H_1^* calculated based on quasi-steady theory from 5% decreased $dC_{Fy}/d\alpha$ (inclined solid line), and Scruton number (dot line) at α = +9°.

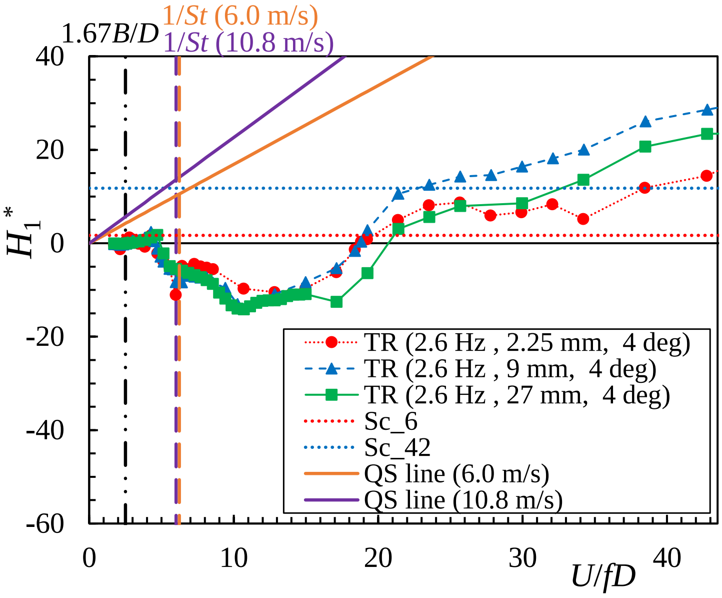

Fig. H.23 Aerodynamic damping H_1^* of TR section obtained from forced vibration test (marker) for the forced vibrating double amplitudes ($2\eta_0$) of 0.025D, 0.1D, and 0.3D, H_1^* calculated based on quasi-steady theory from 5% decreased $dC_{Fy}/d\alpha$ (inclined solid line), and Scruton number (dot line) at α = +4°.

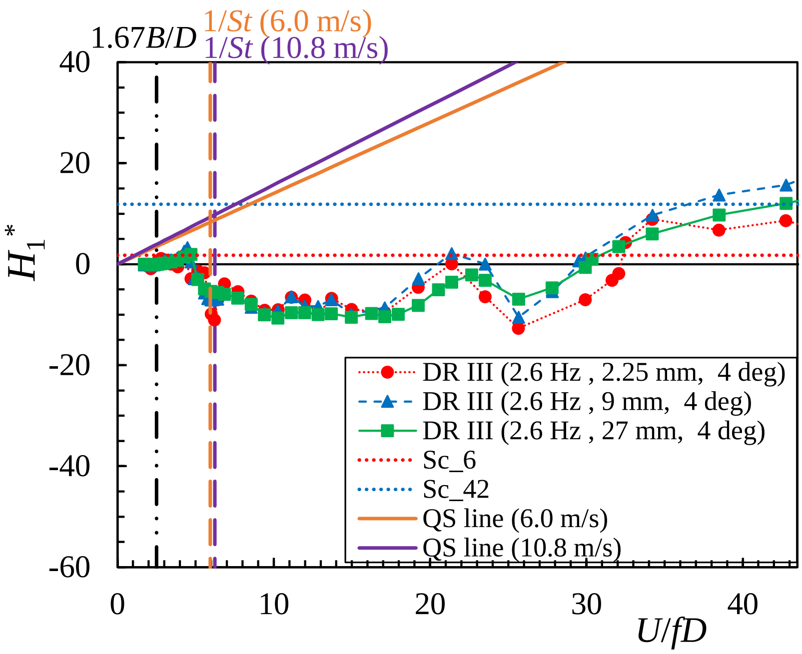

Fig. H.24 Aerodynamic damping H_1^* of DR III section obtained from forced vibration test (marker) for the forced vibrating double amplitudes ($2\eta_0$) of 0.025*D*, 0.1*D*, and 0.3*D*, H_1^* calculated based on quasi-steady theory from 5% decreased $dC_{Fy}/d\alpha$ (inclined solid line), and Scruton number (dot line) at α = +4°.

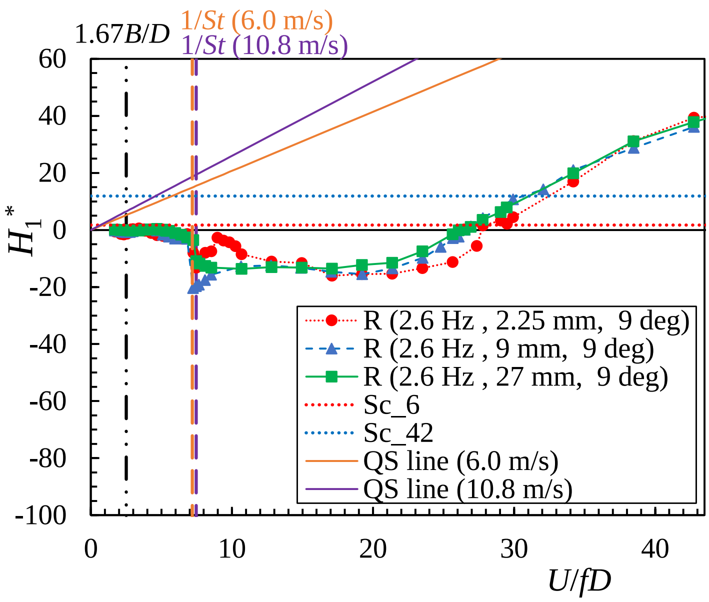

Fig. H.25 Aerodynamic damping H_1^* of R section obtained from forced vibration test (marker) for the forced vibrating double amplitudes ($2\eta_0$) of 0.025*D*, 0.1*D*, and 0.3*D*, H_1^* calculated based on quasi-steady theory from 10% increased $dC_{Fy}/d\alpha$ (inclined solid line), and Scruton number (dot line) at α = +9°.

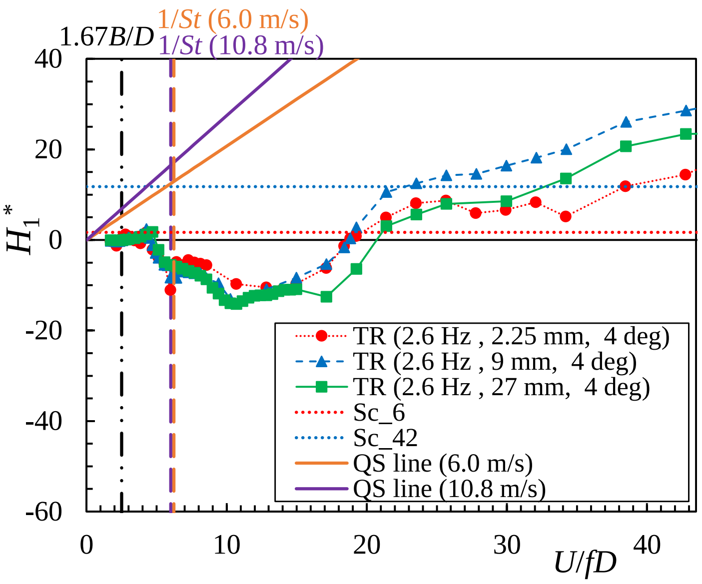

Fig. H.26 Aerodynamic damping H_1^* of TR section obtained from forced vibration test (marker) for the forced vibrating double amplitudes ($2\eta_0$) of 0.025D, 0.1D, and 0.3D, H_1^* calculated based on quasi-steady theory from 10% increased $dC_{Fy}/d\alpha$ (inclined solid line), and Scruton number (dot line) at α = +4°.

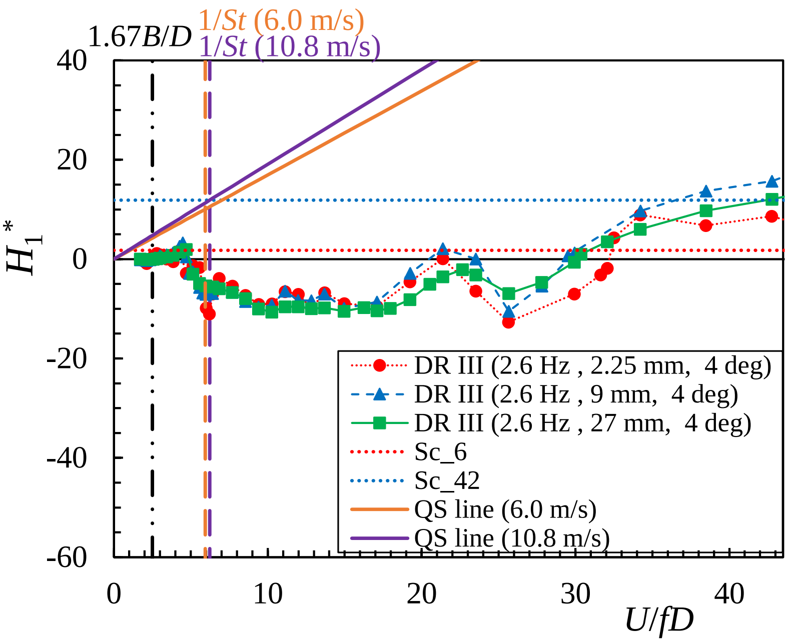

Fig. H.27 Aerodynamic damping H_1^* of DR III section obtained from forced vibration test (marker) for the forced vibrating double amplitudes ($2\eta_0$) of 0.025D, 0.1D, and 0.3D, H_1^* calculated based on quasi-steady theory from 10% increased $dC_{Fy}/d\alpha$ (inclined solid line), and Scruton number (dot line) at α = +4°.

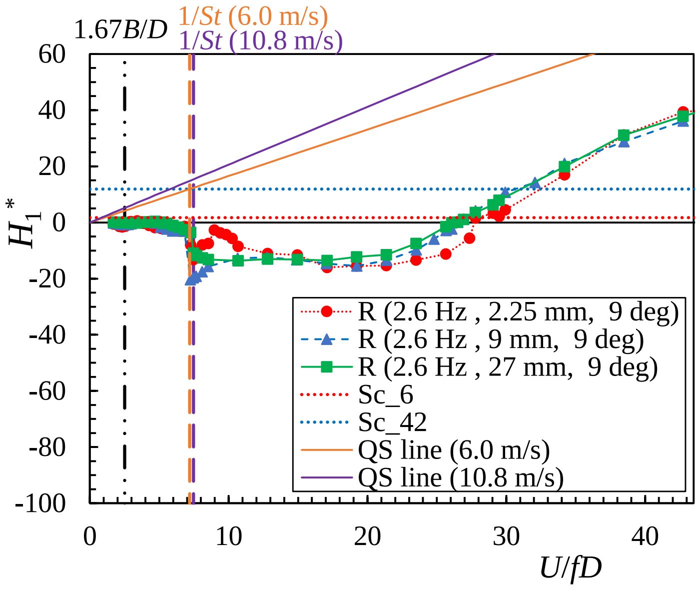

Fig. H.28 Aerodynamic damping H_1^* of R section obtained from forced vibration test (marker) for the forced vibrating double amplitudes ($2\eta_0$) of 0.025D, 0.1D, and 0.3D, H_1^* calculated based on quasi-steady theory from 10% decreased $dC_{Fy}/d\alpha$ (inclined solid line), and Scruton number (dot line) at α = +9°.

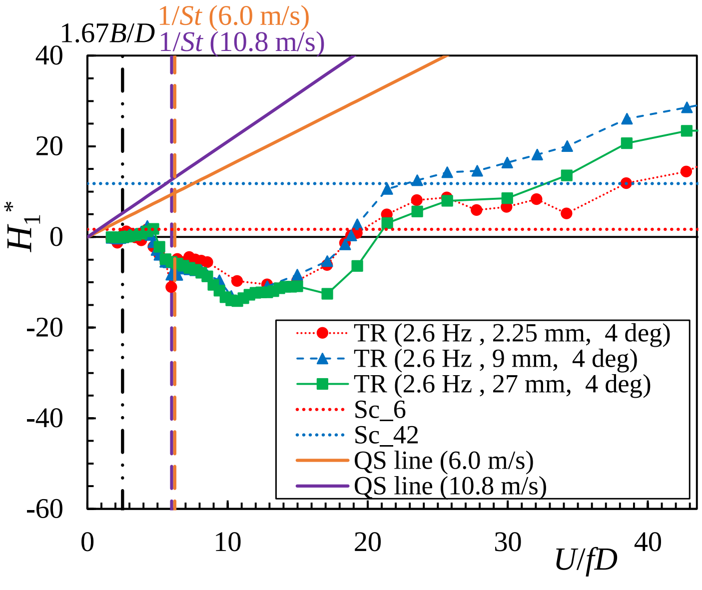

Fig. H.29 Aerodynamic damping H_1^* of TR section obtained from forced vibration test (marker) for the forced vibrating double amplitudes ($2\eta_0$) of 0.025D, 0.1D, and 0.3D, H_1^* calculated based on quasi-steady theory from 10% decreased $dC_{Fy}/d\alpha$ (inclined solid line), and Scruton number (dot line) at α = +4°.

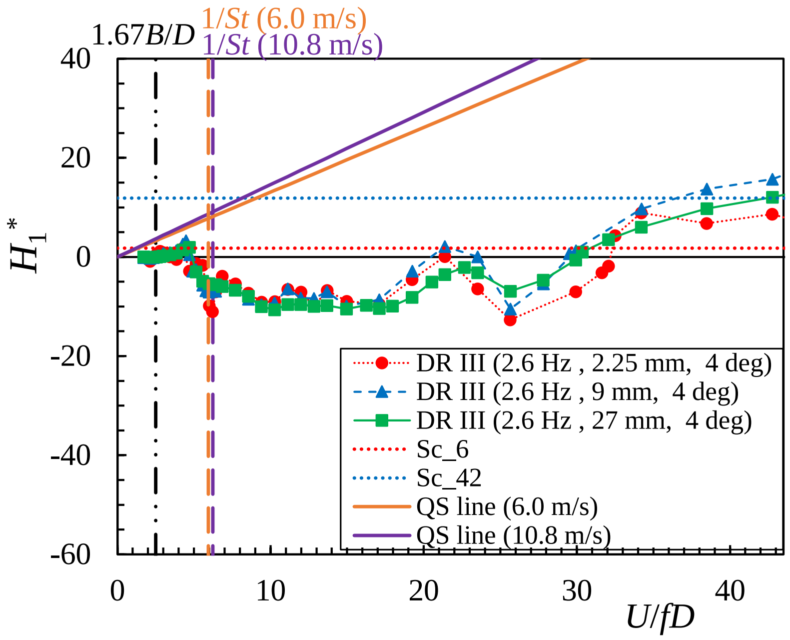

Fig. H.30 Aerodynamic damping H_1^* of DR III section obtained from forced vibration test (marker) for the forced vibrating double amplitudes ($2\eta_0$) of 0.025D, 0.1D, and 0.3D, H_1^* calculated based on quasi-steady theory from 10% decreased $dC_{Fy}/d\alpha$ (inclined solid line), and Scruton number (dot line) at α = +4°.